

This is an informal report intended for use as a preliminary or working document

# GEND

General Public Utilities • Electric Power Research Institute • U.S. Nuclear Regulatory Commission • U.S. Department of Energy

## TMI-2 CORE BORE EXAMINATIONS VOLUME 2 - APPENDICES

~~6-29-95~~  
7-29-96

Douglas W. Akers  
Charles S. Olsen  
Bruce A. Pregger

Malcolm L. Russell  
Richard K. McCardell

LOAN COPY

THIS REPORT MAY BE RECALLED  
AFTER TWO WEEKS. PLEASE  
RETURN PROMPTLY TO:

INEL TECHNICAL LIBRARY

Prepared for the  
U.S. Department of Energy  
Three Mile Island Operations Office  
Under Contract No. DE-AC07-76ID01570

## DISCLAIMER

This book was prepared as an account of work sponsored by an agency of the United States Government. Neither the United States Government nor any agency thereof, nor any of their employees, makes any warranty, express or implied, or assumes any legal liability or responsibility for the accuracy, completeness, or usefulness of any information, apparatus, product or process disclosed, or represents that its use would not infringe privately owned rights. References herein to any specific commercial product, process, or service by trade name, trademark, manufacturer, or otherwise, does not necessarily constitute or imply its endorsement, recommendation, or favoring by the United States Government or any agency thereof. The views and opinions of authors expressed herein do not necessarily state or reflect those of the United States Government or any agency thereof.

GEND- INF-092

**TMI-2 CORE BORE EXAMINATIONS  
VOLUME 2 -- APPENDICES**

**Douglas W. Akers  
Charles S. Olsen  
Malcolm L. Russell  
Richard K. McCardell  
Bruce A. Pregger**

**Published January 1990**

**EG&G Idaho, Inc.  
Idaho Falls, Idaho 83415**

**Prepared for the  
U.S. Department of Energy  
Idaho Operations Office  
Under DOE Contract No. DE-AC07-76ID01570**



## CONTENTS

APPENDIX A--TMI-2 LOWER CORE REGION SAMPLE SELECTION .....	A-1
APPENDIX B--SAMPLE PREPARATION AND EXAMINATION METHODS .....	B-1
APPENDIX C--VISUAL EXAMINATIONS .....	C-1
APPENDIX D--DENSITY AND POROSITY DATA .....	D-1
APPENDIX E--OPTICAL METALLOGRAPHY AND SEM DATA .....	E-1
APPENDIX F--BETA-GAMMA AUTORADIOGRAPHY DATA .....	F-1
APPENDIX G--ELEMENTAL ANALYSIS RESULTS .....	G-1
APPENDIX H--RADIOCHEMICAL EXAMINATION RESULTS .....	H-1
APPENDIX I--DATA QUALIFICATION .....	I-1
APPENDIX J--QUANTITATIVE WDS ANALYSIS .....	J-1



**APPENDIX A**

**TMI-2 LOWER CORE REGION SAMPLE SELECTION**





## APPENDIX A

### TMI-2 LOWER CORE REGION SAMPLE SELECTION

The TMI-2 lower core region samples include samples from both the 32,700 kg (estimated) consolidated region and the fuel assemblies (rod bundles) that retained their original geometry below the consolidated region. The material was collected on three occasions during the defueling program as follows:

- 5 core boring in July 1986 after removal of the loose debris between the cavity at the top of the core and the consolidated region<sup>a</sup>
- By defueling tooling in December 1986 after the consolidated region had been pulverized by drilling 409 holes in an overlapping pattern with a solid-faced bit
- By defueling tooling in late January 1987 after removal of most of the pulverized core material that remained in the core region above the rod bundle geometry after the overlapping hole drilling. Only 25% (8100 kg) of the pulverized core material was retrieved from the consolidated region after the drilling. The remainder is assumed to have relocated to the rod bundles and the reactor vessel lower plenum.

The total collection of material from the lower core region weighed approximately 187 kg and was composed of the following:

---

a. E. L. Tolman et al., TMI-2 Core Bore Acquisition Summary Report, EGG-TMI-7385, Revision 1, February 1987.

<u>Collection Date</u>	<u>Sample Mass (kg)</u>	<u>Sample Description</u>
July 1986 (core bores)	130	Cores, rocks, and fragments from the consolidated region, rod bundle rods and tubes from below the consolidated region and one lower end fitting core from 10 core positions as identified in Table A-1.
December 1986	53	Rocks and fragments from the consolidated region at core positions F6, H8, and M11.
Late January 1987	4	Rocks and fragments from the consolidated region at core positions H9 and K9.

Table A-2 contains the list of samples that were selected and/or evolved from the 187 kg of material from the consolidated and lower rod bundle regions of the core.

All eight cores of consolidated material were subdivided by one of the two sectioning schemes shown in Figure A-1. The specific sectioning diagrams are shown in Appendix E.

The rock-size samples were selected on the basis of size (> 2.5 cm in one dimension), distinctive feature, and/or density. A large (24 kg) rock of consolidated region material from the December 1986 sample collection near core position M11 was returned to storage in TMI-2 fuel canister D-174 because it was too large to handle with the existing sample examination tooling. The initial selection of rock samples was based on size and distinctive feature. After photographing and measurement of density, a final selection of rocks for examination at the INEL was made. The final selection emphasized selection of rocks with midrange and extremes of density to investigate the reasons for the range (9.7 to 5.4 g/cm<sup>3</sup>) and apparent stratification of density in the consolidated region.



TABLE A-2. TMI-2 LOWER CORE REGION SAMPLE LIST

Sample No. <sup>b</sup>	Sample Description			Remarks
	Type	Mass (g)	Density (g/cm <sup>3</sup> )	
<u>6 cm Dia Cores:</u>				
D08-P1:	Lower Crust	632	7.05	Subdivided
D08-P1-A		--	--	CSNI-KFK
D08-P1-B		--	--	ANL-E
D08-P1-C		--	--	INEL (Chem)
D08-P1-D		--	--	INEL (Met)
D08-P1-E		--	--	CSNI-France
D08-P1-F		--	--	CSNI-Canada
D08-P2:	Side Crust	494	7.59	Subdivided
D08-P2-A1		--	--	INEL (Chem)
D08-P2-A2		--	--	INEL (Met)
D08-P2-A3		--	--	
D08-P2-B		--	--	CSNI-JRC
D08-P2-C		--	--	Japan
D08-P2-D		--	--	Japan
D08-P2-E		--	--	Korea
D08-P3:	Upper Crust	746	9.74	Subdivided
D08-P3-A1		--	--	CSNI-JRC
D08-P3-A2		--	--	Japan
D08-P3-A3		--	--	Japan
D08-P3-A4		--	--	Japan
D08-P3-A5		--	--	
D08-P3-B		--	--	CSNI-UK
D08-P3-C		--	--	CSNI-Sweden
D08-P3-D1		--	--	INEL (Chem)
D08-P3-D2		--	--	INEL (Met)
D08-P3-D3		--	--	Japan
D08-P3-D4		--	--	Japan
D08-P3-E		--	--	Japan
G08-P11:	Upper Crust	1847	8.24	Subdivided
G08-P11-A		--	--	
G08-P11-B		--	--	INEL (Chem)
G08-P11-C		--	--	INEL (Met)
G08-P11-D		--	--	Japan
G08-P11-E		--	--	INEL (Chem)
G08-P11-F		--	--	INEL (Met)
G08-P11-G		--	--	Japan
G08-P11-H		--	--	CSNI-Switzerland
G08-P11-I		--	--	INEL (Met)
G08-P11-J		--	--	
G08-P11-K		--	--	Japan

TABLE A-2. (Continued)

Sample No. <sup>b</sup>	Sample Description			Remarks
	Type	Mass (g)	Density (g/cm <sup>3</sup> )	
<u>6 cm Dia Cores (continued)</u>				
G12-P1:	Ceramic	513	7.57	Subdivided
G12-P1-A		--	--	ANL-E
G12-P1-B		--	--	CSNI-KFK
G12-P1-C1		--	--	CSNI-UK
G12-P1-C2		--	--	CSNI-Sweden
G12-P1-D1		--	--	CSNI-France
G12-P1-D2		--	--	INEL (Chem)
G12-P1-D3		--	--	INEL (Met)
G12-P1-D4		--	--	Japan
G12-P1-D5		--	--	CSNI-Canada
G12-P1-E		--	--	INEL (Chem)/Japan
K09-P1:	Lower Crust	1303	7.21	Subdivided
K09-P1-A		--	--	
K09-P1-B		--	--	CSNI-UK
K09-P1-C		--	--	INEL (Chem)/Korea
K09-P1-D		--	--	INEL (Met)
K09-P1-E		--	--	ANL-E
K09-P1-F		--	--	CSNI-KFK
K09-P1-G		--	--	INEL (Met)
K09-P1-H		--	--	CSNI-Canada
K09-P2:	Upper Crust	913	7.87	Subdivided
K09-P2-A		--	--	CSNI-KFK
K09-P2-B		--	--	CSNI-UK
K09-P2-C1		--	--	
K09-P2-C2		--	--	INEL (Chem)/Korea
K09-P2-D		--	--	INEL (Met)
K09-P2-E		--	--	ANL-E
K09-P2-F		--	--	CSNI-Switzerland
007-P4:	Side or Upper Crust	728	8.78	Subdivided
007-P4-A		--	--	Japan
07-P4-B		--	--	CSNI-KFK
007-P4-C1		--	--	
007-P4-C2		--	--	INEL (Chem)
007-P4-D		--	--	INEL (Met)
007-P4-E		--	--	CSNI-JRC
007-P4-F		--	--	Japan

TABLE A-2. (Continued)

Sample No. <sup>b</sup>	Sample Description			Remarks
	Type	Mass (g)	Density (g/cm <sup>3</sup> )	
<u>Core Bore Rocks:</u>				
D04-P2-D		27.2		ANL-E
D04-P2-A		19.7	8.9	INEL (Met&Chem)
D04-P2-B		19.1		CSNI-UK
D04-P2-C		6.8	9.4	Japan
D04-P1-B		4.6		CSNI
D04-P1-A		1.3		
D08-P4-A		67.98	8.67	INEL (Met&Chem)
D08-P4-D		62.02		ANL-E
D08-P4-B		51.84		
D08-P4-C		37.63	7.77	INEL (Met&Chem)
G08-P10-A		268.60	8.24	INEL (Met&Chem)
G08-P7-A		198.00	7.35	INEL (Met&Chem)
G08-P9-A		163.20	7.34	INEL (Met&Chem)
G08-P6-B		157.80	7.62	INEL (Met&Chem)
G08-P5-B		120.00	7.96	INEL (Met&Chem)
G08-P8-A		118.50	7.40	INEL (Met&Chem)
G08-P4-B		60.49		ANL-E
G08-P4-A		55.14	7.45	CSNI-KFK
G08-P5-A		50.06		CSNI-KFK
G08-P8-C		50.03		CSNI-Switzerland
G08-P8-B		39.11		
G08-P7-B		38.45		ANL-E
G08-P7-C		36.10	8.80	INEL (Met&Chem)
G08-P9-B		33.78		ANL-E
G08-P6-A		21.10	7.69	Japan
G12-P9-A		132.18	7.65	INEL (Met&Chem)
G12-P4-A		90.48	7.84	INEL (Met&Chem)
G12-P8-A		82.16		ANL-E
G12-P10-A		64.28		CSNI-JRC
G12-P2-B		60.93	8.47	INEL (Met&Chem)
G12-P10-B		54.65		CSNI-Sweden
G12-P8-B		48.93	7.66	Japan
G12-P2-E		46.71		CSNI-JRC
G12-P3-A		45.41	7.70	Japan
G12-P2-D		40.93	8.33	Japan
G12-P7-A		40.75		
G12-P6-A		40.60		
G12-P4-B		38.91		
G12-P6-E		36.92		CSNI-JRC

TABLE A-2. (Continued)

Sample No. <sup>b</sup>	Sample Description		Remarks
	Type	Mass (g) Density (g/cm <sup>3</sup> )	
<u>Core Bore Rocks (continued):</u>			
G12-P5-A		34.87	
G12-P9-B		33.54	CSNI-JRC
G12-P2-C		30.25	
G12-P10-D		29.03	
G12-P10-C		28.95	CSNI-KFK
G12-P2-A		28.35	
G12-P8-C		28.18	
G12-P6-B		25.14	
G12-P9-C		24.90	
G12-P6-C		24.30	
G12-P10-E		24.18	
G12-P9-D		20.45	
G12-P6-D		19.84	
G12-P3-B		19.01	
G12-P8-D		18.04	
K09-P3-L		75.55	ANL-E
K09-P4-G		67.73	CSNI-Canada
K09-P4-E		66.30	
K09-P4-D		61.34	6.92 INEL (Met&Chem)
K09-P3-A		55.80	7.56 INEL (Met&Chem)
K09-P4-F		46.96	
K09-P3-D		43.82	7.44 INEL (Met&Chem)
K09-P3-M		41.63	7.50 CSNI-France
K09-P4-H		38.33	6.66
K09-P4-N		37.93	
K09-P3-C		37.73	Korea
K09-P3-J		35.12	
K09-P4-L		34.58	
K09-P4-M		33.56	ANL-E
K09-P4-J		26.83	ANL-E
K09-P3-F		26.68	7.78 INEL (Met&Chem)
K09-P3-H		24.54	
K09-P4-B		24.53	7.42
K09-P4-A		24.33	Korea (Radchem)
K09-P3-G		23.97	CSNI-UK
K09-P3-I		23.87	7.52
K09-P3-E		23.65	
K09-P4-I		23.17	
K09-P1-B		19.98	
K09-P3-B		19.47	CSNI-KFK
K09-P4-K		19.24	

TABLE A-2. (Continued)

Sample No. <sup>b</sup>	Sample Description			Remarks
	Type	Mass (g)	Density (g/cm <sup>3</sup> )	
<u>Core Bore Rocks (continued):</u>				
K09-P3-K		18.88		
K09-P4-C		18.85		CSNI-KFK
N05-P1-D		35.55	8.28	INEL (Met&Chem)
N05-P1-H		22.25	9.09	INEL (Met&Chem)
N05-P1-F		18.06		Japan
N05-P1-A		10.50	7.97	INEL (Met&Chem)
N05-P1-E		10.34		CSNI-JRC
N05-P1-G		9.60		
N05-P1-B		5.97		CSNI-KFK
N5-P1-C		3.59		
N12-P1-A		145.64		ANL-E
N12-P1-B		0.66		Japan
007-P6		76.03	5.43	INEL (Met&Chem)
007-P5		34.45		CSNI-France
007-P8-B		21.80		CSNI-KFK
007-P8-C		19.98		
007-P8-A		7.24		
007-P1-A		4.48	7.61	INEL/Japan
007-P3		?		CSNI-KFK
007-P1-B		?		
009-P1-A		30.00	6.91	INEL (Met&Chem)
009-P1-B		20.44	7.22	INEL (Met&Chem)
<u>Post-Drilling Rocks:</u>				
F6-P1		936	7.5	
F6-P2		794	7.3	
F6-P3		540	7.7	
F6-P4		233	7.3	
F6-P5		199	7.3	
F6-P6		75	7.3	
F6-P7		52	7.4	
F6-P8		46	7.5	
F6/H8-P1		1901	7.7	
F6/H8-P2		638	7.5	
F6/H8-P3		224	6.6	
F5/H8-P4		262	7.5	
F6/H8-P5		178	6.5	
F6/H8-P6		202	6.7	



TABLE A-2. (Continued)

Sample No. <sup>b</sup>	Sample Description			Remarks
	Type	Mass (g)	Density (g/cm <sup>3</sup> )	
<u>Post-Drilling Rocks (continued):</u>				
F6/H8-P7		189	7.9	
F6/H8-P8		144	8.5	
F6/H8-P9		121	6.5	
F6/H8-P10		109	6.9	
Big rock (from M11)		24000	--	Returned to fuel canister D-174
M11-P1		1671	7.5	
M11-P2		1075	7.6	Japan
M11-P3		265	8.0	
M11-P4		105	7.3	
M11-P5		91	7.9	
M11-P6		71	7.8	
M11-P7		60	8.2	
M11-P8		56	8.2	
M11-P9		49	7.9	
M11-P10		63	8.4	Japan
H9/K9-P1		86	8.0	
H9/K9-P2		54	7.1	
H9/K9-P3		21	7.9	
H9/K9-P4		26	7.7	Japan
H9/K9-P5		31	7.0	Japan
H9/K9-P6		74	8.1	Japan
H9/K9-P7		24	7.5	
H9/K9-P8		27	7.1	
H9/K9-P9		24	7.3	Korea
H9/K9-P10		26	7.9	
<u>Fuel Rod Lower Ends:</u>				
D04-R9:	123 cm long			Subdivided
D04-R9-2	10 to 20 cm <sup>a</sup>			INEL (Met)
D04-R9-4	38 to 48 cm <sup>a</sup>			INEL (Met)
D04-R9-6	64 to 74 cm <sup>a</sup>			INEL (Met)
D04-R9-8	107 to 117 cm <sup>a</sup>			INEL (Met)
D04-R12:	122 cm long			Subdivided
D04-R12-2	11 to 21 cm <sup>a</sup>			Japan
D04-R12-4	38 to 48 cm <sup>a</sup>			Japan
D04-R12-6	56 to 66 cm <sup>a</sup>			Japan
D04-R12-8	107 to 117 cm <sup>a</sup>			Japan

TABLE A-2. (Continued)

Sample No. <sup>b</sup>	Sample Description			Remarks
	Type	Mass (g)	Density (g/cm <sup>3</sup> )	
<u>Fuel Rod Lower Ends (continued):</u>				
D08-R4:	69 cm long, with gadolinia:			Subdivided  INEL (UO <sub>2</sub> -Gd <sub>2</sub> O <sub>3</sub> <sub>chem</sub> )
D08-R4-2	13 to 23 cm <sup>a</sup>			
D08-R4-4	33 to 38 cm <sup>a</sup>			
D08-R4-6	53 to 63 cm <sup>a</sup>			
D08-R6:	61 cm long, with gadolinia:			Subdivided
D08-R6-2	11.5 to 21.5 cm <sup>a</sup>			
D08-R6-4	28 to 38 cm <sup>a</sup>			
D08-R6-6	48 to 58 cm <sup>a</sup>			
G08-R6:	64 cm long			Subdivided
G08-R6-2	15 to 25 cm <sup>a</sup>			
G08-R9:	64 cm long			Subdivided INEL (Met) INEL (Met) INEL (Met)
G08-R9-2	11 to 21 cm <sup>a</sup>			
G08-R9-4	28 to 38 cm <sup>a</sup>			
G08-R9-6	43 to 53 cm <sup>a</sup>			
G12-R2:	110 cm long			Subdivided
G12-R2-2	13 to 23 cm <sup>a</sup>			
G12-R2-4	41 to 51 cm <sup>a</sup>			
G12-R2-6	64 to 74 cm <sup>a</sup>			
G12-R2-8	94 to 104 cm <sup>a</sup>			
G12-R4:	105 cm long			Subdivided ANL-E ANL-E ANL-E
G12-R4-2	13 to 23 cm <sup>a</sup>			
G12-R4-4	38 to 48 cm <sup>a</sup>			
G12-R4-6	74 to 84 cm <sup>a</sup>			
G12-R8:	105 cm long			Subdivided
G12-R8-2	11.5 to 21.5 cm <sup>a</sup>			
G12-R8-4	38 to 48 cm <sup>a</sup>			
G12-R8-6	61 to 71 cm <sup>a</sup>			
G12-R8-8	91.5 to 101.5 cm <sup>a</sup>			
				CSNI-Canada

TABLE A-2. (Continued)

Sample No. <sup>b</sup>	Sample Description		Remarks
	Type	Mass (g) Density (g/cm <sup>3</sup> )	
<u>Fuel Rod Lower Ends (continued):</u>			
K06-R1-2:	16.5 cm long		Core elevation unknown
K09-R5:	42 cm long		Subdivided
K09-R5-2	11 to 21 cm <sup>a</sup>		INEL (Met)
K09-R5-4	22 to 32 cm <sup>a</sup>		INEL (Met, clad SD Chem)
K09-R5-5	32 to 42 cm <sup>a</sup>		INEL (Met)
K09-R9:	41 cm long		Subdivided
K09-R9-2	10 to 20 cm <sup>a</sup>		ANL-E
K09-R9-4	23 to 33 cm <sup>a</sup>		ANL-E
K09-R9-5	33 to 41 cm <sup>a</sup>		ANL-E
K09-R14:	51 cm long		Subdivided
K09-R14-2	10 to 20 cm <sup>a</sup>		
K09-R14-4	23 to 33 cm <sup>a</sup>		CSNI-UK
K09-R14-5	33 to 43 cm <sup>a</sup>		CSNI-UK
N05-R2:	120 cm long		Subdivided
N05-R2-2	11.5 to 21.5 cm <sup>a</sup>		
N05-R2-4	41 to 51 cm <sup>a</sup>		
N05-R2-6	71 to 81 cm <sup>a</sup>		
N05-R2-8	104 to 114 cm <sup>a</sup>		
N05-R5:	119 cm long		Subdivided
N05-R5-2	15 to 25 cm <sup>a</sup>		
N05-R5-4	46 to 56 cm <sup>a</sup>		
N05-R5-6	76 to 86 cm <sup>a</sup>		
N05-R5-8	102 to 112 cm <sup>a</sup>		
N12-R4:	112 cm long		Subdivided
N12-R4-2	15 to 25 cm <sup>a</sup>		
N12-R4-4	46 to 56 cm <sup>a</sup>		
N12-R4-6	76 to 86 cm <sup>a</sup>		

TABLE A-2. (Continued)

Sample No. <sup>b</sup>	Sample Description		Remarks
	Type	Mass (g) Density (g/cm <sup>3</sup> )	
<u>Fuel Rod Lower Ends (continued):</u>			
N12-R9:	113 cm long		Subdivided
N12-R9-2	11 to 21 cm <sup>a</sup>		
N12-R9-4	33 to 43 cm <sup>a</sup>		
N12-R9-6	63.5 to 73.5 cm <sup>a</sup>		
N12-R9-8	84 to 94 cm <sup>a</sup>		
N12-R11:	113 cm long		Subdivided
N12-R11-2	11 to 21 cm <sup>a</sup>		
N12-R11-4	24 to 34 cm <sup>a</sup>		
N12-R11-6	63.5 to 73.5 cm <sup>a</sup>		CSNI-Switzerland
N12-R11-8	96.5 to 106.5 cm <sup>a</sup>		CSNI-Switzerland
007-R3:	67.3 cm long		Subdivided
007-R3-2	10 to 20 cm <sup>a</sup>		
007-R3-4	30.5 to 40.5 cm <sup>a</sup>		
007-R3-6	51 to 61 cm <sup>a</sup>		
007-R5:	66 cm long		Subdivided
007-R5-2	10 to 20 cm <sup>a</sup>		
007-R5-4	30.5 to 40.5 cm <sup>a</sup>		
007-R5-6	51 to 61 cm <sup>a</sup>		
009-R6:	72 cm long		Subdivided
009-R6-2	13 to 23 cm <sup>a</sup>		
009-R6-3	23 to 28 cm <sup>a</sup>		
009-R6-4	28 to 38 cm <sup>a</sup>		
009-R6-6	48 to 58 cm <sup>a</sup>		
009-R11:	69 cm long		Subdivided
009-R11-2	13 to 23 cm <sup>a</sup>		
009-R11-3	23 to 28 cm <sup>a</sup>		
009-R11-4	28 to 38 cm <sup>a</sup>		
009-R11-6	48 to 58 cm <sup>a</sup>		

TABLE A-2. (Continued)

Sample No. <sup>b</sup>	Sample Description		Remarks
	Type	Mass (g) Density (g/cm <sup>3</sup> )	
<u>Control Rod/Guide Tube Lower Ends:</u>			
D04-R8:	122 cm long		Subdivided
D04-R8-2	11.5 to 21.5 cm <sup>2</sup>		INEL (Met)
D04-R8-4	33 to 43 cm <sup>2</sup>		INEL (Met)
D04-R8-6	66 to 76 cm <sup>2</sup>		INEL (Met)
D04-R8-8	104 to 114 cm <sup>2</sup>		INEL (Met)
D08-R7:	84 to 94 cm long		Subdivided
D08-R7-2	18 to 28 cm <sup>2</sup>		
D08-R7-4	41 to 51 cm <sup>2</sup>		
D08-R7-6	53 to 63 cm <sup>2</sup>		
K09-R13:	49.5 cm long		Subdivided
K09-R13-2	5 to 15 cm <sup>2</sup>		INEL (Met)
K09-R13-4	20 to 30 cm <sup>2</sup>		INEL (Met)
K09-R13-6	36 to 46 cm <sup>2</sup>		INEL (Met)
N12-R7:	117 cm long		Subdivided
N12-R7-2	8 to 18 cm <sup>2</sup>		
N12-R7-4	28 to 38 cm <sup>2</sup>		
N12-R7-6	61 to 71 cm <sup>2</sup>		
N12-R7-8	81 to 92 cm <sup>2</sup>		
N12-R7-10	107 to 117 cm <sup>2</sup>		INEL (Met and SS Clad SD Chem)
N12-R13:	52 cm long		Subdivided
N12-R13-2	5 to 15 cm <sup>2</sup>		ANL-E
N12-R13-4	25 to 35 cm <sup>2</sup>		ANL-E
N12-R13-6	46 to 56 cm <sup>2</sup>		ANL-E
O07-R7:	74 cm long w/poss. solidified core mat'l:		Subdivided
O07-R7-2	10 to 20 cm <sup>2</sup>		
O07-R7-4	53 to 63 cm <sup>2</sup>		
O07-R7-6	64 to 74 cm <sup>2</sup>		INEL (Met)
O09-R7:	109 cm long w/poss. solidified core mat'l:		Subdivided
O09-R7-2	5 to 15 cm <sup>2</sup>		
O09-R7-4	23 to 33 cm <sup>2</sup>		
O09-R7-6	46 to 56 cm <sup>2</sup>		

TABLE A-2. (Continued)

Sample No. <sup>b</sup>	Sample Description		Remarks
	Type	Mass (g) Density (g/cm <sup>3</sup> )	
<u>Control Rod/Guide Tube Lower Ends (continued):</u>			
009-R8:	109 cm long		Subdivided
009-R8-2	5 to 15 cm <sup>a</sup>		
009-R8-4	23 to 33 cm <sup>a</sup>		
009-R8-6	43 to 53 cm <sup>a</sup>		
<u>Burnable Poison Rod/Guide Tube Lower Ends:</u>			
G08-R11:	30.5 cm long		Subdivided
G08-R11-2	10 to 20 cm <sup>a</sup>		INEL (BP Chem)
G12-R13:	88 cm long		Subdivided
G12-R13-2	20 to 30 cm <sup>a</sup>		INEL (BP Chem)
G12-R13-4	66 to 76 cm <sup>a</sup>		CSNI-KFK
R12-R16:	98 cm long		Subdivided
G12-R16-2	23 to 33 cm <sup>a</sup>		CSNI-KFA
G12-R16-4	56 to 66 cm <sup>a</sup>		CSNI-KFK
N05-R7:	122 cm long		Subdivided
N05-R7-2	5 to 15 cm <sup>a</sup>		ANL-E
N05-R7-4	48 to 58 cm <sup>a</sup>		ANL-E
N05-R7-6	76 to 86 cm <sup>a</sup>		ANL-E
N05-R7-8	99 to 109 cm <sup>a</sup>		ANL-E
<u>Instrument Tube Lower Ends:</u>			
D04-R1:	79 cm long		Subdivided
D04-R1-2	10 to 20 cm <sup>a</sup>		
D04-R1-4	41 to 51 cm <sup>a</sup>		
D04-R1-6	63.5 to 73.5 cm <sup>a</sup>		
D08-R8:	49.5 cm long		Subdivided
D08-R8-2	8 to 18 cm <sup>a</sup>		
D08-R8-4	25 to 35 cm <sup>a</sup>		
D08-R8-6	38 to 48 cm <sup>a</sup>		

TABLE A-2. (Continued)

Sample No. <sup>b</sup>	Sample Description		Remarks
	Type	Mass (g) Density (g/cm <sup>3</sup> )	
<u>Instrument Tube Lower Ends (continued):</u>			
G08-R3:	56 cm long w/solidified core material:		Subdivided
G08-R3-2	4 to 14 cm <sup>a</sup>		INEL (Met, IT & SCM Chem)
G08-R3-4	16.5 to 17.5 cm <sup>a</sup>		INEL (Met & sleeve SD Chem)
G08-R3-6	36 to 46 cm <sup>a</sup>		INEL (Met & sleeve SD Chem)
G12-R12:	113 cm long w/poss. solidified core material:		Subdivided
G12-R12-2	8 to 18 cm <sup>a</sup>		Japan
G12-R12-4	28 to 38 cm <sup>a</sup>		Japan
G12-R12-6	69 to 79 cm <sup>a</sup>		Japan
G12-R12-8	97 to 107 cm <sup>a</sup>		Japan
K09-R4:	39 cm long		Subdivided
K09-R4-2	10 to 20 cm <sup>a</sup>		Japan
K09-R4-4	25 to 35 cm <sup>a</sup>		Japan
N05-R15:	60 cm long		Subdivided
N05-R15-2	25 to 35 cm <sup>a</sup>		INEL (Met)
007-R4:	67 cm long		Subdivided
007-R4-2	10 to 20 cm <sup>a</sup>		
007-R4-4	30.5 to 40.5 cm <sup>a</sup>		
007-R4-6	51 to 61 cm <sup>a</sup>		

a. Distance above rod or tube bottom.

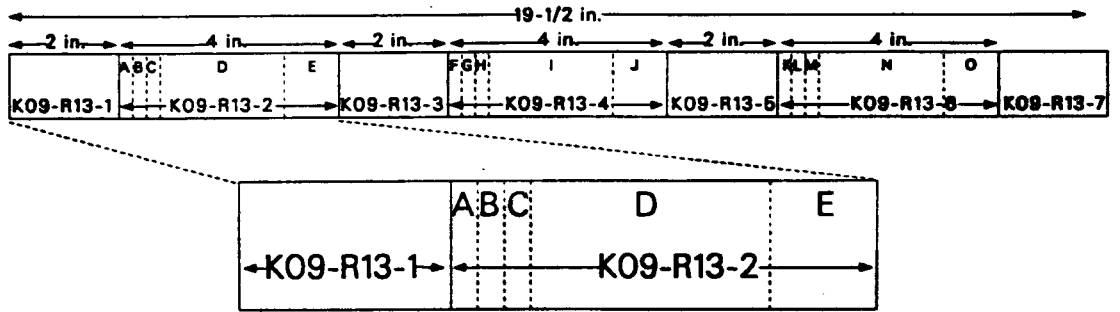
b. Alpha-numeric prefix corresponds to the TMI-2 core position origin of the sample.





The rod and tube samples were selected on the basis of representativeness and/or interaction with other core materials. Sections 10 cm long were cut from each rod or tube, as shown in Figure A-2.

Further subdivision of samples occurred to produce the special geometries needed for the examination methods. The 10 cm long rod and tube sections were subdivided, including a 0.6 cm long section for metallurgical examinations, a 2.5 cm long section for radiochemical analysis of the surface deposits, and an occasional whole fuel or burnable poison pellet for elemental and/or radiochemical analyses. Microcores (6.35 mm dia) were obtained from the core and rock samples for dissolution and subsequent radiochemical and wet-chemistry analysis. Other microcores (11.1 mm dia) were cut from the metallurgical mounts for remounting for subsequent SEM examinations.



<u>Sample No.</u>	<u>Location</u>		<u>Comments</u>
	<u>Bottom</u>	<u>Top</u>	
K09-R13-1	0	2	Remnant
K09-R13-2	2	6	
K09-R13-2A	0	1/4	Remnant
K09-R13-2B	1/4	1/2	Met
K09-R13-2C	1/2	3/4	Remnant
K09-R13-2D	3/4	3	
K09-R13-2E	3	4	Rad chemistry

P814 CSO-488-20

Figure A-2. Section Diagram (K09-R13 Control Rod).

**APPENDIX B**  
**EXAMINATION TECHNIQUES**



## APPENDIX B

### EXAMINATION TECHNIQUES

This Appendix presents a brief overview of techniques used during examination of the TMI-2 core bore samples, including physical, metallurgical, chemical, and radiochemical examinations.

Upon arrival at the INEL, the core bores were contained in a split tube that consisted of two semi-cylindrical tubes held together with tightly wrapped piano wire. The core barrel was placed on the disassembly-and-examination fixture, where the drill bit (including the end-fitting remnant) was removed. The core bores, contained in their split-tube assemblies and gamma-scanning containers, were received at the ARA Hot Cells.

#### Physical Examinations

##### Visual/Photographic

A visual examination of the intact core bores was performed and recorded using a 35-mm single lens reflex (SLR) camera body and a B&W video camera attached to a Kollmorgen periscope at the camera and Filar eyepiece ports, respectively. A "data back" attached to the SLR camera door was used to record identification numbers on the negatives. At the ARA Hot Cells, each core bore was placed on a movable table and moved incrementally under the periscope while overlapping photographs were taken to produce mosaic photographs of each core bore. Axial location was determined by including a scale in each photograph. At selected locations, high-magnification photographs also were taken to record details of the crust layers, rod stubs, and rocks. Video recordings were used to record the overall appearance of the core bores as well as individual rod stubs after they were removed from the core bores. Cutting operations, such as the removal of the jamming collar on selected core bores, were also video recorded.

Individual debris samples larger than 2.5 cm were individually photographed using the method described above. A scale was also included in

each photograph to define the magnification used and the sample size. In some cases, the sample was photographed in different orientations to document important surface features.

### Mass

The mass of each intact core bore was measured within  $\pm 0.1$  kg using a dynamometer. After the surface of the core bore was exposed by removing one-half of the split tube, the core bore was weighed by suspending the split tube half containing the core bore from a dynamometer. This total weight of the core bore and split tube was corrected for the known weight of the other split tube half.

The mass of each rock-type sample larger than 2.5 cm was determined with an electronic top loader balance with a capacity of 3000 g and a precision of 0.01 g.

### Density

The sample density of selected samples was determined using a standard immersion technique. For samples weighing less than 630 g, matrix density was determined within  $\pm 0.05$  g/cm<sup>3</sup> using an analytical balance for samples weighing less than 150 g and a triple beam balance for samples weighing less than 630 g. For larger samples, an electronic balance was used, allowing the matrix density to be determined within  $\pm 0.08$  g/cm<sup>3</sup>.

### Beta-Gamma Autoradiography

Beta-gamma autoradiography was performed on samples selected for SEM analysis to evaluate the distribution of radioactivity in different phases of the samples. The film packet containing x-ray film (wrapped in plastic to prevent contamination) was placed on the sample for a period of about 15 s to attain adequate exposure levels. The actual exposure time for each sample was recorded. Samples were autoradiographed separately unless multiple specimens were contained in the same metallographic mount. Additionally,

radiation field measurements were taken for comparison purposes. The radiation levels were recorded only for those samples to be shipped to the TAN hot cells.

## Metallurgical Examinations

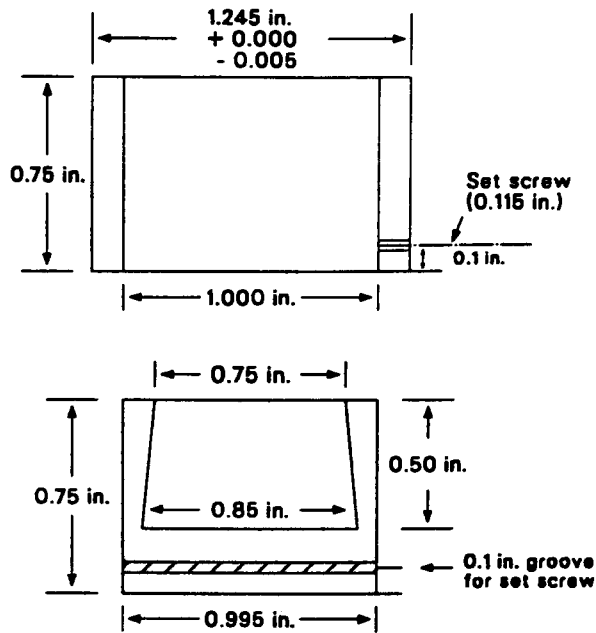
### Optical Metallography

Optical metallography at magnifications up to about 500X was performed on polished and etched sample cross sections using a Leitz Model MM5RT light microscope.

Small samples (<19 mm diameter) were mounted in 31.8-mm diameter brass mounts (Figure B-1) using a low melting lead/bismuth alloy to hold the sample in place. The sample was then placed in the mount with the surface to be examined facing up. For large samples (>19.8 mm diameter), a 12.7-cm diameter aluminum ring placed in a groove in an aluminum plate (Figure B-2) was used for mounting. In this method, the sample was placed with the face to be examined facing downward towards the bottom plate. After epoxy was poured around the sample, the mount was placed in a vacuum to fully impregnate the sample. After the epoxy had cured, the ring containing the epoxied sample was removed from the base plate, exposing the surface to be examined.

The following grinding and polishing sequence was used to prepare the TMI-2 core debris samples for optical metallography:

- Coarse grind with water-lubricated silicon carbide 120 grit paper with a whirlamat
- Medium grind with 240 and 400 grit paper (Wash between grit sizes)
- Final grind with 600 grit paper
- Initial polish with 6 mm diamond grit in mineral oil-type fluid on a hard paper with a whirlamat



L242-KM276-02

Figure B-1. Schematic drawing of 1-1/4 in. metallographic mount.

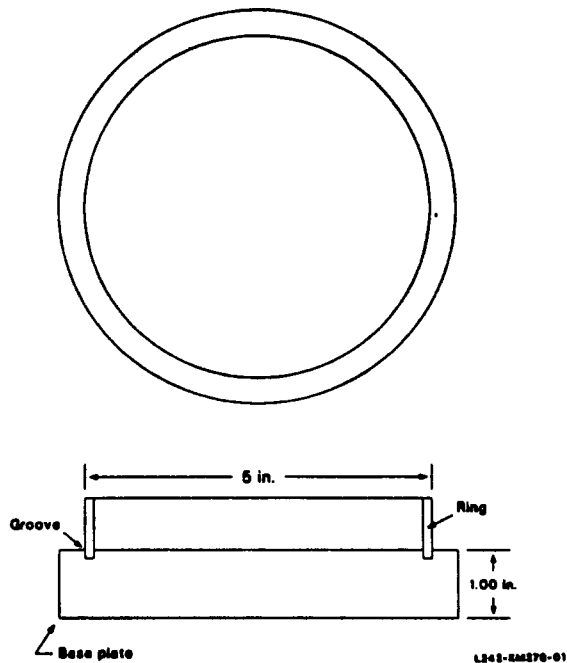


Figure B-2. Schematic drawing of 5 in. metallographic mount.



- Final polish with 3 mm diamond grit in mineral oil on a short nap nylon cloth.

For ceramic samples a swab-etching technique was used with varying etchants times depending on the sample, but generally for about a minute or less. The fuel etchant was 85% hydrogen peroxide ( $H_2O_2$ ), and 15% sulphuric acid ( $H_2SO_4$ ).

For metallic phases, a zircaloy etch was used. This etch also was useful in characterizing the microstructure of the Ag-In-Cd control rod materials. This etch contained 19% nitric acid ( $HNO_3$ ), 19% water, 28% lactic acid, and 7% hydrofluoric acid (HF).

### Scanning Electron Microscopy

Scanning electron microscope samples were removed from metallographic samples by core drilling. A 1.27-cm outer diameter diamond-tipped corer was inserted into a drill press, and the sample was mounted onto the drill press base. A template developed from a photomicrograph was taped to the specimen and used as a guide to position the drill within 1 mm of the desired location. The sample was removed from the core drill and mounted using a lead/bismuth alloy into a brass SEM mount.

Energy dispersive X-ray spectroscopy (EDS) was used to determine the elemental composition of a sample by measuring the energy and intensity of characteristic X-rays generated in the material when bombarded by an electron beam in a SEM. A solid state detector is used to acquire the spectrum, providing a simultaneous acquisition of the entire detectable X-ray energy range (1-20 keV, corresponding to peaks of elements with atomic numbers 11 and greater). This made EDS useful for quick area surveys of elemental content as a preliminary to detailed WDS analysis. Two factors limited the utility of EDS spectra: high sample-induced radiation background (due to the close proximity of detector to sample) and the relatively poor resolution inherent in solid-state X-ray detection. As an example of the latter, the energies of the major peak clusters for U, Ag, Cd, In, and Sn overlap and

were impossible to separate analytically. Consequently, EDS was only used qualitatively.

Wavelength dispersive X-ray spectroscopy (WDS) is similar to EDS except that the X-rays generated by the electron beam are separated by wavelength through a diffracting crystal, and a gas filled proportional counter is used as the detector. The detector is physically scanned across the spectrum of diffracted X-rays and generates a signal on a point-by-point basis. Acquisition is slow, but results in a very high resolution spectrum.

WDS was used to provide elemental data of two types: qualitative X-ray dot maps, and spectra for quantitative analysis. Dot maps are produced by tuning the spectrometer to the peak of the element of interest and rastering the electron beam across the area of interest. Spectrometer output is correlated to beam position, and a picture of the area is constructed in which relative brightness corresponds to beam-generated X-ray intensity, and thereby to concentration of the element. The images show the relative distribution of elements in an area.

WDS can be used to ascertain precise elemental compositions in very small (<10  $\mu\text{m}$ ) regions of a sample. The peak heights of unknowns are compared to those of well characterized standards. This method is described in detail in Appendix J.

### SEM System Configuration

The SEM/WDS laboratory was configured and hardware was modified to allow examination of highly radioactive, contaminated specimens. Lower core SEM specimens from TMI ranged from 5 to greater than 50 R/h (beta-gamma) at contact. The microscope column was installed in a hot cell in the Hot Cell Annex at Test Area North, and electrically interconnected with the control console and operating system electronics situated in a nearby room. Samples were stored in a second hot cell connected to the SEM cell by a remote transfer drawer. Sample loading was performed with master/slave manipulators. Operations were performed remotely, including changing the

objective aperture and alignment; inserting/retracting the optical focusing microscope; opening/closing the specimen chamber door; resetting the specimen stage position; and refilling the EDS dewar.

The SEM was a JEOL JSM-840 with Tracor/Northern (T/N) 5600 stage automation. It was fitted with a T/N EDS and three JEOL WDS spectrometers. The EDS spectrometer was controlled by a T/N 5500 system, which also performed spectrum analysis and image digitizing and analysis. The WDS spectrometers were controlled by the T/N 5600 system that also controlled the motion of the sample stage.

The EDS detecting crystal was shielded from the sample by a tungsten disk 2 mm thick with a 0.5 mm hole through the center. This shielding reduced the radiation induced background to the point that useful spectra were obtained, although in order to acquire a suitably intense signal through the pinhole, very high beam currents (200 - 300 nA) had to be employed.

Three WDS spectrometers, containing two different diffracting crystals, were attached to the SEM column. Crystals in the system included lead stearate (STE, d spacing 35A), thallium acid phthalate (TAP, d spacing 13.0A), pentaerythritol (PET, d spacing 4.37A), and lithium fluoride (LiF, d spacing 2.01A). Two of the spectrometers contained both PET and LiF, while the third held TAP and STE. The duplication of crystals is a time saving device designed to acquire more than one element simultaneously with the same type of crystal. The TMI material examinations used only TAP, PET and LiF crystals. The STE was not used because it was intended for oxygen and other light elements which the TAP detected with greater resolution. Specific crystals used for the different elements detected in the lower core samples are listed below.

- TAP: Al, O
- PET: Sn, In, Ag, U, Cd, Mo, Tc, Ru, Pd, Zr
- LiF: Ni, Fe, Cr

## Chemical Examinations

### Inductively Coupled Plasma Spectrometry

Dissolved solid samples are nebulized and pulse-injected into an inductively (radio frequency) heated plasma, causing all elements present to emit characteristic light wavelengths. The light is separated on a diffraction-grating monochromator, and the wavelength intensities are sequentially measured by a photomultiplier tube. (As such, inductively coupled plasma (ICP) spectrometry is a refinement of atomic emission spectroscopy.) This technique generally is free of elemental interferences, is highly accurate, and has a detection threshold of approximately 0.001 at% (10 ppm).

## Radiochemical Examinations

### Gamma Spectroscopy

The initial radiochemical analysis performed was gamma spectroscopy. This technique is based on gamma-ray emissions that produce a spectrum specific to individual radionuclide species. The spectra were analyzed by a computerized gamma spectroscopy system using DEC PDP-15 and PDP-11/44 computers with a GAUSS VI analysis program.<sup>a</sup> This program (a) identifies the radionuclides associated with the gamma-ray energy peaks, and (b) determines their emission rates corrected for detector efficiency, random pulse summing, and decay during the count. The values were converted to disintegration rates by dividing them by the gamma-ray emission probability. The equipment was fabricated at EG&G Idaho and calibrated using standards of the National Bureau of Standards.

Dissolved portions of samples were diluted and analyzed in 60 mL bottles at calibrated distances with a computerized Ge(Li) gamma

---

a. J. E. Klein, M. H. Putnam, R. H. Helmer, *GAUSS VI, A Computer Program for the Automatic Analysis of Gamma Rays from Germanium Spectrometers*, ANRC-13, June 1973.

spectroscopy system. They were analyzed as point source geometries at distances from the detector ranging up to 195 cm. The mass of each portion analyzed was less than or equal to 100 mg to keep the specific radionuclide concentration low and to minimize the effects of mass attenuation that were evaluated and corrected. The uncertainty of the gamma spectroscopy analysis method is less than  $\pm 10\%$ , with the exception of those radionuclides whose concentrations were determined using low energy gamma rays ( $^{152}\text{Eu}$  and  $^{125}\text{Sb}$ ). The uncertainty associated with these radionuclides is approximately  $\pm 30\%$ .

### Neutron Activation/Delayed Neutron Analysis

The fissile/fertile material content was measured by neutron activation/delayed neutron analysis at the Coupled Fast Reactivity Measurement Facility (CFRMF). The total fissile/fertile material content was measured by remotely exposing individual 1 x 5-cm long cylinders containing sample material to a fast spectrum neutron flux in the central region of the CFRMF core. The cylinder was removed after a 1 min exposure; the delayed neutrons were measured after about 40 s, using a He-3 detector in a hydrogen moderator.

The fissile material content was determined by exposing the cylinder to a thermal spectrum neutron flux, causing only the uranium-235 and plutonium-239 within the sample to fission and emit delayed neutrons. It was assumed that the quantity of plutonium-239 was insignificant ( $\sim 2$  wt% based on theoretical predictions). However, a bias between 5% and 8% may have resulted. The fertile material contents were determined by subtracting the measured fissile material content (uranium-235 and plutonium-239) from the total fissile/fertile material content using appropriate calibrations. Calibration measurements were made using both mass and various enrichment standards (depleted uranium, natural uranium, 4.3% enriched uranium, and 93% enriched uranium).

## Iodine-129, Strontium-90, and Tellurium Analyses

Analyses for strontium-90 and iodine-129 were performed on dissolved sample material. After an organic separation, the volatile sample fraction was analyzed via neutron activation with a subsequent gamma spectroscopy analysis. The iodine-129 present in the dissolved material was activated to iodine-130, a gamma-ray-emitting radionuclide. The sample material then was analyzed via gamma spectrometry, and the iodine-129 concentration calculated from the measured iodine-130.

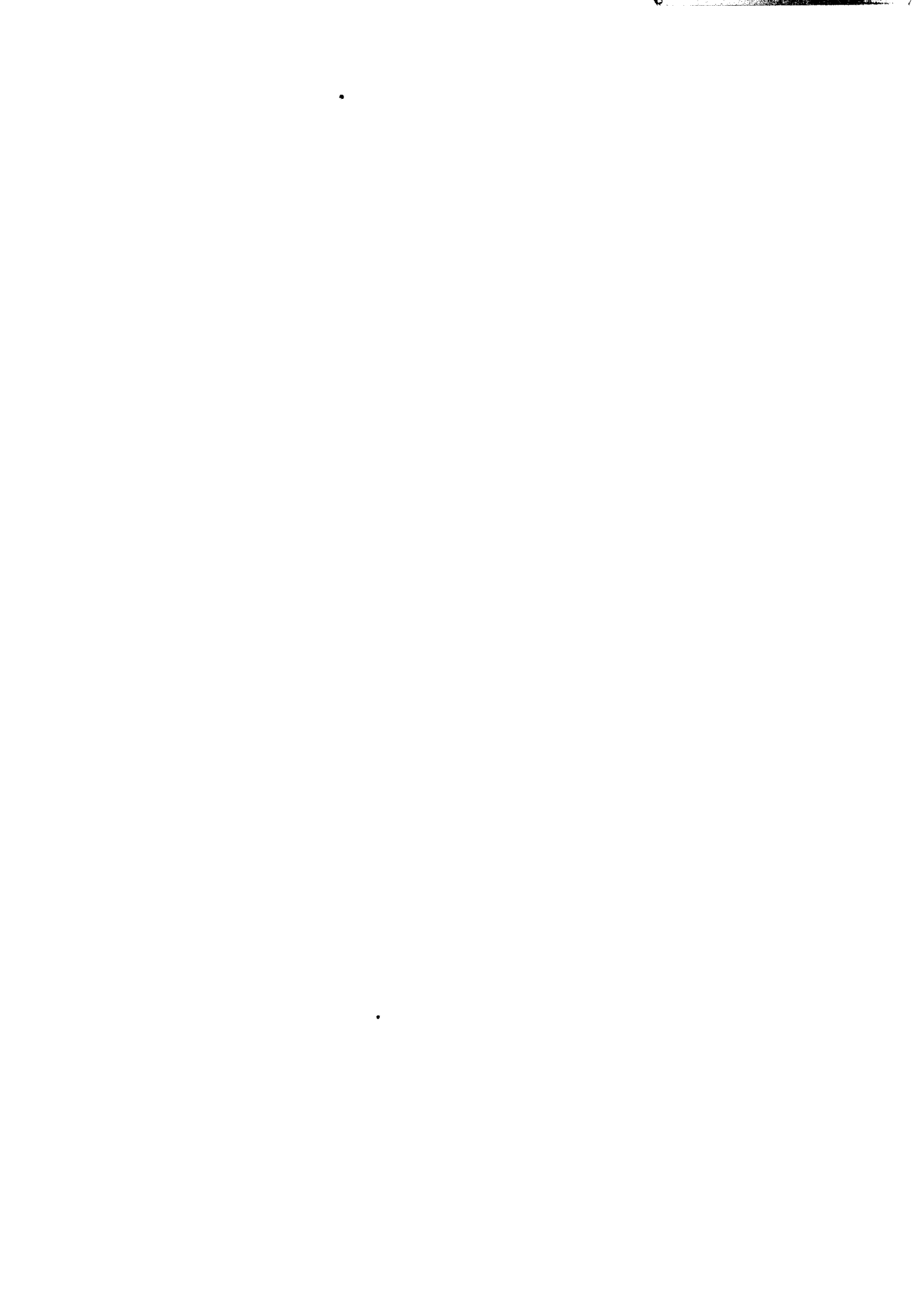
The strontium-90 analysis was performed on the nonvolatile sample fractions by precipitating the strontium carrier and strontium-90 from the other radionuclides, followed by beta analysis performed in a liquid scintillation counter (Packard Tricarb 3385).

The tellurium analyses were performed by two methods. Analyses were performed for tellurium on all samples using ICP; however, the detection limit for this method is near the core average concentration for tellurium in the TMI-2 core, which causes many analysis results to be at the detection limit. Consequently, a more sensitive analysis technique based on neutron activation analysis had been developed.

The tellurium analysis technique based on neutron activation analysis has a detection limit at the nanogram/gram level. In this method, a chemical separation is performed to remove the elemental tellurium with an appropriate tracer (tellurium-123m) from a dissolved sample of material. Chemical separations are then performed and the sample loaded on a resin column, which is then activated to determine the production of tellurium-131 from tellurium-130. Tellurium-130 is a naturally occurring isotope that is also produced by fission; however, there is no known source of this isotope at TMI-2.

There is a total uncertainty associated with the strontium-90 and tellurium analyses of  $\pm 10$  to  $\pm 20\%$ . Uncertainties associated with these analysis results are from the sample dissolution and measurement methods

used. The uncertainty associated with the dissolution is due to potential material losses on glassware surfaces and the occasional presence of small (<10%) amounts of insoluble material after the dissolution. However, for some samples, the uncertainties are  $\pm 30$  to  $\pm 50\%$  due to uncertainties in sample weight for small (<10 mg) samples and losses during dissolution as determined from comparing uranium analysis results from the fissile/fertile and chemical analyses.





**APPENDIX C**

**VISUAL EXAMINATIONS**



## APPENDIX C

### VISUAL EXAMINATIONS

Although ten core bores were extracted from TMI-2, only nine were examined. The tenth core bore, (K06), only contained a 12-cm long fuel rod fragment. This rod was broken at each end so that its location in the core could not be determined. Because the location could not be ascertained and other fuel rods were available, this piece was discarded.

The nine core bores were visually examined and weighed. The visual examination was recorded by 35-mm color film and video recordings, as described in Appendix B. From these nine core bores, samples from the fuel rods, large particles, and plugs from crusts were extracted. This Appendix documents the results of these nondestructive examinations.

The total mass of the ten core bores was 130.48 kg (Table C-1). Excluding core bore K06, which contained a small piece of fuel rod, the average mass per core bore is 14.5 kg. With the exception of core bore D08, the lighter core bores consisted of a lesser amount of fuel rods and more loose debris. Of the 130.48 kg, 14.71 kg was loose debris. The remaining mass of 115.77 kg was fuel rods. Particles larger than 2.5 cm were extracted from the loose debris, which totaled 11.55 kg or 78.5% of the loose debris.

The visual appearance of each of the core bores is shown from the mosaic photograph of each core bore in Figures C-1 - C-3. At the bottom of the core bore, a jamming collar which covered the lower spacer grid prevented the loss of the core bore when it was removed from the reactor.

#### Core Bore D04

The longest fuel rod in core bore D04 was about 157.5 cm long; most of the rods were about 129.2 cm. A number of the rods were torn open by the

TABLE C-1. CORE BORE DEBRIS MASS AND LARGE PARTICLES

<u>Core Bore</u>	<u>Total mass (kg)</u>	<u>Loose debris mass (g)</u>	<u>Large particles<sup>a</sup> mass (g)</u>	<u>Number of particles<sup>a</sup></u>
D04	19.1	77	77	6
D08	18.1	2287	2092	7
G08	12.7	3476	3232	16
G12	15.9	2638	1731	30
K06	0.08	0	0	--
K09	10.9	4951	3209	30
N05	17.0	114	114	8
N12	13.9	146	146	2
O07	10.7	936	896	7
O09	12.4	89	50	2

a. Particles larger than 25 mm

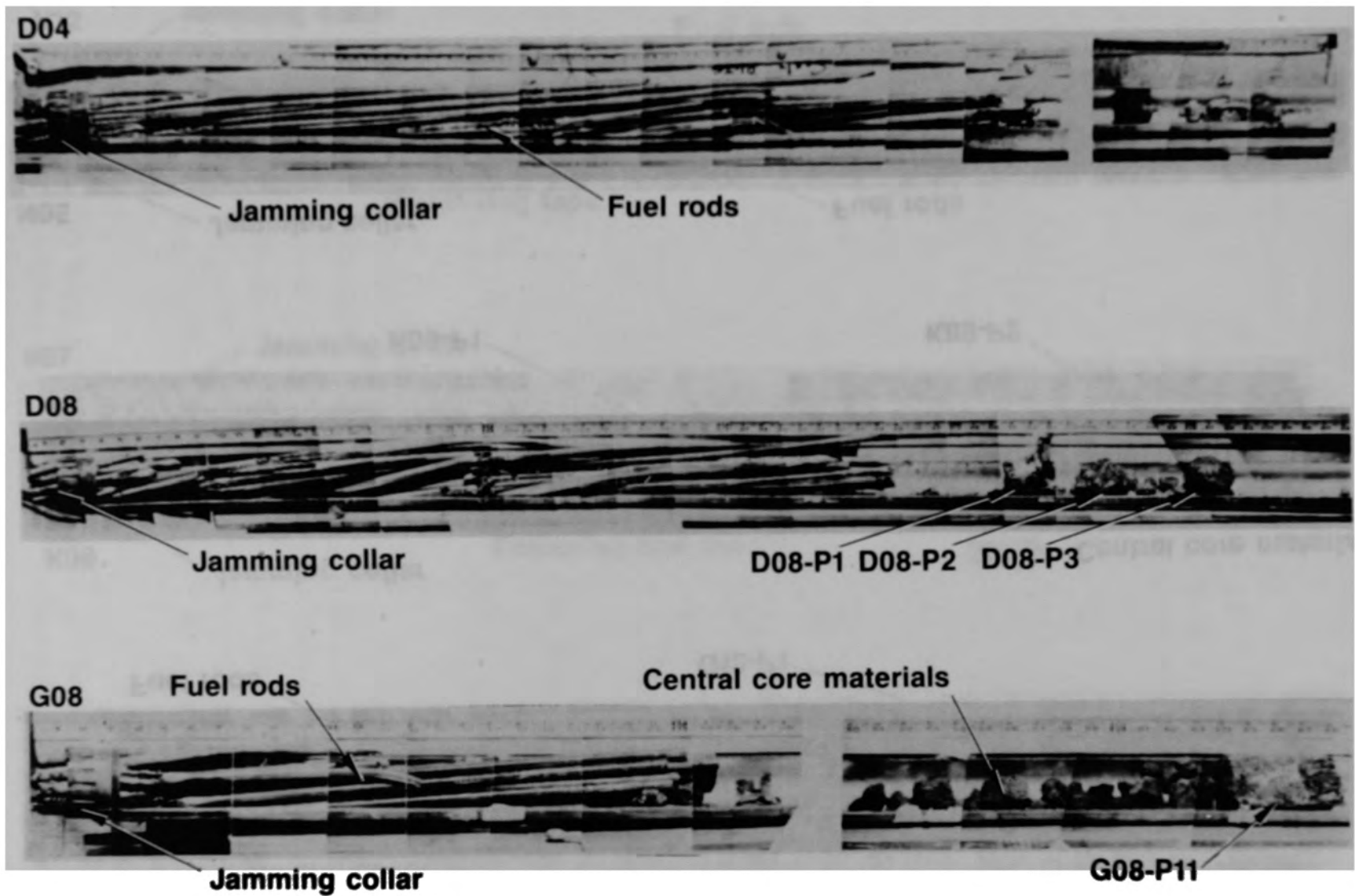


Figure C-1. Mosaic photographs of core bore samples D04, D08, and G08.

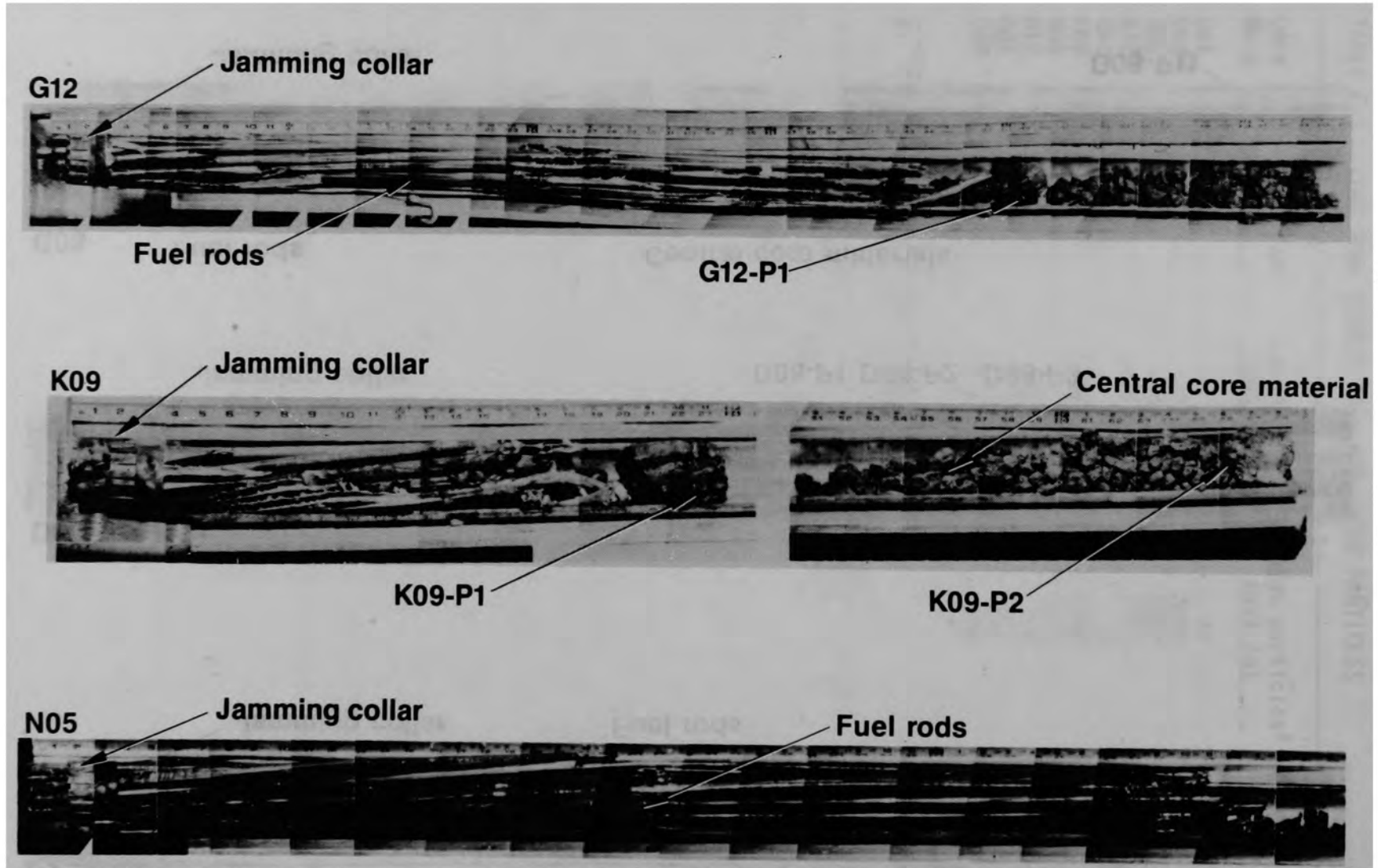


Figure C-2. Mosaic photographs of core bore samples G12, K09, and N05.

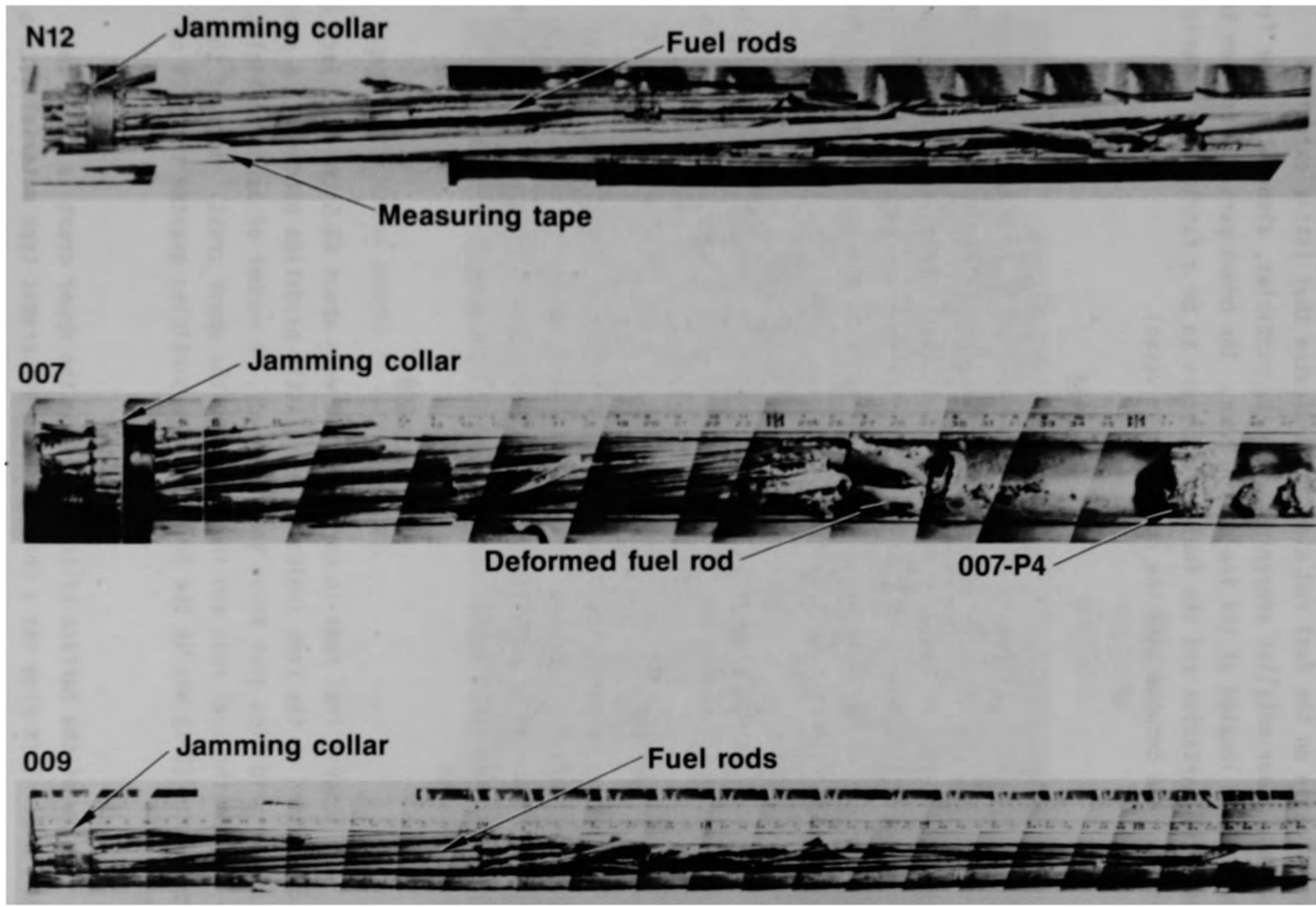


Figure C-3. Mosaic photographs of core bore samples N12, 007, and 009.

core-boring operation exposing fragments of the fuel rods. The lack of discoloration on the fuel rod cladding indicates that little oxidation occurred. Four metallic appearing rock-like particles, along with some fine debris, were located at the top of the core. The brown particle between the cluster of particles and the fuel rods appears to be a fabric type material that may have dropped into the open reactor vessel.

#### Core Bore D08

The longest fuel rod in core bore D08 was about 114.3 cm. The rods were torn open by the core-boring operation exposing fragments of fuel. The lack of oxidation on the fuel rod cladding indicates that little oxidation took place. This core bore contained three large crust samples as shown in Figure C-1. Two of these are from the lower crust, and the third one at the top of the core bore came from the upper crust.

The upper crust plug was a coherent mass of ceramic-type material with very fine dispersions of metallics, as indicated by bright metallic-looking flakes.

The group of particles located between the upper and middle plugs is shown in Figure C-4. Most of these particles appear to be ceramic with a substantial amount of metallic inclusions. The particle near the top of the figure contains large voids.

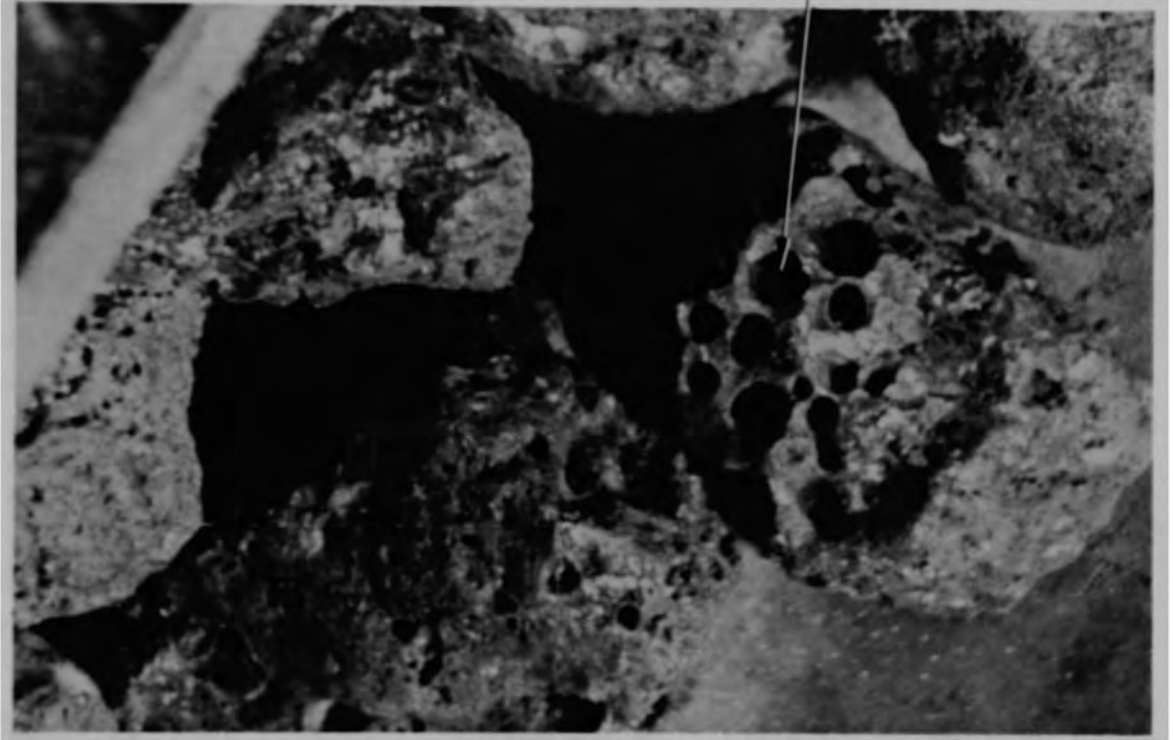
#### Core Bore G08

The longest fuel rods in core bore G08 were about 63.5 cm. The lack of discoloration on the rods indicates very little oxidation occurred. A piece of spacer grid lies just above the fuel rods. A number of large particles lie between the fuel rods and the plug from the upper crust. Most of the loose debris (93%) was in the form of large particles greater than 2.5 cm diameter.

A view of the surface of the plug from the upper crust is shown in Figure C-5. This plug was a coherent mass of ceramic-type material with a

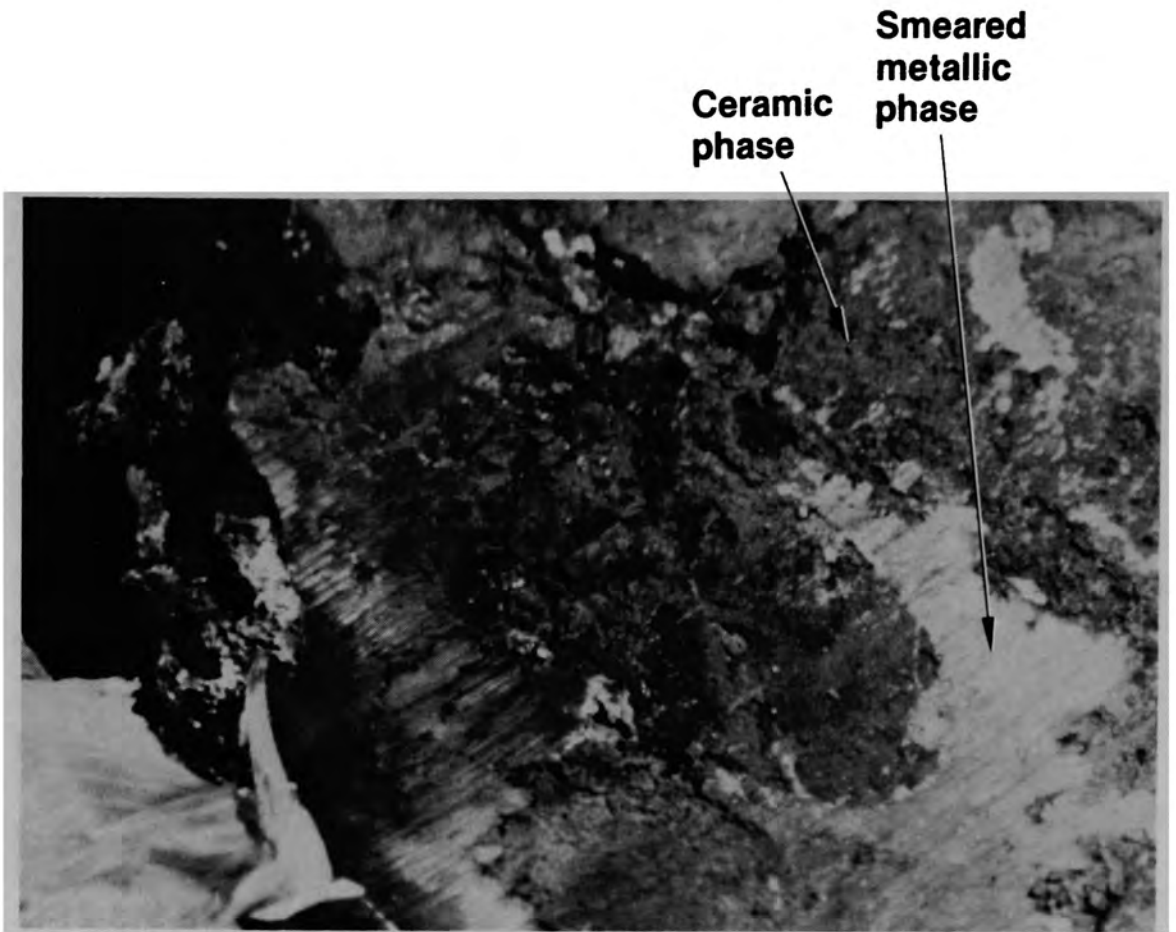


**Void in  
ceramic  
particle**



**86-513-21-13**

Figure C-4. Loose debris in core bore D08.



86-513-9-11

Figure C-5. Metallic inclusions in upper crust sample G08-P11.

large amount of metallic materials dispersed in the crevices and cracks. The ductility of these metallics is indicated by the smearing of the metallics over the surface of the plug as a result of the core-boring operations. Another view of this plug shows numerous fissures and cracks along with some metallics smeared over the surface (Figure C-6).

A particle between some fuel rods is shown in Figure C-7. The rounded surfaces of this particle indicate that it was a previously molten metallic globule.

### Core Bore G12

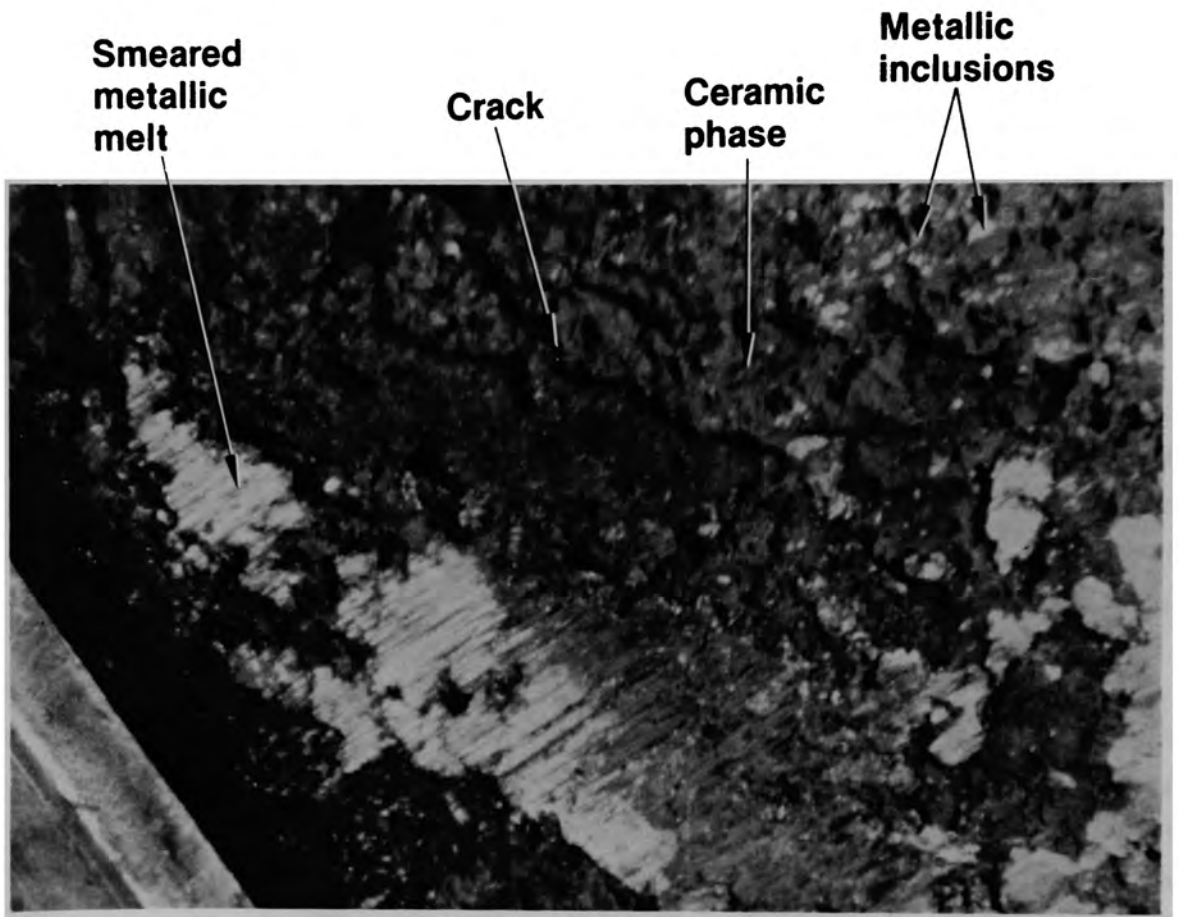
The longest fuel rods in core bore G12 were about 111.8 cm. The lack of discoloration on the fuel rods indicates very little oxidation occurred. A number of large particles lie between the fuel rods and the top of the core. A plug from the peripheral crust lies just above the fuel rods. A large part of the loose debris (65%) was in the form of large particles greater than 2.5 cm diameter.

A view of the surface of the plug from the peripheral crust is shown in Figure C-8. This crust was a coherent mass of ceramic-type material with a large amount of metallic materials dispersed in the matrix. This view is from a transition zone from a dull, grayish surface that is relatively smooth to an area that appears freshly fractured with numerous cracks and fissures. The metallics appear bright and reflective.

Several particles located near the top of the core bore are shown in Figure C-9. A piece of the piano wire that held the split tube together is shown in this figure. The particles contain some large pores but little fine porosity. The surfaces are very irregular.

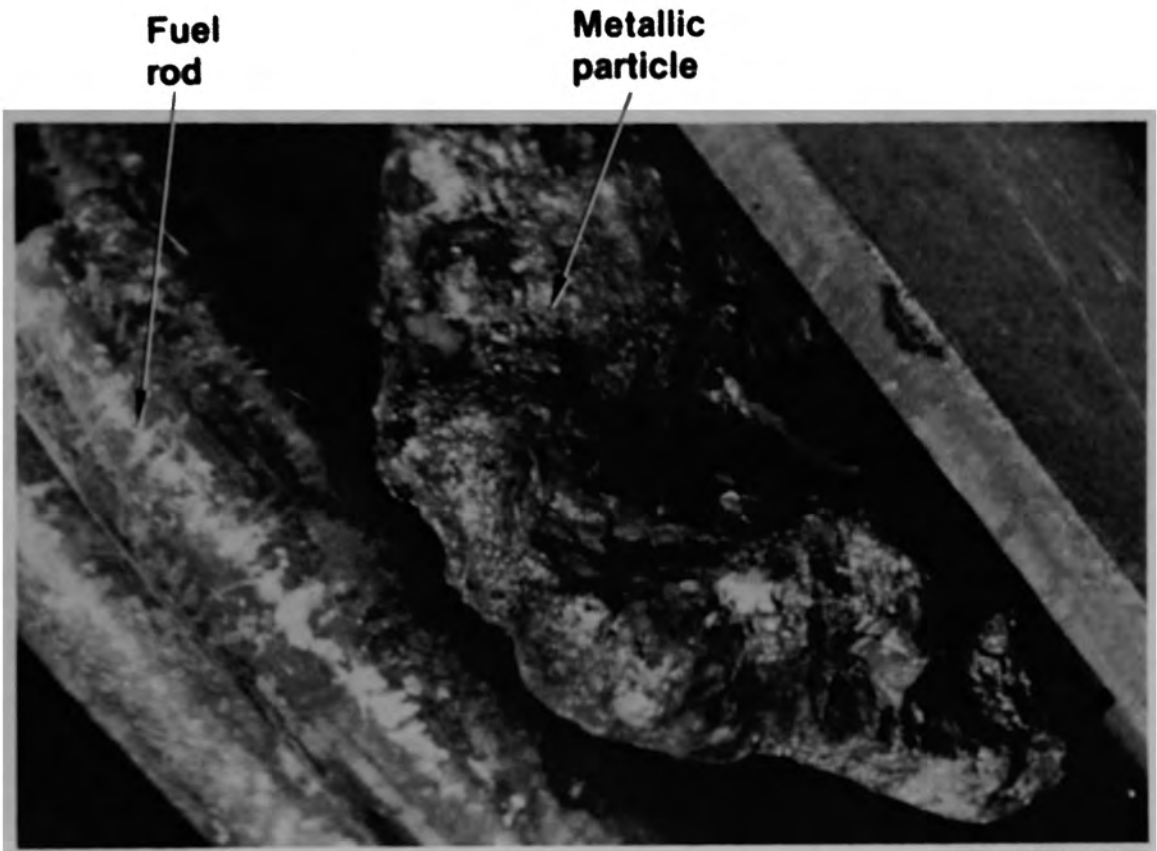
### Core Bore K09

The longest fuel rods in core bore K09 were about 48.3 cm, which is the smallest of any of the core bores. The fuel rods were severely damaged from the core-boring operations and exhibited extensive ductility, as exhibited



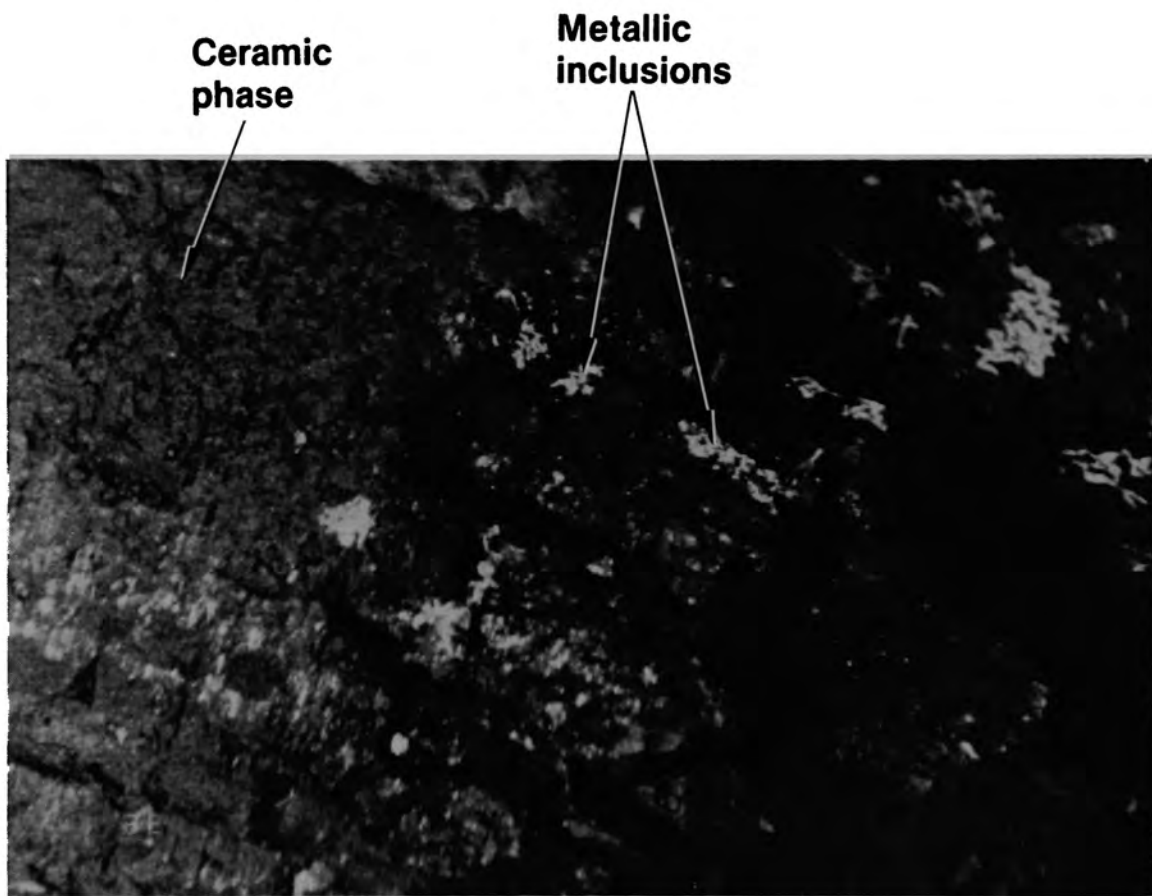
86-513-10-4

Figure C-6. Fissures and cracks in G08-P11.



86-513-9-15

Figure C-7. Partially metallic particle in core bore G08.



**86-513-12-1**

Figure C-8. Surface appearance of G12-P1.

**Piano wire used  
to hold core bore**

**Loose  
particles**



**86-513-12-5**

Figure C-9. Loose particles in core bore G12.

by the bent and twisted shapes. The fuel rod cladding did not exhibit much discoloration from oxidation. A plug from the lower crust (K09-P1) lies just above the fuel rods, and one from the upper crust (K09-P2) is located at the top of the core bore. A number of large particles lie between the two plugs. The loose debris (65%) was in the form of large particles greater than 2.5 cm diameter.

The upper crust sample was a coherent mass of ceramic material with finely dispersed metallics in the matrix. A view of the plug from the lower crust is shown in Figure C-10. A remnant of a fuel pellet is present at the edge of the plug.

Several particles are shown in Figure C-11. The one in the center of the figure appears to be a ceramic particle with a fine dispersion of metallics distributed through the particle. It contains some large voids with some fine porosity. The surrounding particles are very irregular in shape and contain some large voids.

#### Core Bore N05

The longest fuel rods in core bore N05 were about 121.9 cm. The fuel rods were slightly damaged at about 61 cm (24 in.). The rods were slightly discolored indicating some oxidation.

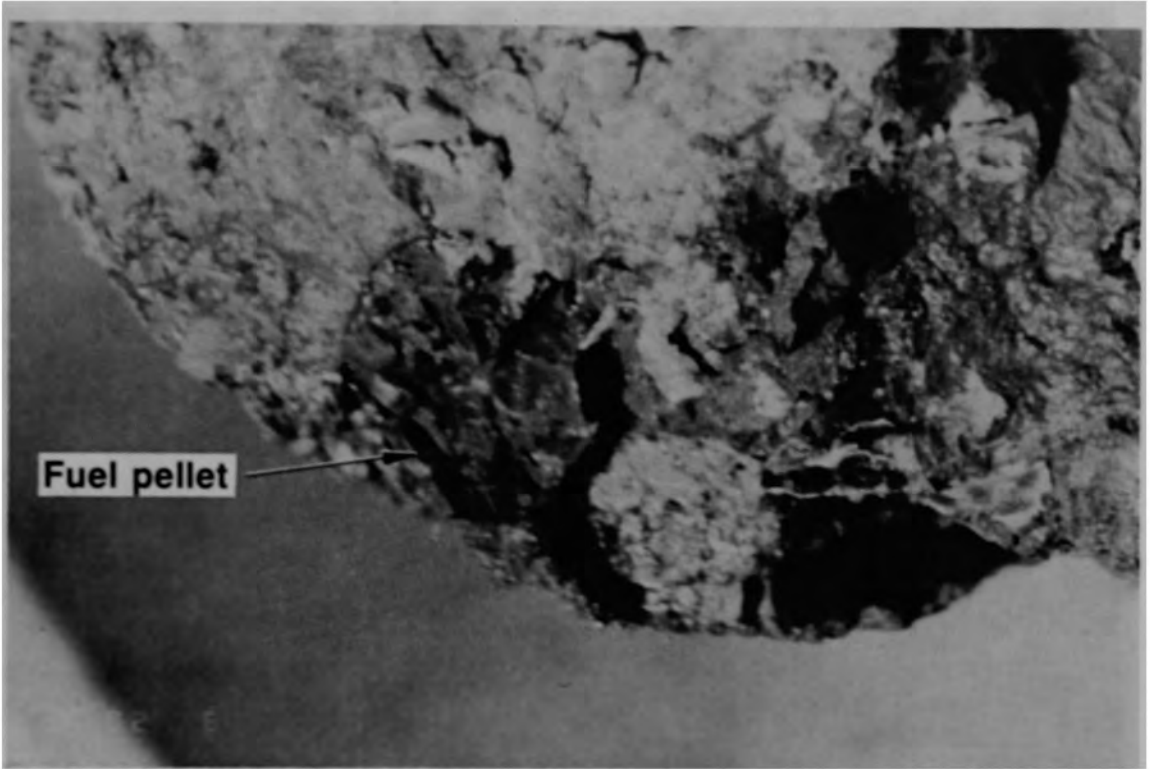
#### Core Bore N12

The fuel rods varied in length and were damaged extensively from the core-boring operation. This core bore weighed 13.6 kg and contained only about 146 g of debris. A control rod that was previously molten at the endtip is shown in Figure C-12.

#### Core Bore 007

The longest fuel rods in core bore 007 were about 68.6 cm. The fuel rods were cut and twisted from the core-boring operation and exhibited





**86-513-22-30**

Figure C-10. Surface appearance of lower crust K09-P1.



**86-513-22-22**

Figure C-11. Ceramic particles in K09 core bore.



**86-513-5-29**

Figure C-12. Prior-molten control rod from core bore N12.

extensive ductility, as exhibited by the bent and twisted shapes. The fuel rod cladding did not exhibit much discoloration from oxidation. A plug from the peripheral crust lies above the fuel rods. This plug resembled the ceramic upper crust material. This core bore contained only a small amount of loose debris. The fuel rod damage and some of the small fuel fragments are shown in Figure C-13.

The surface of the plug from the peripheral crust is shown in Figure C-14. This crust was a coherent mass of ceramic material with metallics embedded in the cracks and crevices. The metallics have been smeared over the surface as a result of the core-boring operations.

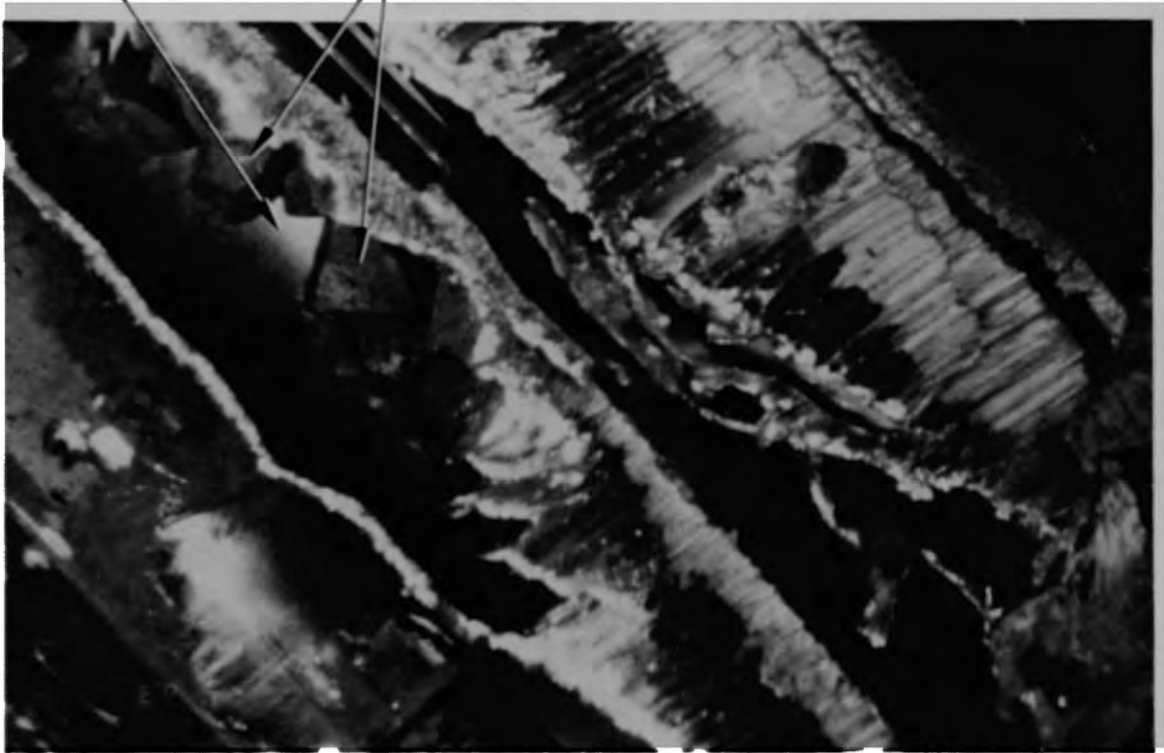
A large particle is shown in Figure C-15. This particle contains a number of metallic inclusions and folds or fissures in the ceramic phase.

#### Core Bore 009

The fuel rods in core bore 009 were about 165 cm long and were damaged from the core-boring operation. A few rods were cut, but more were bent and twisted, exhibiting ductility in the cladding. This core bore weighed 12.4 kg. A control rod that was previously molten is shown in Figure C-16.

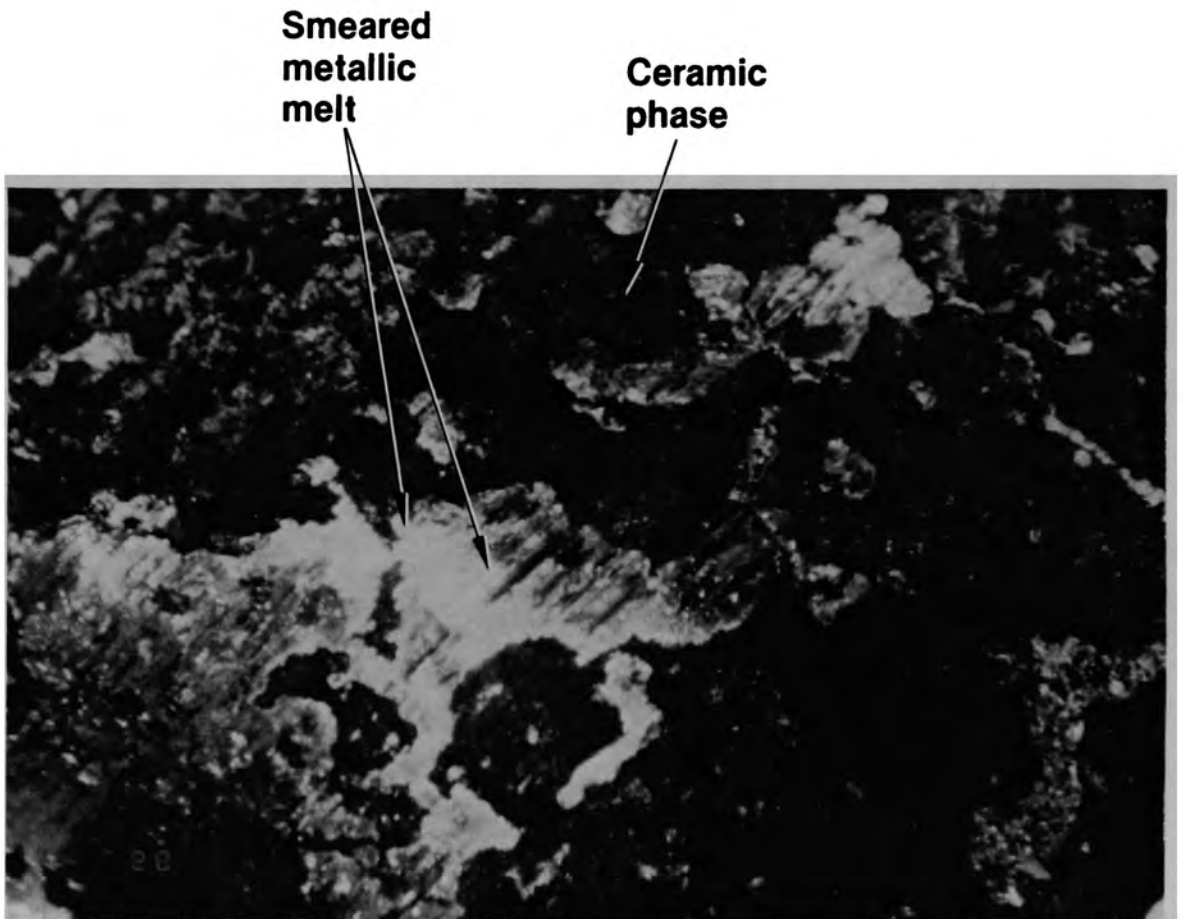
**Damaged  
cladding**

**Fuel  
fragments**



**86-513-13-17**

Figure C-13. Fuel fragments inside damaged fuel rod in core bore 007.



86-513-13-23

Figure C-14. Surface appearance of peripheral crust (007-P4).



**86-513-13-25**

Figure C-15. Particle from core bore 007.



86-513-7-26

Figure C-16. Melted material at tip of rod stub.



**APPENDIX D**

**DENSITIES OF SELECTED TMI-2 CORE BORE SAMPLES**



## APPENDIX D

### DENSITY DATA

The densities are listed in Table D-1 for 36 "rock-type" samples selected from the nine core bores, eight plugs from the lower, upper, and peripheral crusts, and 38 other samples that were obtained after the core-boring operations.

The densities varied from 5.45 g/cm<sup>3</sup> to 9.736 g/cm<sup>3</sup>. The lowest density is for a metallic particle containing large voids. The highest density is for a large plug sample from the upper crust. The measured densities reflect a broad range because the measured densities depend upon the composition (the amount of ceramic and metallic constituents and the composition of each of these phases) and the porosity. For specific types of samples, as determined from the metallographic examination, the density of metallic particles varied between 5.45 and 8.78 g/cm<sup>3</sup>; the density of the ceramic particles varied between 6.923 and 8.79 g/cm<sup>3</sup>, and the density for mixed metallic and ceramic particles varied between 7.63 and 9.08 g/cm<sup>3</sup>.

TABLE D-1. DENSITY OF SELECTED SAMPLES

Sample ID	Weight (g)	Density (g/cm <sup>3</sup> )
D04-P2-A	19.06	8.93
D04-P2-C	6.16	9.38
D08-P1	632.27	7.25
D08-P2	494.25	7.56
D08-P3	746.75	9.73
D08-P4-A	67.35	8.67
D08-P4-C	36.98	7.77
F6-P1	936.30	7.51
F6-P2	794.70	7.30
F6-P3	539.80	7.72
F6-P4	222.62	7.27
F6-P5	198.91	7.30
F6-P6	75.17	7.30
F6-P7	52.08	7.40
F6-P8	45.56	7.52
F6/H8-P1	1901.00	7.69
F6/H8-P2	638.40	7.50
F6/H8-P3	223.86	6.61
F6/H8-P4	262.05	7.51
F6/H8-P5	178.09	6.52
F6/H8-P6	201.54	6.72
F6/H8-P7	189.23	7.94
F6/H8-P8	144.24	8.53
F6/H8-P9	121.36	6.51
F6/H8-P10	109.48	6.94
G08-P11	1847.53	8.24
G08-P4-A	55.52	7.71
G08-P5-B	116.06	7.96
G08-P6-A	20.46	7.69
G08-P6-B	153.62	7.62
G08-P7-A	193.84	7.35
G08-P7-C	36.10	8.79
G08-P8-A	114.26	7.40
G08-P9-A	158.94	7.38
G08-P10-A	263.78	8.24
G12-P1	520.80	7.56
G12-P2-B	60.54	8.46
G12-P2-D	40.54	8.32
G12-P3-A	45.02	7.70
G12-P4-A	90.48	7.75
G12-P8-B	48.51	7.66
G12-P9-A	131.45	7.63
H9/K9-P1	86.17	7.98
H9/K9-P2	54.13	7.06
H9/K9-P3	21.08	7.89
H9/K9-P4	26.12	7.73
H9/K9-P5	30.57	7.00

TABLE D-1. (continued)

Sample ID	Weight (g)	Density (g/cm <sup>3</sup> )
H9/K9-P6	74.01	8.09
H9/K9-P7	23.77	7.47
H9/K9-P8	27.48	7.12
H9/K9-P9	24.04	7.29
H9/K9-P10	25.67	7.89
K09-P1-A	1306.54	7.31
K09-P2	912.98	7.86
K09-P3-A	55.15	7.56
K09-P3-D	43.17	7.44
K09-P3-F	26.03	7.78
K09-P3-I	23.22	7.52
K09-P3-M	40.98	7.49
K09-P4-A	10.28	7.13
K09-P4-B	23.90	7.41
K09-P4-D	60.69	6.92
K09-P4-H	37.68	6.65
M11-P1	1671.00	7.47
M11-P2	1075.30	7.63
M11-P3	264.60	7.99
M11-P4	104.80	7.28
M11-P5	91.30	7.85
M11-P6	70.80	7.79
M11-P7	60.00	8.17
M11-P8	55.90	8.19
M11-P9	49.20	7.86
M11-P10	62.70	8.44
N05-P1-A	9.85	7.97
N05-P1-D	34.90	8.27
N05-P1-H	21.65	9.08
N12-P1-B	0.66	8.86
O07-P1-A	4.09	7.61
O07-P4	732.58	8.78
O07-P6	75.65	5.45
O09-P1-A	29.61	6.90
O09-P1-B	20.05	7.21



APPENDIX E  
OPTICAL METALLOGRAPHY AND SEM DATA





## APPENDIX E

### OPTICAL METALLOGRAPHY AND SEM DATA

This appendix provides additional details from the metallographic and scanning electron microscope examinations of the nine core bores obtained from the TMI-2 reactor. These results serve to further illustrate the points that were made in Section 3, by providing additional representative photographs of the various regions. A perspective of the locations of these samples is provided in Figure E-1, which shows the end state configuration of the TMI-2 reactor. Samples were obtained from the lower, upper, and peripheral regions of the crust, as well as from the previously molten core region contained within the crust, and the intact region below the lower crust.

#### Lower Crust

##### D08-P1

A photograph of the D08-P1 plug from the lower crust is shown in Figure E-2. The crust sample was 5.1 cm long and 6.4 cm in diameter. The plug weighed 631.77 g and had a density of  $7.00 \text{ g/cm}^3$ . The circumference of the plug contained appreciable metallic material that was smeared over most of the surface, apparently as a result of the core boring operation. An enlarged view of the surface of this sample is provided in Figure E-3. This photograph shows fuel pellets surrounded by an agglomeration of previously molten material.

The sectioning scheme for this plug is shown in Figure E-2. A 0.64-cm thick transverse cross section was first taken from the top end. Half of the plug was then cut into longitudinal slices designated as B, C, and D. The other half of the plug was cut into two quarter sections designated as E and F. Section C was used for radiochemical analyses, and Section D was metallographically examined at the INEL. The other sections were held for examinations by the organizations shown in Figure E-2.

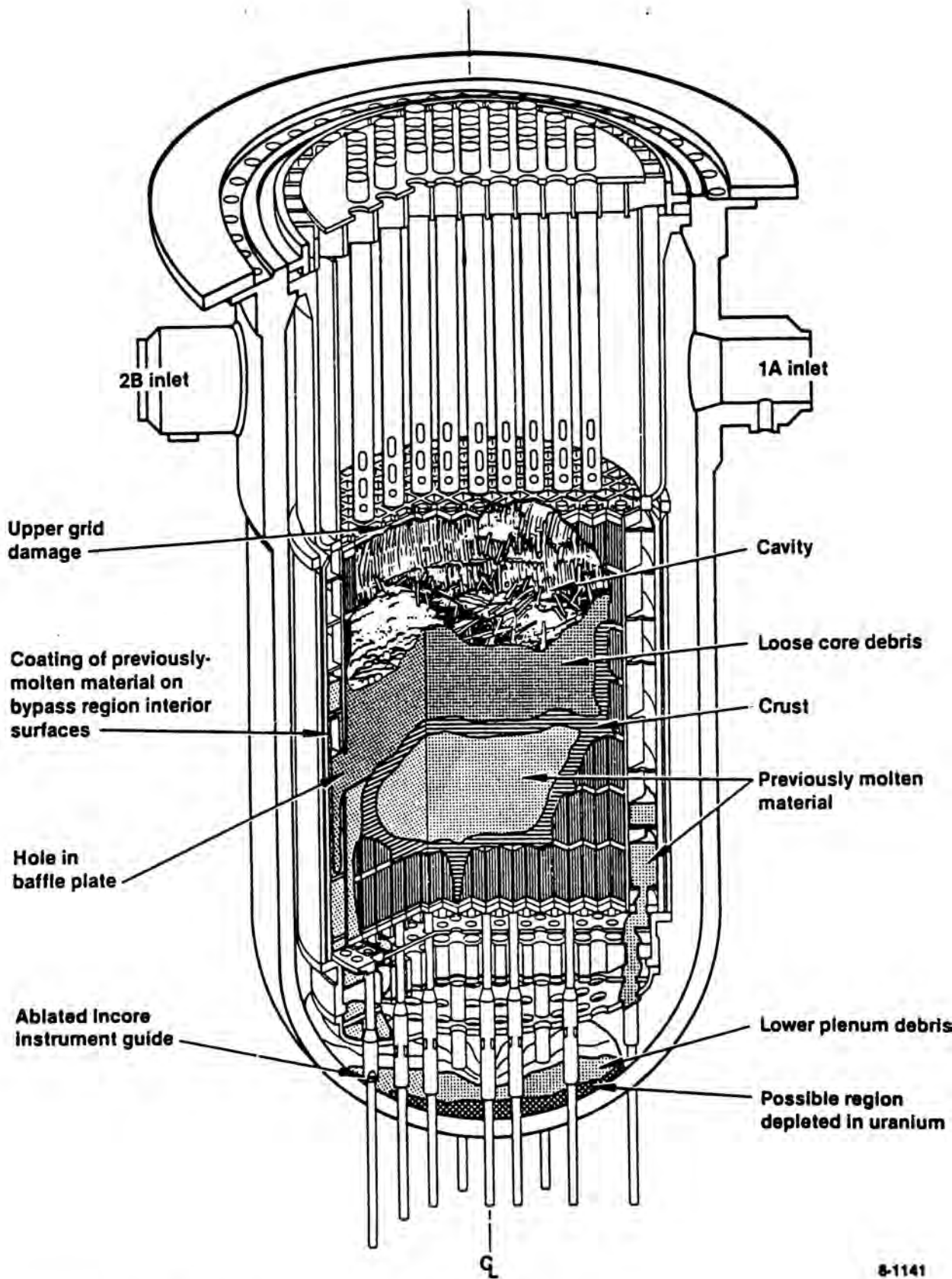


Figure E-1. TMI-2 core end-state configuration.

- A - Germany-KFK
- B - ANL
- C - INEL Rad Chem
- D - INEL Met
- E - France
- F - Canada

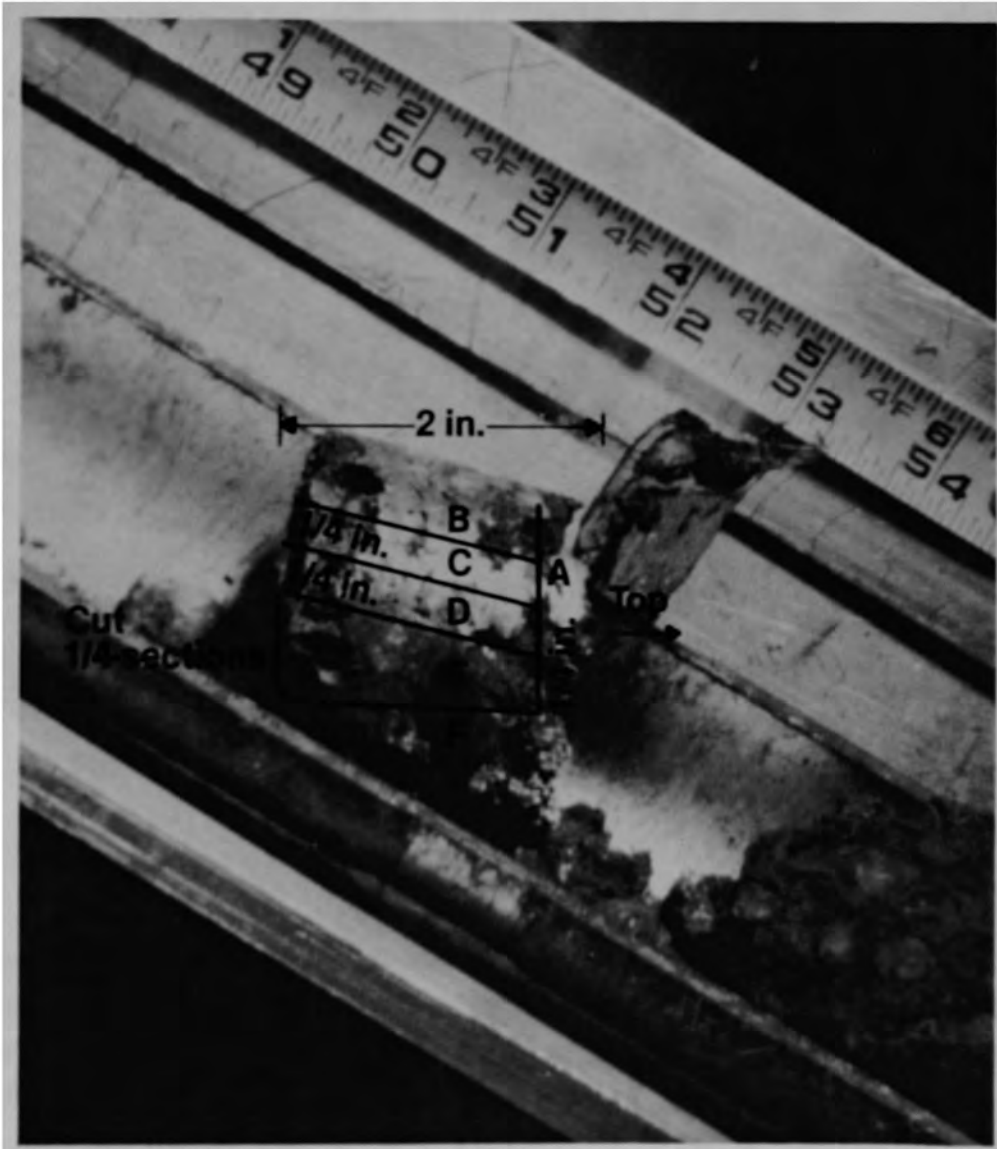
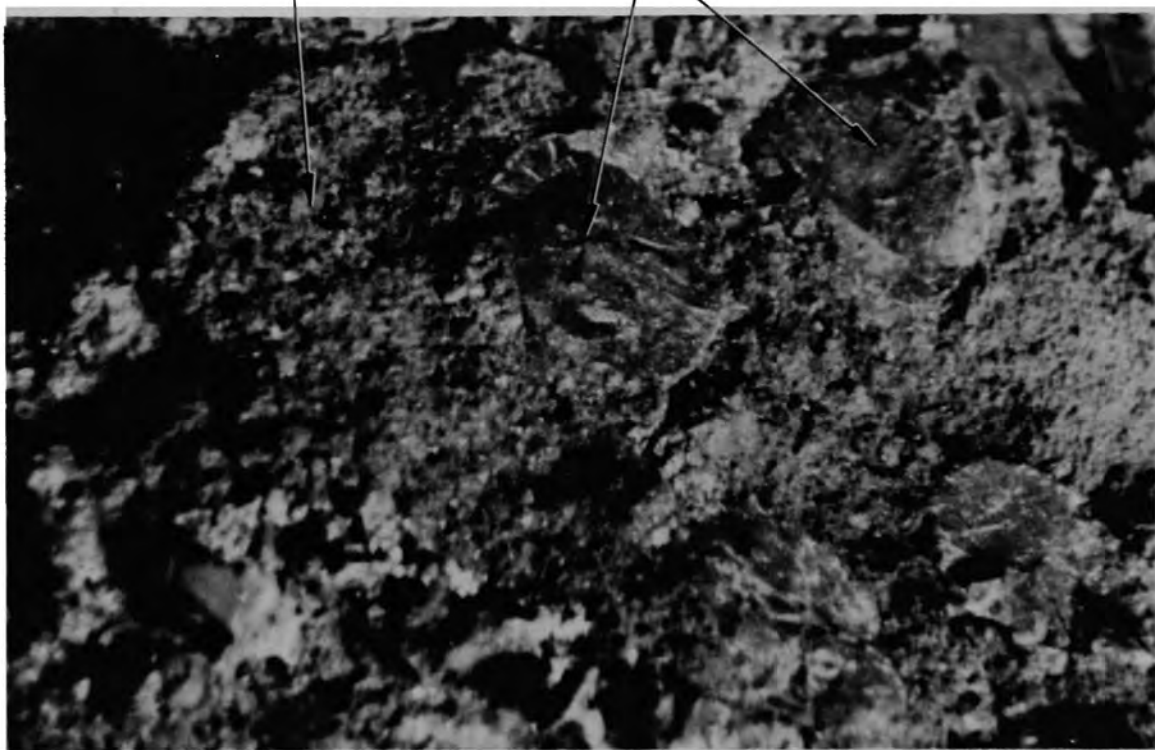


Figure E-2. Sectioning diagram for lower crust sample D08-P1.

**Previously  
molten  
material**

**Fuel  
pellets**



**86-513-21-7**

Figure E-3. Enlarged view of the surface of lower crust sample D08-P1.

The as-cut transverse section D08-P1-A is shown in Figure E-4. It shows an agglomerate of fuel pellets surrounded by prior-molten material, similar to Figure E-3. The melt appears to be a mixture of ceramic and metallic melts.

The as-polished longitudinal cross section of D08-P1-D is shown in Figure E-5. This cross section contained two recognizable fuel pellets surrounded by prior molten material. The zircaloy cladding had been liquefied by the metallic melt.

The typical fuel structure is shown in Figure E-6. The  $UO_2$  grain size was about 6  $\mu m$ , and grain boundary separation had occurred. This separation resulted in the subsequent pullout of grains during the preparation of this sample. The grain boundary separation may have been caused by reduction of the fuel by the surrounding metallic melt, which would have resulted in hypostochiometric  $UO_2$  and liquid uranium metal along the grain boundaries. Figure E-7 shows a fuel pellet remnant that has apparently been partially liquefied by the surrounding metallic melt, as evidenced by the irregular surface.

Typical microstructures in the metallic melt are presented in Figures E-8 and E-9. These microstructures consisted of both single phase melt globules and laminar eutectic structures. SEM examinations were not conducted on the samples to provide elemental analysis, but the metallic melts were most likely composed of various mixtures of the structural components (Zr, Fe, Cr, Ni, Ag, and In).

#### D08-P2

A photograph of lower crust sample D08-P2 is shown in Figure E-10. The crust sample was 3.8 cm long and 6.4 cm in diameter. This plug weighed 494.29 g and had a density of 7.6 g/cm<sup>3</sup>. Although this plug was located above D08-P1, it is believed to be a part of the lower crust because it was also an agglomerate of fuel pellets embedded in prior-molten metallic and ceramic phases. From the combined lengths of D08-P1 and D08-P2, the thickness of the bottom crust was estimated to be 8.9 cm.

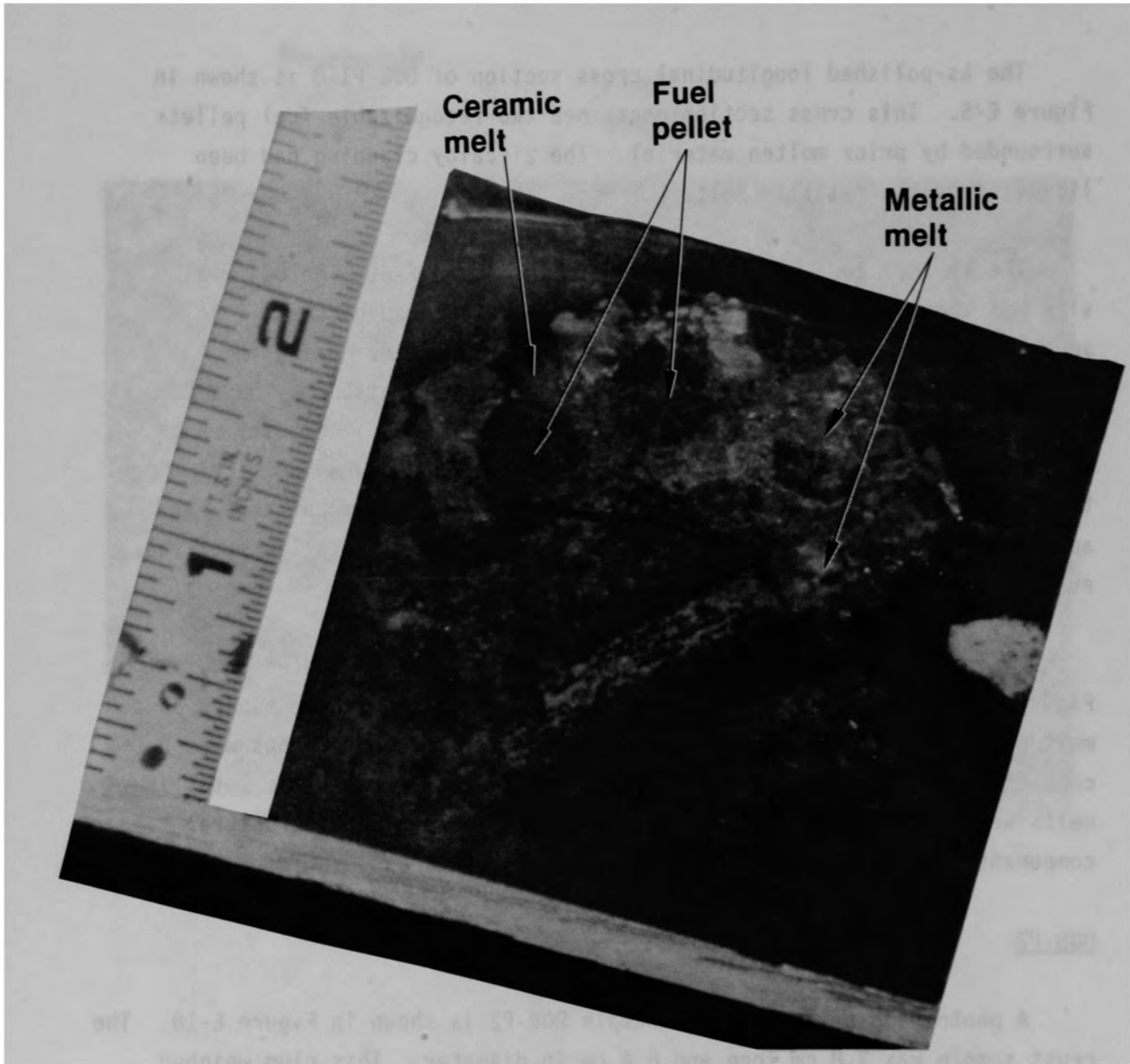
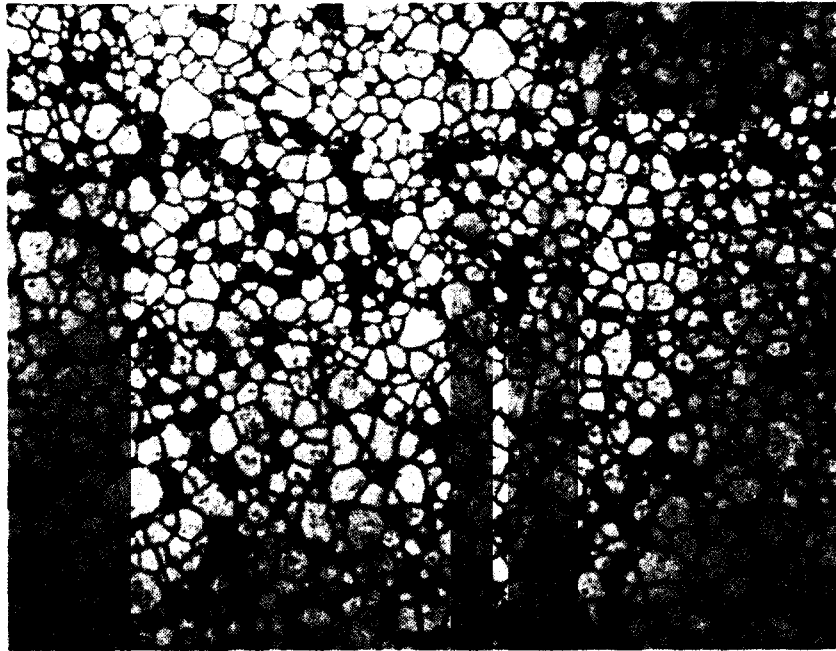


Figure E-4. As-cut transverse section D08-P1-A.



Figure E-5. Longitudinal cross section D08-P1-D from lower crust.



20  $\mu\text{m}$

Fuel etch

87M-875

Figure E-6. Grain boundary separation in fuel pellet in D08-P1-D.



[[ 3 ]]

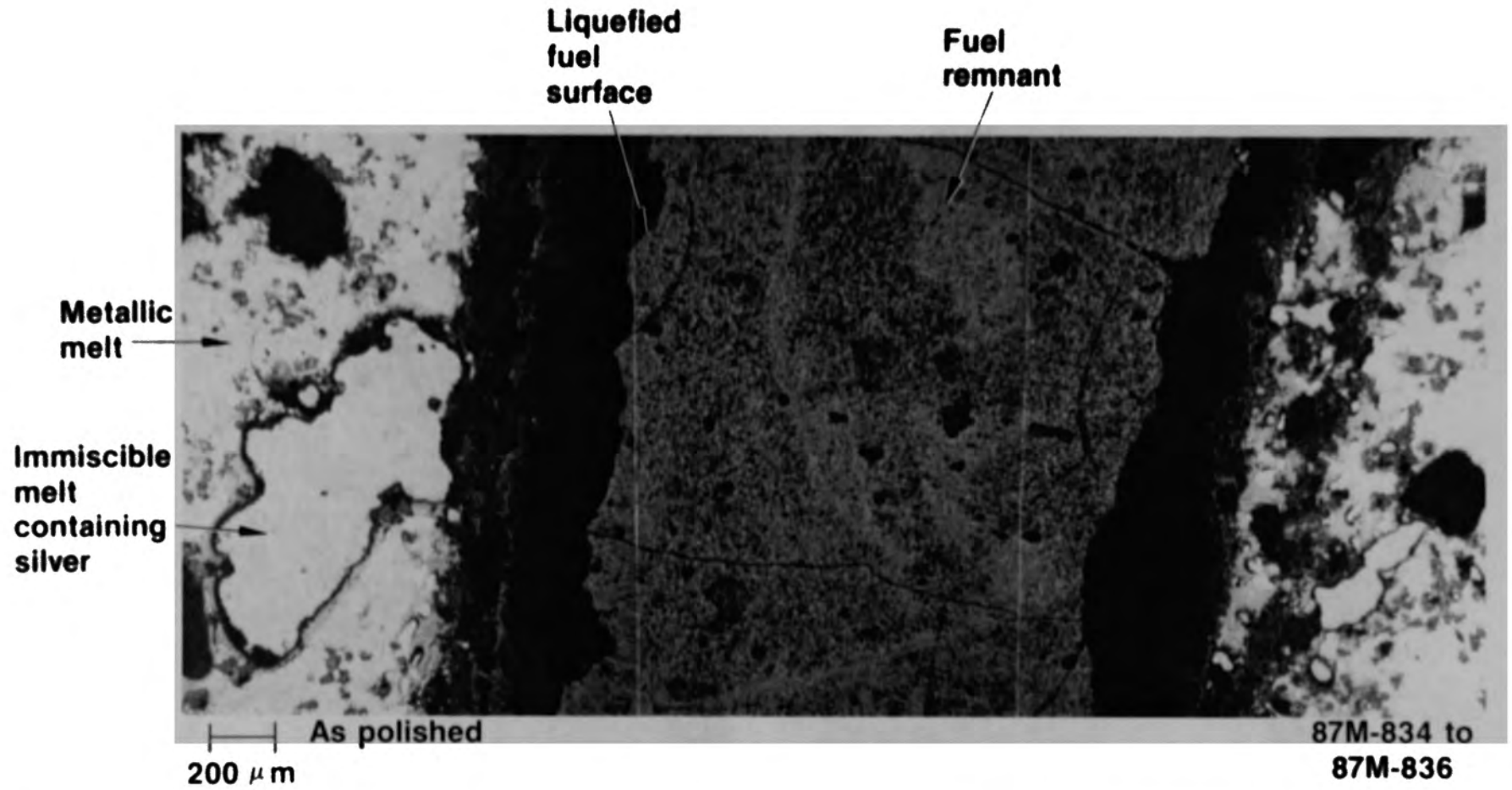


Figure E-7. Partially liquefied fuel pellet in lower crust sample D08-P1-D.

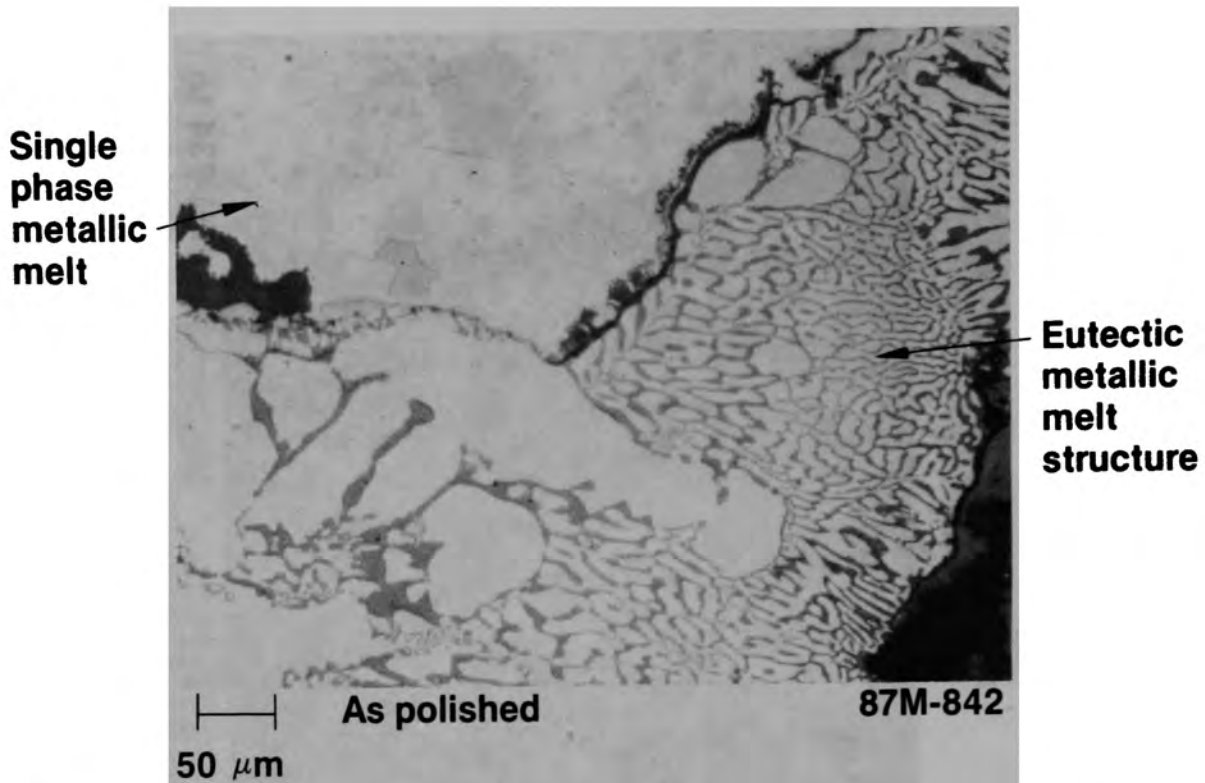


Figure E-8. Various metallic melt structures at surface of metallic globule in lower crust (D08-P1-D).

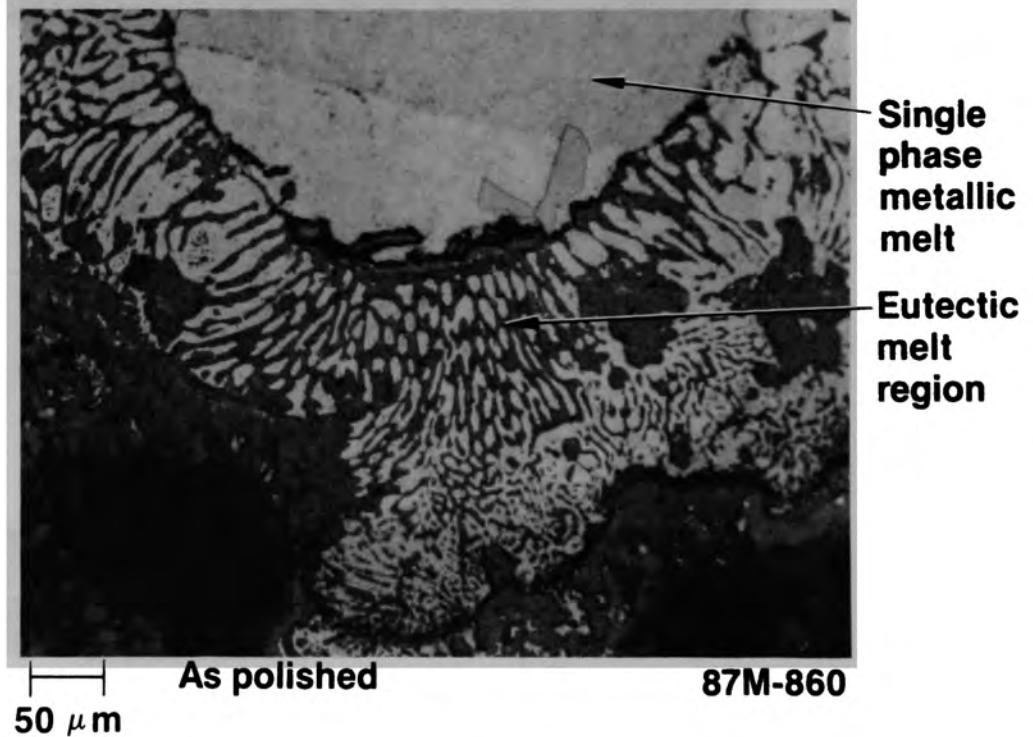
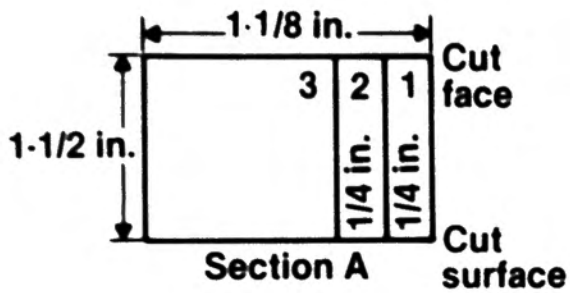


Figure E-9. Laminar eutectic metallic melt structure at surface of metallic inclusion in lower crust (D08-P1-D).



- A-1 - INEL Rad Chem
- A-2 - INEL Met
- A-3 - Germany-JRC
- B - Germany-JRC
- C - Japan
- D - Japan
- E - Korea

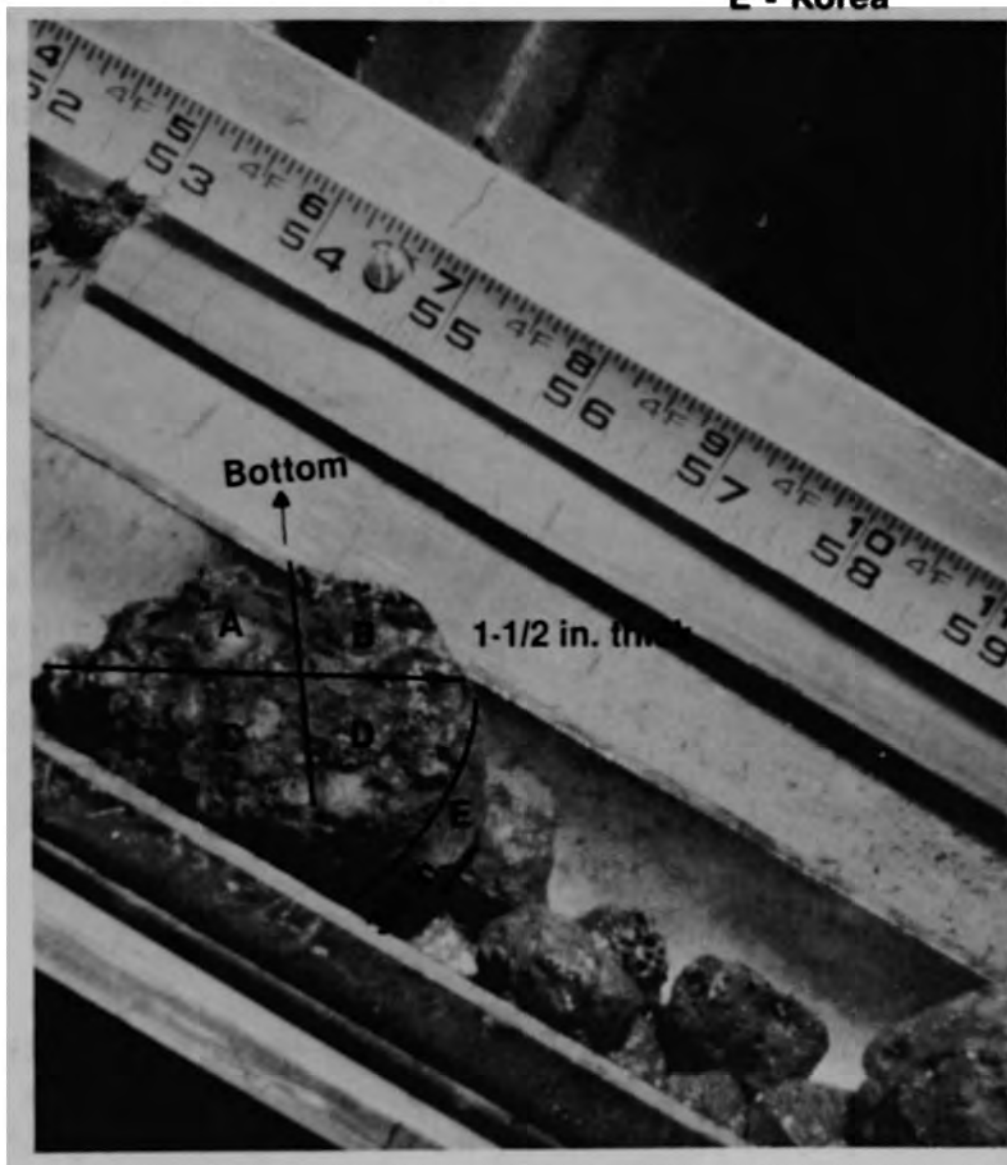


Figure E-10. Overview of D08-P2 lower crust sample.

The sectioning diagram for this plug is provided in Figure E-10. A 0.95-cm thick transverse cross section was obtained from the top end to show a complete view of the plug. The remainder of the sample was then cut into four quarter sections, and from one of these quarter sections (Section A) two 0.64-cm pie-shaped wafers were cut. Section A-1 was used for radiochemical analyses, and Section A-2 was used for metallographic examination.

A transverse section of D08-P2-E, shown in Figure E-11, reveals an agglomerate of fuel pellets embedded in a prior molten mixture of ceramic and metallic phases. The structure appears very similar to that which was observed on transverse section D08-P1-A (Figure E-4).

The as-polished transverse cross section from quarter section D08-P2-A2 is shown in Figure E-12. This cross section shows the remnants of three fuel pellets embedded in a matrix of predominately metallic melt and the locations where further detailed metallographic examinations were conducted.

Metallographic examination of Area 1 indicated that the cladding had oxidized and reacted with the fuel (Figure E-13). The interaction zone is indicated by the region containing the large amount of porosity adjacent to the  $ZrO_2$ . Metallic melt had flowed into the cracks in the fuel pellets and completely filled voids in the ceramic fuel. This metallic melt was primarily a single phase solid solution, which contained areas of immiscible metallic melts; however, two phase metallic melt structures and some ceramic melt were observed in Area 2 of this sample (Figure E-14). The composition of these phases was not determined.

#### K09-P1

The photograph of the lower crust sample from central core position K09 is shown in Figure E-15. The crust sample was 8.6 cm long and 6.4 cm in diameter. This plug weighed 1302.59 g, and the density was  $7.21 \text{ g/cm}^3$ .

The sectioning diagram for the plug is shown in Figure E-15. A 1.27-cm thick transverse cross section was taken from the top end to show a complete view of a cross section of this plug. Half of the remaining sample was then

E-15

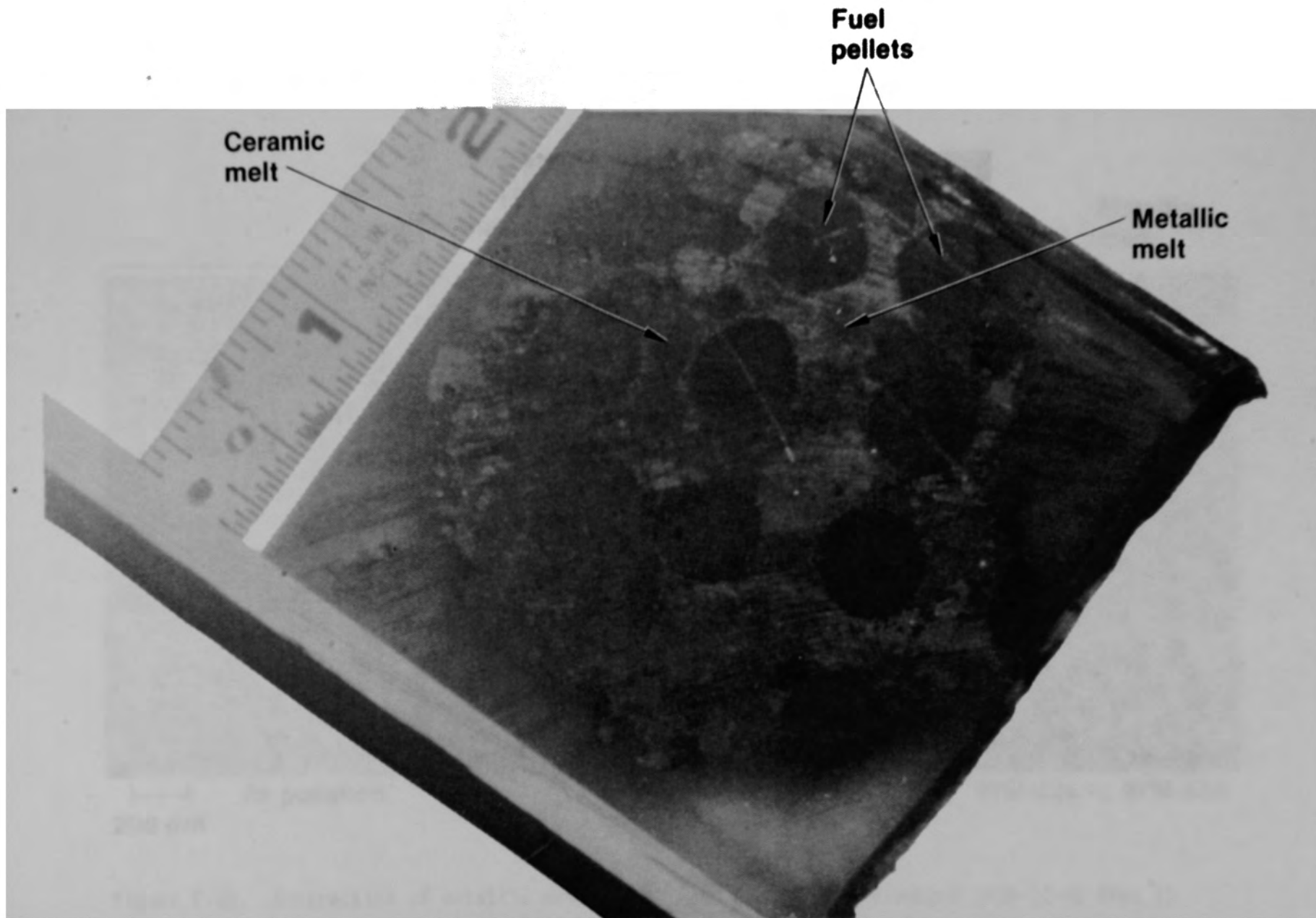


Figure E-11. As-cut transverse section D08-P2-E from the lower crust.



Figure E-12. As-polished transverse section D08-P2-A2.

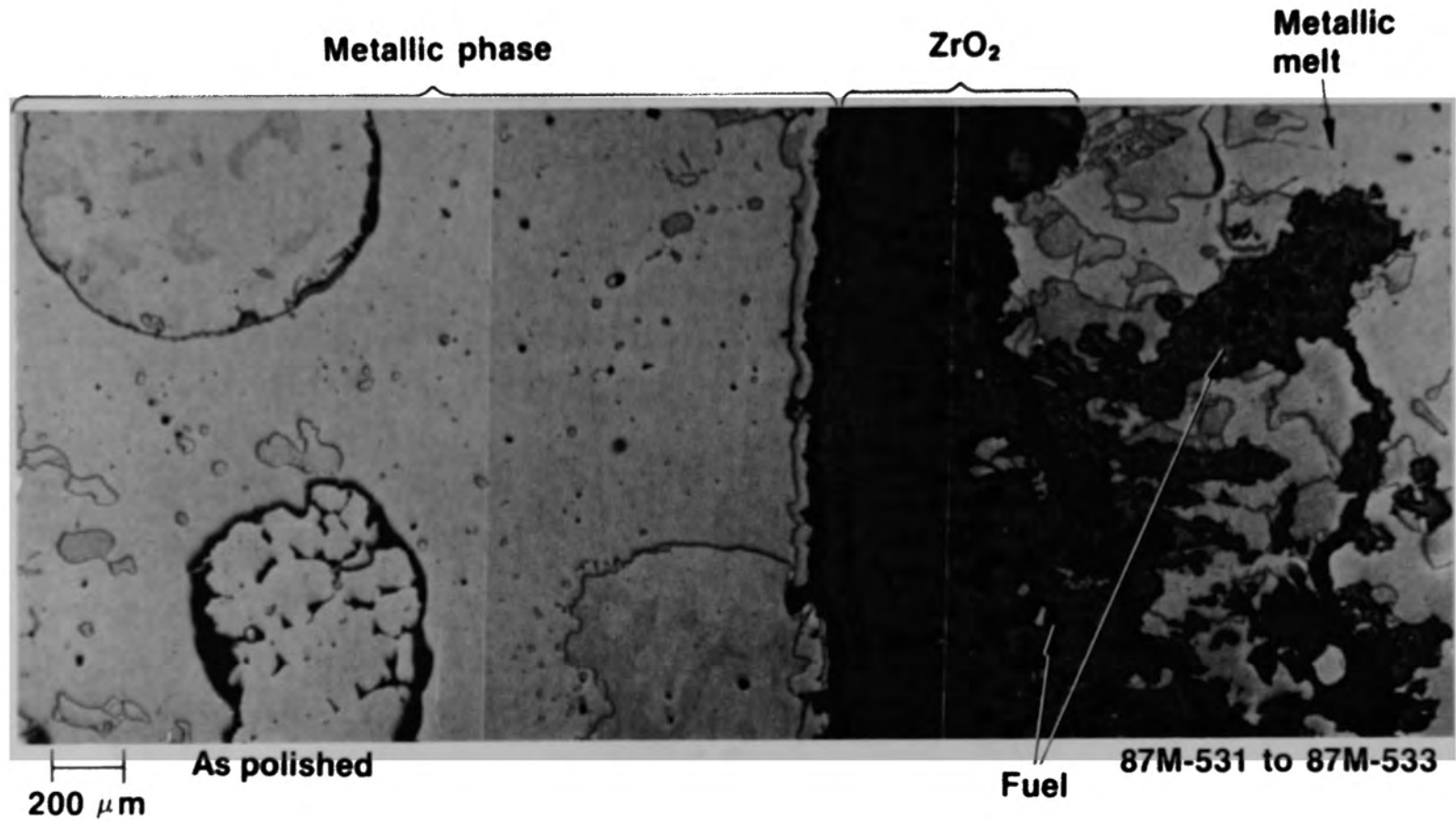


Figure E-13. Interaction of metallic melts with fuel and oxidized cladding (D08-P2-A2 Area 1).

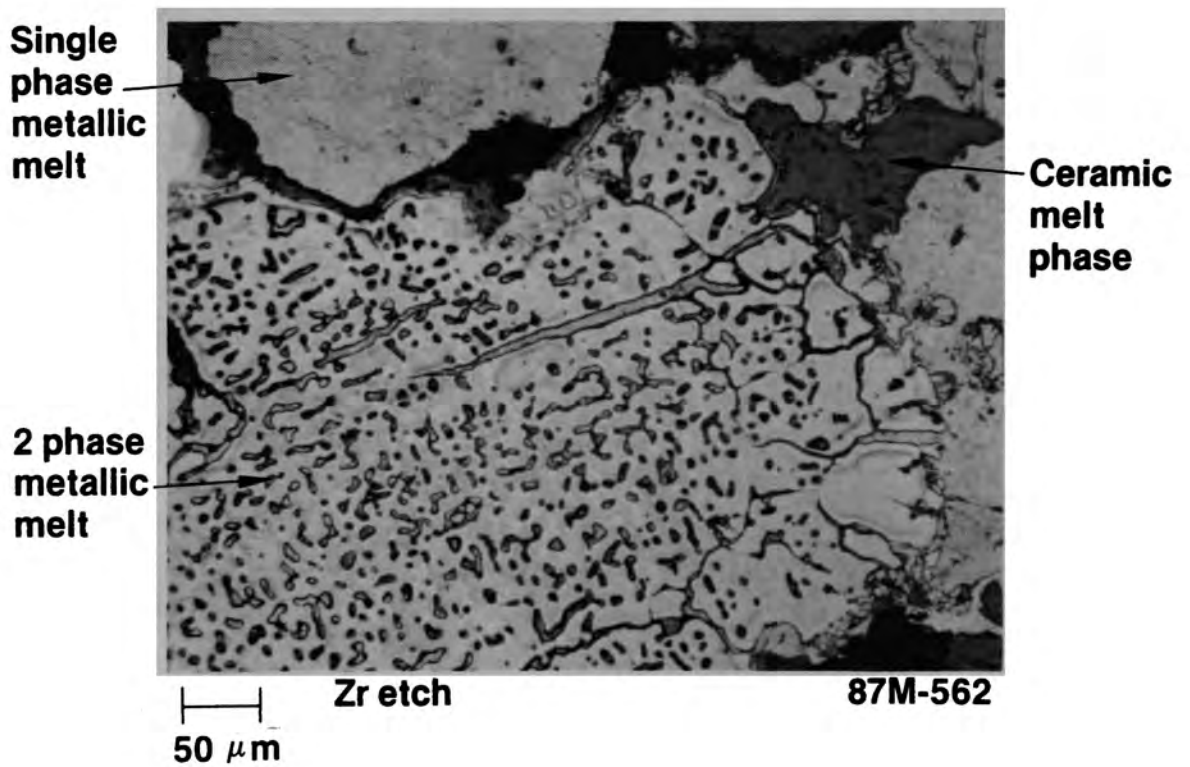


Figure E-14. Typical structures of prior molten metallic melt (D08-P2-A2 Area 2).



- A - Canada
- B - United Kingdom
- C - Rad Chem; Korea
- D - INEL Met
- E - ANL
- F - Germany-KFK
- G - Met
- H - Rad Chem

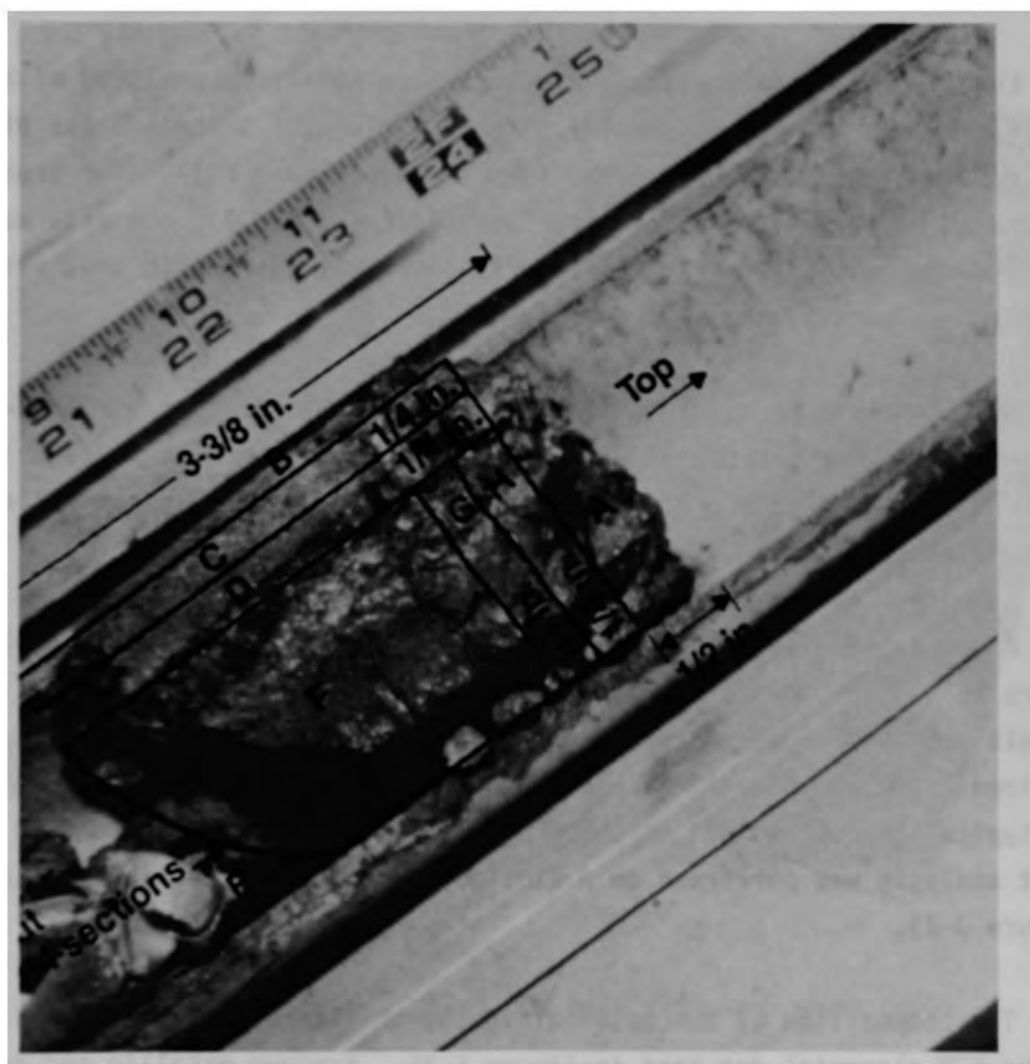


Figure E-15. Overview of K09-P1 lower crust sample.

cut into longitudinal slices designated as B, C, and D. The other half of the sample was cut into two quarter sections, and from one of these sections two 0.64-cm thick wafers were cut (Sections G and H). Sections D and G were used for metallographic examinations; Sections H and a portion of section C were used for radiochemical analyses, with most of section C being allocated for Korea.

The transverse section (K09-P1-A) shows an agglomerate of prior molten material surrounding fuel pellets (Figure E-16). It is very similar to transverse sections through the D08 lower crust samples.

Longitudinal metallographic cross section K09-P1-D consisted of a metallic melt surrounding intact fuel pellet stacks. Several areas of this sample were examined in detail, as indicated in Figure E-17. Two areas were located at axial pellet/pellet interfaces (Areas 1 and 2); one area was in the flow channel between two fuel stacks (Area 3); the fourth area was in a region where most of the fuel was gone.

Small samples were also drilled from this cross section for SEM/WDS examinations. The microcores were obtained from the locations shown in Figure E-18; however, microcore K09-P1-D5 was not examined because the microstructure was similar to K09-P1-D4.

An enlarged view of Area 1 at the pellet/pellet interface is shown in Figure E-19. The melt flowed into the dished interfaces between the fuel pellets and into cracks in the fuel. The melt adjacent to the fuel was oxidized. Small precipitates of fuel were present in the metallic melt, and the typical microstructure of these particles is shown in Figure E-20. WDS point analysis was performed on a similar area as described in Appendix J (Figure J-7).

The composition of the material in the pellet/pellet interface is shown in the SEM elemental dot maps in Figure E-21. Various metallic and ceramic phases consisting of complex mixtures of Zr, Sn, Fe, Cr, Ni, U, and O were present. Ag and In were present as an immiscible metallic melt phase. WDS point analysis was also performed in these areas as described in Appendix J (Figure J-8).

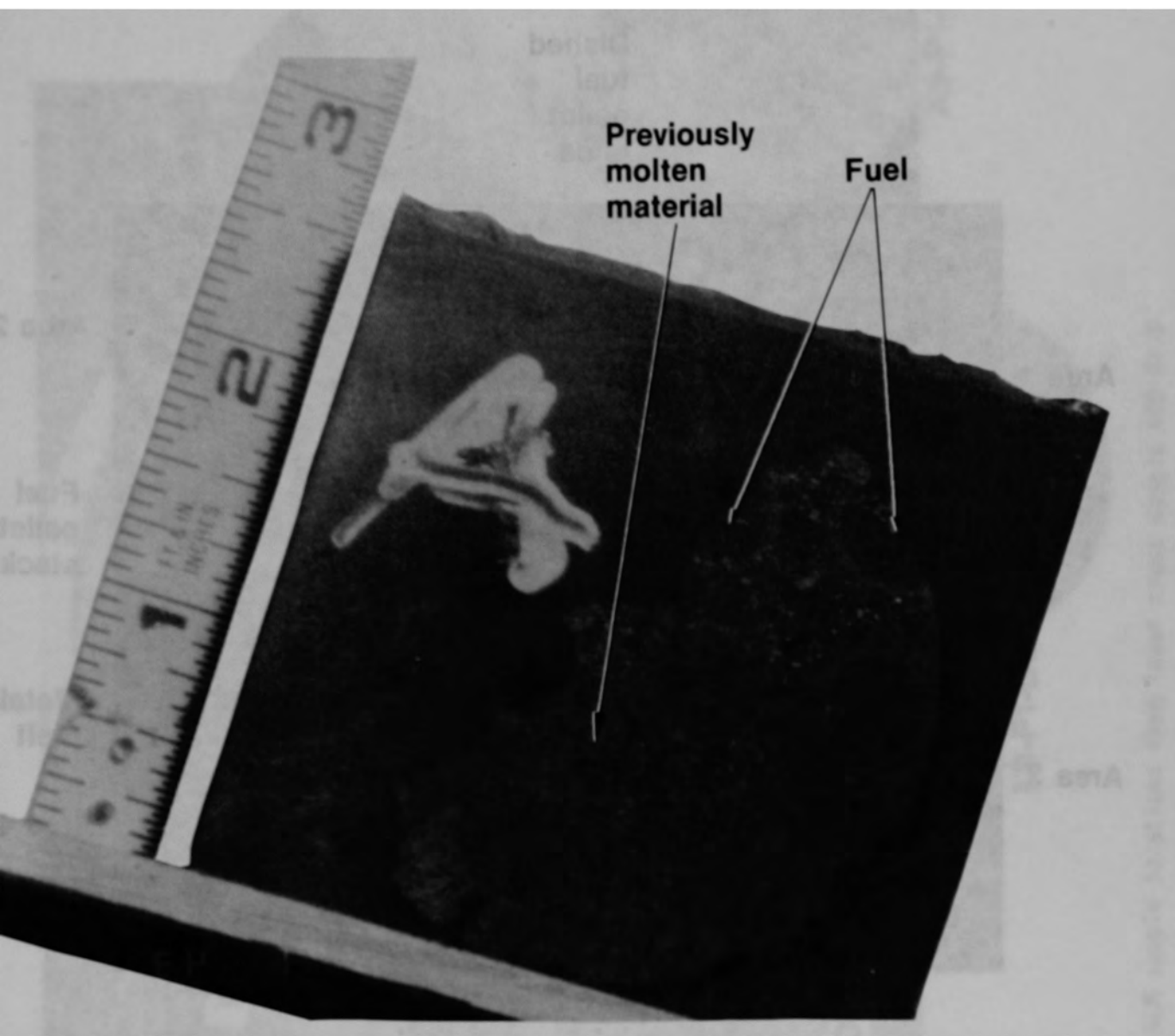


Figure E-16. As-cut transverse section K09-P1-A from the lower crust.

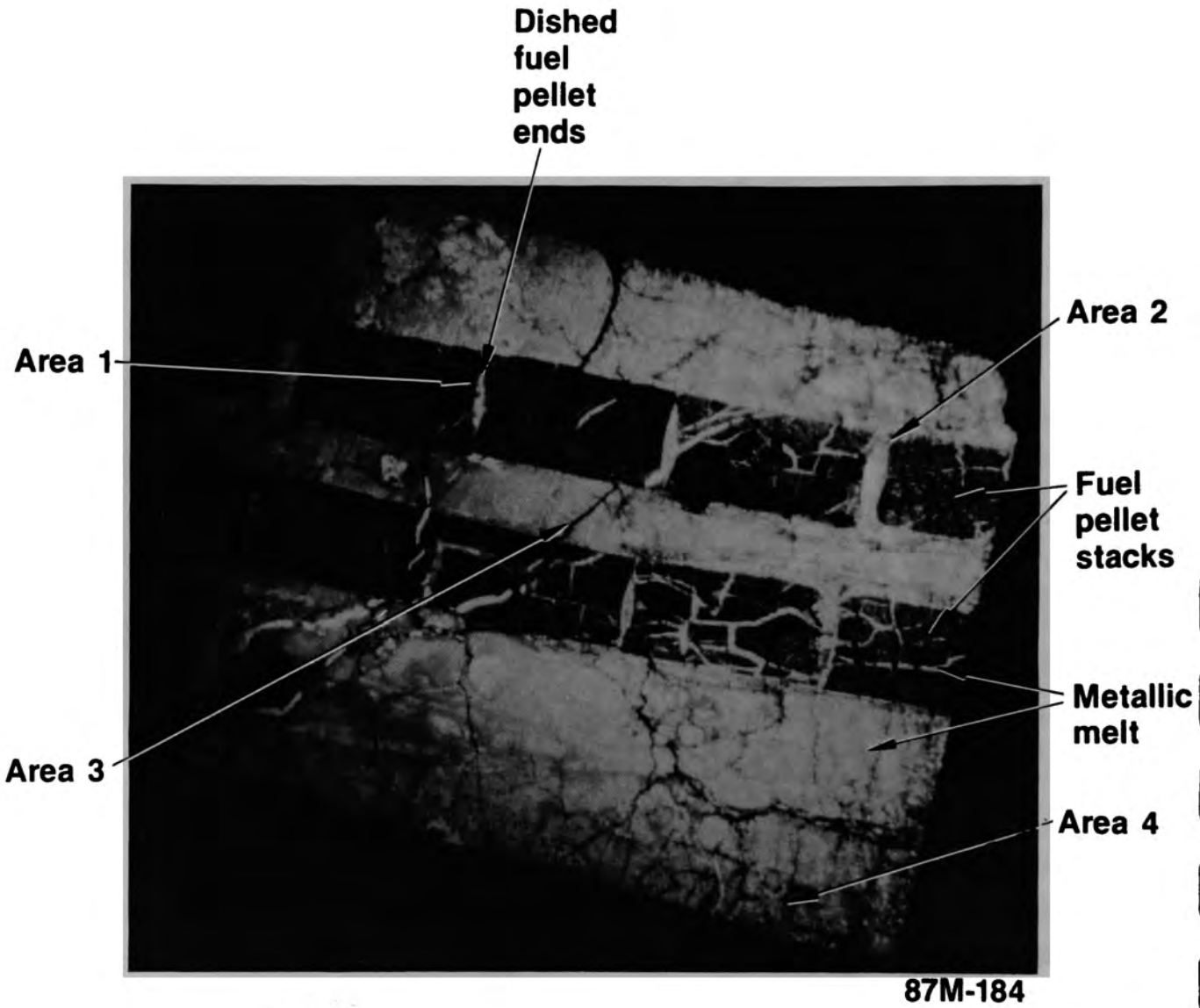


Figure E-17. Metallic melt surrounding fuel pellet stacks in lower crust (K09-P1-D).

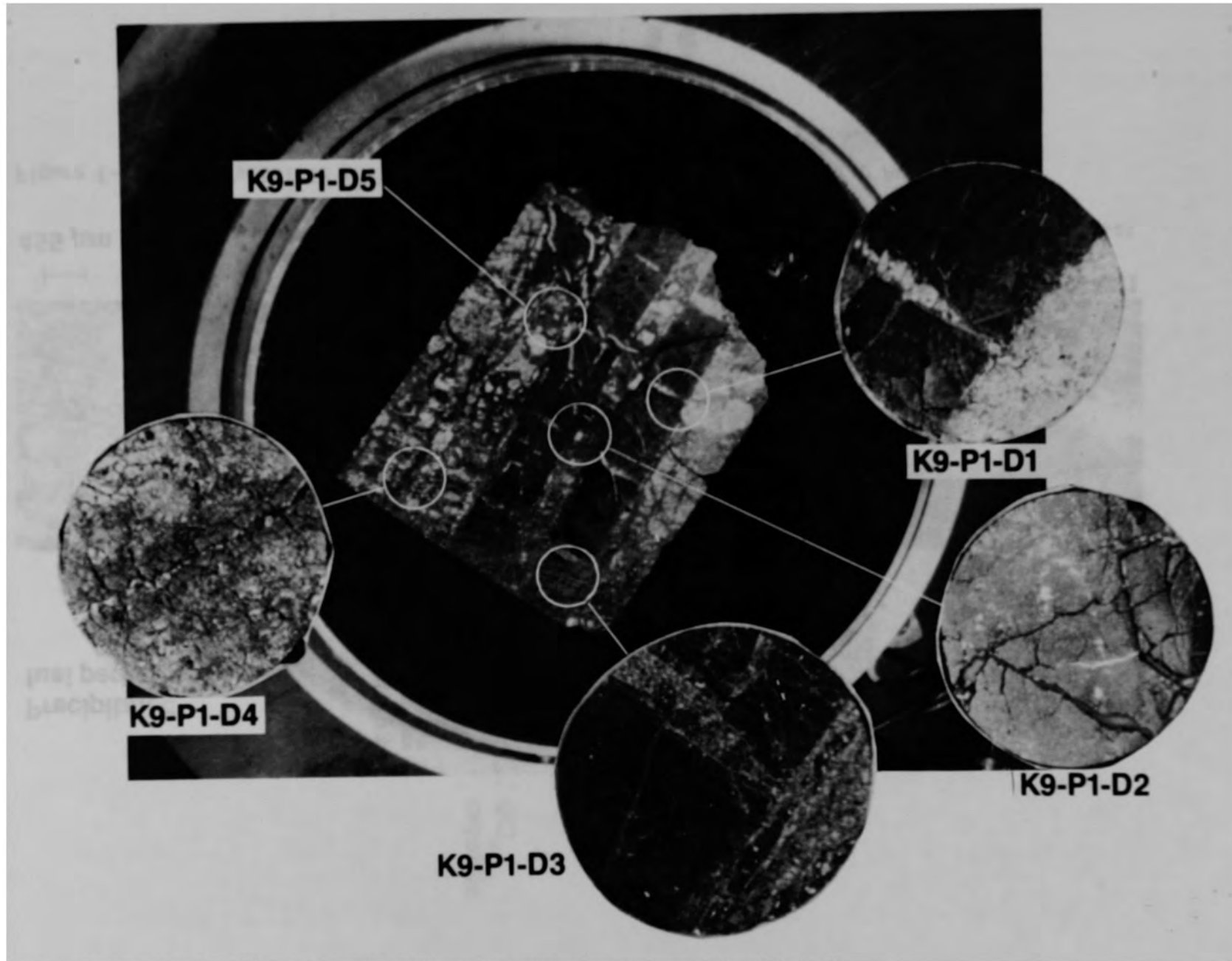


Figure E-18. SEM sample locations from lower crust sample K09-P1-D.

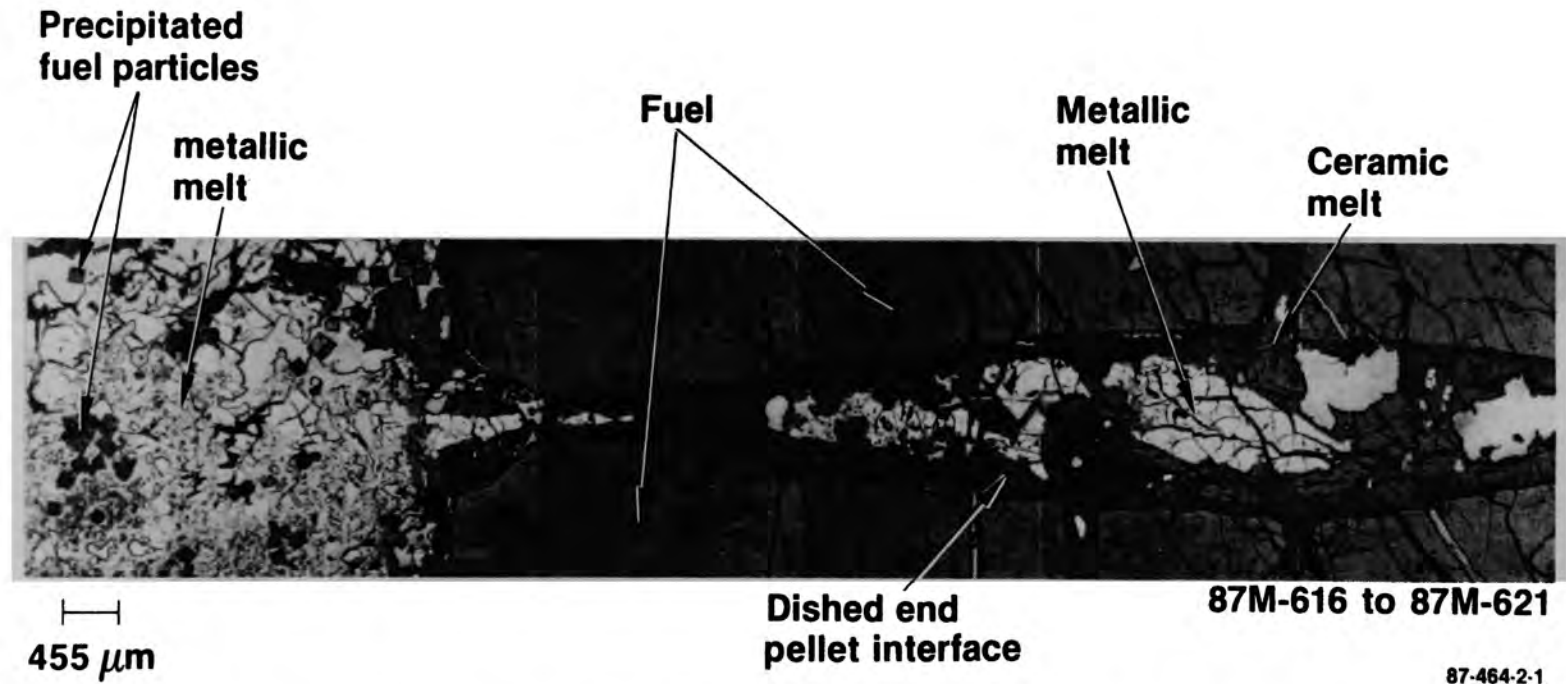


Figure E-19. Fuel/metallic melt interaction at dished interface (K09-P1-D Area 1).

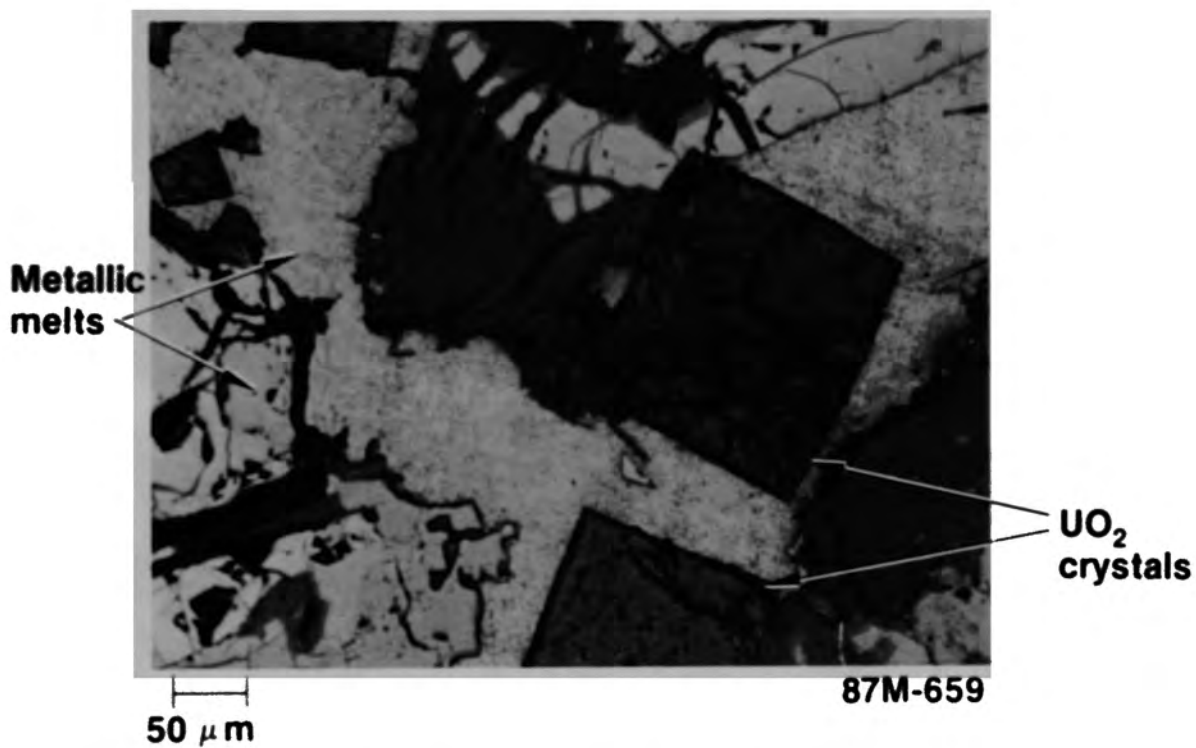


Figure E-20. Recrystallized UO<sub>2</sub> crystals in metallic melt (K09-P1-D1).

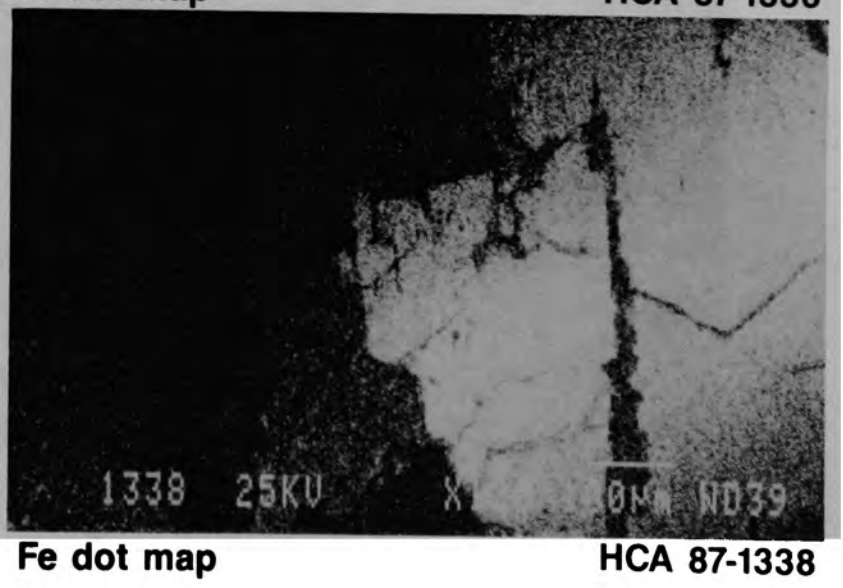
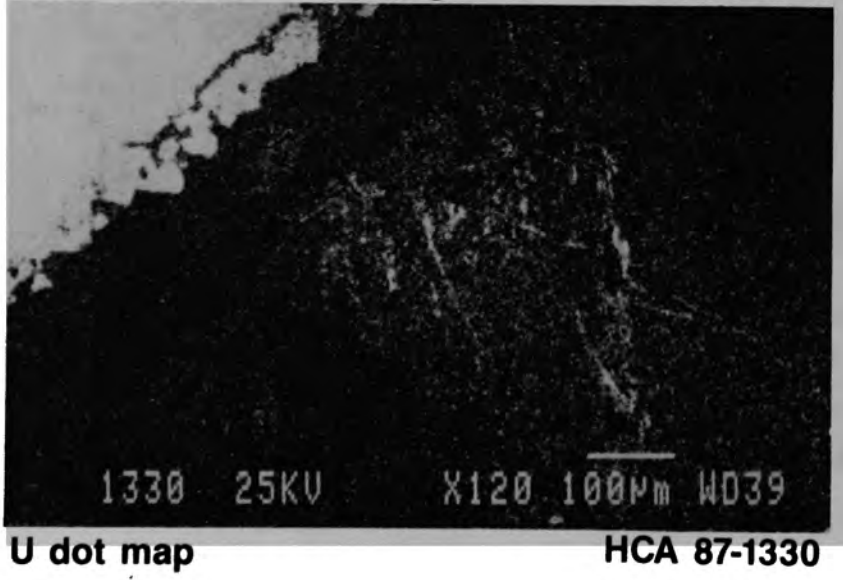
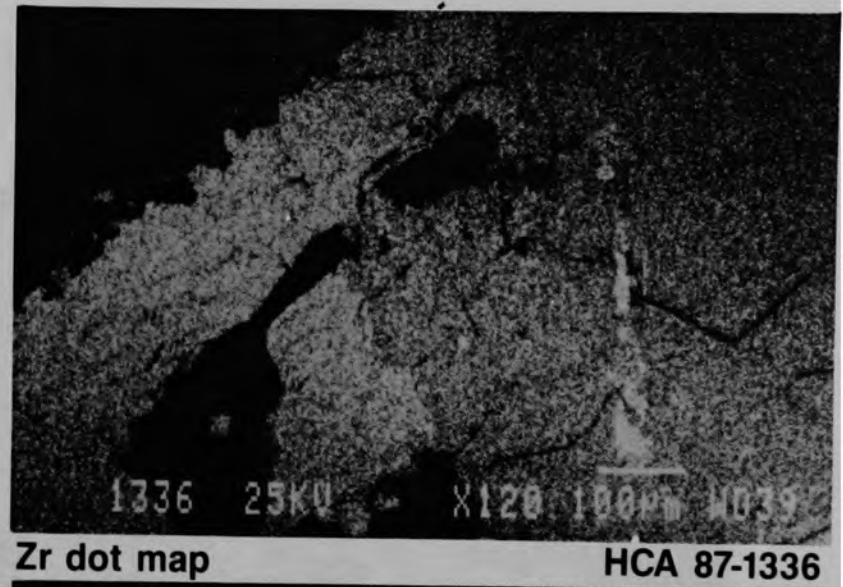
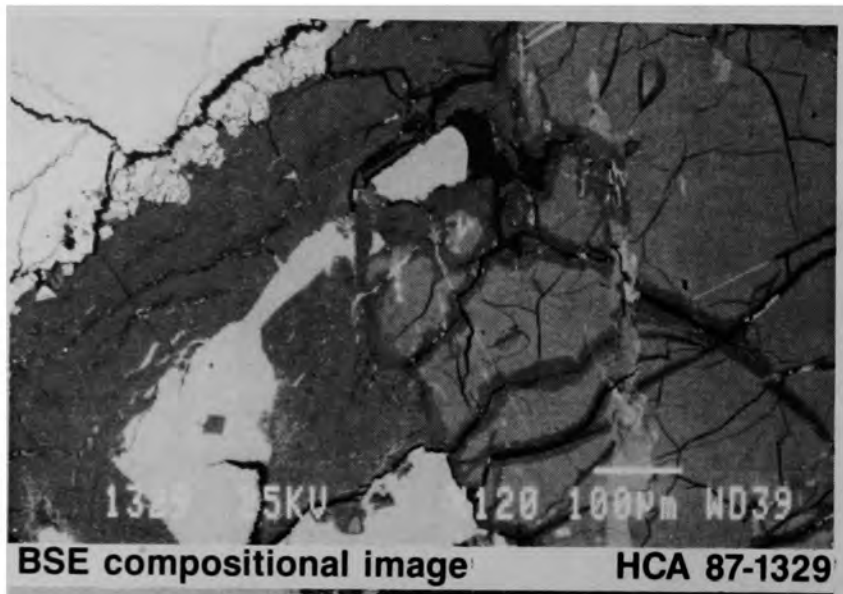


Figure E-21. Material interactions in pellet/pellet interface (K09-P1-D1).



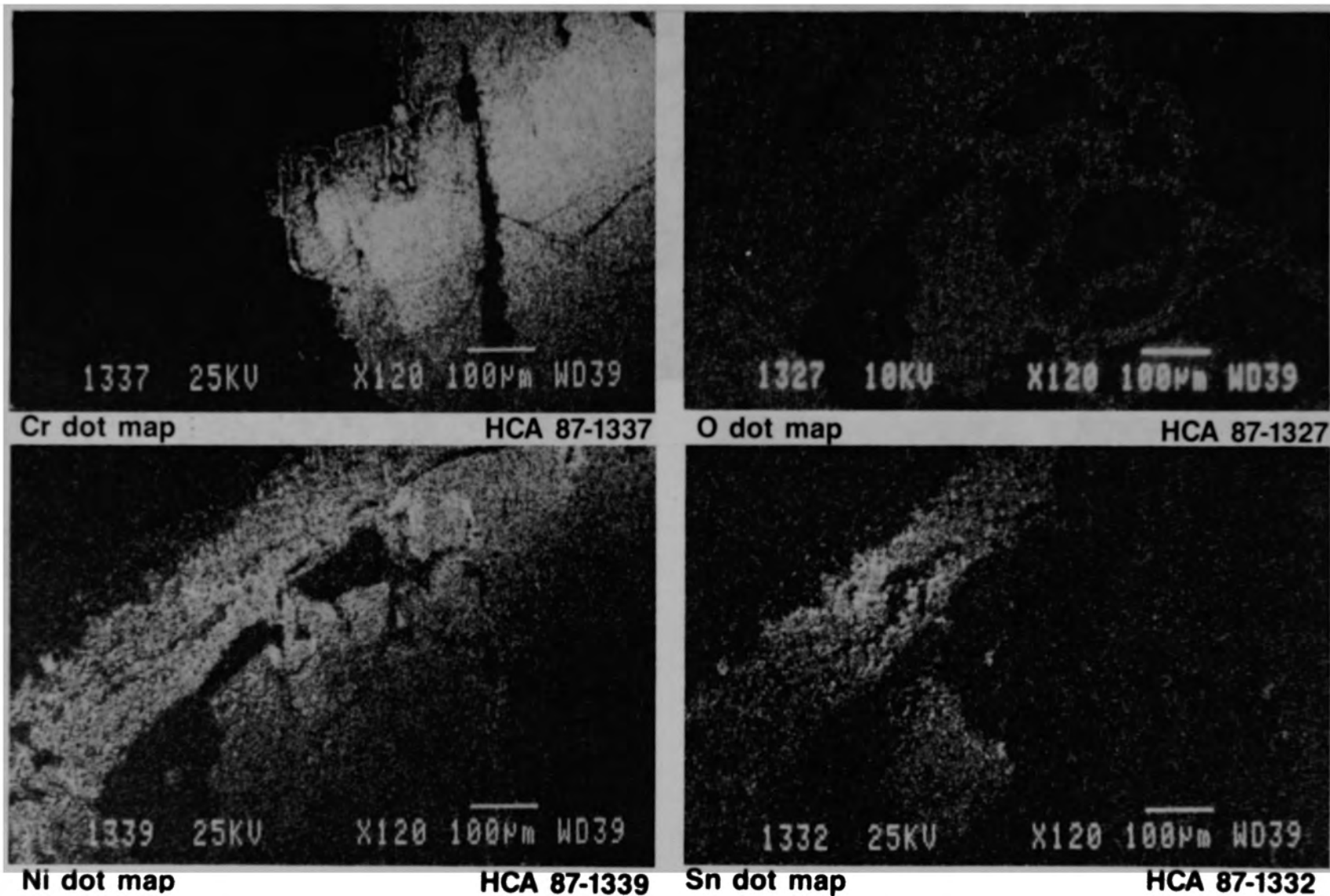


Figure E-21. (Continued)

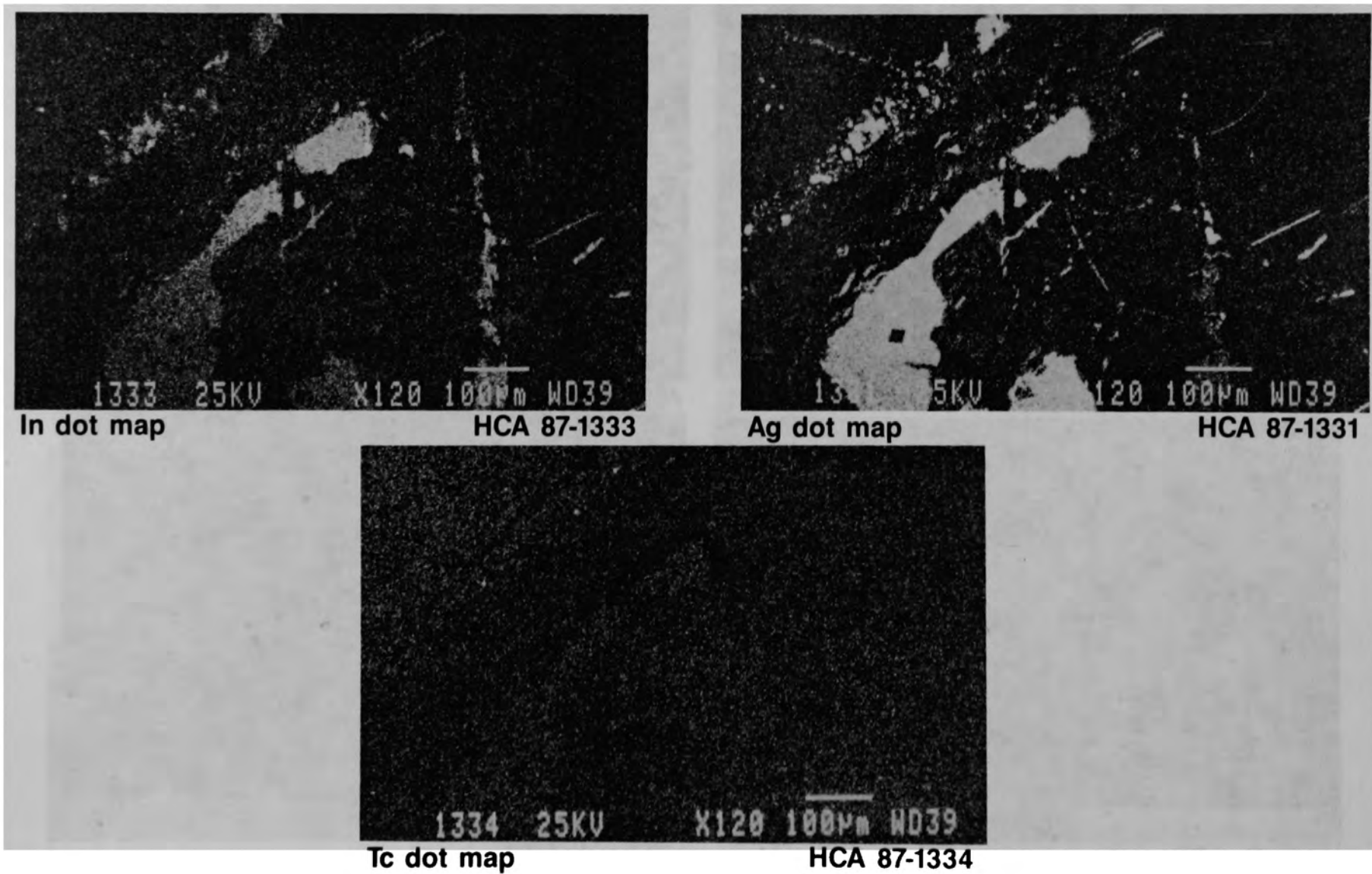


Figure E-21. (Continued)

The microstructure of the area next to the fuel pellet in Area 2 of Figure E-17 is shown in Figure E-22. The fuel is severely fragmented, and the oxidized cladding remnant was partially dissolved by the metallic melt. Any unoxidized zircaloy cladding would probably have been dissolved by molten silver or liquefied by eutectic interactions with iron or nickel.

The backscattered electron image of SEM sample K09-P1-D3, extracted from Area 2 in Figure E-17, is shown in Figure E-23. The compositions of the major phases in this area are summarized in Figure E-24. Precipitated crystals of  $UO_2$  are surrounded by prior molten material with a few Ag/In particles. The dissolution of the fuel is indicated by the mixed oxide of uranium, zirconium, and iron.

Figure E-25 shows the material in the flow channel between the fuel columns in Area 3 of Figure E-17. This structure is similar to the material in the flow channel in Area 1, in which the molten material is primarily metallic with small  $UO_2$  precipitates.

A backscattered electron image of microcore K09-P1-D2, extracted from Area 3 in Figure E-17, is shown in Figure E-26. This figure shows the areas which were examined in detail, and the significant results are discussed below.

The composition of material at Area C is shown in Figure E-27. This sample contains a vein of Ag-In melt located in a crack in a ceramic matrix of  $(U,Zr)O_2$  melt material, which also contains metallic melt regions consisting primarily of Zr, Fe, Cr, Ni, and Sn. WDS point analysis was also performed in this area as described in Appendix J (Figure J-10).

A series of elemental dot maps from Area D in the  $UO_2$  pellet shows fuel that was dissolved in a Zr, Ni, Fe metallic melt which penetrated along a crack in the fuel (Figure E-28).

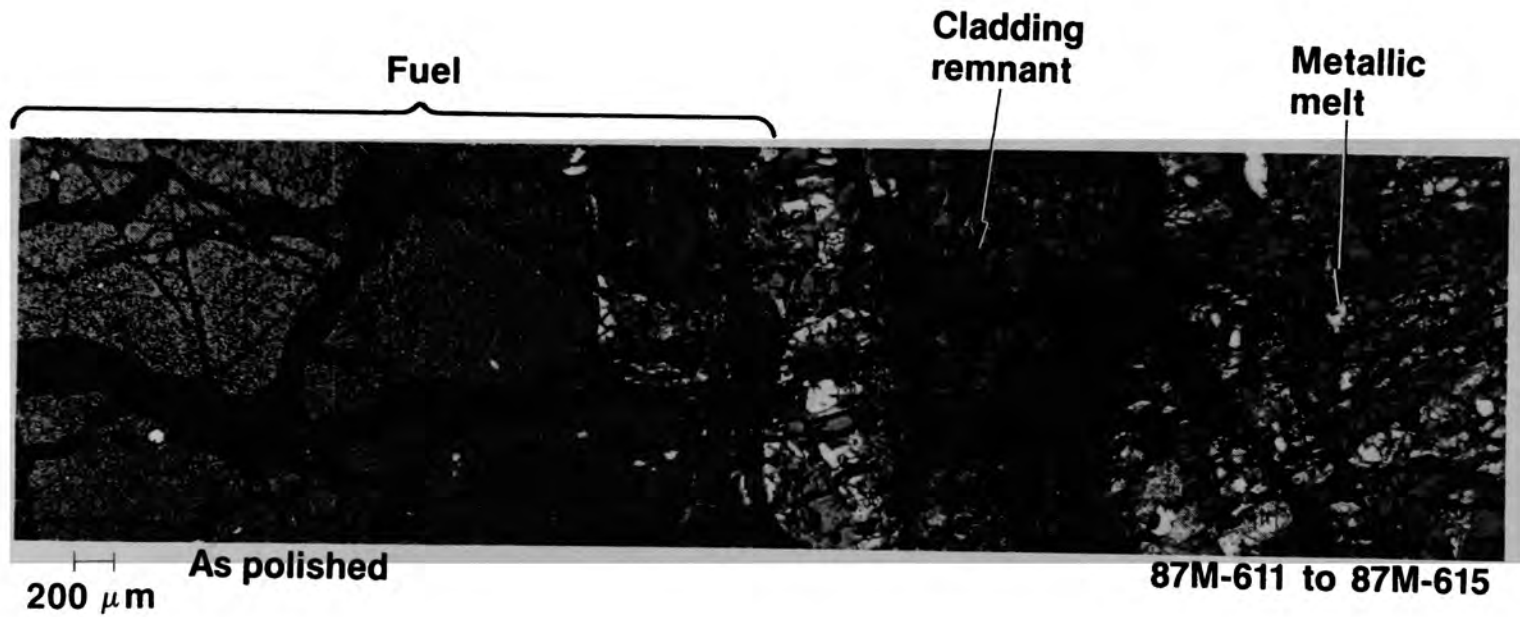


Figure E-22. Cladding oxidation and dissolution near fuel pellet (K09-P1-D Area 2).

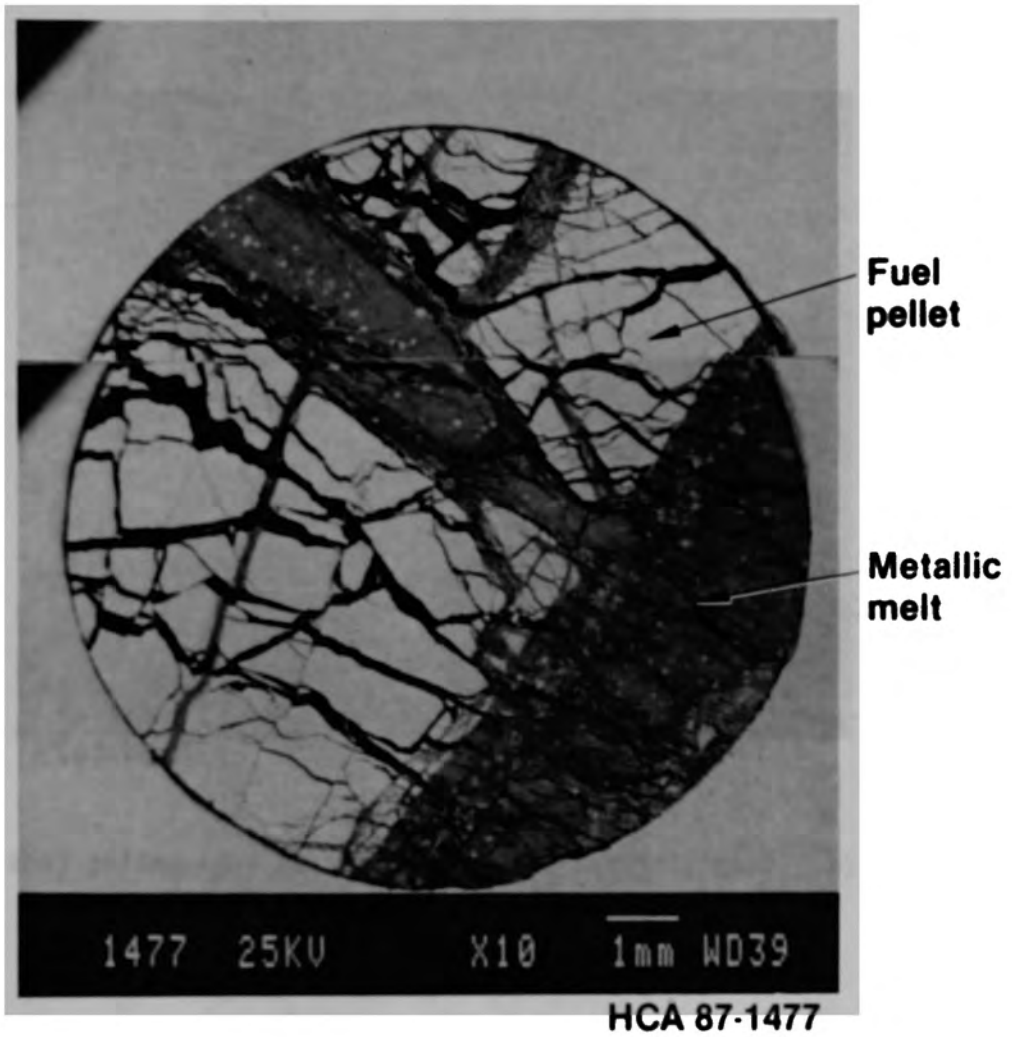


Figure E-23. Backscattered electron image of fuel/melt interface (K09-P1-D3).

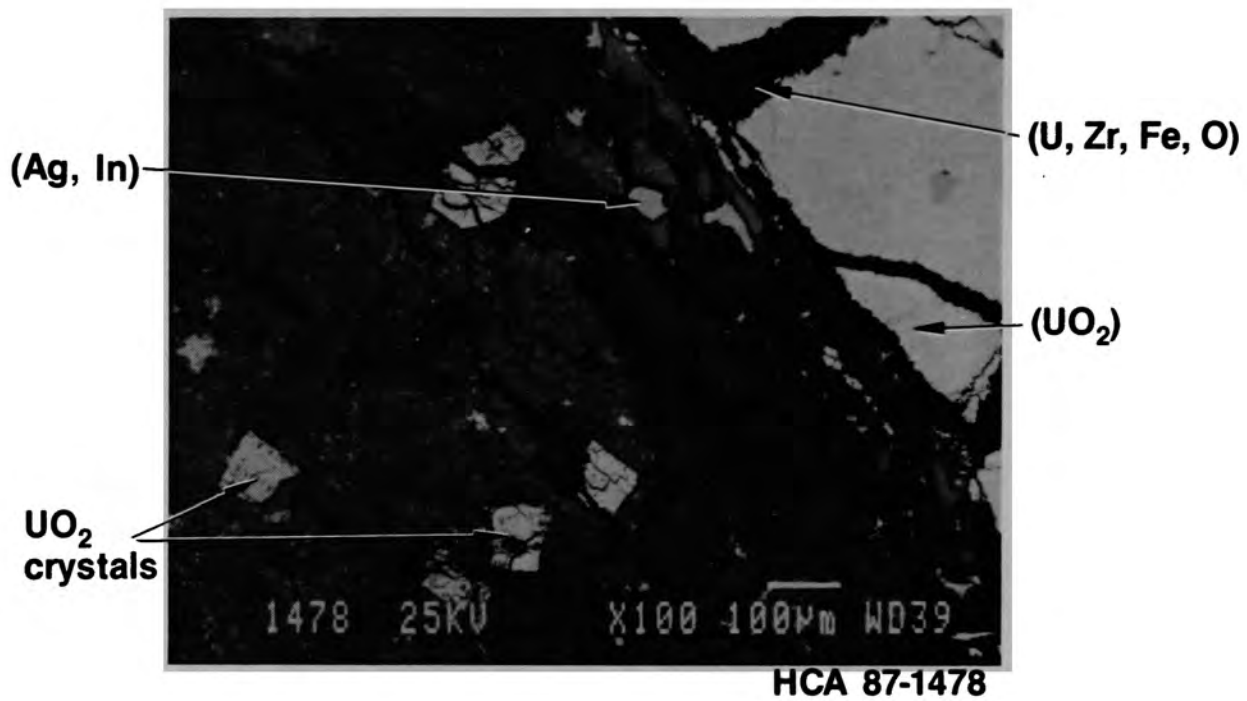


Figure E-24. Compositions in melt adjacent to fuel pellet (K09-P1-D3).

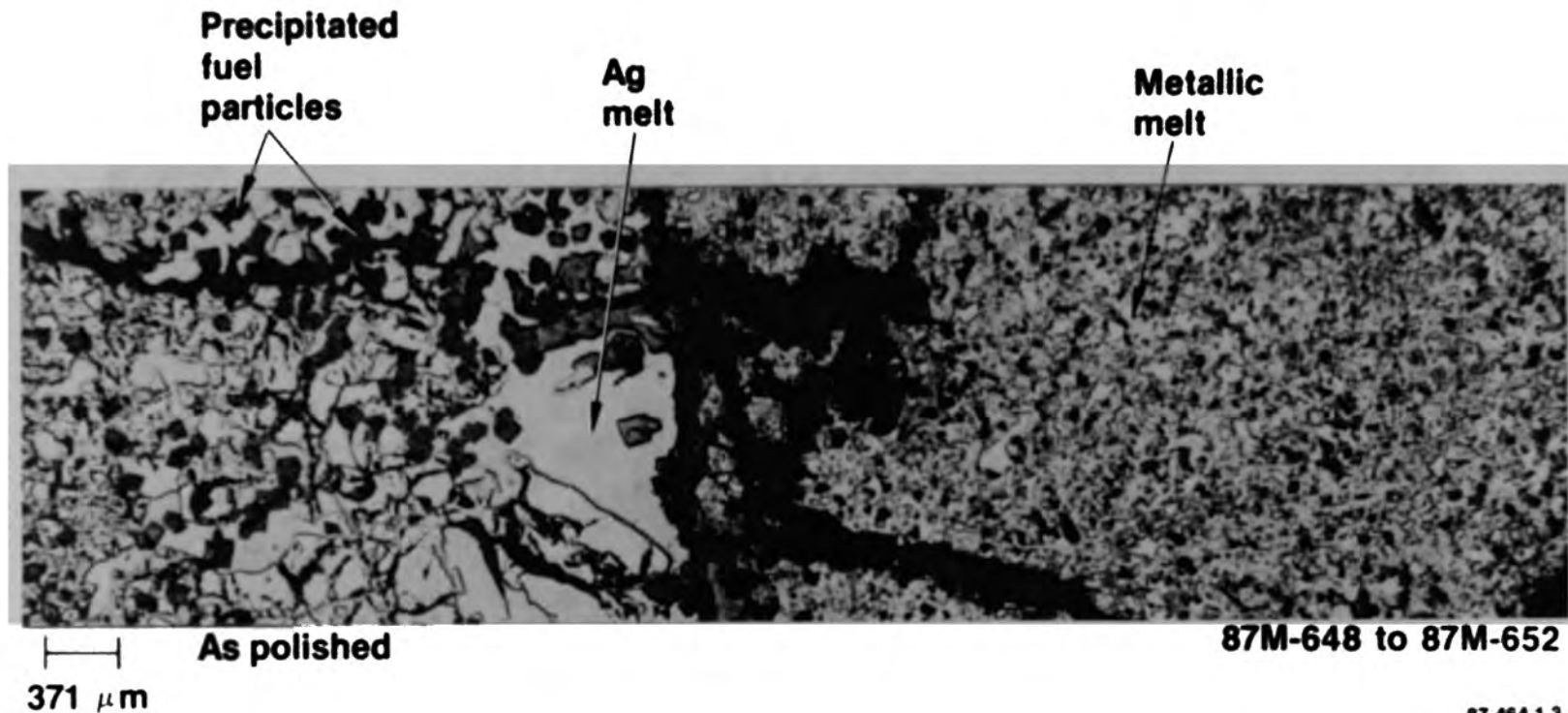


Figure E-25. Microstructure of melt in flow channel in lower crust (K09-P1-D).

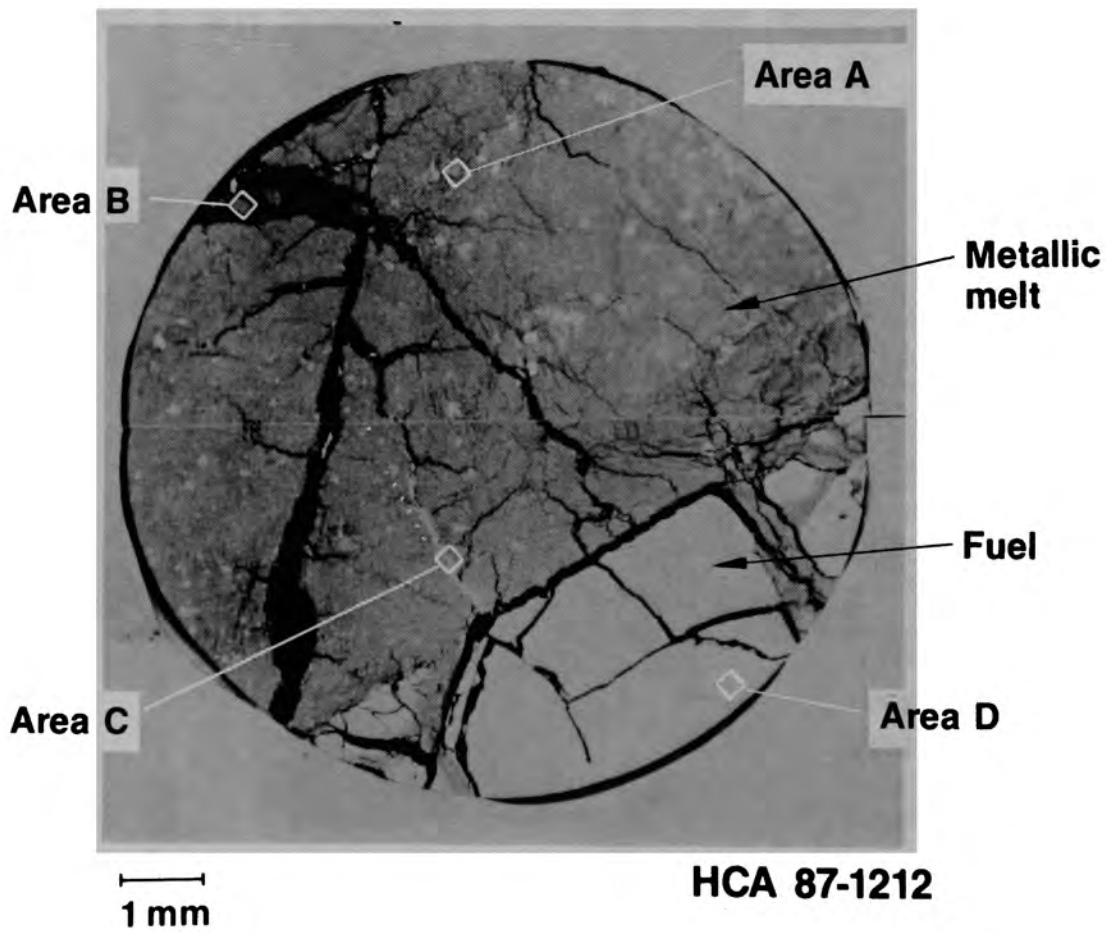


Figure E-26. Backscattered electron image of fuel/melt interface (K09-P1-D2).



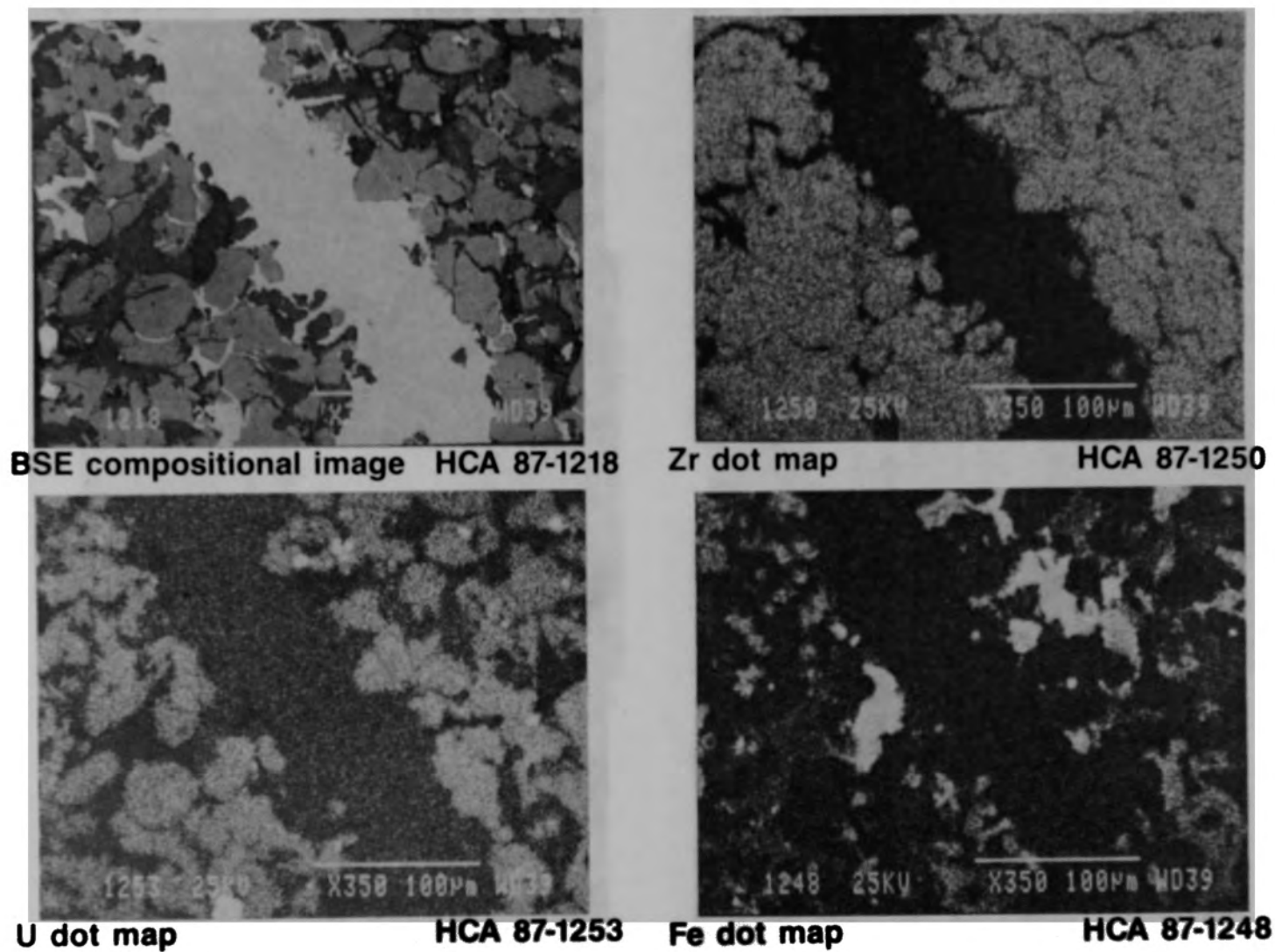
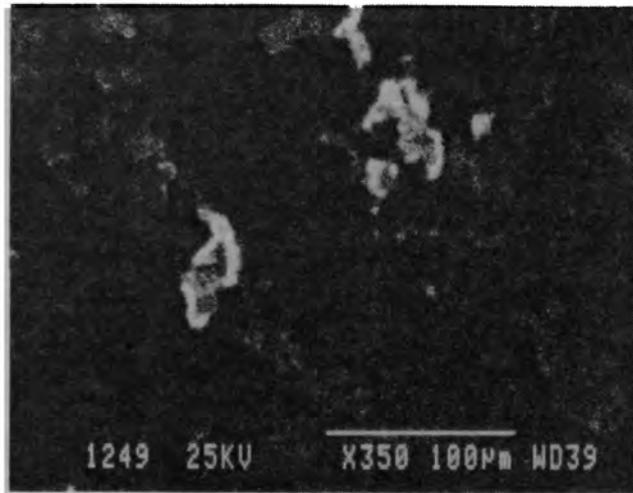
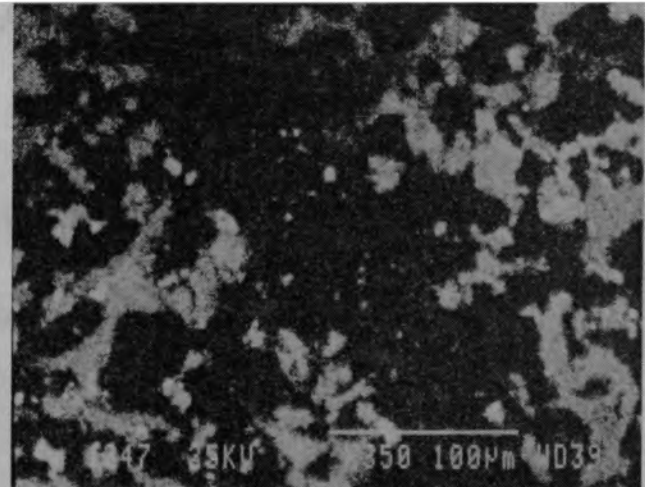


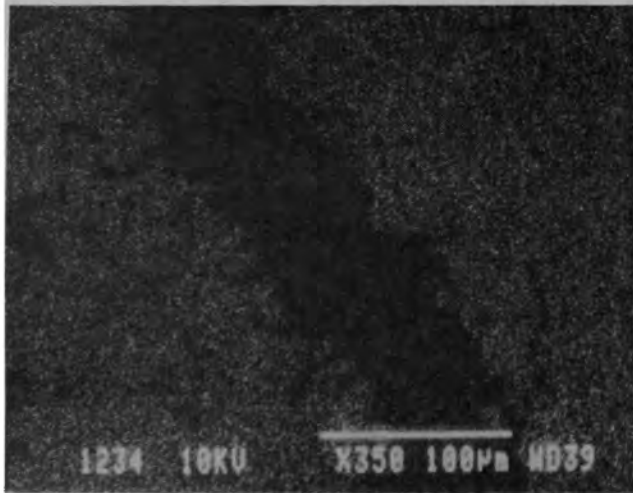
Figure E-27. Silver veins in  $UO_2/ZrO_2$  mixed oxides (K09-P1-D2 Area C).



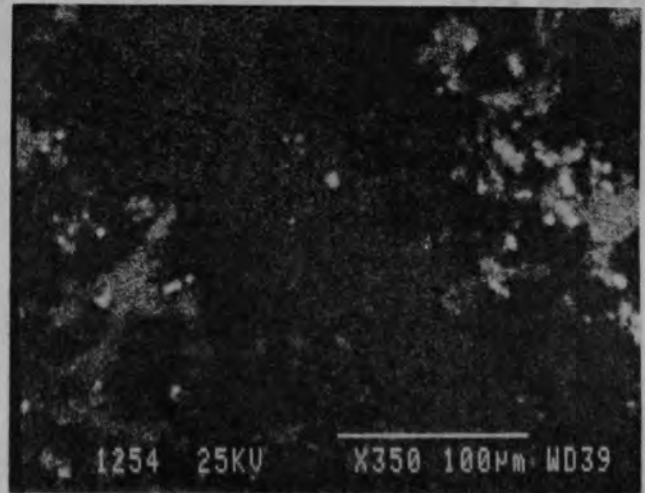
**Cr dot map HCA 87-1249**



**Ni dot map HCA 87-1242**



**O dot map HCA 87-1234**



**Sn dot map HCA 87-1254**

Figure E-27. (Continued)

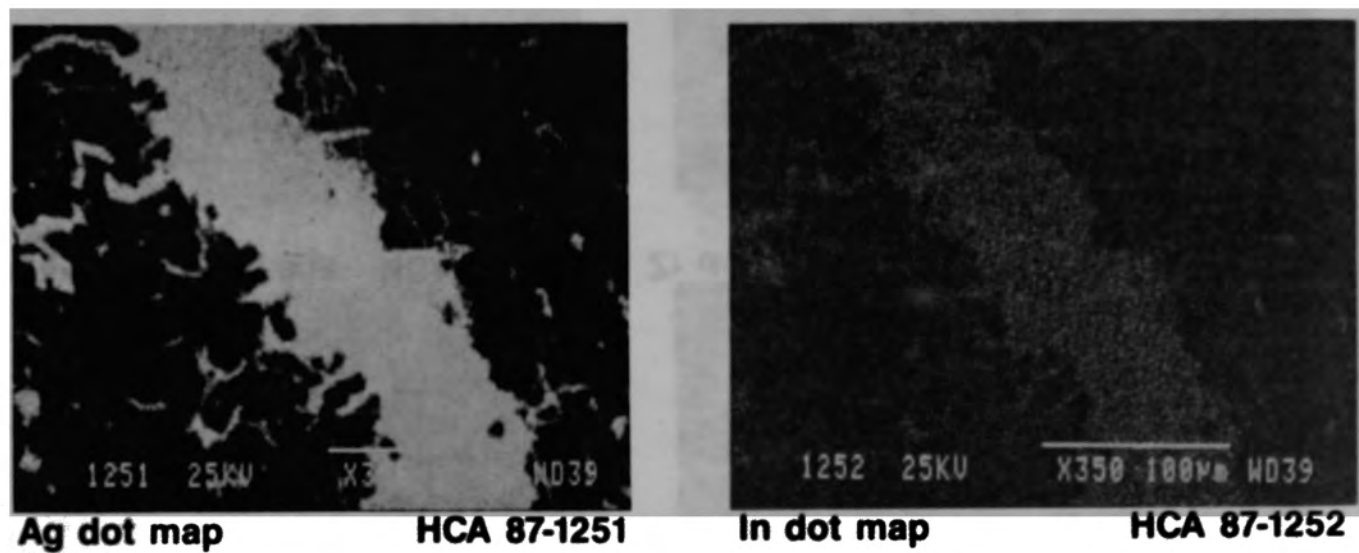
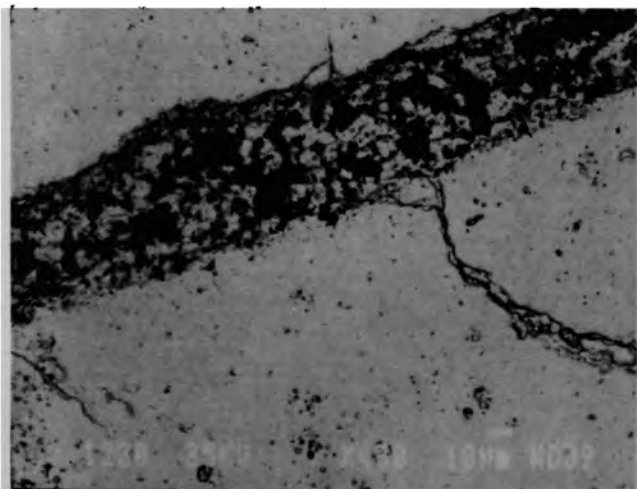
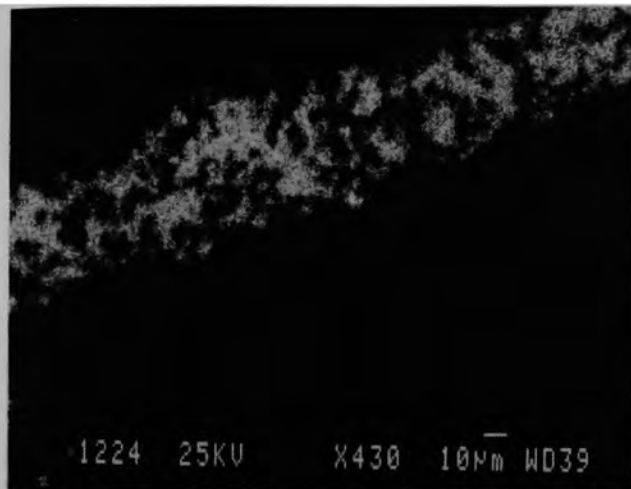


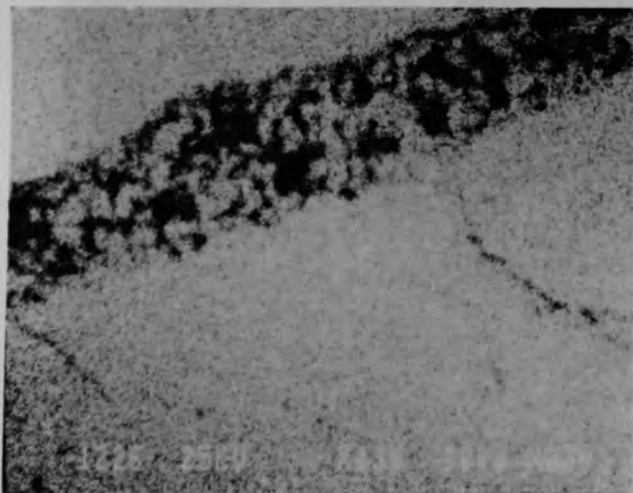
Figure E-27. (Continued)



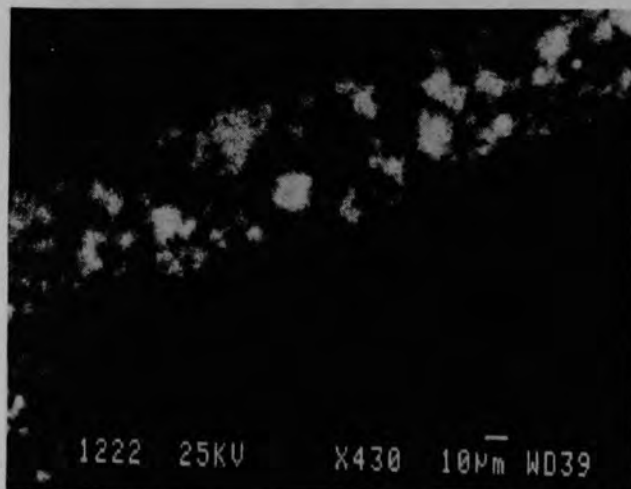
BSE compositional image HCA 87-1220



Zr dot map HCA 87-1224



U dot map HCA 87-1226



Fe dot map HCA 87-1222

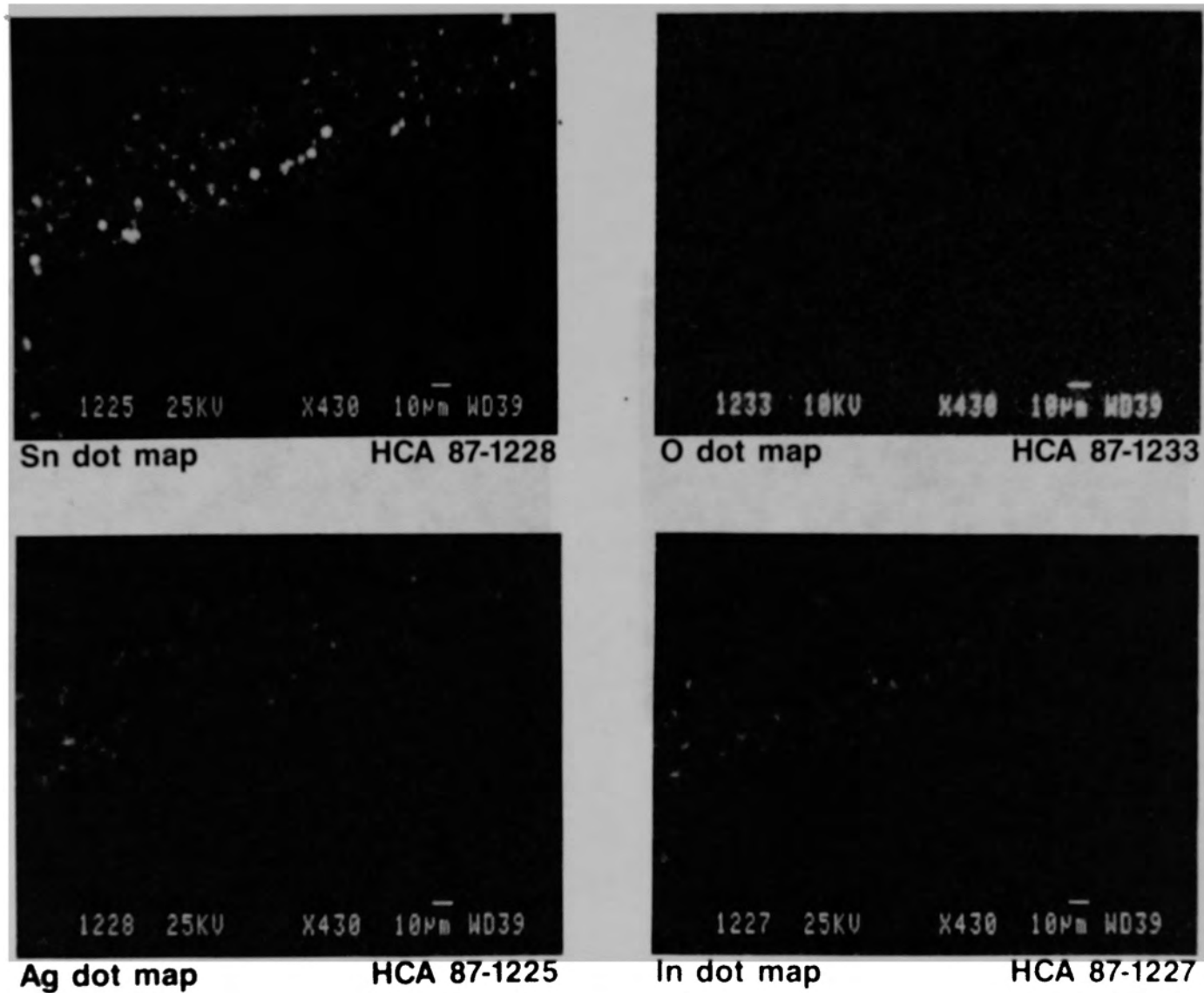


Figure E-28. (Continued)

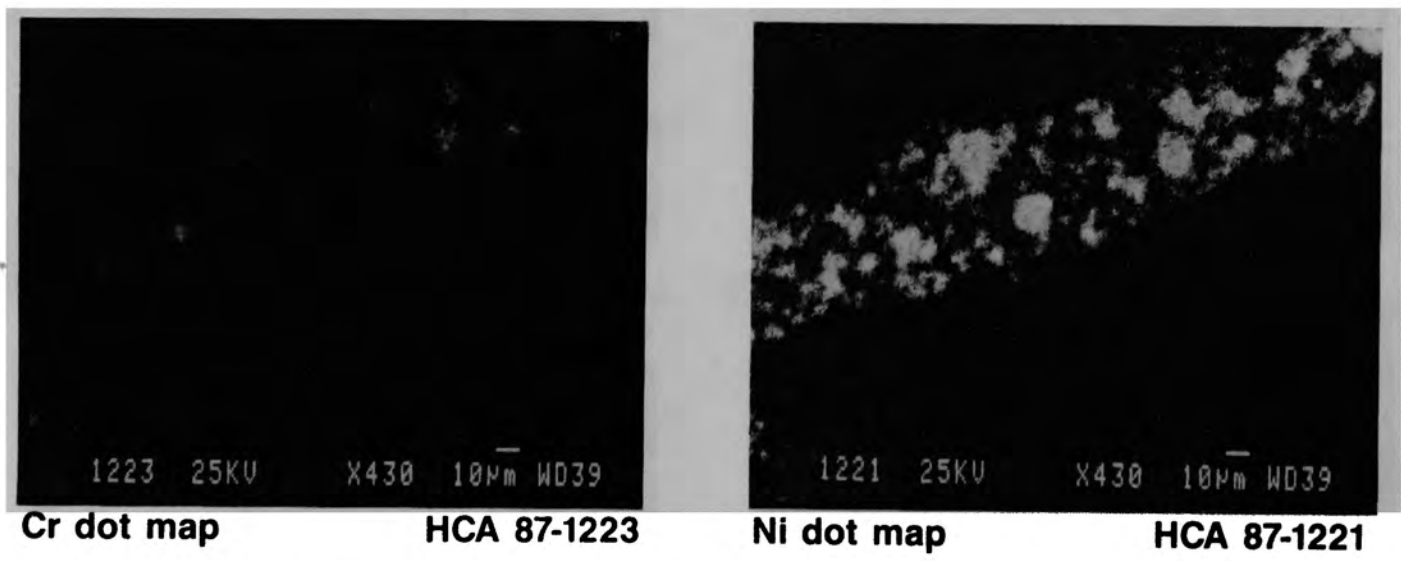


Figure E-28. (Continued)

Figure E-29 is a photomicrograph from K09-P1-D Area 4 (Figure E-17), which shows three fuel remnants surrounded by metallic melt. Precipitated fuel crystals are once again apparent in the metallic melt. Figures E-30 and E-31 show in greater detail the diversity in the melt microstructures in this area. Figure E-30 shows the precipitated  $UO_2$  crystals in the metallic melt. These fragments varied between 50 and 100  $\mu m$ . Figure E-31 shows metallic melts penetrating and dissolving the fuel remnants.

Transverse section K09-P1-G is shown in Figure E-32. This section contained two fuel pellets that were surrounded by cladding that was severely attacked by the metallic melt. An area of the metallic melt adjacent to the fuel is shown in more detail in Figure E-33. The cladding has essentially been dissolved by the metallic melt, and a number of different metallic phases are present. Precipitated  $UO_2$  crystals are once again apparent in the metallic melt.

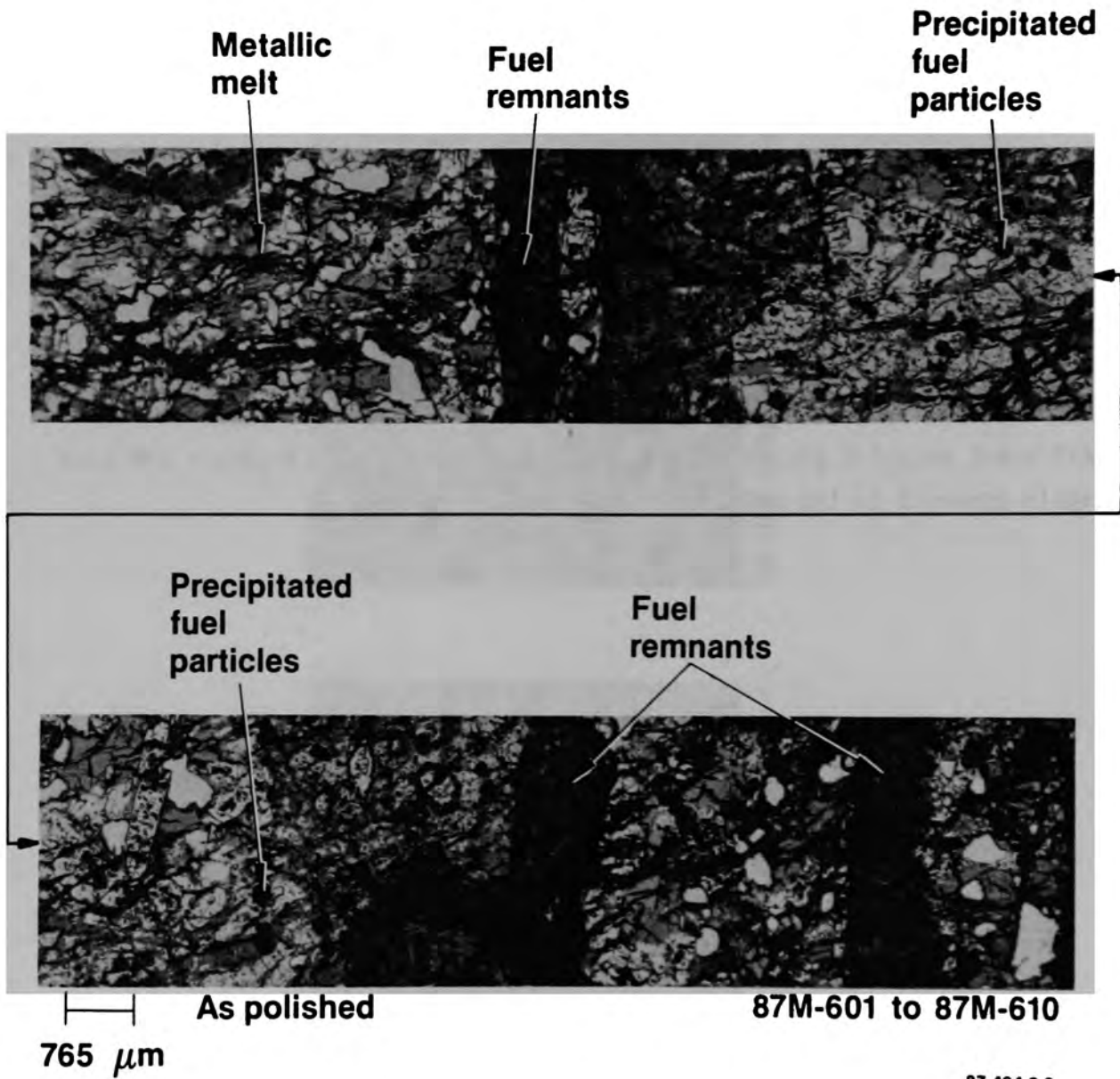
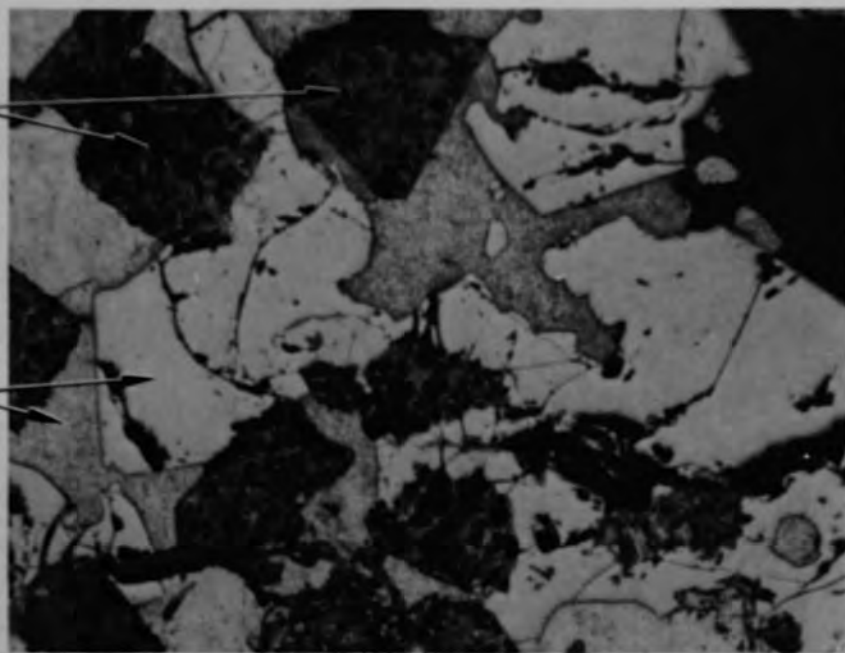


Figure E-29. Fuel/metallic melt interactions in lower crust (K09-P1-D2 Area 4).



**UO<sub>2</sub>  
precipitates**

**Metallic  
melts**



50 μm

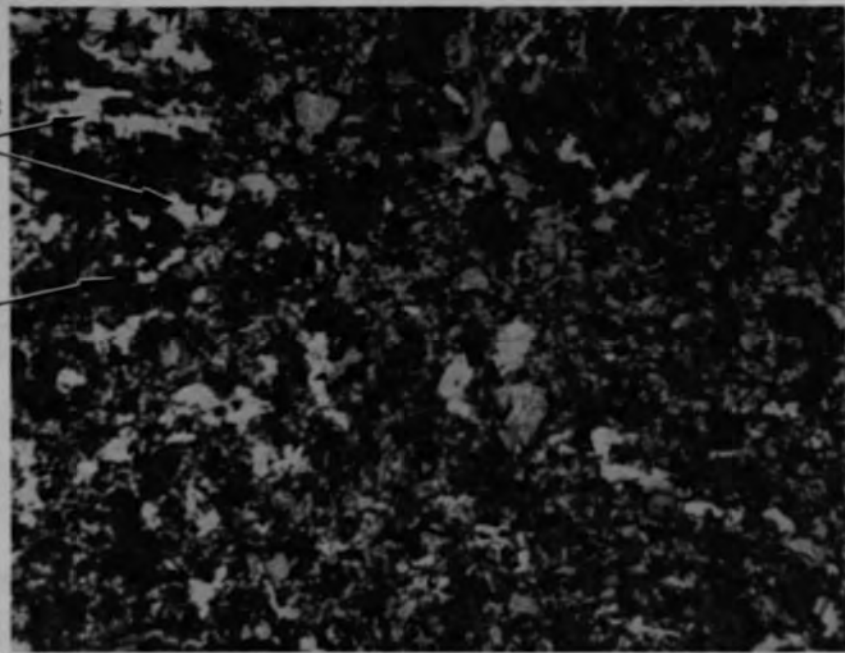
**As polished**

**87M-663**

Figure E-30. UO<sub>2</sub> precipitates in metallic melt in lower crust (K09-P1-D Area 4).

**Metallic  
melts**

**Fuel  
remnants**

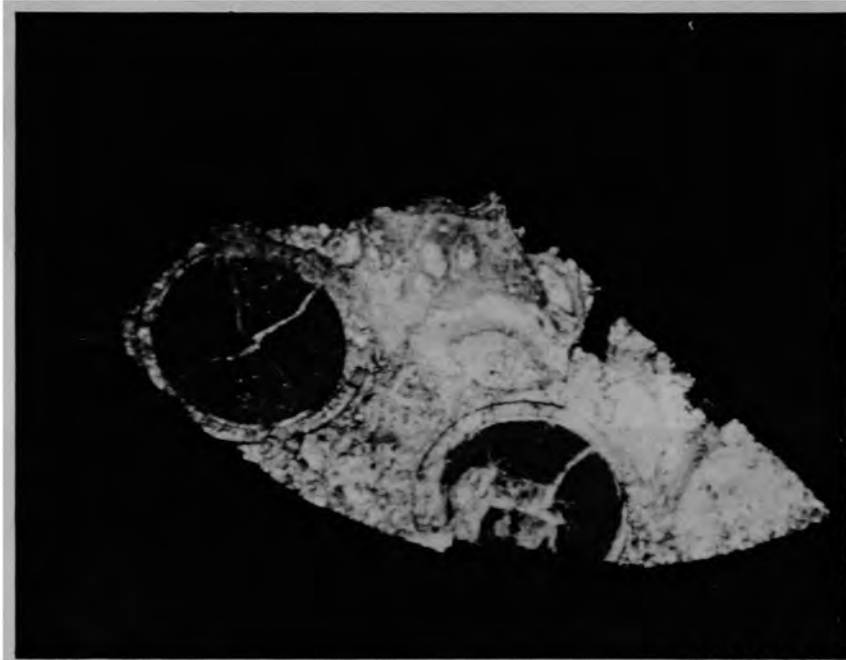


50 μm

**As polished**

**87M-664**

Figure E-31. Metallic melt penetration into fuel remnants (K09-P1-D Area 4).



**87M-384**

Figure E-32. Transverse cross section of K09-P1-G from the lower crust.

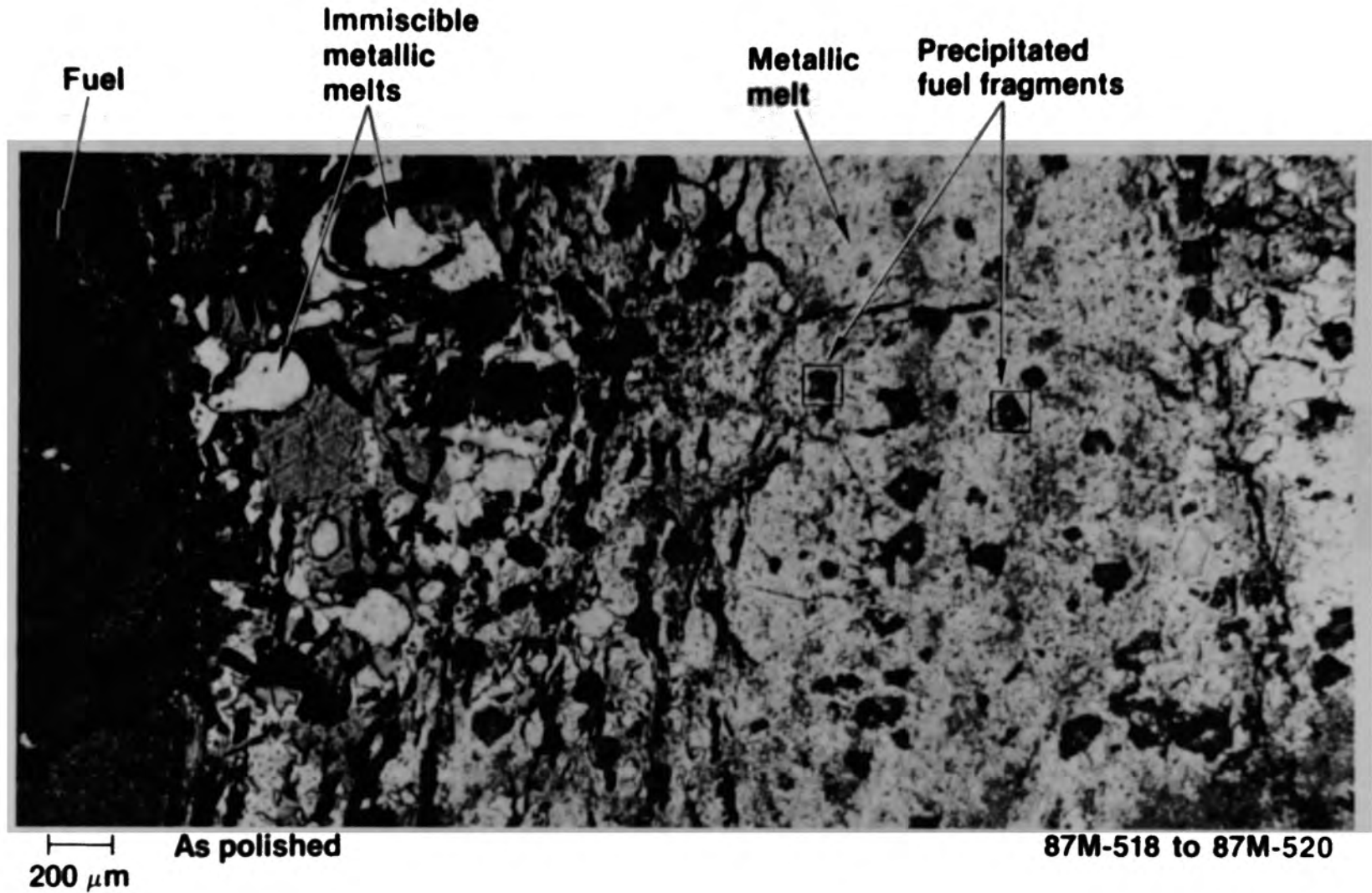


Figure E-33. Metallic melt structure in lower crust with precipitated fuel particles (K09-P1-G).

## Upper Crust

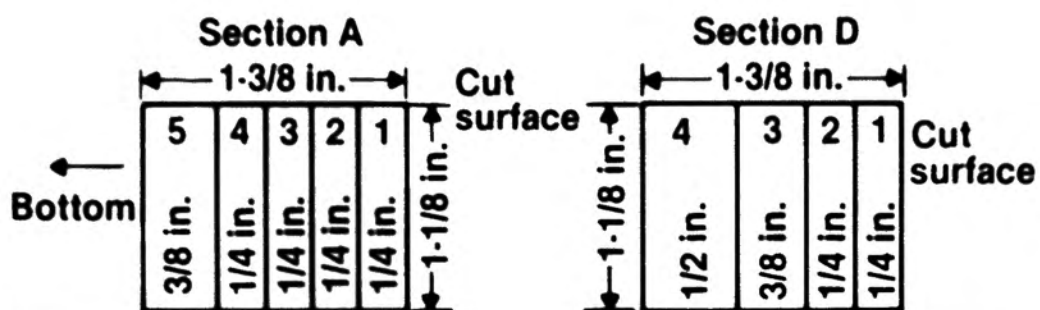
### D08-P3

A photograph of a plug from the upper crust at central core position D08 is shown in Figure E-34. The crust sample was 4.5 cm long and 6.4 cm in diameter. This plug weighed 746.47 g and had a density of 9.74 g/cm<sup>3</sup>.

Figure E-34 also shows the sectioning diagram for this plug. A 0.95-cm thick transverse cross section (Section D08-P3-E) was cut from one end to show a transverse view of the plug. The remaining plug was then cut into quarter sections designated A, B, C, and D. Two of these quarter sections were cut into wafers, five from section A and four from section D, as shown in Figure E-34. Section D08-P3-D1 was used for radiochemical analyses, and section D08-P3-D2 was used for metallographic examinations at the INEL.

The polished section of D08-P3-D2 shows a ceramic melt with extensive metallic inclusions (Figure E-35). The typical microstructure of D08-P3-D2 is shown in Figure E-36. The matrix is ceramic with a large amount of porosity. The as-polished structure shows metallic globules with fine porosity or second-phase precipitates. At the surface of these metallic globules there was a very fine lamellar structure representing eutectic solidification. Another example of the sample microstructure is shown in Figure E-37. Again, the matrix is ceramic with a large amount of porosity and a few metallic inclusions. A few microcracks are also present.

After the metallographic examinations, a small microcore was drilled from this cross section for SEM elemental analysis. The location of this microcore is shown in Figure E-38. The backscattered electron image of this microcore is shown in Figure E-39. This photograph shows the area that was examined on the SEM. This area was at the interface between two metallic inclusions.



- A-1 - Germany-JRC
- A-2 - Canada
- A-3 - Japan
- A-4 - Japan
- A-5 - Japan
- B - United Kingdom
- C - Sweden
- D-1 - INEL Rad Chem
- D-2 - INEL Met
- D-3 - Japan
- D-4 - Japan
- E - Japan

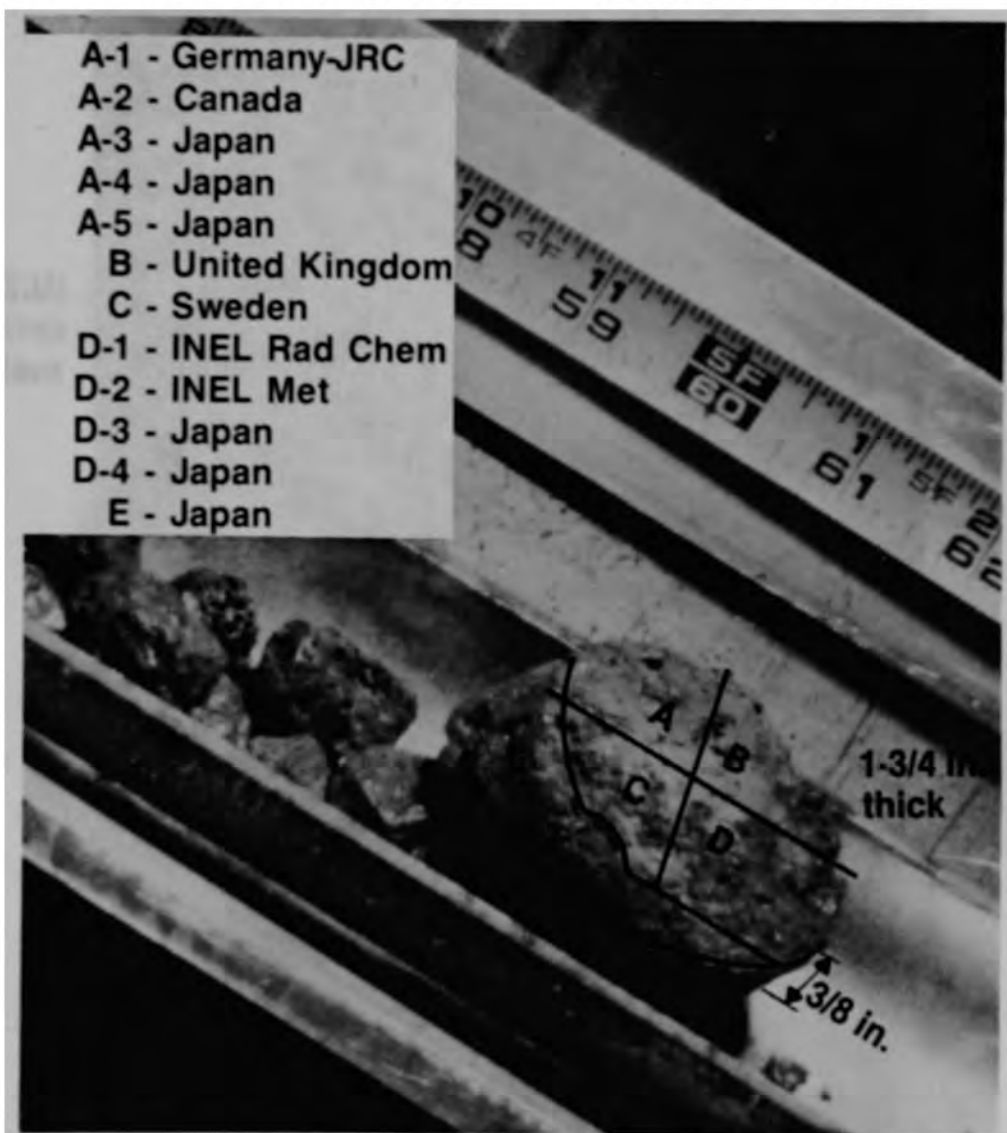


Figure E-34. Overview of sample D08-P3 from the upper crust.

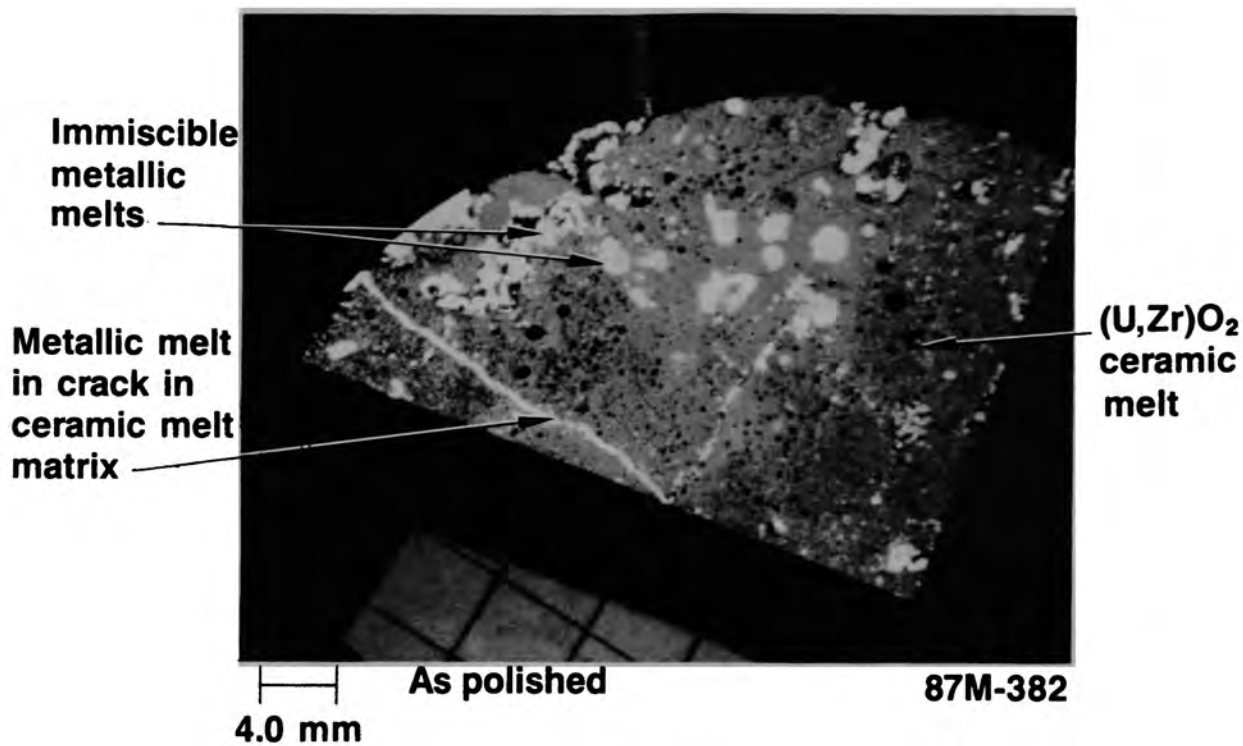


Figure E-35. Cross section D08-P3-D2 from the upper crust.

E-49

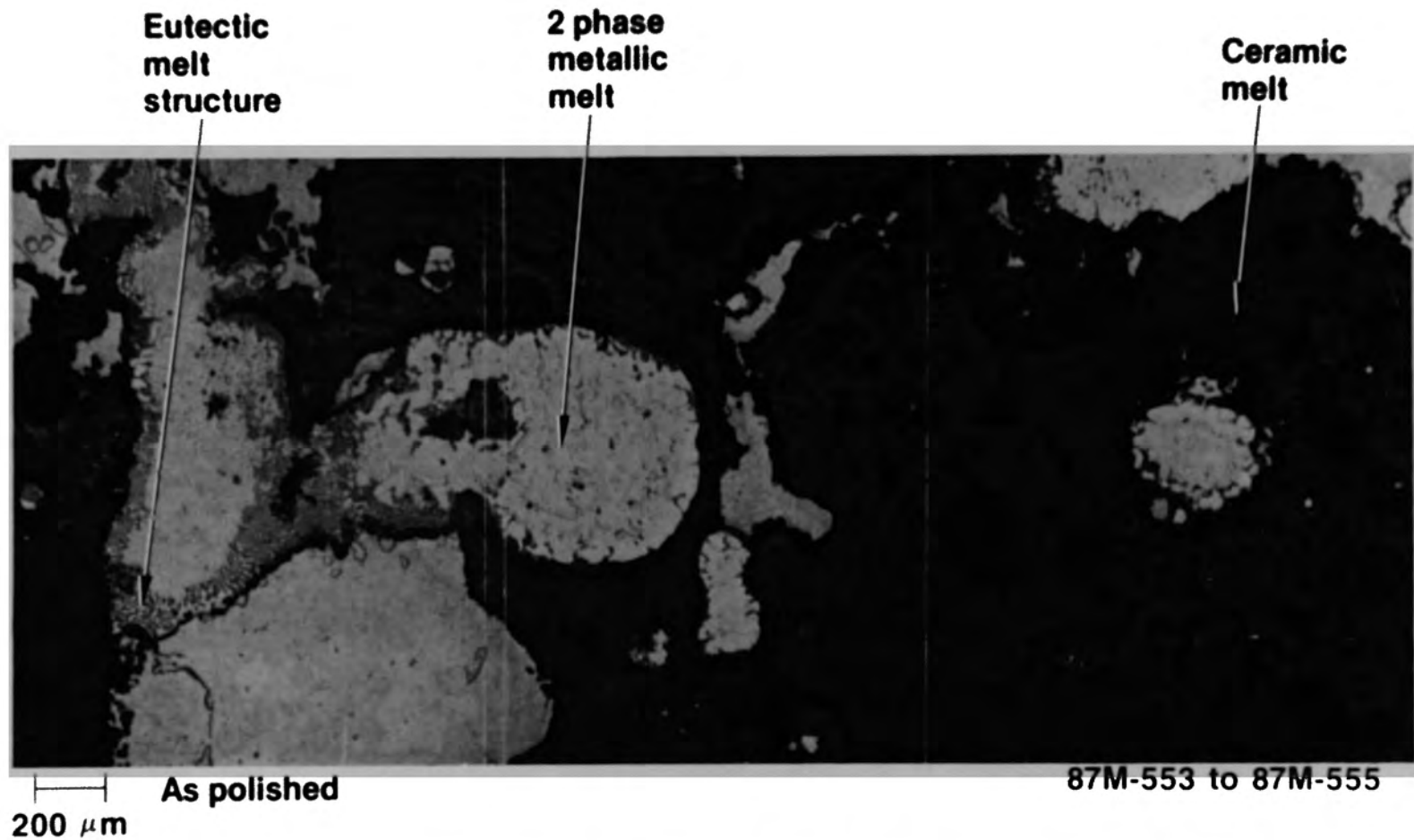


Figure E-36. Metallic inclusions in ceramic matrix of D08-P3-D2.

E-50

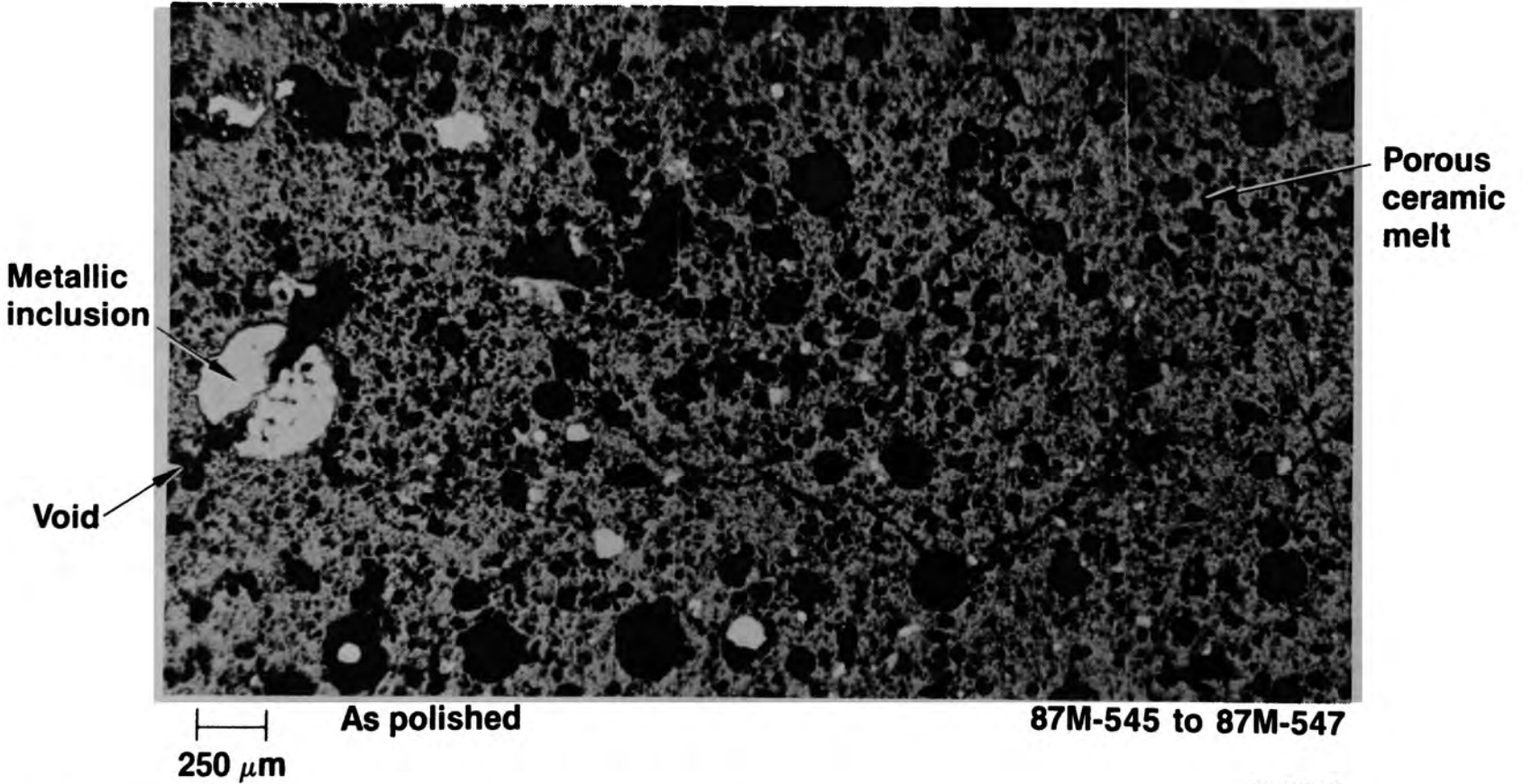


Figure E-37. Metallic inclusions and pores (D08-P3-D2).





**87M-382 and 87M-955**

Figure E-38. SEM sampling location in D08-P3-D2.

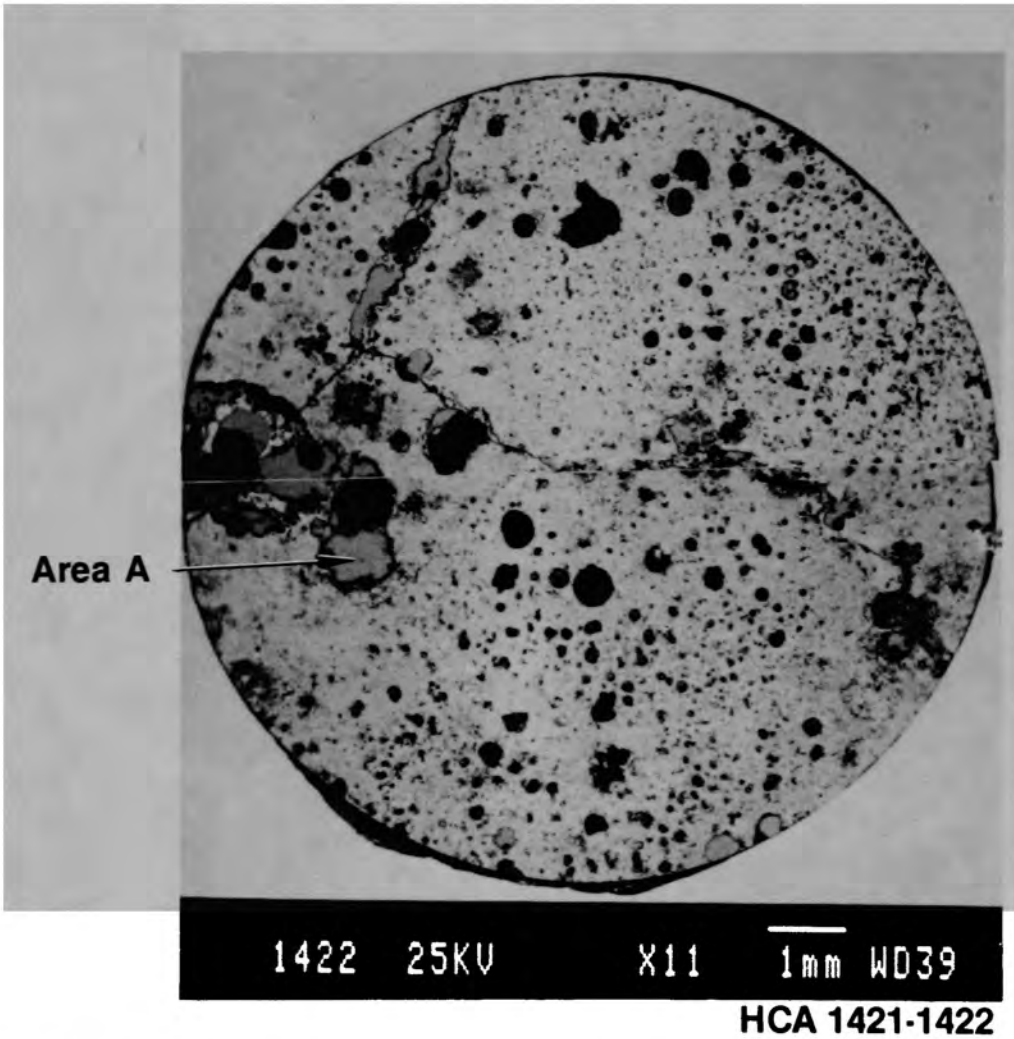


Figure E-39. Backscattered electron image of microcore D08-P3-D2 from upper crust.

The elemental dot maps of this area are shown in Figure E-40. The immiscible metallic phase at the bottom is (Ag,In,Cd) control rod alloy. Other metallic phases include predominantly (Ni,Sn) and (Fe,Cr,Mo,Ni), with a ceramic (Zr,Sn,O) phase separating the metallic phase at the top of the image. The fission products Pd and Ru were distributed in small concentrations throughout the metallic phases. A layer of uranium and iron oxides was also present.

#### K09-P2

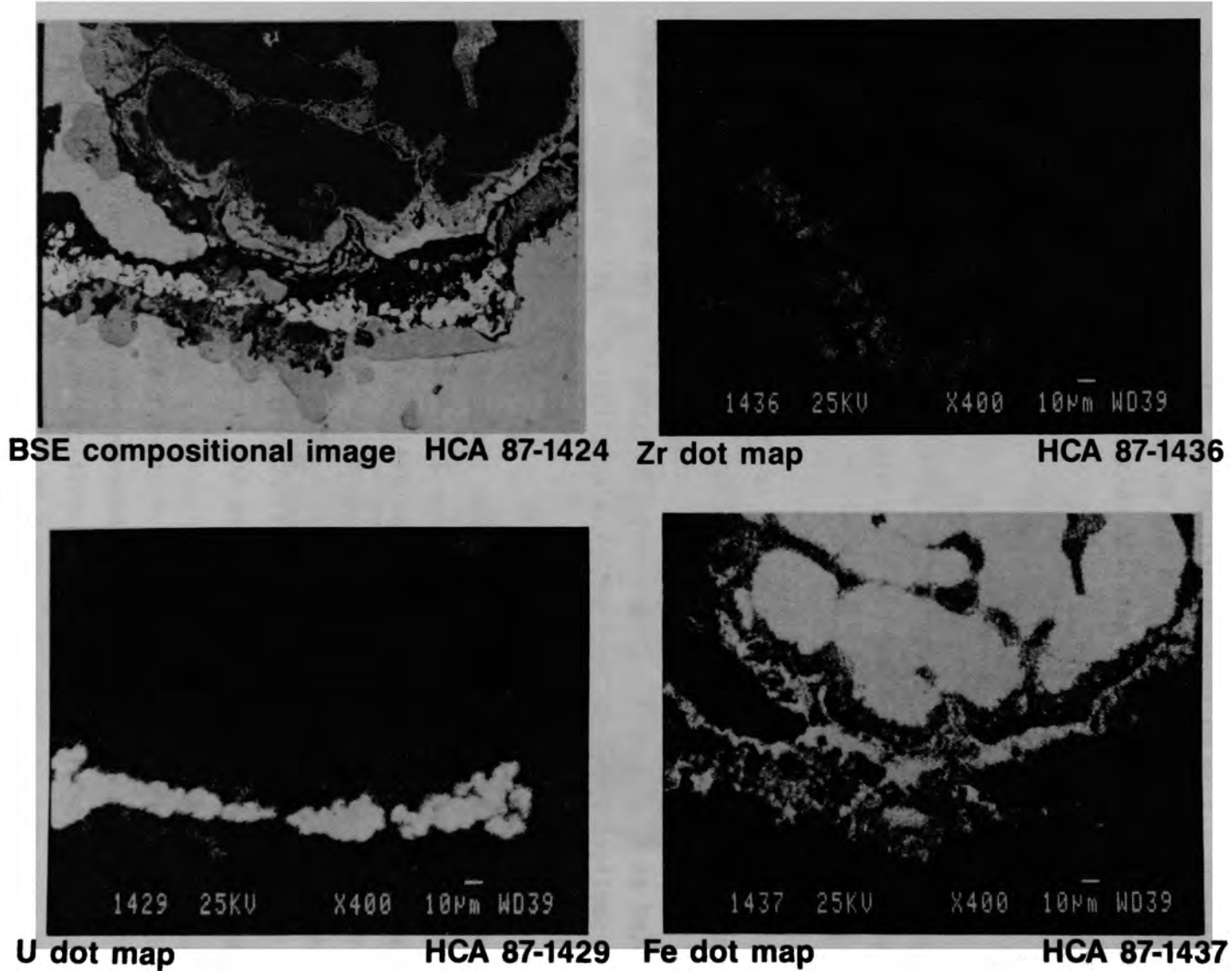
A photograph of upper crust sample K09-P2 is shown in Figure E-41. The sample was 6.4 cm long and 6.4 cm in diameter. This plug weighed 912.81 g and had a density of 7.80 g/cm<sup>3</sup>.

The sectioning scheme for this plug is also outlined in Figure E-41. A 0.95 cm thick transverse cross section was first cut from the top end. Half of the remaining plug was then cut into longitudinal slices designated as B, C, and D. The other half of the plug was cut into two quarter sections E and F. Section D was metallographically examined at the INEL.

Most of the significant results from the metallographic examinations of sample K09-P2-D were discussed in Section 3.1. The sample basically consisted of a mixture of ceramic and metallic melts. Some of the results of SEM analysis of small microcores drilled from this cross section are discussed here. The microcores were taken from the locations shown in Figure E-42, which also shows the overall condition of the sample. After the samples were drilled, it was decided not to examine microcore K09-P2-D2.

A backscattered electron image of microcore K09-P2-D1 is shown in Figure E-43. Area A is the interface between two metallic inclusions that was examined in detail, and a higher magnification backscattered electron image of this area is shown in Figure E-44.

The elemental dot maps for this area are shown in Figure E-45. These dot maps show the two immiscible metallic melts that are composed of



BSE compositional image HCA 87-1424

Zr dot map

HCA 87-1436

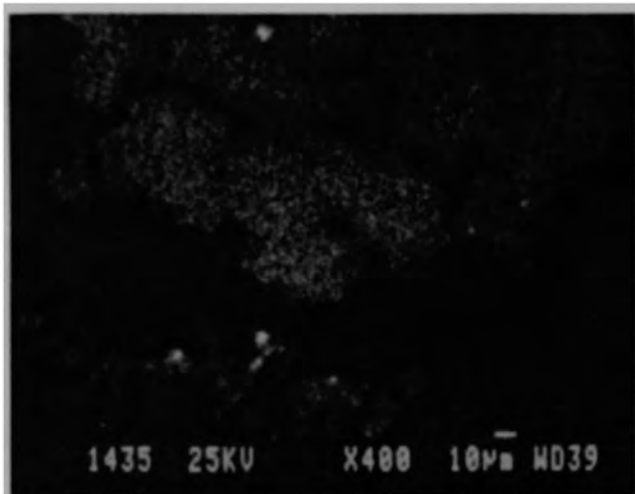
U dot map

HCA 87-1429

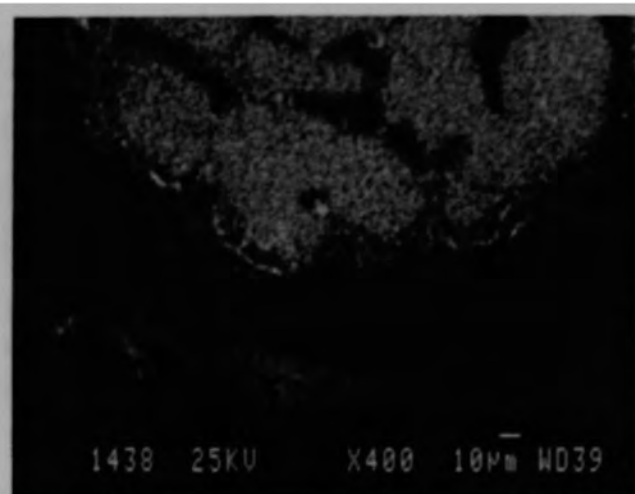
Fe dot map

HCA 87-1437

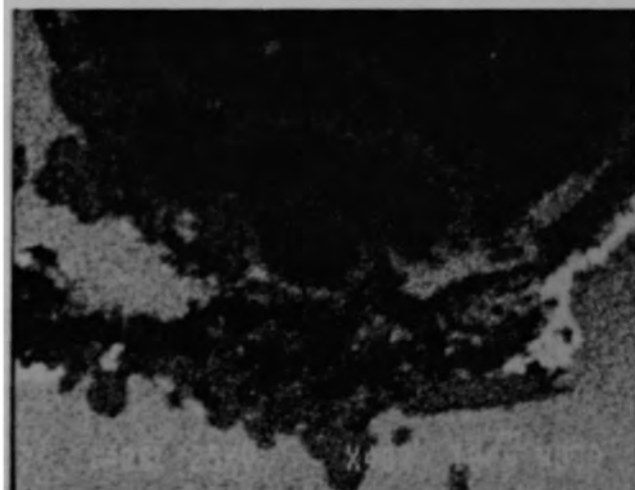
Figure E-40. Elemental composition at interface of metallic inclusions in D08-P3-D2 Area 1.



Mo dot map HCA 87-1435



Cr dot map HCA 87-1438



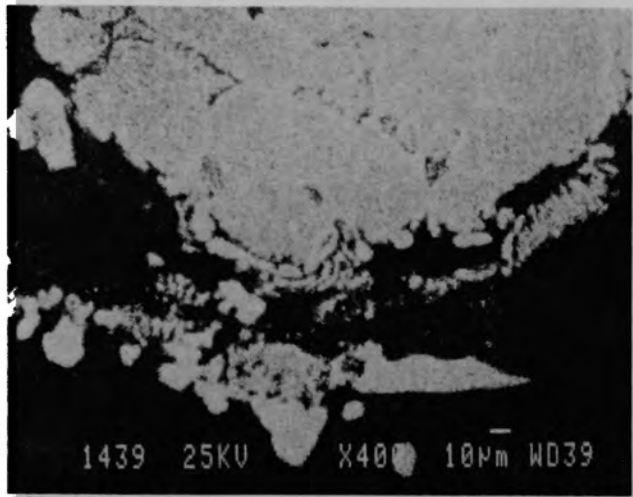
In dot map HCA 87-1428



Cd dot map HCA 87-1430

Figure E-40. (Continued)

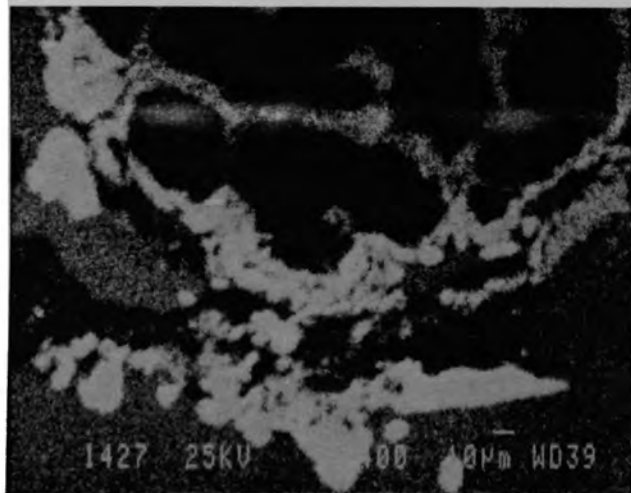
*J. S. 10*



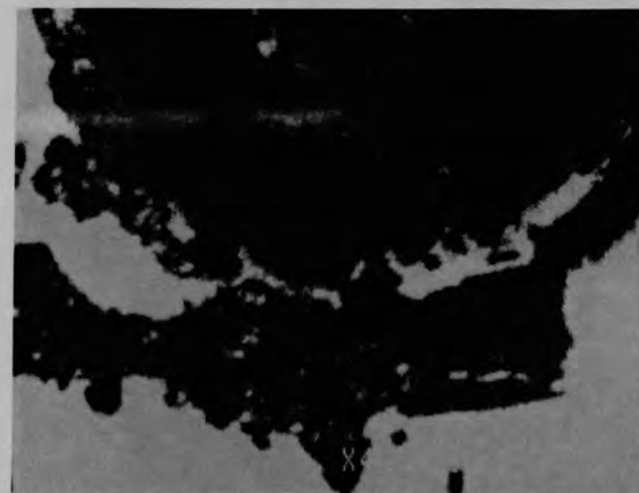
Ni dot map HCA 87-1439



O dot map HCA 87-1426



Sn dot map HCA 87-1427



Ag dot map HCA 87-1431

Figure E-40. (Continued)

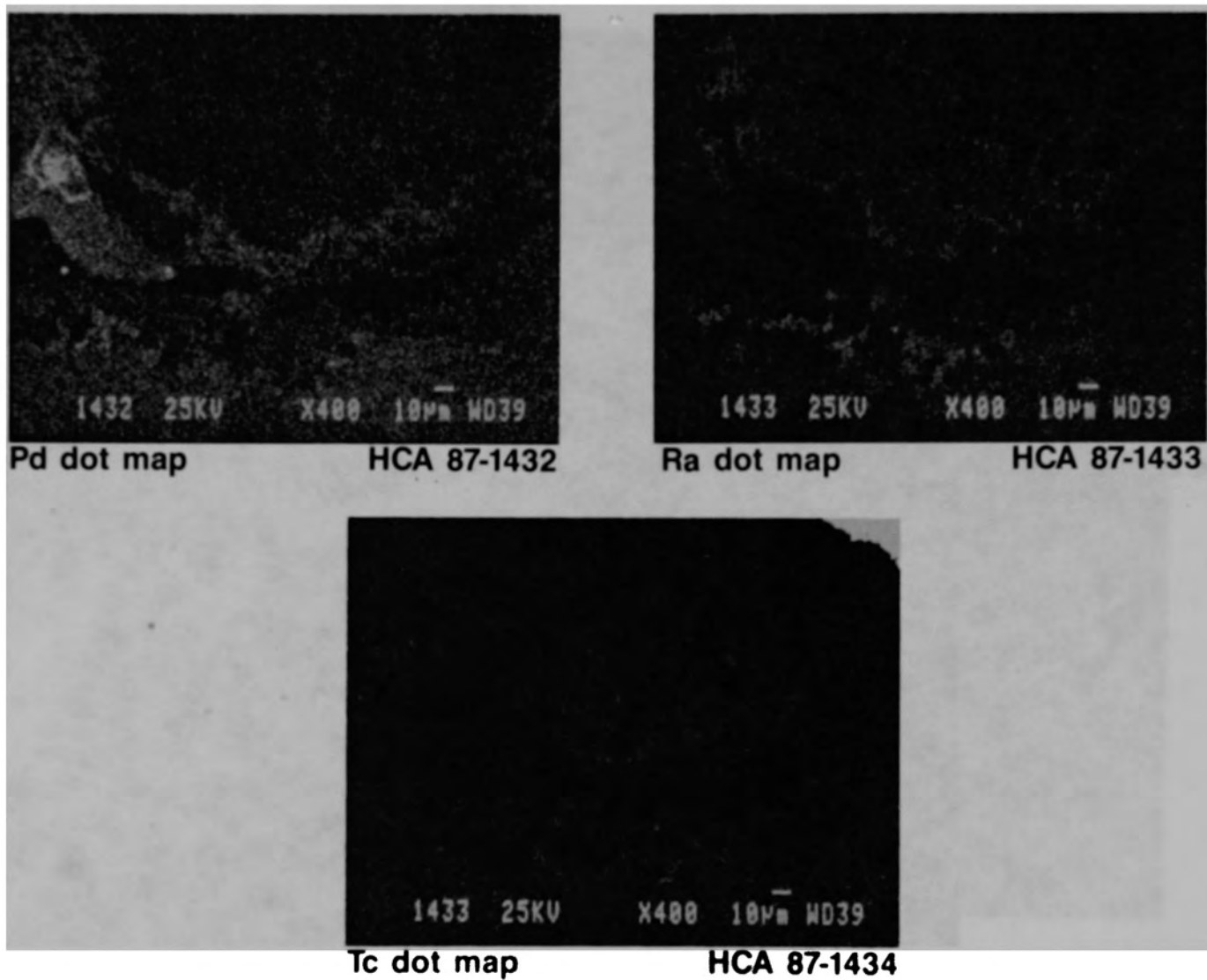


Figure E-40. (Continued)

- A - Germany-KFK
- B - United Kingdom
- C - Korea
- D - INEL Met
- E - ANL
- F - Switzerland



Figure E-41. Sectioning diagram for upper crust sample K09-P2.



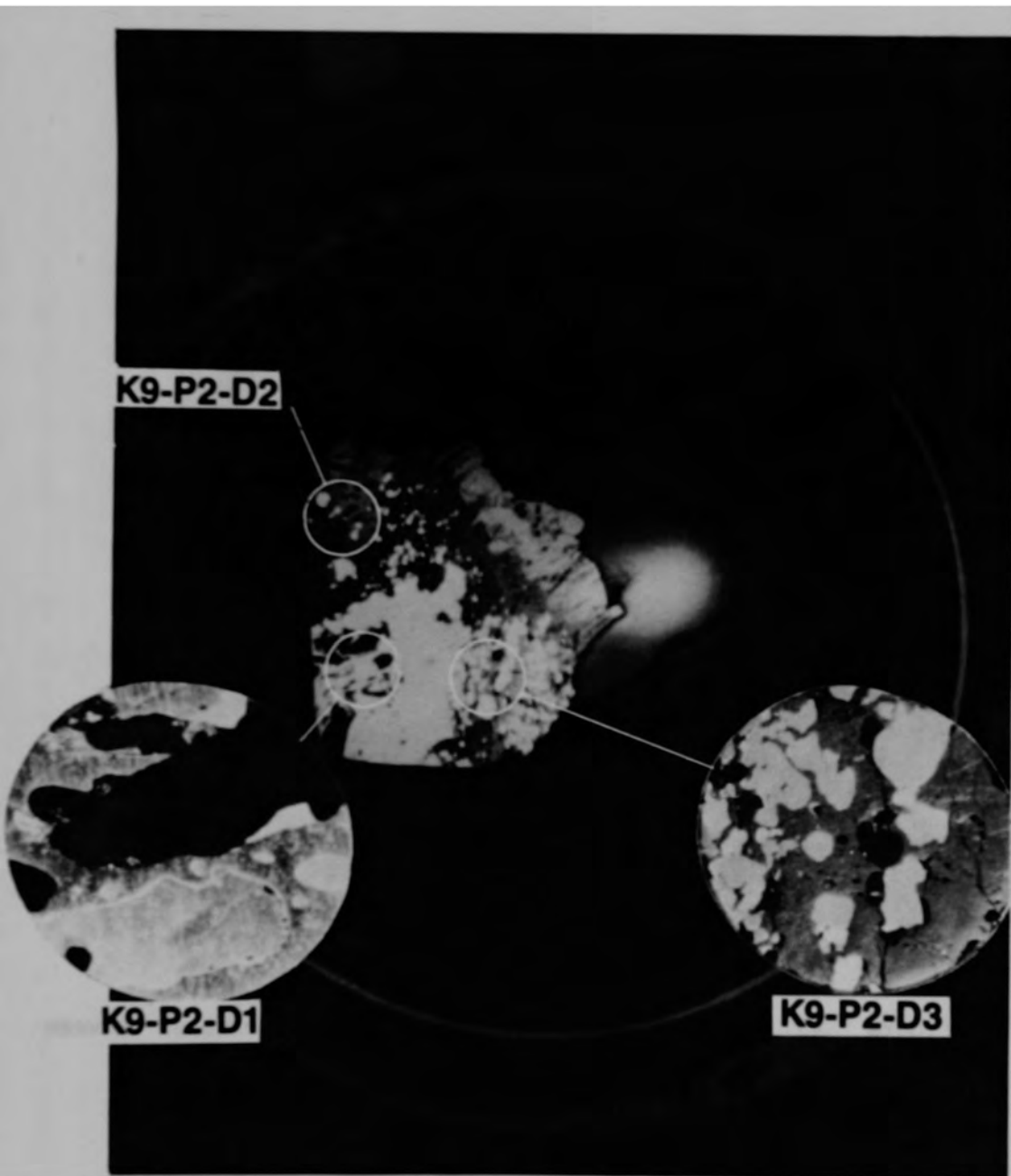


Figure E-42. SEM sample locations in K09-P2-D.



**HCA 1462-1463**

Figure E-43. Backscattered electron image of interfaces between metallic inclusions (K09-P2-D1).

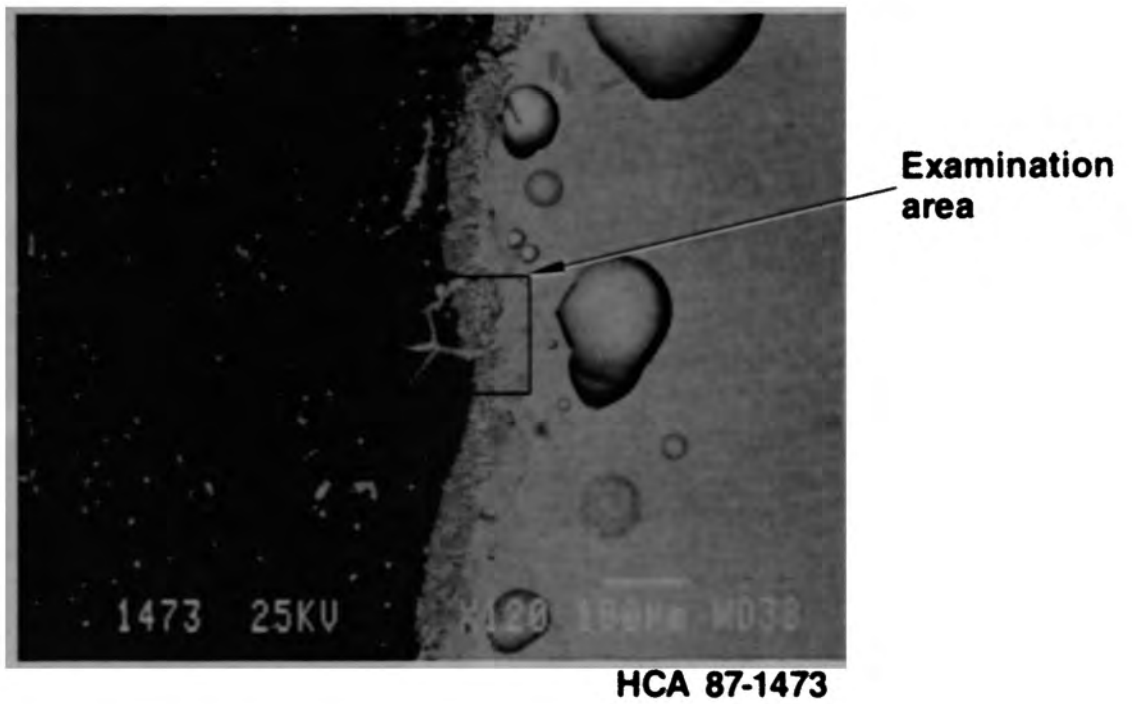
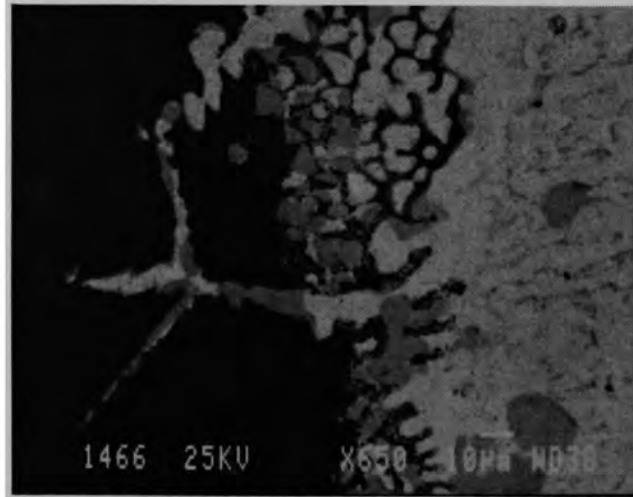
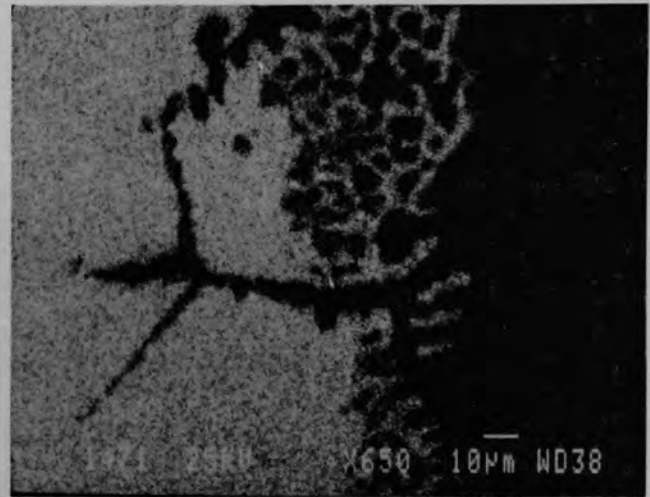


Figure E-44. Backscattered electron image of the interface between two metallic phases (K09-P2-D1 Area A).

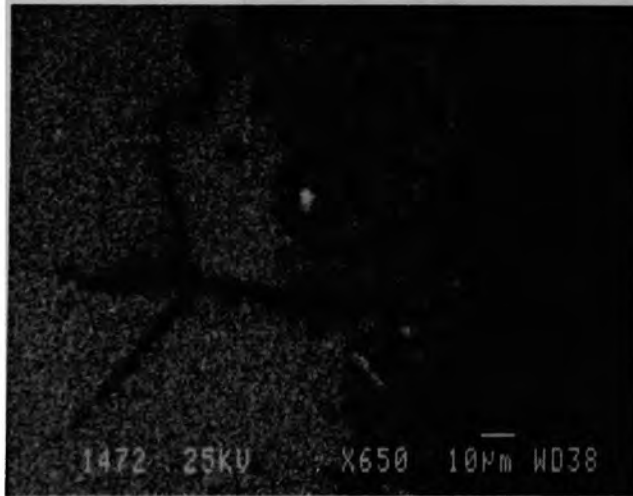


**BSE compositional image HCA 87-1466**



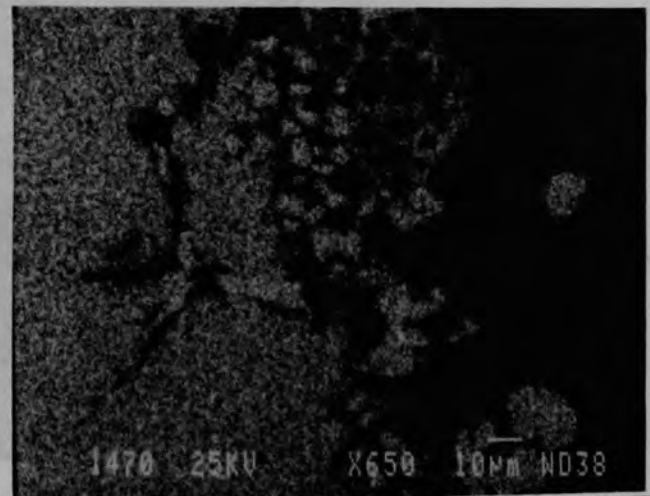
**Fe dot map**

**HCA 87-1471**



**Cr dot map**

**HCA 87-1472**



**Ni dot map**

**HCA 87-1470**

**Figure E-45. Distribution of elements at interface between metallics.**

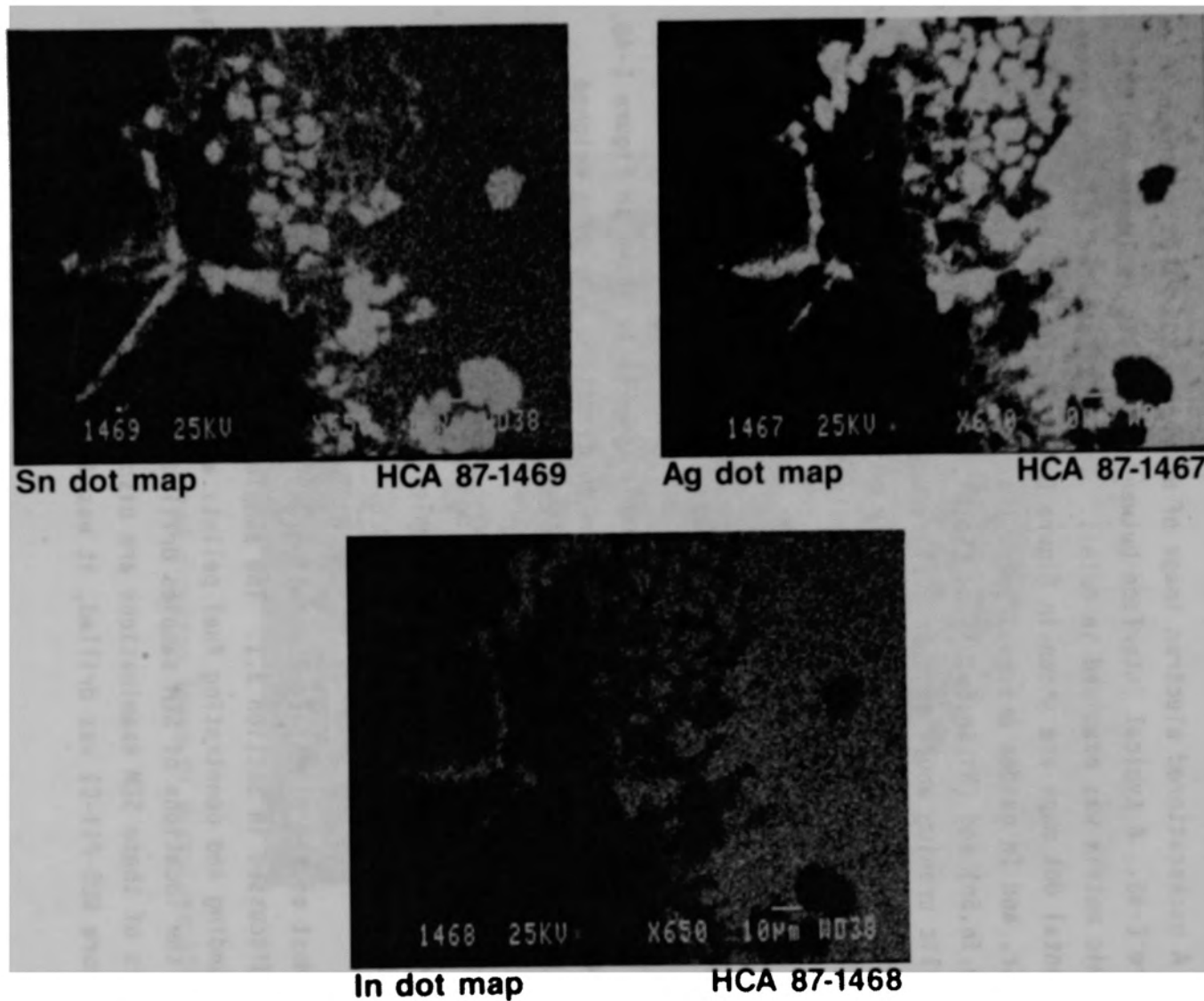


Figure E-45. (Continued)

(Fe,Cr,Ni) and (Ag,In), with Sn being partitioned between the two phases. A WDS quantitative analysis was performed in one location in this area as described in Appendix J (Figure J-6).

A backscattered electron image of microcore K09-P2-D3 is shown in Figure E-46. A typical interface between a metallic inclusion and the ceramic matrix was examined in detail. The backscattered electron image and elemental dot maps are shown in Figure E-47. In the top right corner are Zr, Cr, and In oxides phases. Below this are metallic layers of (U,Ag,In,Sn) and (Ni,Sn,Fe,U) and (Fe,Ni,Mo). The apparent presence of metallic uranium would suggest fuel reduction to hypostochiometric  $UO_{2-x}$  and liquid metallic uranium. The only major bundle constituent capable of reducing  $UO_2$  is Zr, which in the immediate vicinity is only present as an oxide in the ceramic phase.

#### G08-P11

The photograph of upper crust sample G08-P11 is shown in Figure E-48. The sample was 11.5 cm long and 6.4 cm in diameter. The plug weighed 1847.17 g and had a density of  $8.24 \text{ g/cm}^3$ .

The sectioning scheme for the plug is outlined in Figure E-48. The plug was sectioned as shown, with samples C, F, and I being metallographically examined at the INEL.

Most of the significant metallographic results from sample G08-P11-C were discussed in Section 3.1. The sample consisted of metallic melt surrounding and penetrating fuel pellets as shown in Figure E-49, which also shows the locations of SEM samples drilled from this cross section. The details of these SEM examinations are discussed here, although after microcore G08-P11-C1 was drilled, it was decided not to examine it on the SEM.

A backscattered electron image of microcore G08-P11-C3 is shown in Figure E-50. Area A is the interface between two metallic phases; Area B is



Figure E-46. Backscattered electron image of microcore K09-P2-D3.

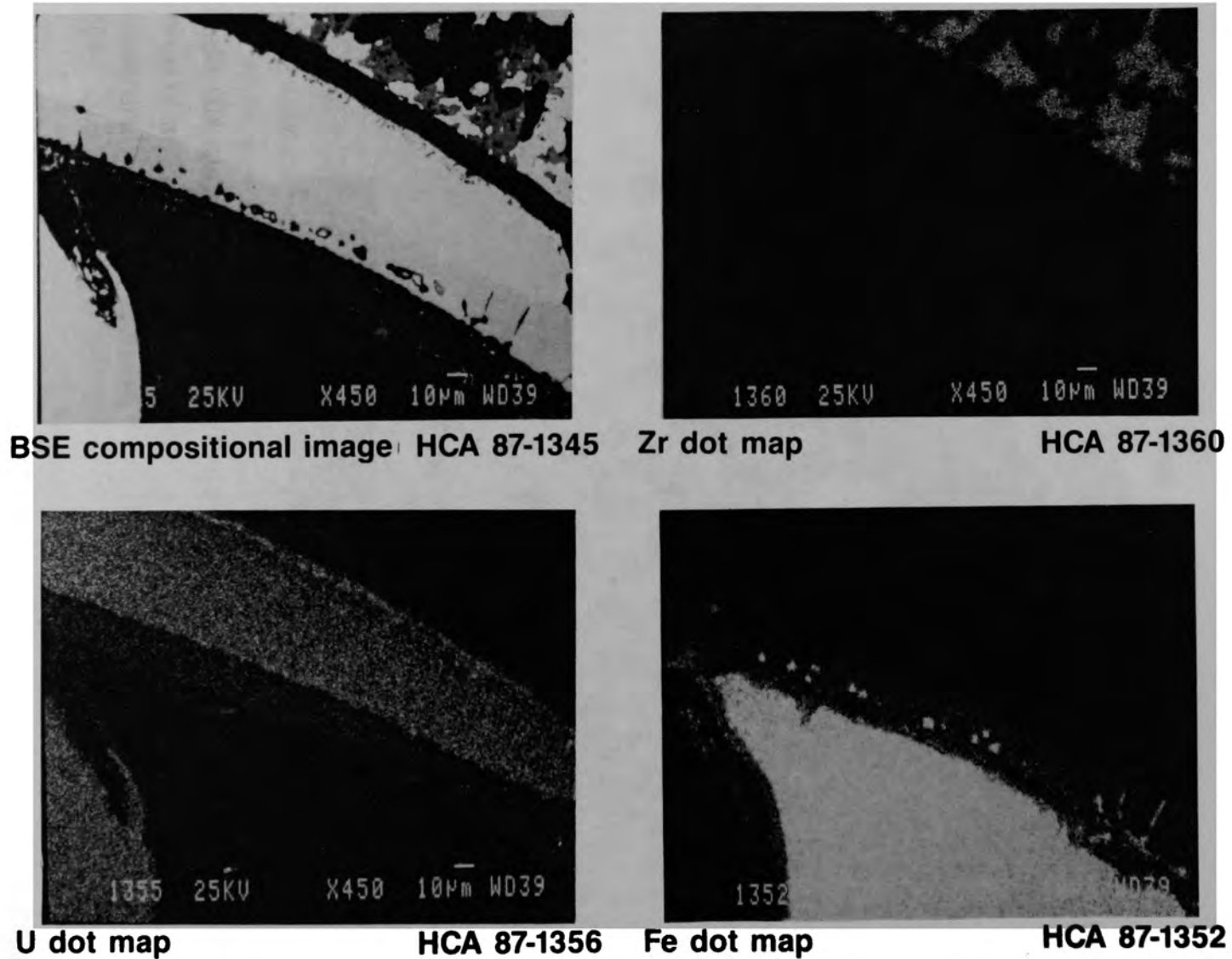


Figure E-47. Element distribution at interface between metallic particle and ceramic matrix (K09-P2-D3).



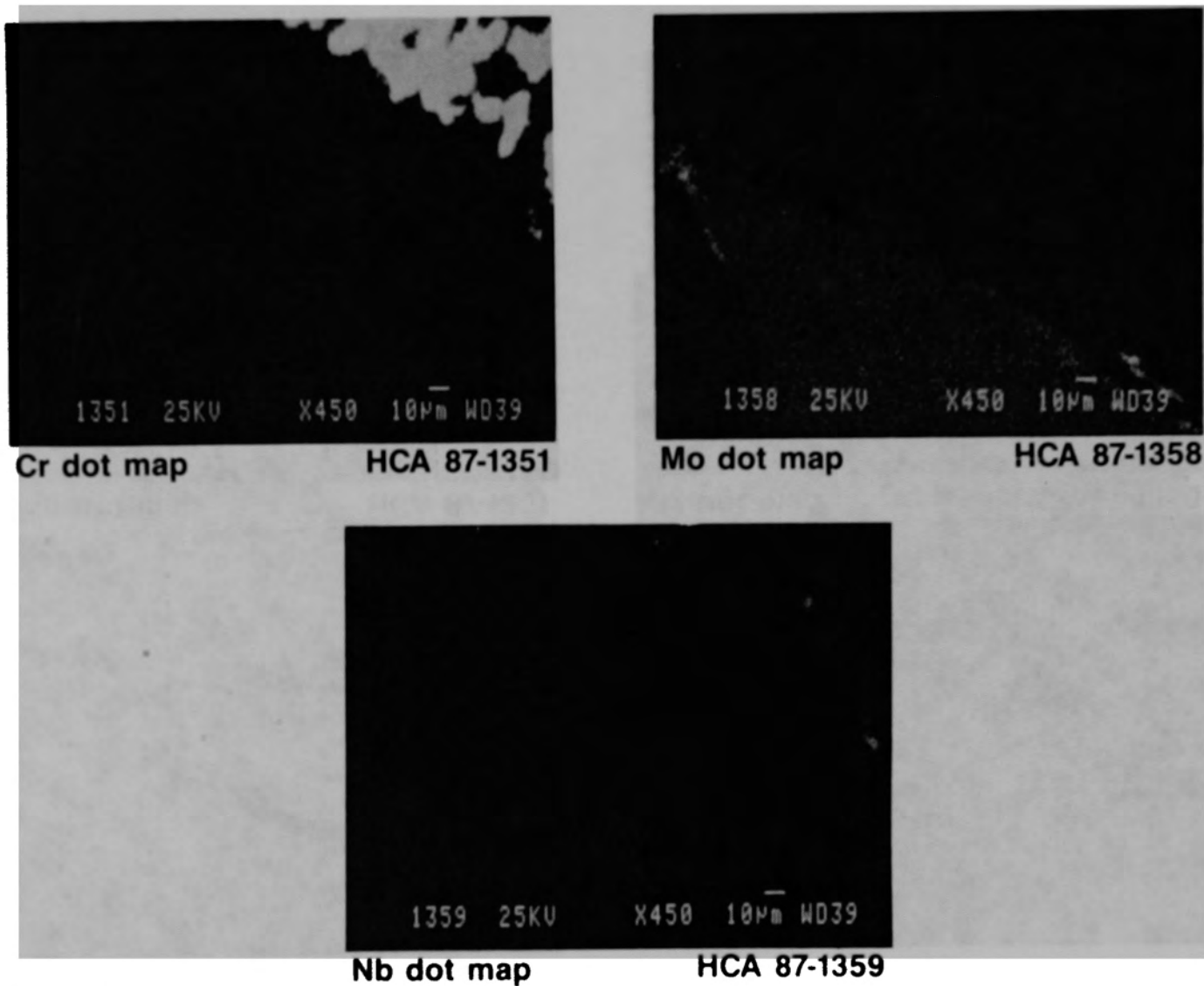


Figure E-47. (Continued)

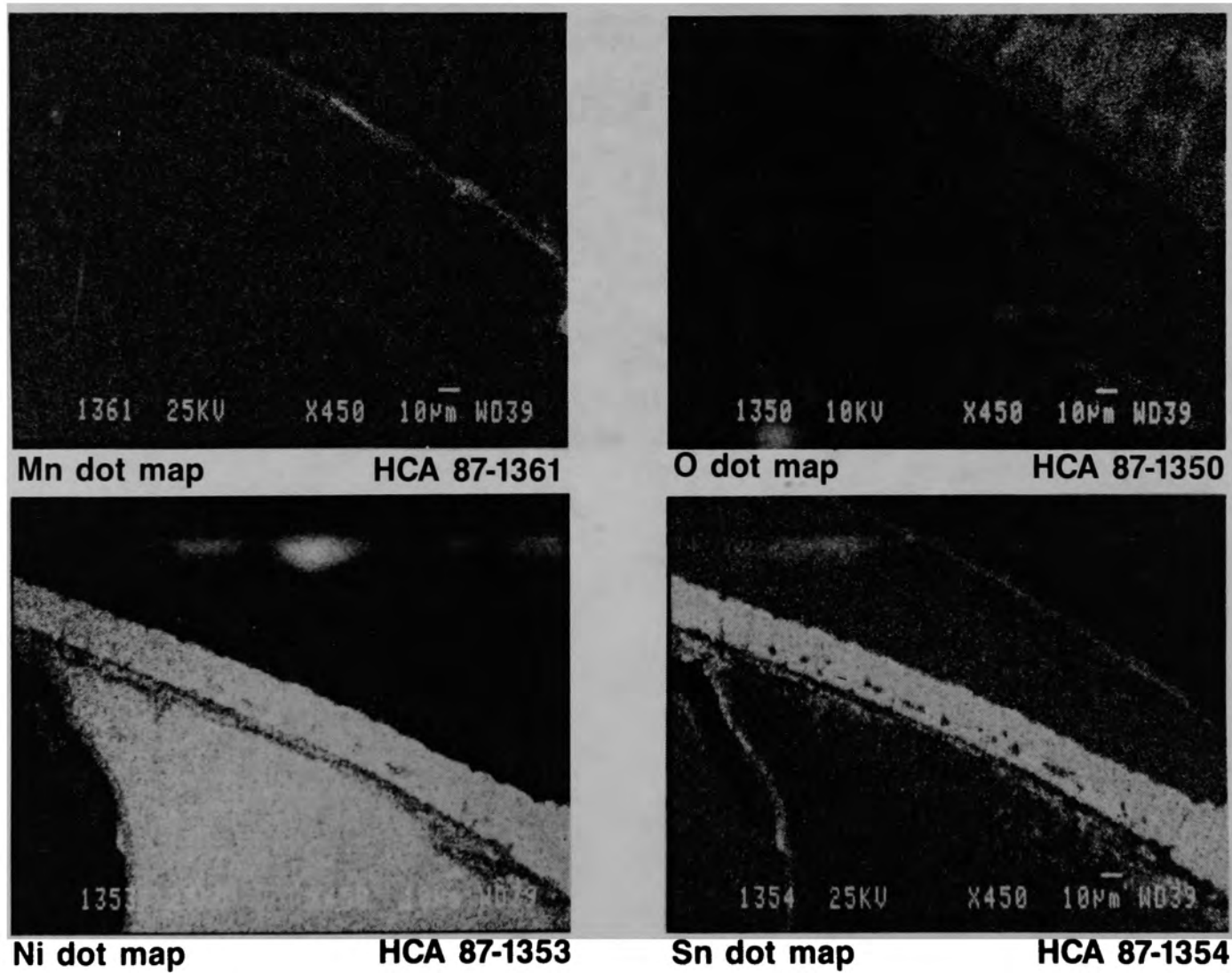


Figure E-47. (Continued)

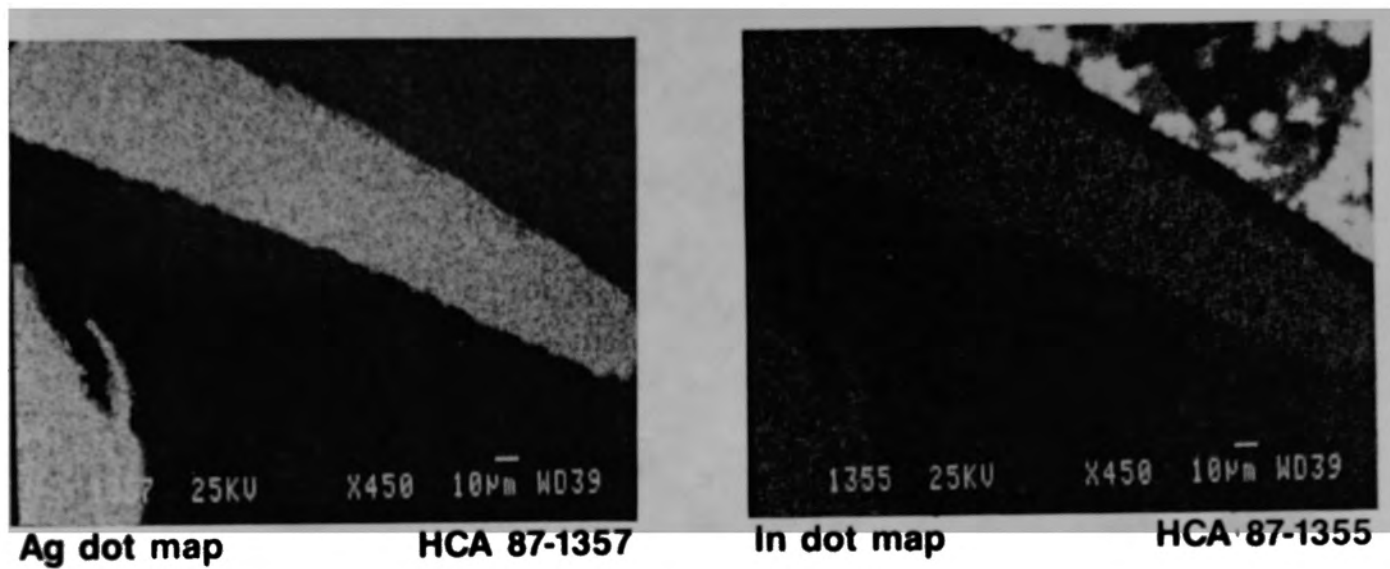


Figure E-47. (Continued)

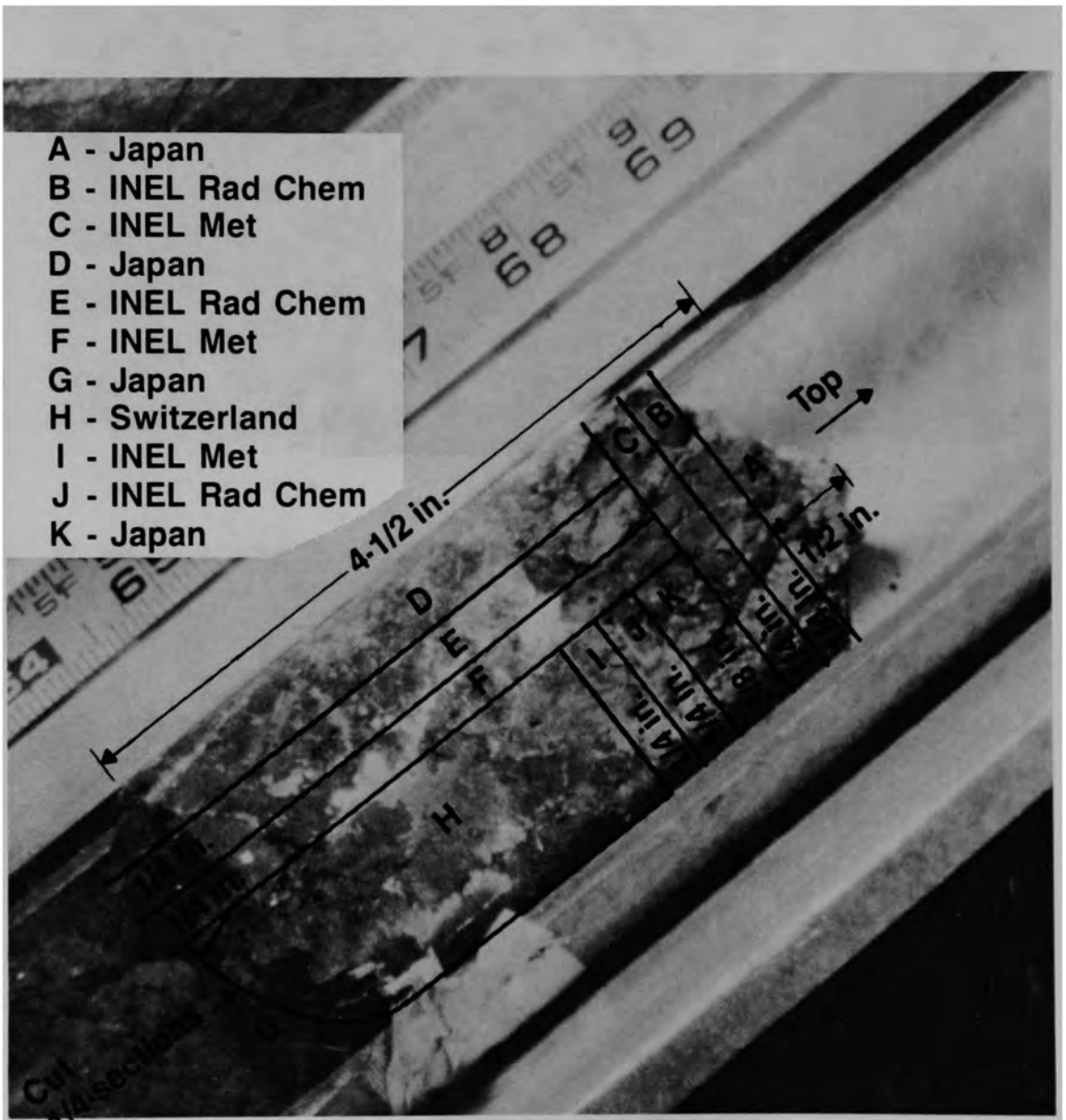


Figure E-48. Overview of G08-P11 upper crust sample.

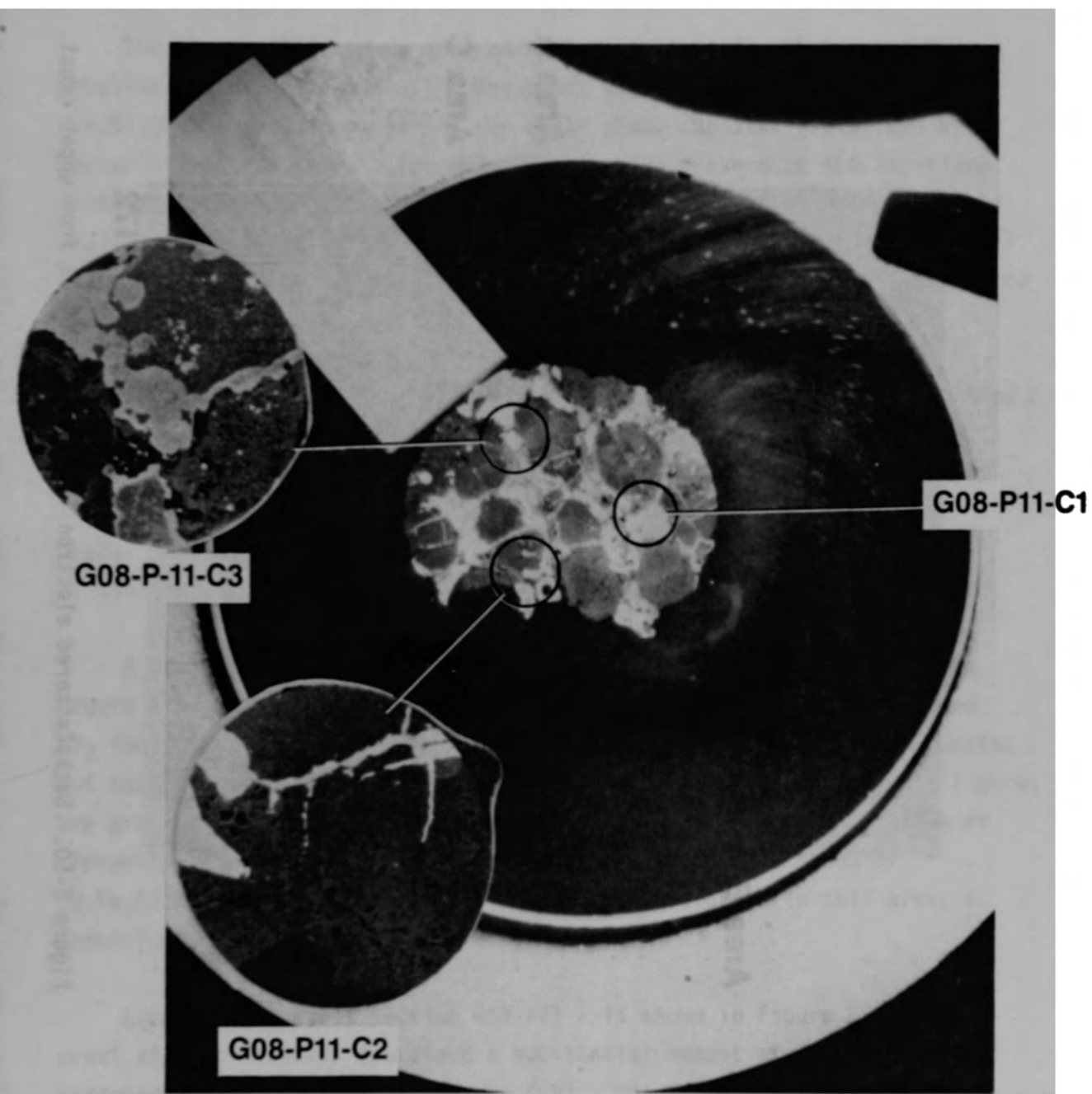


Figure E-49. Locations for SEM samples from upper crust sample G08-P11-C.

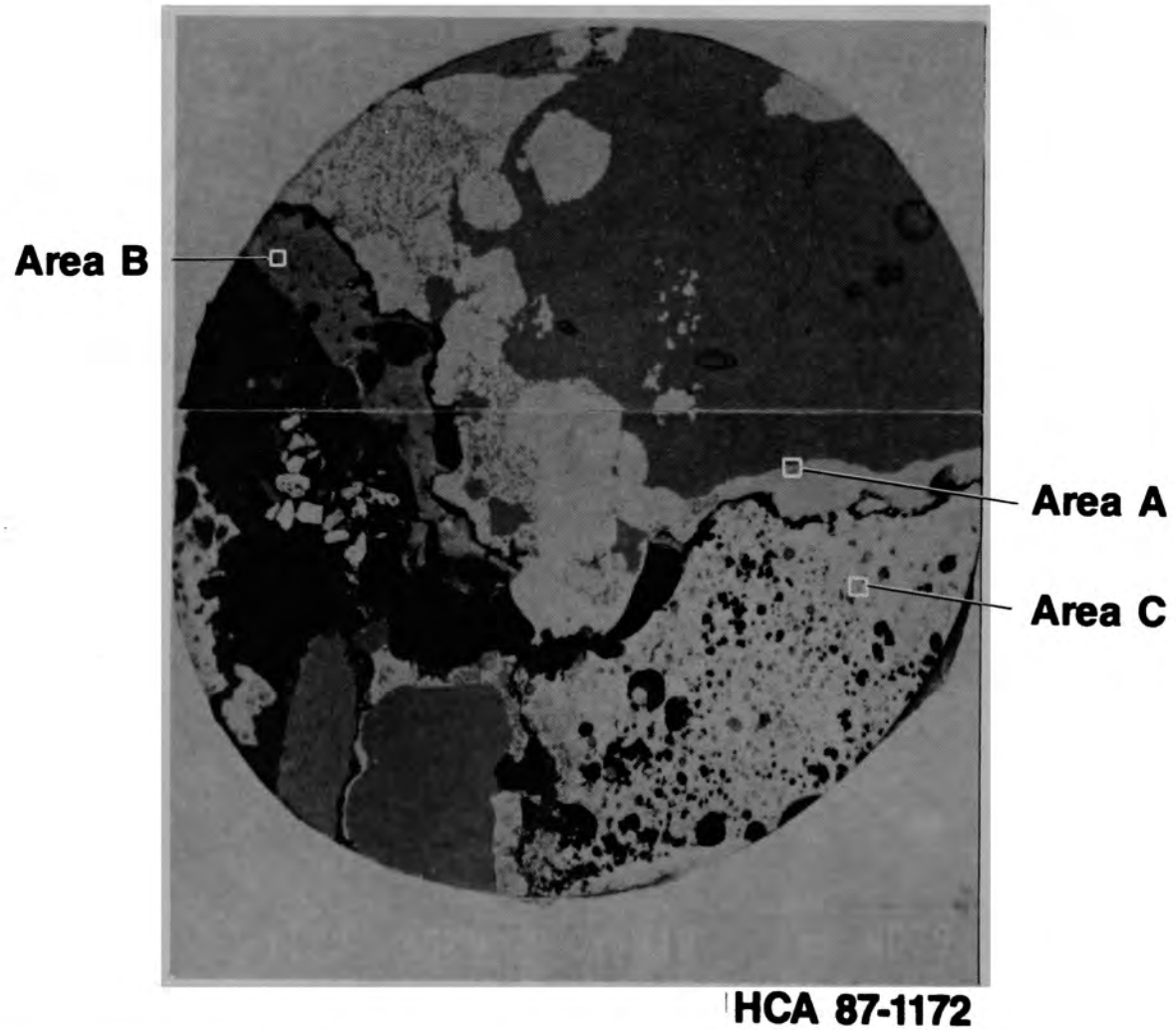


Figure E-50. Backscattered electron image of G08-P11-C3 from upper crust.

a ceramic layer adjacent to a metallic phase; and Area C contains a metallic inclusion inside a  $UO_2$  fuel pellet. Only areas A and C are discussed here.

The elemental dot maps at Area A show the interface between two metallic phases (Figure E-51). One phase contains (Ag,In,Sn) with (Fe,Ni,Cr,Sn) inclusions, while the other phase contains (Fe,Ni,Cr) with inclusions of (Ag,In). A (Ni,Sn) phase is also present at the interface. These dot maps demonstrate the immiscibility of (Fe,Ni,Cr) melts from the stainless steel and Inconel components, and (Ag,In) melts from the control rods. The tin from the zircaloy is alloyed with nickel and the control rod materials.

The elemental dot maps for the metallic inclusion in the fuel at Area C are shown in Figure E-52. The matrix is  $UO_2$  with inclusions of Zr, Fe, Ni, and Cr. Several immiscible phases are present in the large metallic inclusion. These include (Ag,In,Cd,Sn), (Ni,Sn,Fe,In), (Ni,Sn), and  $Cr_2O_3$ . These immiscible phases are similar to those observed in Area A of this same sample.

A backscattered electron image of microcore G08-P11-C2 is shown in Figure E-53. Area A is near an interface between oxidized cladding and  $UO_2$  fuel, and an overview of this area is shown in Figure E-54. Elemental dot maps, obtained to characterize the region within the box in this figure, are presented in Figure E-55. These dot maps indicate some diffusion of zirconium into the fuel and a eutectic microstructure composed of (U,Fe,Ni,Ag,Cr). WDS point analysis was also performed in this area, as described in Appendix J (Figure J-5).

Longitudinal cross section G08-P11-F is shown in Figure E-56. The crust at this location contained a substantial amount of metallic melt surrounding and penetrating the  $UO_2$  fuel. About half of this cross section was ceramic melt. A number of different areas were examined, as shown in Figure E-56.

E-74

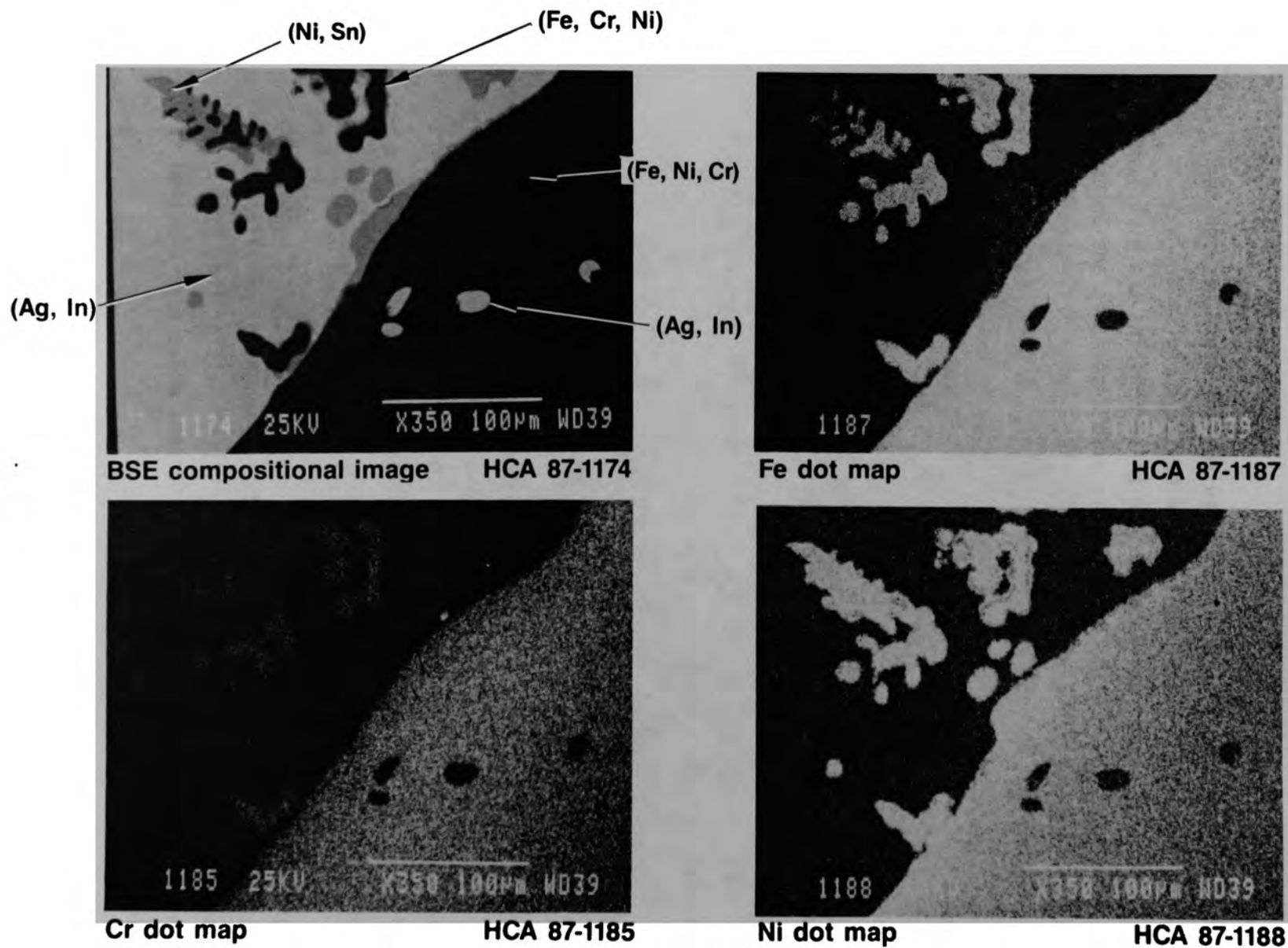
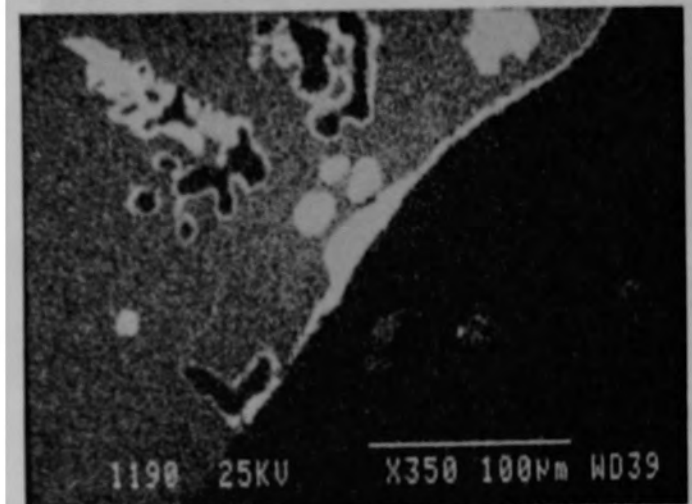
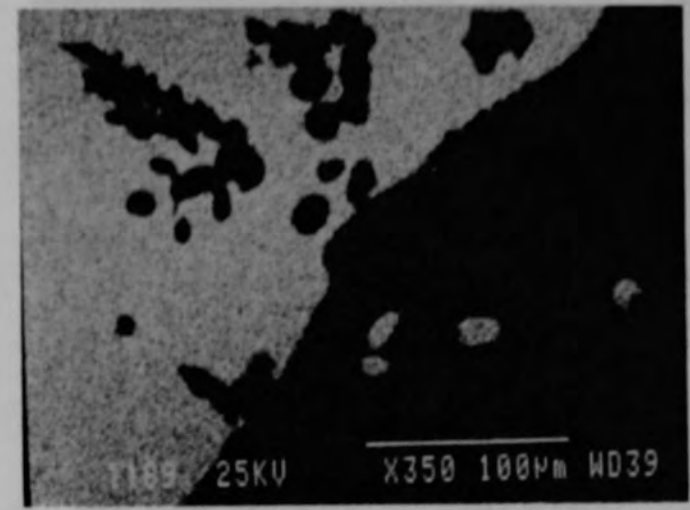


Figure E-51. Elemental dot maps of interface between immiscible metallic melts (G08-P11-C3 Area A).

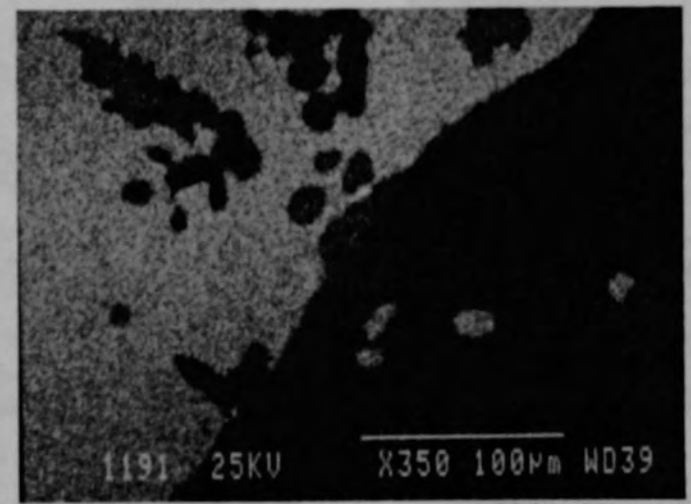




Sn dot map HCA 87-1190



Ag dot map HCA 87-1189



In dot map HCA 87-1191

Figure E-51. (Continued)

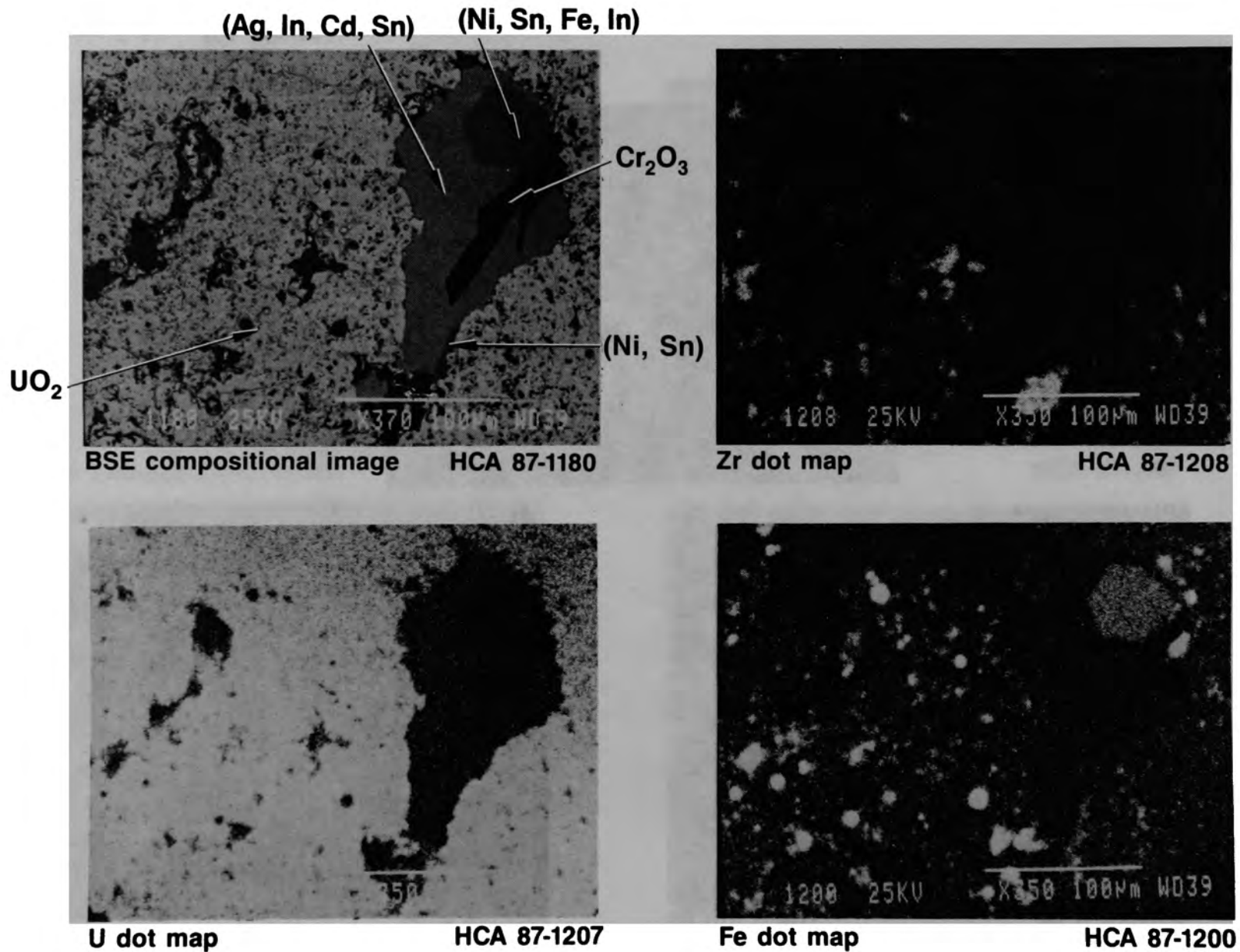
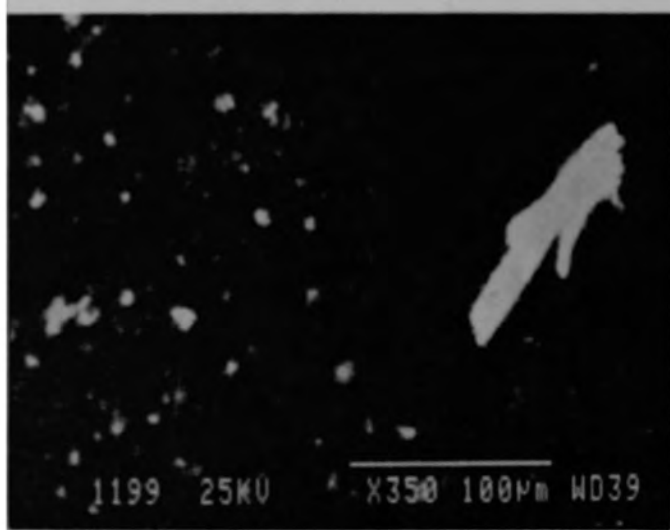
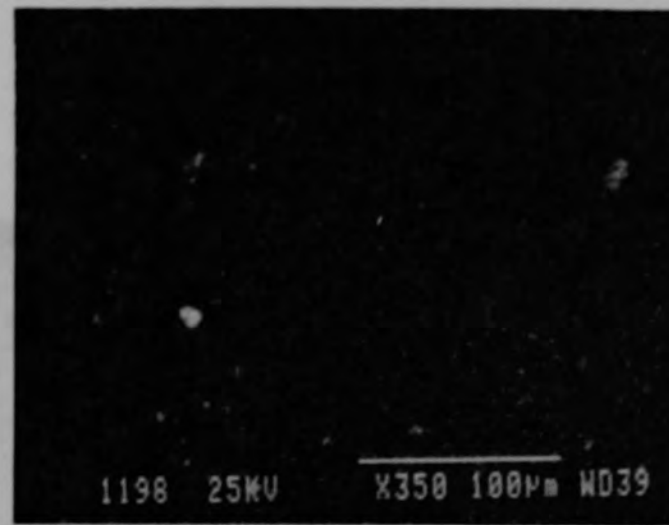


Figure E-52. Metallic inclusions in uranium dioxide fuel (G08-P11-C3 Area C).



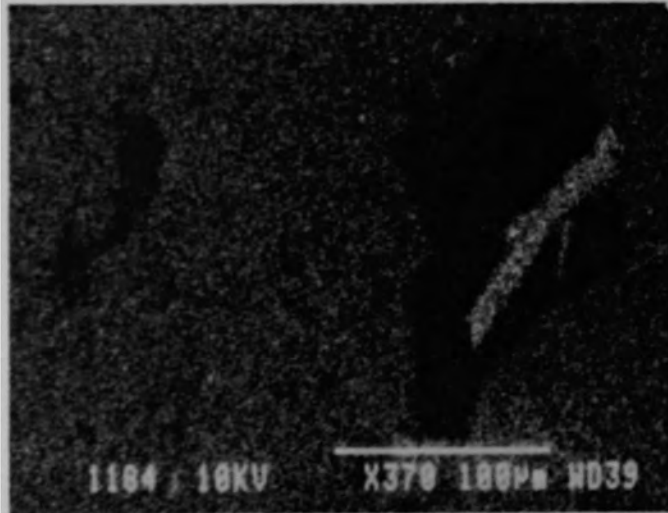
Cr dot map

HCA 87-1199



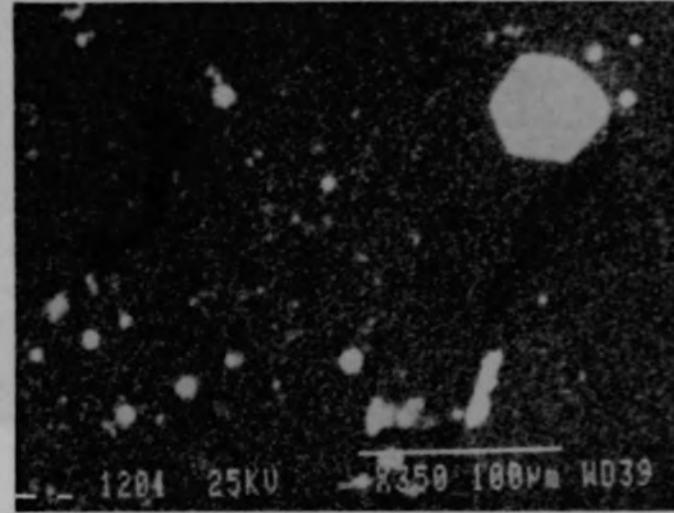
Mn dot map

HCA 87-1198



O dot map

HCA 87-1184



Ni dot map

HCA 87-1201

Figure E-52. (Continued)

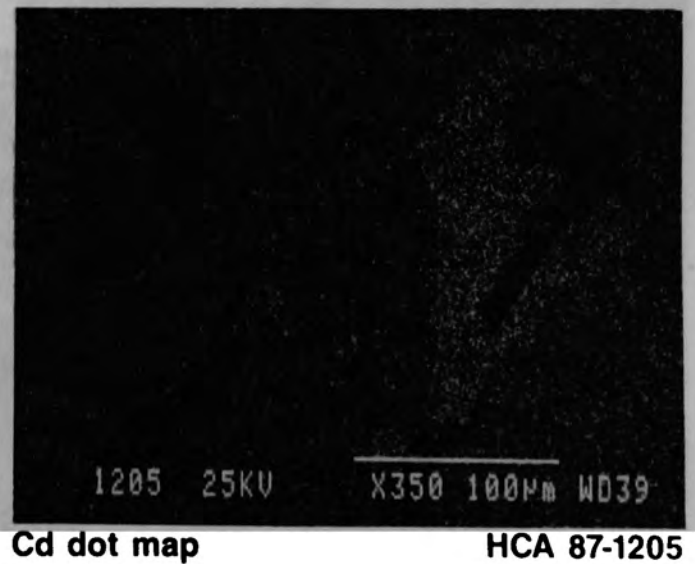
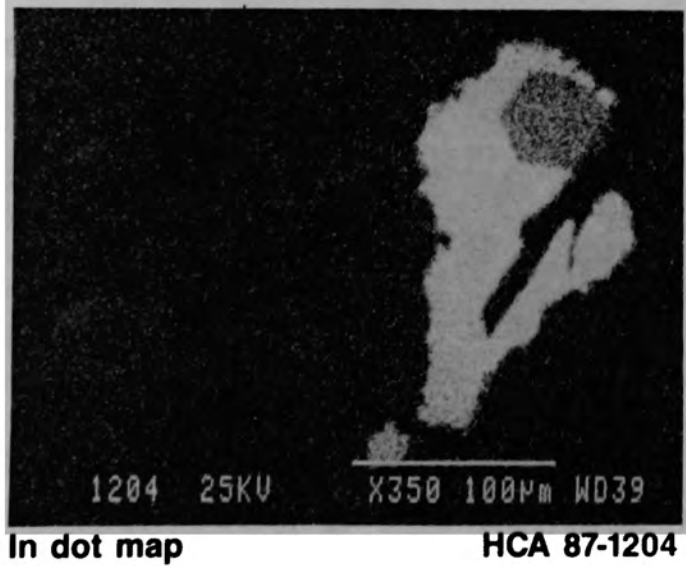
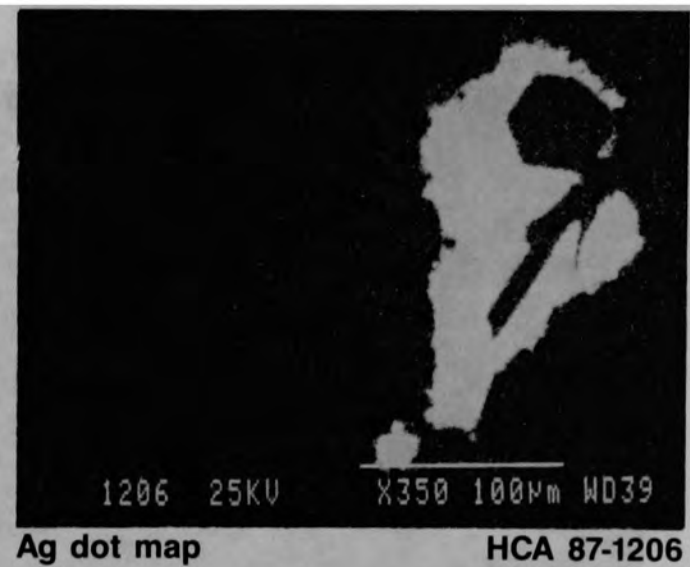
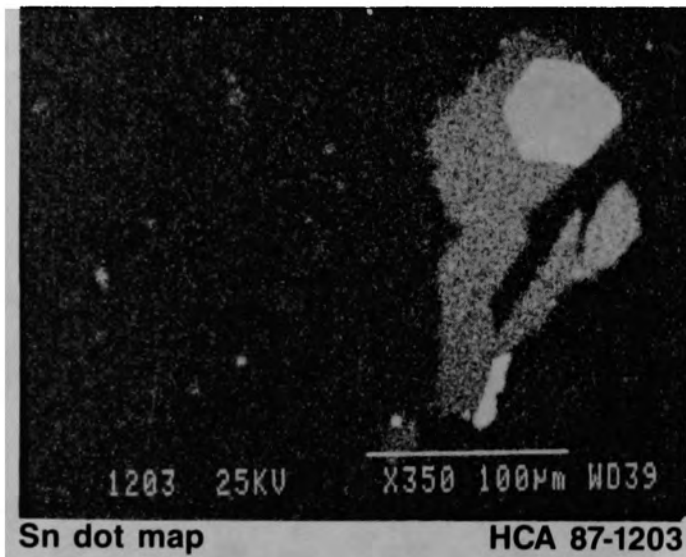
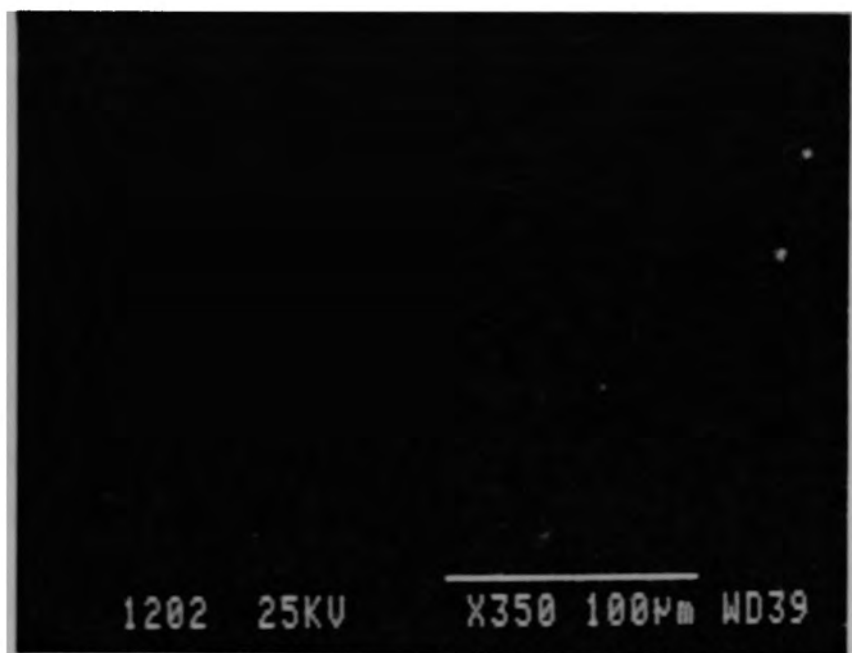


Figure E-52. (Continued)



**Tc dot map**

**HCA 87-1202**

Figure E-52. (Continued)

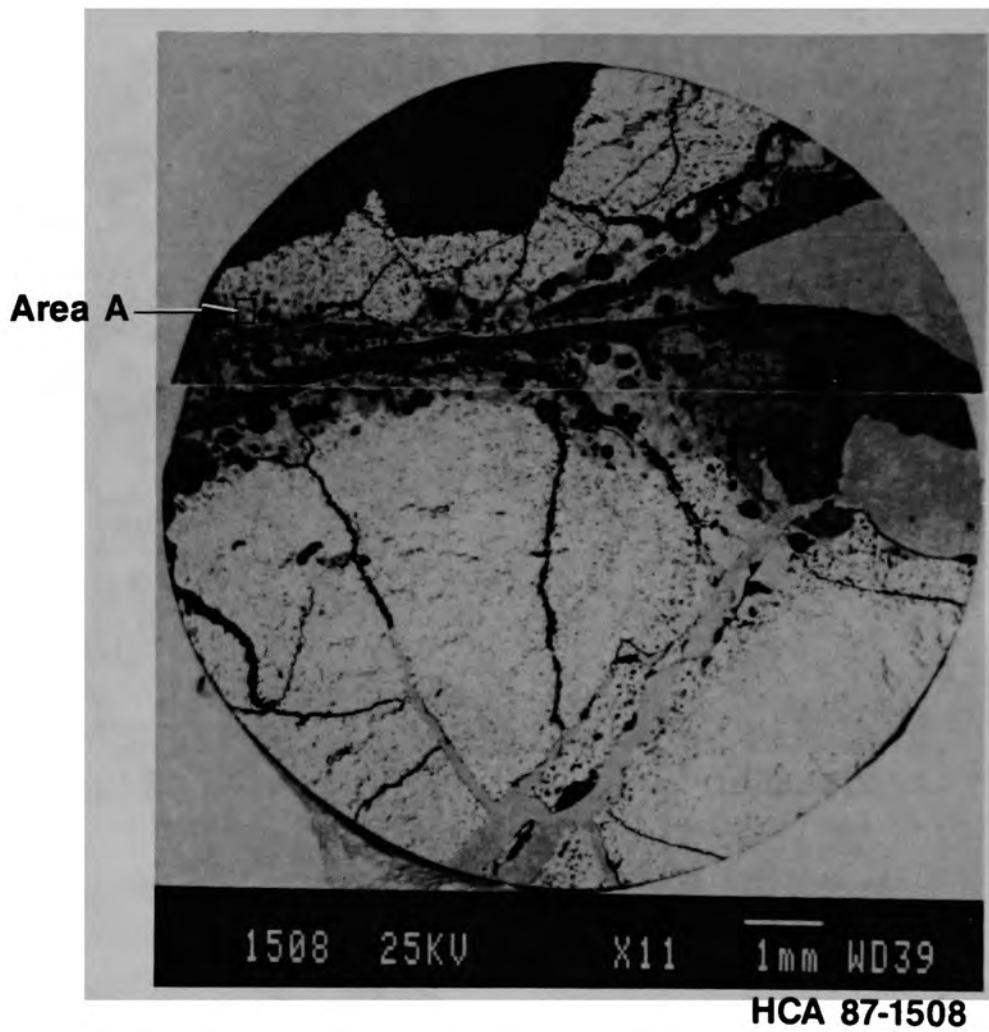


Figure E-53. Backscattered electron image of microcore G08-P11-C2 from upper crust.

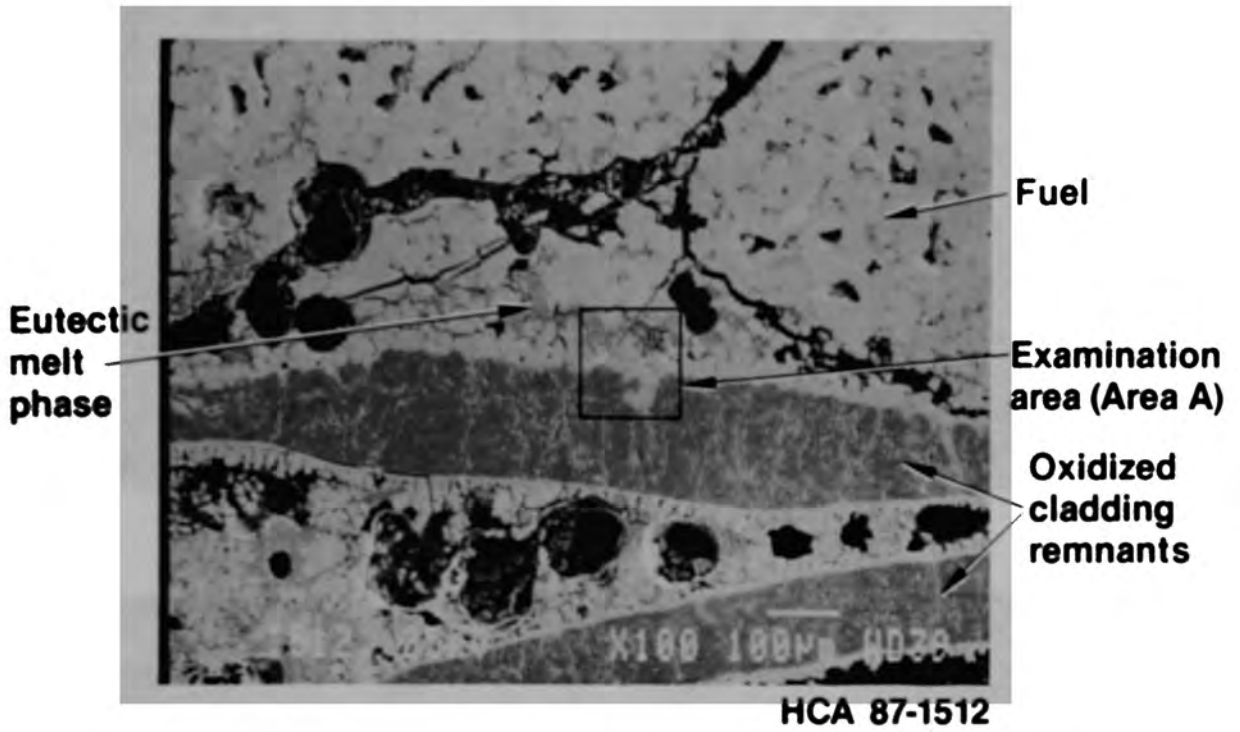


Figure E-54. Backscattered electron image overview of interaction of metallics with fuel and cladding (G08-P11-C2 Area A).

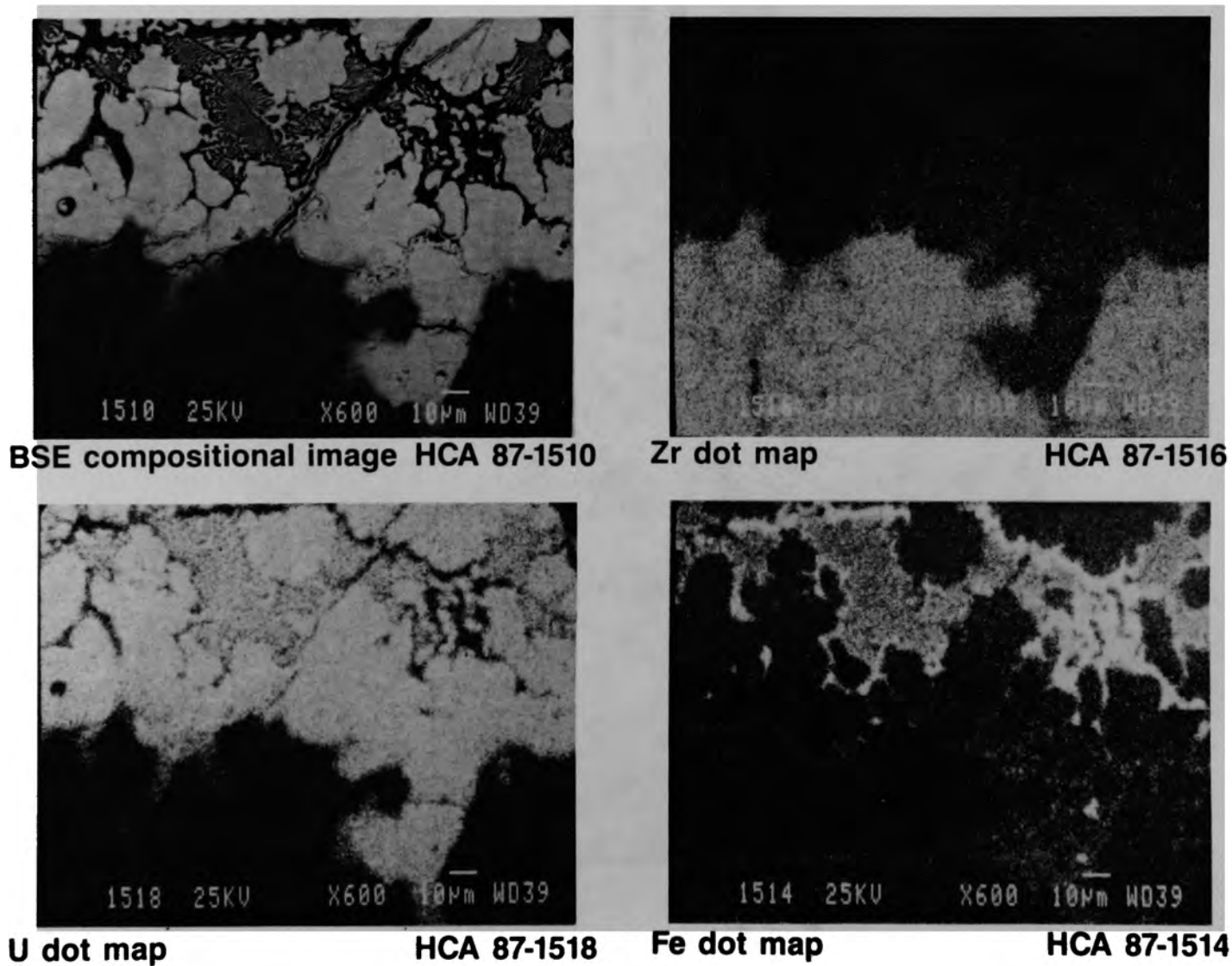
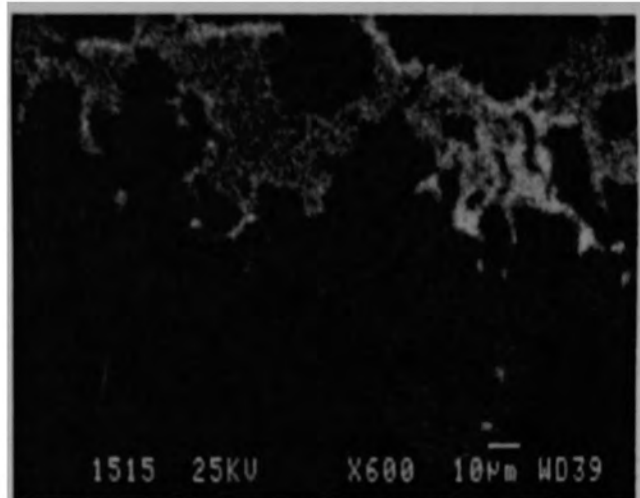


Figure E-55. Elemental distribution at cladding/fuel interface in upper crust sample G08-P11-C2 (Area A).

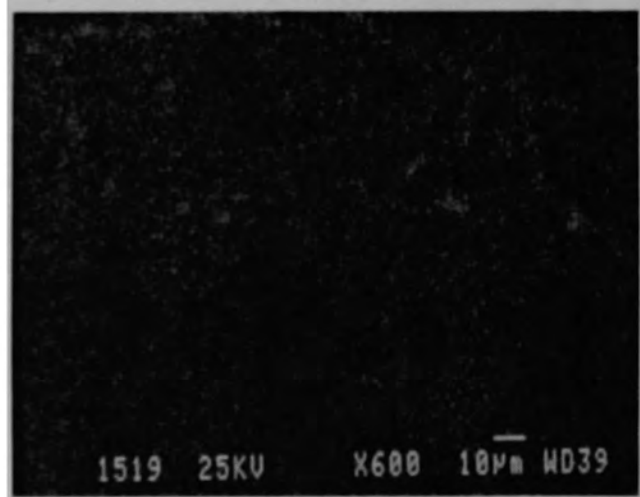




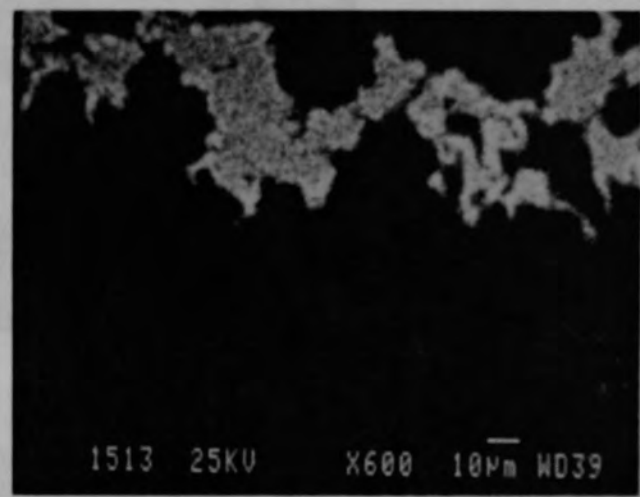
Ni dot map HCA 87-1515



O dot map HCA 87-1520



Sn dot map HCA 87-1519



Ag dot map HCA 87-1517

Figure E-55. (Continued)

E-84

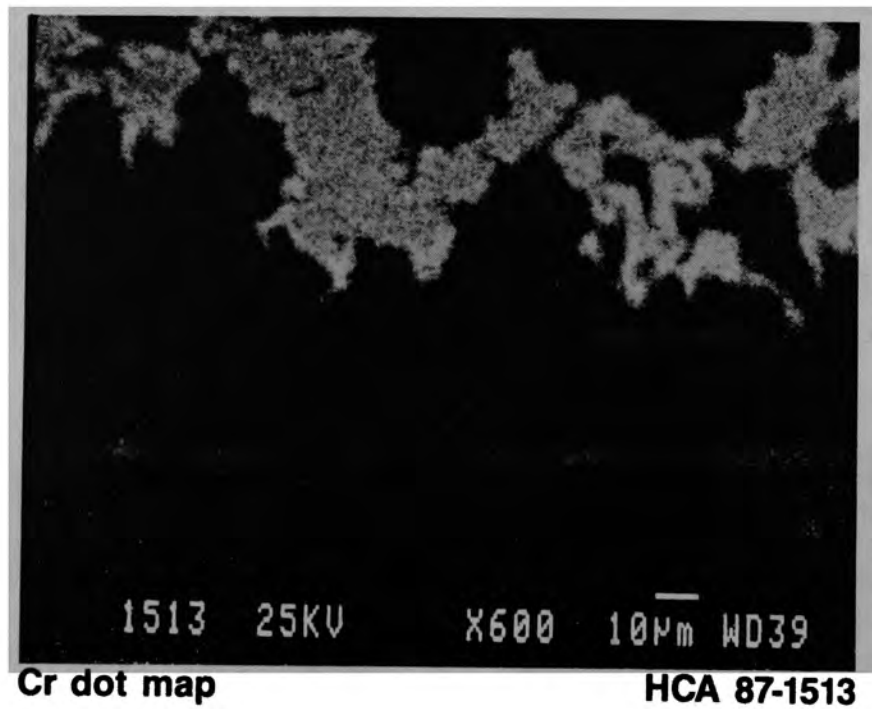
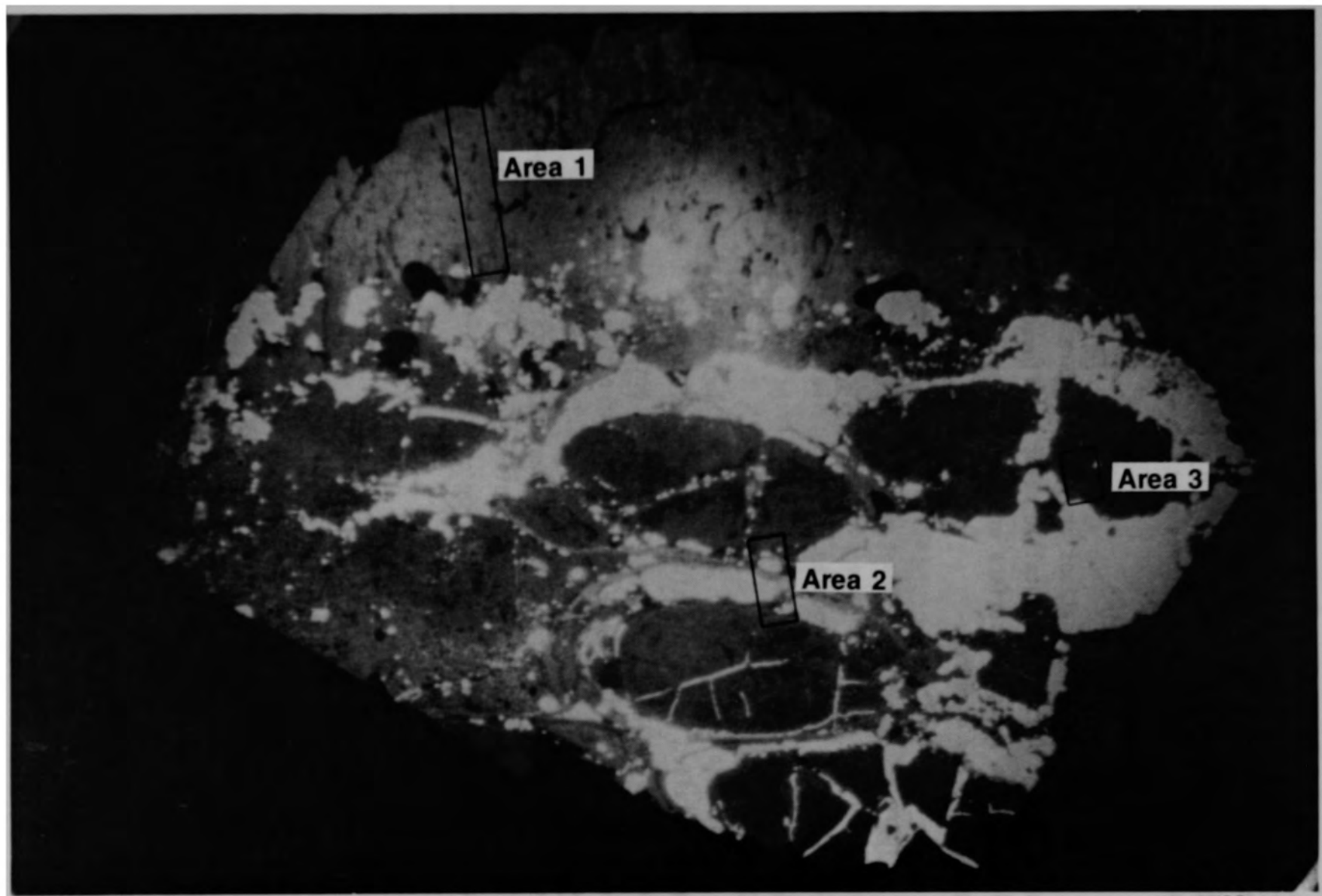


Figure E-55. (Continued)



87M-496

Figure E-56. Cross section from G08-P11-F.

The microstructure of the material in G08-P11-F Area 1 is shown in Figures E-57 and E-58. The microstructure in Figure E-57 shows a matrix of  $(U,Zr)O_2$  with areas of mottled structure near some of the grain boundaries. The area within these mottled regions is shown in more detail in Figure E-58.

Metallographic examinations at Area 2 (Figure E-59) indicated that the cladding was oxidized, and metallic melts had flowed between the cladding and fuel. The irregular surface of the fuel suggests that some fuel liquefaction had occurred.

Figure E-60 shows multiphase metallic melt adjacent to the fuel in Area 3 of G08-P11-F. Extensive porosity was present in the fuel, and metallic inclusions were located throughout the fuel. The metallic globule next to the fuel contains a number of different metallic phases.

Transverse cross section G08-P11-I is shown in Figure E-61. This sample contained a substantial amount of metallic melt surrounding and penetrating  $UO_2$  fuel. Figure E-62 shows the metallic melt structure at Area 1. This area includes a two-phase layer of immiscible melts, coating a multiphase metallic melt. Metallographic examination of Area 2 (Figure E-63) shows a large amount of two phase metallic melt surrounding a fuel fragment. This fuel fragment contained extensive porosity and some metallic inclusions in the voids. The irregular surface suggests that it may have been partially liquefied.

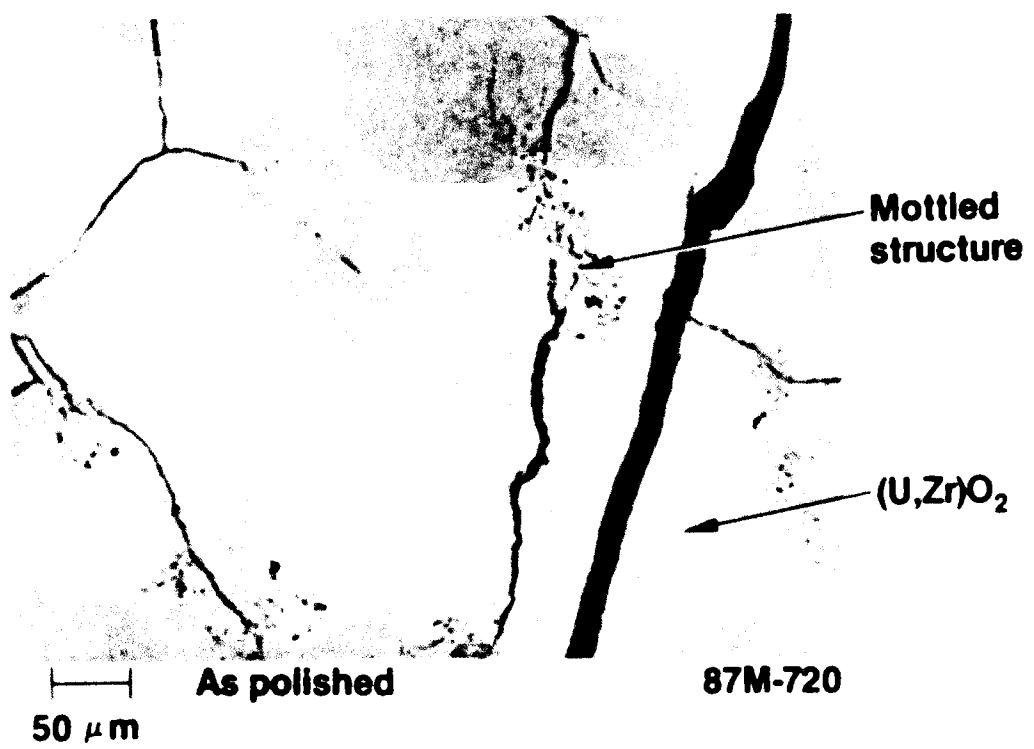


Figure E-57. Mottled structure in  $(U,Zr)O_2$ .

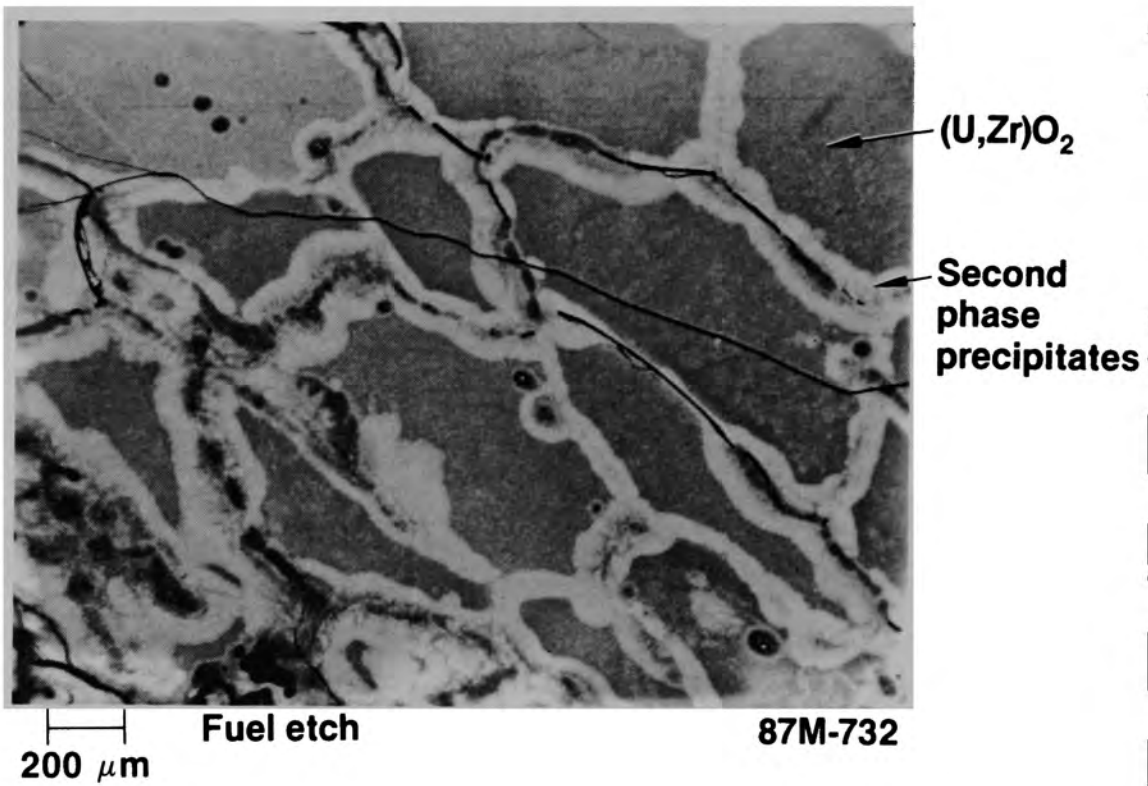


Figure E-58. Second-phase precipitates along  $(U,Zr)O_2$  grain boundaries (G08-P11-F Area 1).

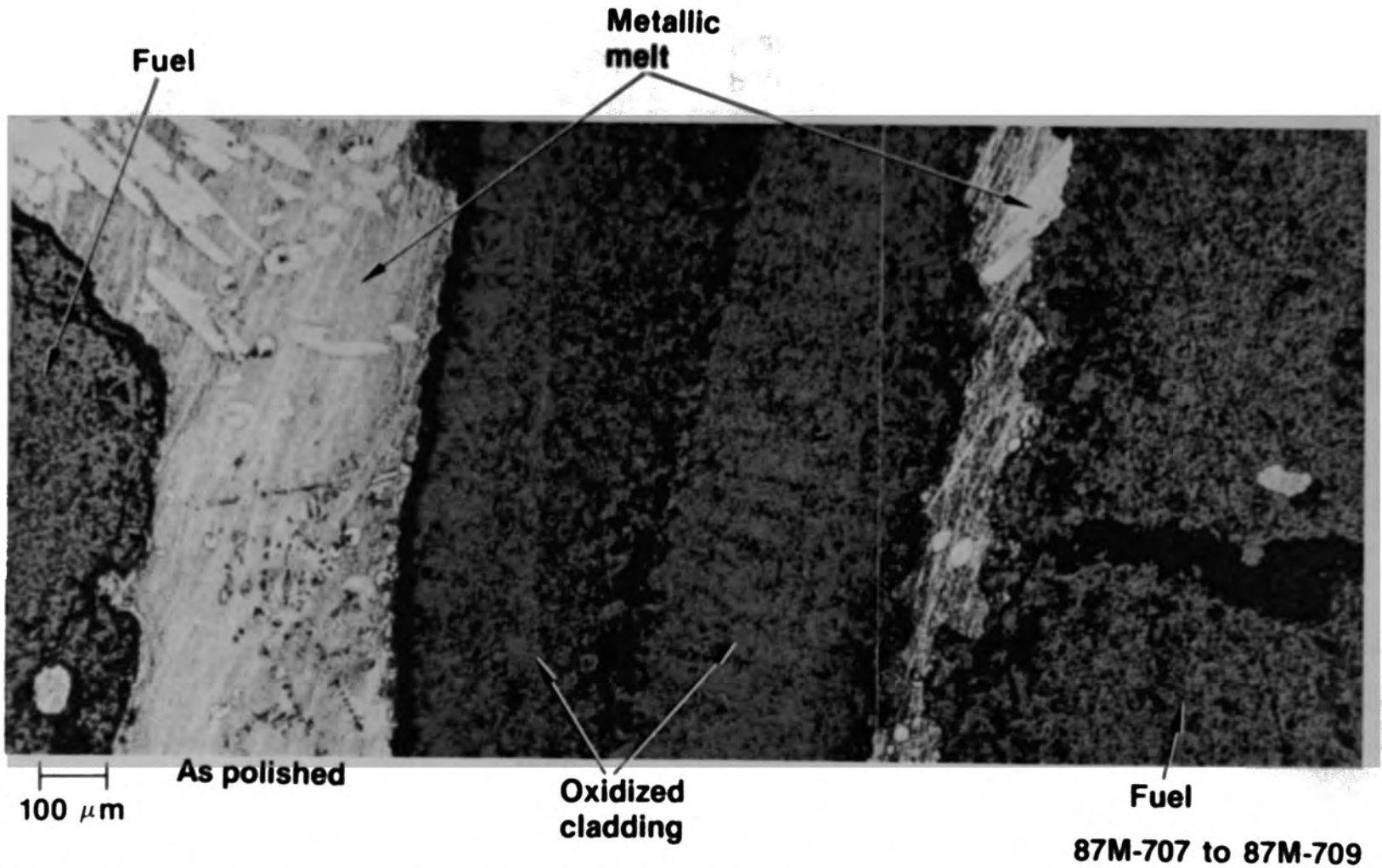


Figure E-59. Interaction of metallic material with fuel and oxidized cladding (G08-P11-F Area 2).

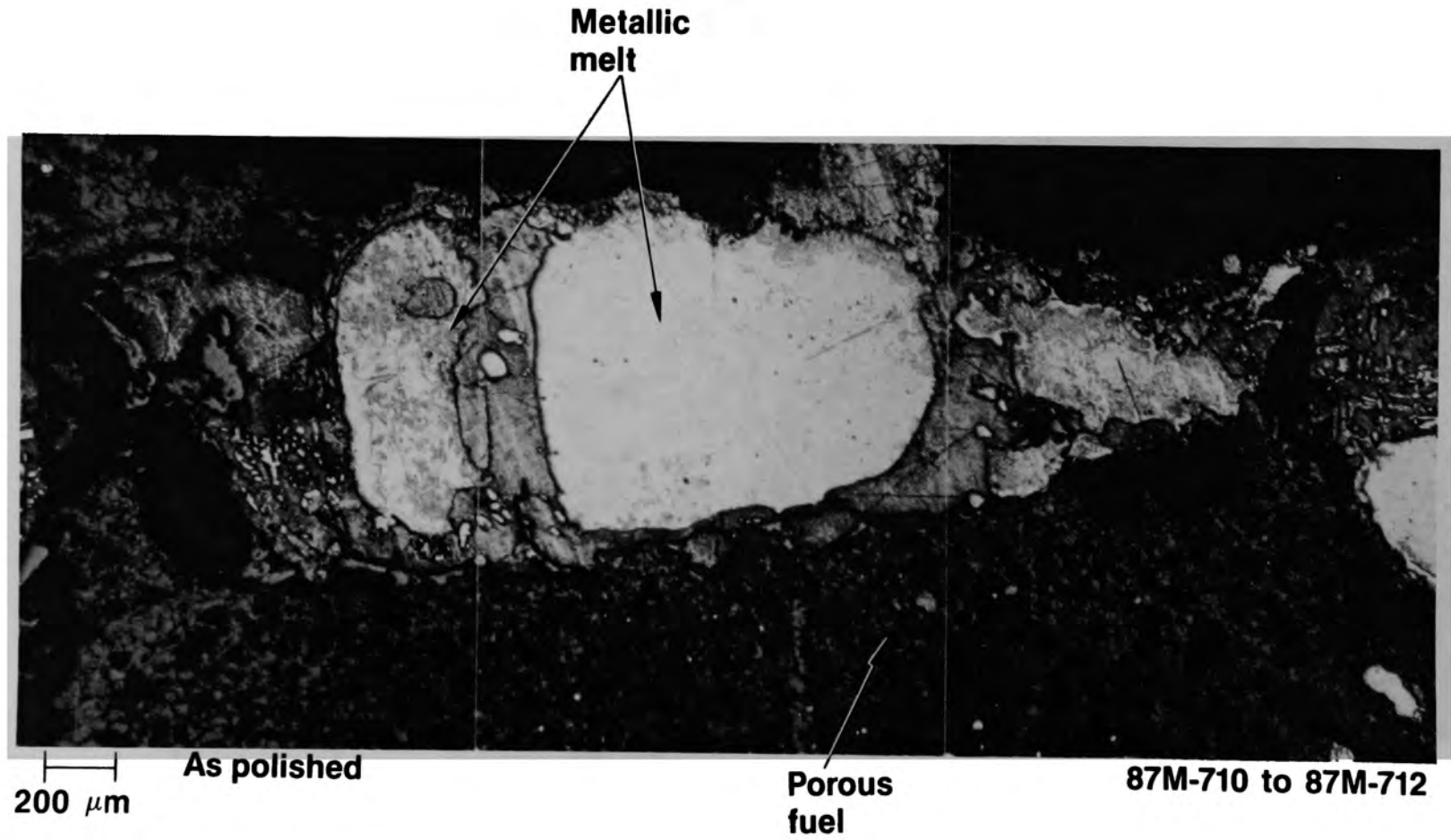


Figure E-60. Metallic inclusion adjacent to fuel (G08-P11-F Area 3).



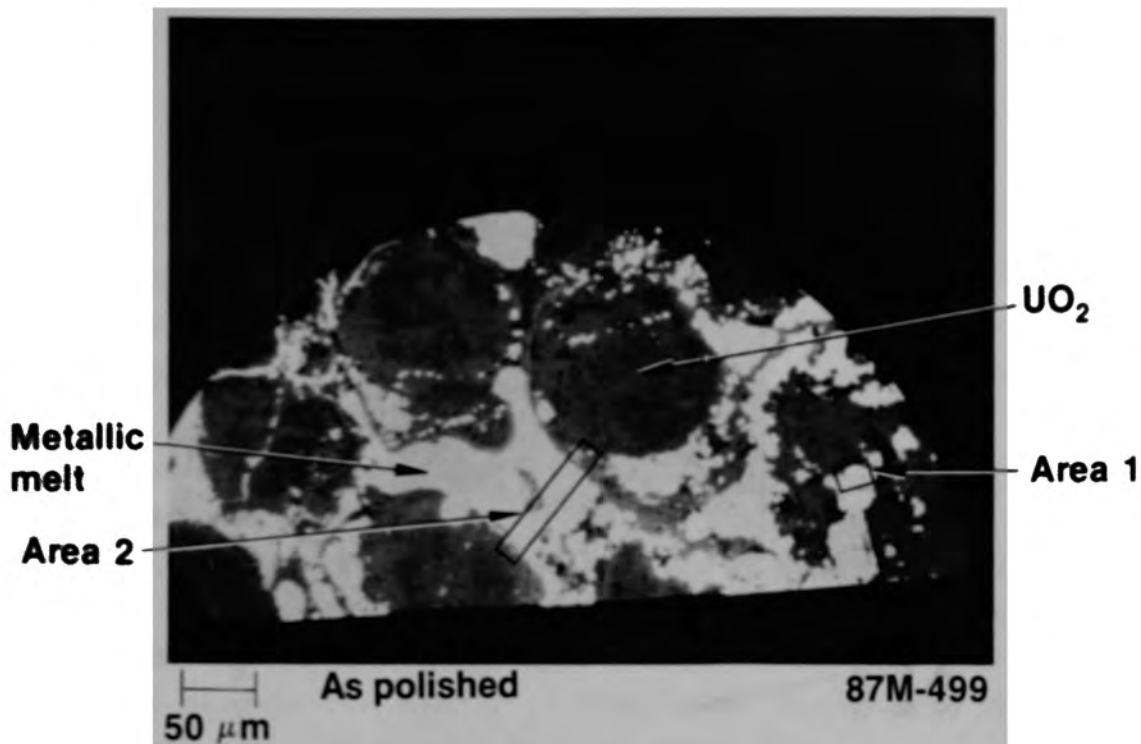


Figure E-61. Transverse cross section G08-P11-I.

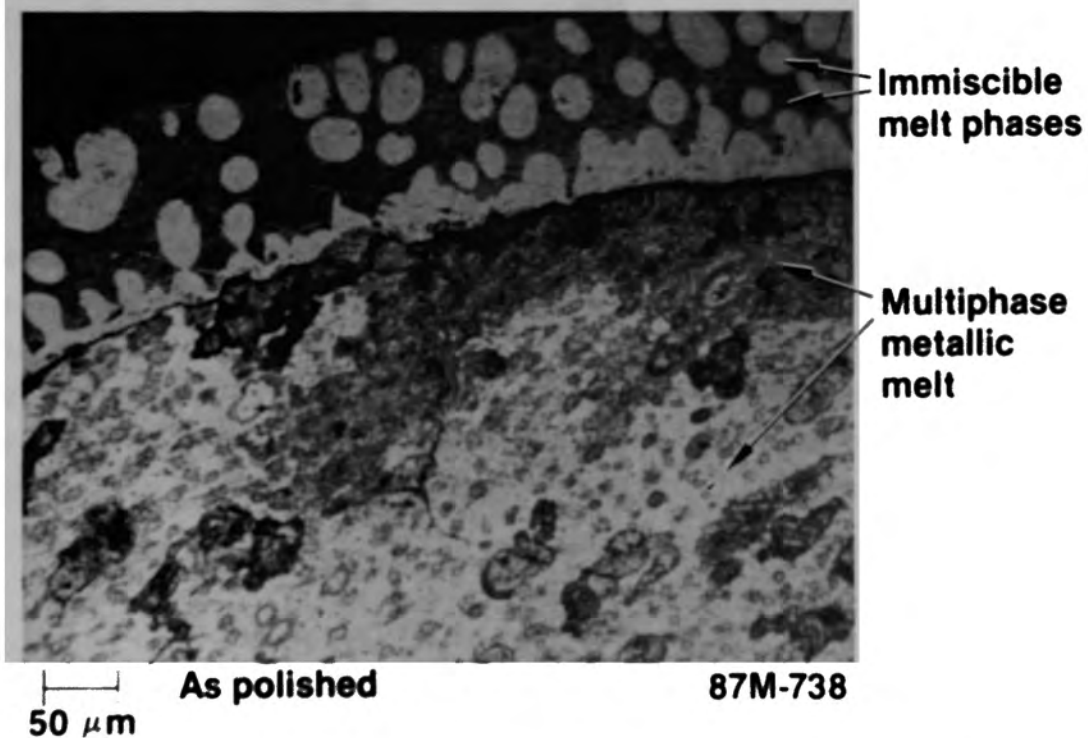


Figure E-62. Interface between two metallic melts (G08-P11-I Area 1).

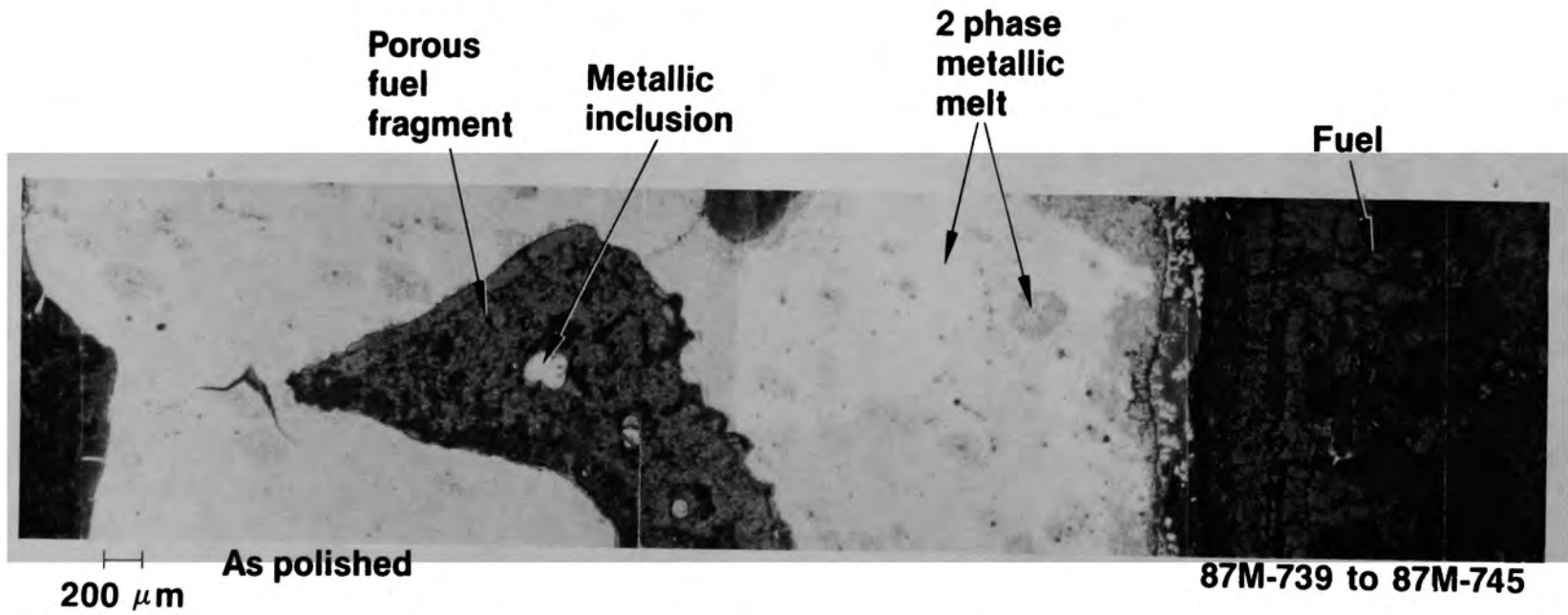


Figure E-63. Previously molten metallic melt material surrounding a fuel fragment (G08-P11-I Area 2).

## Peripheral Crust

### G12-P1

A photograph of peripheral crust sample G12-P1 is shown in Figure E-64. The sample was 5.1 cm long and 6.4 cm in diameter. This plug weighed 512.12 g and had a density of  $7.57 \text{ g/cm}^3$ .

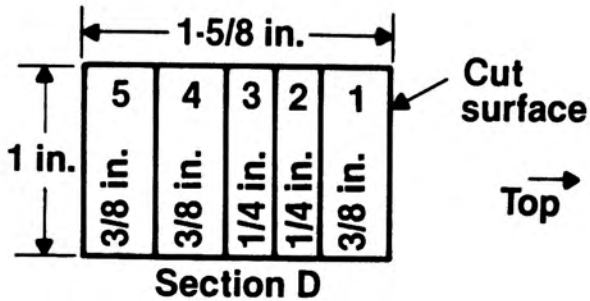
The sectioning diagram for this crust sample is also shown in Figure E-64. A 0.95-cm thick transverse section (Section E) was cut from the top end to show a transverse view of the plug in the rough cut condition; it was never polished and photographed. The remaining plug was cut into four quarter sections designated as A, B, C, and D. Section D was further cut into five wafers, as shown in the diagram, and Section G12-P1-D3 was metallographically examined at the INEL.

Cross section G12-P1-D3 is shown in Figure E-65. The sample was composed of previously molten ceramic material. This figure also indicates the area that was examined in detail.

Figure E-66 shows the typical structure of the  $(\text{U,Zr})\text{O}_2$  ceramic melt material at Area 1. This area contains several large pores that are surrounded by a mottled phase. A small microcore was subsequently drilled from this area for elemental analyses to identify the composition of this mottled phase. The backscattered electron image of this microcore is shown in Figure E-67. The elemental dot maps for this area are shown in Figure E-68. The matrix consists of  $(\text{U,Zr})\text{O}_2$  with a secondary phase composed of  $(\text{Fe,Cr,Al,Ni,O})$ . This secondary phase is the cause of the mottled structure in Figure E-66.

### 007-P4

A photograph of peripheral crust sample 007-P4 is shown in Figure E-69. The sample was 5.1 cm long and 6.4 cm in diameter. This plug weighed 727.90 g and had a density of  $8.78 \text{ g/cm}^3$ .



- A - ANL
- B - Germany-KFK
- C-1 - United Kingdom
- C-2 - Sweden
- E - Japan
- D-1 - France
- D-2 - INEL Rad Chem
- D-3 - INEL Met
- D-4 - Japan
- D-5 - Canada

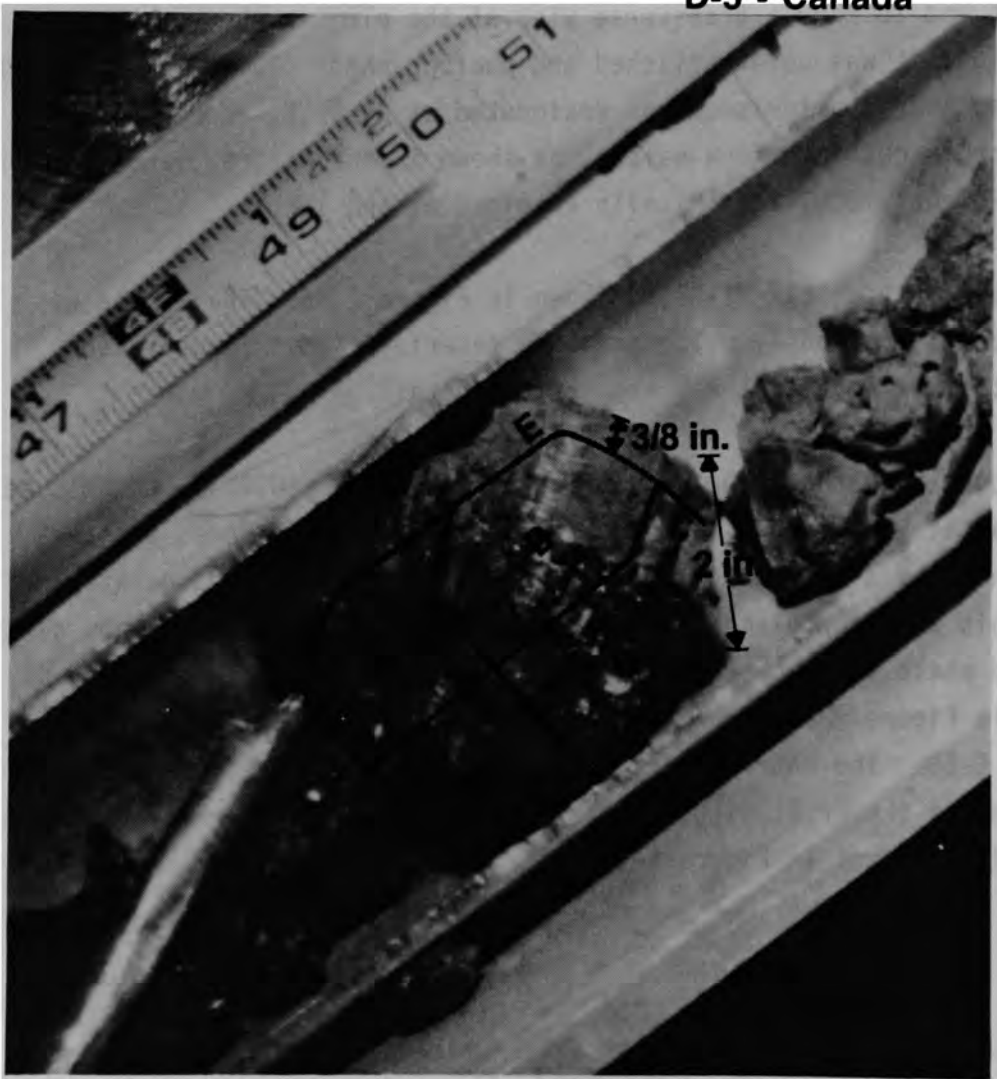
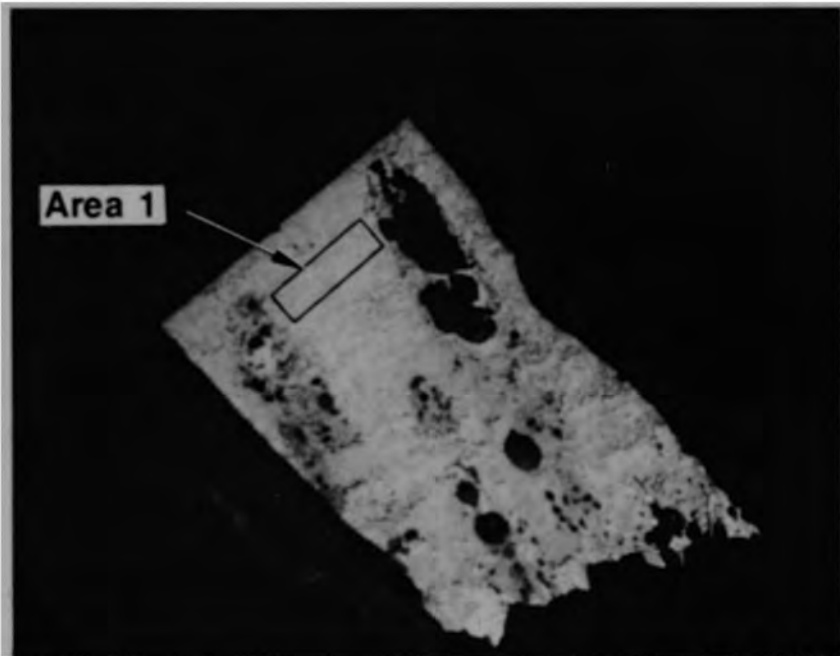


Figure E-64. Section diagram and overall view of peripheral crust sample G12-P1.



**87M-385**

Figure E-65. Transverse cross section from peripheral crust G12-P1-D3.

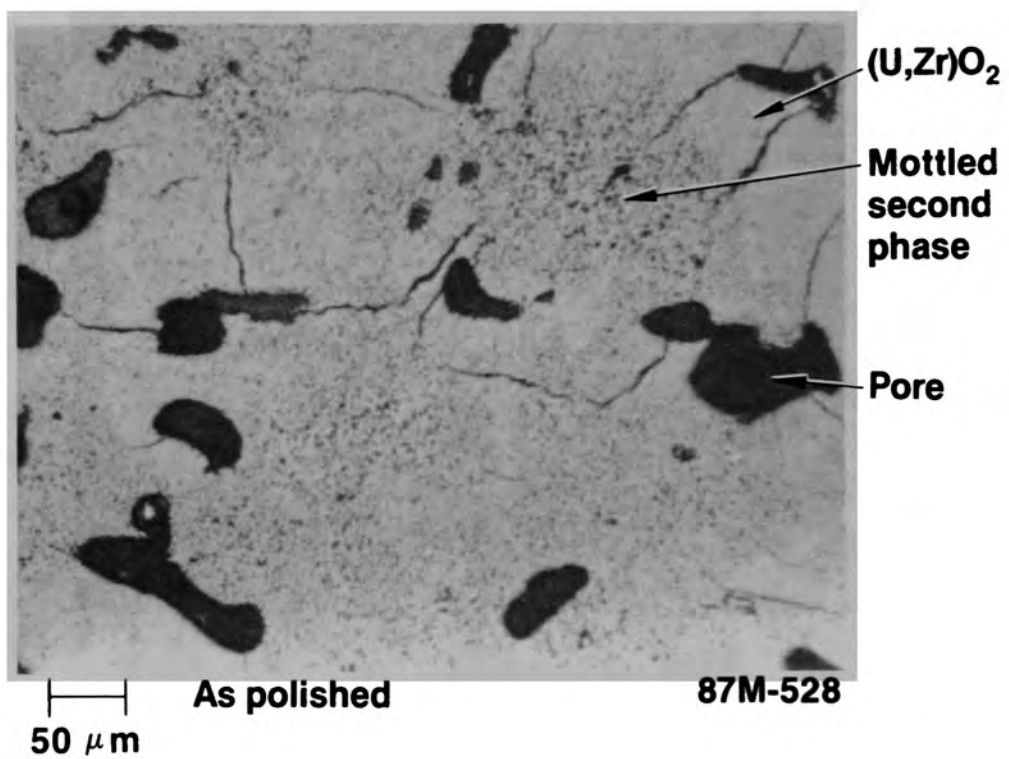


Figure E-66. Structure of ceramic melt in peripheral crust sample G12-P1-D3 Area 1.

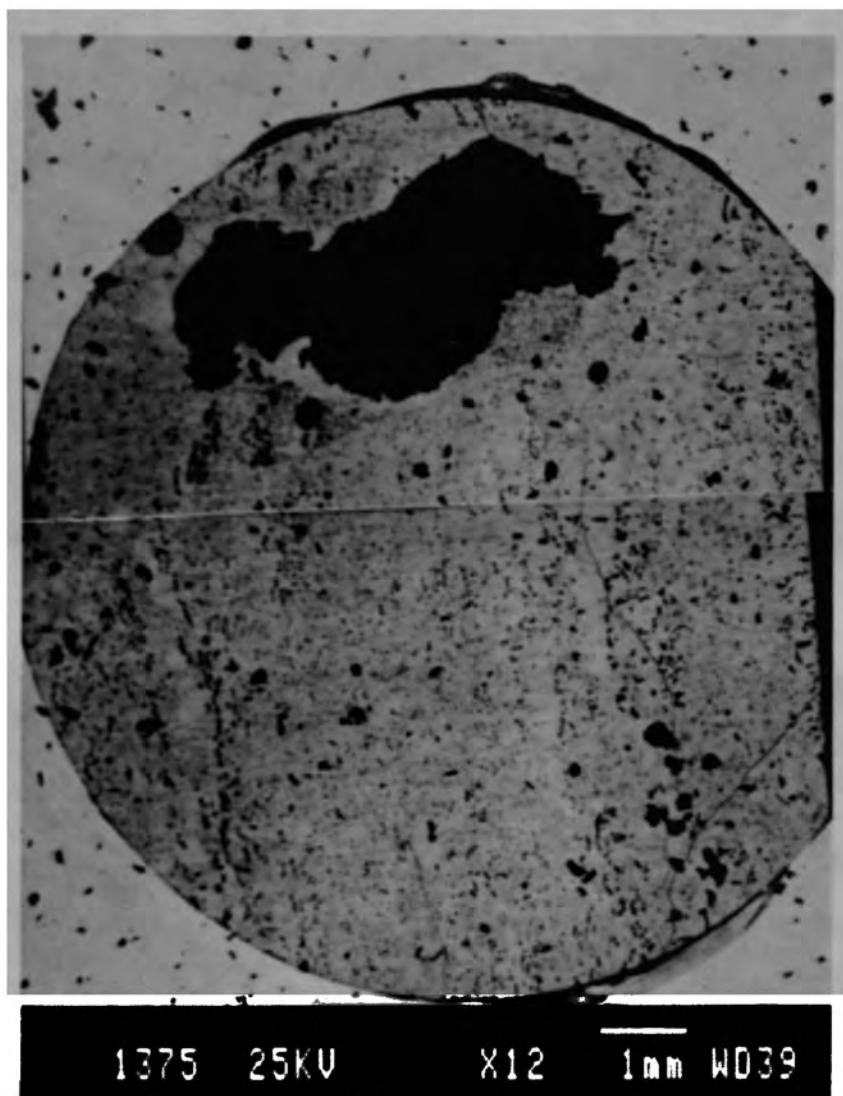
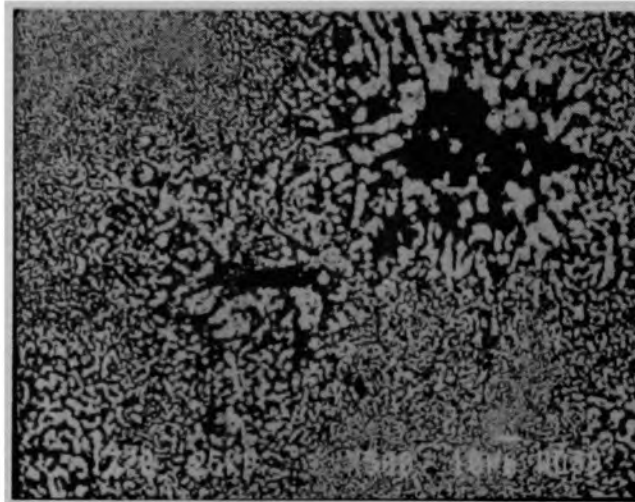
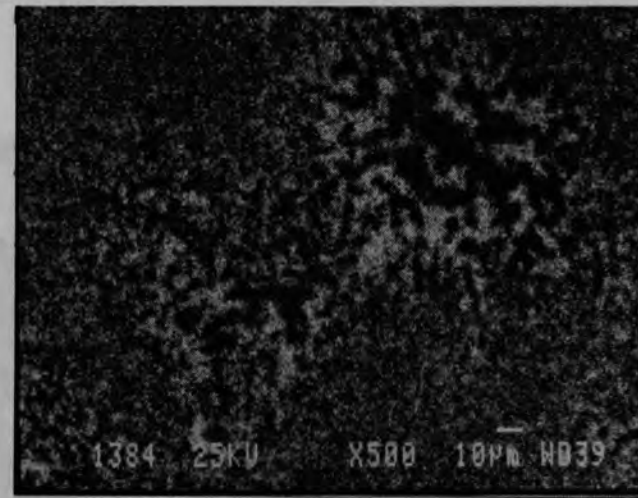


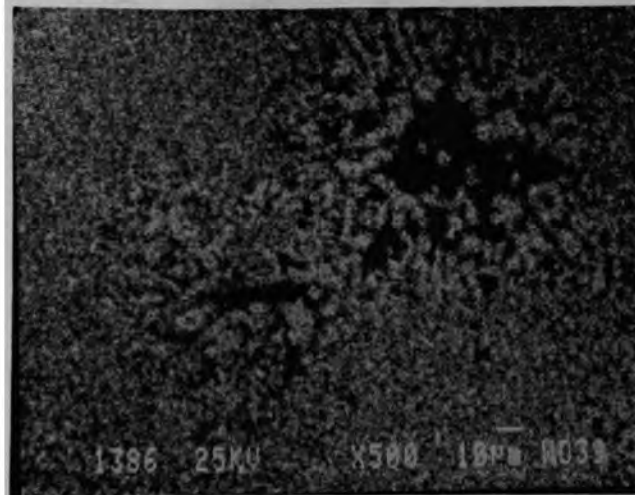
Figure E-67. Backscattered electron image of microcore G12-P1-D3.



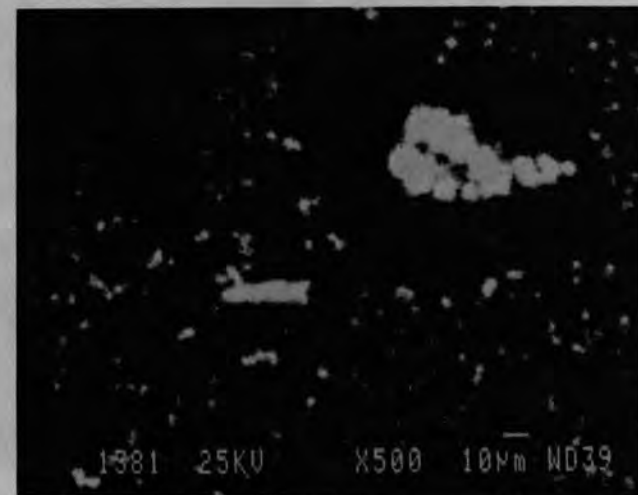
**BSE compositional image HCA 87-1378**



**Zr dot map HCA 87-1384**



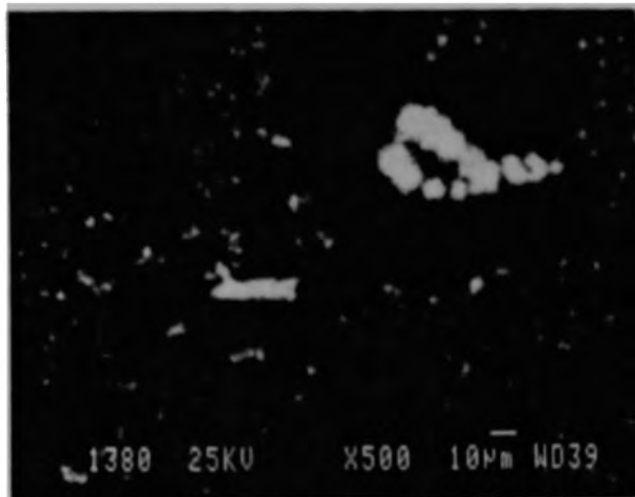
**U dot map HCA 87-1386**



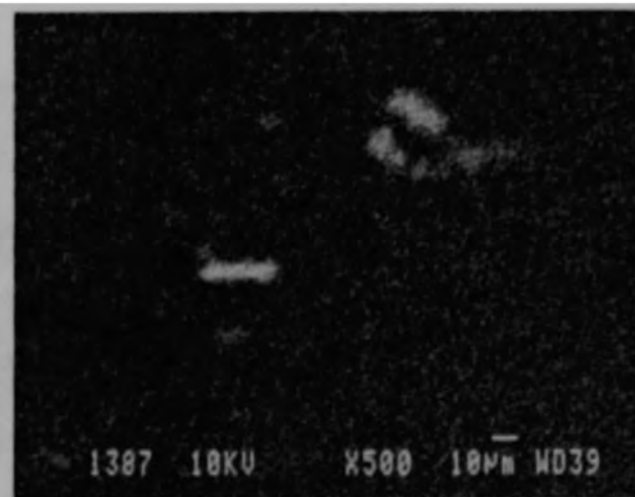
**Fe dot map HCA 87-1381**

Figure E-68. Elemental analysis of ceramic melt in G12-P1-D3 Area 1.

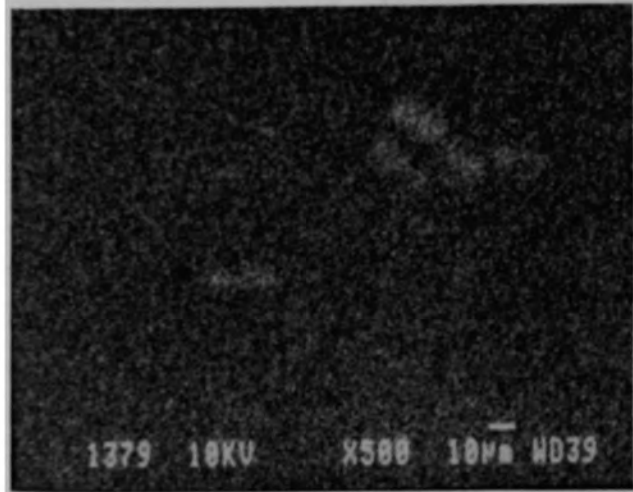




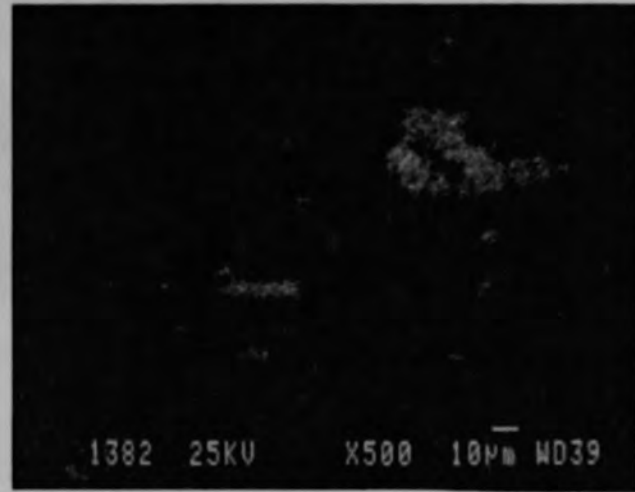
Cr dot map HCA 87-1380



Al dot map HCA 87-1387

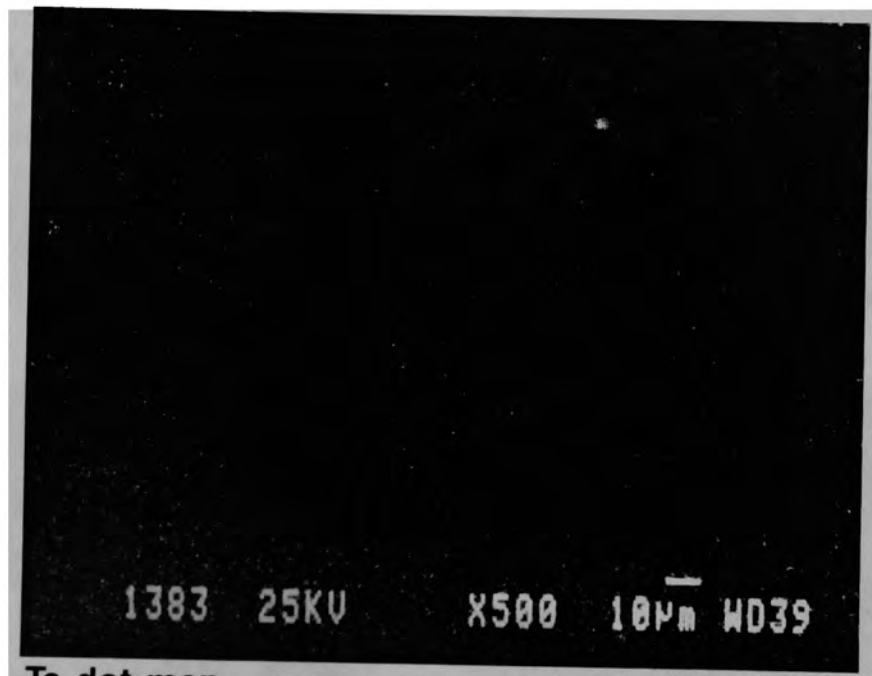


O dot map HCA 87-1379



Ni dot map HCA 87-1382

Figure E-68. (Continued)



Tc dot map

HCA 87-1383

Figure E-68. (Continued)

- A - Japan
- B - Germany-KFK
- C - Rad Chem
- D - Met
- E - Germany-JRC
- F - Japan

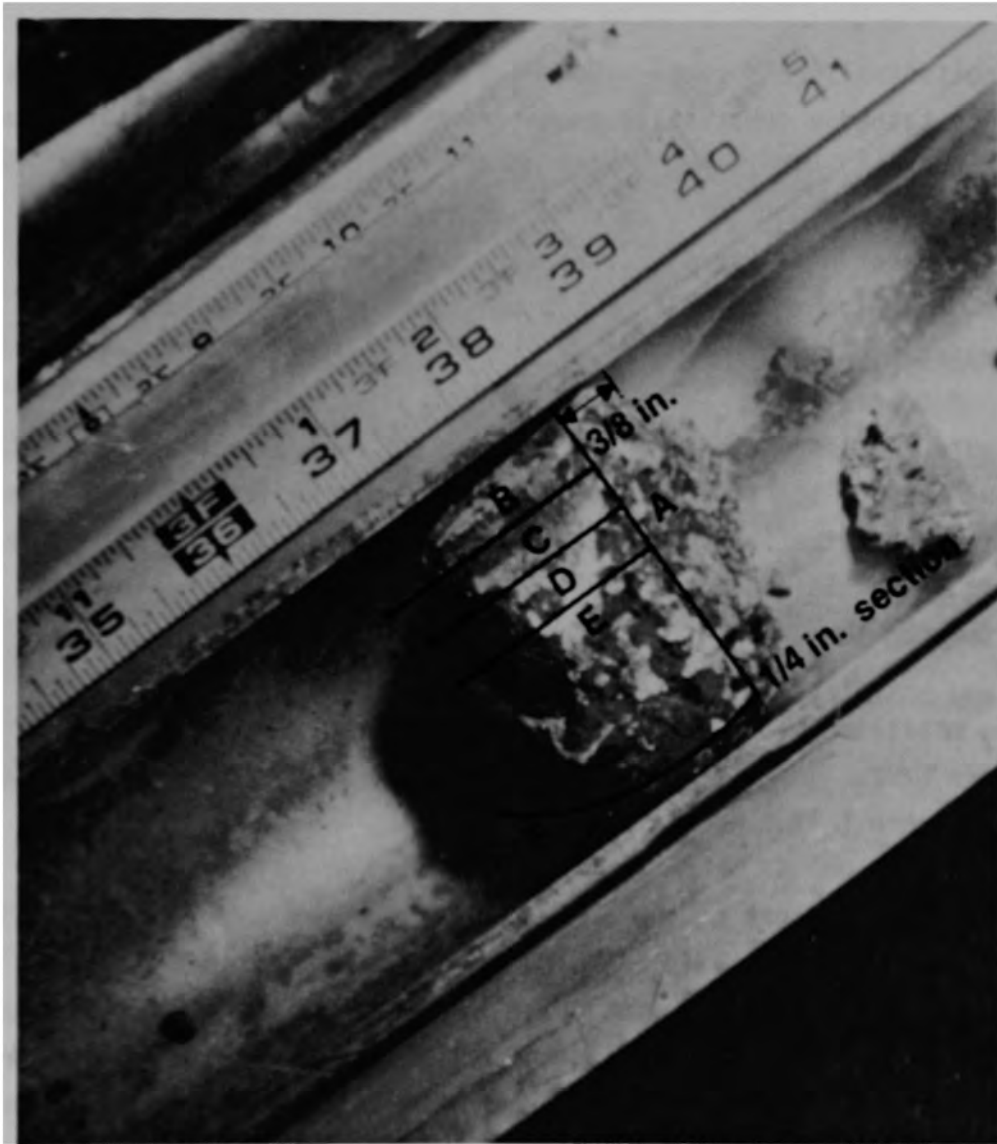


Figure E-69. Overview of peripheral crust sample 007-P4.

The sectioning diagram for this plug is also depicted in Figure E-69. A 0.95-cm thick cross section was taken from the top end to show a complete transverse view of the plug in the rough cut condition; it was never polished and photographed. Half of the remaining plug was then cut into longitudinal slices designated as B, C, and D. The other half of the plug was cut into two quarter sections E and F. Section C was used for radiochemical analyses, and Section D was used for metallographic examination at the INEL.

Longitudinal cross section 007-P4-D is shown in Figure E-70. The sample contained a substantial amount of metallic melt surrounding fuel pellet remnants. The irregular shape of these fuel remnants indicates extensive fuel liquefaction as a result of interactions with the metallic melt. A number of different areas were examined on this cross section; however, the discussion will be limited to a few representative photographs.

Figure E-71 shows the interface between a fuel pellet and the metallic melt in Area 3. The fuel is very porous and has an irregular surface, which indicates the fuel was in the process of being liquefied by the metallic melt. Some metallic melt flowed into the fuel and formed inclusions in the voids.

The metallic melt had a dendritic microstructure in Area 2 are shown in Figure E-72. In other areas the melt was a solid solution, as can be seen in Figure E-71.

The microstructure of the ceramic phase in Area 1 is shown in Figure E-73. The matrix is composed of  $(U,Zr)O_2$  with a mottled structure concentrated near the pores in the melt. This mottled structure was previously identified (peripheral crust sample G12-P1) as being a secondary phase composed of structural oxides. This phase can be expected to have a lower melting point than the  $(U,Zr)O_2$ , and the segregation of this mottled phase near the gas pores in the melt is consistent with gas being concentrated in the last material to solidify.

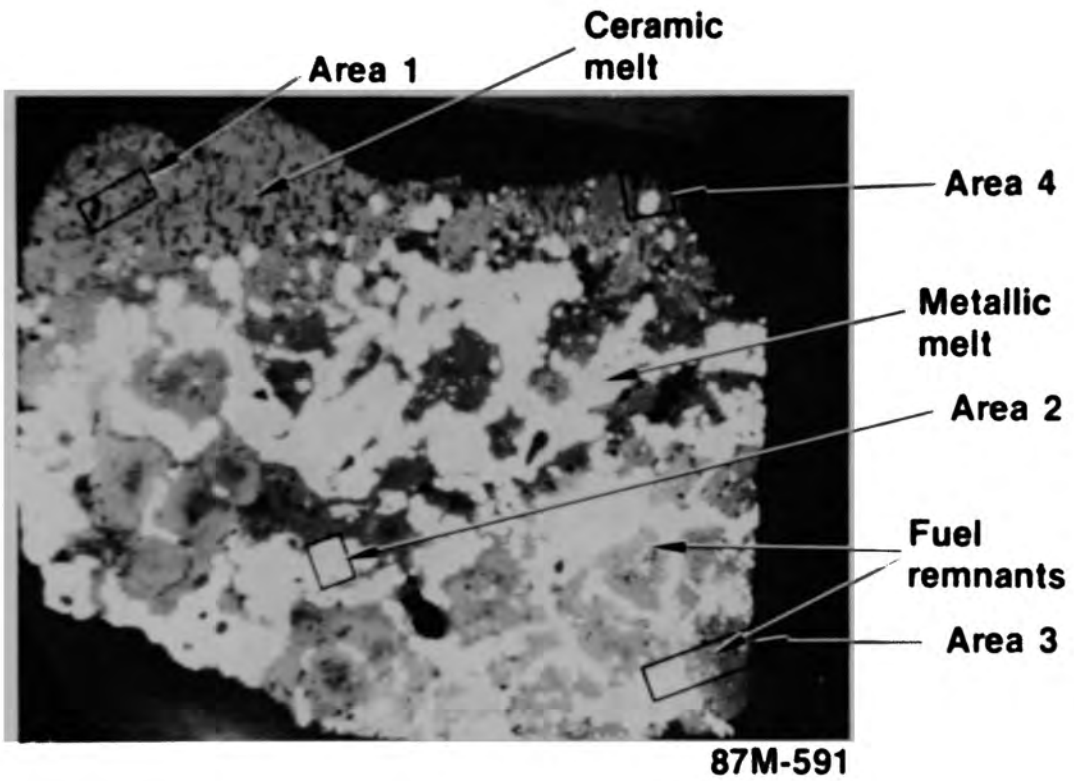


Figure E-70. Longitudinal cross section 007-P4-D from peripheral crust.

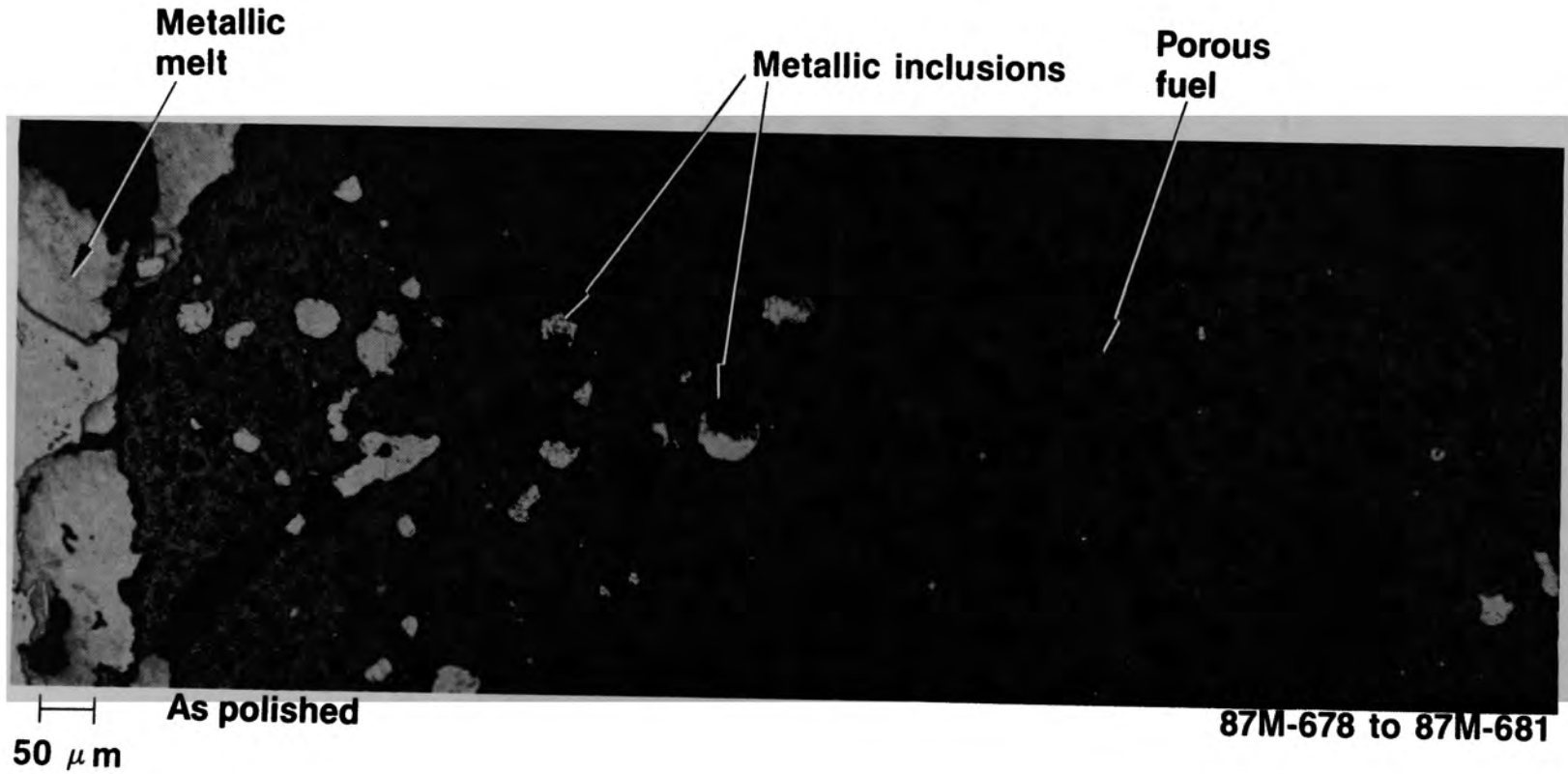
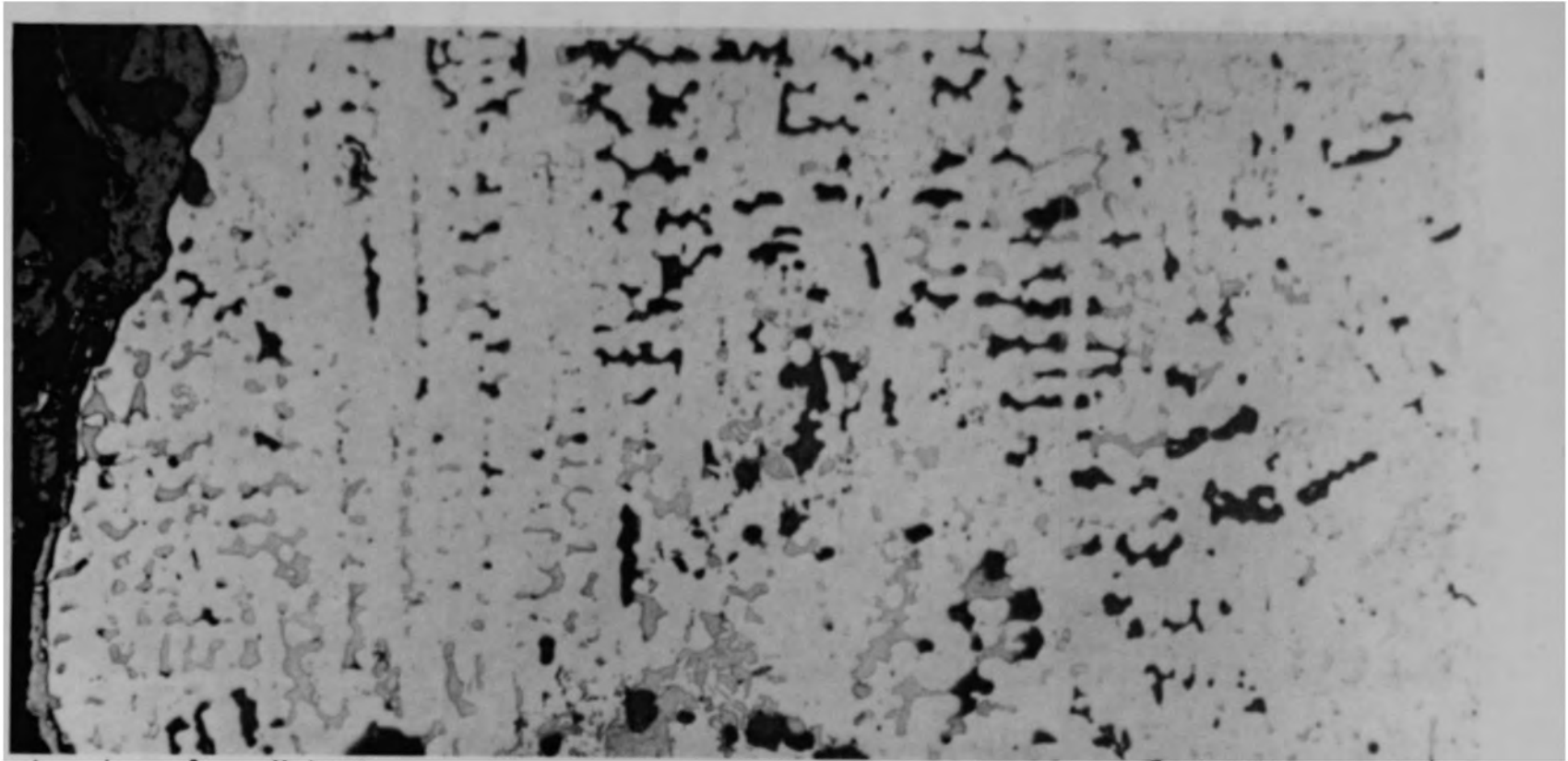


Figure E-71. Penetration of metallic melt into partially liquefied fuel (007-P4-D Area 3).



100  $\mu$ m

As polished

87M-685 to 87M-687

Figure E-72. Dendritic structure of metallic melt (007-P4-D Area 2).

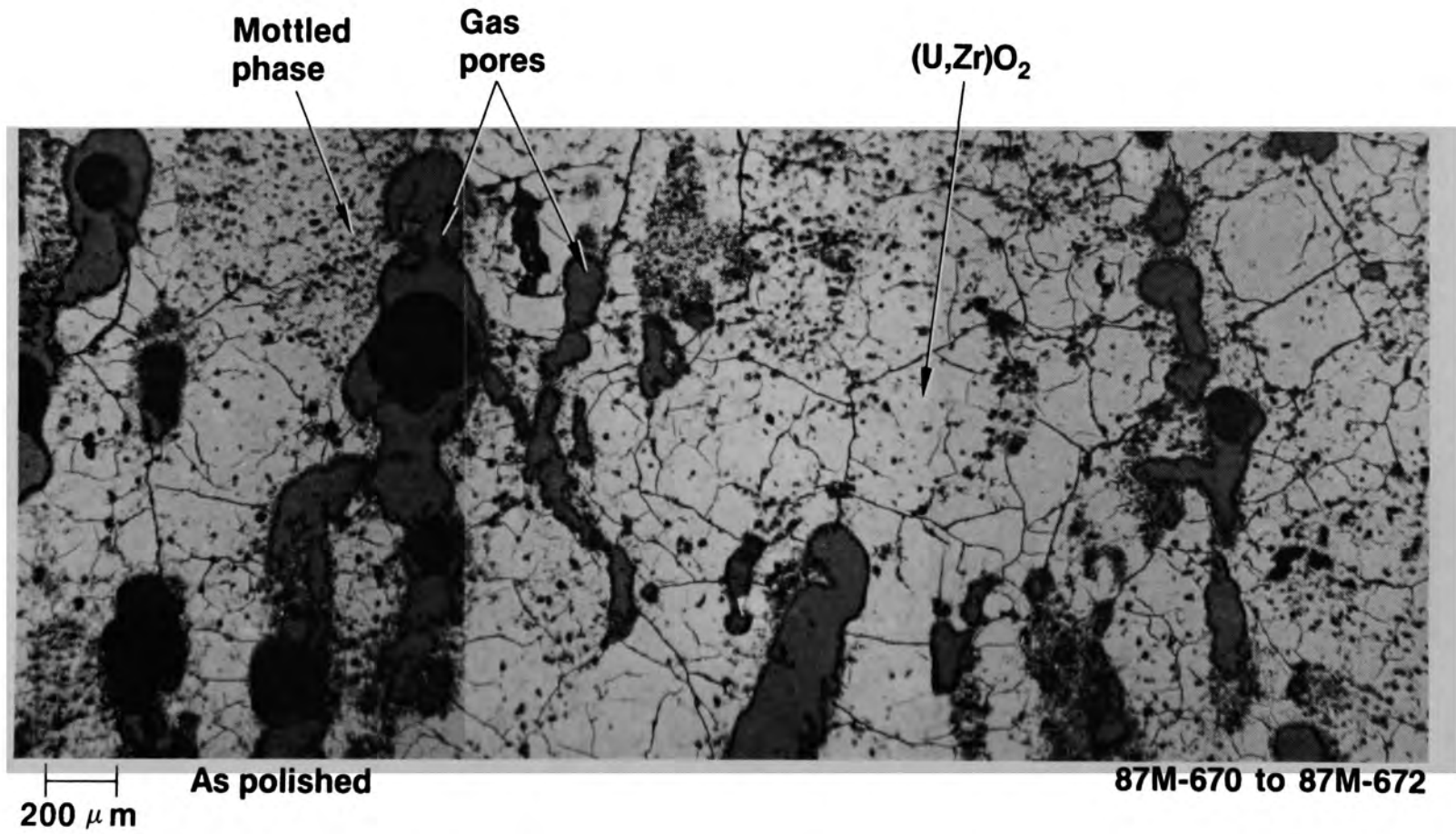


Figure E-73. Porosity and mottled phase (U,Zr)O<sub>2</sub> ceramic melt (007-P4-D Area 1).



## Central Consolidated Core Region

Examinations of particles >25 mm from the central consolidated core region indicated a wide variation in the composition of these materials. Some particles were entirely ceramic, a few were entirely metallic, and many were mixtures of metallic and ceramic phases. Samples from each category are discussed.

### Metallic Samples

D04-P2-A A metallic particle removed from the D04 core position is shown in Figure E-74. This particle appears to be almost entirely metallic, with stringers of metallics at one end of the particle. This particle weighed 19.07 g and had a density of 8.9 g/cm<sup>3</sup>.

A cross section from this particle is presented in Figure E-75. The microstructure of this particle is shown in Figure E-76, and it shows the presence of (Ag,In,Cd) control rod material. The presence of voids in the overall cross section indicates that this material was previously molten. This particle appears to be the molten endtip of a control rod.

009-P1-A Particle 009-P1-A is shown in Figure E-77. This sample weighed 29.62 g and had a density of 6.9 g/cm<sup>3</sup>.

The cross section of 009-P1-A is shown in Figure E-78. The matrix consisted of a dendritic metallic melt with spherical inclusions. Within the spherical inclusions were spherical voids or ceramic inclusions.

Elemental dot maps of a typical inclusion are shown in Figure E-79. The matrix consisted primarily of (Fe,Ni) with small inclusions of Ag, Sn, and In. The larger spherical inclusion contained Ag, In, and Sn. The dark spherical inclusion within the inclusion was Cr<sub>2</sub>O<sub>3</sub>. The presence of molten Cr<sub>2</sub>O<sub>3</sub> indicates that temperatures were in excess of 2266 K in this region.



Figure E-74. Overview of metallic sample D04-P2-A from the consolidated core region.

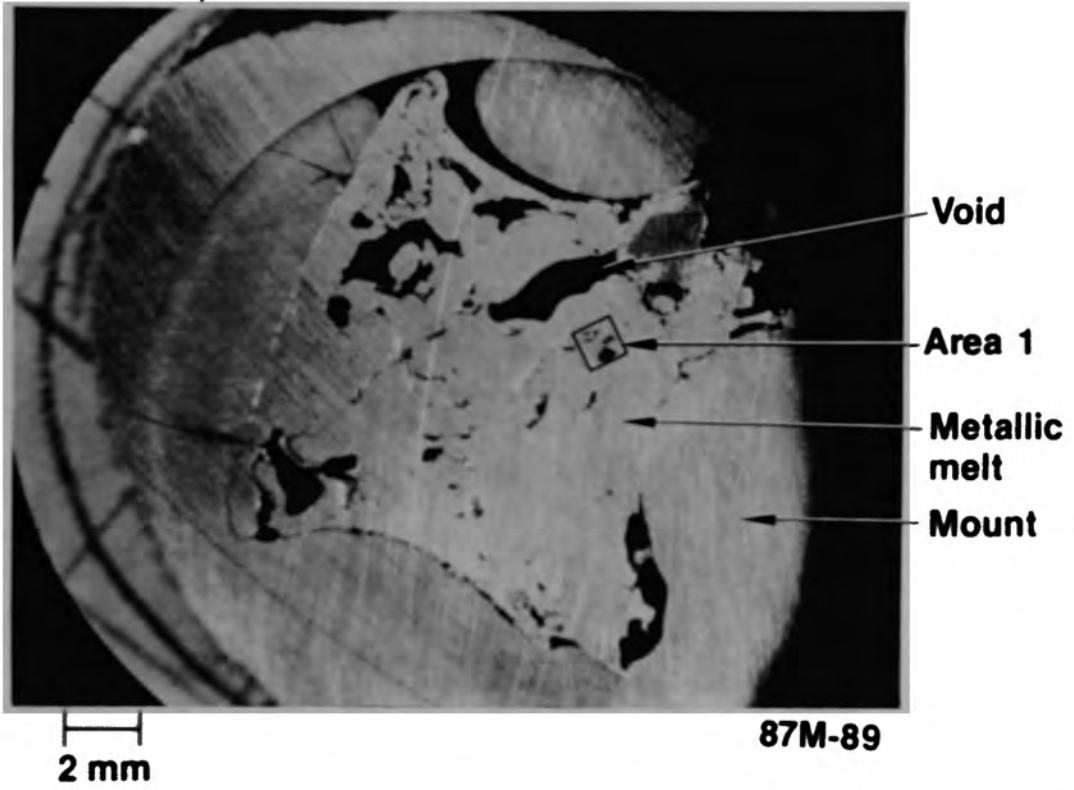
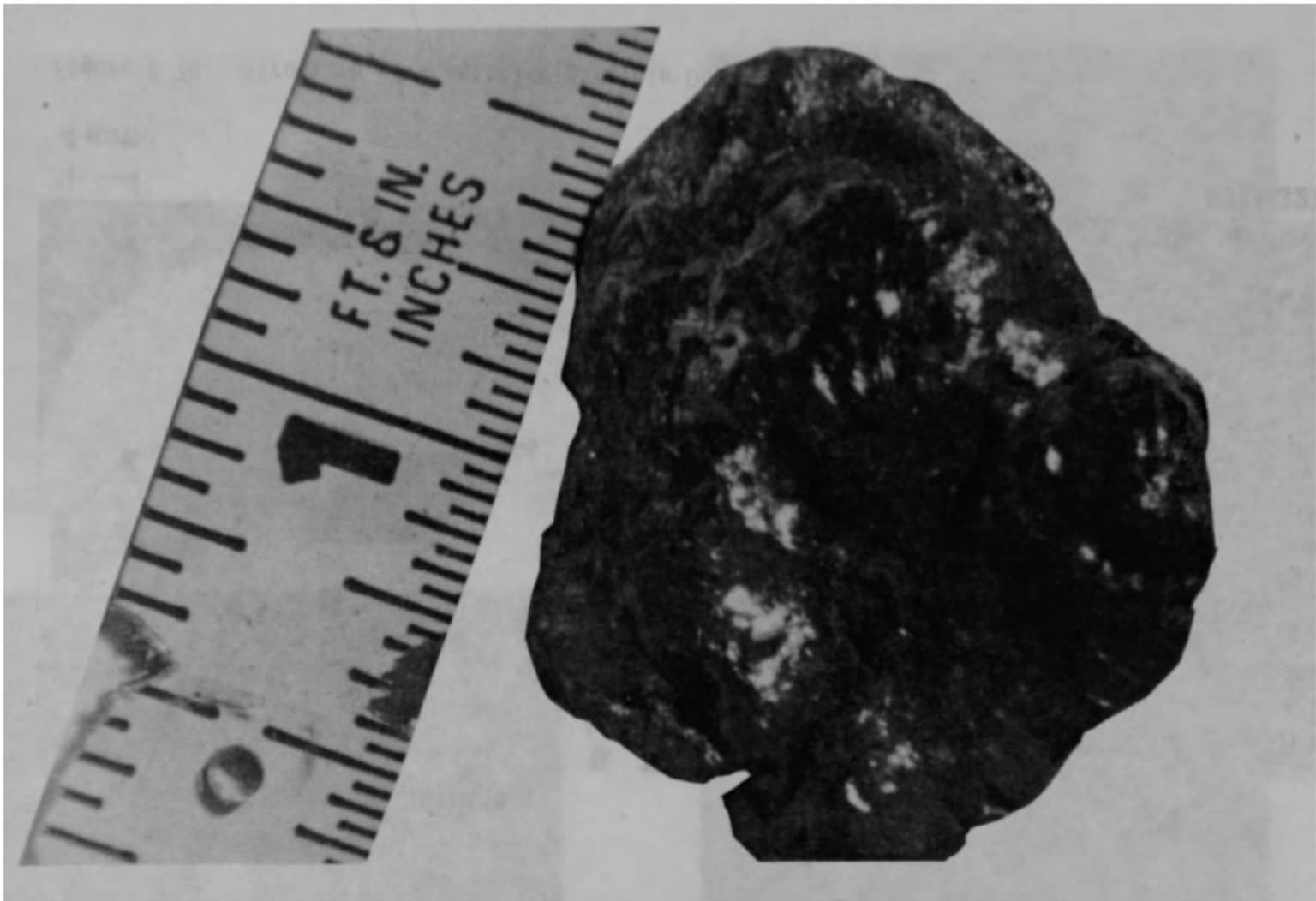


Figure E-75. Cross section of D04-P2-A from consolidated core region.



Figure E-76. Previously molten Ag-In-Cd alloy.



86-614-1-1

Figure E-77. Metallic particle 009-P1-A from consolidated core region.

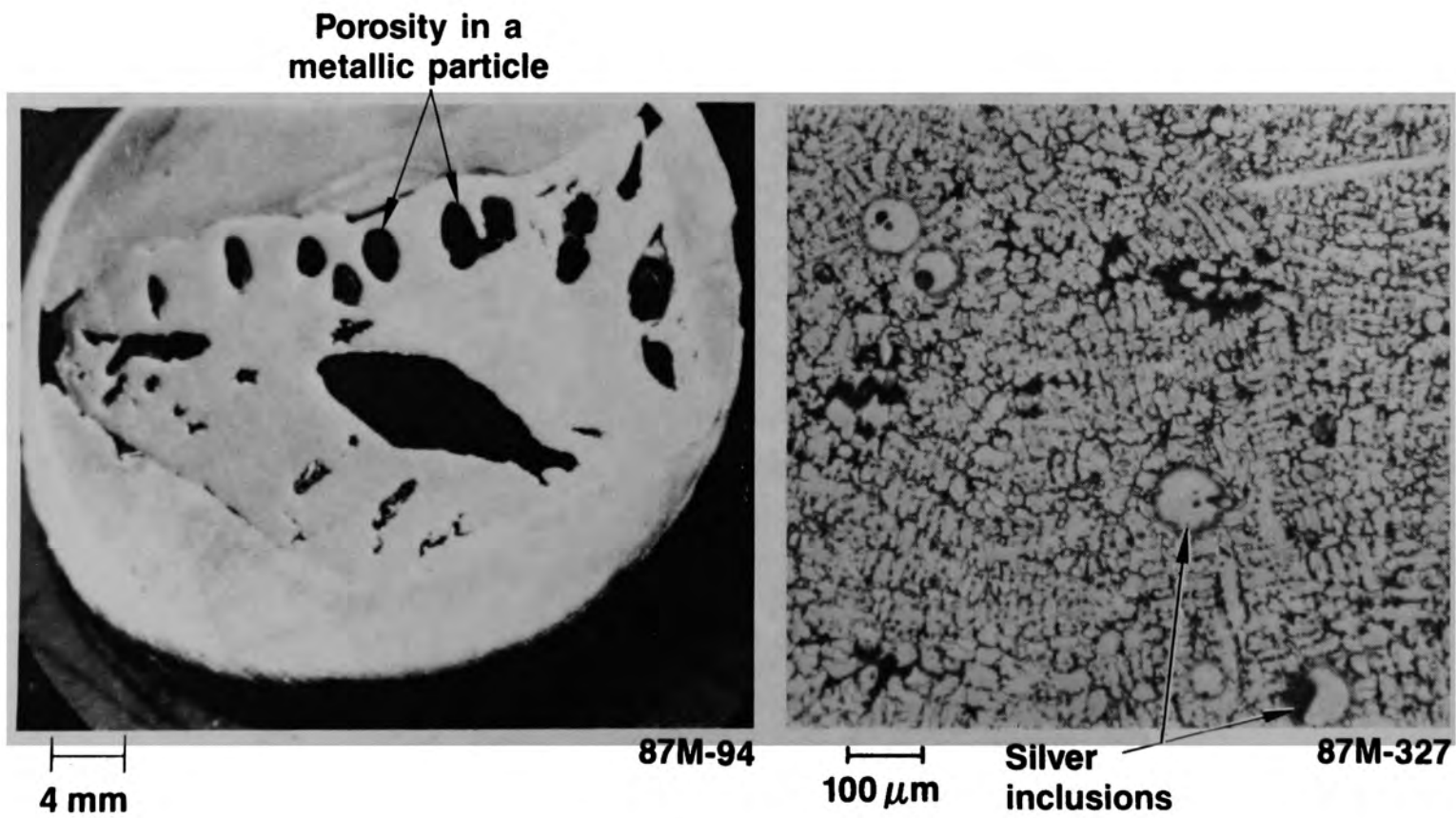
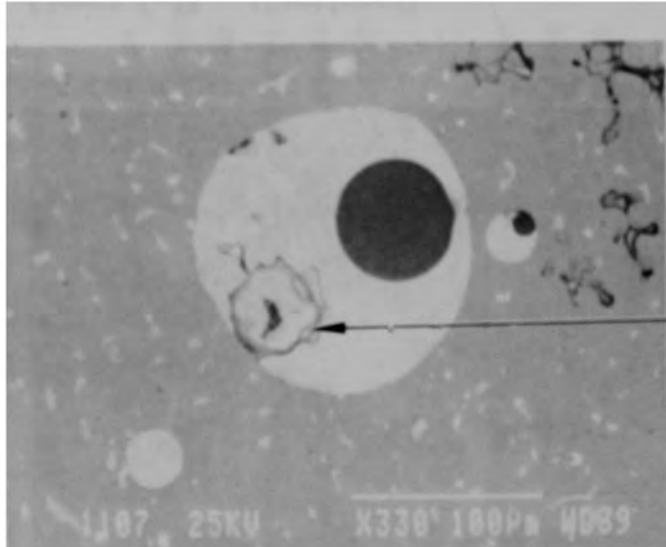
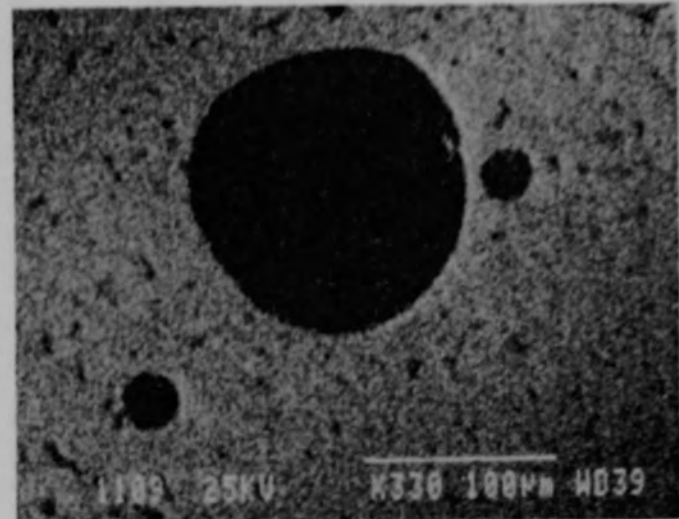


Figure E-78. Structure of a metallic particle 009-P1-A.

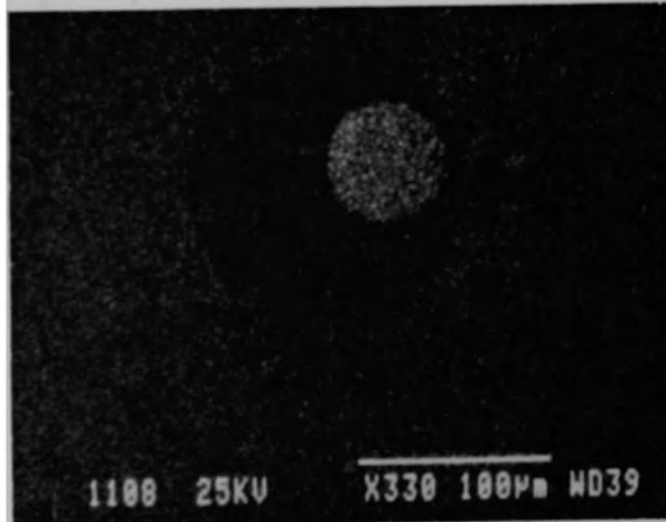


BSE compositional image HCA 87-1107

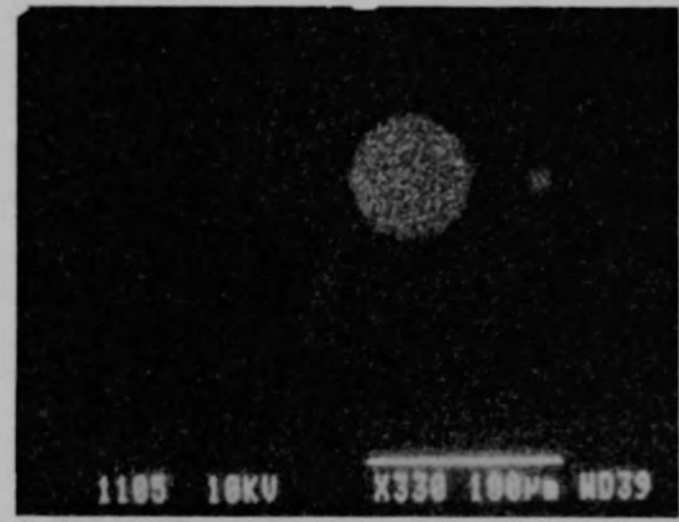
Area 4



Fe dot map HCA 87-1109

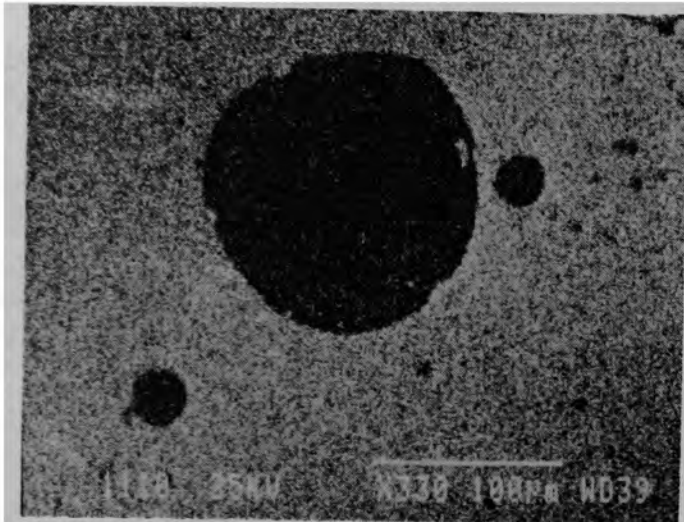


Cr dot map HCA 87-1108



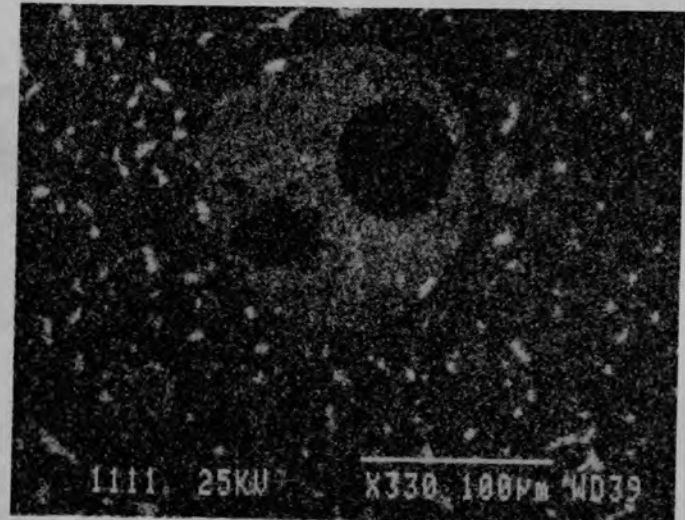
O dot map HCA 87-1105

Figure E-79. Silver inclusion in metallic matrix.



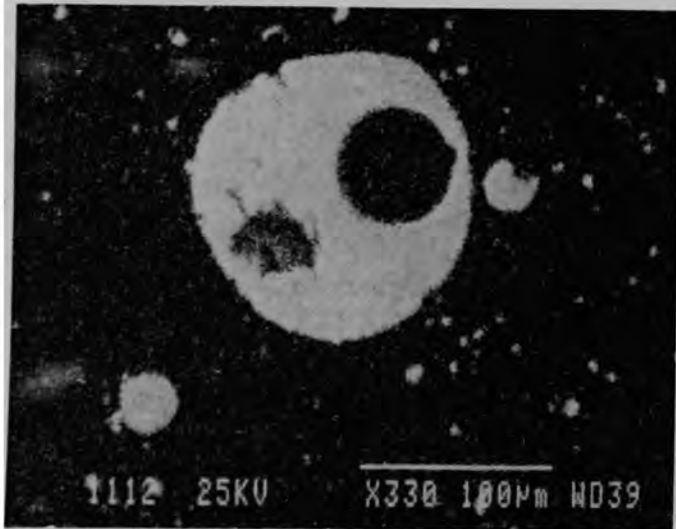
Ni dot map

HCA 87-1110



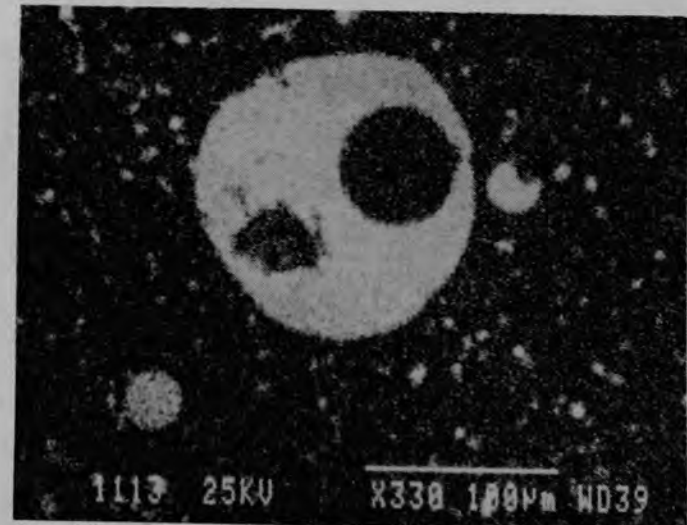
Sn dot map

HCA 87-1111



Ag dot map

HCA 87-1112



In dot map

HCA 87-1113

Figure E-79. (Continued)



009-P1-B The second metallic particle from core bore 009 was very similar to the first one (Figure E-80). The particle was blackish in appearance with some bright areas, indicating a metallic luster. This sample weighed 20.06 g. and the density was 7.2 g/cm<sup>3</sup>.

A cross section from this particle is shown in Figure E-81. The particle contained some very large voids, and the microstructure was a dendritic metallic melt as shown in Figure E-82. A few spherical particles were embedded in the matrix, and inside these spherical particles were voids or inclusions of other materials, very similar to the inclusions seen on sample 009-P1-A.

007-P1-A This metallic particle is shown in Figure E-83. The particle weighed 4.1 g and had a density of 7.6 g/cm<sup>3</sup>.

A cross section from this particle is shown in Figure E-84. Like the other metallic particles, this particle contained large voids indicative of previously molten material. The typical microstructure is shown in Figure E-85, which shows a dendritic metallic melt.

007-P6 This particle appeared ceramic, with some small protrusions showing a metallic luster (Figure E-86). The particle weighed 75.67 g and had a density of 5.4 g/cm<sup>3</sup>, which was the lowest density of all the particle samples.

The cross section through this sample is shown in Figure E-87. This cross section shows that the particle was mostly metallic with some ceramic regions. Large voids and smaller porosity are apparent, and these are shown in more detail in Figure E-88. The large amount of closed porosity in this metallic melt is the cause of the low overall measured density. The dendritic structure of the metallic melt in Area B is shown in Figures E-89 and E-90.

A SEM sample was drilled from the location shown in Figure E-87. The backscattered electron image in Figure E-91 shows the porosity distribution in this sample. Elemental analysis of the area shown in Figure E-92

E-116



Figure E-80. Overview of metallic sample 009-P1-B from the central consolidated region.

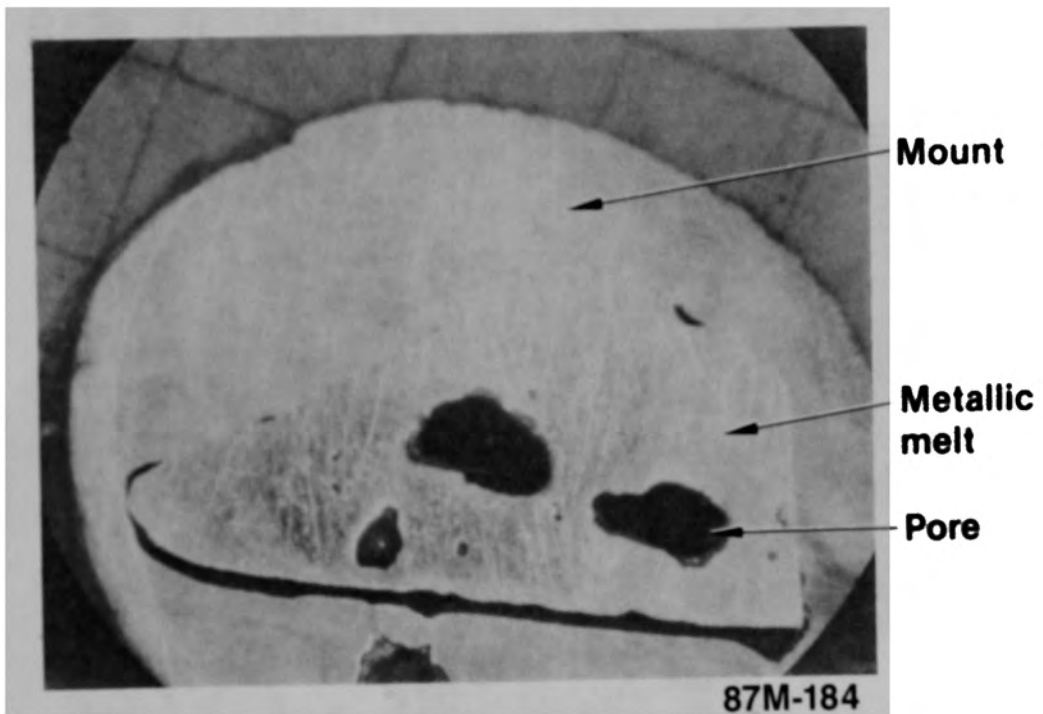


Figure E-81. Metallic melt with large pores (009-P1-B).

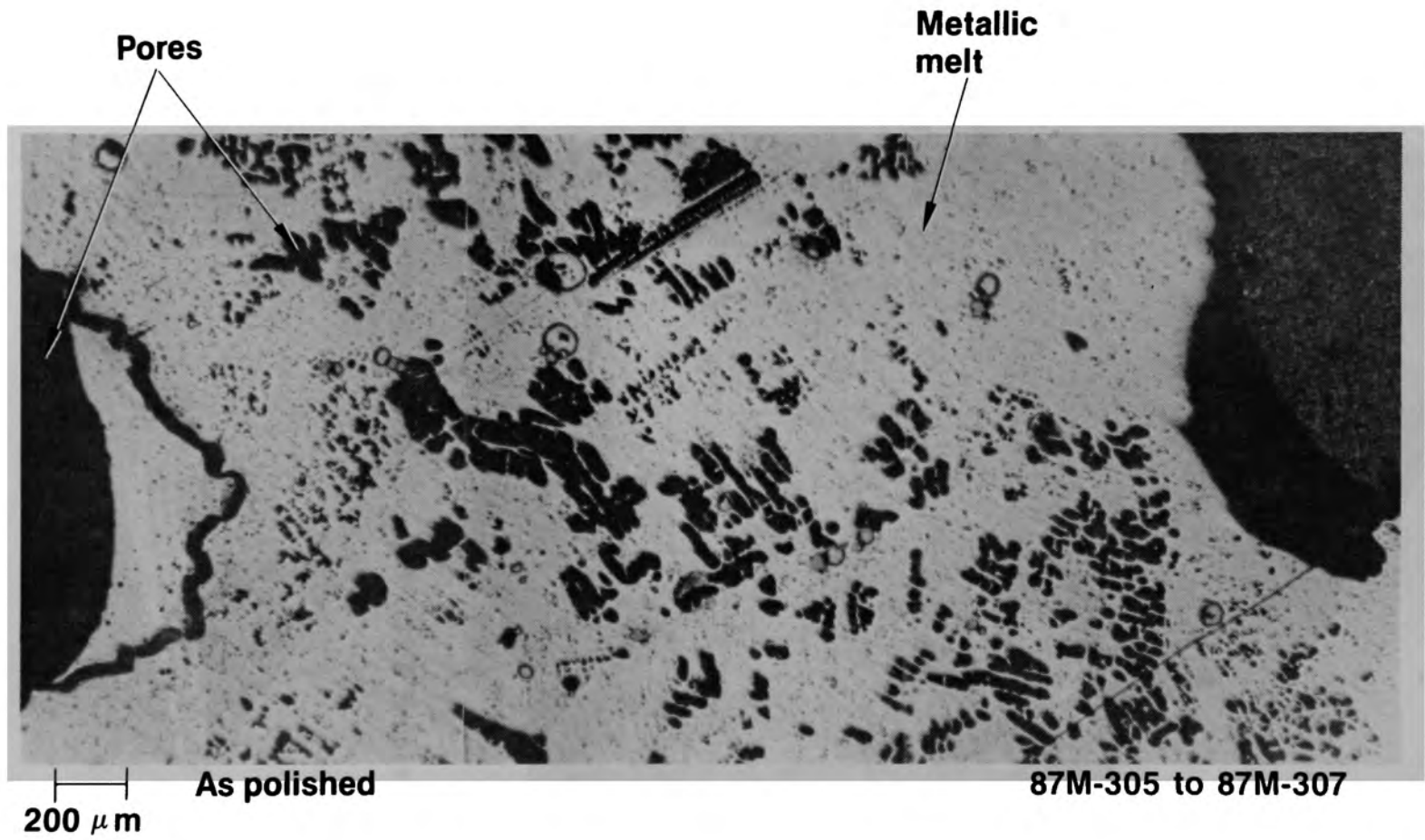
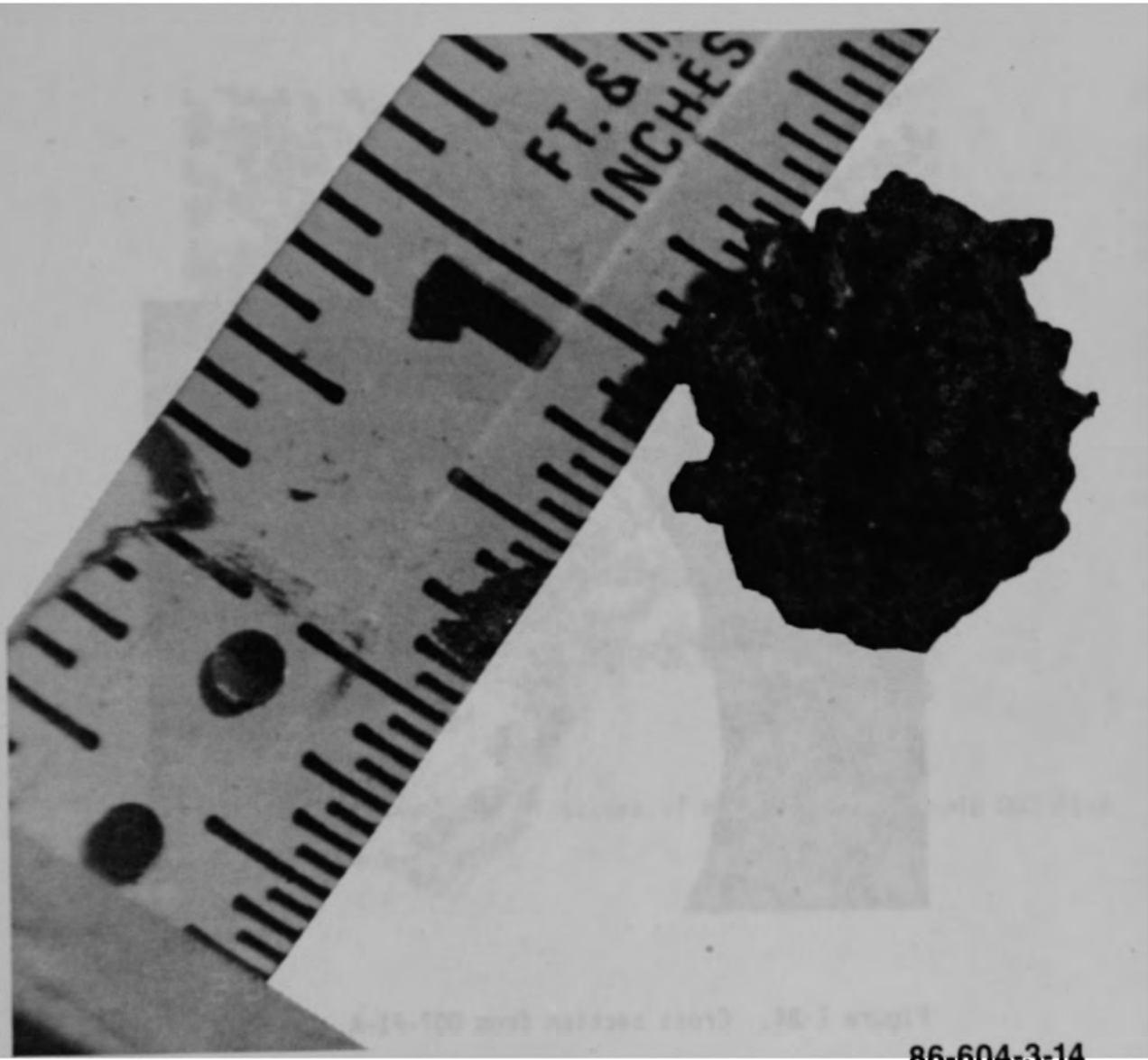


Figure E-82. Dendritic structure of metallic melt (009-P1-B).



86-604-3-14

Figure E-83. Overview of metallic sample 007-P1-A from the consolidated core region.



87M-95

Figure E-84. Cross section from 007-P1-A.

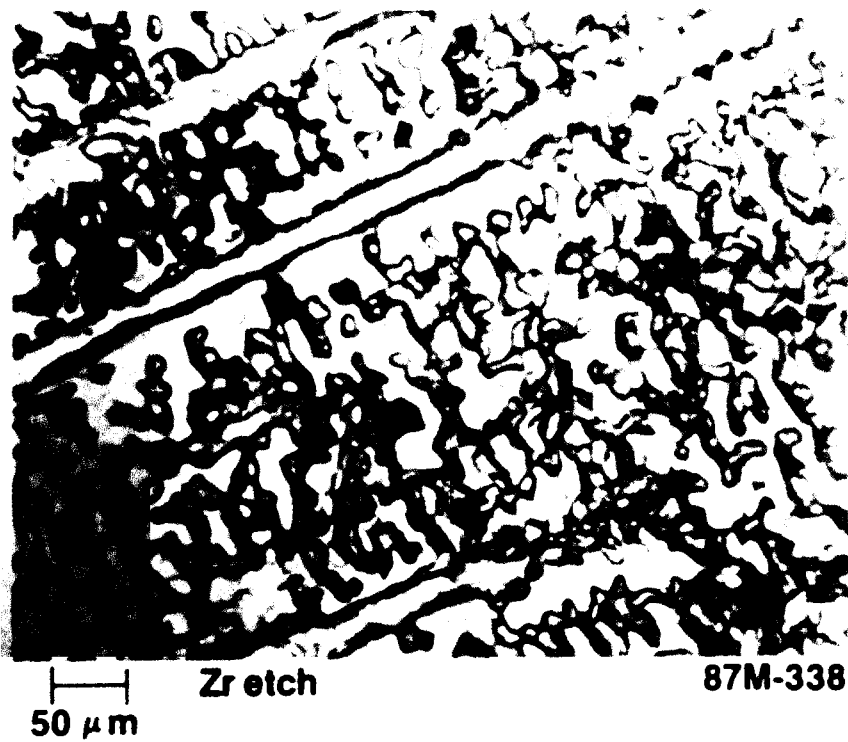


Figure E-85. Dendritic structure of metallic melt sample 007-P1-A.



Figure E-86. Overview of metallic sample 007-P6 from the consolidated core region.



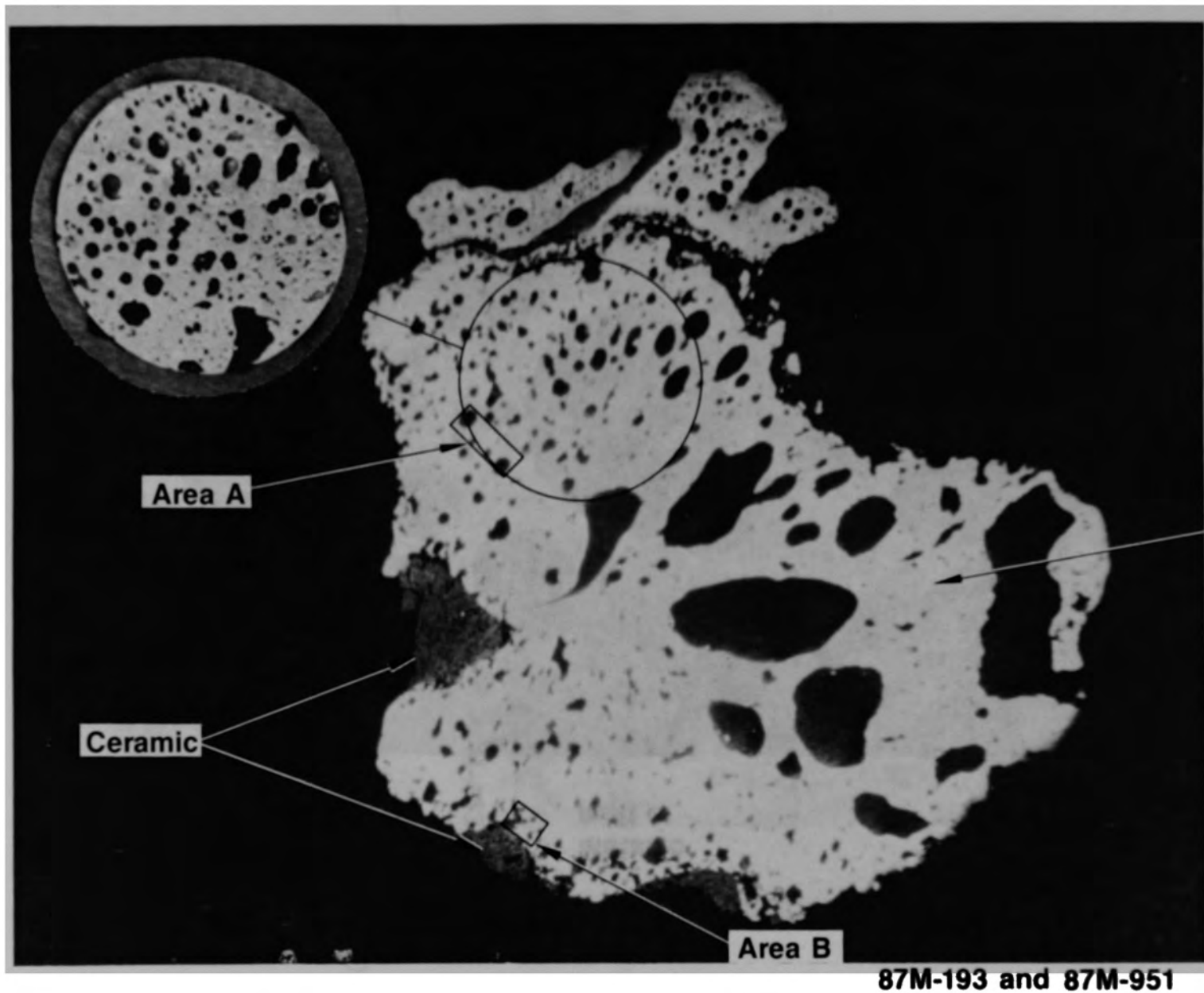


Figure E-87. Cross section and microcore location of metallic sample 007-P6.

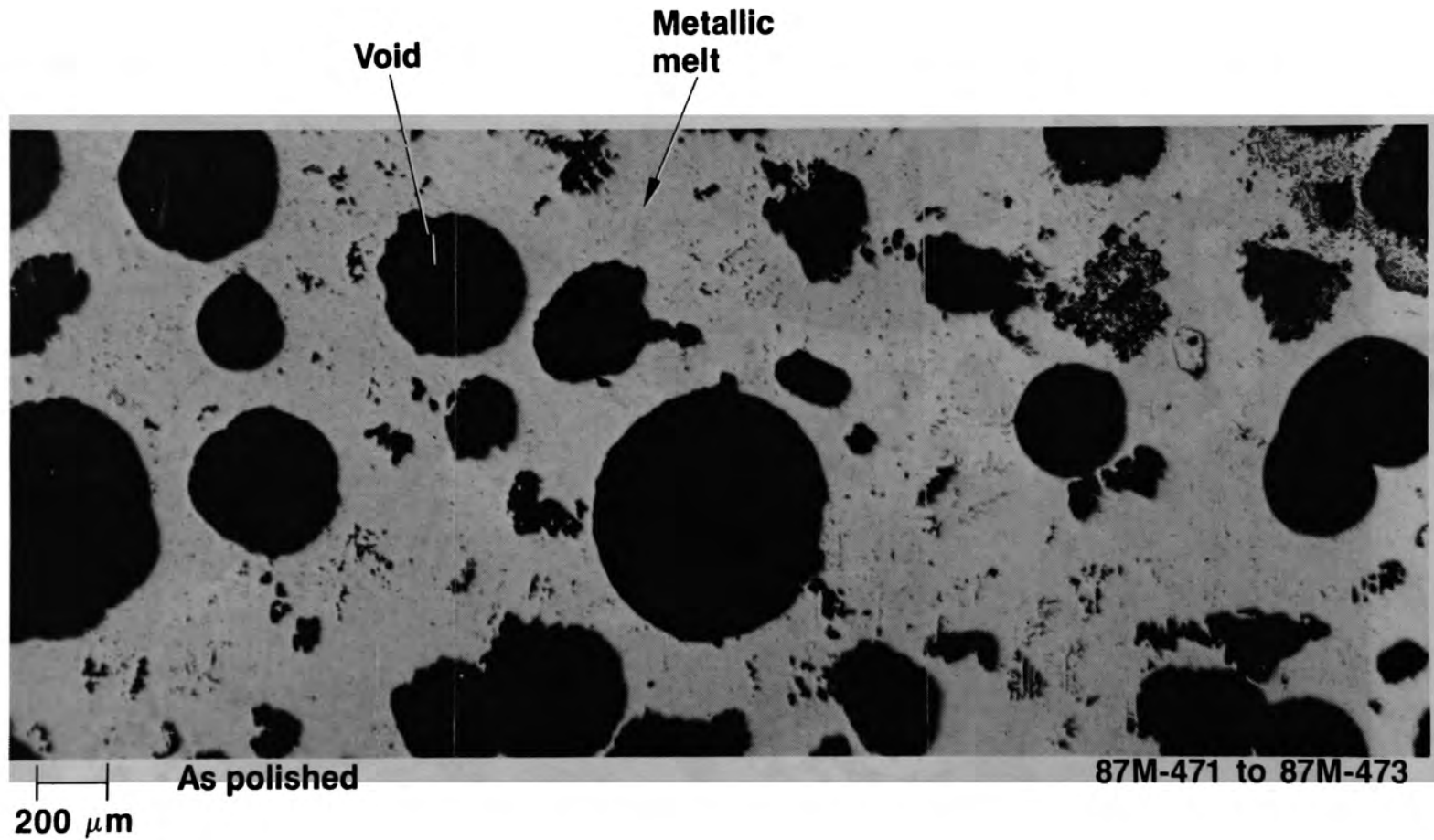


Figure E-88. Spherical voids and closed porosity in metallic matrix of sample 007-P6 Area A.

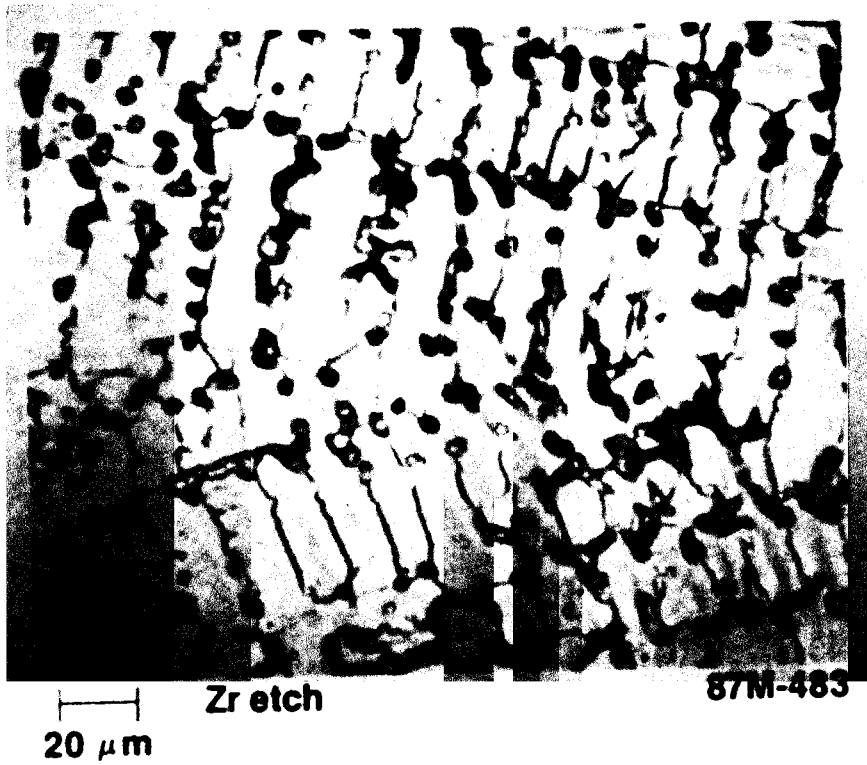


Figure E-89. Dendritic growth in metallic phase (007-P6 Area B).

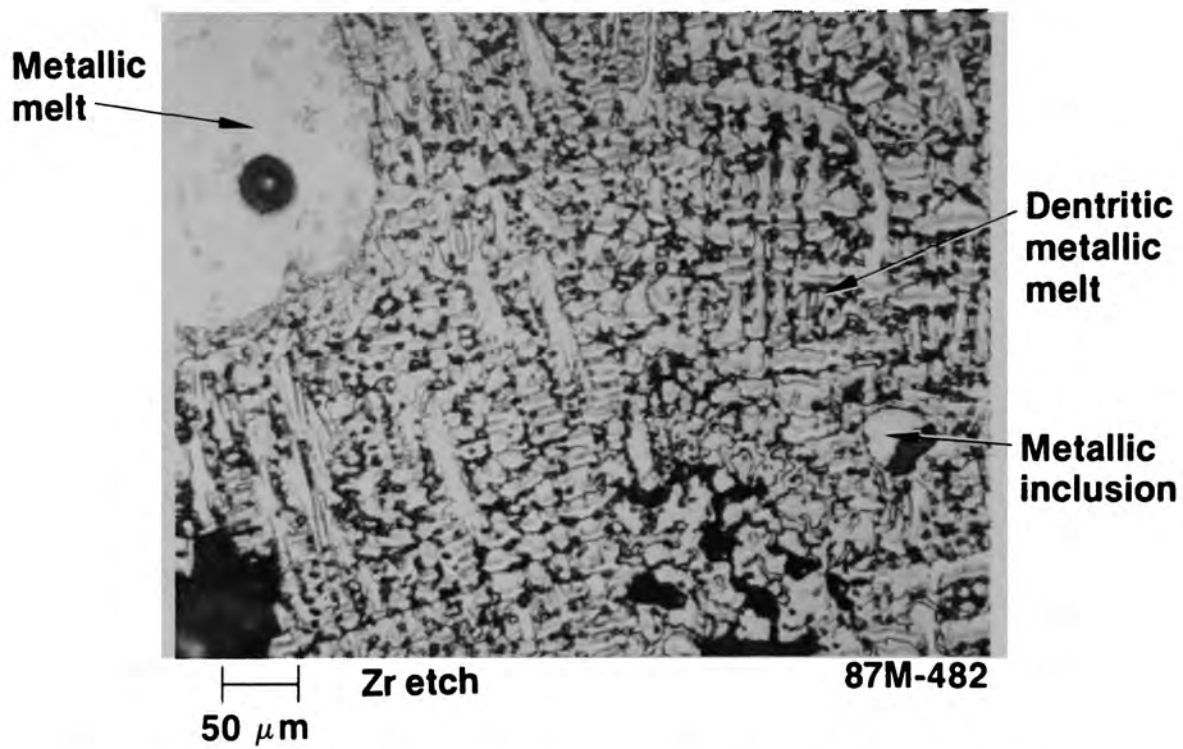


Figure E-90. Dendritic growth in metallic phase (007-P6 Area B).

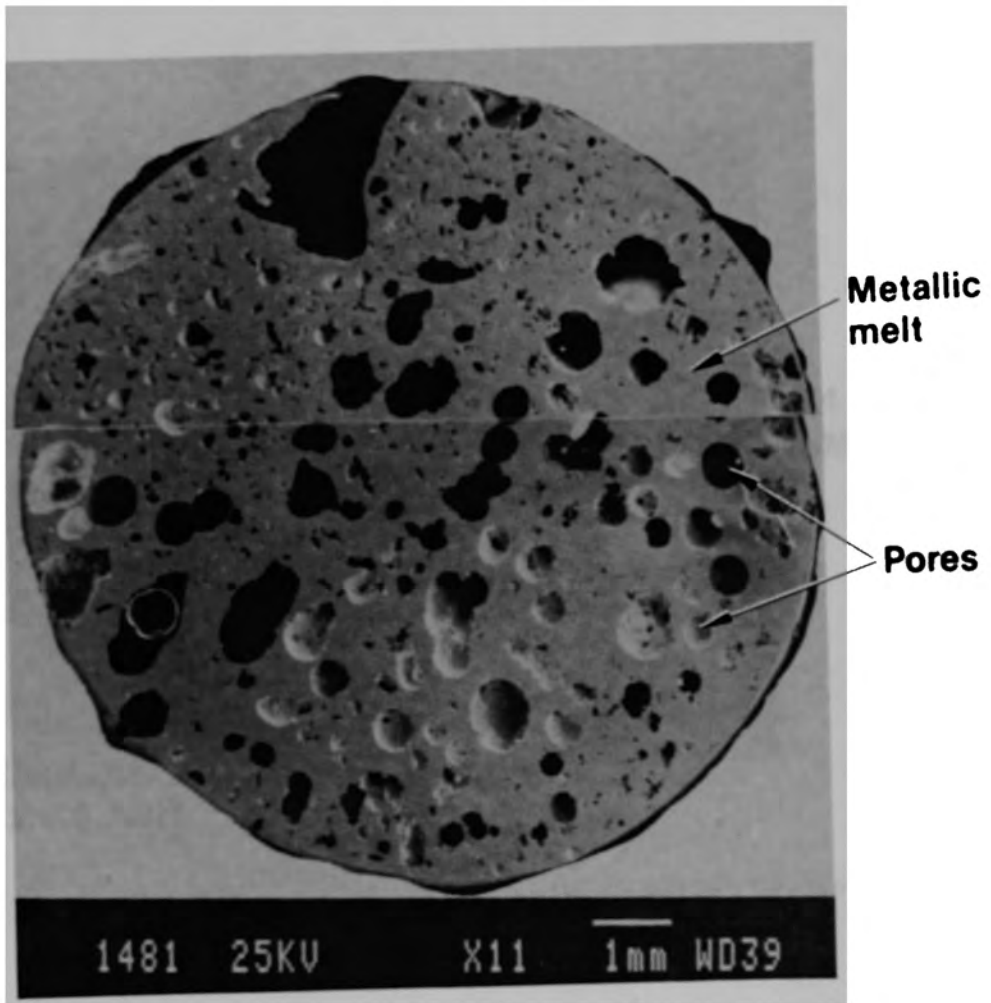
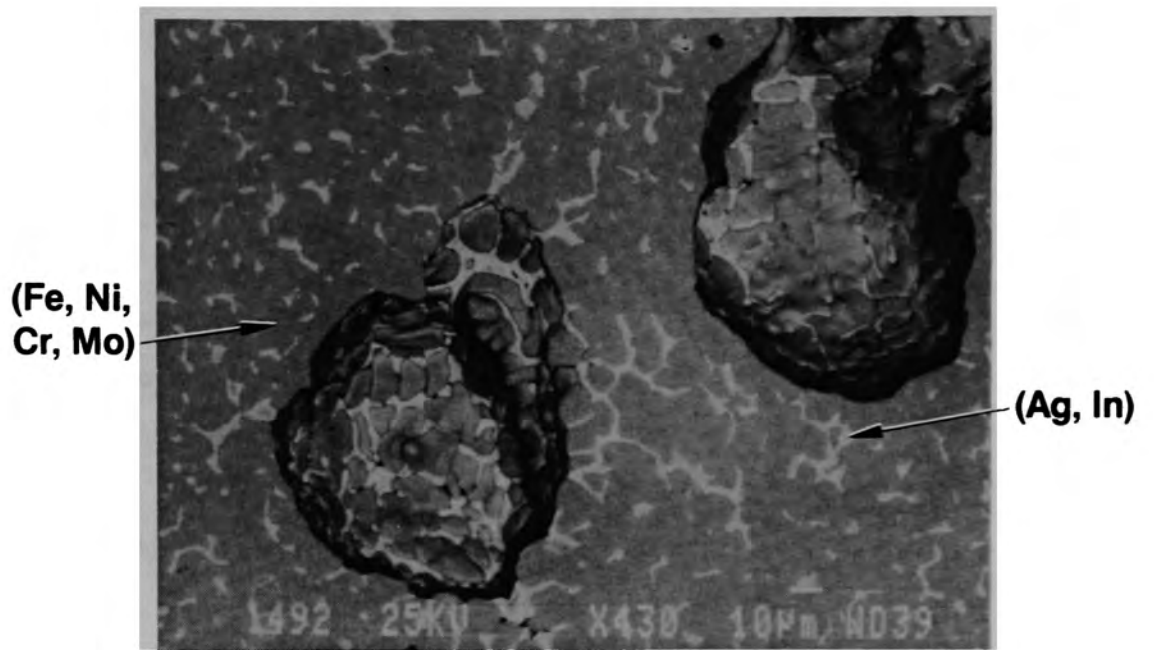


Figure E-91. Backscattered electron image of microcore from 007-P6.



**HCA 87-1492**

Figure E-92. Element distribution in metallic melt in 007-P6.

indicated that the matrix was composed of Fe and Ni with a small amount of Cr and Mo. Ag and In had also precipitated in the grain boundaries.

## Ceramic Particles

D08-P4-A This particle is shown in Figure E-93. It weighed 67.35 g and had a density of  $8.7 \text{ g/cm}^3$ . A cross section from this particle, shown in Figure E-94, shows a few large voids. As shown in Figure E-95, this particle was composed of  $(\text{U,Zr})\text{O}_2$  with some structural oxides mixed in the areas where the microstructure had a mottled appearance.

D08-P4-C The overall view of this particle is shown in Figure E-96. This particle weighed 37.00 g and had a density of  $7.80 \text{ g/cm}^3$ . A cross section through this particle, shown in Figure E-97, shows the extent of porosity in this particle. The typical microstructure is shown in Figure E-98. Metallic inclusions were distributed throughout the  $(\text{U,Zr})\text{O}_2$  matrix, and structural oxides had precipitated in the grain boundaries.

G08-P5-B A photograph of this particle is shown in Figure E-99. It weighed 116.06 g and had a density of  $8.0 \text{ g/cm}^3$ . A cross section through this particle is shown in Figure E-100. Voids are evident in this cross section along with a few microcracks. The typical microstructure is shown in Figure E-101. It consists of structural oxides mixed in a matrix of  $(\text{U,Zr})\text{O}_2$ .

G08-P6-B The overall view of this particle is shown in Figure E-102, which shows some surface porosity and the ceramic nature of the rock. The sample weighed 153.62 g and had a density of  $7.6 \text{ g/cm}^3$ .

After the metallographic examinations a small microcore was drilled from this cross section for elemental analysis. The backscattered electron image of the microcore is shown in Figure E-103. This image shows the area that was examined in detail on the SEM. A backscattered electron image of this detailed area is shown in Figure E-104. This region consists of areas of  $(\text{U,Zr})\text{O}_2$ , with a eutectic phase along the grain boundaries. This microstructure is very similar to other areas which were previously identified as containing structural oxides (see Figure E-68 in peripheral crust appendix section).





Figure E-93. Overview of ceramic sample D08-P4-A from the consolidated core region.

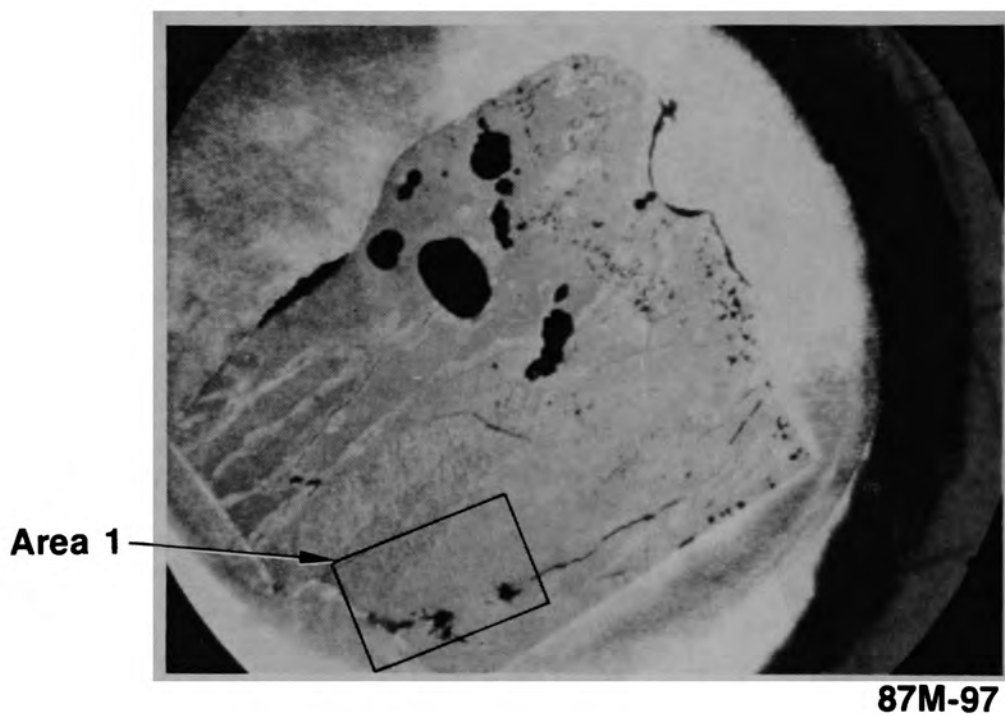


Figure E-94. Cross section from D08-P4-A.

(U, Zr)O<sub>2</sub> containing  
structural oxides

(U, Zr)O<sub>2</sub> ceramic melt



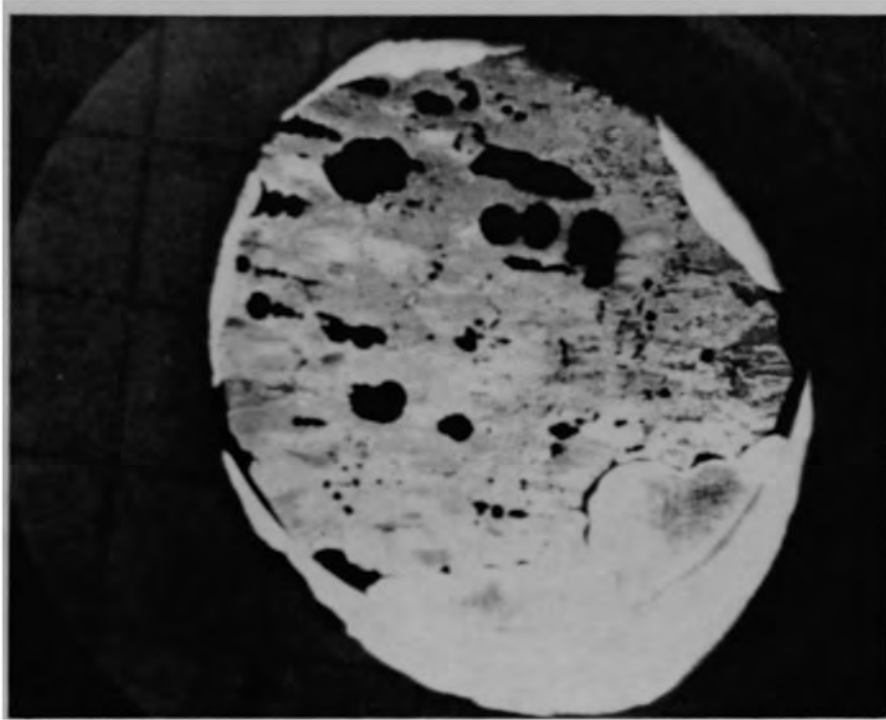
As polished  
200 μm

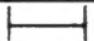
87M-179 to 87M-181

Figure E-95. Structural oxides in (U,Zr)O<sub>2</sub> ceramic melt.



Figure E-96. Overview of ceramic sample D08-P4-C from the consolidated core reg



  
**2.3 mm**

**87M-92**

Figure E-97. Cross section from D08-P4-C.

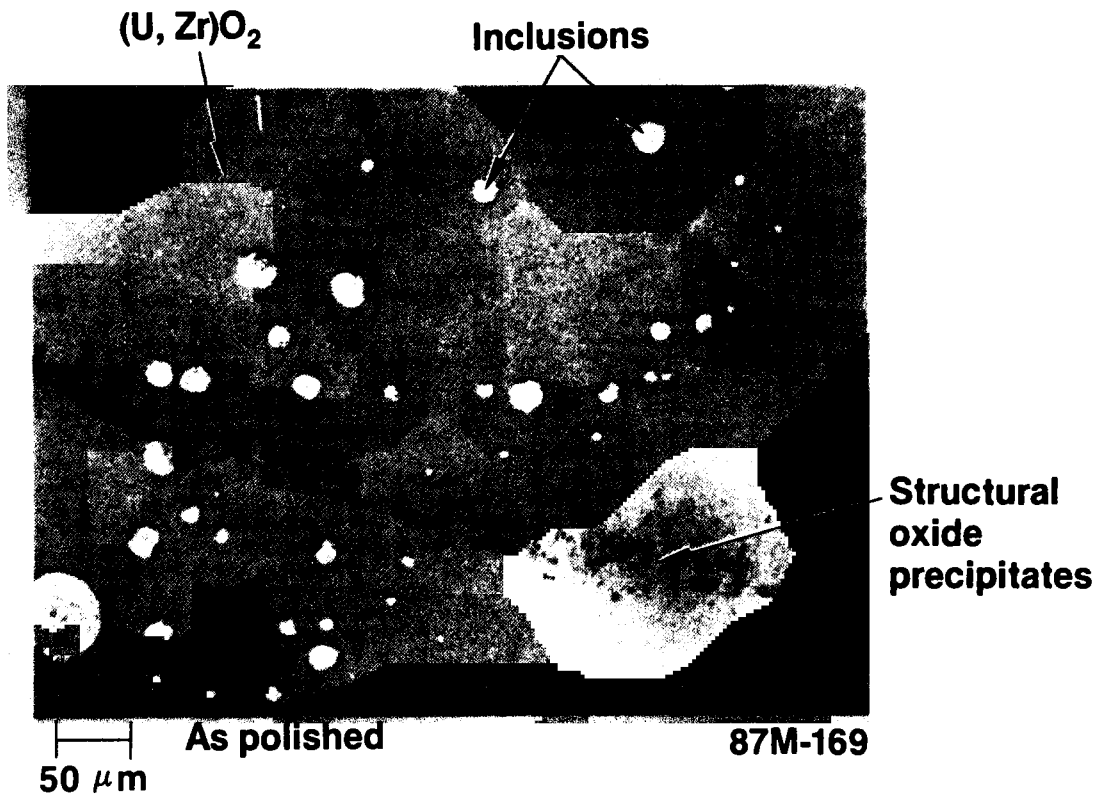


Figure E-98. Metallic inclusions in (U,Zr)O<sub>2</sub> (D08-P4-C).

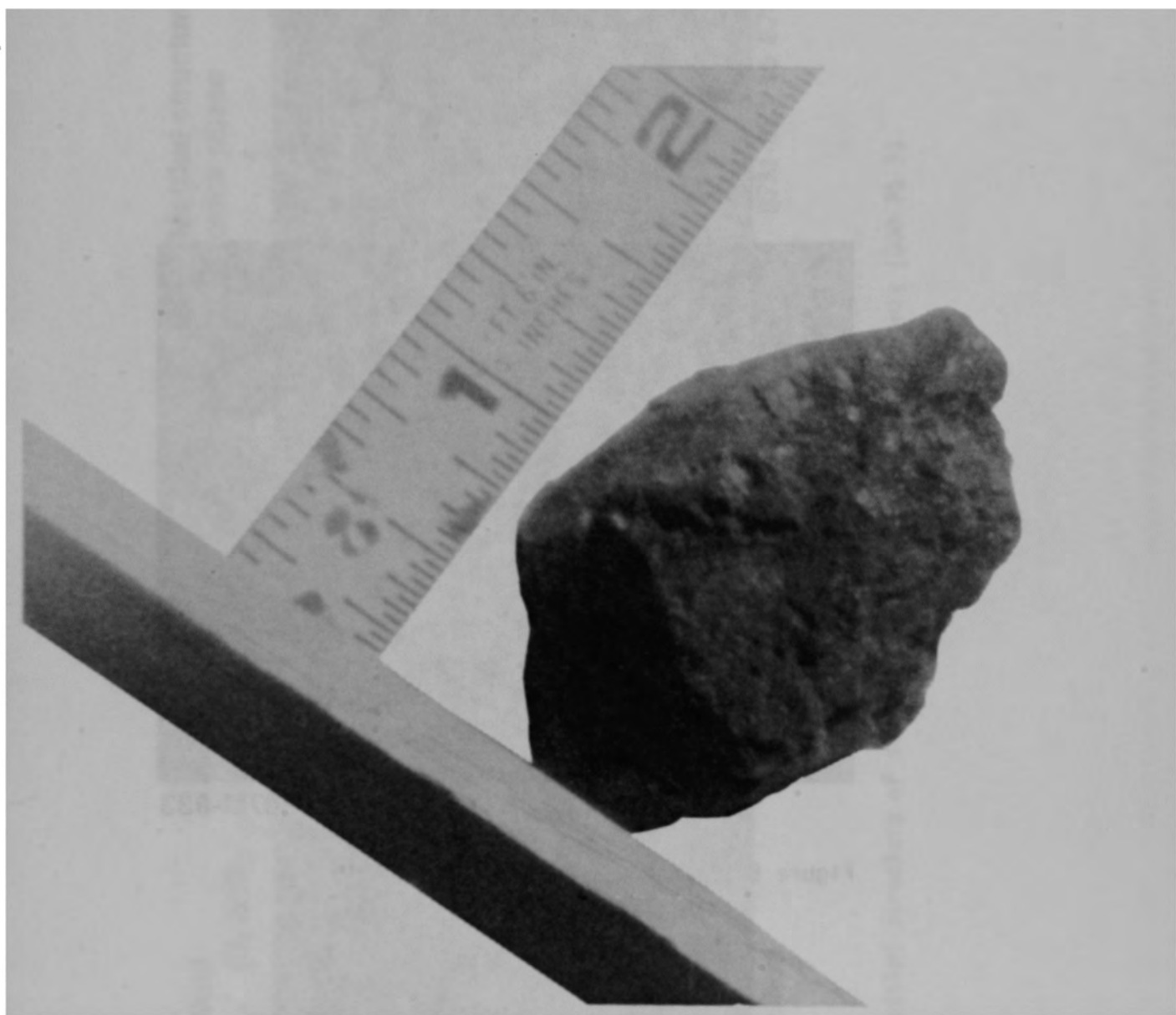


Figure E-99. Overview of ceramic sample G08-P5-B from the consolidated core region.



**87M-833**

Figure E-100. Cross section from G08-P5-B.



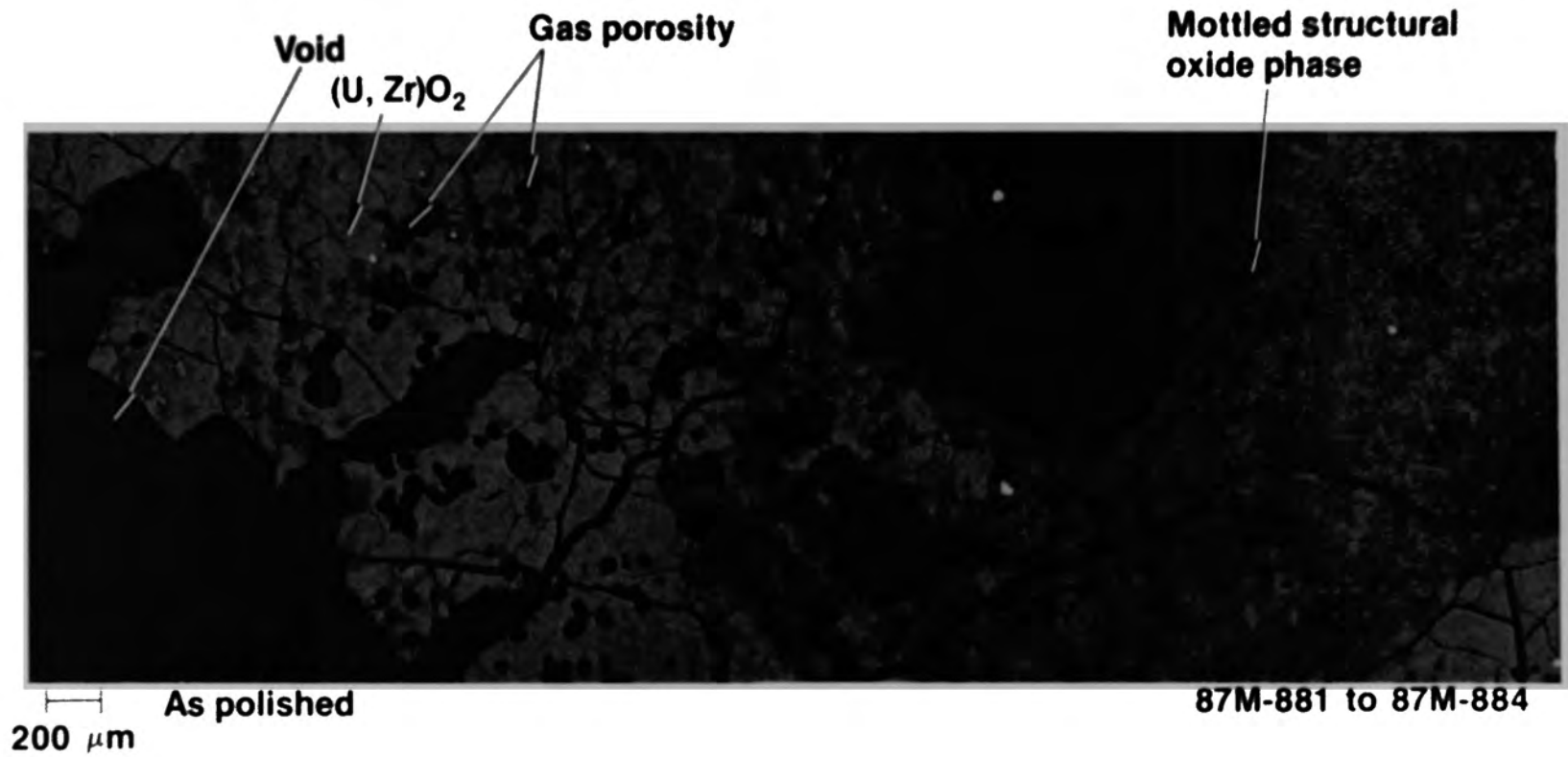


Figure E-101. Mottled structure of structural oxides in (U,Zr)O<sub>2</sub> matrix (G08-P5-B).

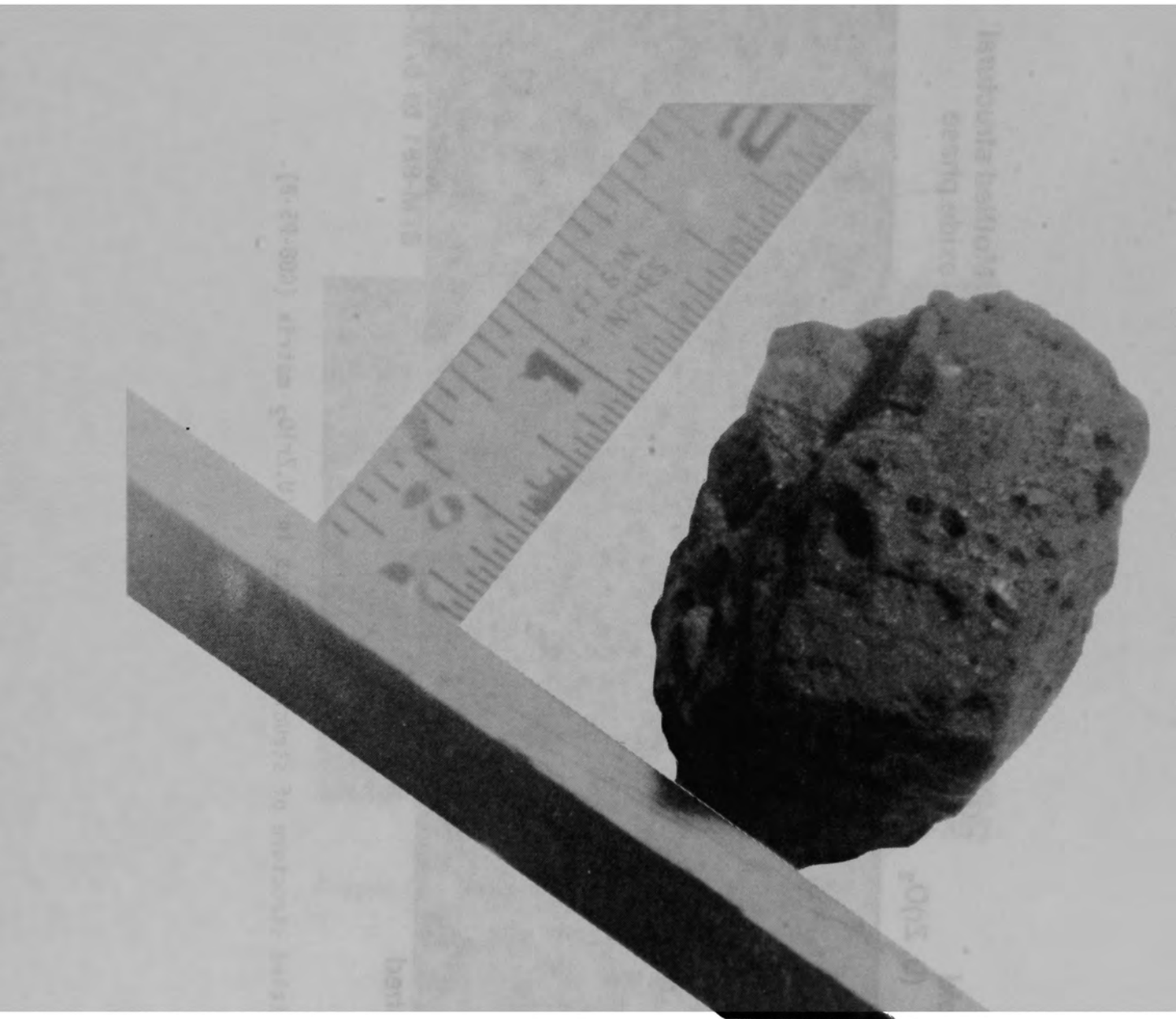


Figure E-102. Ceramic sample G08-P6-B from the consolidated core region.

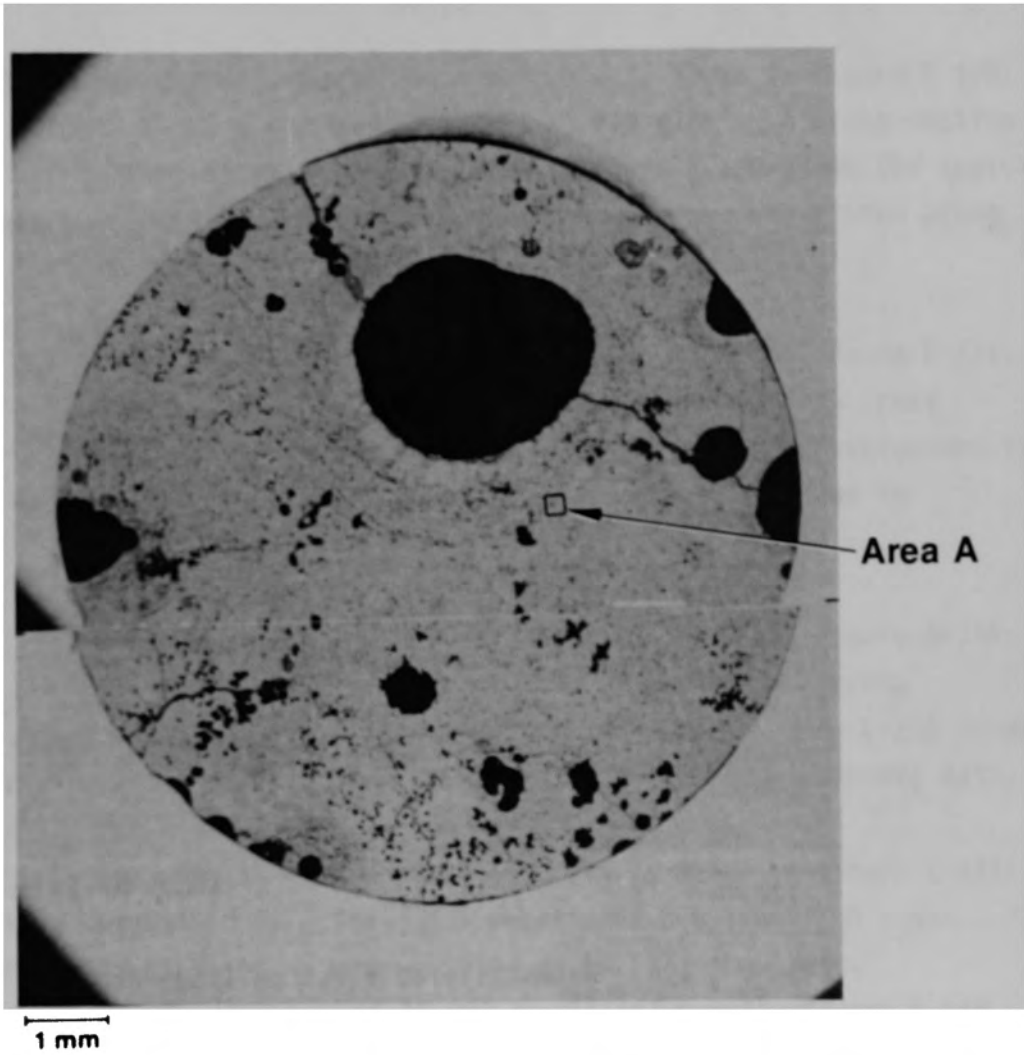


Figure E-103. Backscattered electron image of microcore G08-P6-B1.

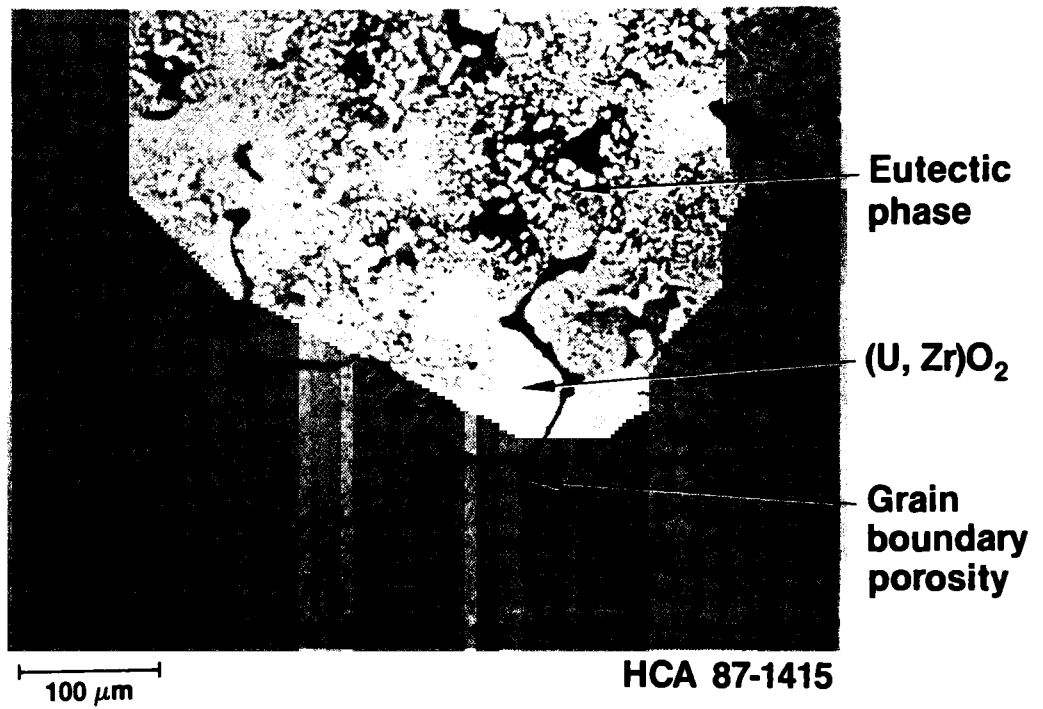


Figure E-104. Backscattered electron image of grain boundary eutectics in G08-P6-B1.

G08-P7-A The overall view of this particle is shown in Figure E-105. This sample weighed 193.84 g and had a density of  $7.8 \text{ g/cm}^3$ . A cross section from this particle is shown in Figure E-106. As shown in Figure E-107, the typical microstructure consisted of  $(\text{U,Zr})\text{O}_2$  ceramic melt with regions of structural oxides mixed in the melt.

G08-P7-C The overall view of this particle is shown in Figure E-108. This rock weighed 36.10 g and had a density of  $8.8 \text{ g/cm}^3$ . A cross section from this particle is shown in Figure E-109. Figure E-110 shows the typical microstructure of  $(\text{U,Zr})\text{O}_2$  melt with structural oxides concentrated along the grain boundaries.

G08-P8-A The overall view of this particle is shown in Figure E-111. This sample weighed 114.26 g and had a density of  $7.4 \text{ g/cm}^3$ . A cross section from this particle is shown in Figure E-112. The microstructure is typically  $(\text{U,Zr})\text{O}_2$  melt with structural oxides mixed in as shown in Figure E-113.

G08-P9-A The overall view of this particle is shown in Figure E-114. This rock weighed 158.94 g and had a density of  $7.3 \text{ g/cm}^3$ . A cross section through this particle is shown in Figure E-115. Figure E-116 shows the typical microstructure of structural oxides and  $(\text{U,Zr})\text{O}_2$  ceramic melt.

G12-P2-B The overall view of this particle is shown in Figure E-117. This particle weighed 60.51 g and had a density of  $8.5 \text{ g/cm}^3$ . A cross section from this particle is shown in Figure E-118. The typical microstructure of structural oxides in  $(\text{U,Zr})\text{O}_2$  is shown in Figure E-119. However, after etching, another area of the particle showed a banded structure of a light phase embedded in an oxide matrix (Figure E-120). This area is shown in more detail in Figure E-121, which shows a darker precipitate in the center of the band.

G12-P4-A The overall view of this particle is shown in Figure E-122. This rock weighed 90.48 g and had a density of  $7.7 \text{ g/cm}^3$ . A cross section from this particle shows partially molten fuel pellet remnants encased in a



Figure E-105. Overview of ceramic sample G08-P7-A.

**86-604-1-25**

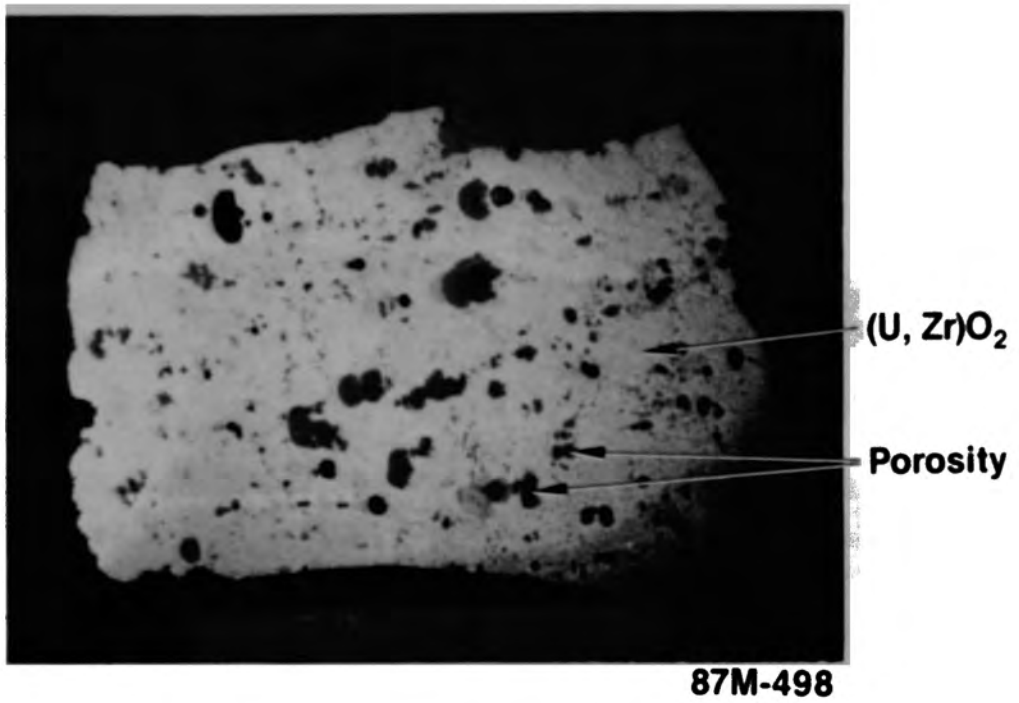


Figure E-106. Cross section of ceramic sample G08-P7-A.

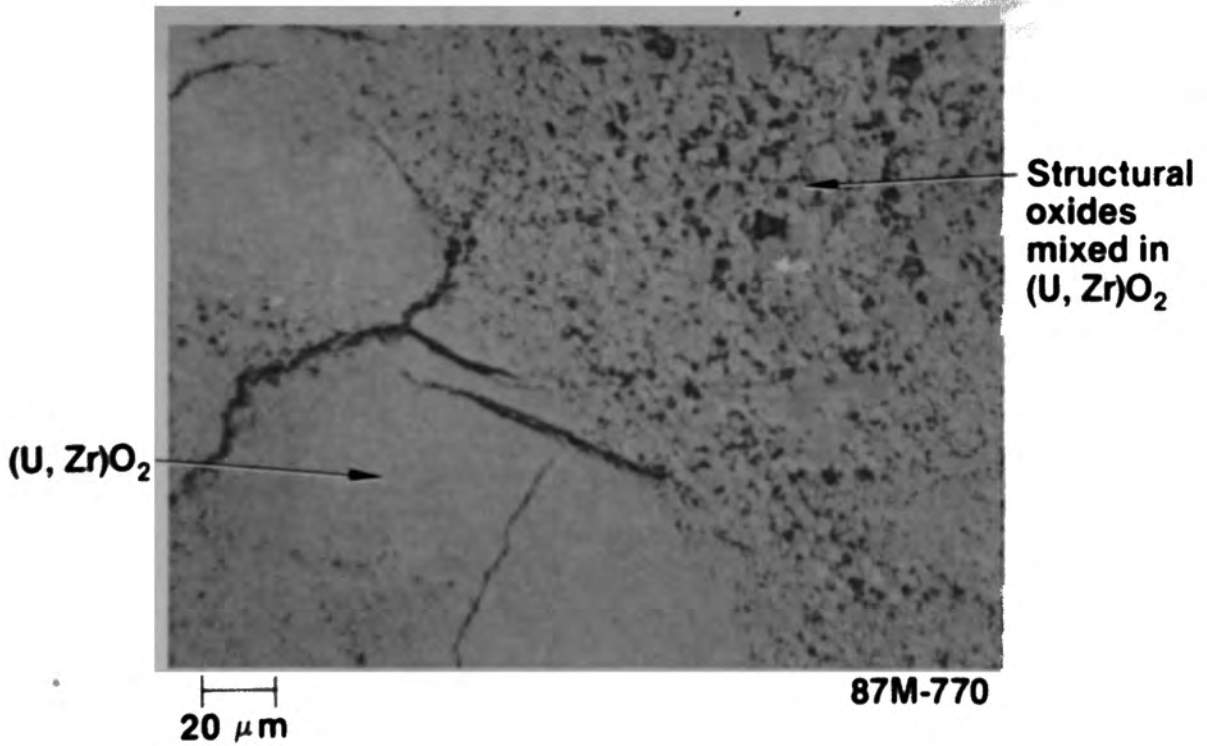


Figure E-107. Microstructure of sample G08-P7-A.



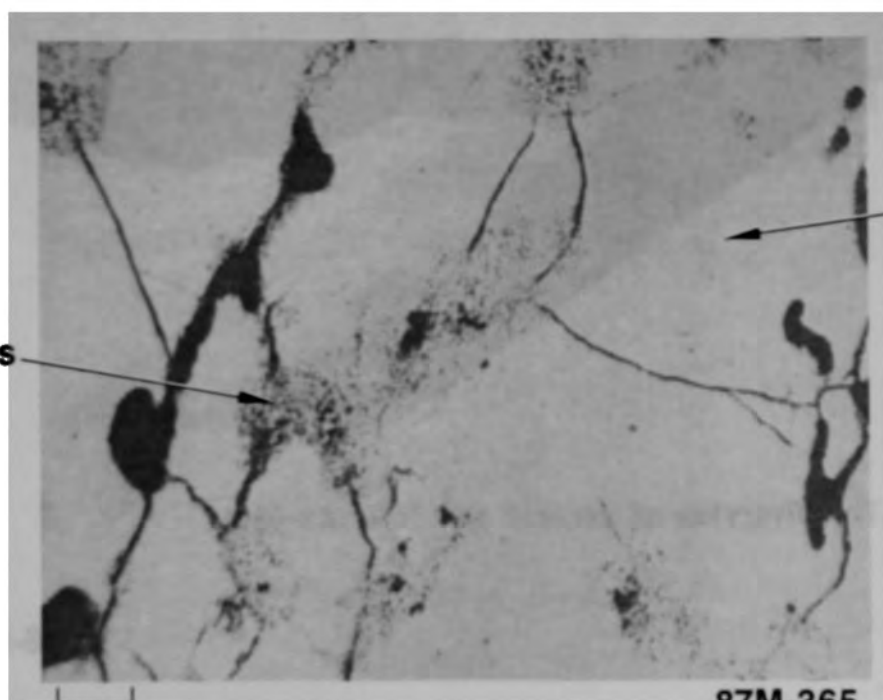




2 mm

87M-88

Figure E-109. Cross section of ceramic sample G08-P7-C.



Grain  
boundary  
precipitates

(U, Zr)O<sub>2</sub>

50  $\mu$  m

87M-365

Figure E-110. Grain boundary precipitates and mottled structure in G08-P7-C.



Figure E-111. Overview of ceramic particle G08-P8-A.

**86-604-1-26**



**87M-497**

Figure E-112. Cross section from G08-P8-A.

E-150

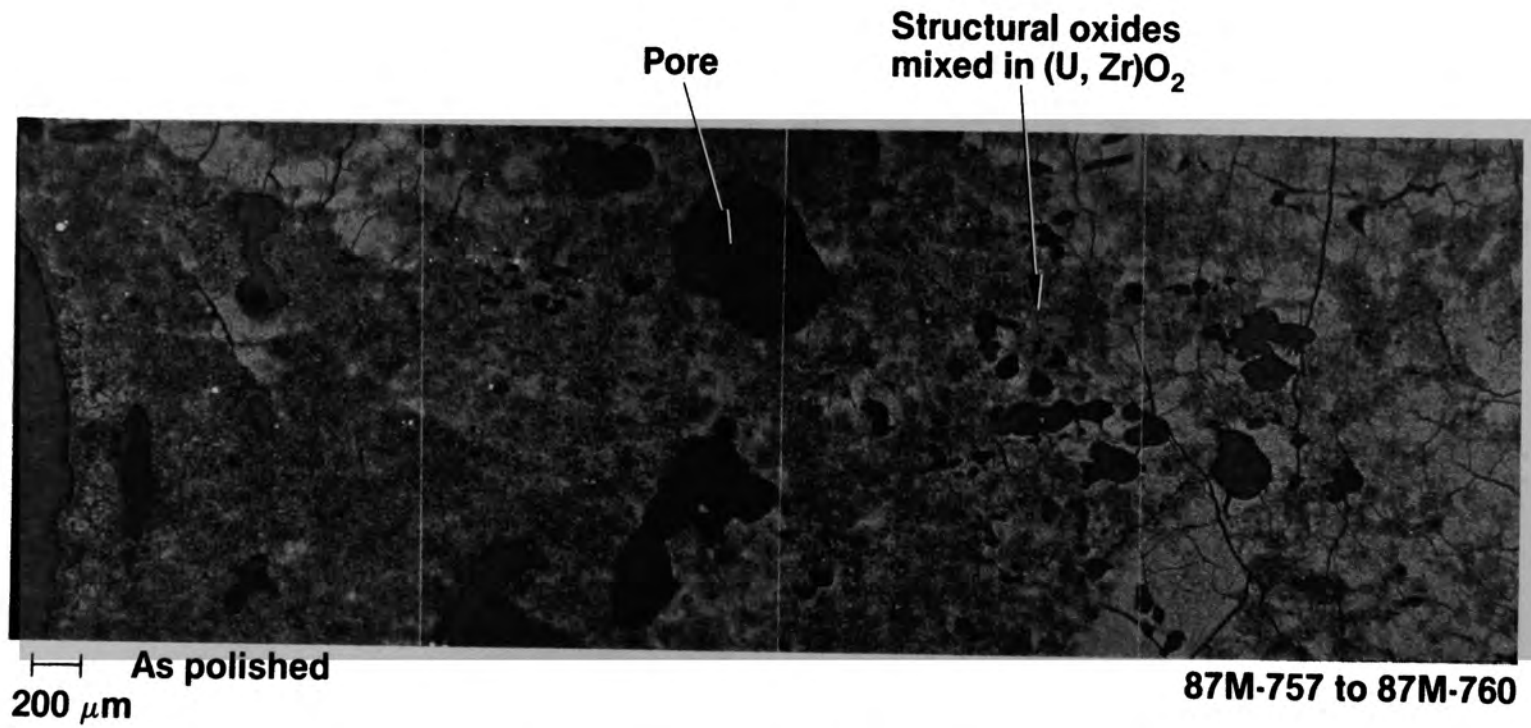


Figure E-113. Microstructure of ceramic sample G08-P8-A.

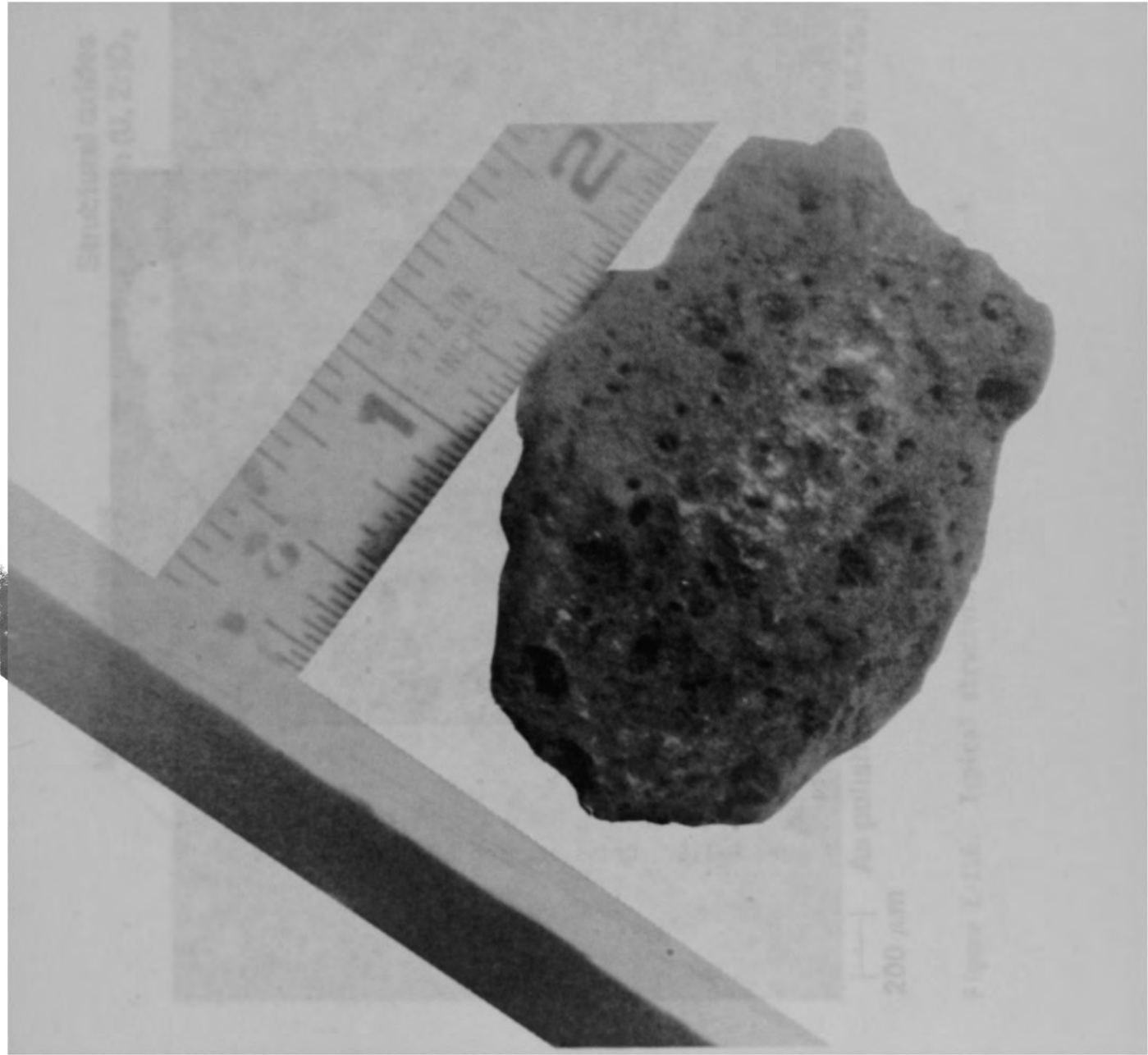


Figure E-114. Overview of ceramic sample G08-P9-A from the consolidated core region.



2 mm

87M-830

Figure E-115. Cross section of sample G08-P9-A.

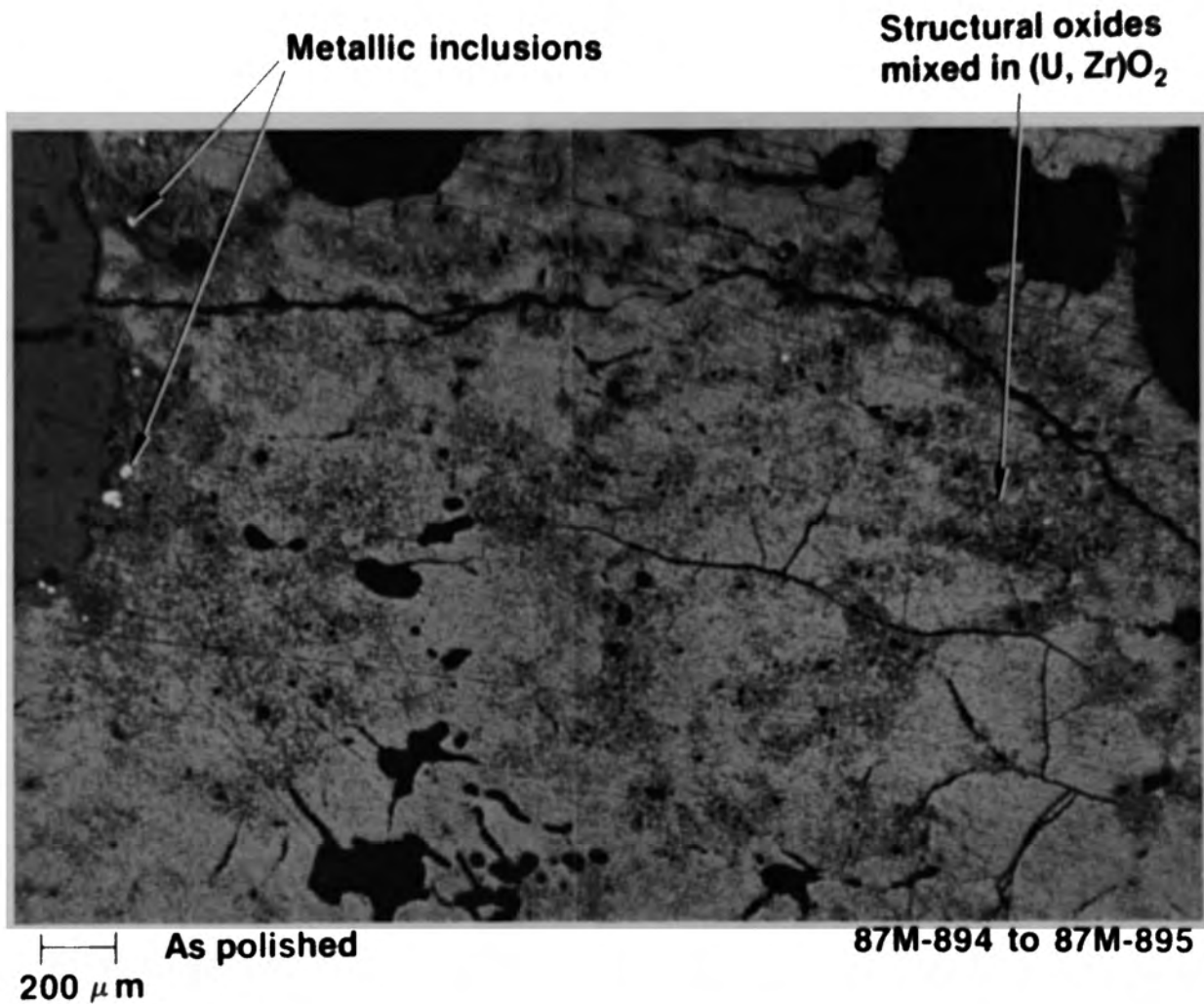
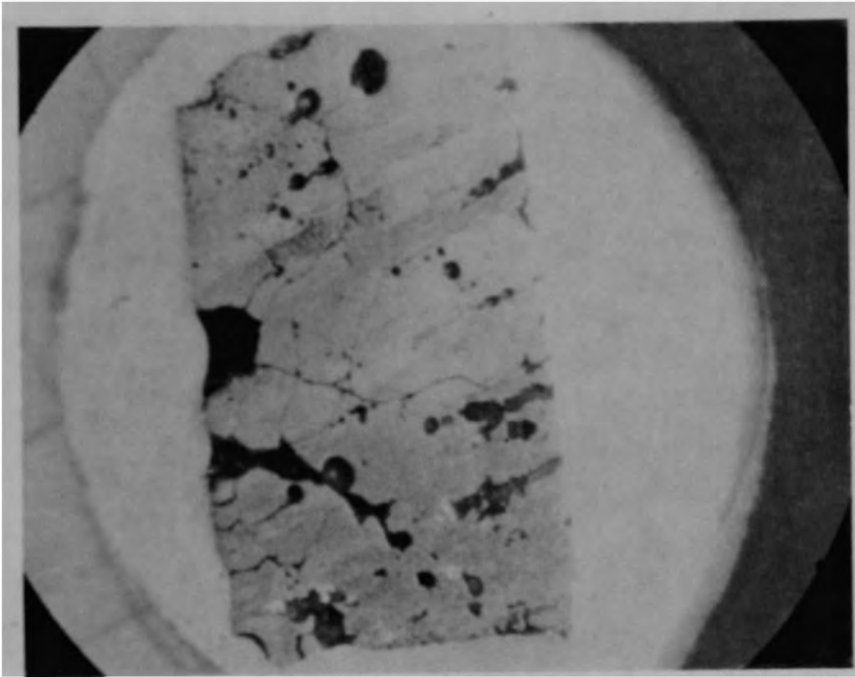


Figure E-116. Typical structure of ceramic matrix in G08-P9-A.



Figure E-117. Overview of ceramic sample G12-P2-B from the consolidated core region.





**87M-90**

Figure E-118. Cross section of G12-P2-B.

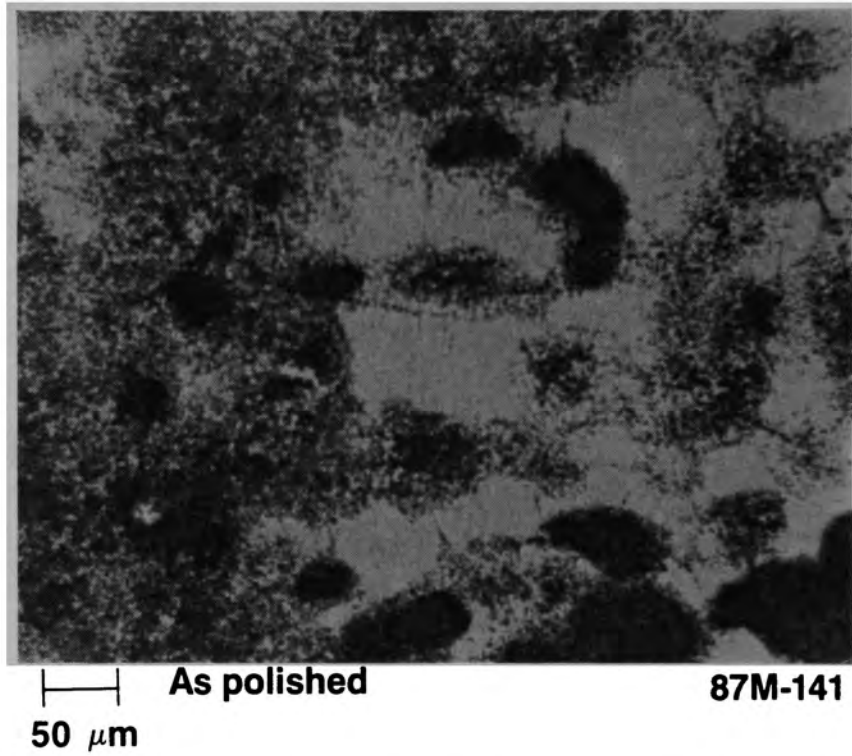
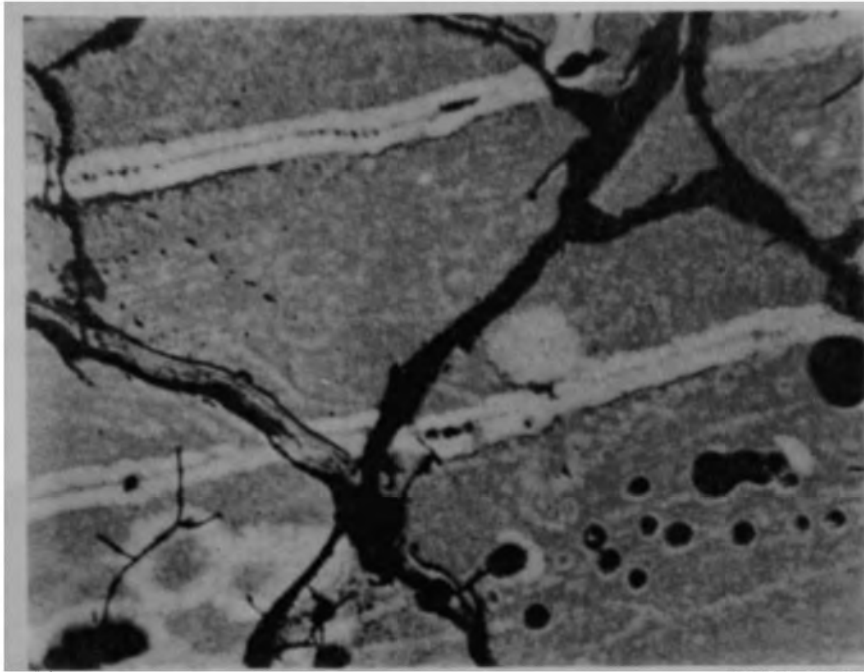


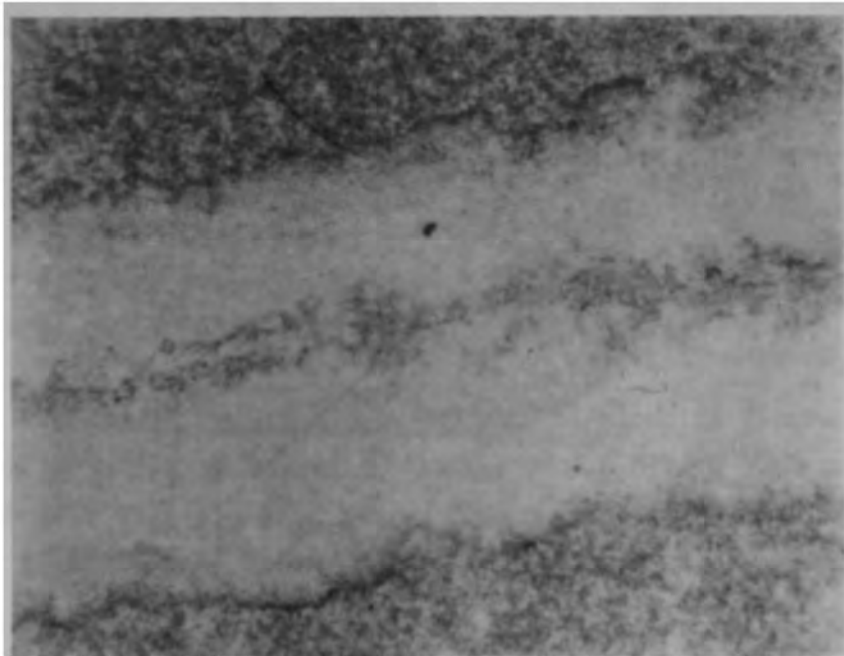
Figure E-119. Structural oxides and pores in  $(U,Zr)O_2$  in sample G12-P2-B.



—|—| Fuel etch  
50  $\mu\text{m}$

87M-156

Figure E-120. Banded structure in  $(\text{U,Zr})\text{O}_2$  matrix (G12-P2-B).



—|—| Fuel etch  
20  $\mu\text{m}$

87M-157

Figure E-121. Dark stringer within band (G12-P2-B).

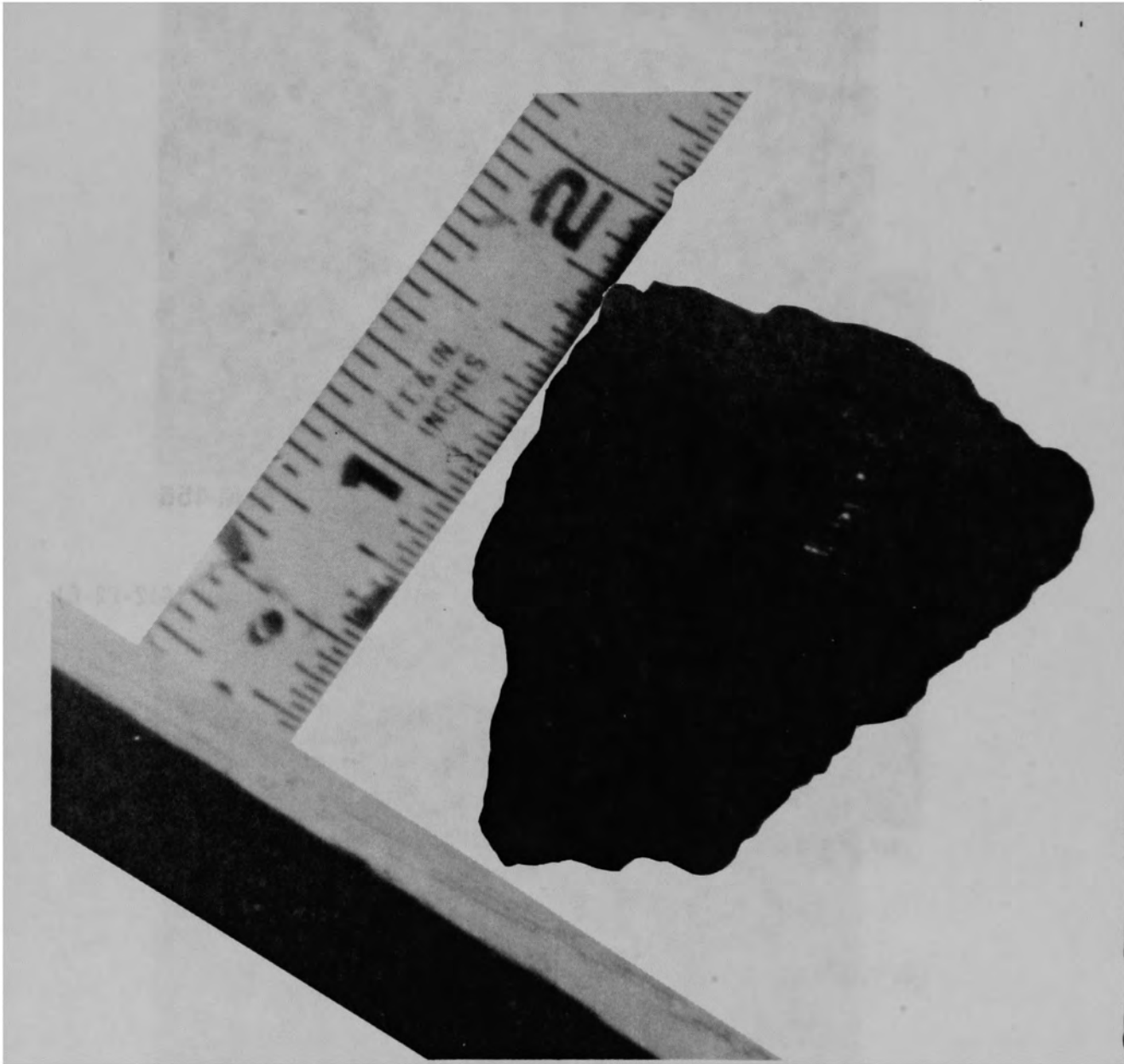


Figure E-122. Overall view of ceramic sample G12-P4-A.

86-604-5-20

ceramic matrix of  $(U,Zr)O_2$  (Figure E-123). Large voids were present in the partially molten fuel. This microstructure was previously discussed in Section 3.4.

K09-P3-A This particle is shown in Figure E-124. The particle weighed 55.15 g and had a density of  $7.6 \text{ g/cm}^3$ . A cross section from this particle is shown in Figure E-125. The microstructure consisted of structural oxides mixed in  $(U,Zr)O_2$  as shown in Figure E-126.

K09-P3-D This particle is shown in Figure E-127. The particle weighed 43.19 g and had a density of  $7.4 \text{ g/cm}^3$ . A cross section from this particle is shown in Figure E-128. The typical microstructure of structural oxides in  $(U,Zr)O_2$  is shown in Figure E-129.

K09-P3-F This sample is shown in Figure E-130. The particle weighed 26.04 g and had a density of  $7.8 \text{ g/cm}^3$ . A cross section through this particle is shown in Figure E-131. The typical microstructure of structural oxides concentrated along grain boundaries in the  $(U,Zr)O_2$  is shown in Figure E-132. A backscattered electron image of this cross section is shown in Figure E-133. The elemental dot maps for the area shown in Figure E-133, are shown in Figure E-134. These dot maps show regions of  $(U,Zr)O_2$  and a second phase composed of  $(Fe,Cr,Ni,Al,O)$ .

K09-P4-A The overall view of this particle is shown in Figure E-135. This particle weighed 10.28 g and had a density of  $7.1 \text{ g/cm}^3$ . A cross section of this particle is shown in Figure E-136. Figure E-137 shows the typical structural oxides mixed in the ceramic  $(U,Zr)O_2$  melt.

K09-P4-D The overall view of this particle is shown in Figure E-138. This particle weighed 23.9 g and had a density of  $6.9 \text{ g/cm}^3$ . The cross section through this particle is shown in Figure E-139. The typical microstructure of structural oxides in  $(U,Zr)O_2$  is shown in Figure E-140.

A backscattered electron image of the cross section is shown in Figure E-141. This figure shows the different areas which were examined in

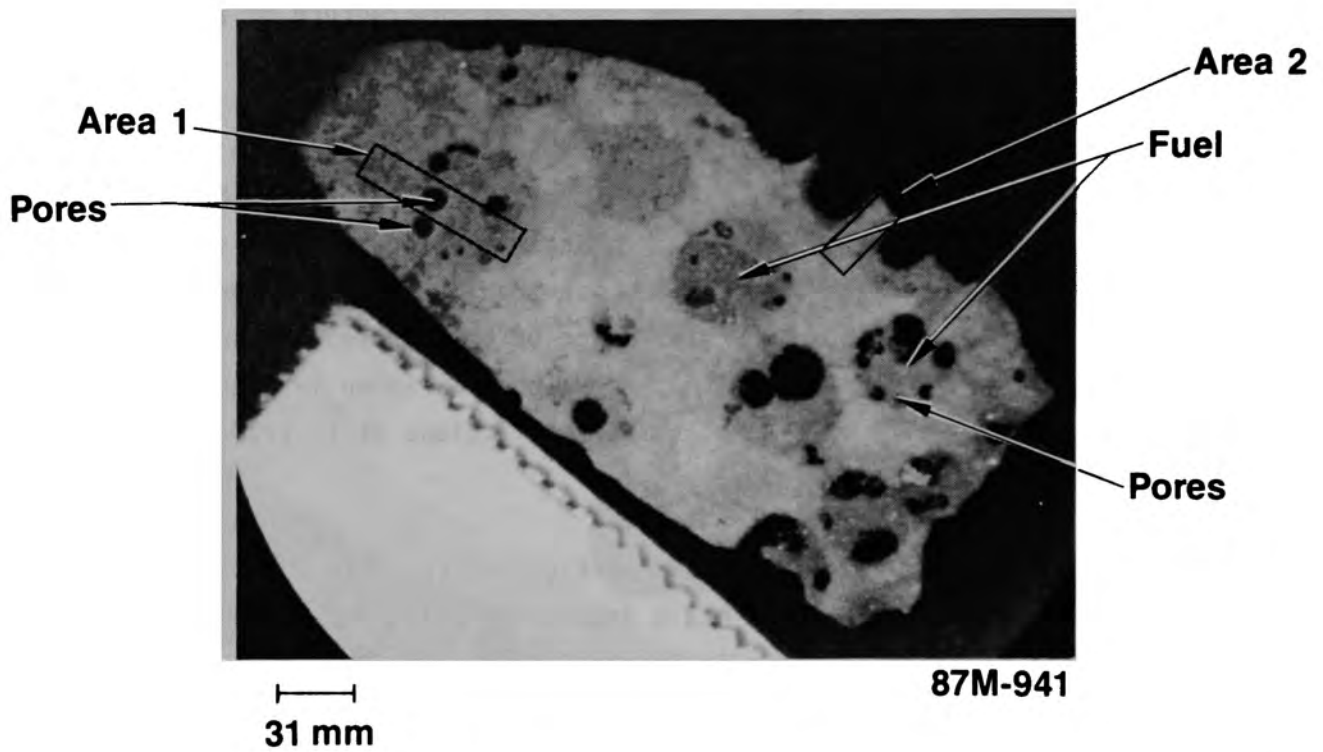


Figure E-123. Distribution of pores adjacent to fuel pellet remnants (G12-P4-A).

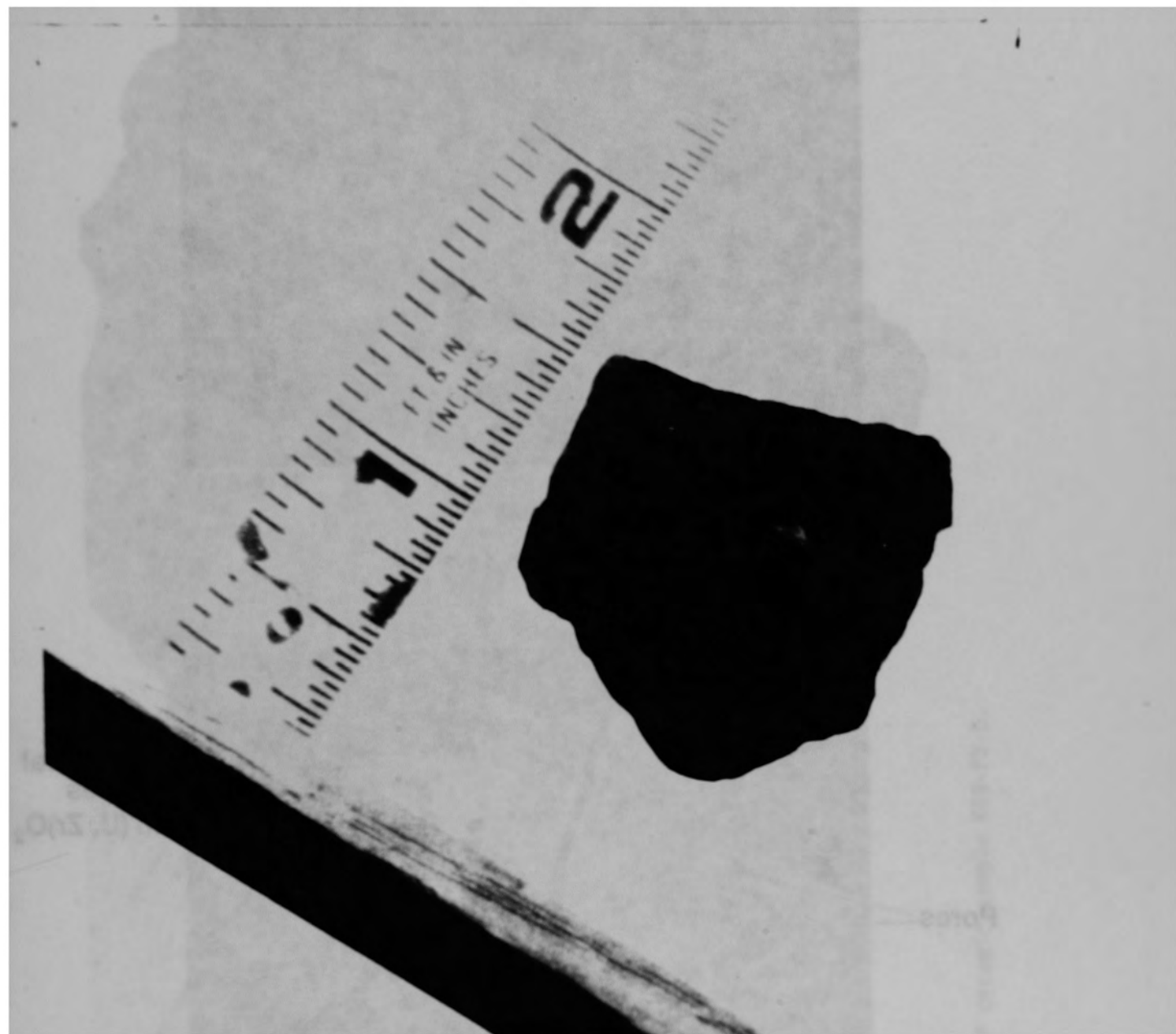


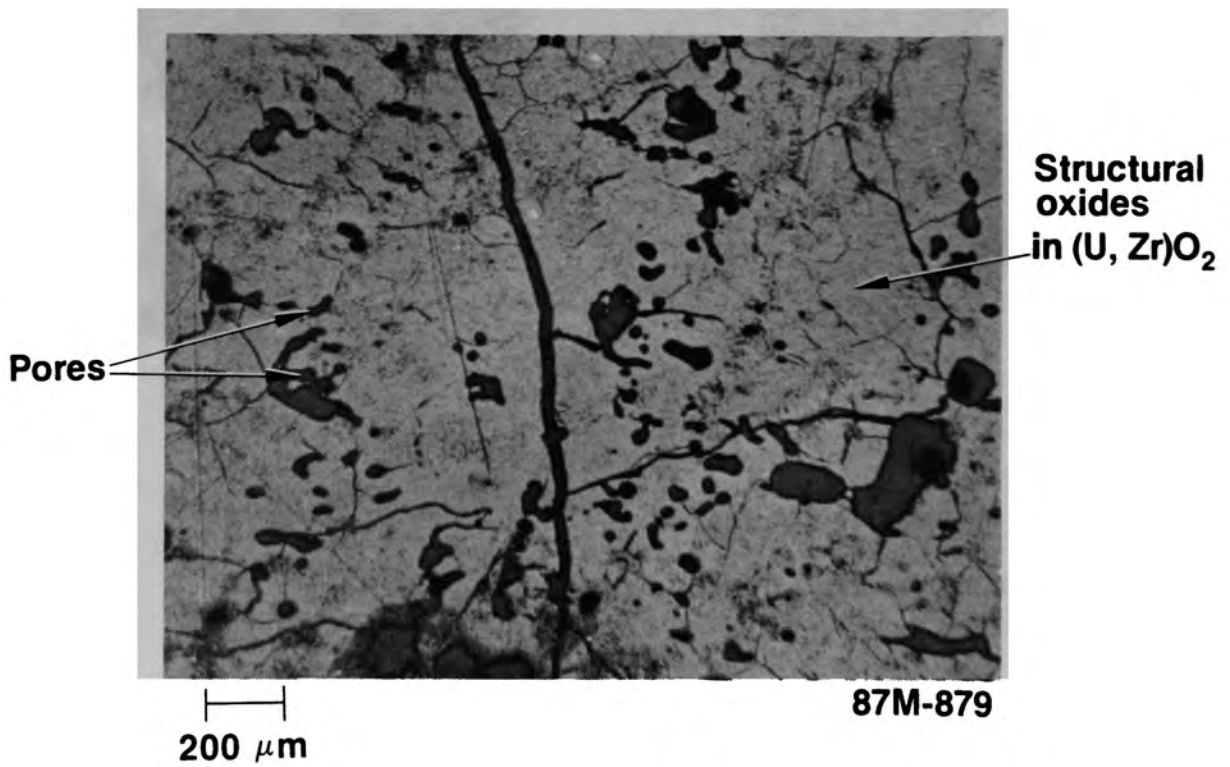
Figure E-124. Overview of ceramic sample K09-P3-A.

86-604-3-24



87M-831

Figure E-125. Cross section from K09-P3-A.



200 μm

87M-879

Figure E-126. Typical microstructure of K09-P3-A.



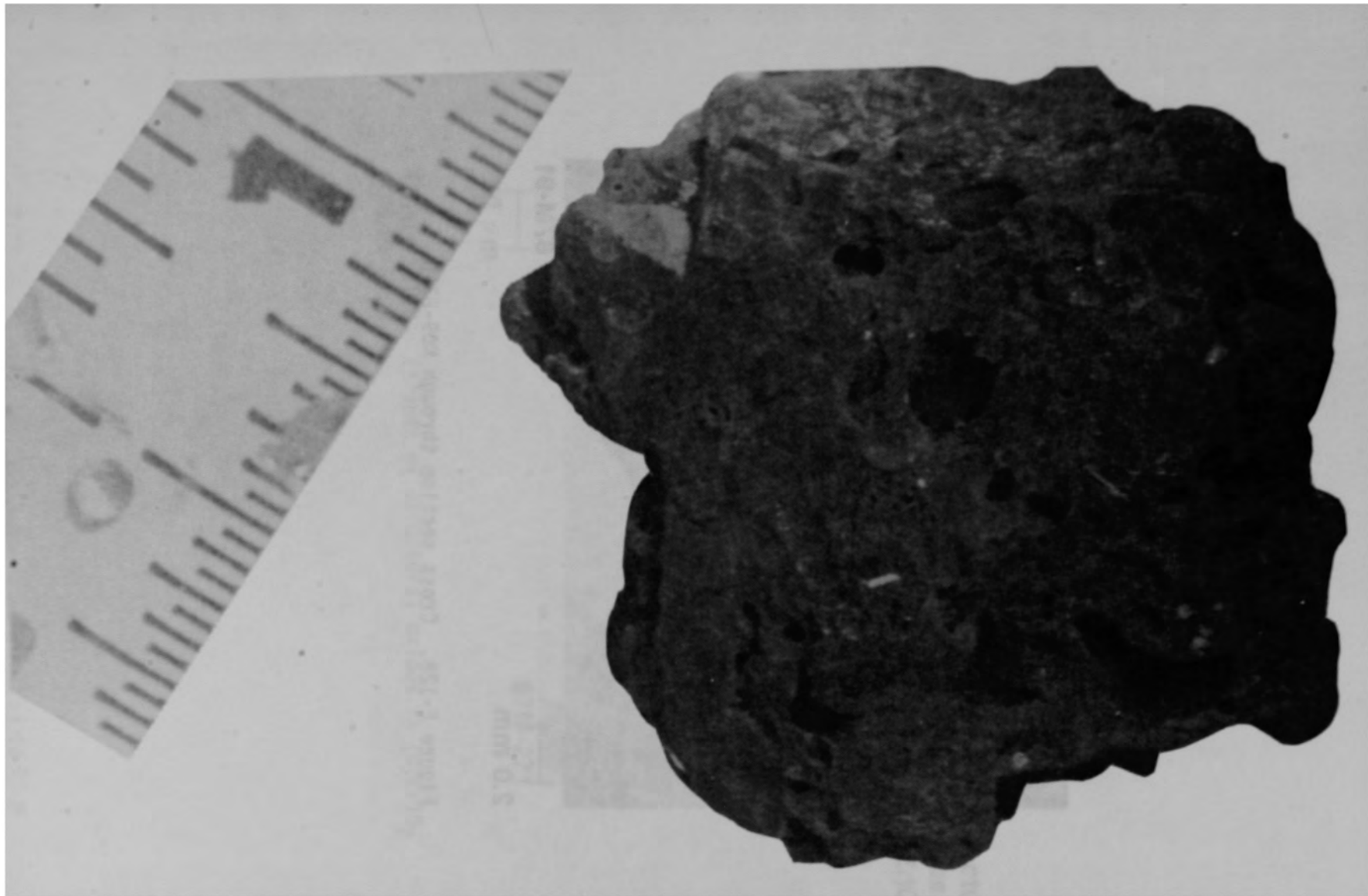
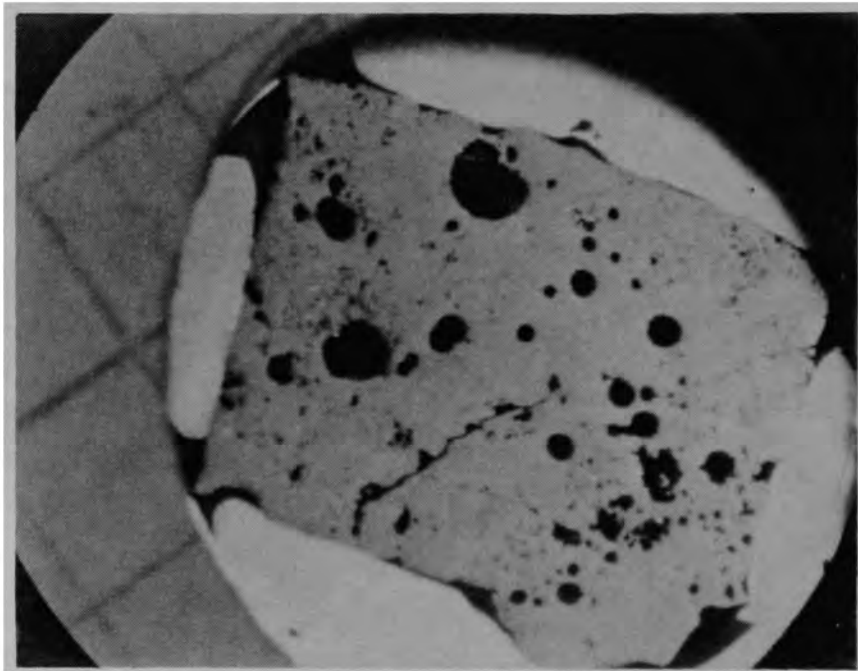


Figure E-127. Overview of ceramic sample K09-P3-D.



2.0 mm

87M-91

Figure E-128. Cross section through K09-P3-D.

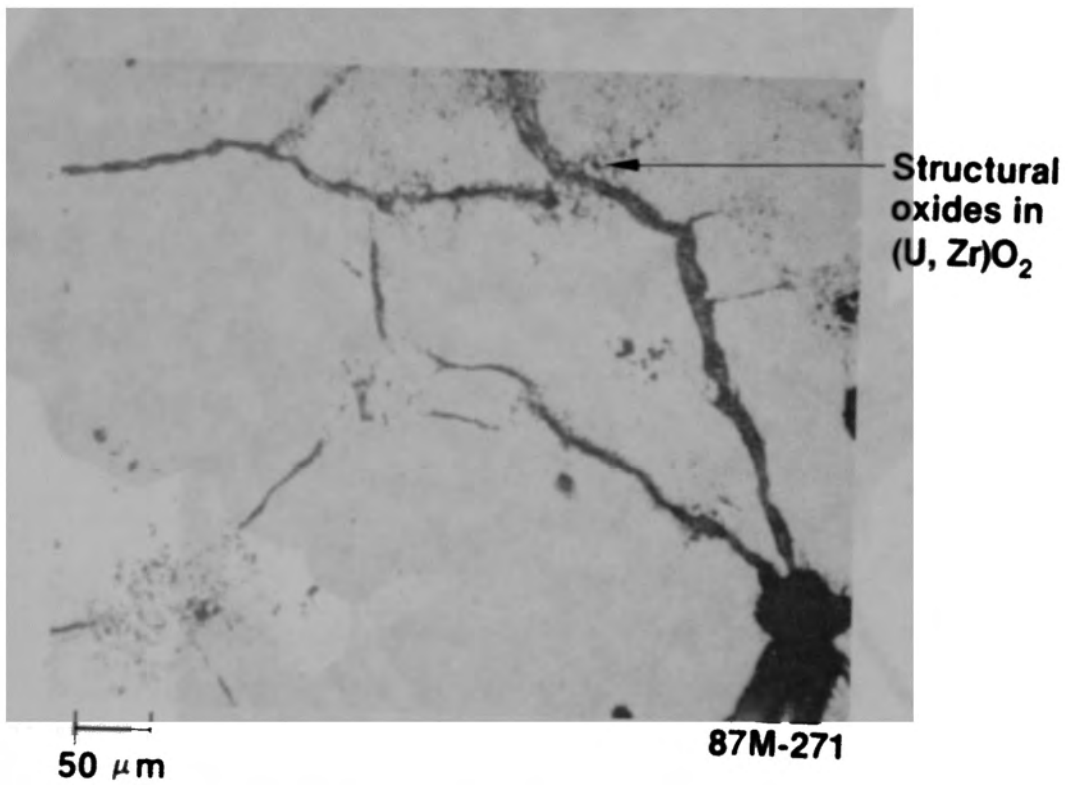


Figure E-129. Islands of structural oxides in  $(U, Zr)O_2$  (K09-P3-D).



Figure E-130. Overview of ceramic sample K09-P3-F from the consolidated core region

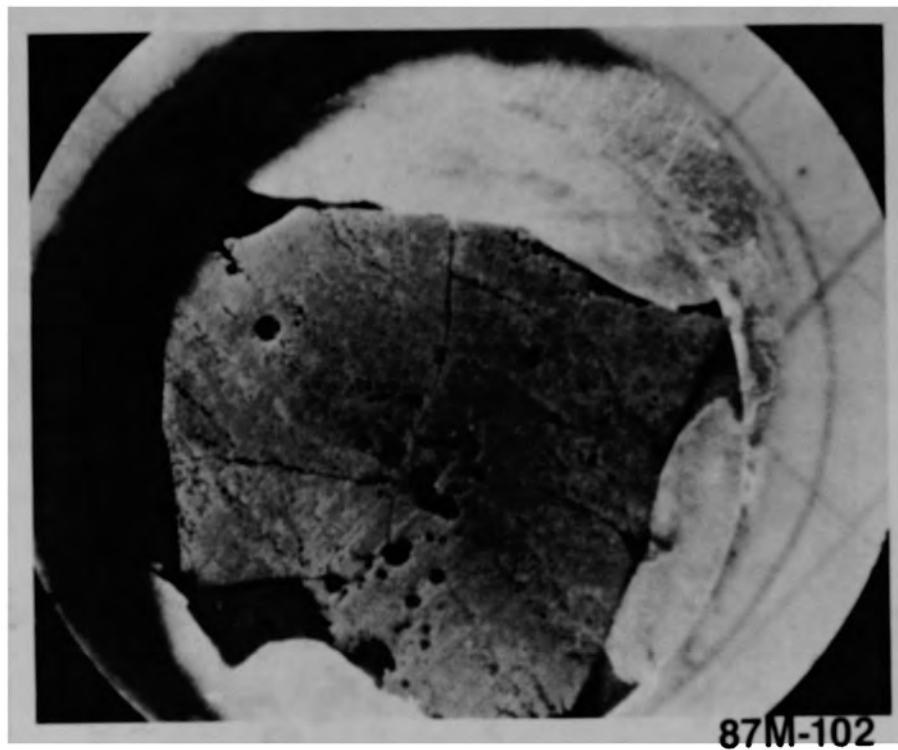


Figure E-131. Cross section of K09-P3-F.

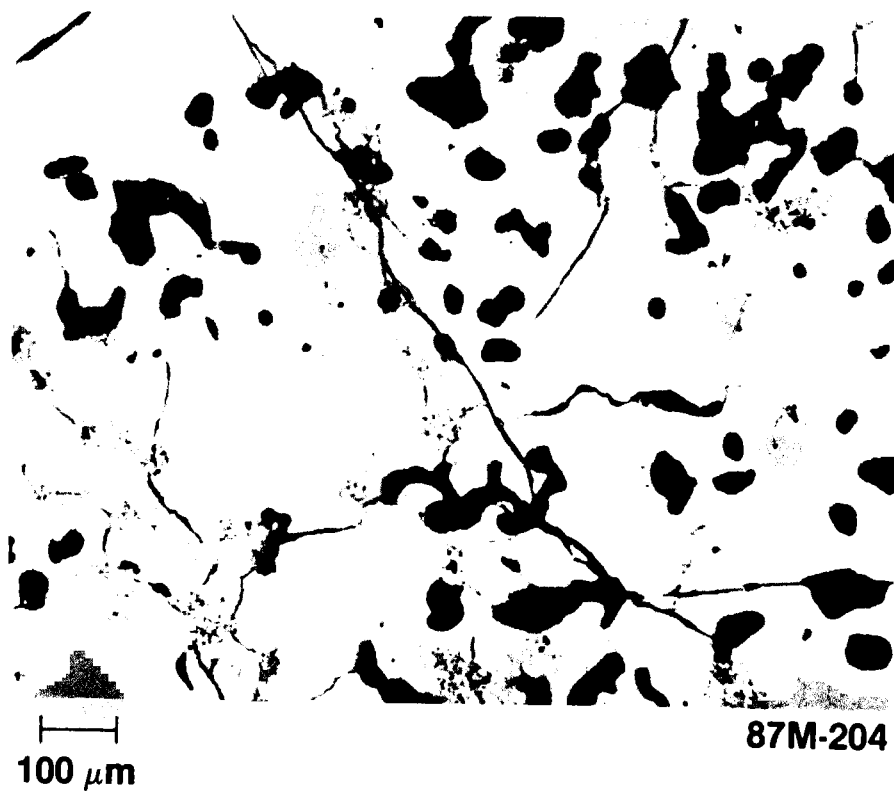
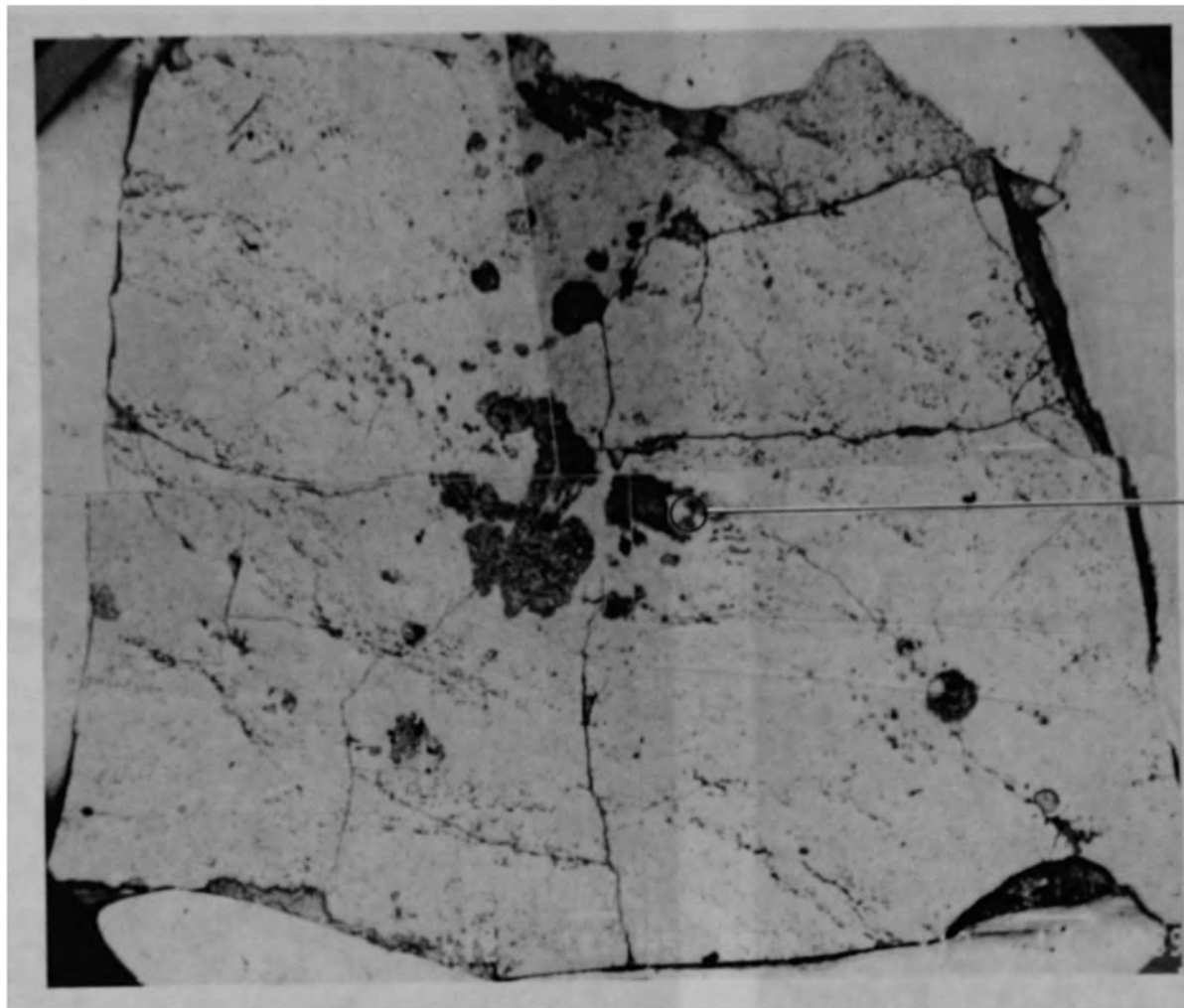


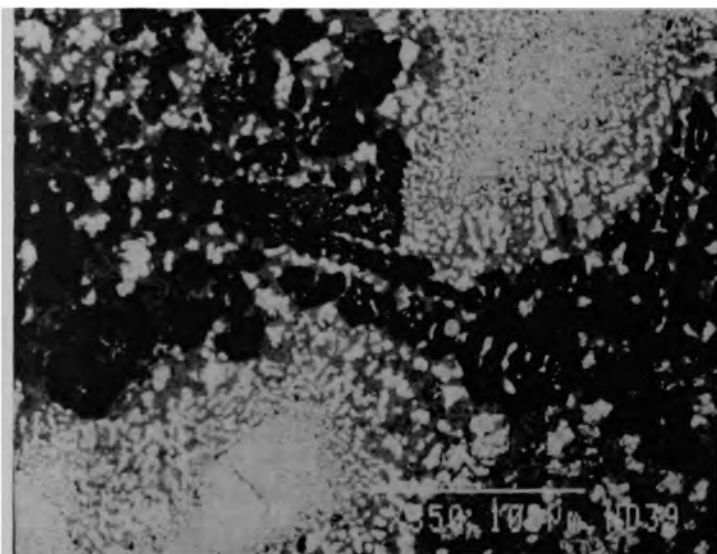
Figure E-132. Porosity and grain boundary precipitates in K09-P3-F.

E-169

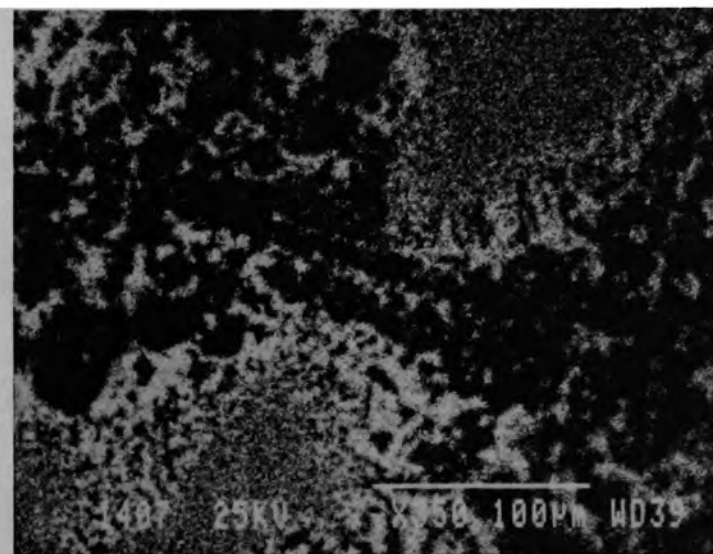


**Examination  
area**

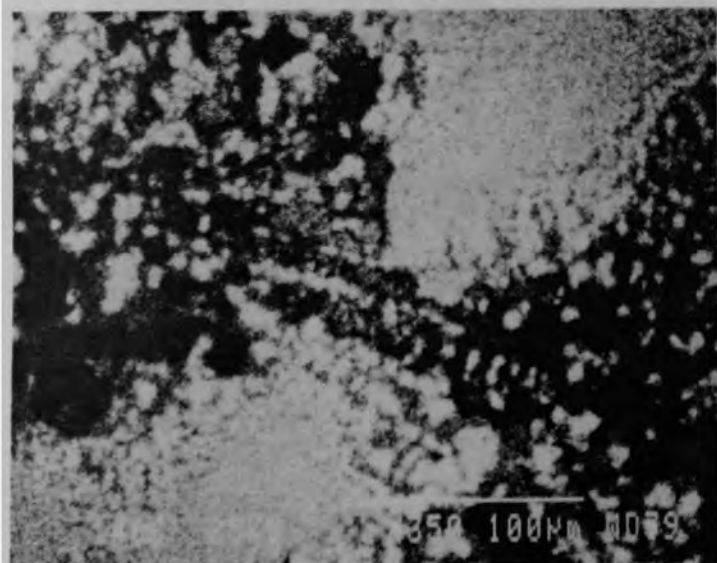
Figure E-133. SEM examination location (K09-P3-F).



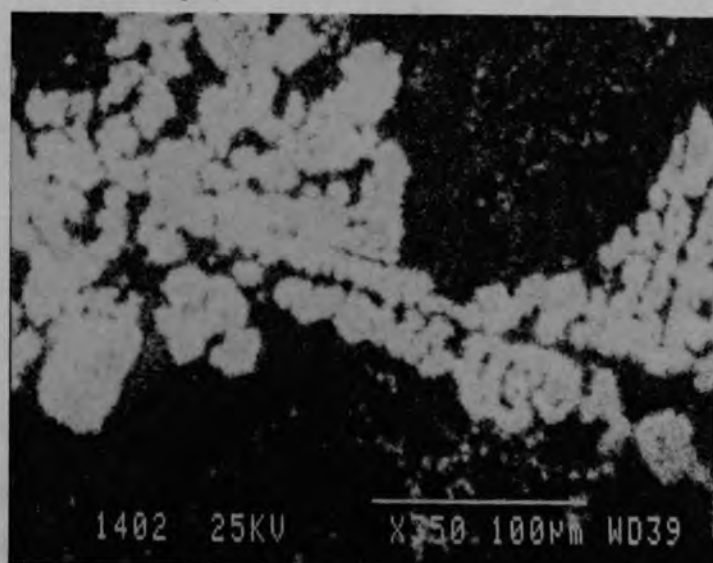
**BSE compositional image HCA 87-1399**



**U dot map HCA 87-1406**



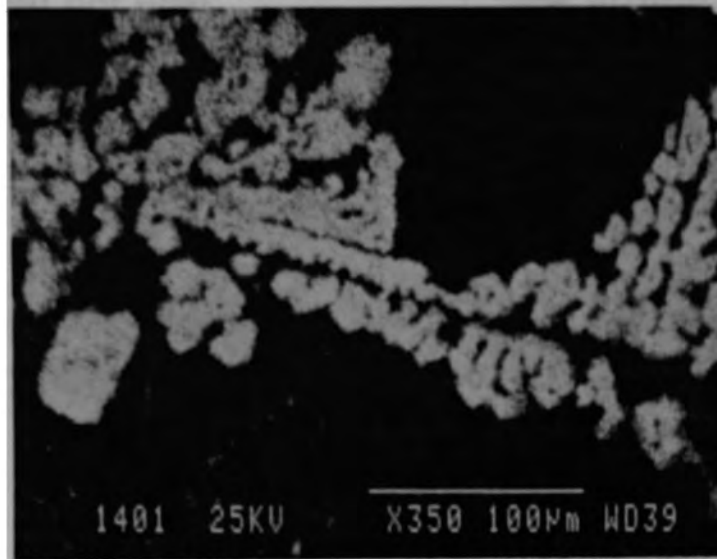
**Zr dot map HCA 87-1407**



**Fe dot map HCA 87-1402**

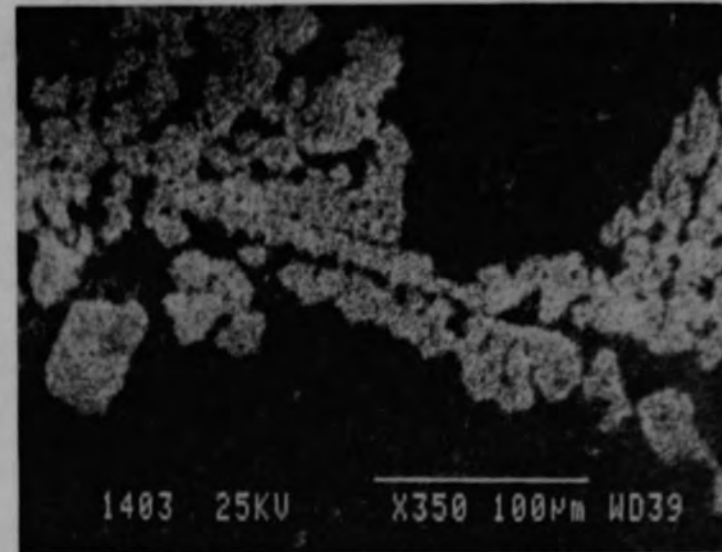
Figure E-134. Structural materials in  $(U,Zr)O_2$  matrix (K09-P3-F).





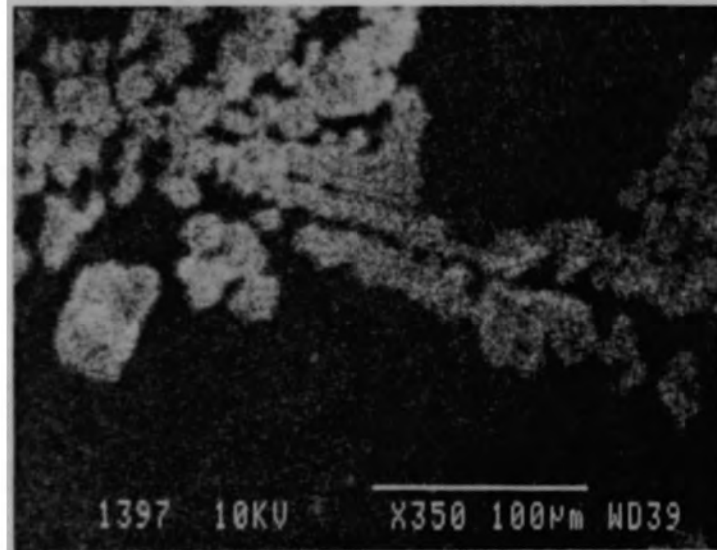
Cr dot map

HCA 87-1401



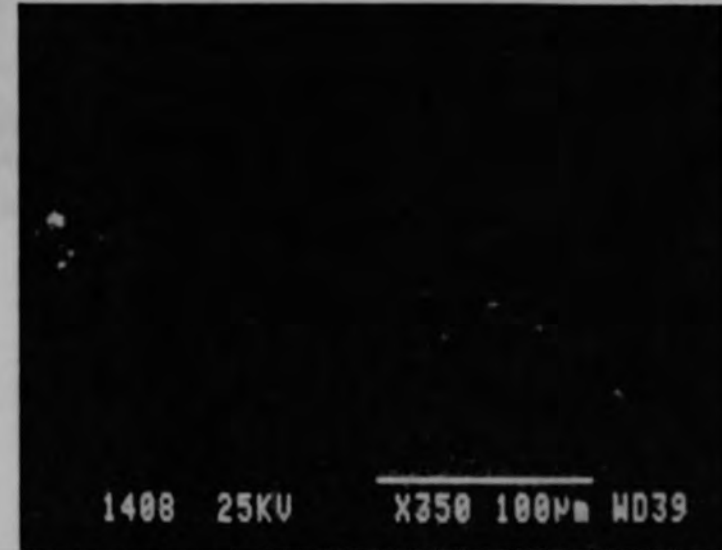
Ni dot map

HCA 87-1403



Al dot map

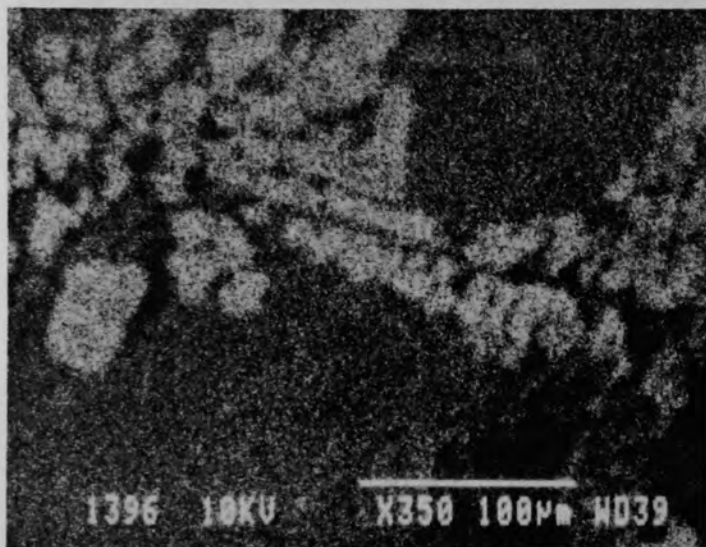
HCA 87-1397



Mo dot map

HCA 87-1408

Figure E-134. (Continued)



O dot map

HCA 87-1396



Sn dot map

HCA 87-1405



Ag dot map

HCA 87-1410



Tc dot map

HCA 87-1409

E-173

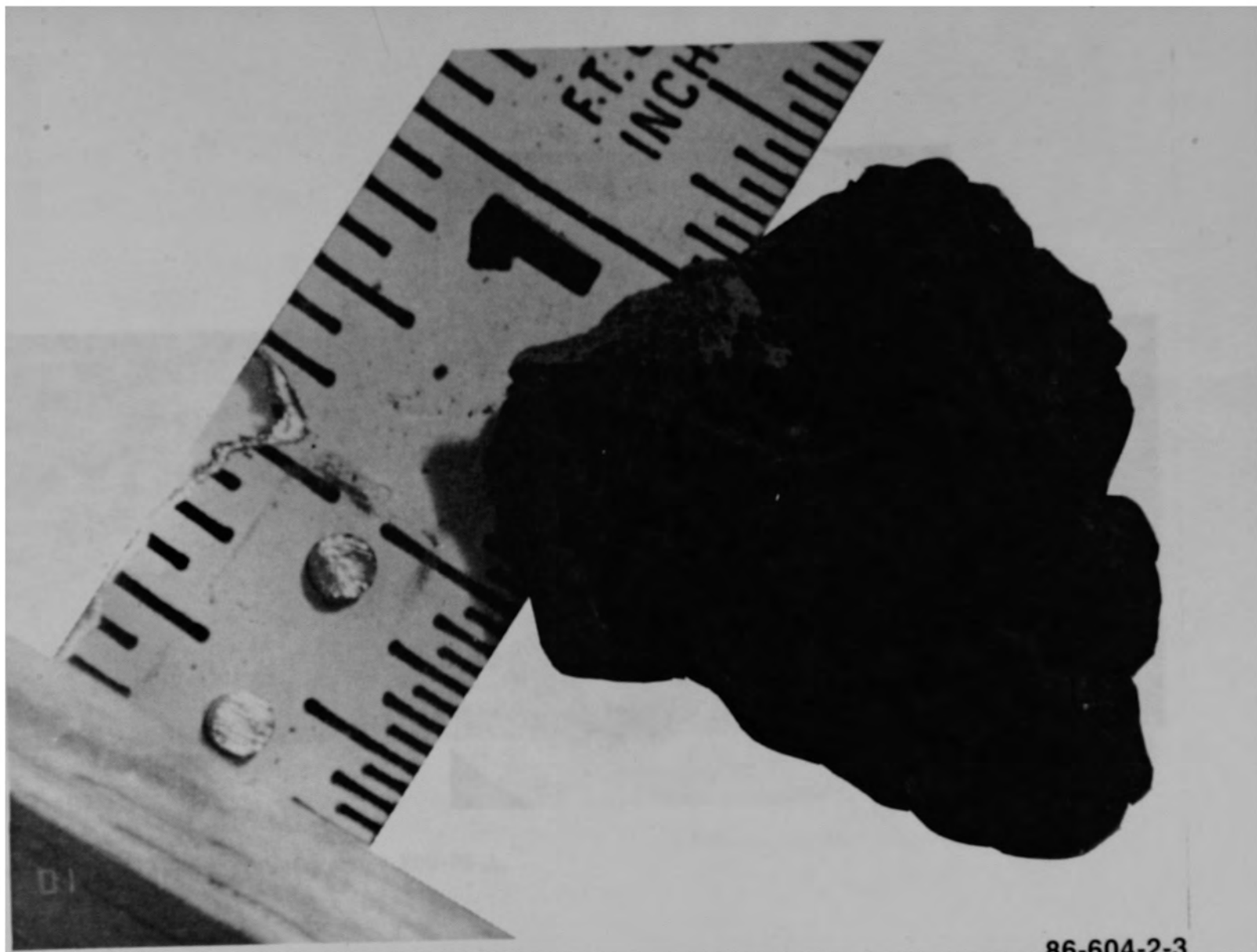
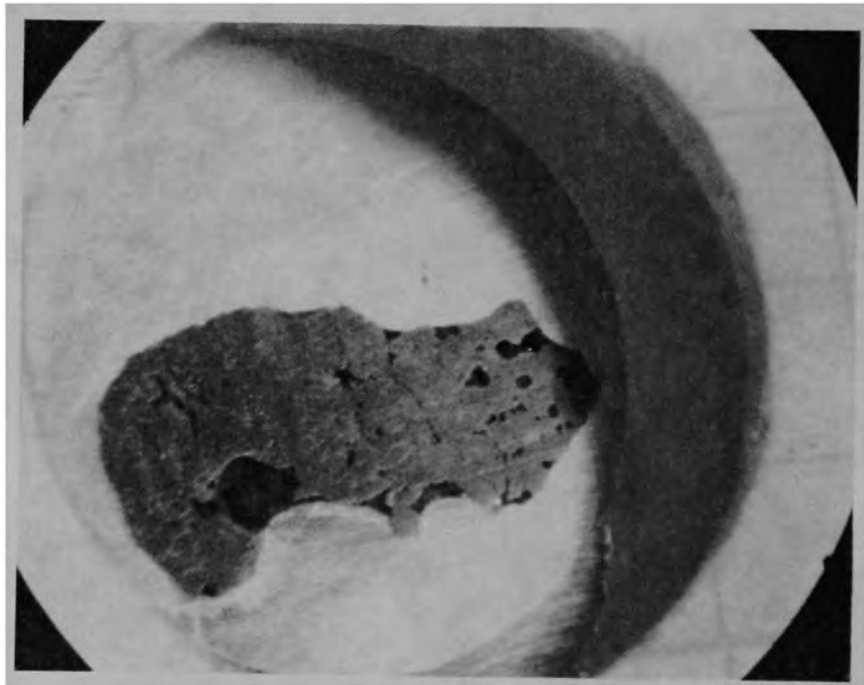


Figure E-135. Overview of ceramic sample K09-P4-A from the consolidated core region.



**87M-87**

Figure E-136. Cross section from K09-P4-A.

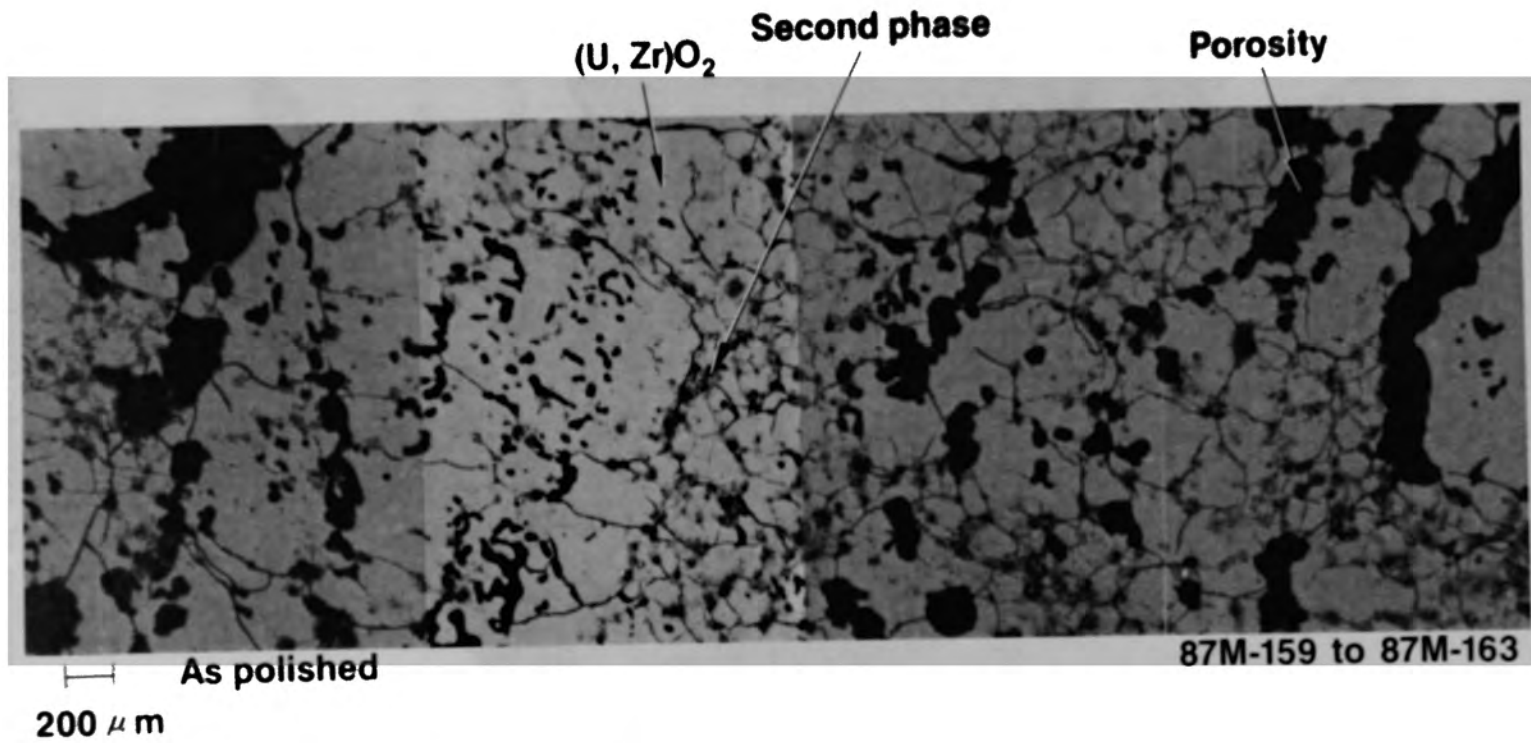
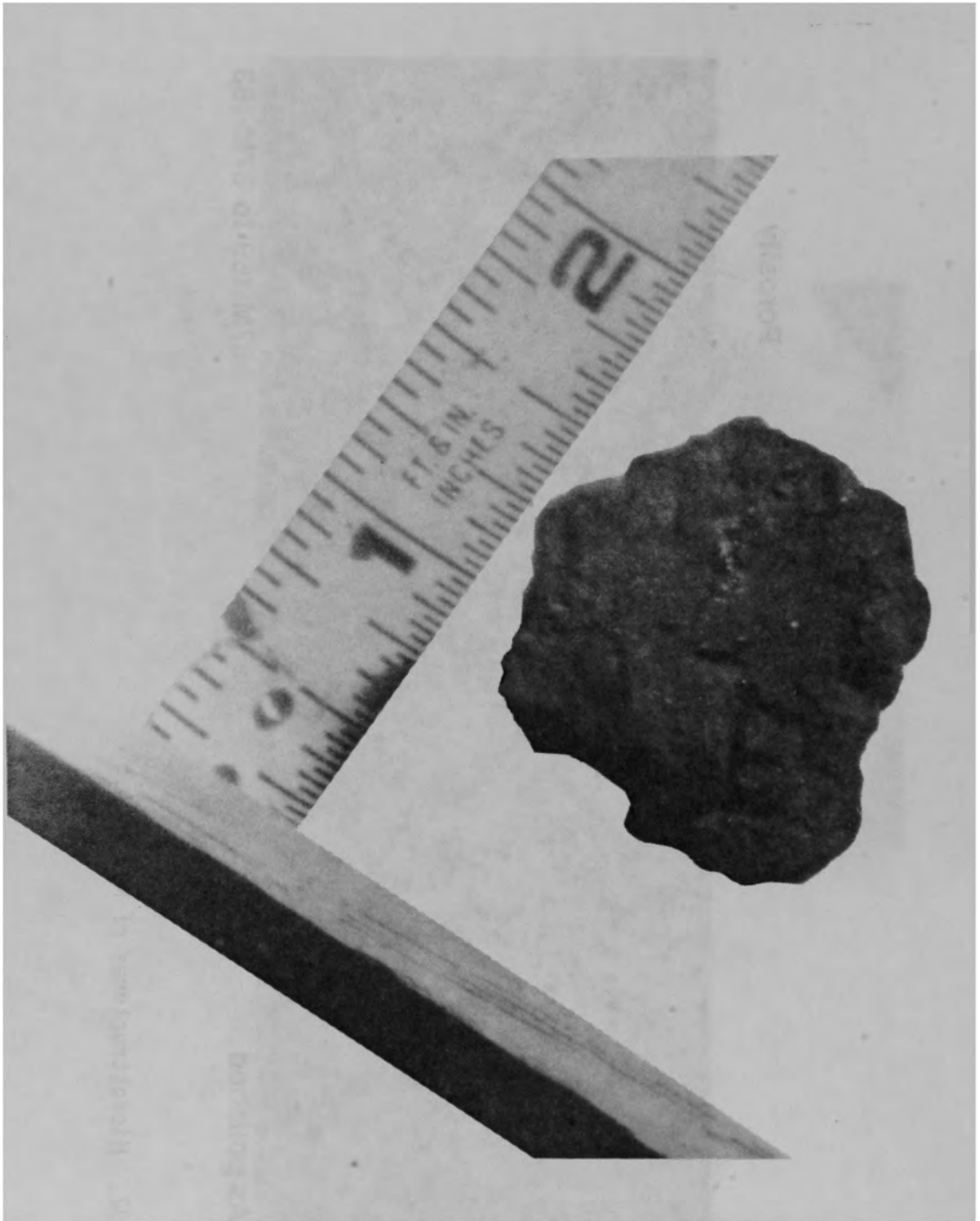


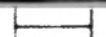
Figure E-137. Microstructures of K09-P4-A.



**86-604-3-22**

Figure E-138. Overview of ceramic sample K09-P4-D from the consolidated region.



  
2 mm

87M-98

Figure E-139. Cross section from K09-P4-D.



Figure E-140. Structural oxides around pores in  $(\text{UZr})\text{O}_2$  matrix.



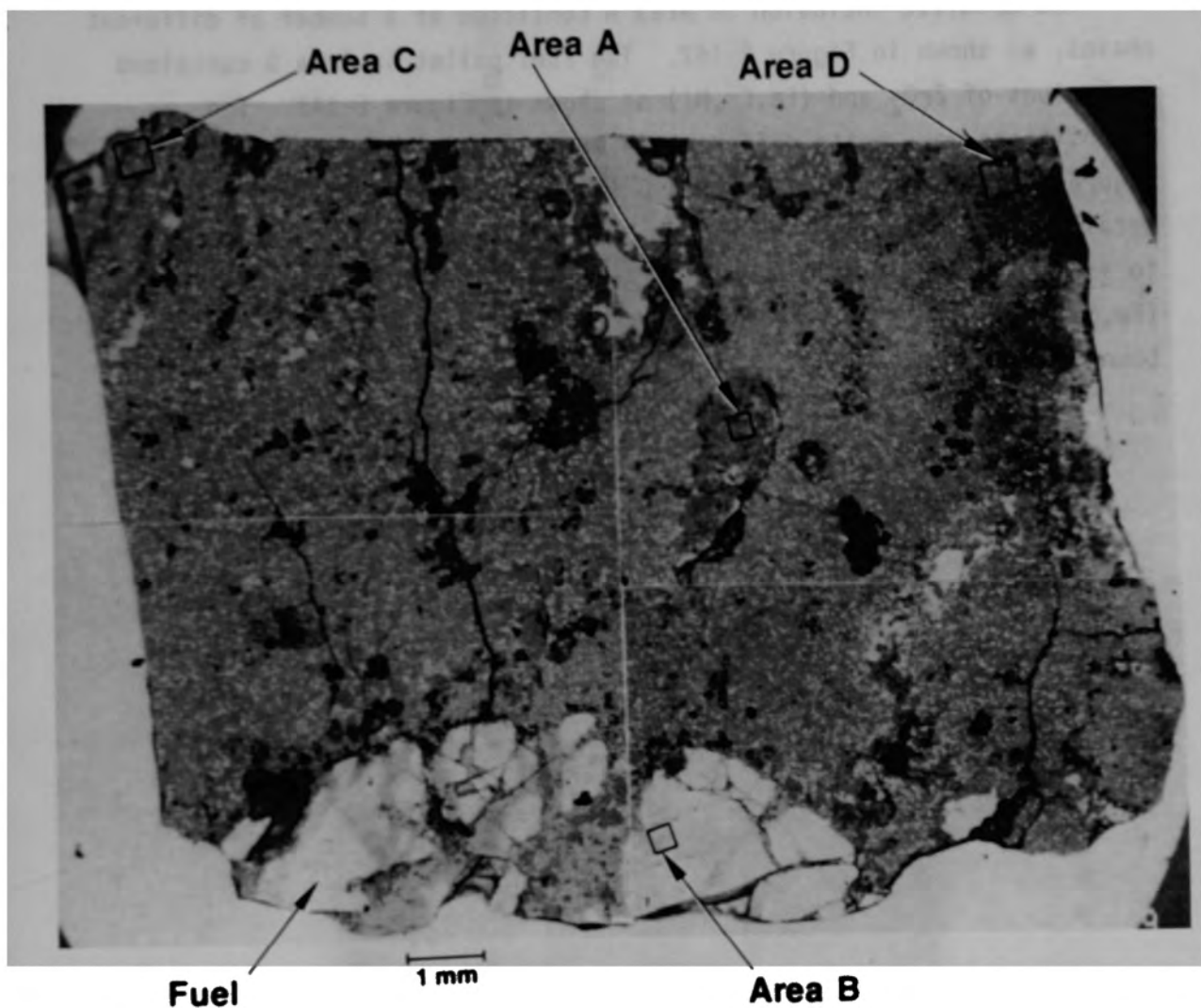


Figure E-141. Backscattered electron image of K09-P4-D cross section.

detail on the SEM. Area A represents a metallic inclusion; Area B is the  $UO_2$  fuel, and Areas C and D represent the matrix composition of this sample.

The metallic inclusion in Area A consisted of a number of different phases, as shown in Figure E-142. The fuel pellet in Area B contained inclusions of  $ZrO_2$  and (Fe,Cr,Ni) as shown in Figure E-143. The compositions were quite different in Areas C and D, as shown in Figures E-144 and E-145. In Area C (Figure E-144), consisted primarily of metallic (Fe,Cr,Ni,Sn). Stringers of  $ZrO_2$  were also present, in addition to isolated inclusions of  $UO_2$ . In Area D (Figure E-145) the matrix was (Fe,Ni,Sn,Mo). (U,Zr,O) was precipitated along the (Fe,Ni,Sn,Mo) grain boundaries.

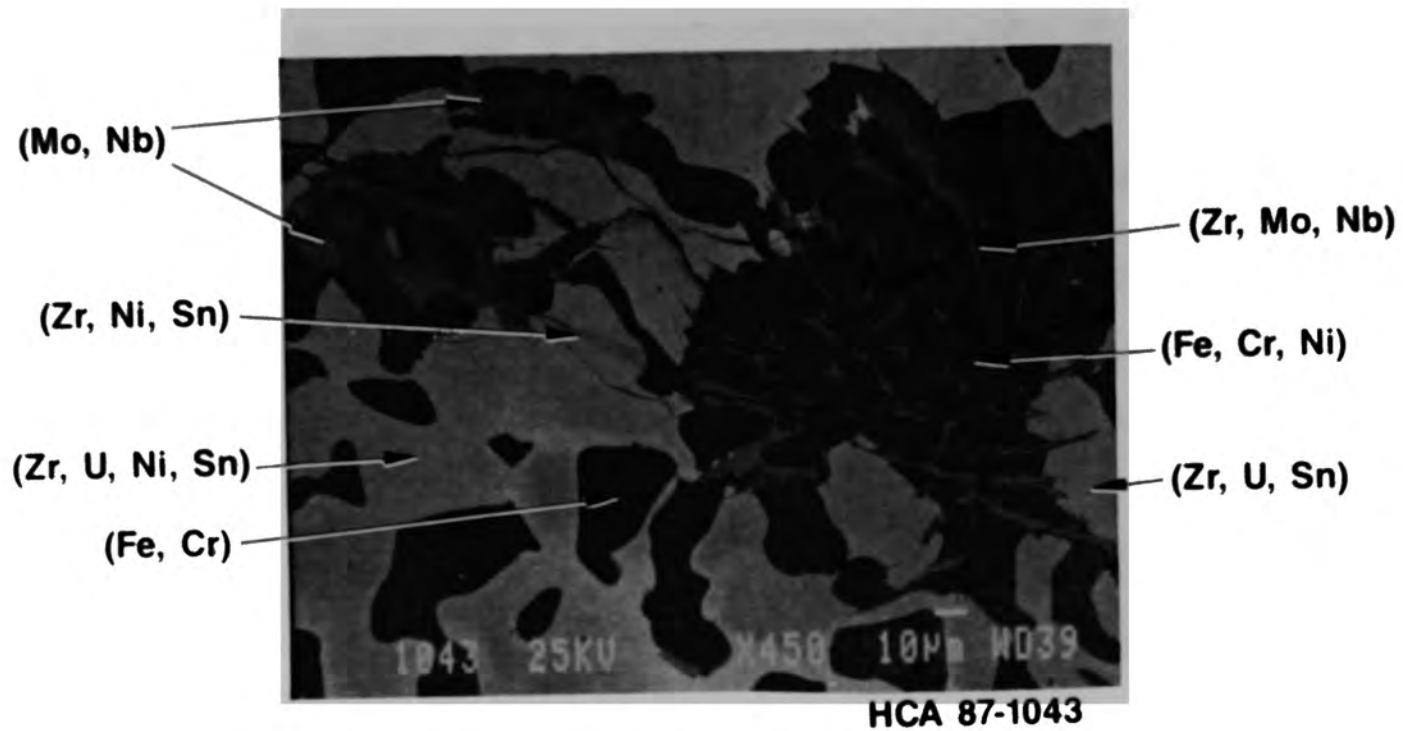


Figure E-142. Elemental composition of metallic inclusion (K09-P4-D Area A).

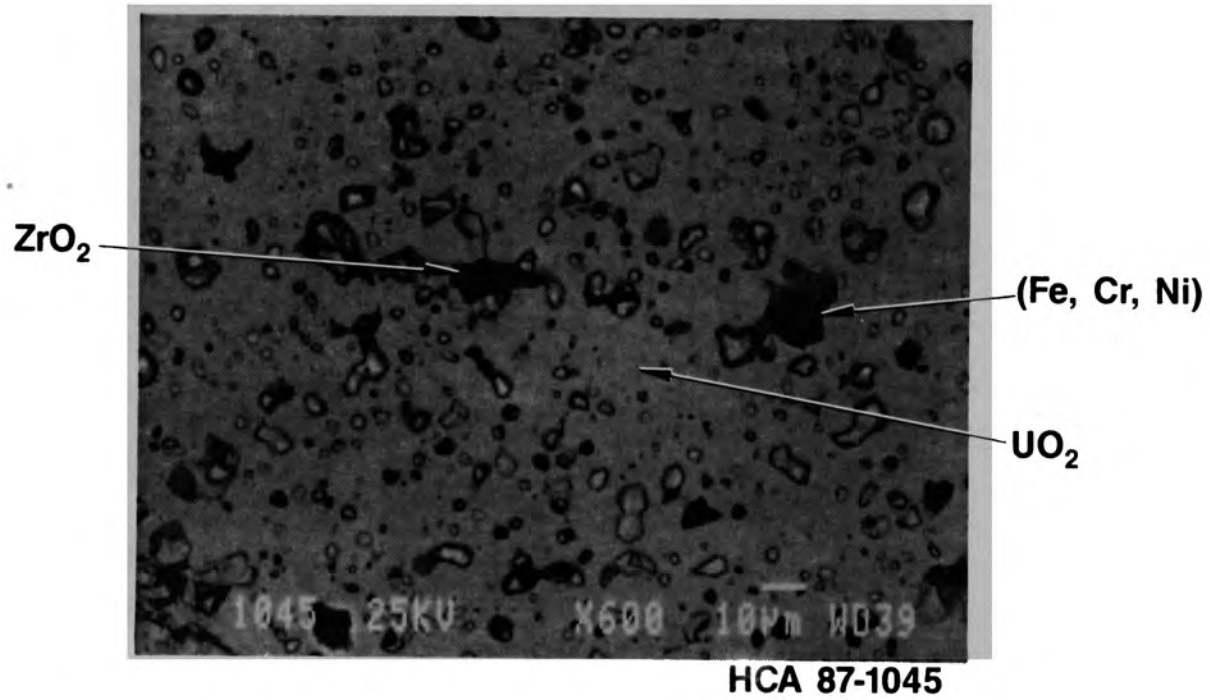


Figure E-143. Elemental composition in fuel (K09-P4-D Area B).

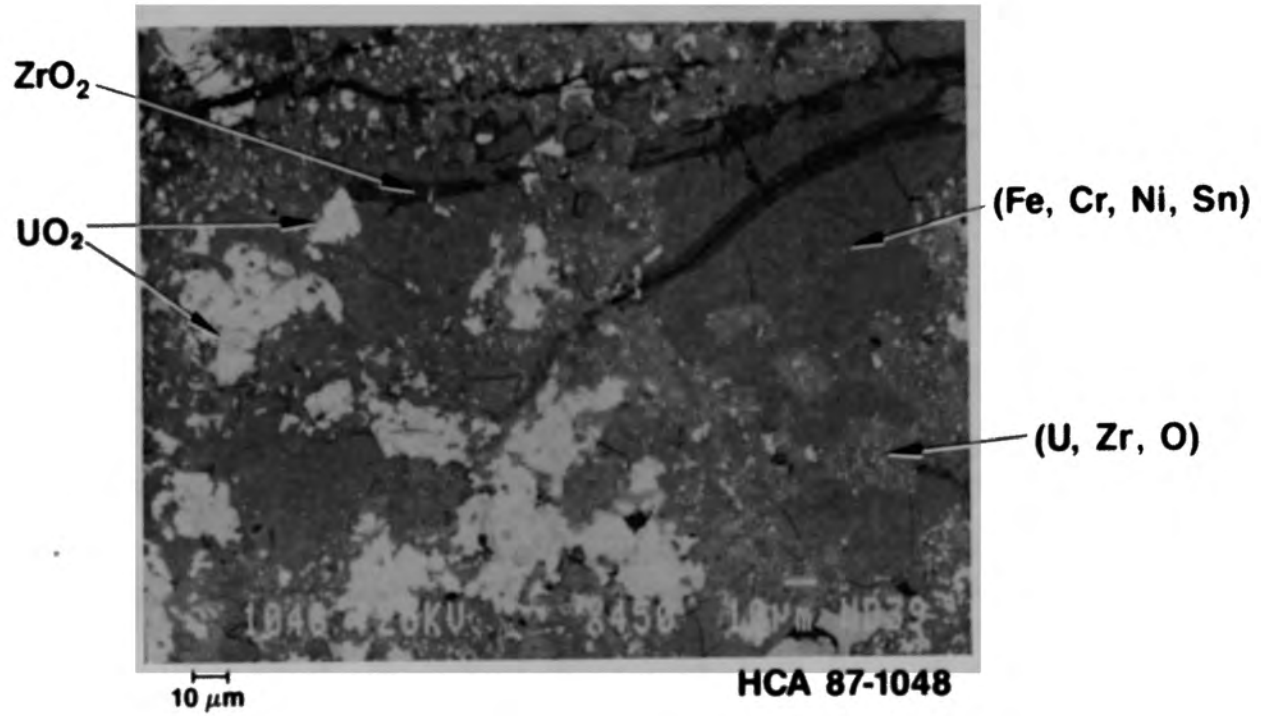


Figure E-144. Elemental composition in K09-P4-D Area C.

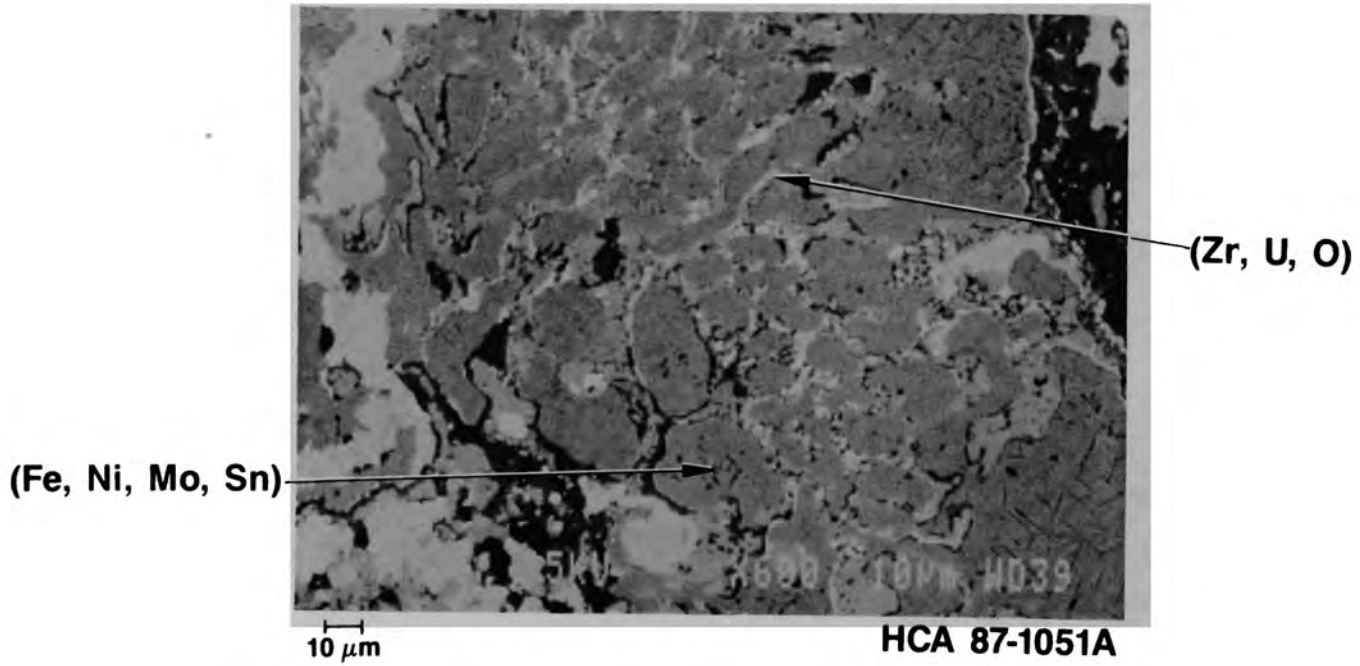


Figure E-145. Elemental composition in K09-P4-D Area D.

## Mixed Metallic and Ceramic Particles

G08-P10-A This particle is shown in Figure E-146). The surface appears oxidized except for some small metallic regions. This particle weighed 223.78 g and had a density of 8.2 g/cm<sup>3</sup>.

A cross section through this particle is shown in Figure E-147. The dendritic microstructure of a metallic inclusion is shown in Figure E-148.

The microstructure of the ceramic matrix is shown in Figure E-149. It shows the typical structural oxides mixed in (U,Zr)O<sub>2</sub>. Grain boundary precipitates are shown in detail in Figure E-150.

A backscattered electron image of a microcore from this sample is shown in Figure E-151. It shows the ceramic matrix with a metallic inclusion in a large void. Area A in this figure was examined to determine the composition of the matrix and the metallic globule.

The elemental analysis is summarized in the backscattered electron image of this interface (Figure E-152.) The matrix consisted of mixed oxides of uranium and zirconium and various metallic phases, as shown in the figure.

G12-P9-A This particle is shown in Figure E-153. The particle appeared partially oxidized, with some unoxidized metallic inclusions at one end of the particle. This particle weighed 131.45 g, and the density was 7.6 g/cm<sup>3</sup>.

To facilitate handling, this particle was cut in half so that the metallic-bearing portion was mounted as one sample (G12-P9-A1), and the ceramic-bearing portion was prepared as another sample (G12-P9-A2).

A cross section from the metallic-bearing portion is shown in Figure E-154. A long fissure extends almost all the way through the center of this sample. A metallic inclusion from this sample is shown in Figure E-155. This globule has a number of second-phase metallics



Figure E-146. Overview of sample G08-P10-A from the consolidated core region.



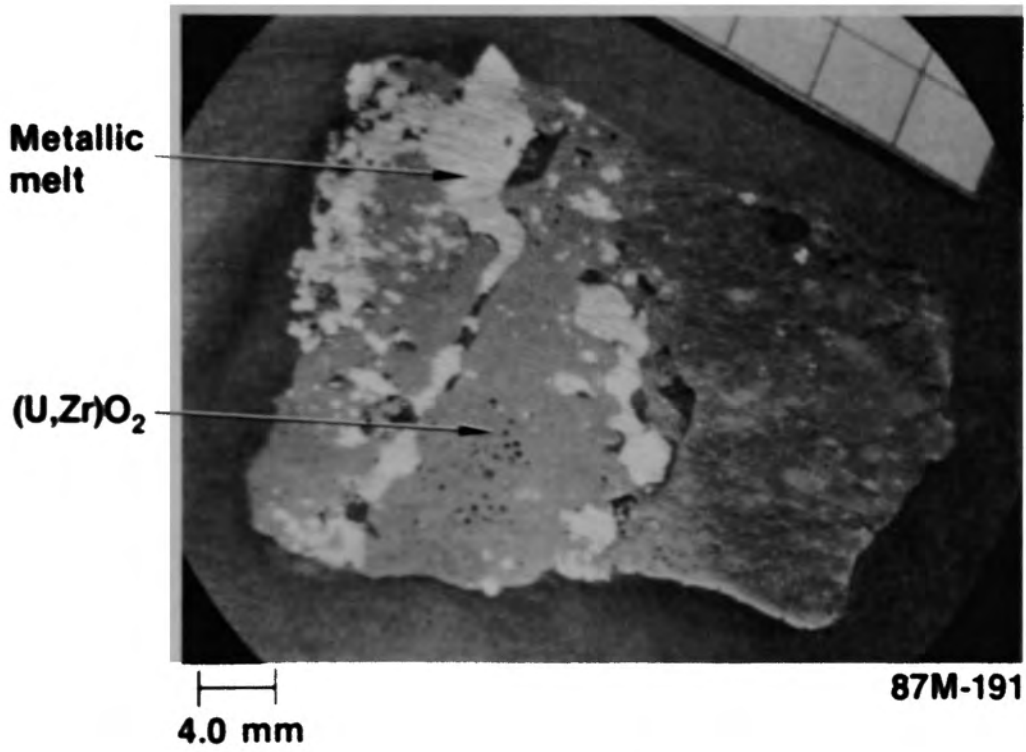


Figure E-147. Cross section from G08-P10-A.

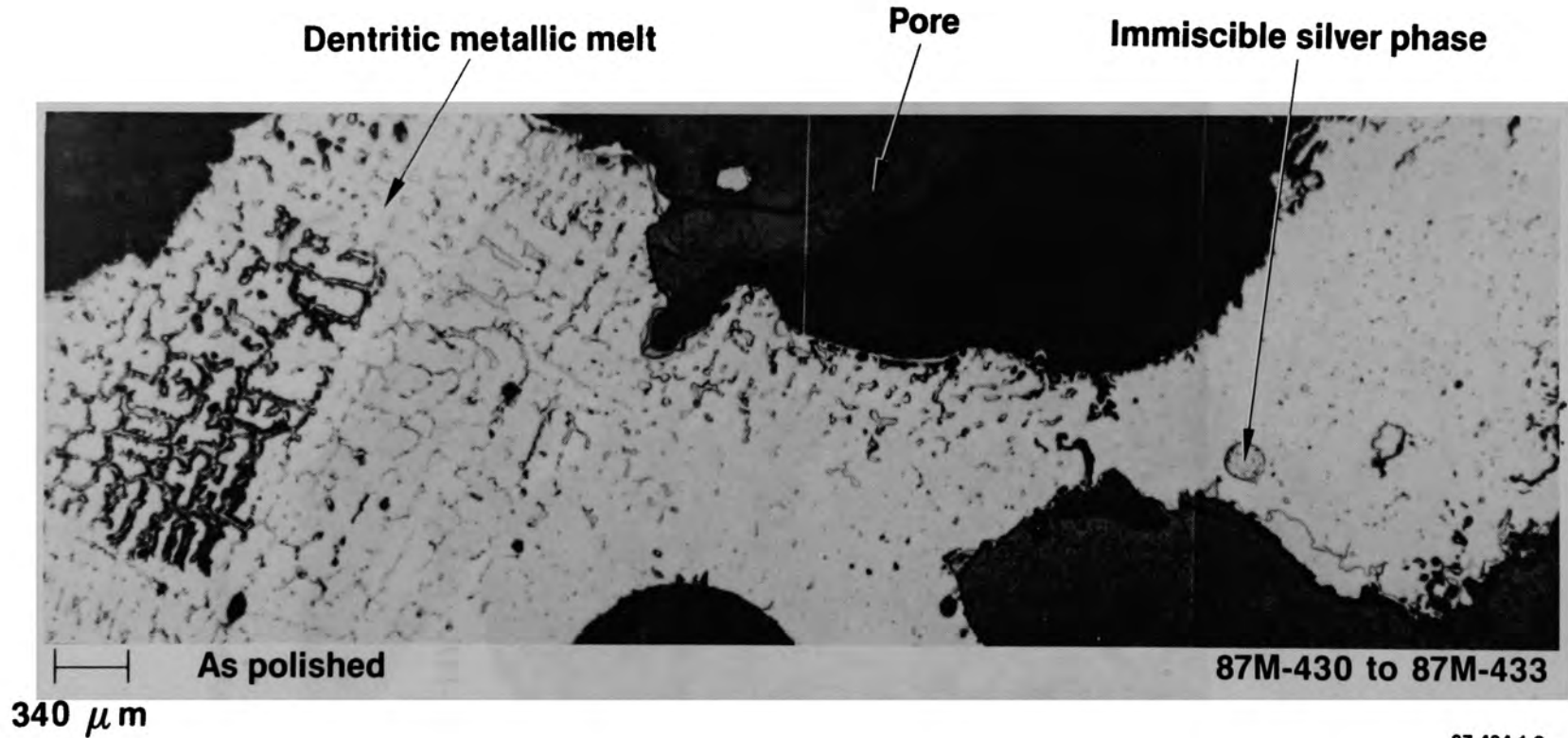


Figure E-148. Metallic inclusions in sample G08-P10-A.

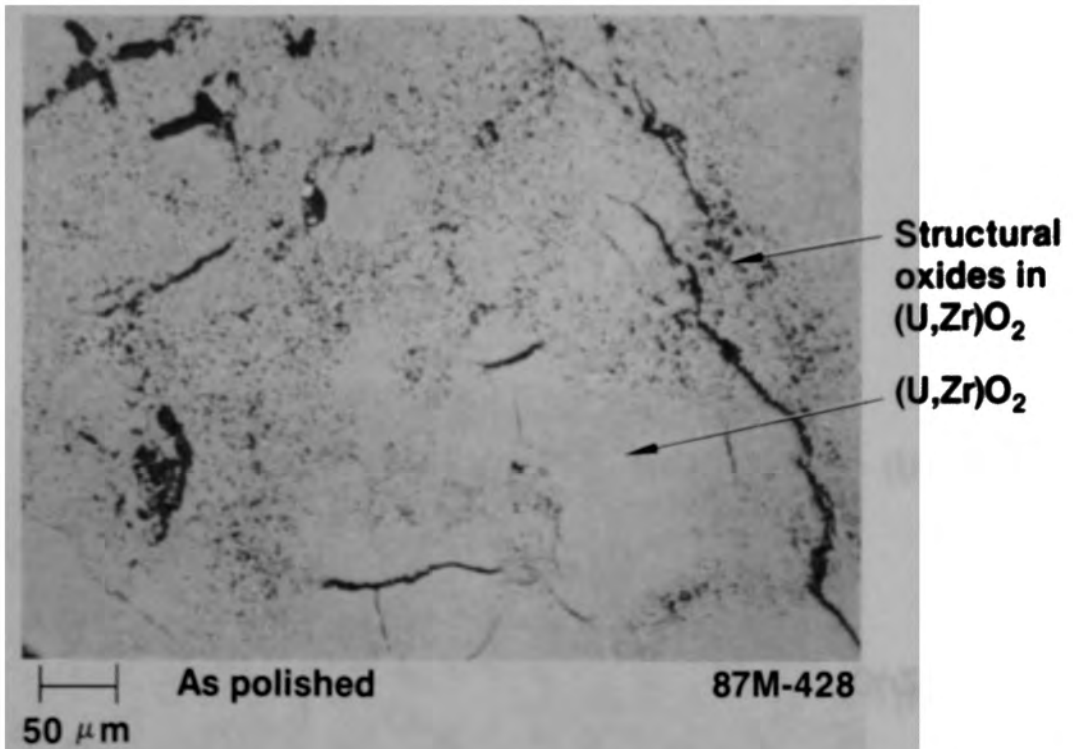


Figure E-149. Mottled structure from structural oxides in  $(U,Zr)O_2$  (G08-P10-A).

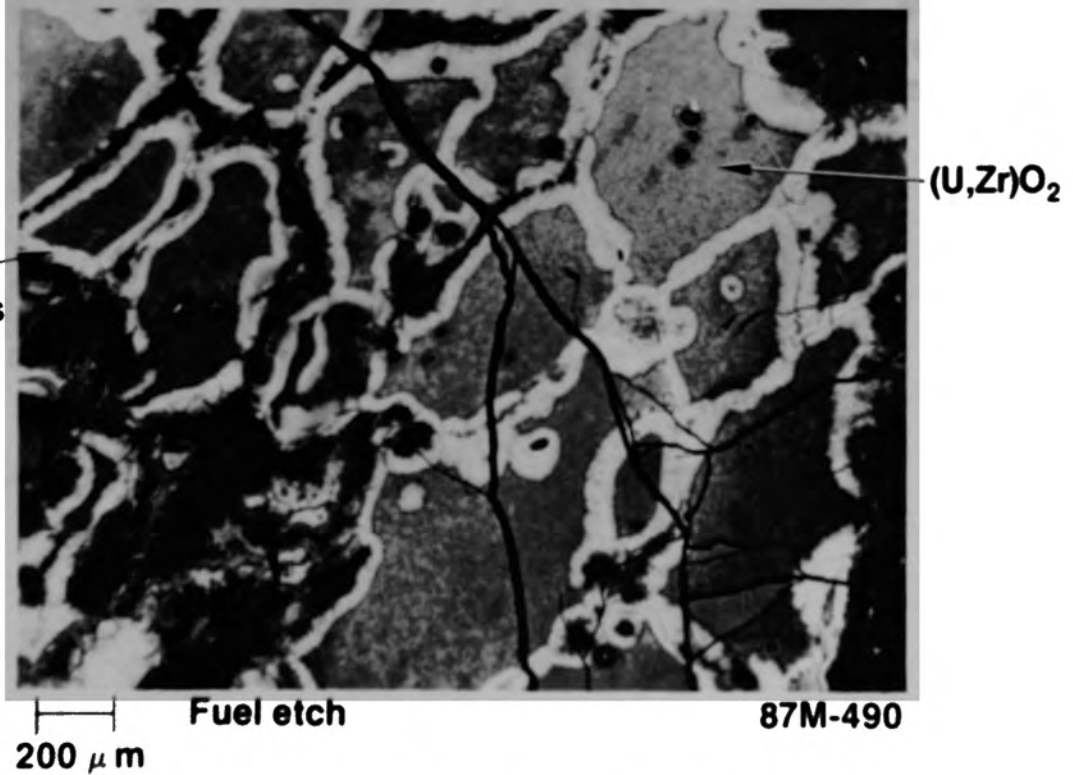


Figure E-150. Grain boundary precipitates in  $(U,Zr)O_2$  (G08-P10-A).

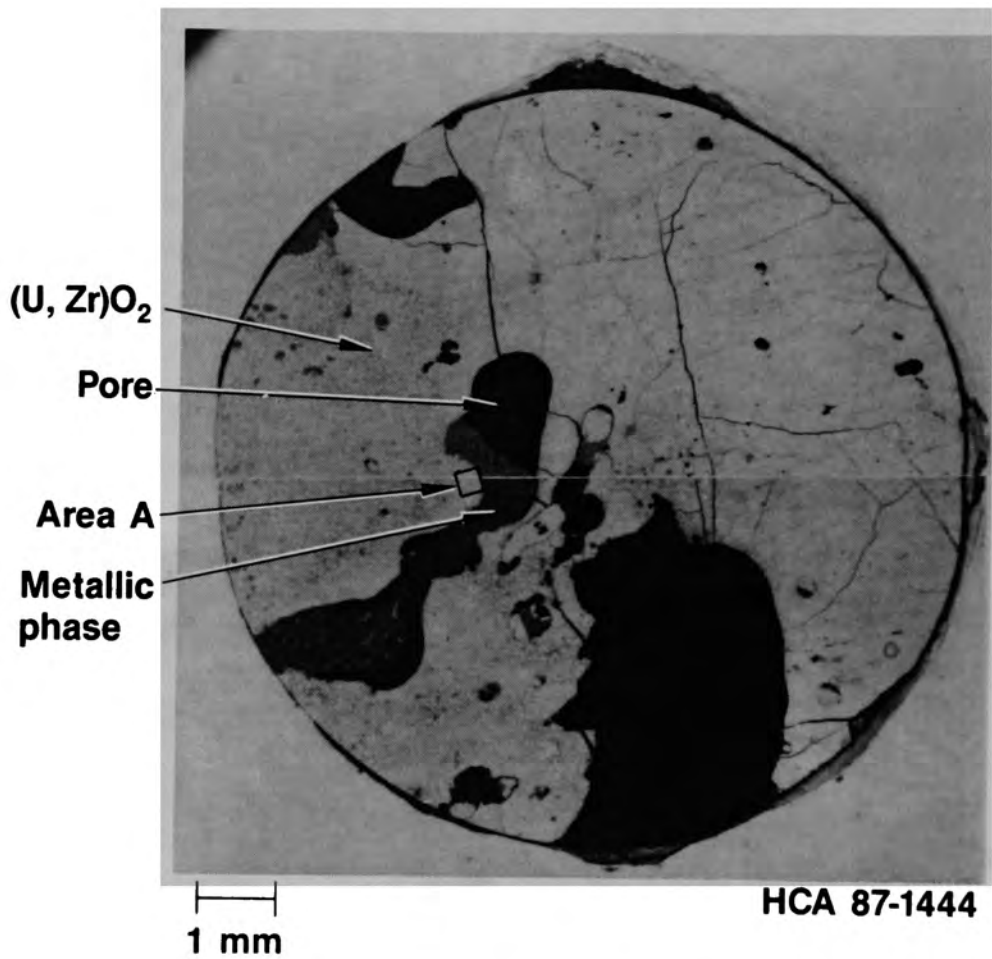


Figure E-151. Backscattered electron image of microcore G08-P10-A2.

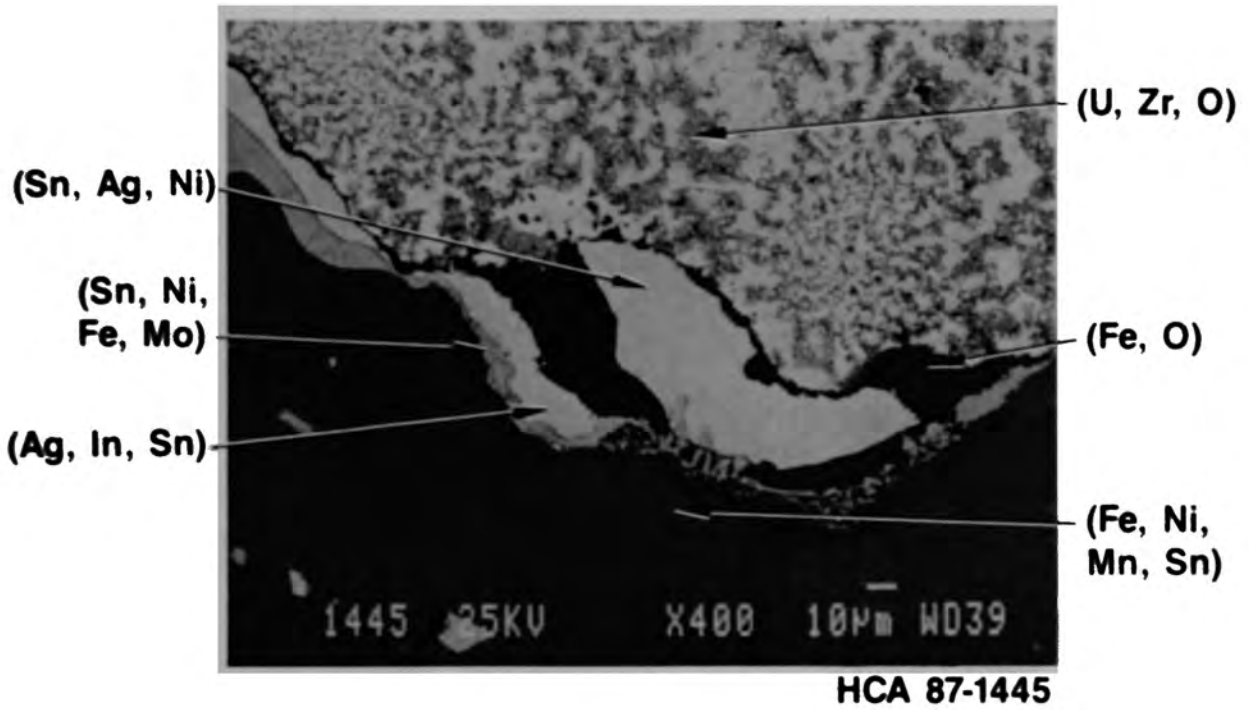


Figure E-152. Elemental distribution in SEM sample G08-P10-A2 Area A.

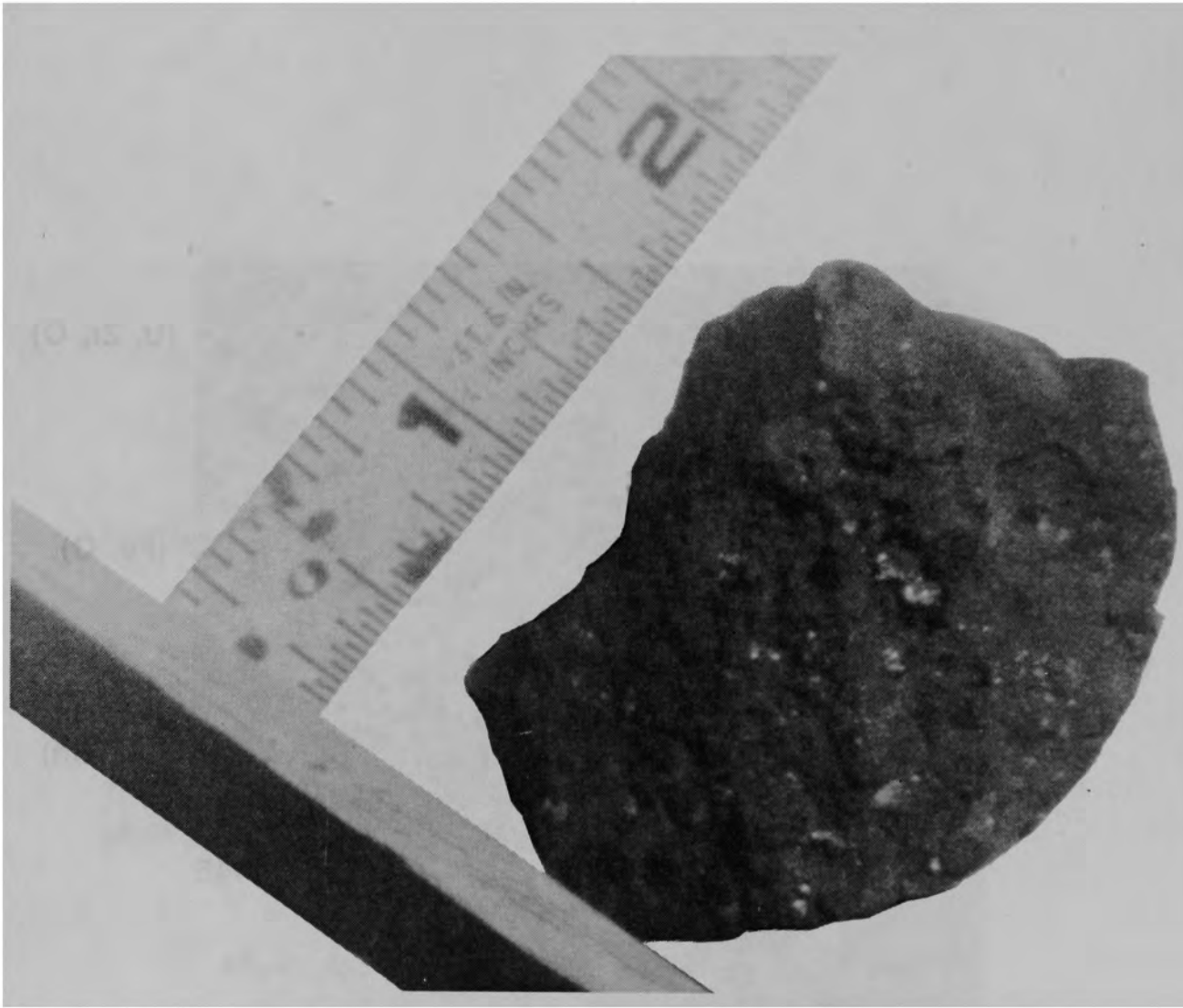


Figure E-153. Overview of particle G12-P9-A.

86-604-1-19

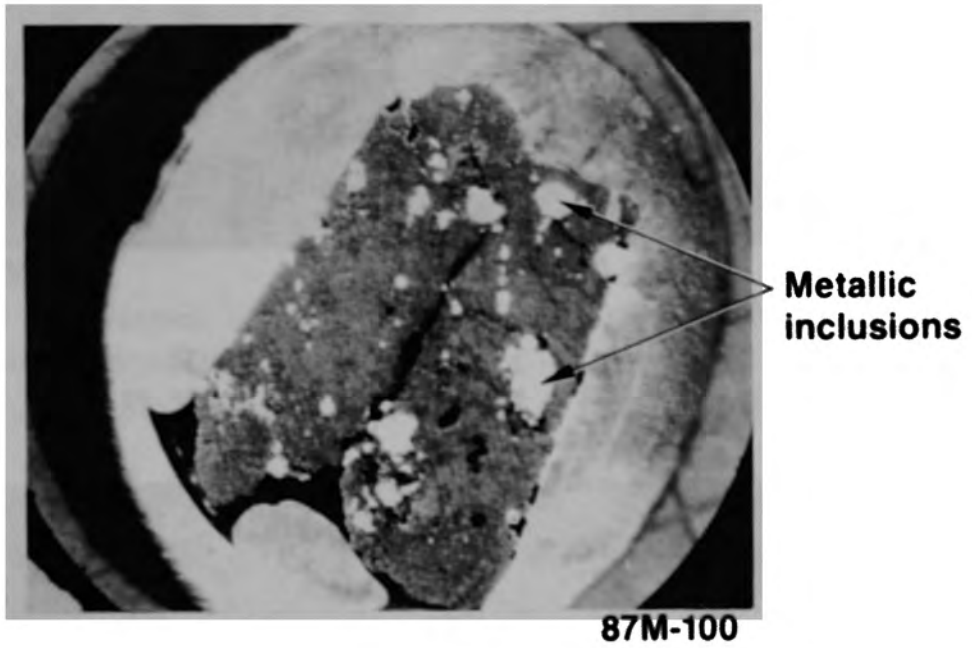


Figure E-154. Cross section of G12-P9-A1.

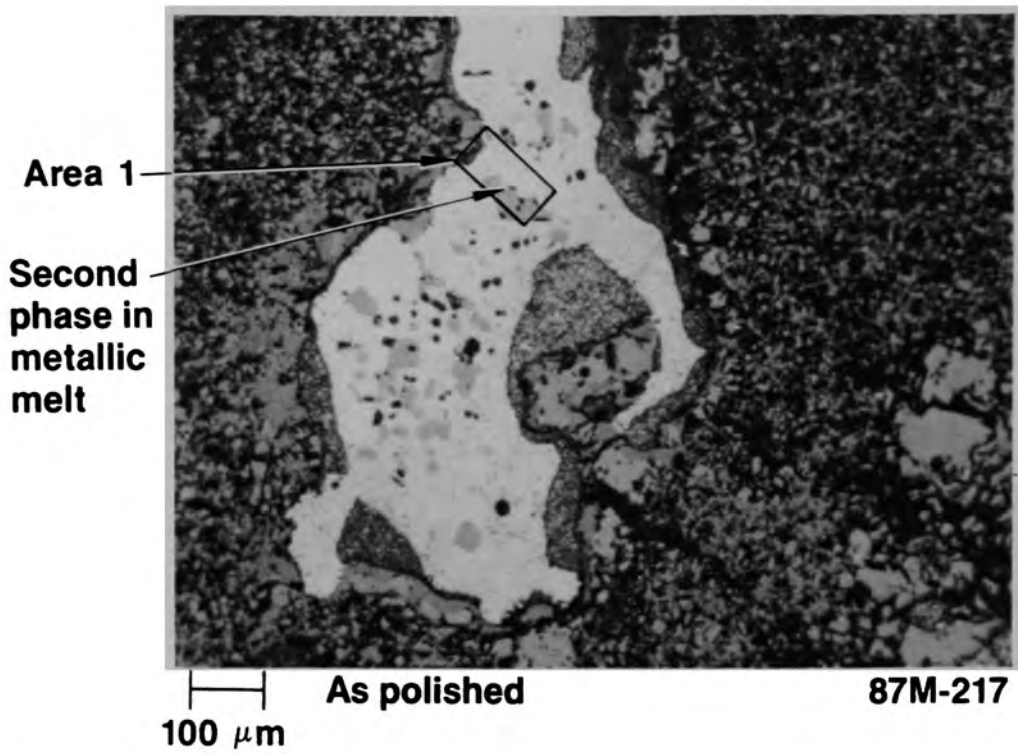


Figure E-155. Metallic inclusion in sample G12-P9-A1.

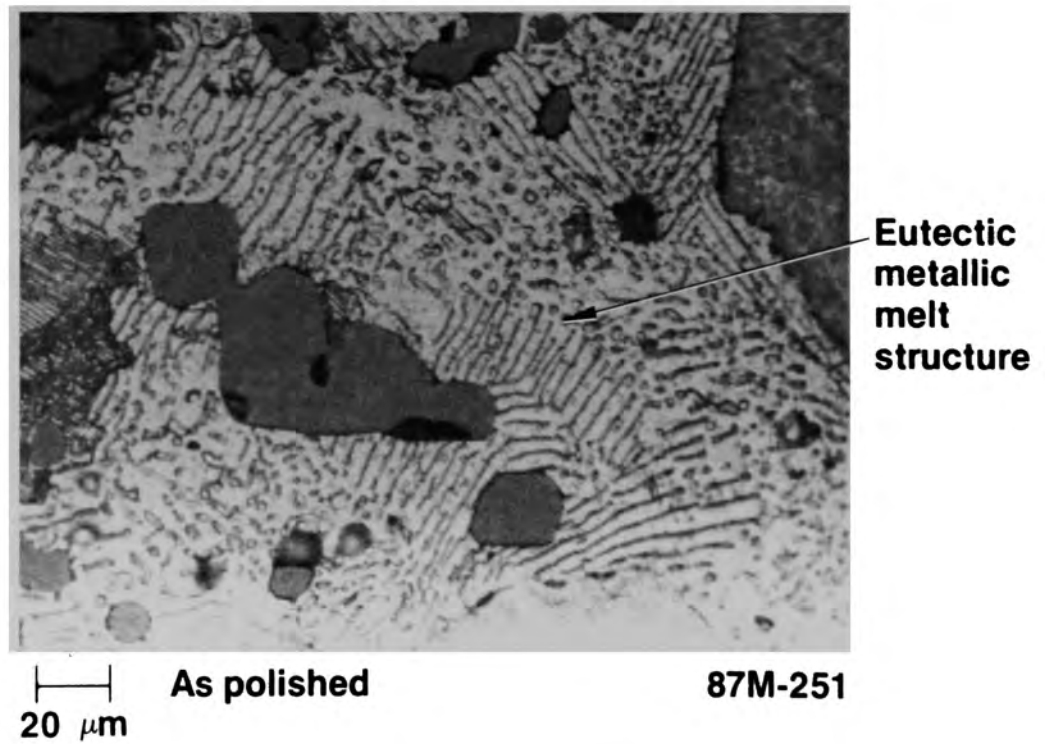


Figure E-156. Second-phase metallic structure (G12-P9-A1 Area 1).



precipitated in the matrix. These second-phase particles were in themselves composed of multiple metallic phases as shown in Figure E-156.

A metallic inclusion in a pore in the ceramic matrix of G12-P9-A1 was examined on the SEM. Inside the pore there were some  $UO_2$  single crystals, as shown in the backscattered electron image in Figure E-157. A secondary electron image of this area is shown in Figure E-158. The rod-shaped material surrounding these  $UO_2$  crystals consisted entirely of iron. Indium crystals were deposited on the surface of these iron crystals.

The cross section of the ceramic portion (G12-P9-A2) is shown in Figure E-159. It shows the structure to be rather homogeneous with a uniform distribution of pores. The typical microstructure consisted of  $(U,Zr)O_2$  with some metallic inclusions, as shown in Figure E-160.

N05-P1-A A photograph of particle N05-P1-A is shown in Figure E-161. This particle has a metallic globule located at one end of the ceramic particle. This particle weighed 9.86 g and had a density of  $8.0 \text{ g/cm}^3$ .

A cross section through this particle is shown in Figure E-162. It shows two distinct and separate ceramic phases surrounded by a metallic melt. The dendritic microstructure of the metallic melt is shown in Figure E-163. The typical microstructure of the ceramic phase is shown in Figure E-164, which consists of various metallic inclusions in a matrix of  $(U,Zr)O_2$ .

N05-P1-D The overall view of particle N05-P1-D is shown in Figure E-165. This particle is a mixture of metallics surrounding the remnants of a fuel pellet. This particle weighed 34.91 g and had a density of  $8.3 \text{ g/cm}^3$ .

The cross section of this particle, along with the details of the microstructure at two locations, is shown in Figure E-166. The remains of a fuel rod are surrounded by a mixture of metallic melts. The photograph at

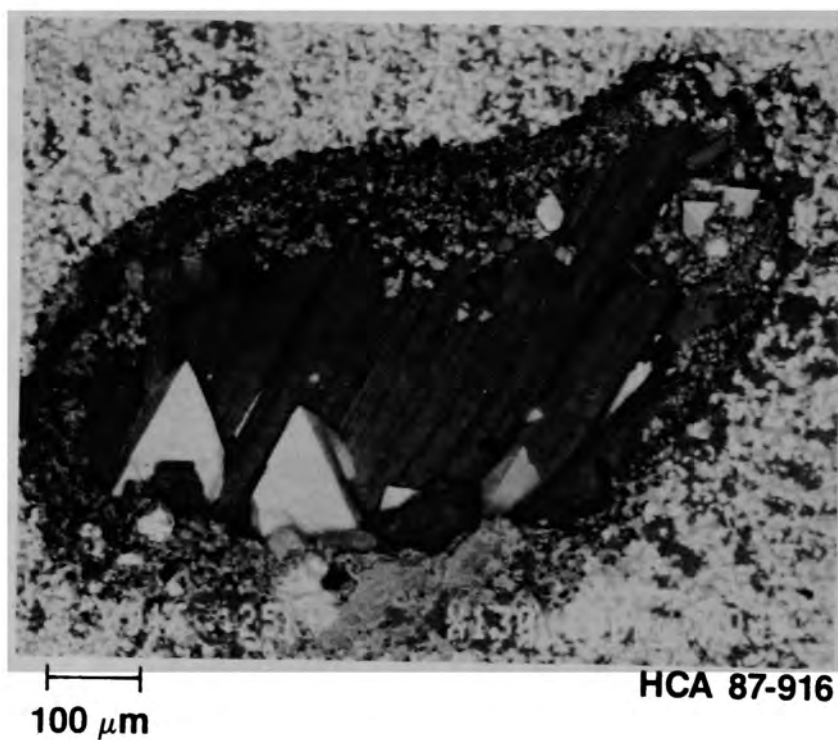


Figure E-157. Backscattered electron image of crystals in pore (G12-P9-A1).

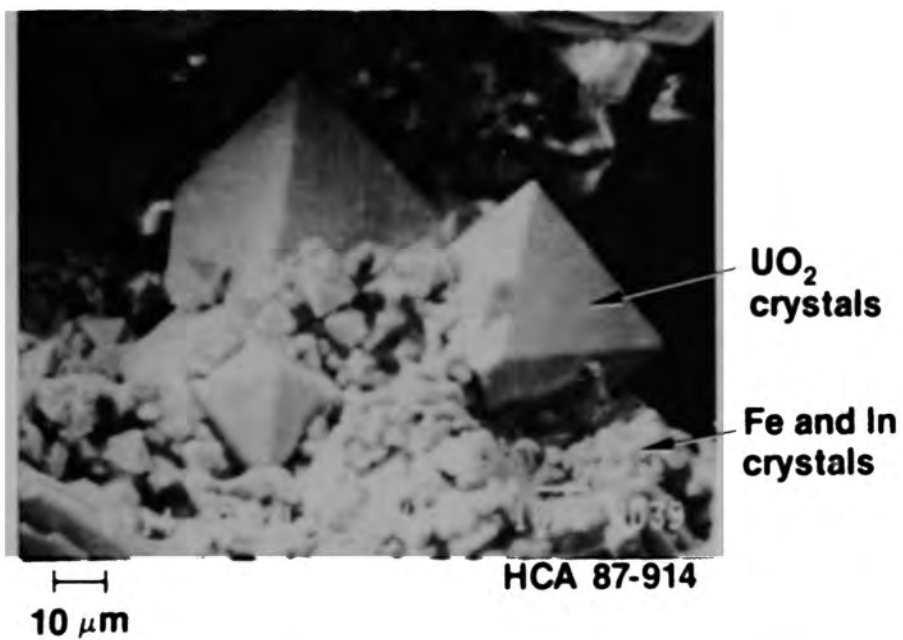


Figure E-158. Secondary electron image of crystals in a pore in G12-P9-A1.

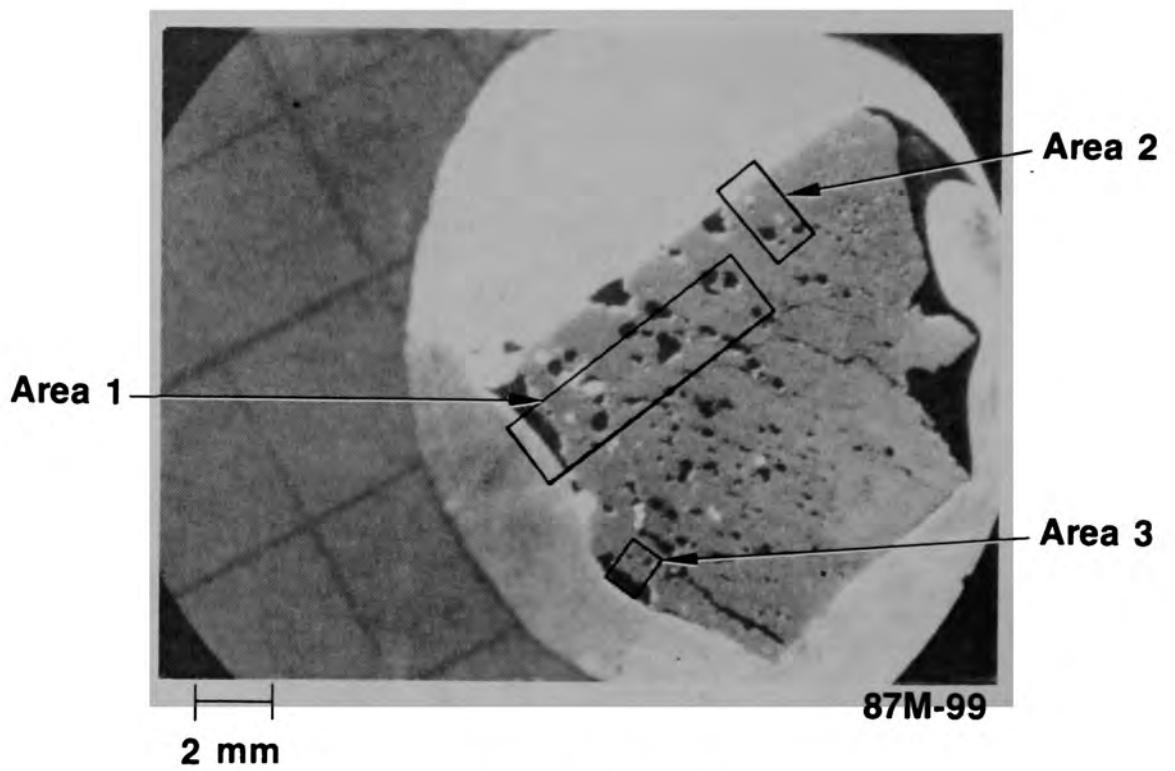


Figure E-159. Cross section from G12-P9-A2.

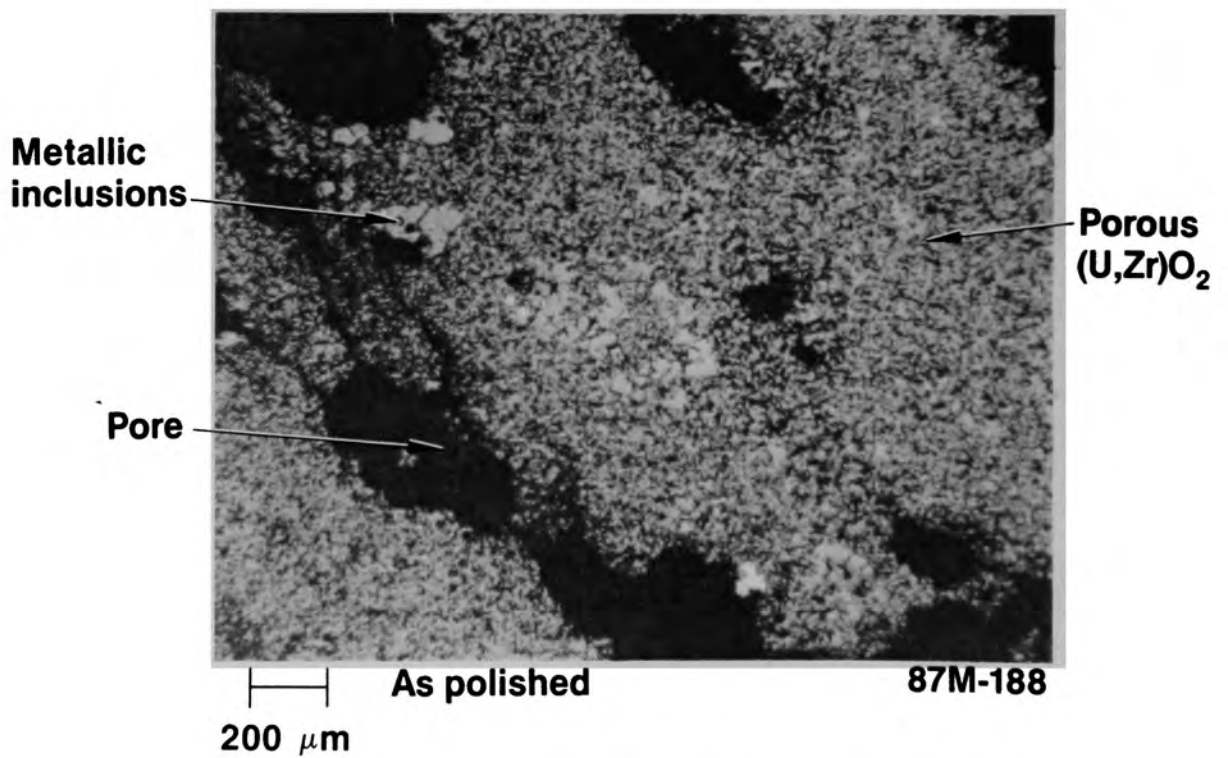


Figure E-160. Porous (U,Zr)O<sub>2</sub> structure in G12-P9-A2.

E-199

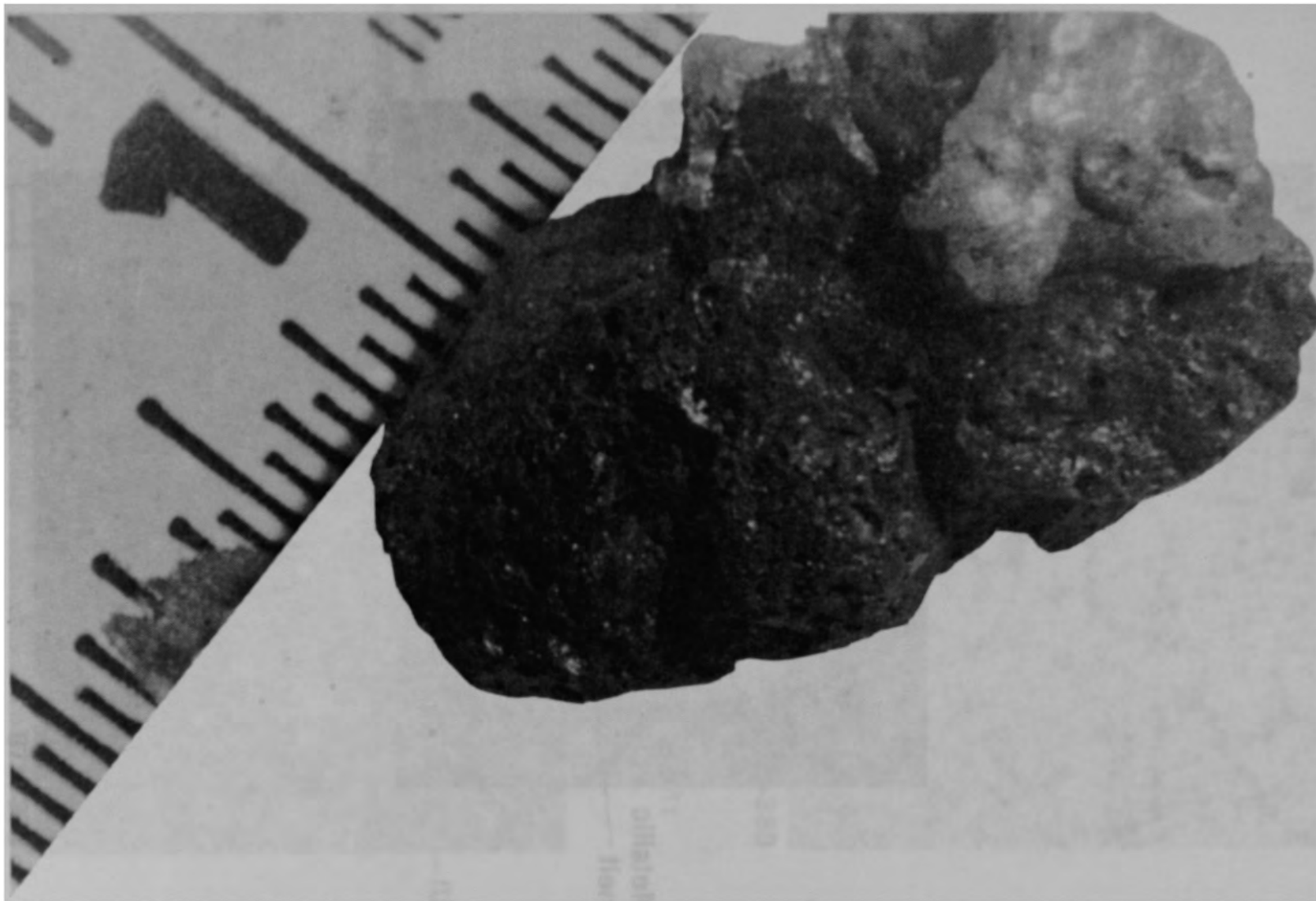


Figure E-161. Overview of sample N05-P1-A.

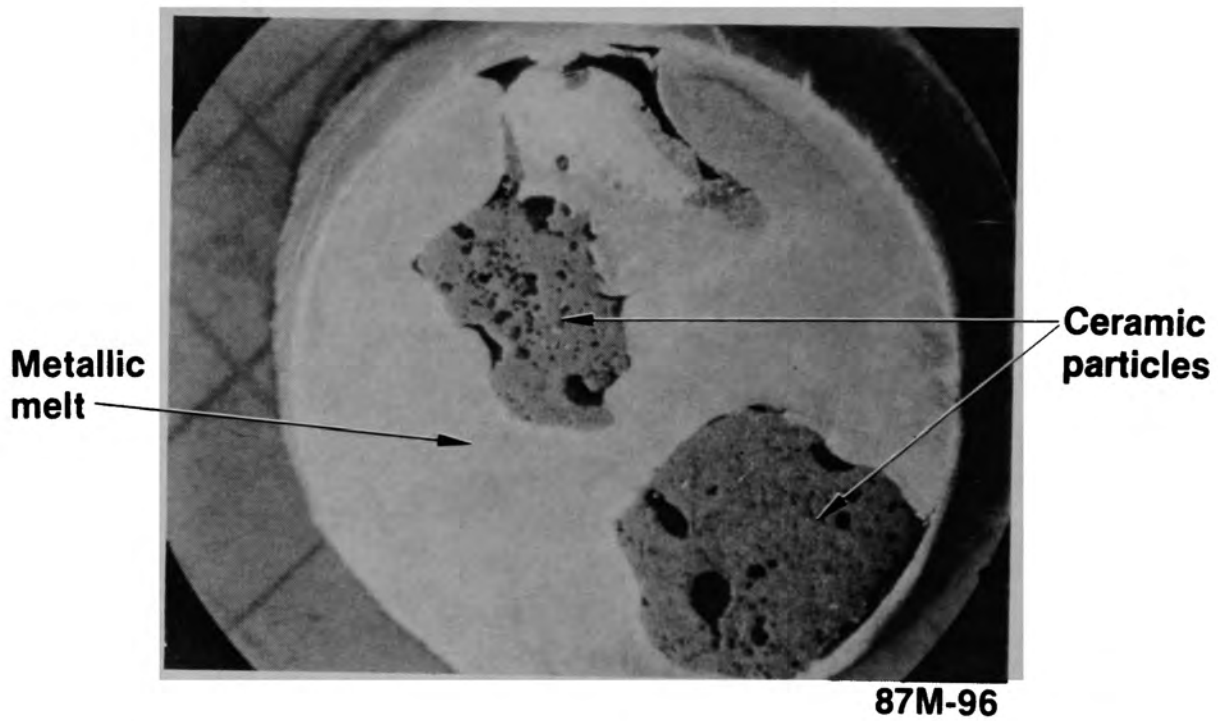


Figure E-162. Cross section of sample N05-P1-A.

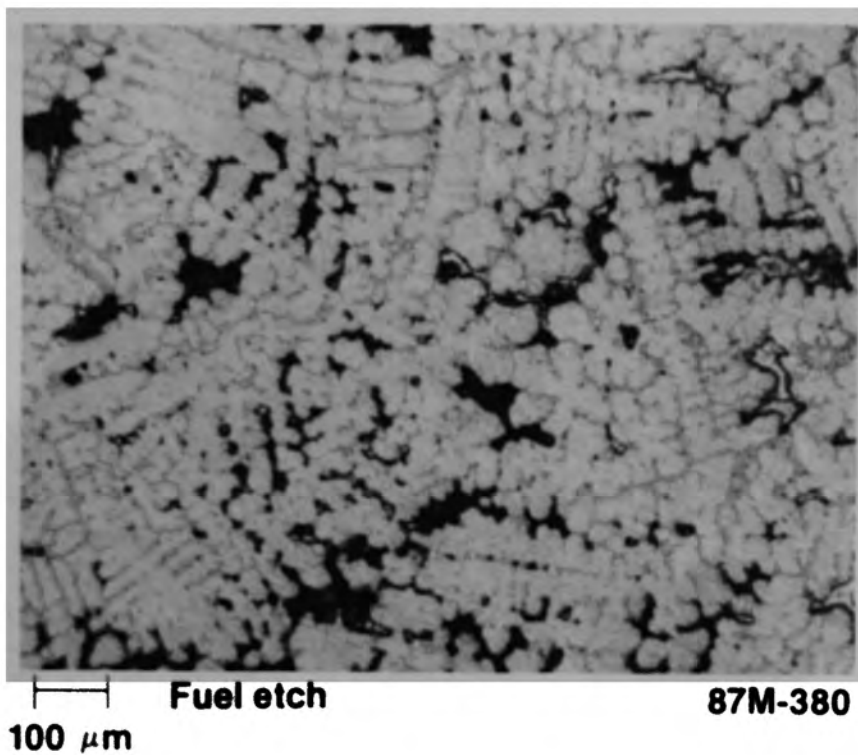


Figure E-163. Dendritic structure of metallic melt (N05-P1-A).

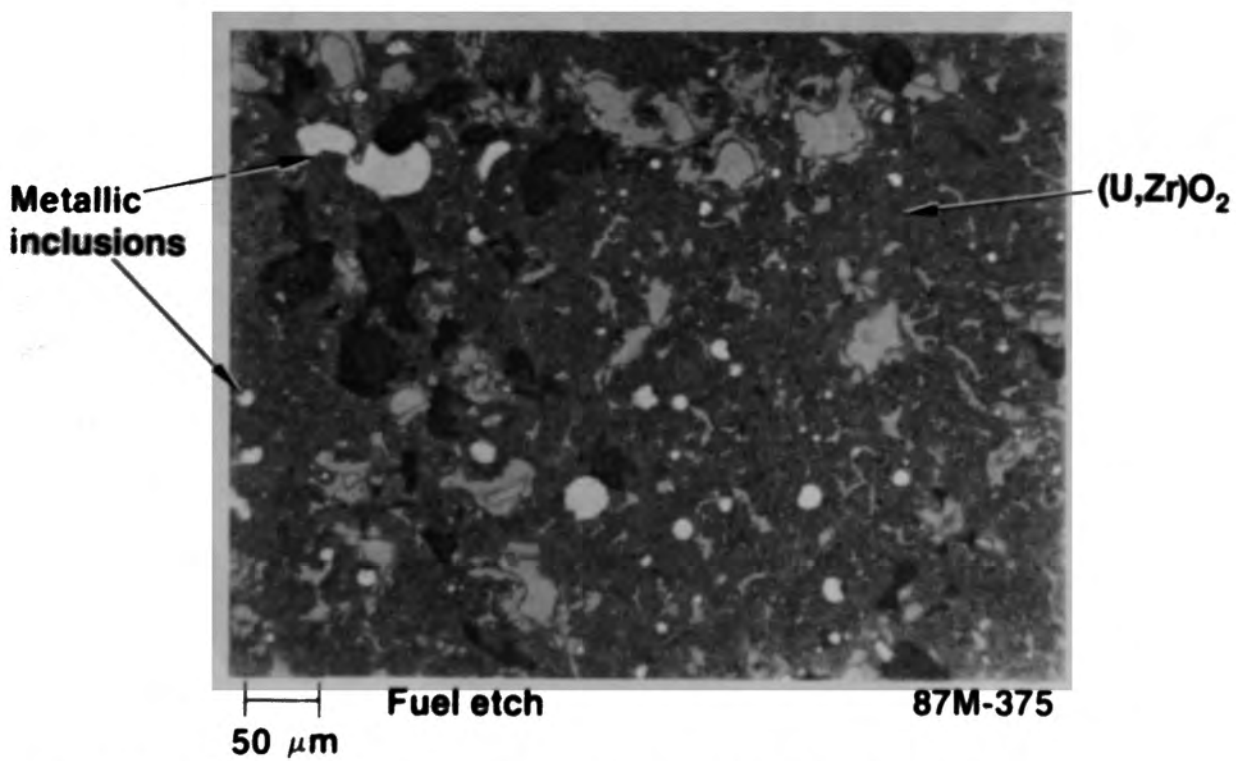


Figure E-164. Metallic inclusions in (U,Zr)O<sub>2</sub> in sample N05-01-A.



Figure E-165. Overview of N05-P1-D.



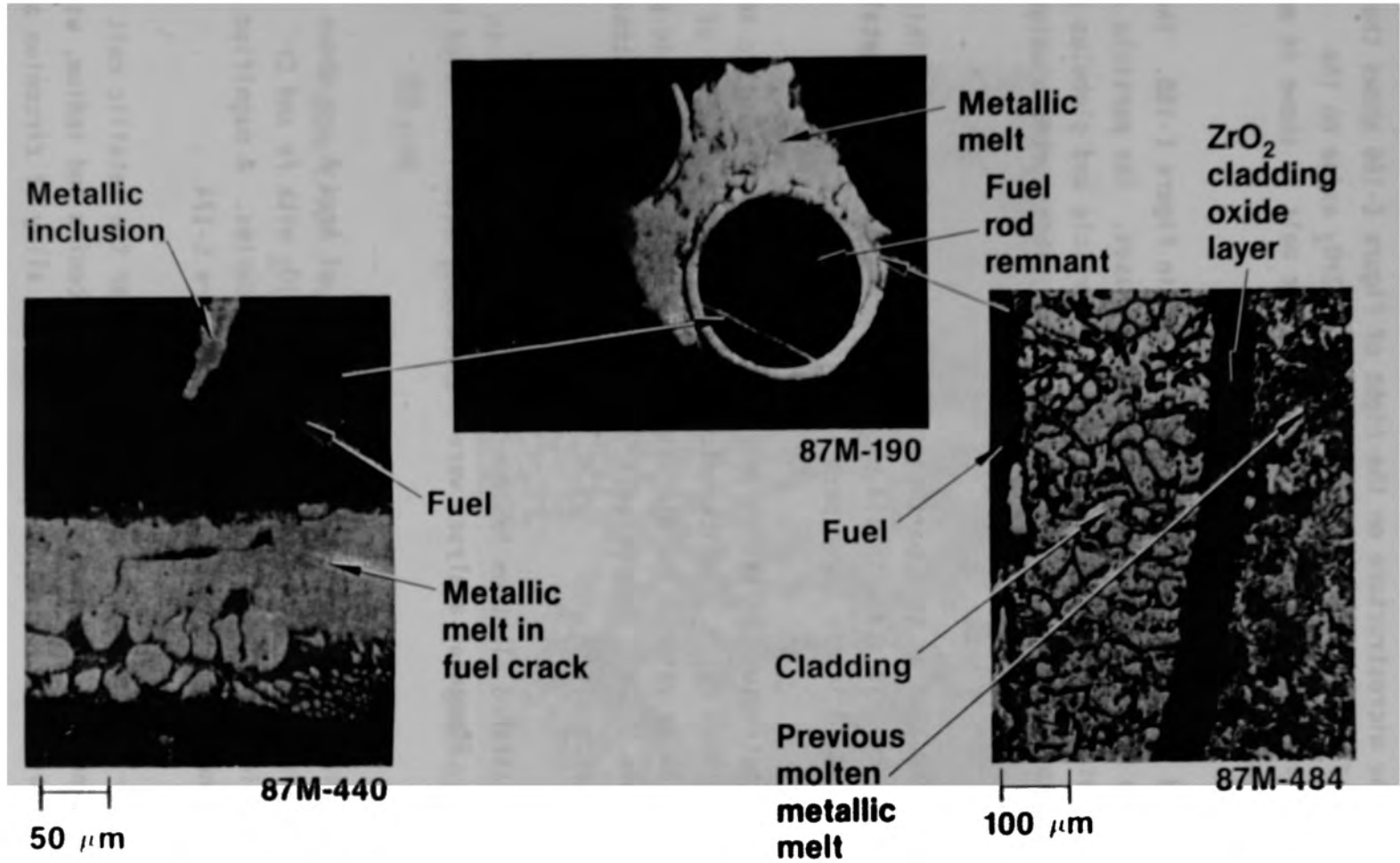


Figure E-166. Fuel pellet surrounded by metallic material (N05-P1-D).

the left shows an area where metallic melt has penetrated along a crack in the fuel. The microstructure on the right of Figure E-166 shows the degradation of the cladding and a thin layer of  $ZrO_2$  oxide on the cladding. The eutectic structure of the metallic melt is shown in more detail in Figure E-167.

N05-P1-H A view of this particle is shown in Figure E-168. The particle is a mixture of ceramic and metallic phases. The particle appears very jagged with stringers extending from the particle and globules of molten material adhering to the larger particle. This particle weighed 21.65 g, and the density was  $9.1 \text{ g/cm}^3$ .

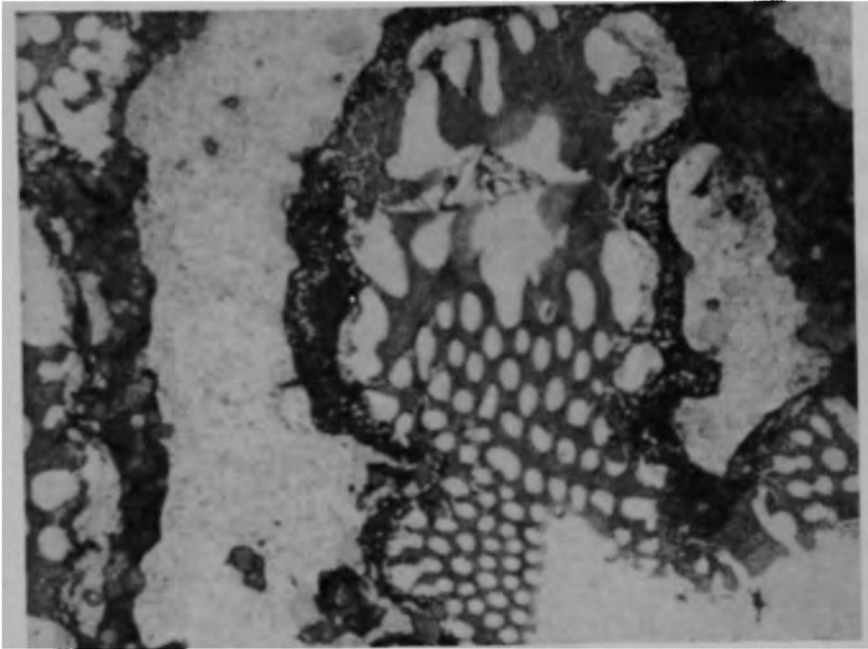
A cross section of this particle is shown in Figure E-169. This section shows ceramic and metallic phases. Round globules of a metallic phase are embedded in the large pores of the ceramic phase.

The microstructure of the ceramic phase with a large metallic inclusion is shown in Figure E-170. The ceramic phase consists of a matrix of fine porosity and large voids. The microstructure of the large metallic phase is shown in Figure E-171. This metallic phase was attacked by the etchant, resulting in etch pits.

A backscattered electron image of the cross section is shown in Figure E-172. Elemental analyses were performed in areas indicated by the letters.

The elemental dot maps of the ceramic phase at Area A are shown in Figure E-173, which shows the matrix to be  $(U,Zr)O_2$  with Fe and Cr structural oxides precipitated in the grain boundaries. A magnified view of the grain boundary precipitates is shown in Figure E-174.

Figure E-175 shows the elemental dot maps for the metallic melt in Area B. The matrix is primarily an alloy of zirconium and indium, with a small amount of silver. The precipitates are an alloy of zirconium and nickel.



As polished  
20  $\mu\text{m}$

87M-439

Figure E-167. Metallic melt in N05-P1-D.

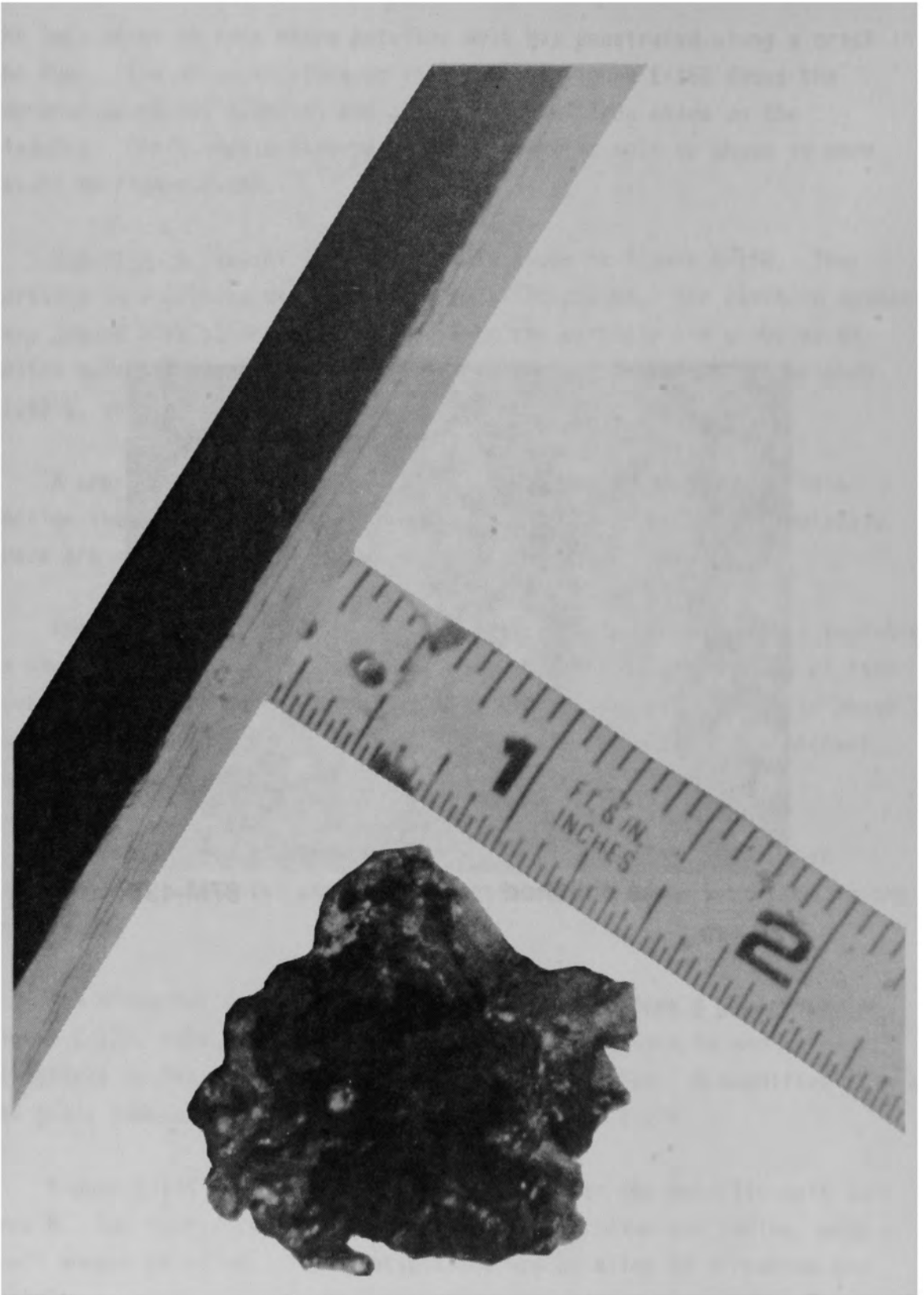


Figure E-168. Overview of N05-P1-H.

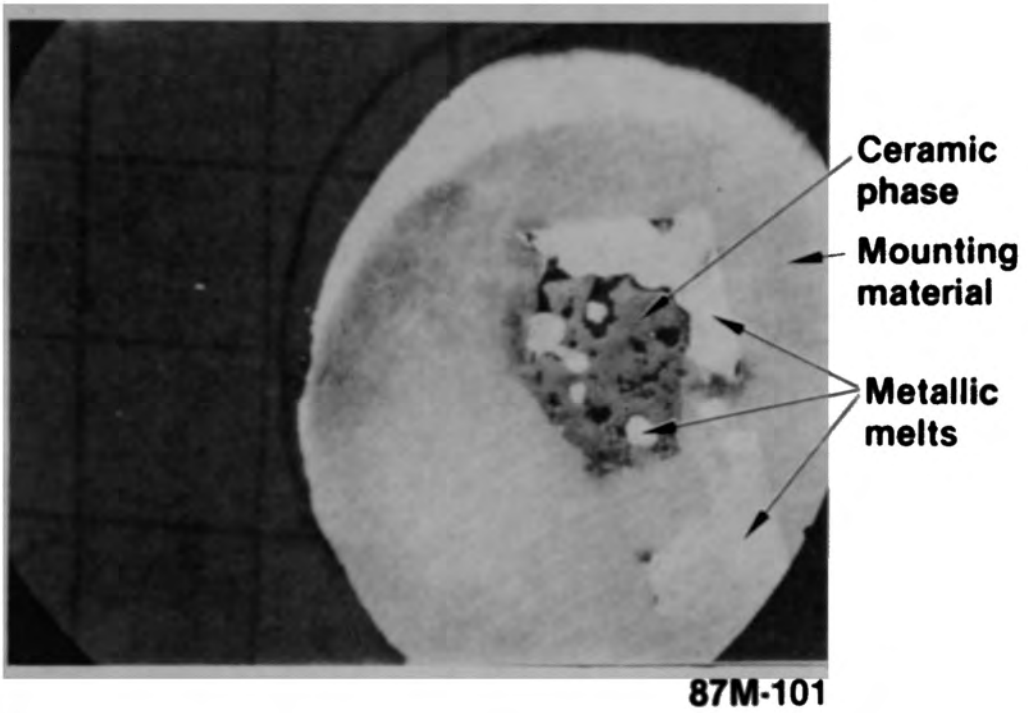


Figure E-169. Cross section of sample N05-P1-H.

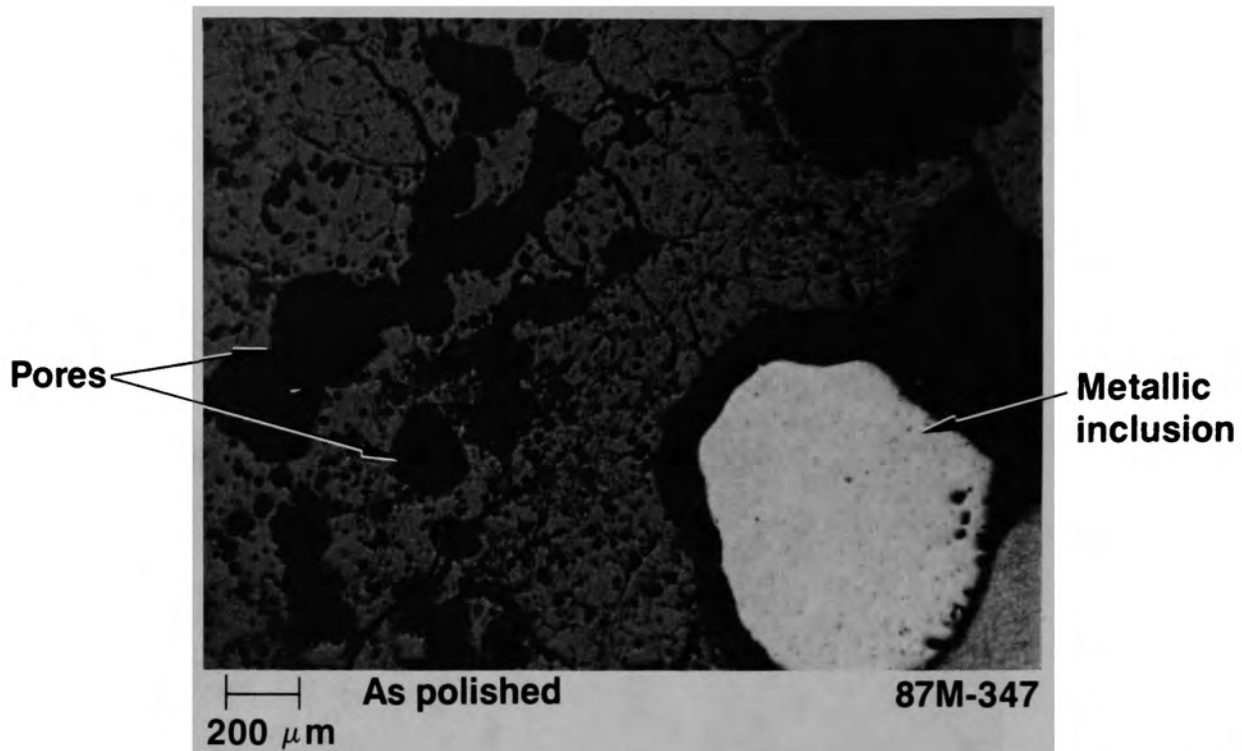


Figure E-170. Metallic inclusion in ceramic phase (N05-P1-H).

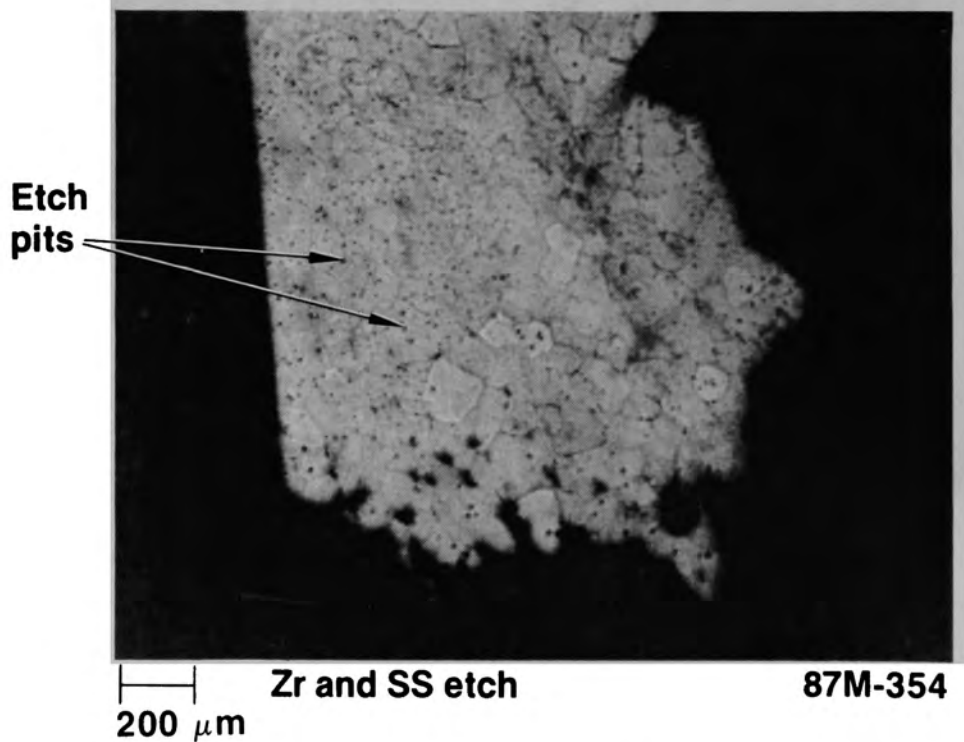


Figure E-171. Metallic inclusion in N05-P1-H.

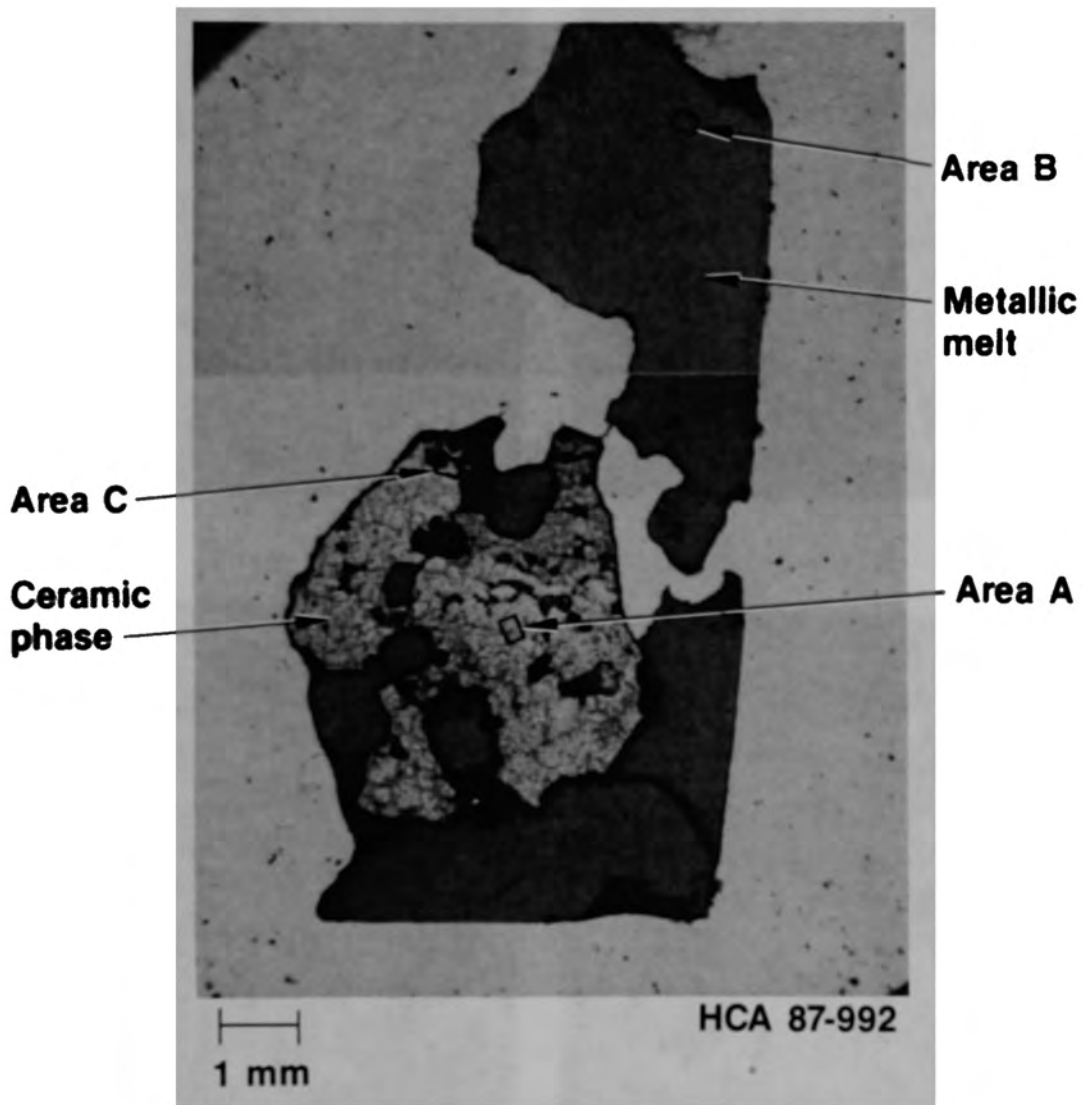
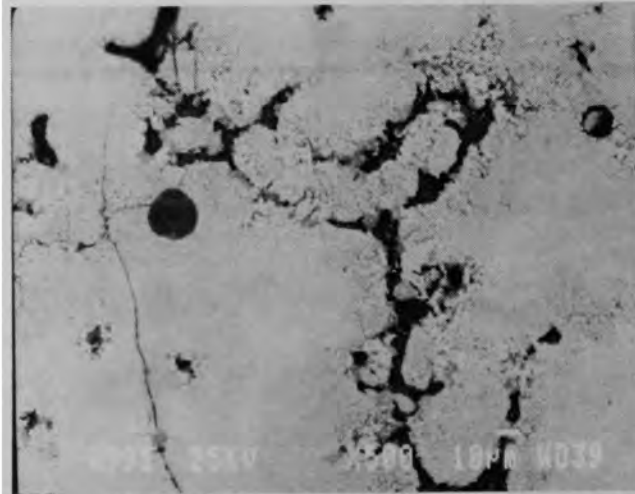
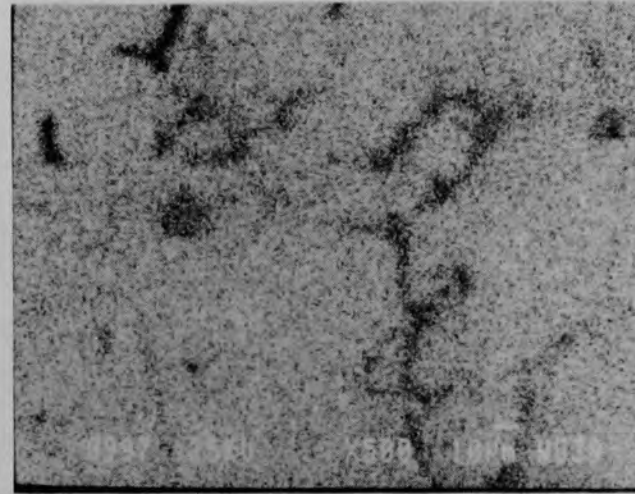


Figure E-172. Backscattered electron image of cross section from N05-P1-H.

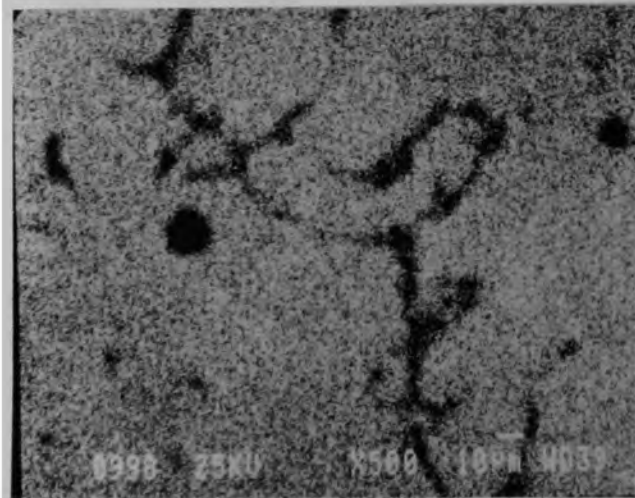


BSE compositional image HCA 87-995



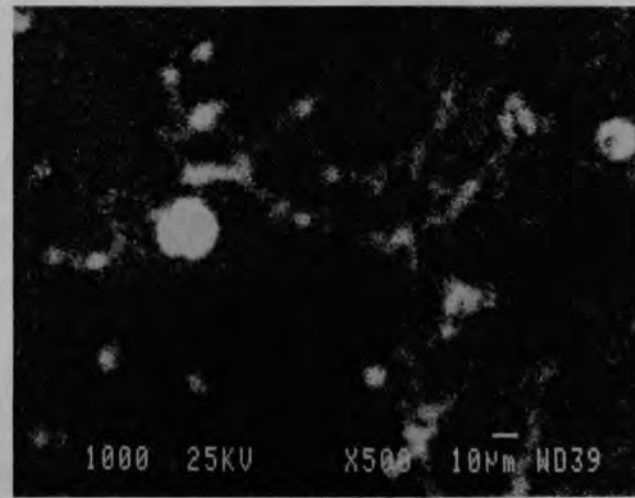
Zr dot map

HCA 87-997



U dot map

HCA 87-998



Fe dot map

HCA 87-1000

Figure E-173. Structural oxides in (U,Zr)O<sub>2</sub> grain boundaries (N05-P1-H Area A).



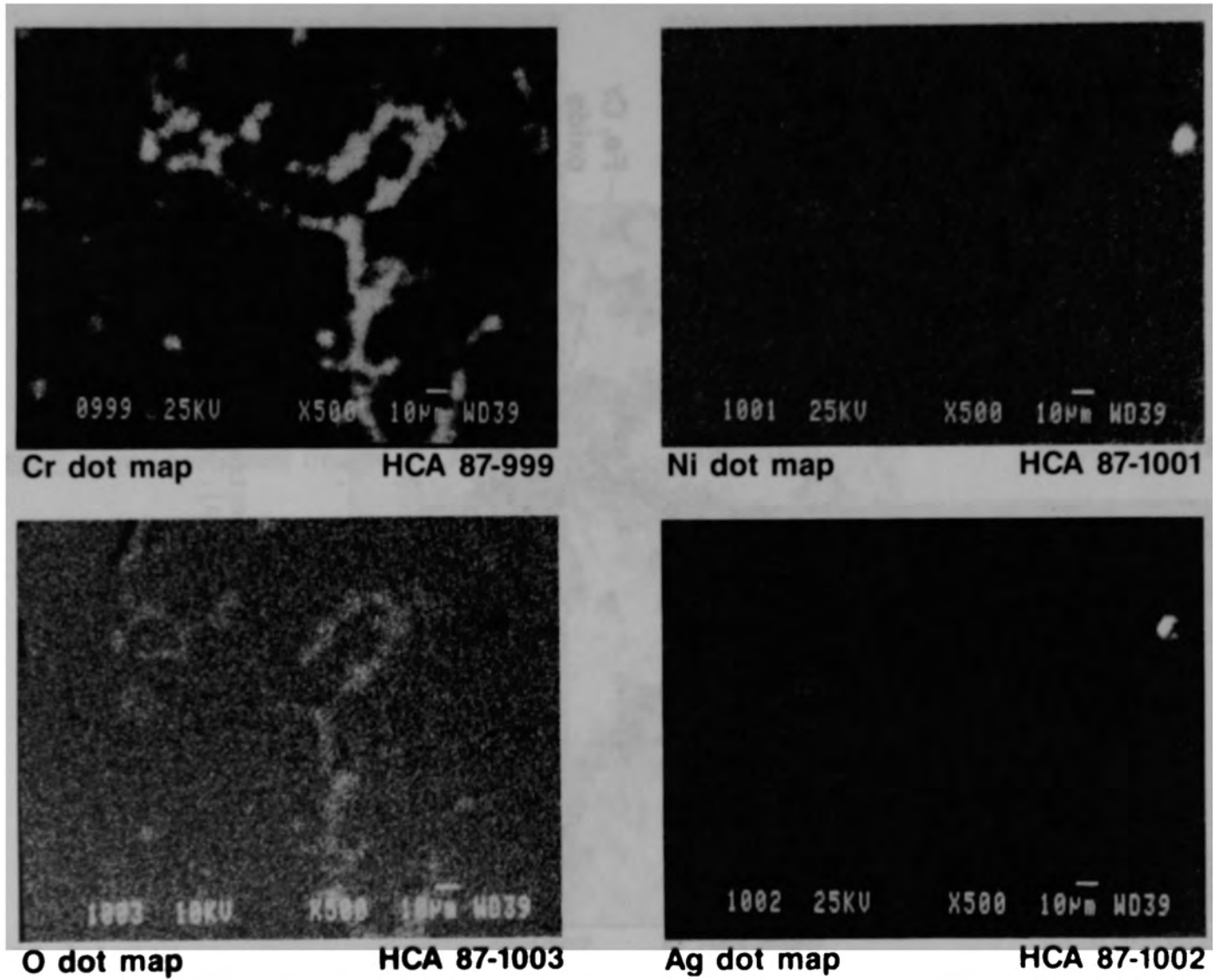


Figure E-173. (Continued)

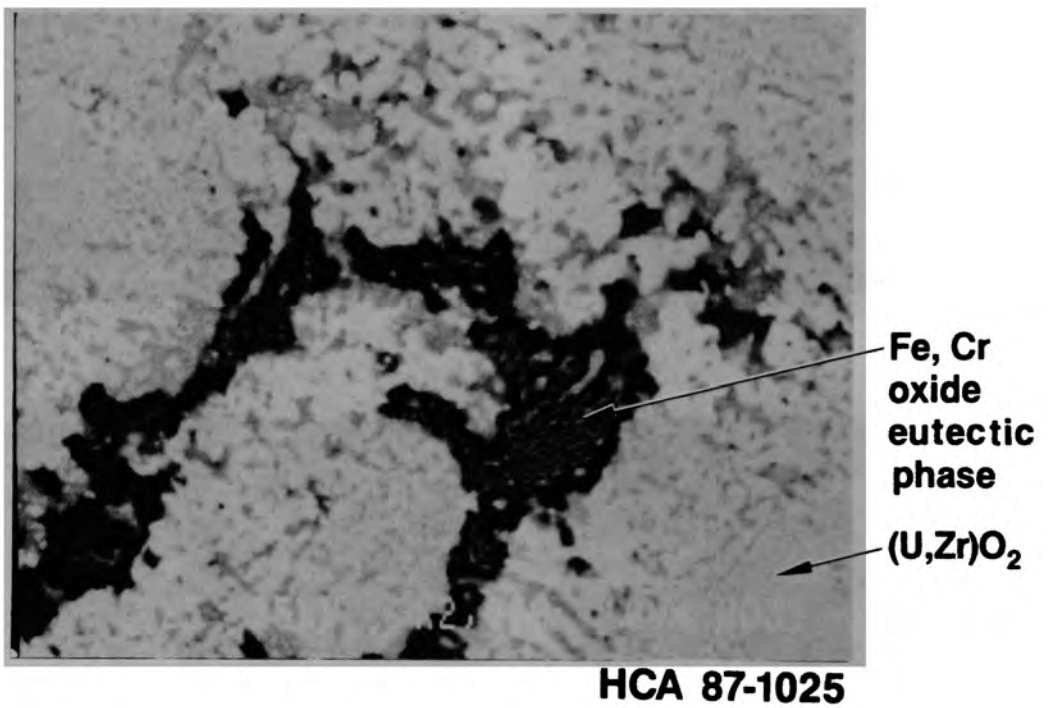


Figure E-174. Backscattered electron image of Fe,Cr oxide phase in (U,Zr)O<sub>2</sub> matrix (N05-P1-H Area A).

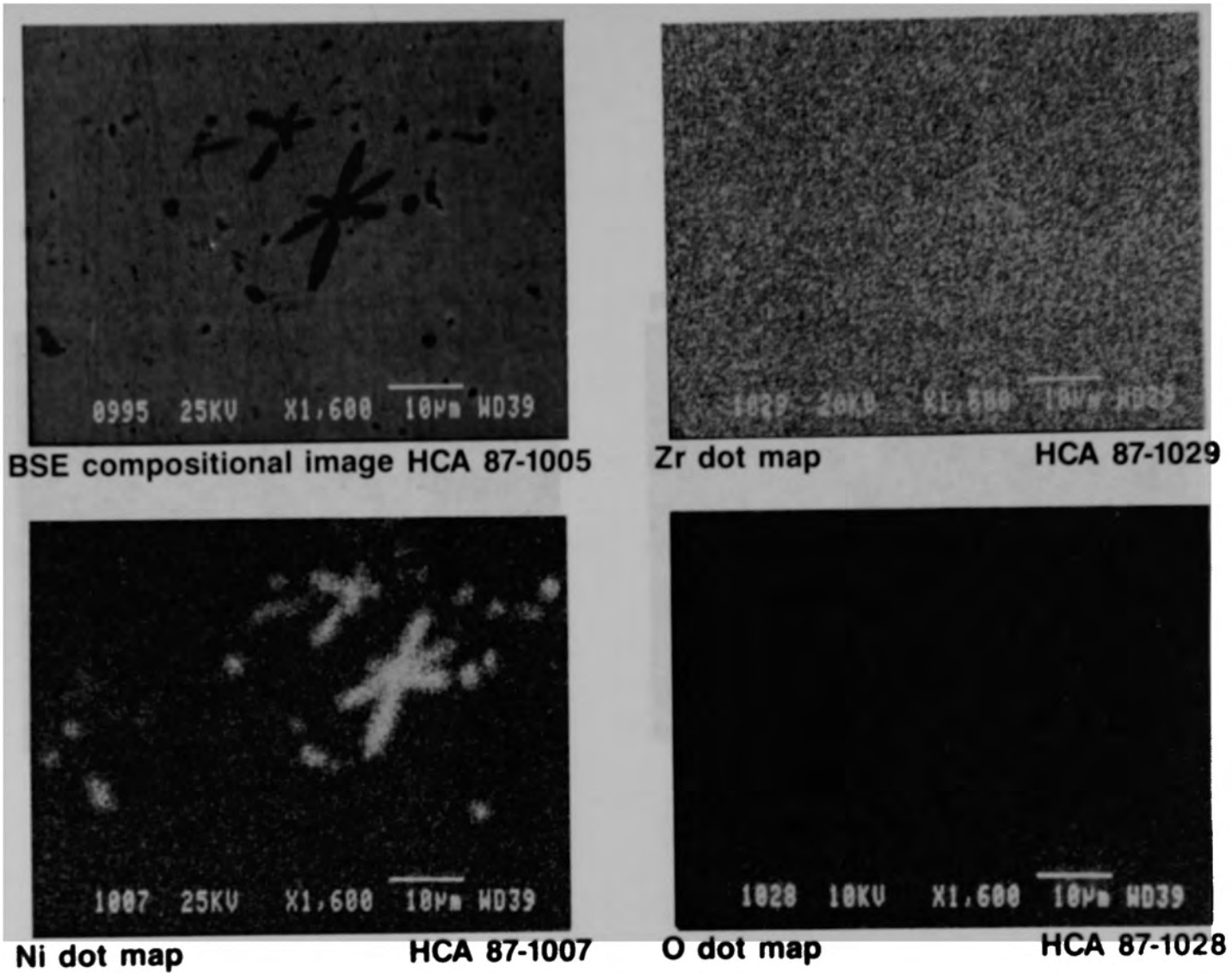


Figure E-175. Element composition of metallic phase in N05-P1-H Area B.

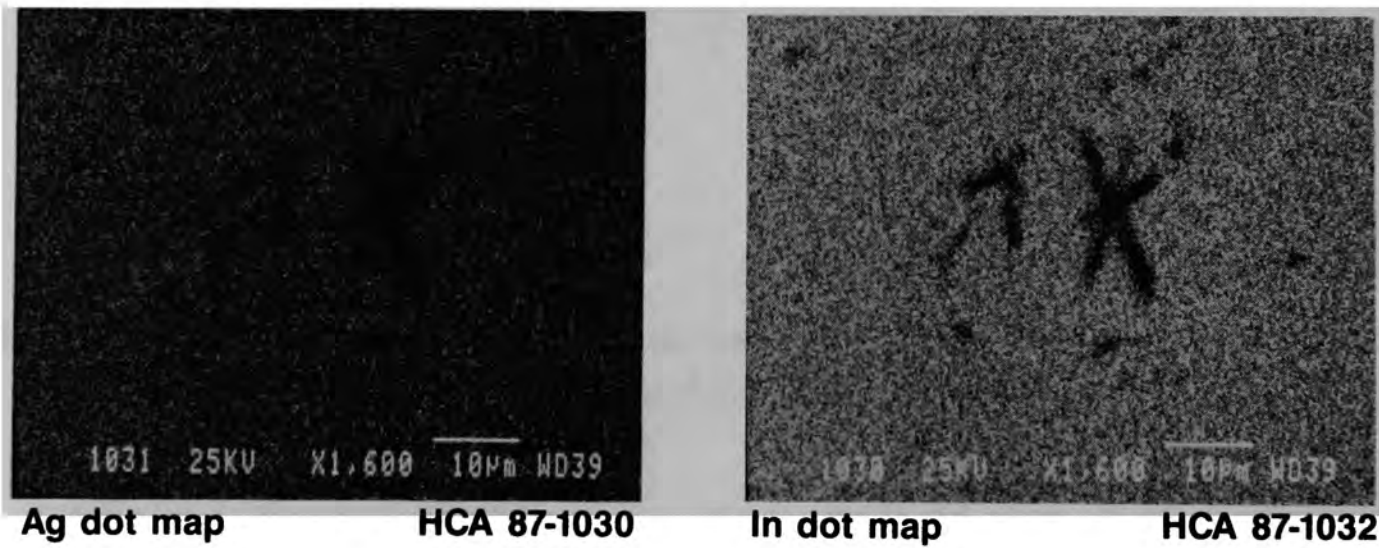
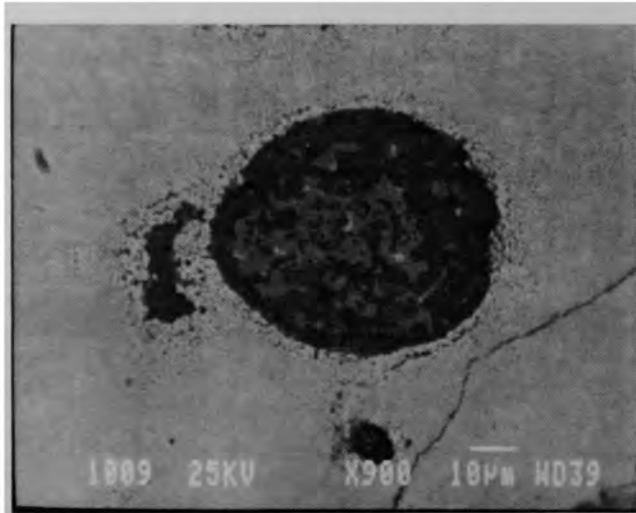
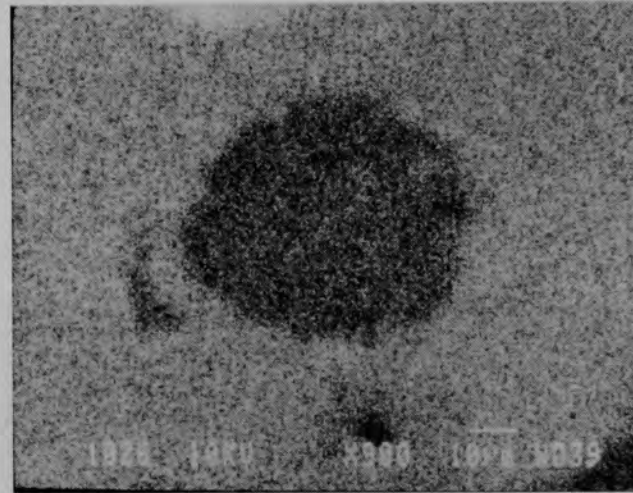


Figure E-175. (Continued)

Figure E-176 shows the elemental dot maps for a metallic inclusion in Area C. These dot maps show a metallic inclusion consisting of Fe-Ni-Cr. A layer of previously molten  $\text{Cr}_2\text{O}_3$  is concentrated on the periphery of the inclusion. This indicates temperatures were in excess of 2266 K.

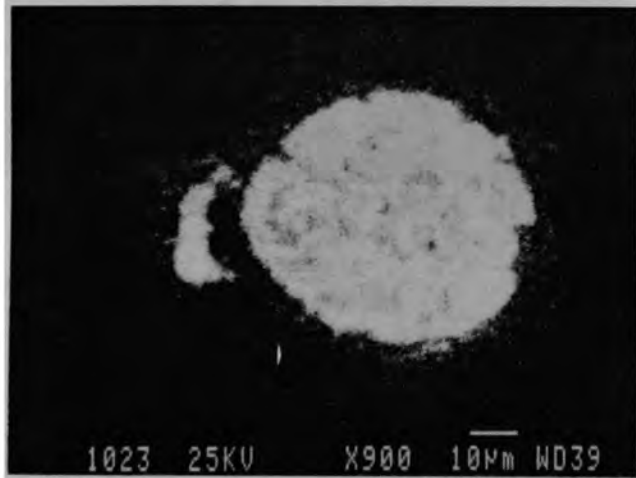


BSE compositional image HCA 87-1009



Zr dot map

HCA 87-1026



Fe dot map

HCA 87-1023



Cr dot map

HCA 87-1021

Figure E-176. Inclusion in mixed oxides of uranium and zirconium.

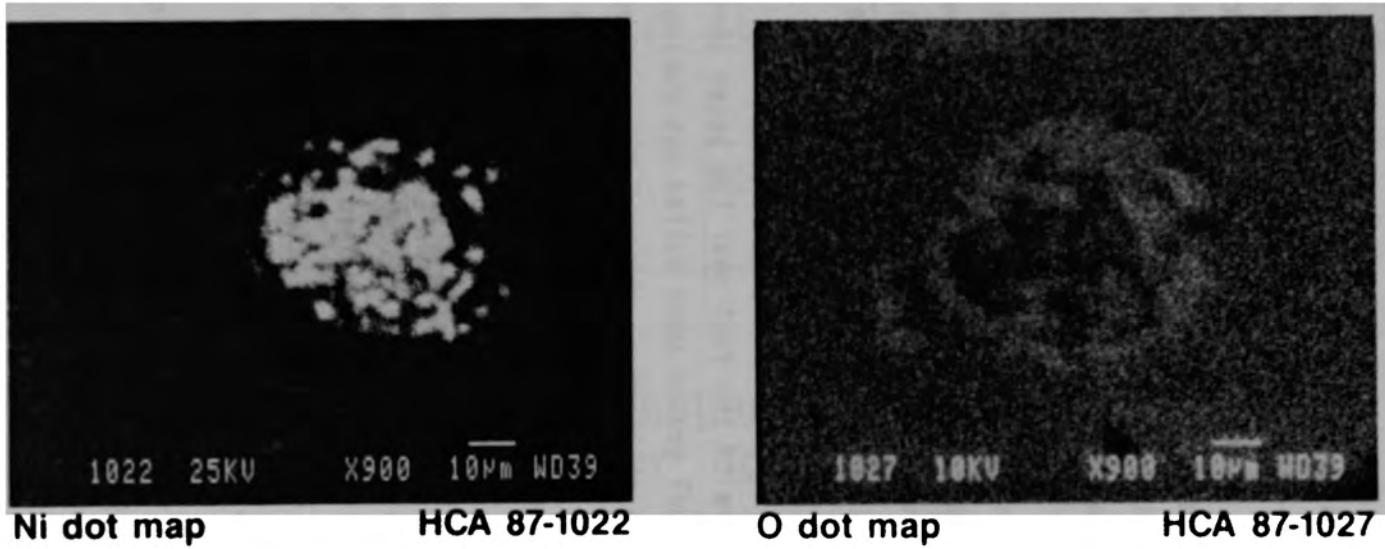


Figure E-176. (Continued)

## Intact Core Components

### D04-R9 Fuel Rod

The sectioning diagram for fuel rod D04-R9 is shown in Figure E-177. Samples D04-R9-2, D04-R9-4, D04-R9-6, and D04-R9-8 were all subdivided and examined in a similar manner, and consequently the detailed sectioning and examination plan is only shown for sample D04-R9-2. All the metallographic samples were very similar, and hence only representative photographs will be presented and discussed.

The cross section of sample D04-R9-2B from near the bottom of the fuel rod is shown in Figure E-178. The as-polished cladding is shown in Figure E-179, which shows some zirconium-hydride precipitates oriented in the circumferential direction. Based upon out-of-pile experiments, the hydride concentration is <25 ppm.<sup>a</sup>

The microstructure of the fuel near the outer surface is shown in Figure E-180. Some fuel grains were pulled out during sample preparation, but the microstructure still shows the as-fabricated porosity contained within the fuel grains, which indicates relatively low temperature conditions. The average grain size was approximately 8  $\mu\text{m}$ .

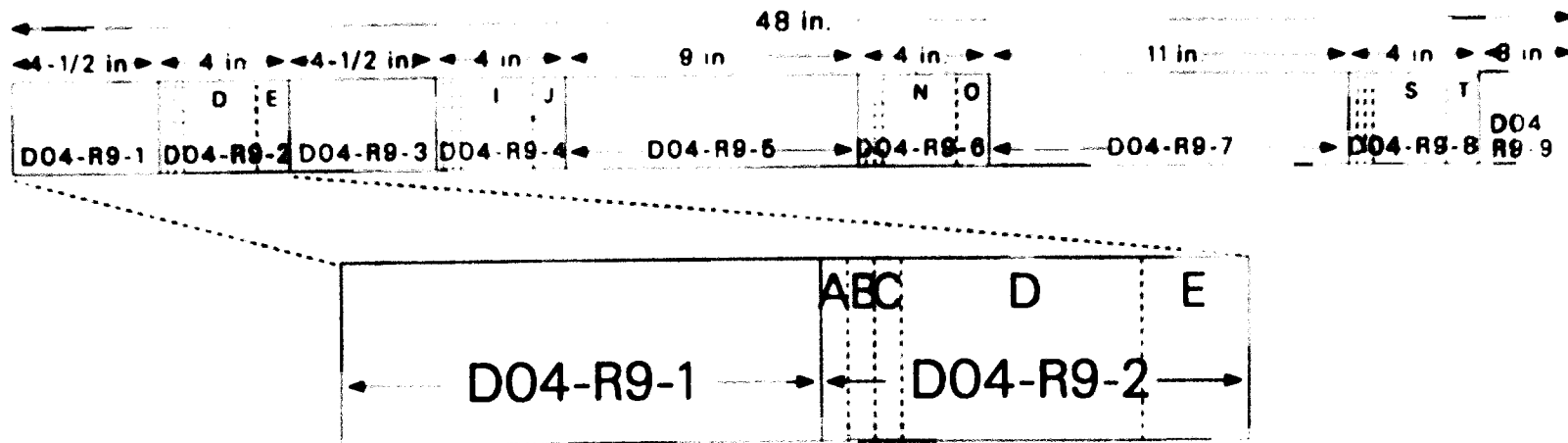
The structure of the cladding in a sample obtained near the top of this fuel rod stub is shown in Figure E-181, which shows minor amounts of zirconium-hydride precipitates oriented in the circumferential direction, similar to sample D04-R9-2B. A thin oxide film (2  $\mu\text{m}$ ) at the top of this rod is shown in Figure E-182.

The structure of the fuel at the center and edge of the fuel pellet of sample D04-R9-8Q are shown in Figures E-183 and E-184, respectively. The fuel microstructure is very similar to D04-R9-2B.

---

a. Barry Z. Hyatt, *Metallographic Hydride Standards for LWR Zircaloy 4 Seed Tuning Based on Out-of-Pile Corrosion Tests*, WAPD-LC(BB)-89, February 1974.





Sample No.	Location		Comments
	Bottom	Top	
D04-R9-1	0	4-1/2	Remnant
D04-R9-2	4-1/2	8-1/2	
D04-R9-2A	0	1/4	Remnant
D04-R9-2B	1/4	1/2	Met
D04-R9-2C	1/2	3/4	Remnant
D04-R9-2D	3/4	3	CSNI
D04-R9-2E	3	4	Rad chemistry

P614 CSO-488-05

Figure E-177. Sectioning diagram for fuel rod D04-R9.

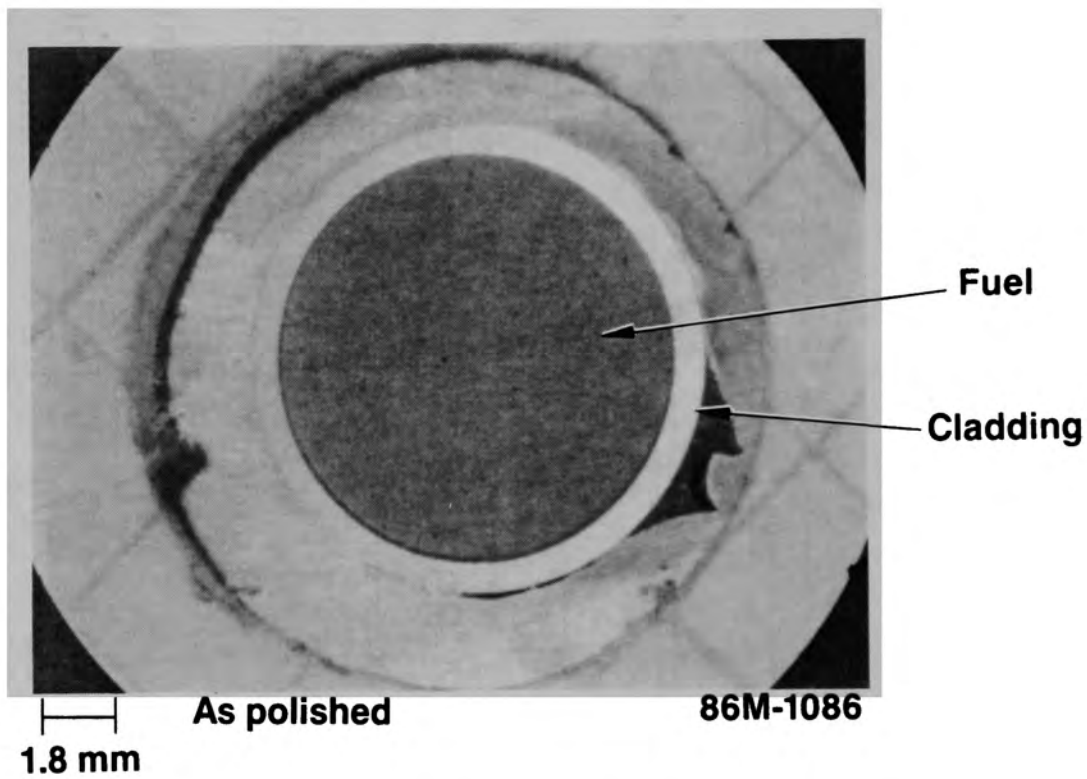
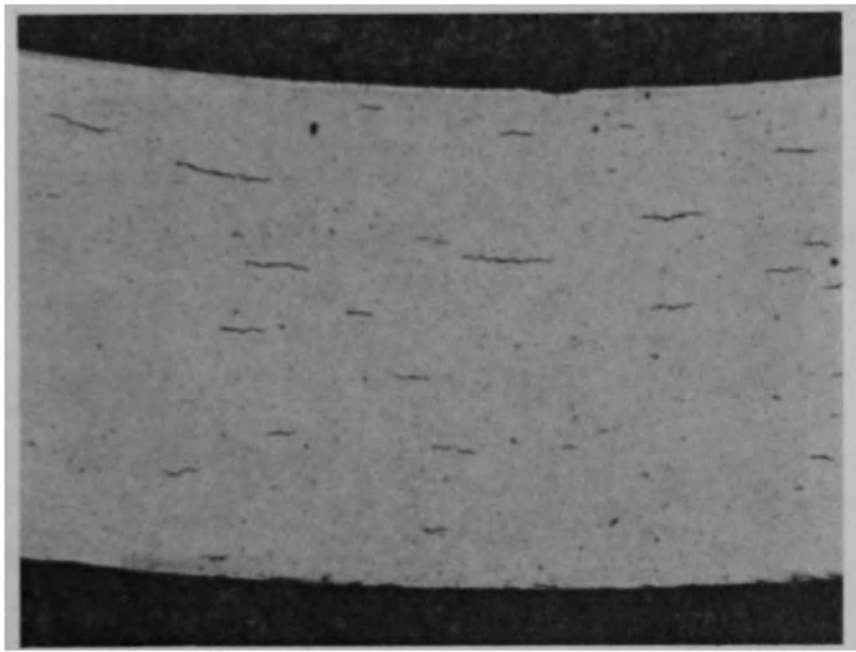


Figure E-178. Cross section D04-R9-2B from the bottom of a fuel rod.

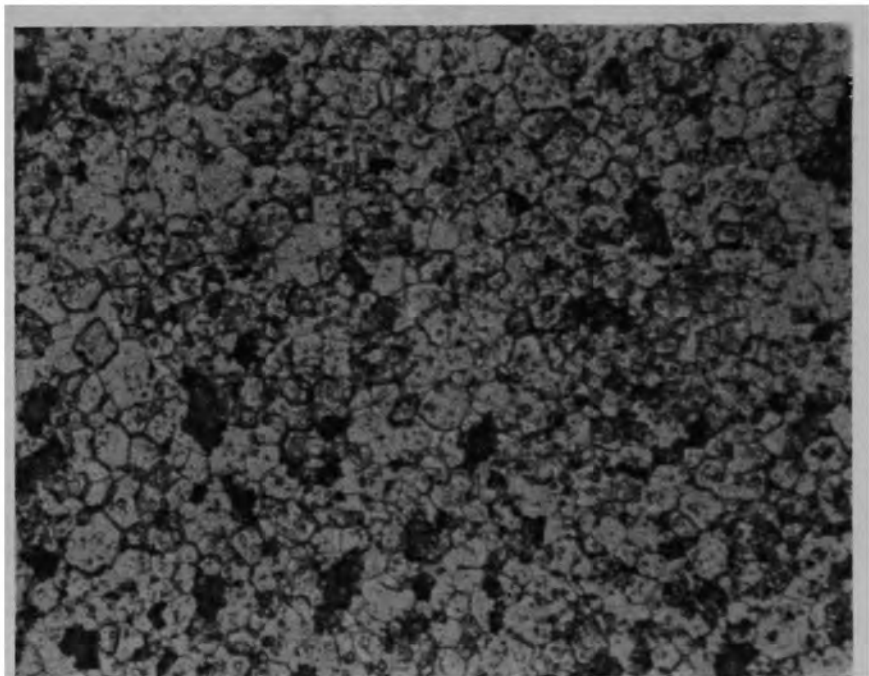


100  $\mu\text{m}$

Zr etch

87M-45

Figure E-179.  $\text{ZrH}_2$  in zircaloy cladding (D04-R9-2B).



—| |—  
20  $\mu\text{m}$

**Fuel etch**

**87M-42**

Figure E-180. Fuel microstructure (D04-R9-2B).

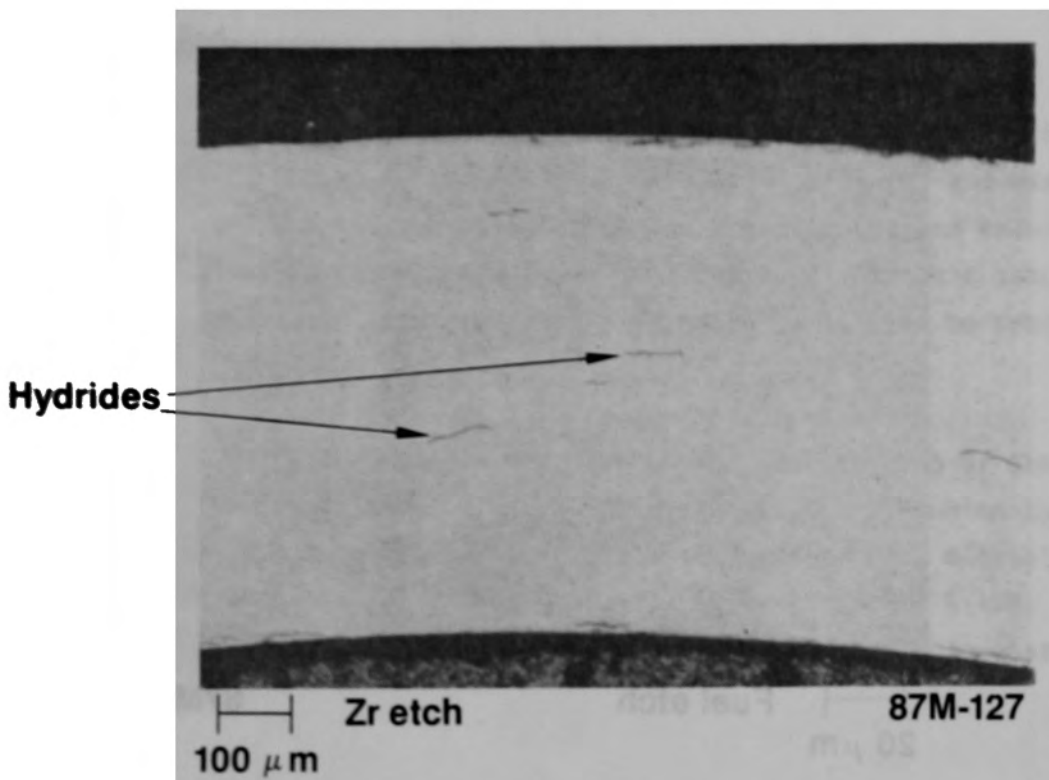


Figure E-181. Zirconium hydrides near top of rod (D04-R9-8Q).

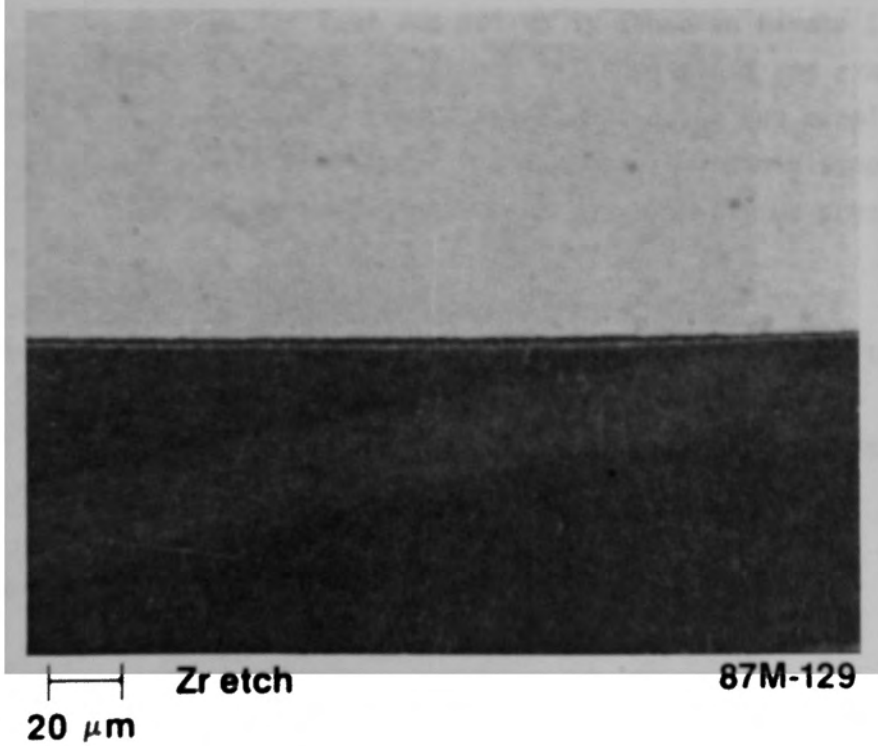
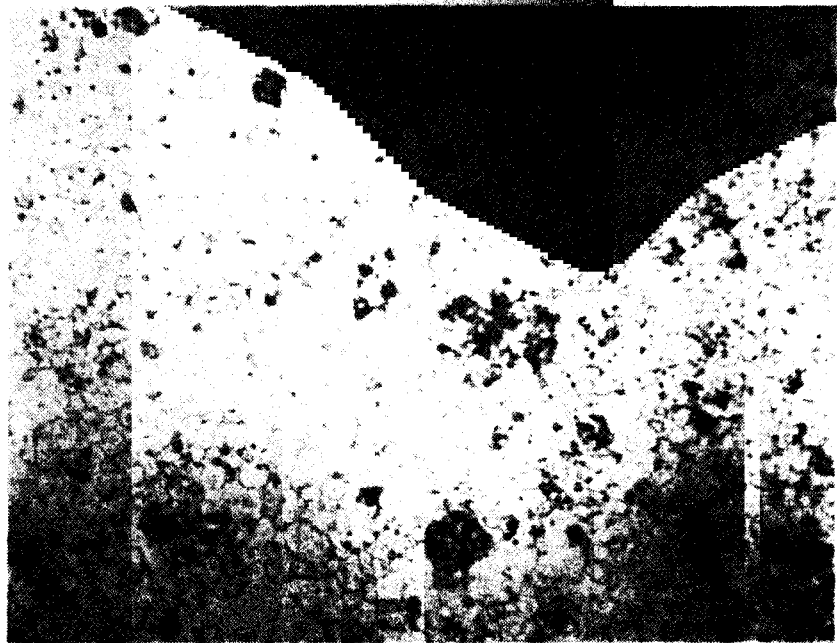


Figure E-182.  $ZrO_2$  layer on cladding (D04-R9-8Q).

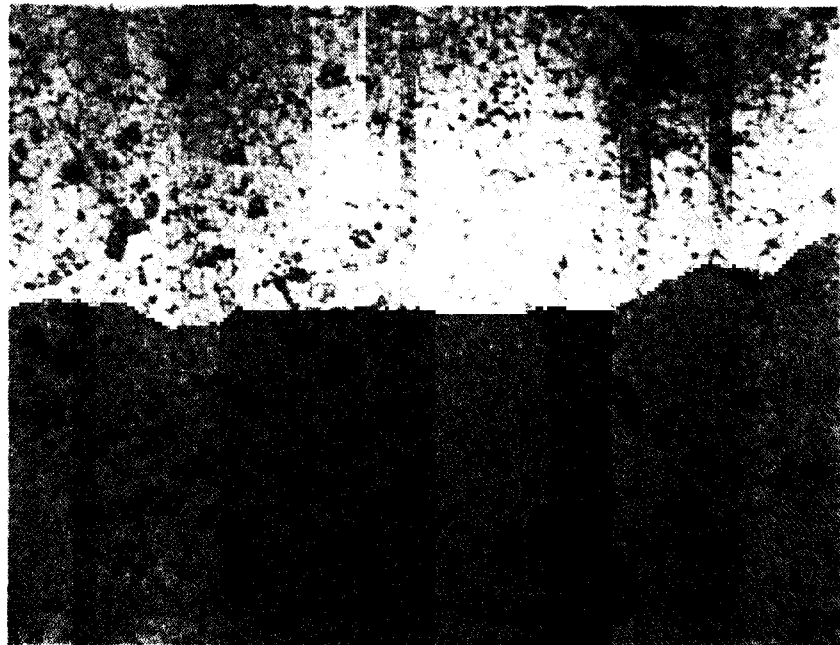


—|—|  
20  $\mu\text{m}$

**Fuel etch**

**87M-121**

Figure E-183. Fuel structure near pellet center (D04-R9-8Q).



—|—|  
20  $\mu\text{m}$

**Fuel etch**

**87M-123**

Figure E-184. Fuel structure near edge of pellet (D04-R9-8Q).

### G08-R9 Fuel Rod

The sectioning diagram for fuel rod G08-R9 is shown in Figure E-185. Samples G08-R9-2, G08-R9-4, and G08-R9-6 were all subdivided and examined in a similar manner, and consequently the detailed sectioning and examination plan is only shown for sample G08-R9-2. All the metallographic samples were very similar, and hence only representative photographs will be presented and discussed.

The cross section of sample G08-R9-6L, from near the top of the fuel rod, is shown in Figure E-186. Figure E-187 shows some zirconium-hydride precipitates oriented in the circumferential direction. The microstructure of the fuel near the center of the pellet is shown in Figure E-188. Both the cladding and fuel microstructures are very similar to those observed on sample D04-R9.

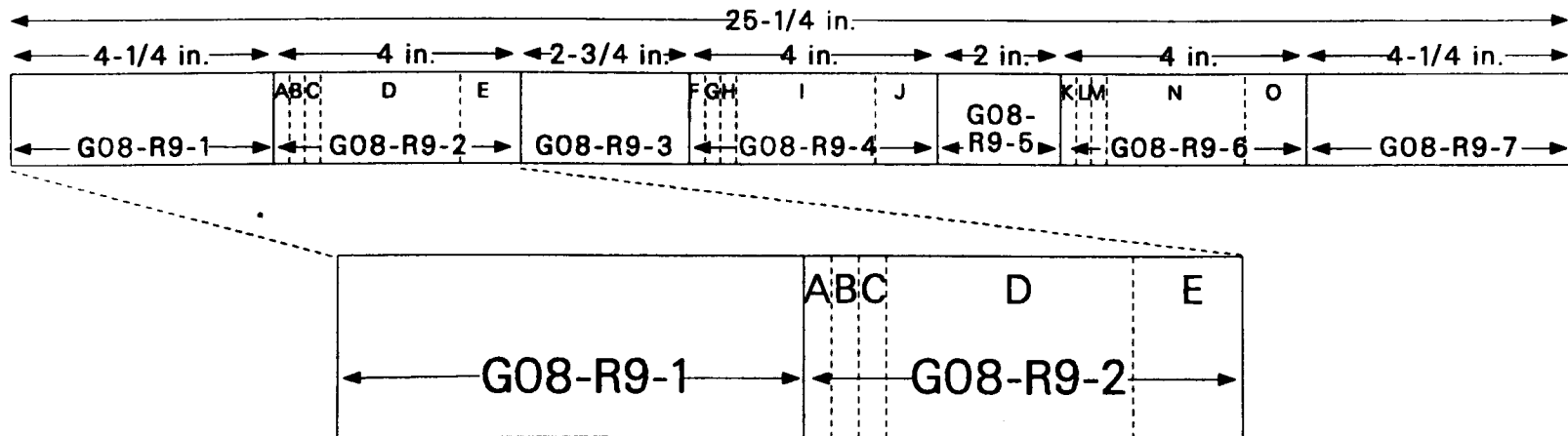
### K09-R5 Fuel Rod

The sectioning diagram for fuel rod K09-R5 is shown in Figure E-189. Samples K09-R5-2, K09-R5-4, and K09-R5-5 were all subdivided and examined in a similar manner, and consequently the detailed sectioning and examination plan is only shown for sample K09-R5-2. All the metallographic samples were very similar, and hence only representative photographs will be presented and discussed.

The cross section of sample K09-R5-5L, obtained from near the top of the fuel rod, is shown in Figure E-190. The cladding and fuel microstructures were very similar to those on the other fuel rods, as shown in Figures E-191 and E-192.

### D04-R8 Control Rod

The sectioning diagram for control rod D04-R8 is shown in Figure E-193. Samples D04-R8-2, D04-R8-4, D04-R8-6, and D04-R8-8 were all subdivided and examined in a similar manner, and consequently the detailed



Sample No.	Location		Comments
	Bottom	Top	
G08-R9-1	0	4-1/4	Remnant
G08-R9-2	4-1/4	8-1/4	
G08-R9-2A	0	1/4	Remnant
G08-R9-2B	1/4	1/2	Met
G08-R9-2C	1/2	3/4	Remnant
G08-R9-2D	3/4	3	CSNI
G08-R9-2E	3	4	Rad chemistry

P614 CSO-488-01

Figure E-185. Sectioning diagram for fuel rod G08-R9.



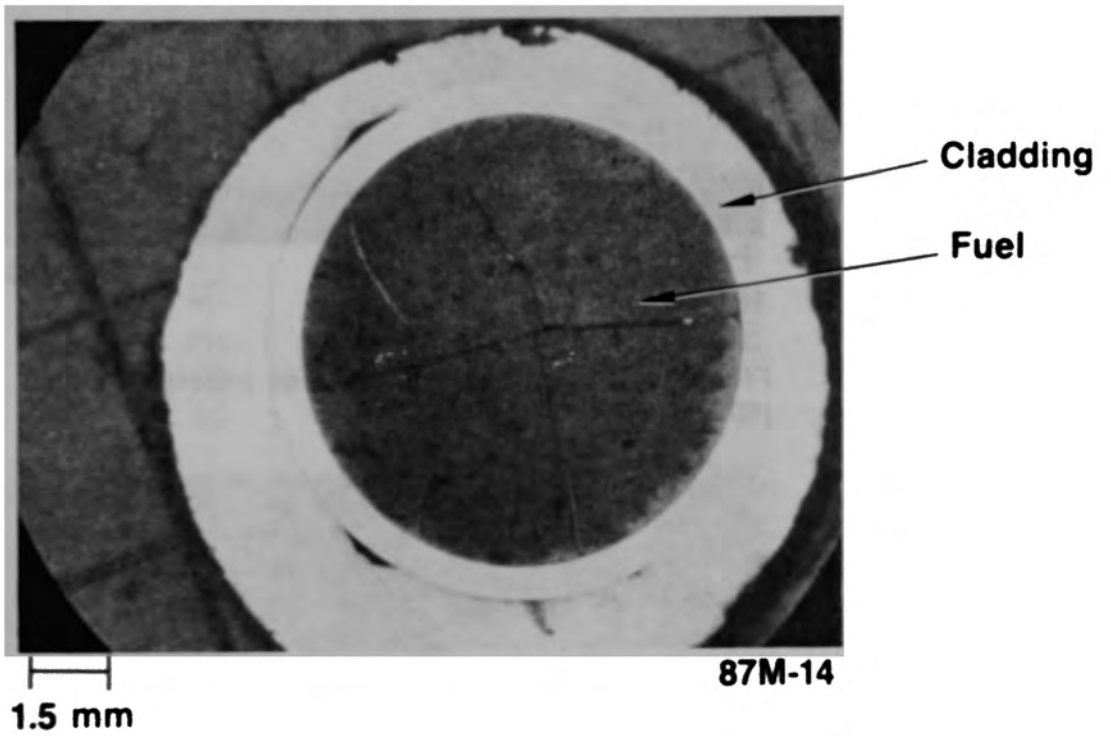


Figure E-186. Cross section near top of fuel rod (G08-R9-6L).

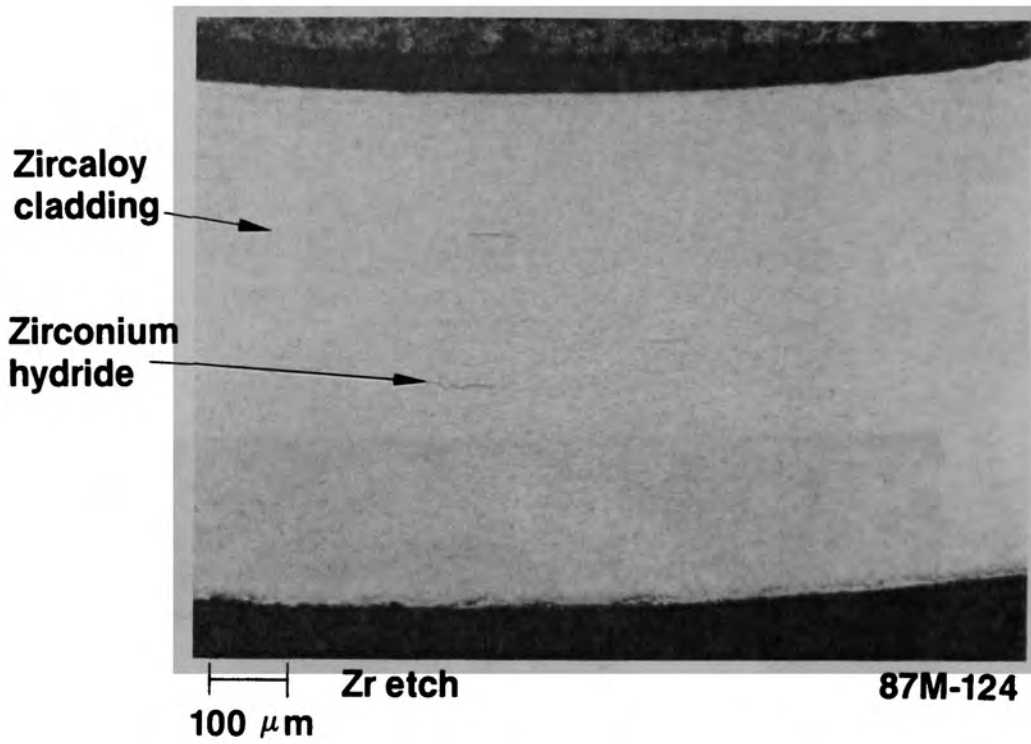


Figure E-187. Zirconium hydride precipitation (G08-R9-6L).

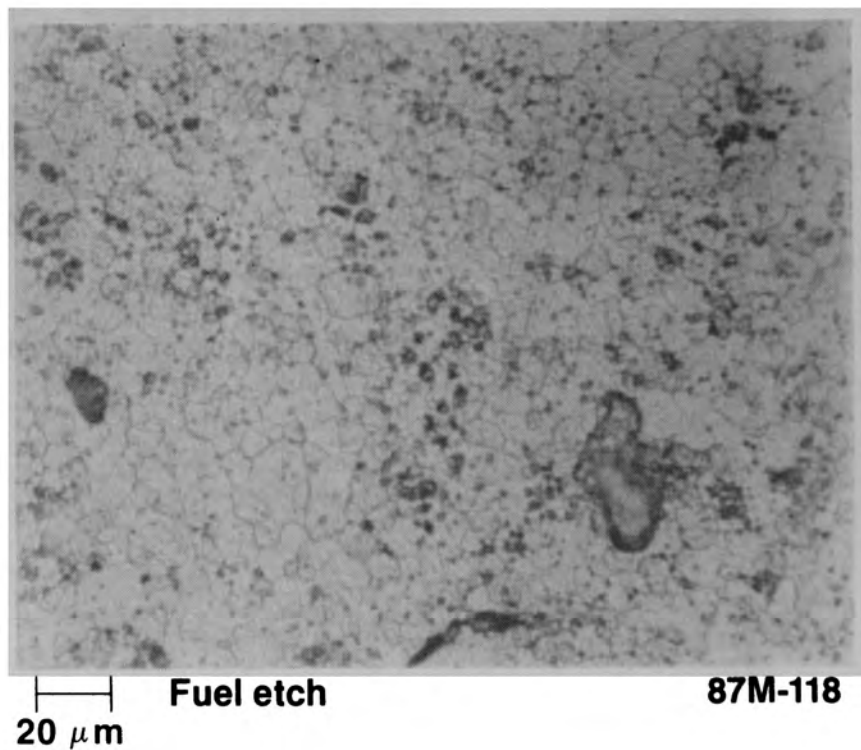
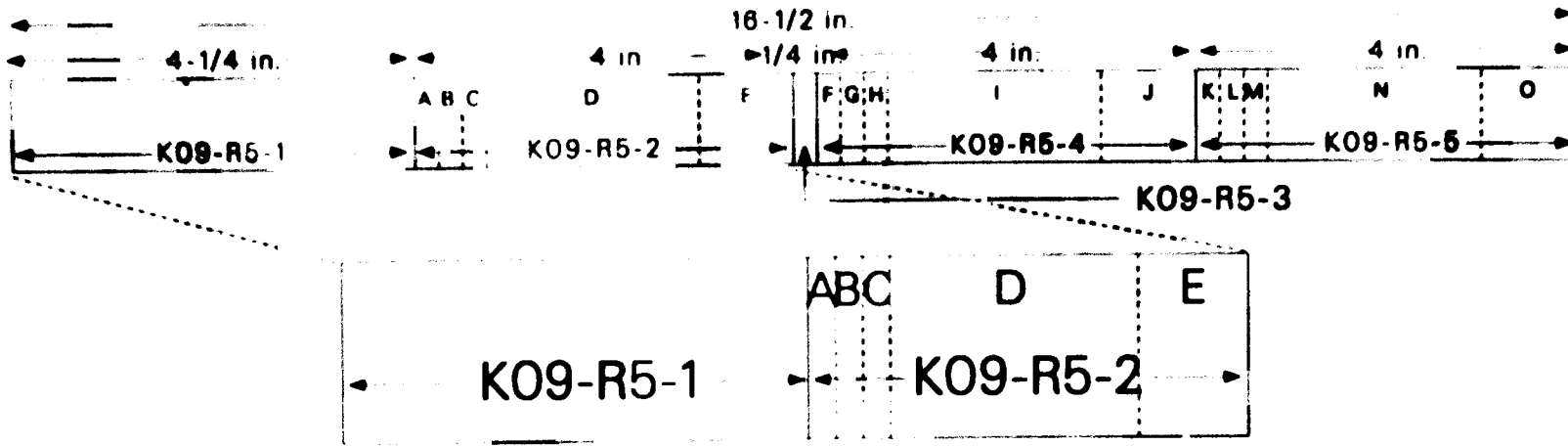


Figure E-188. Fuel structure near center of fuel pellet (G08-R9-6L).



622-3

Sample No.	Location		Comments
	Bottom	Top	
K09-R5-1	0	4-1/4	Remnant
K09-R5-2	4-1/4	8-1/4	
K09-R5-2A	0	1/4	Remnant
K09-R5-2B	1/4	1/2	Met
K09-R5-2C	1/2	3/4	Remnant
K09-R5-2D	3/4	3	CSNI
K09-R5-2E	3	4	Rad chemistry

P614 CSO-488-02

Figure E-189. Sectioning diagram for fuel rod K09-R5.

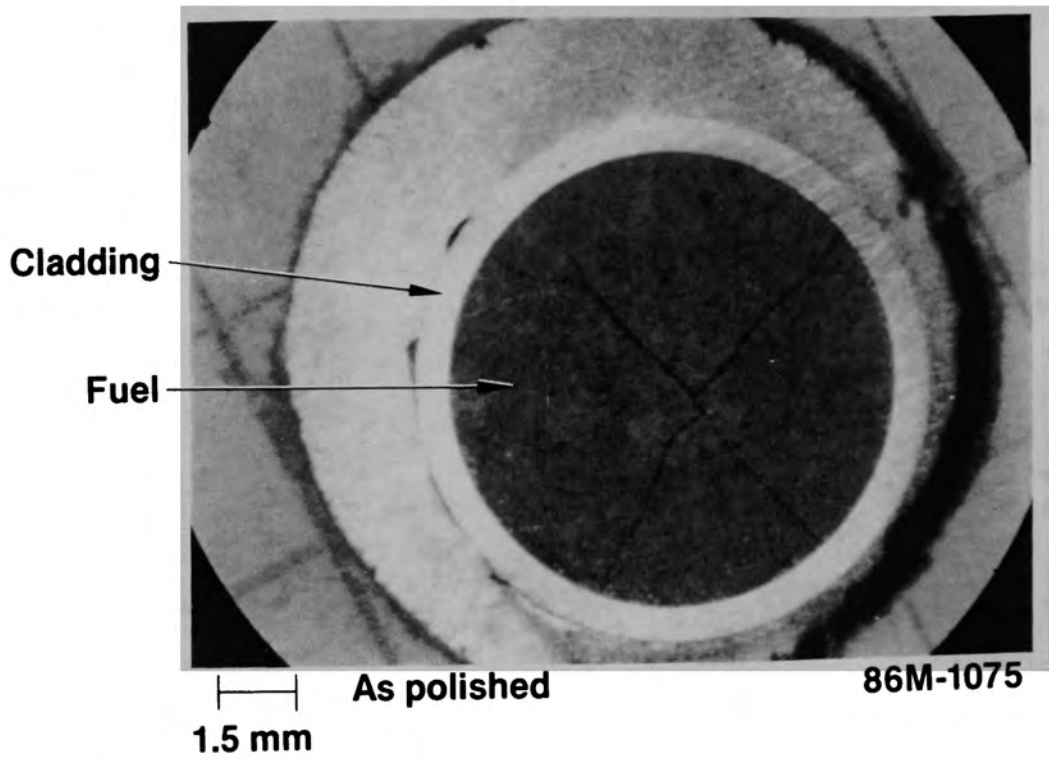


Figure E-190. Cross section near top of fuel rod (K09-R5-5L).

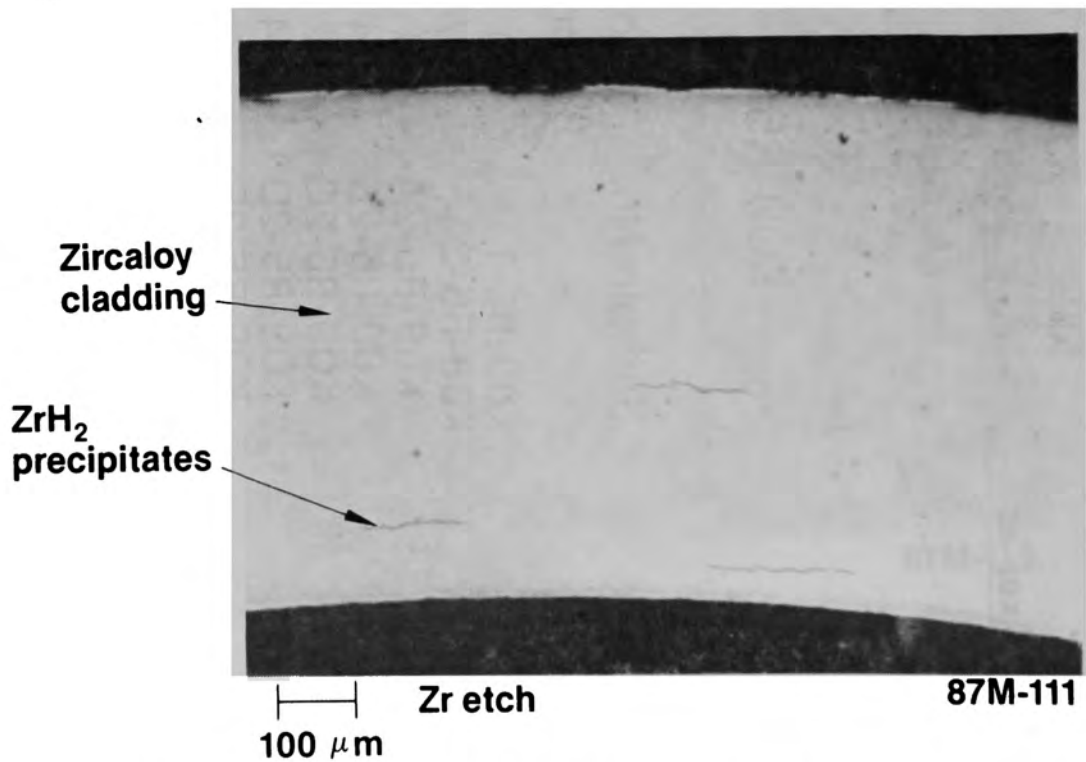
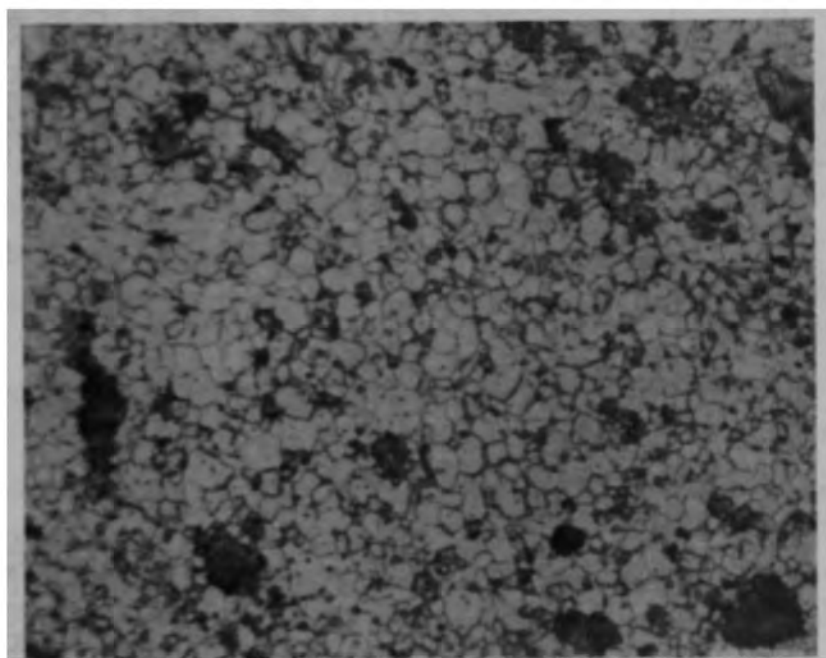


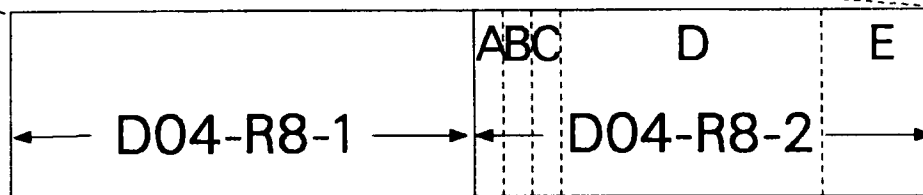
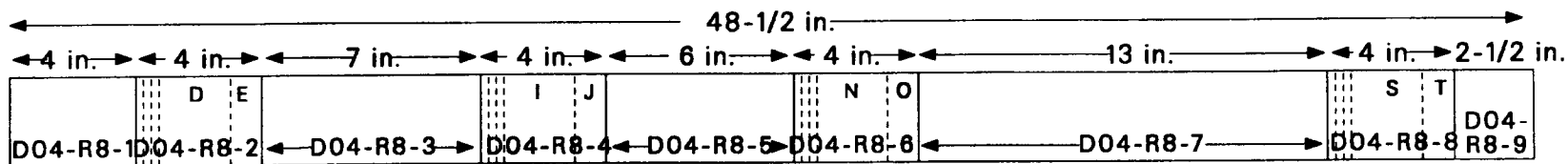
Figure E-191. Zirconium hydrides in cladding (K09-R5-5L).



20  $\mu\text{m}$  Fuel etch

87M-105

Figure E-192. Fuel structure in K09-R5-5L.



<u>Sample No.</u>	<u>Location</u>		<u>Comments</u>
	<u>Bottom</u>	<u>Top</u>	
D04-R8-1	0	4	Remnant
D04-R8-2	4	8	
D04-R8-2A	0	1/4	Remnant
D04-R8-2B	1/4	1/2	Met
D04-R8-2C	1/2	3/4	Remnant
D04-R8-2D	3/4	3	CSNI
D04-R8-2E	3	4	Rad chemistry

P614 CSO-488-06

Figure E-193. Sectioning diagram from control rod D04-R8.

sectioning and examination plan is only shown for sample D04-R8-2. All the metallographic samples were very similar, and hence only representative photographs will be presented and discussed.

Figure E-194 shows cross section D04-R8-2B taken from near the bottom of the control rod. The zircaloy guide tube has been cut in two places as a result of the core-boring operation.

The microstructure of the zircaloy guide tube is shown in Figure E-195. A few more zirconium hydrides were present than in the zircaloy fuel rod cladding that was examined.

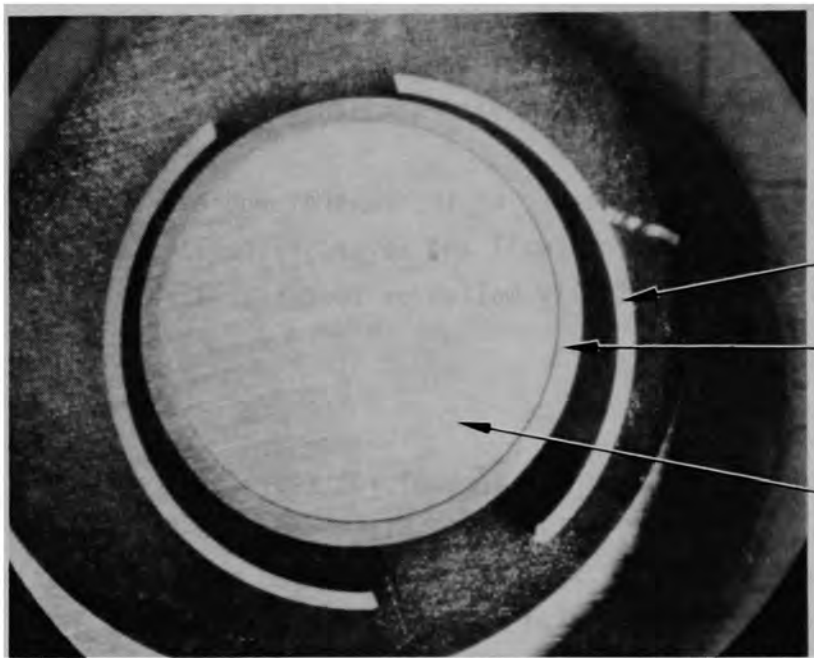
The typical microstructure of the control rod material is shown in Figure E-196. A mixture of small and large grain sizes suggest the (Ag,In,Cd) alloy was partially molten or recrystallized.

#### K09-R13 Control Rod

The sectioning diagram for control rod K09-R13 is shown in Figure E-197. Samples K09-R13-2, K09-R13-4, and K09-R13-6, were all subdivided and examined in a similar manner, and consequently the detailed sectioning and examination plan is only shown for sample K09-R13-2. All the metallographic samples were very similar, and hence only representative photographs will be presented and discussed.

The microstructure of the zircaloy guide tube is shown in Figure E-198, and it is very similar to the guide tube from sample D04-R8. The microstructure of the stainless steel cladding is shown in Figure E-199. This microstructure is typical, and does not indicate any abnormal conditions at this reactor location.

The typical microstructure of the control rod material is shown in Figure E-200. This microstructure is typical for as-fabricated control rod material, which indicates that this material remained intact and that temperatures for this reactor location were less than 1073 K.



**86M-1083**

Figure E-194. Cross section of control rod showing damaged guide tube from core boring (D04-R8-2B).



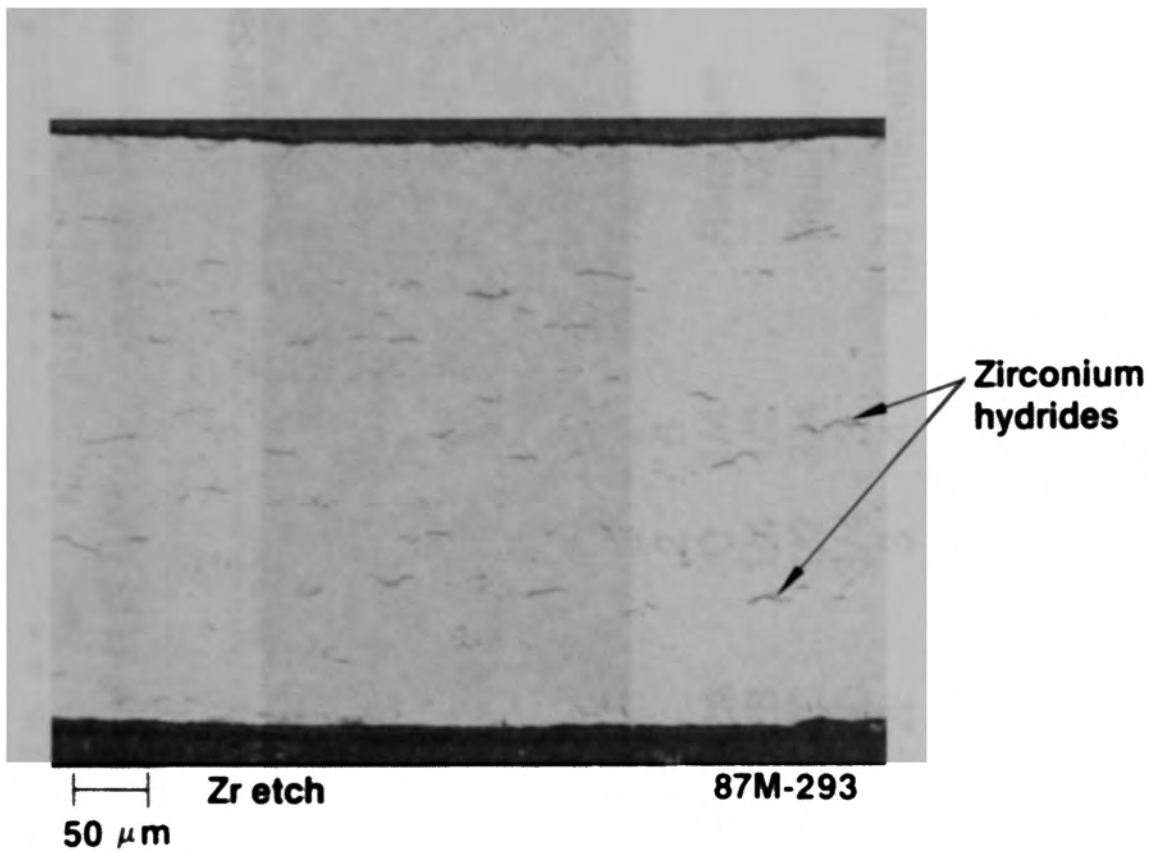
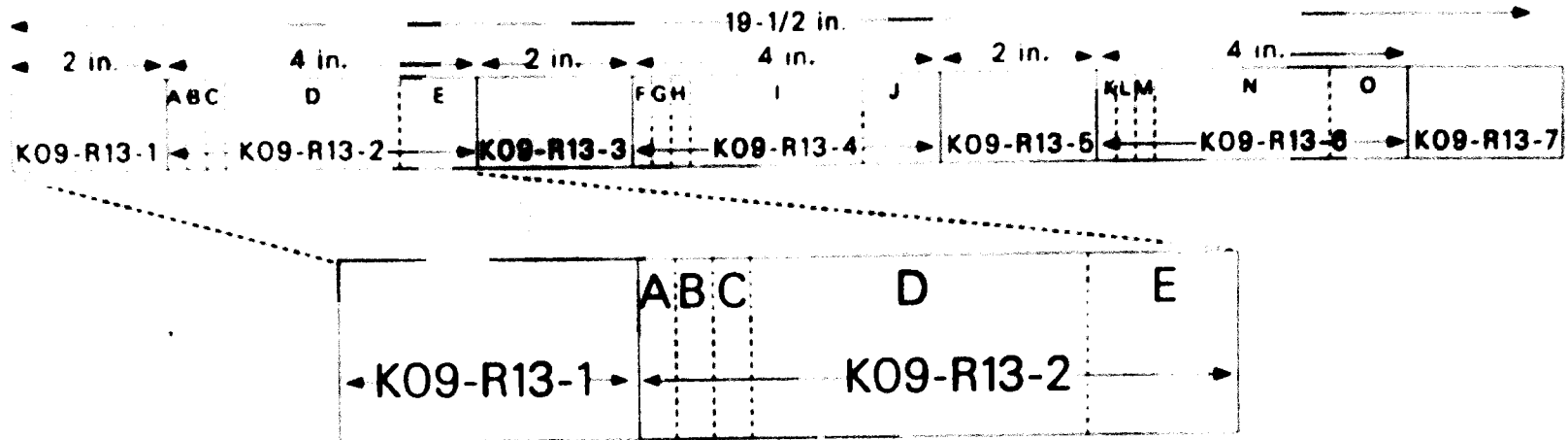


Figure E-195. Microstructure of zircaloy guide tube showing zirconium hydride precipitation.



Figure E-196. Possible melting of Ag-In-Cd alloy.



Sample No.	Location		Comments
	Bottom	Top	
K09-R13-1	0	2	Remnant
K09-R13-2	2	6	
K09-R13-2A	0	1/4	Remnant
K09-R13-2B	1/4	1/2	Met
K09-R13-2C	1/2	3/4	Remnant
K09-R13-2D	3/4	3	
K09-R13-2E	3	4	Rad chemistry

P614 CSO-488-20

Figure E-197. Sectioning diagram for control rod K09-R13.

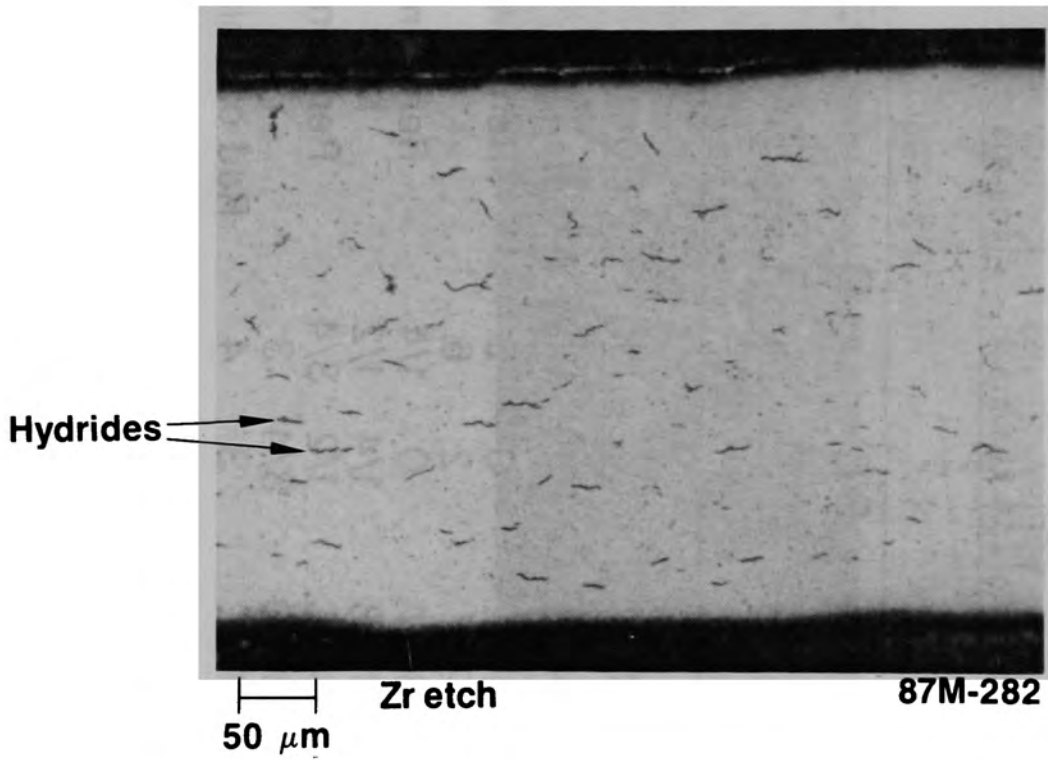
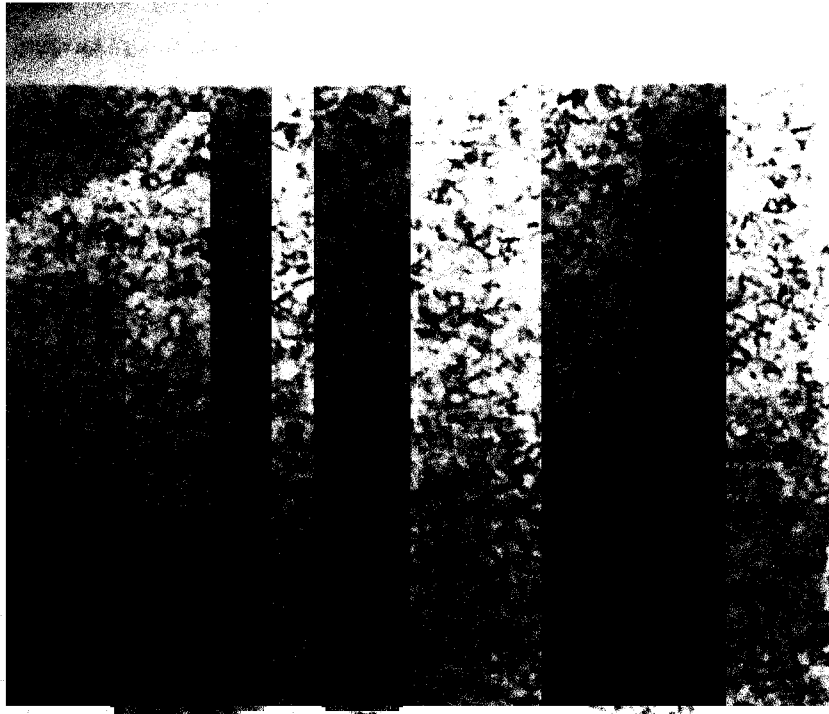


Figure E-198. Hydride precipitation in zircaloy guide tube (K09-R13-2B).



50  $\mu\text{m}$

Stainless steel etch

87M-303

Figure E-199. Microstructure of 304 SS cladding (K09-R13-2B).

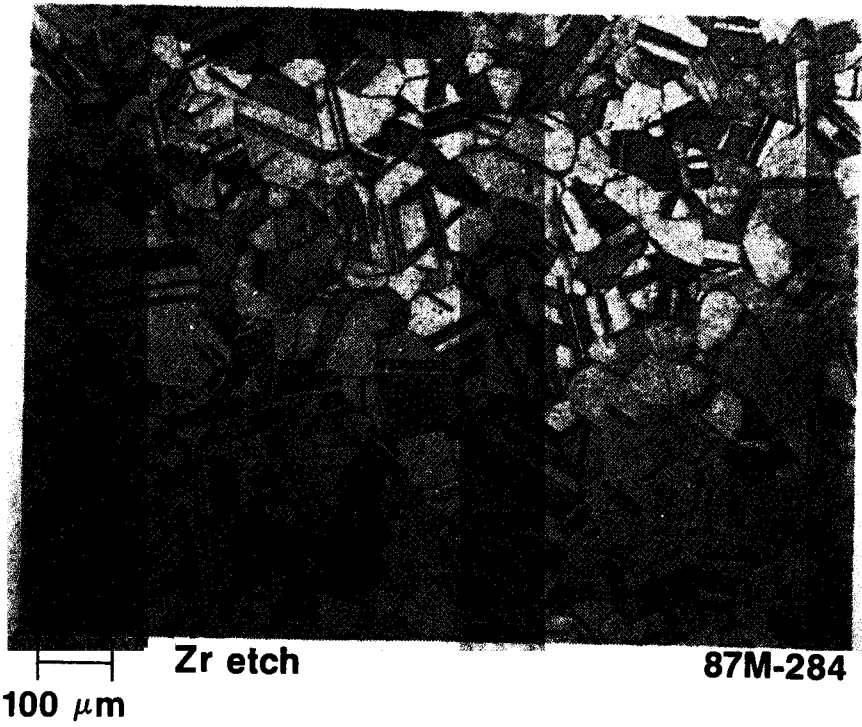


Figure E-200. Intact Ag-In-Cd microstructure (K09-R13-2B).

### N12-R7 Control Rod

The sectioning diagram for this control rod is shown in Figure E-201. The sample at the top of this rod was examined because it had apparently melted.

The cross section sample N12-R7-10Y is shown in Figure E-202. Figure E-203 shows the previously molten (Ag,In,Cd) microstructure from this sample, which indicates temperatures in excess of 1073 K.

### 007-R7 Control Rod

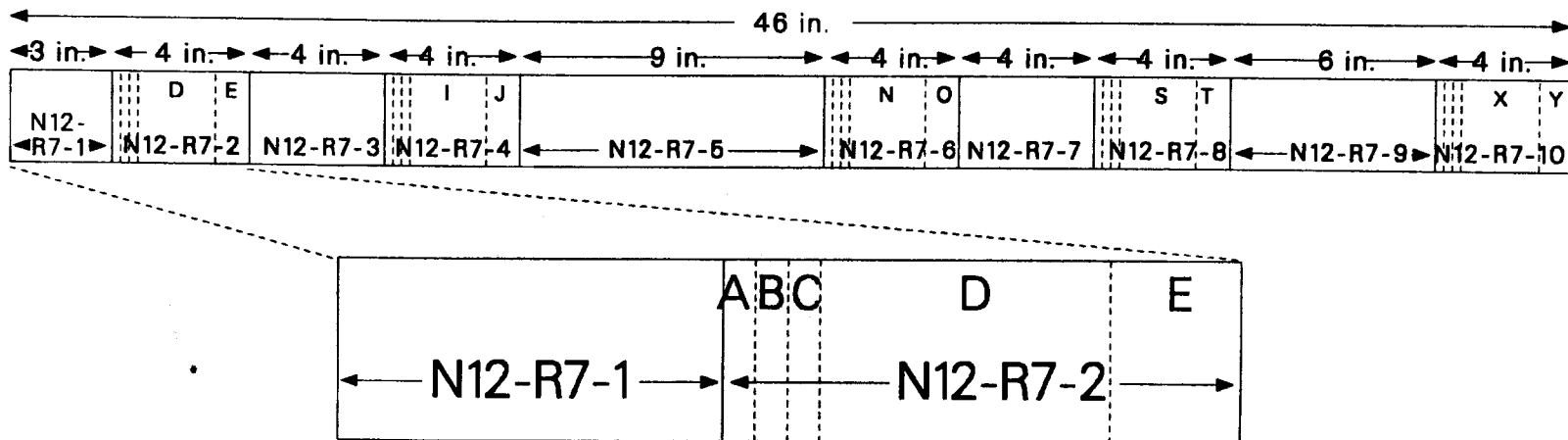
The sectioning diagram for control rod 007-R7 is shown in Figure E-204. Only the sample at the top of this rod (007-R7-60) was examined because it had apparently melted.

The cross section of sample 007-R7-60 is shown in Figure E-205. The microstructure in Area 1 is shown in Figure E-206. The surface coating has been oxidized to a limited extent, and metallic and oxide fragments appear to be trapped in a molten layer covering the intact zircaloy guide tube remnant. The microstructure in Area 2 is shown in Figure E-207. Various metallic melt regions are present.

Figure E-208 shows the results of SEM analysis conducted on this molten material. In addition to (Ag,In,Cd) control material, Fe, Cr, and Ni from the melting of the stainless steel control rod cladding is present, as well as small amounts of  $UO_2$ .

The elemental distribution at Area 1 is shown in Figure E-209, which shows the remnants of a zircaloy guide tube. Various complex melt phases surrounded and interacted with the guide tube remnant.

The interaction of zirconium with indium is illustrated in Figure E-210. Various complex metallic inclusions are present in the Zr-In matrix.



Sample No.	Location		Comments
	Bottom	Top	
N12-R7-1	0	3	Remnant
N12-R7-2	3	7	
N12-R7-2A	0	1/4	Remnant
N12-R7-2B	1/4	1/2	
N12-R7-2C	1/2	3/4	
N12-R7-2D	3/4	3	
N12-R7-2E	3	4	Remnant

P614 CSO-488-03

Figure E-201. Sectioning diagram for control rod N12-R7.



Molten  
(Ag, In, Cd)

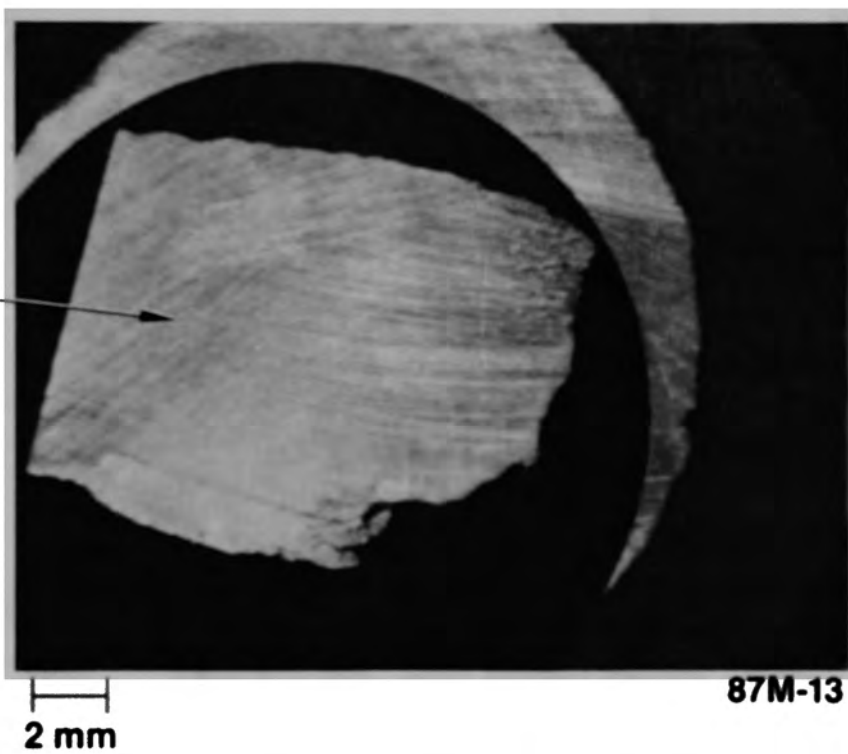


Figure E-202. Molten control rod (N12-R7-10Y).

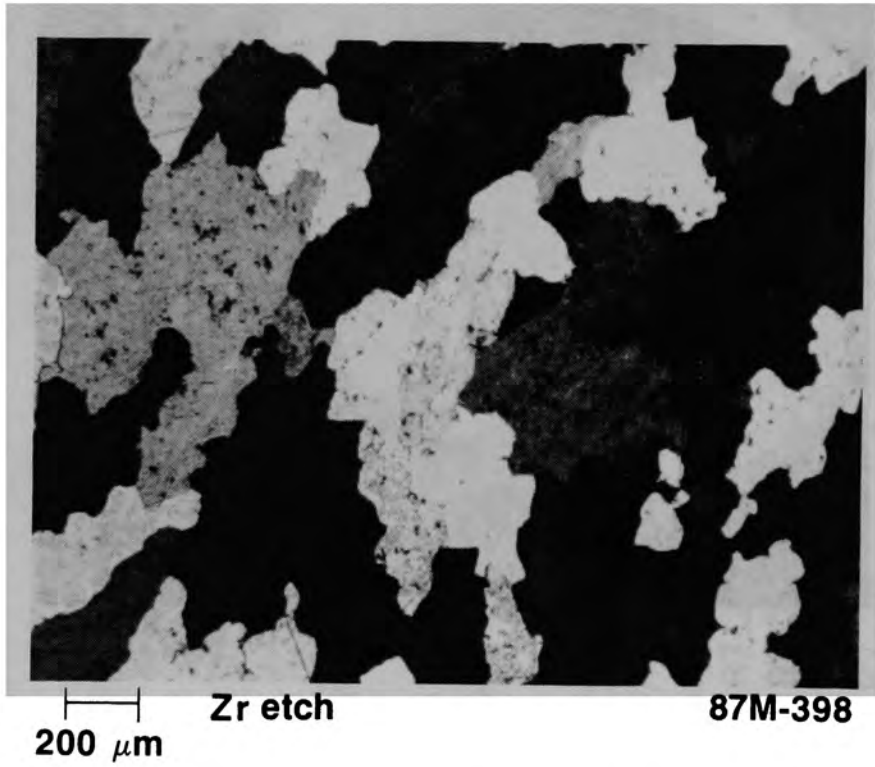
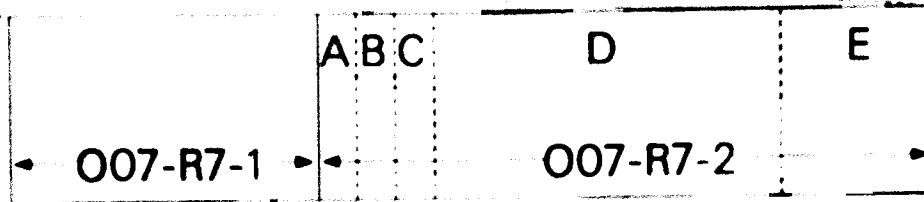
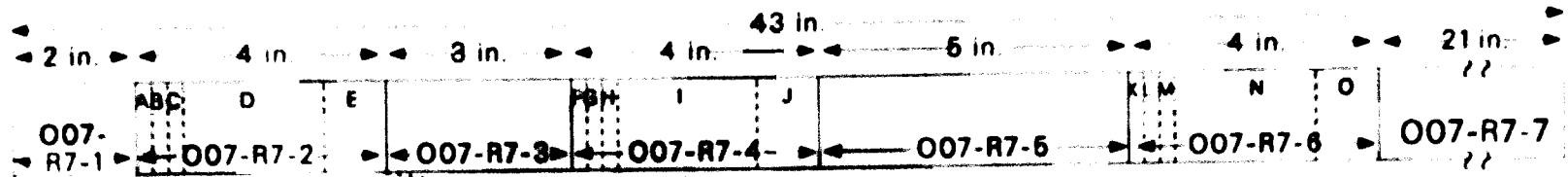


Figure E-203. Molten (Ag,In,Cd) control rod material (N12-R7-10Y).



E-245

Sample No.	Location		Comments
	Bottom	Top	
O07-R3-1	0	2	Remnant
O07-R3-2	2	6	
O07-R7-2A	0	1/4	Remnant
O07-R7-2B	1/4	1/2	
O07-R7-2C	1/2	3/4	
O07-R7-2D	3/4	3	
O07-R7-2E	3	4	Remnant

P614 CSO-488-19

Figure E-204. Sectioning diagram for control rod 007-R7.

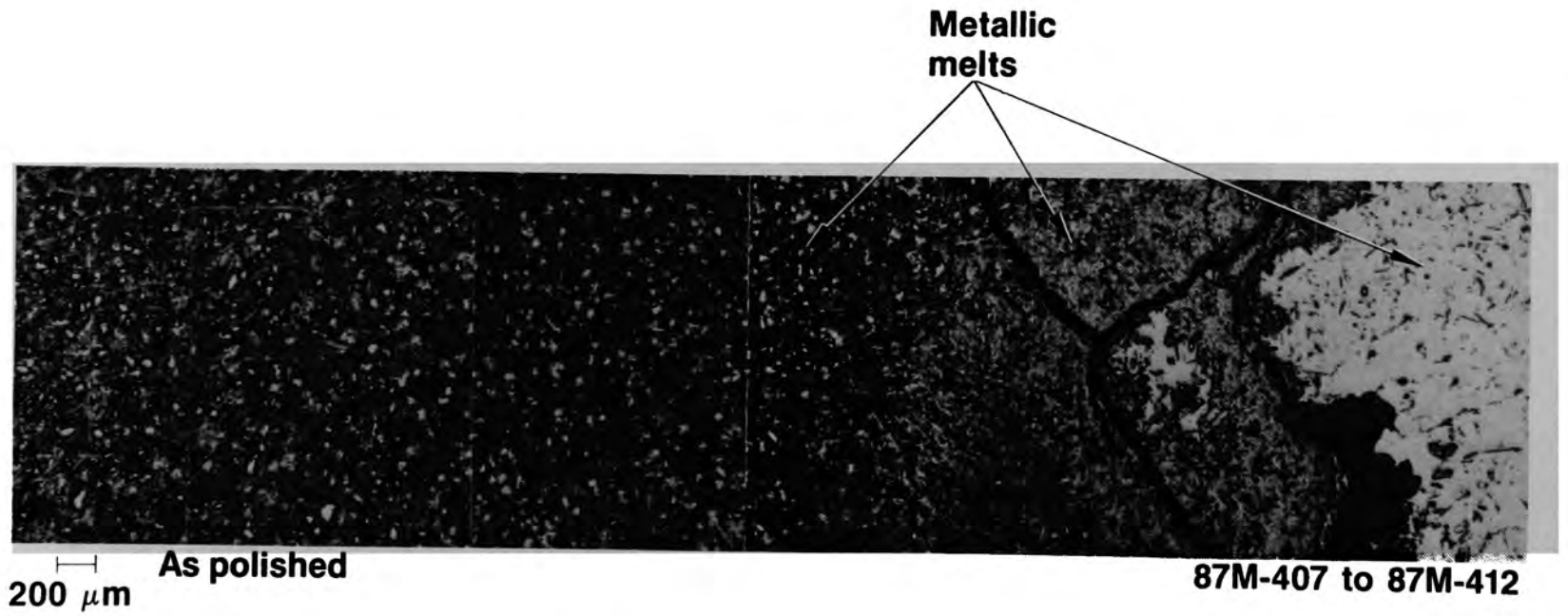


Figure E-207. Microstructure in 007-R7-60 Area 2.

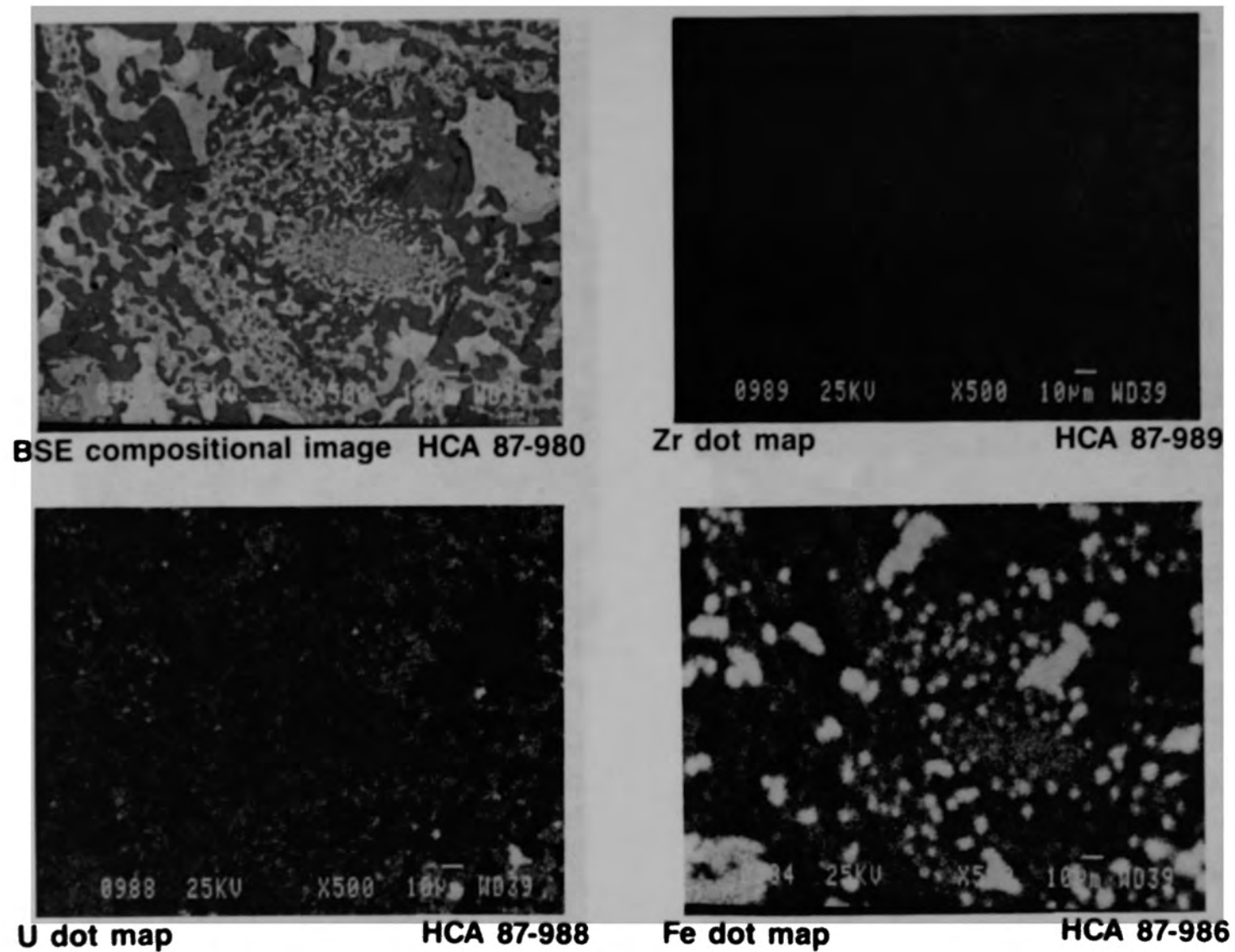


Figure E-208. Material interaction near tip of Ag-In-Cd control rod (007-R7-60).

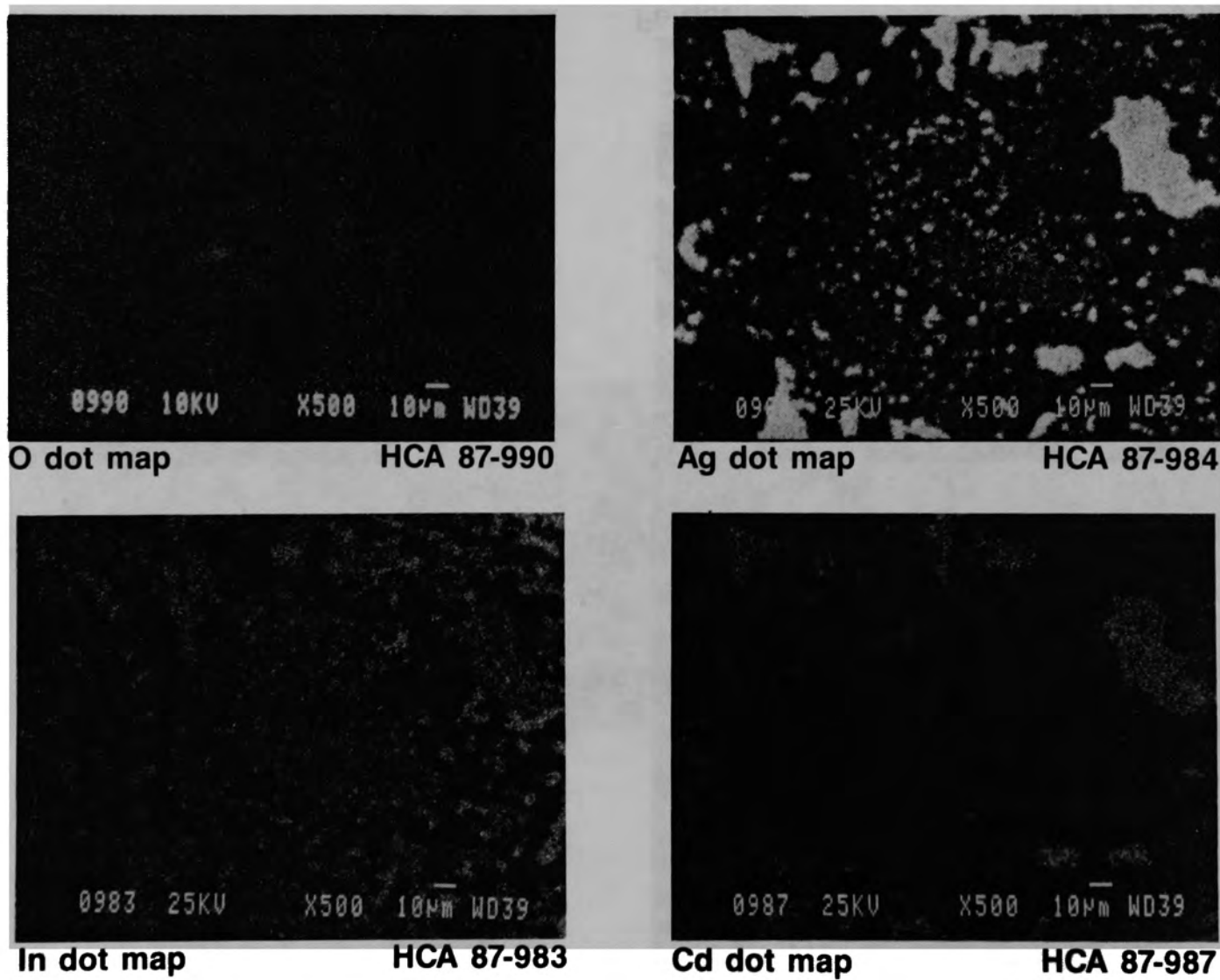


Figure E-208. (Continued)

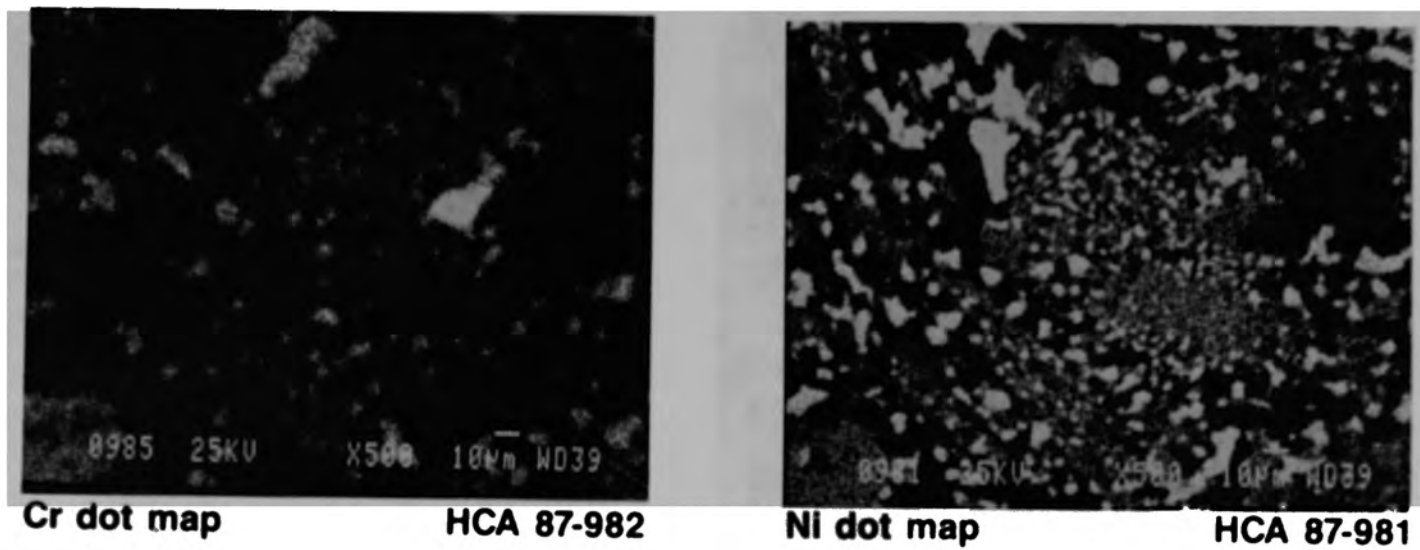


Figure E-208. (Continued)

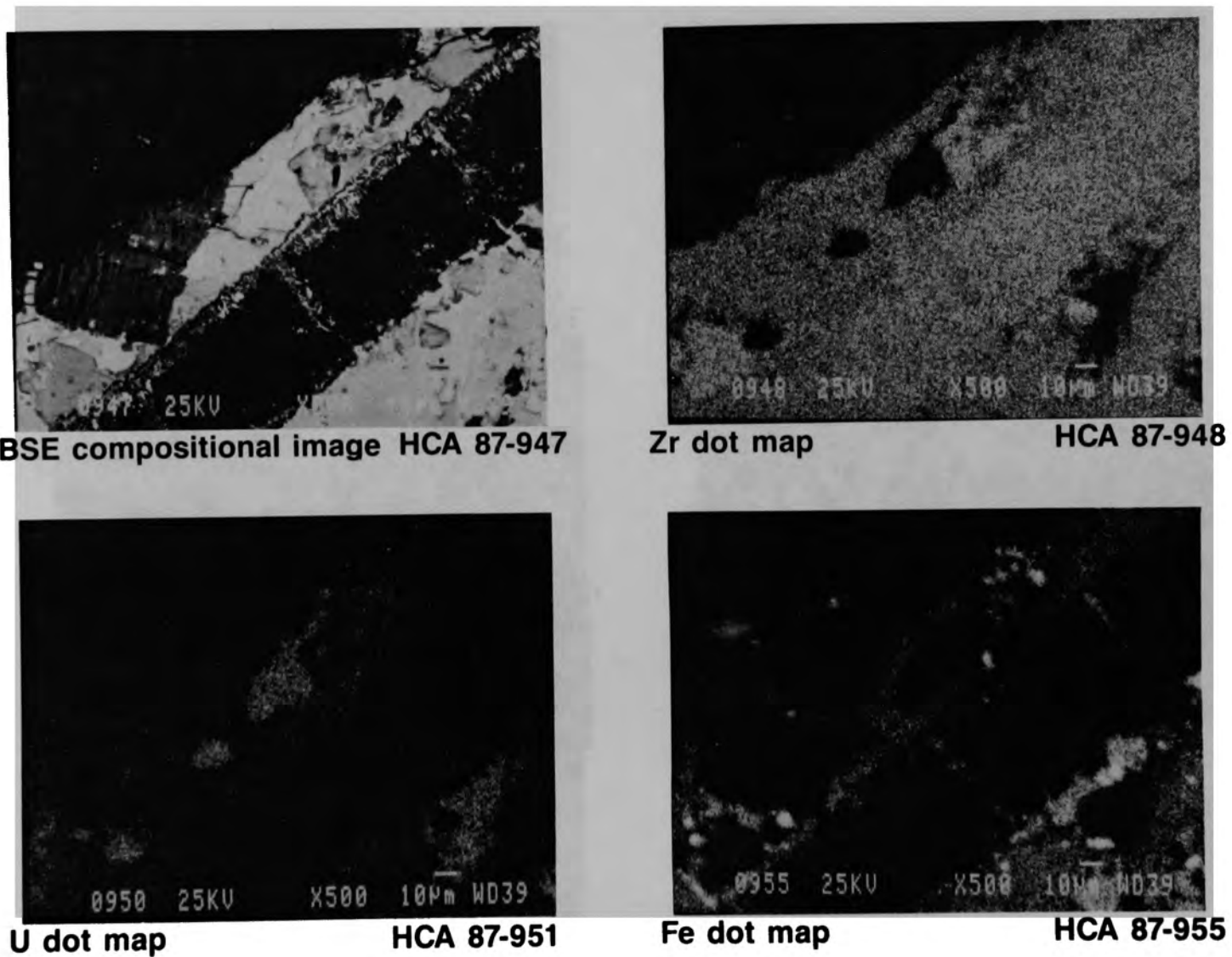


Figure E-209. Surface interaction of Ag-In-Cd control rod (007-R7-60).



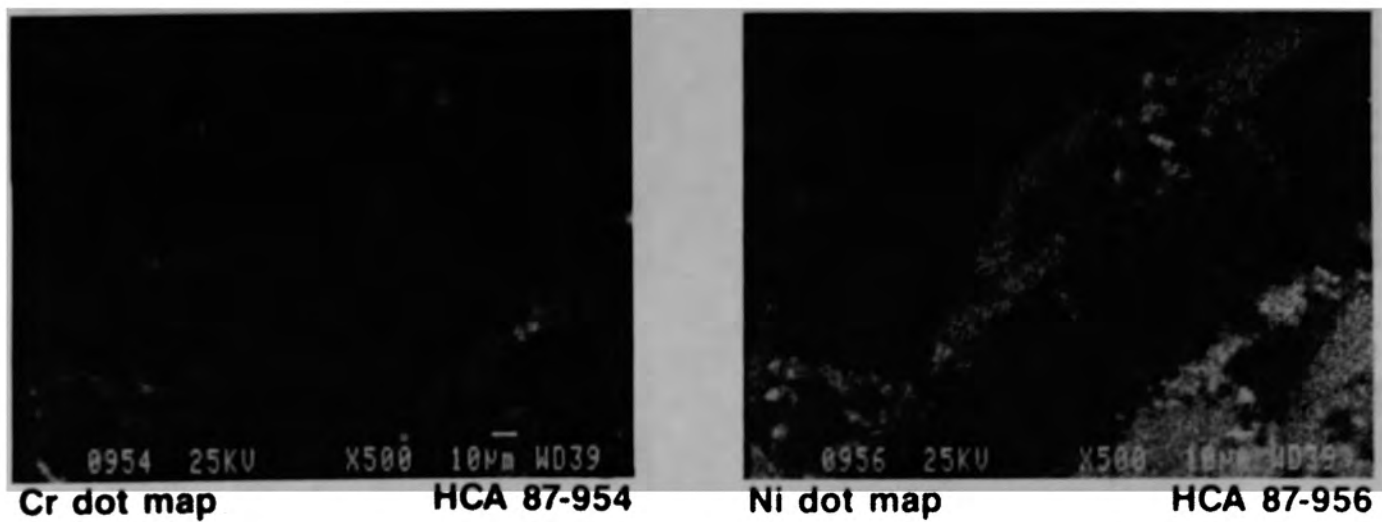
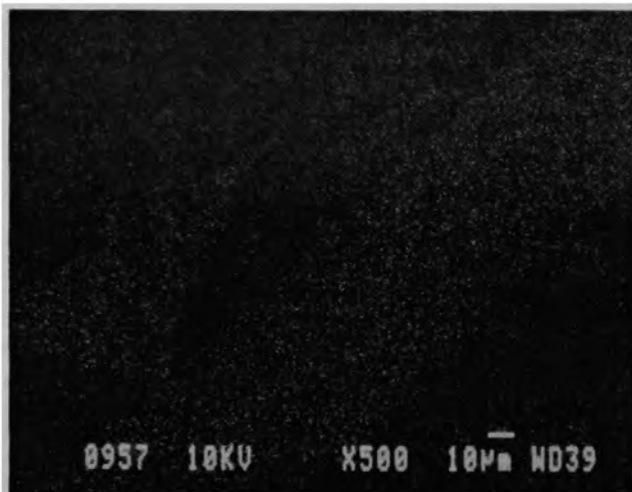


Figure E-209. (Continued)



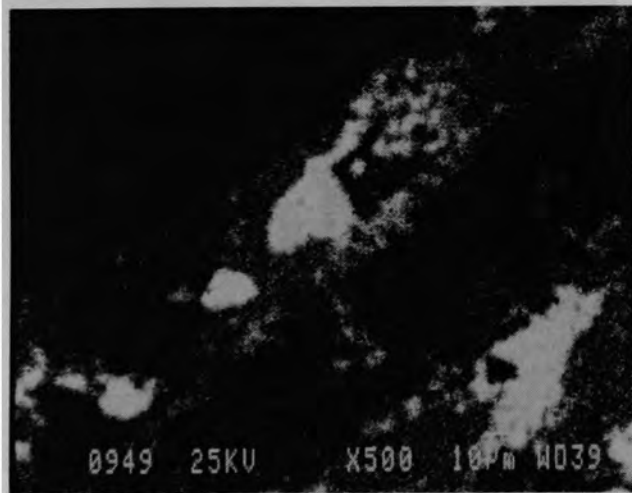
O dot map

HCA 87-957



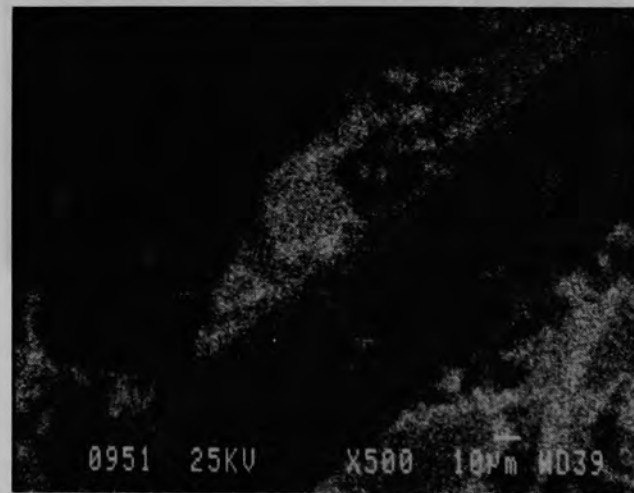
Sn dot map

HCA 87-953



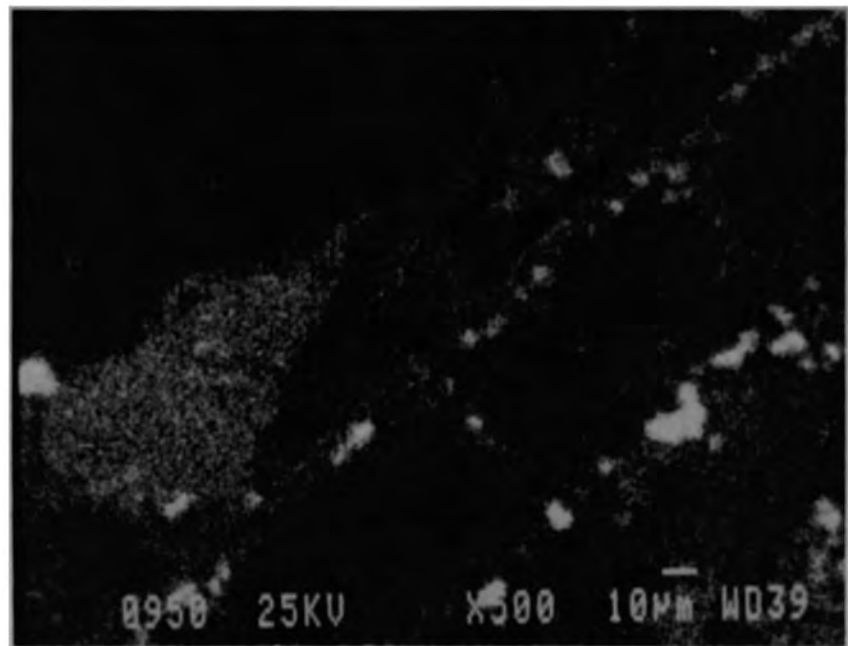
Ag dot map

HCA 87-949



In dot map

HCA 87-952



**Cd dot map**

**HCA 87-950**

Figure E-209. (Continued)

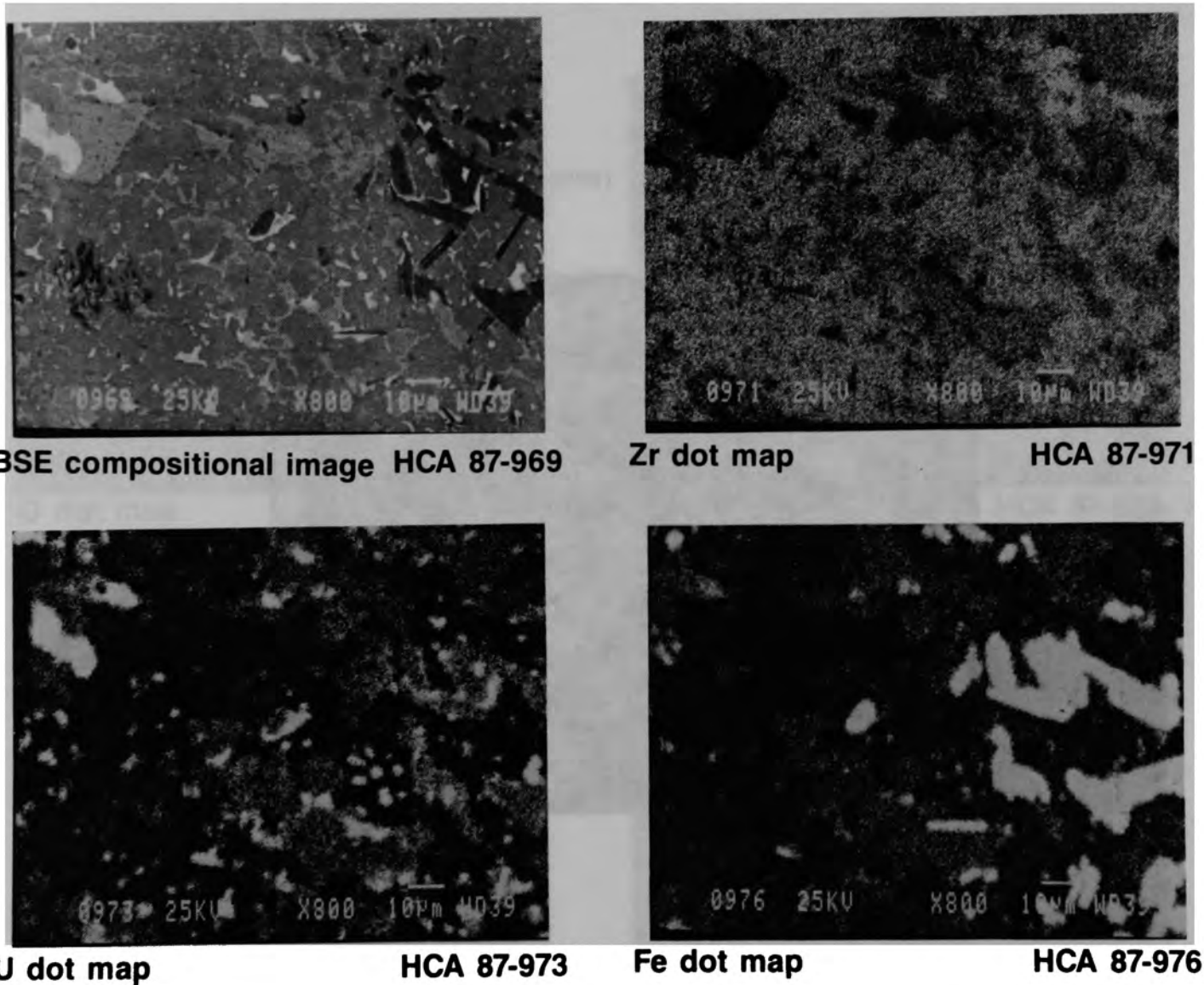
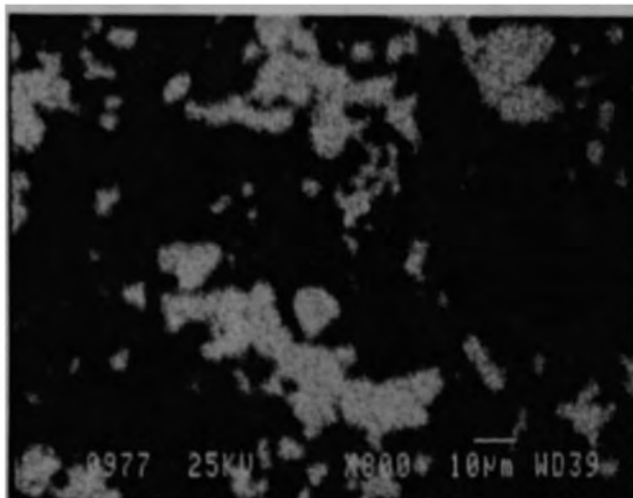


Figure E-210. Interaction zone between core debris and Ag-In-Cd control rod material (007-R7-60).



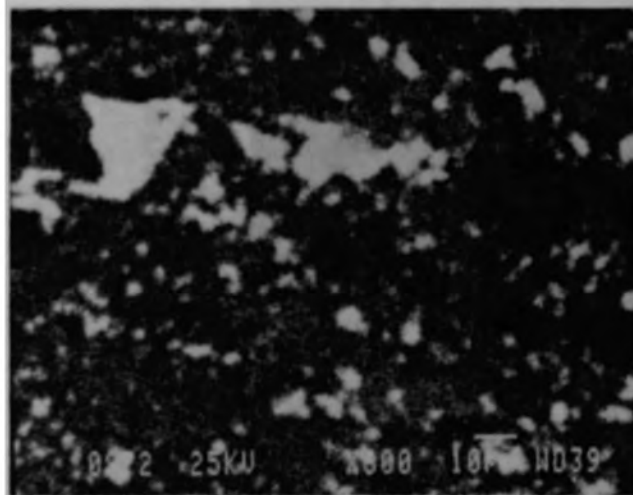
Ni dot map

HCA 87-977



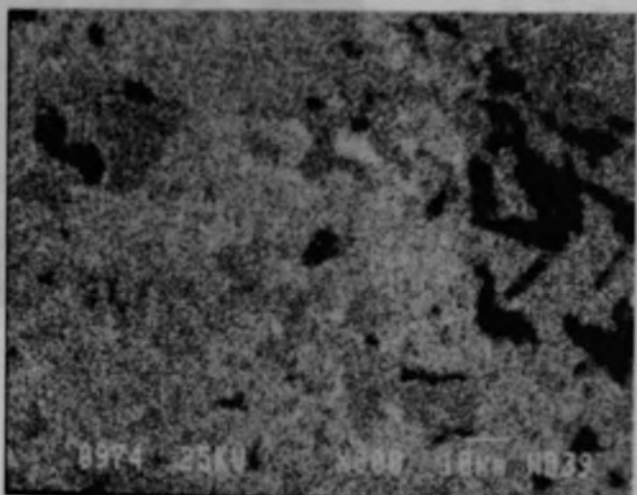
O dot map

HCA 87-978



Ag dot map

HCA 87-972



In dot map

HCA 87-974

Figure E-210. (Continued)

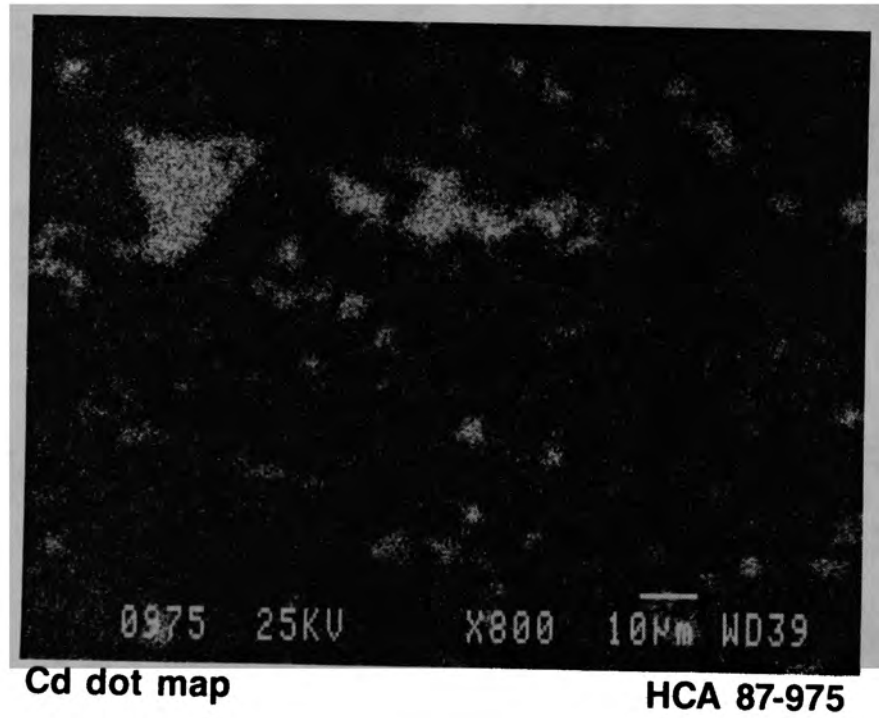


Figure E-210. (Continued)

### N05-R15 Burnable Poison Rod

The sectioning diagram for this rod is shown in Figure E-211. This rod apparently was a burnable poison rod containing boron carbide in alumina. The rod was extensively damaged from the core boring, which is why sample N05-R15-2B was obtained from the center of the rod rather than at the end. However, a sample could not be obtained that contained some of the burnable poison material because it apparently fell out during sample handling.

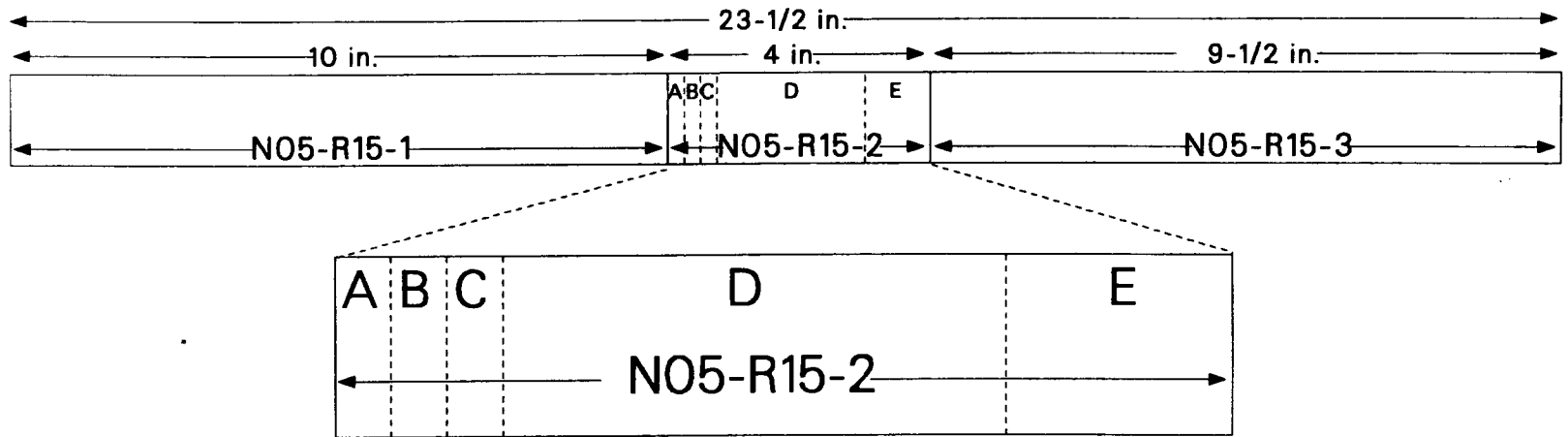
The microstructure of the inner zircaloy cladding is shown in Figures E-212 and E-213. Figure E-212 shows the lack of any hydrides, as determined under bright field conditions. The microstructure in Figure E-213, under polarized light, shows the typical as-fabricated cold-worked microstructure. This indicates that temperatures did not exceed 920 K.

### G08-R3 Instrument Tube

The sectioning diagram for instrument tube G08-R3 is shown in Figure E-214. Samples G08-R3-2, G08-R3-4, and G08-R3-6 were all subdivided and examined in a similar manner, and consequently the detailed sectioning and examination plan is only shown for sample G08-R3-2. All the metallographic samples were very similar, and hence only representative photographs will be presented and discussed.

The cross section of sample G08-R3-4H, taken from the middle of the rod, is shown in Figure E-215. The outer zircaloy guide tube was nicked in one place as a result of the core boring operation.

The zircaloy guide tube had experienced some minor hydriding, as shown in Figure E-216. The structure of the material inside the instrument tube is shown in Figures E-217 and E-218.



E-260

<u>Sample No.</u>	<u>Location</u>		<u>Comments</u>
	<u>Bottom</u>	<u>Top</u>	
N05-R15-1	0	10	Remnant
N05-R15-2	10	14	
N05-R15-2A	0	1/4	Remnant
N05-R15-2B	1/4	1/2	Met
N05-R15-2C	1/2	3/4	Remnant
N05-R15-2D	3/4	3	CSNI
N05-R15-2E	3	4	Rad chemistry

P614 CSO-488-04

Figure E-211. Sectioning diagram for burnable poison rod N05-R15.



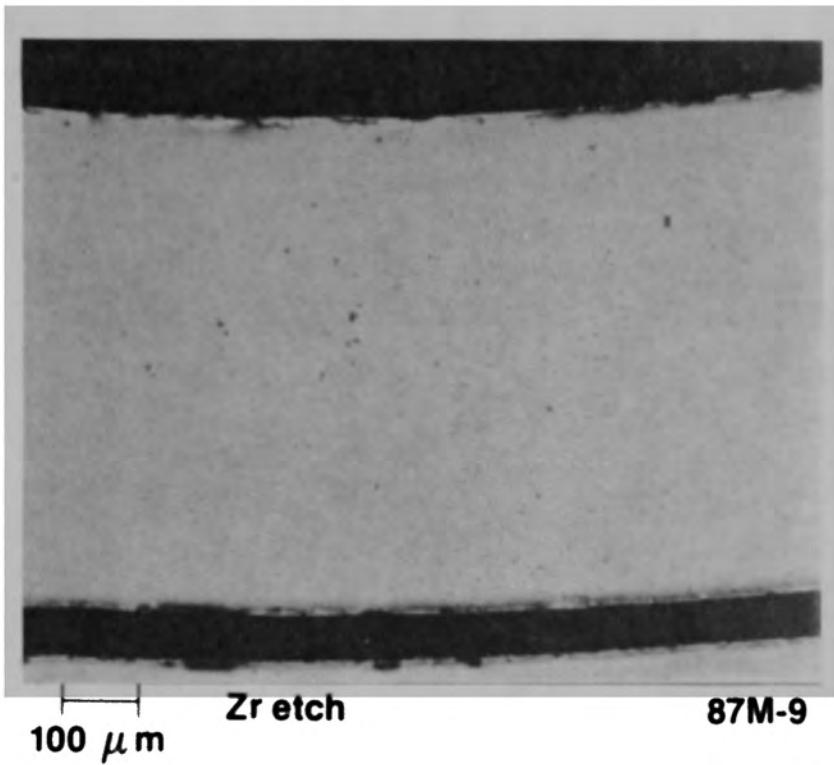
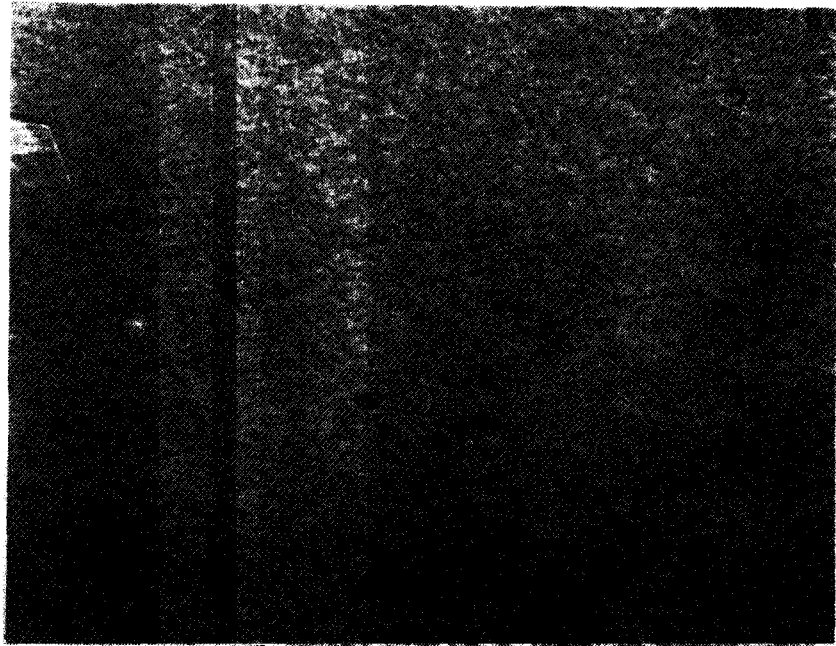


Figure E-212. Typical microstructure of inside tube of N05 burnable poison rod under bright field conditions (N05-R15-2B).

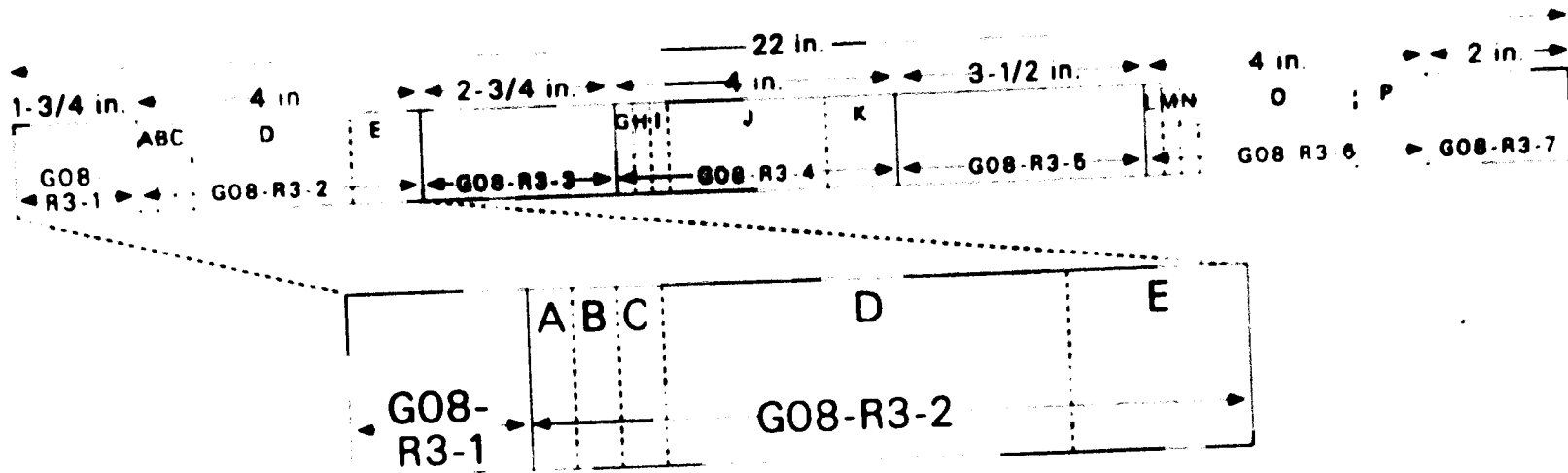


50  $\mu\text{m}$

Zr etch

87M-11

Figure E-213. Microstructure of inner tube of N05 burnable poison rod under polarized light conditions (N05-R15-2B).



E-263

Sample No.	Location		Comments
	Bottom	Top	
G08-R3-1	3/4	1-3/4	Remnant
G08-R3-2	1-3/4	5-3/4	
G08-R3-2A	0	1/4	Remnant
G08-R3-2B	1/4	1/2	Met
G08-R3-2C	1/2	3/4	Remnant
G08-R3-2D	3/4	3	CSNI sample
G08-R3-2E	3	4	Rad chemistry

P614 CSO-488-18

Figure E-214. Sectioning diagram for instrument tube G08-R3.

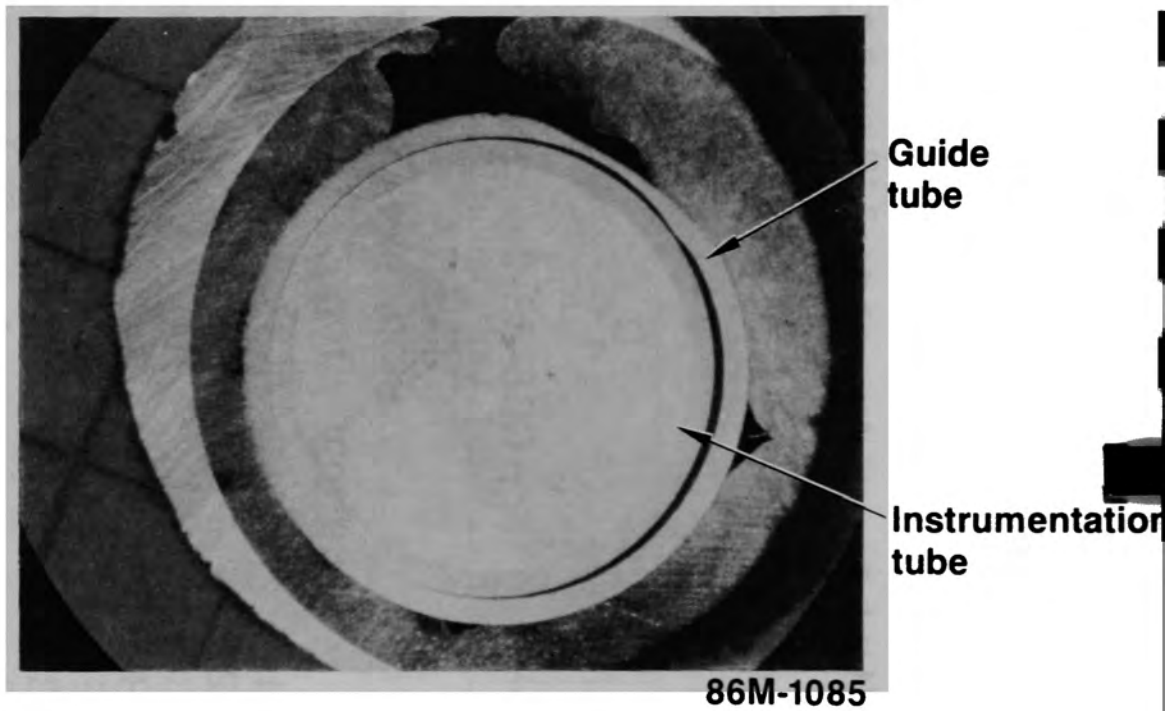


Figure E-215. Instrument tube cross section (G08-R3-4H).

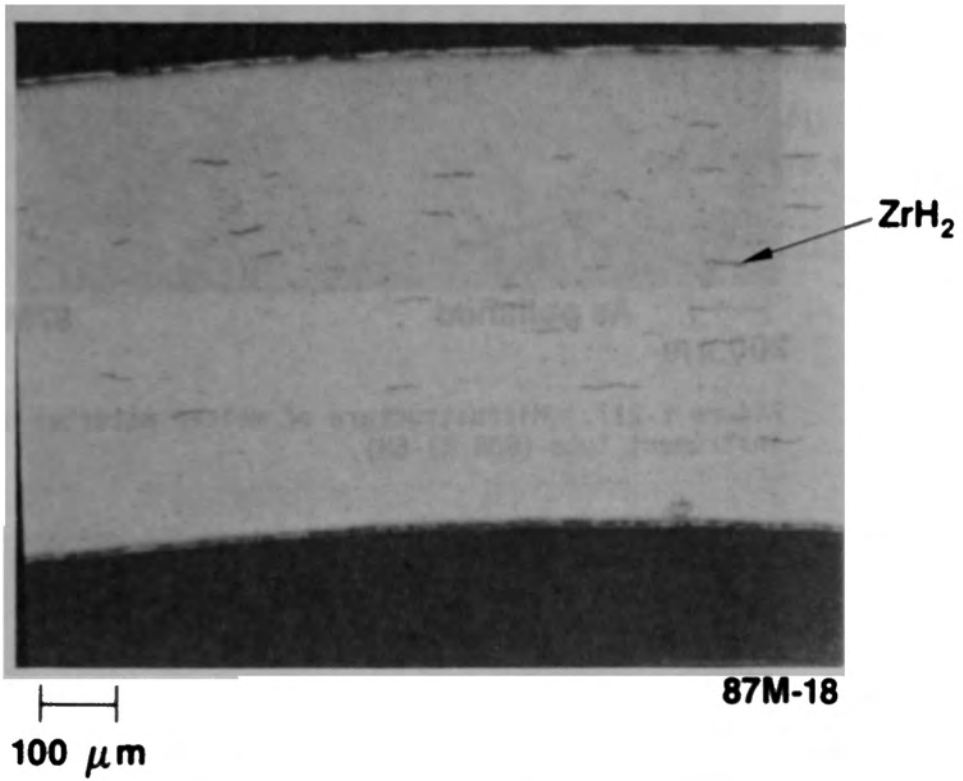
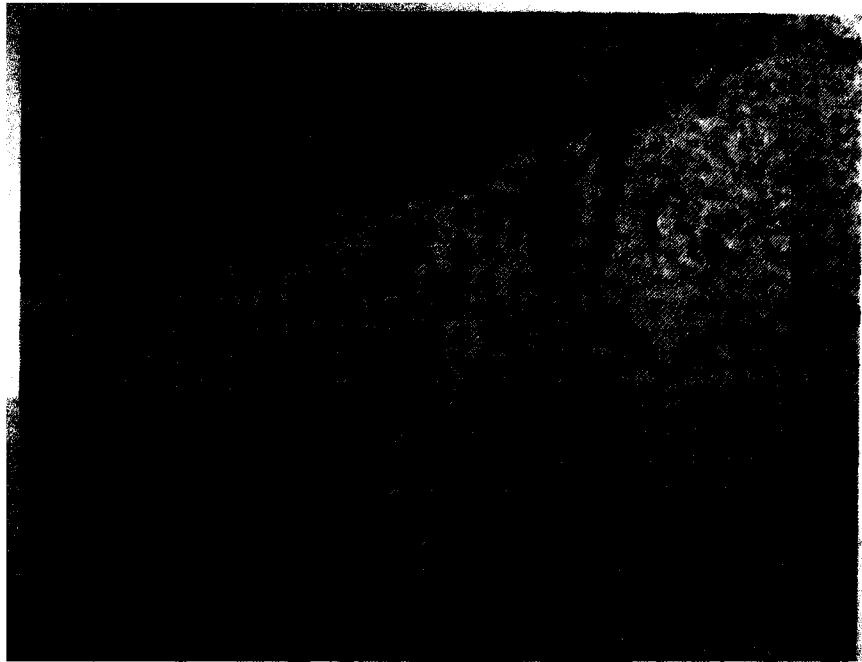


Figure E-216. Hydrided guide tube of instrument tube (G08-R3-6M).



—|—| **As polished**  
200  $\mu\text{m}$

**87M-15**

Figure E-217. Microstructure of molten material in instrument tube (G08-R3-6M).



—|—| **As polished**  
20  $\mu\text{m}$

**87M-72**

Figure E-218. Magnified view of molten material in instrument tube (G08-R3-2B).

The backscattered electron image of a cross section taken near the top of the rod is shown in Figure E-219. The examination locations for the SEM are also shown in this figure. The material inside the instrument tube contains numerous cracks.

The distribution of elements inside the tube is shown in Figure E-220. Previously molten fuel, control material, and structural materials are present.

The distribution of elements in Area C, at the interface between the zircaloy cladding and the molten debris, is shown in Figure E-221. The material is similar to that found in Area B. These data indicate that the instrument tubes provided paths for relocating material.

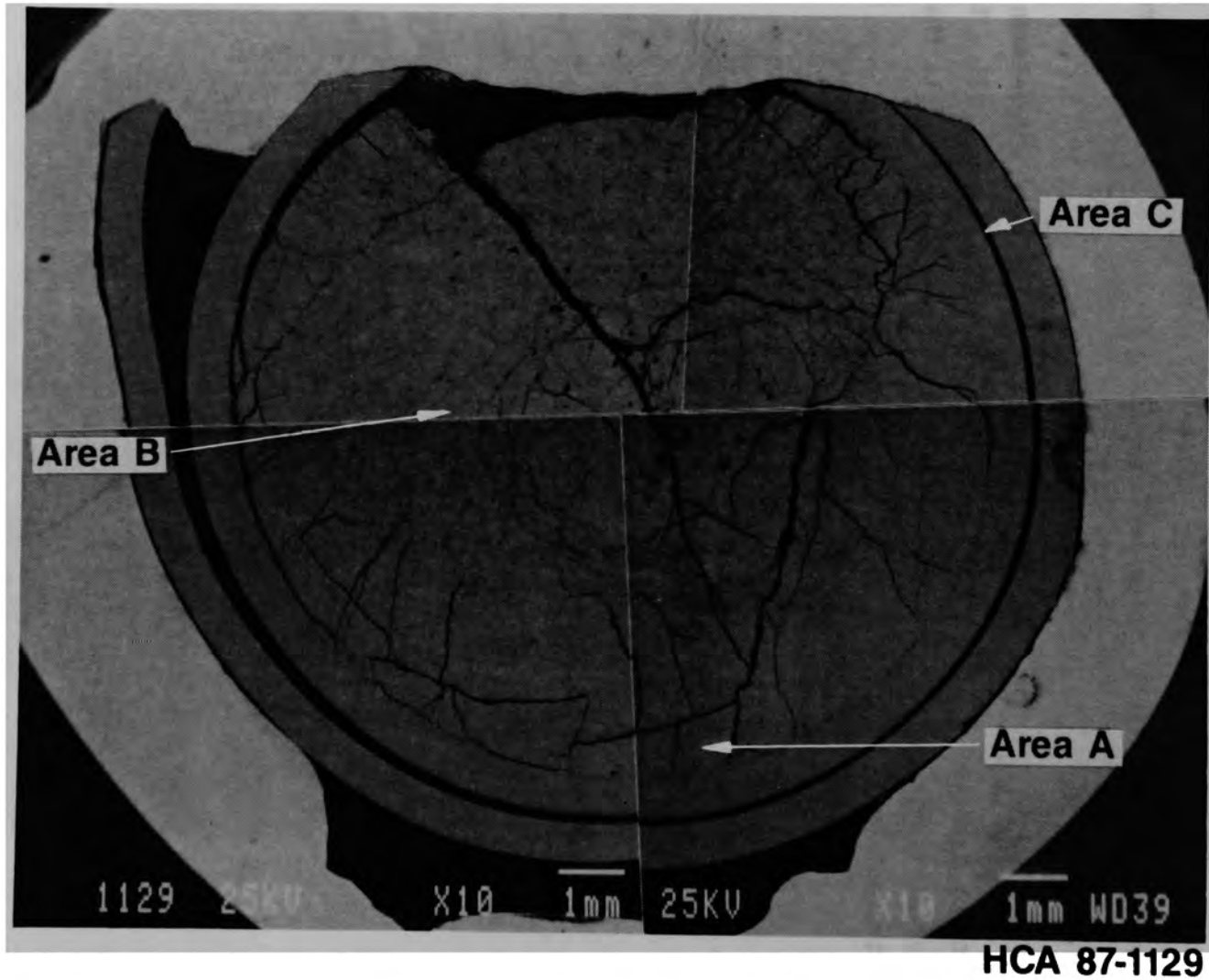
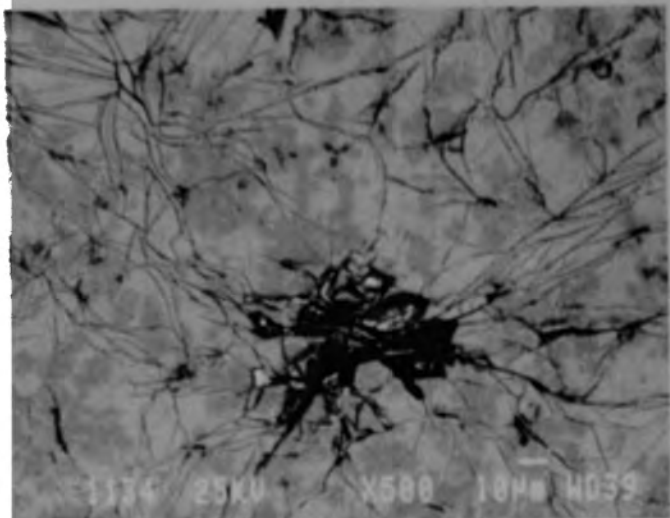


Figure E-219. SEM examination locations in instrument tube G08-R3.

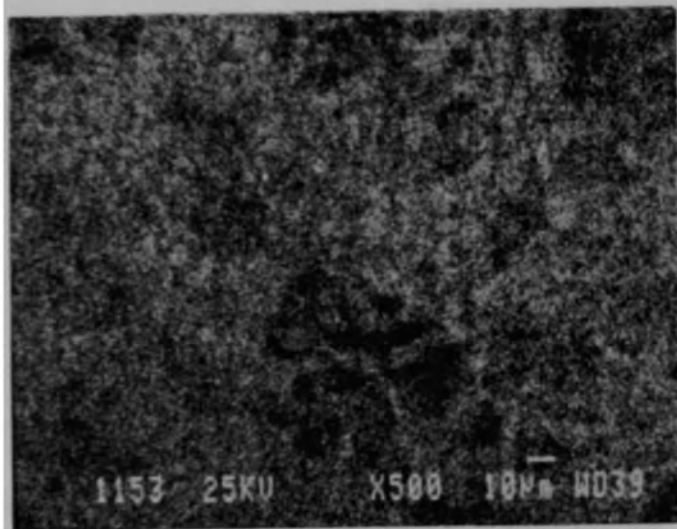




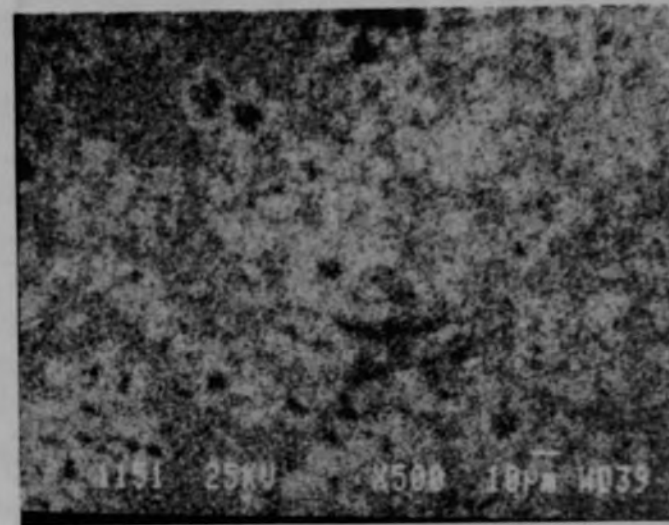
BSE compositional image HCA 87-1134



Zr dot map HCA 87-1158

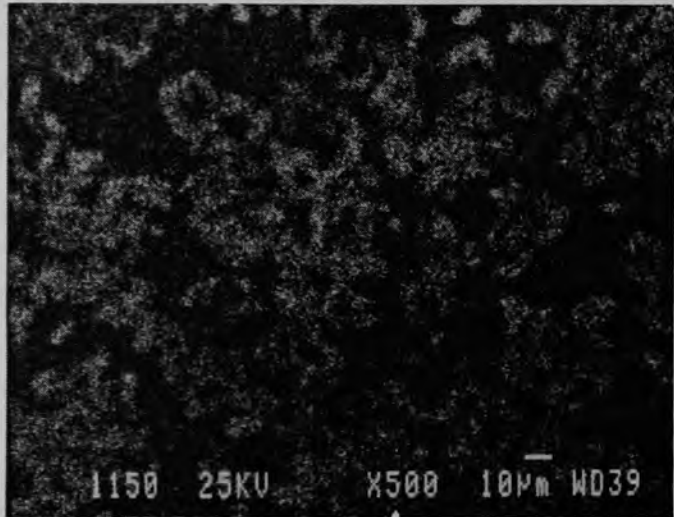


U dot map HCA 87-1153



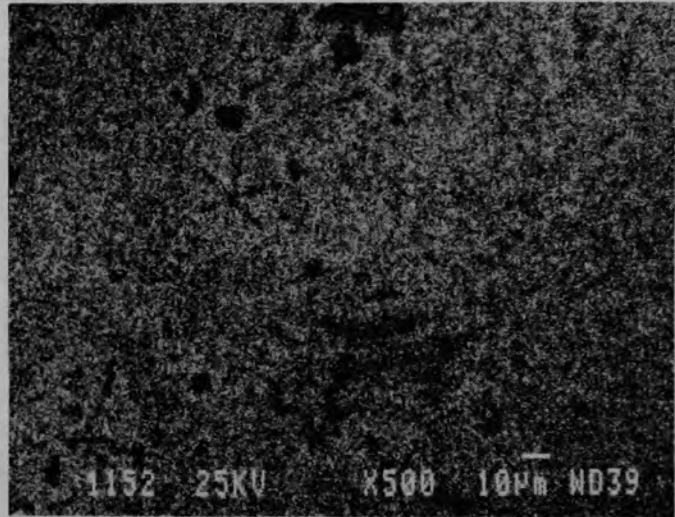
Fe dot map HCA 87-1151

Figure E-220. Material inside instrument tube (G08-R3-6M Area B).



Cr dot map

HCA 87-1150



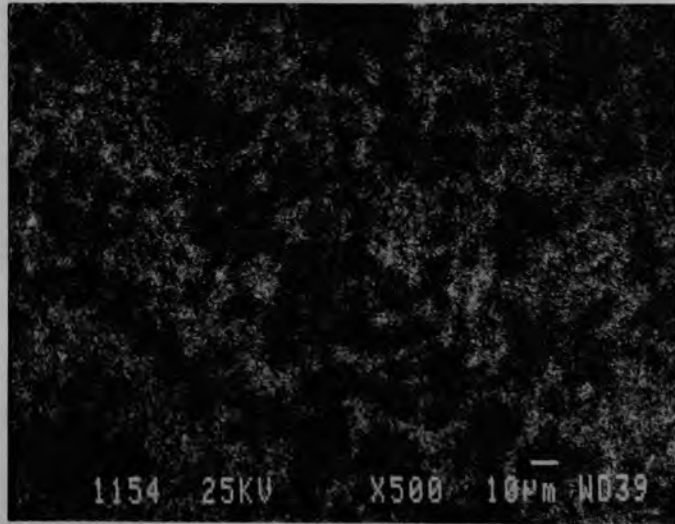
Ni dot map

HCA 87-1152



O dot map

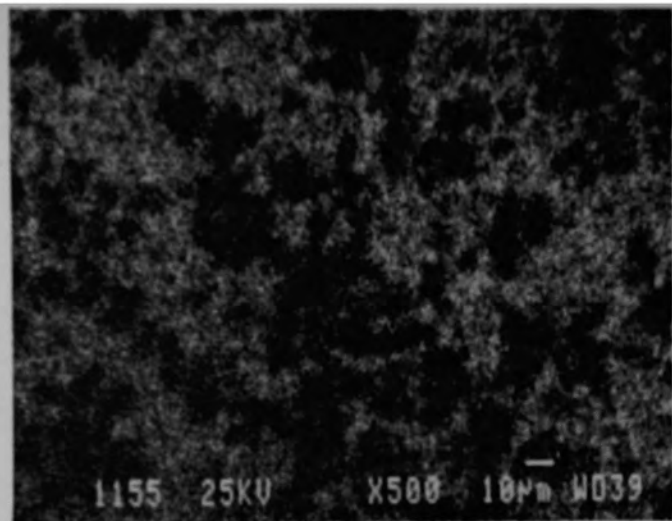
HCA 87-1149



Sn dot map

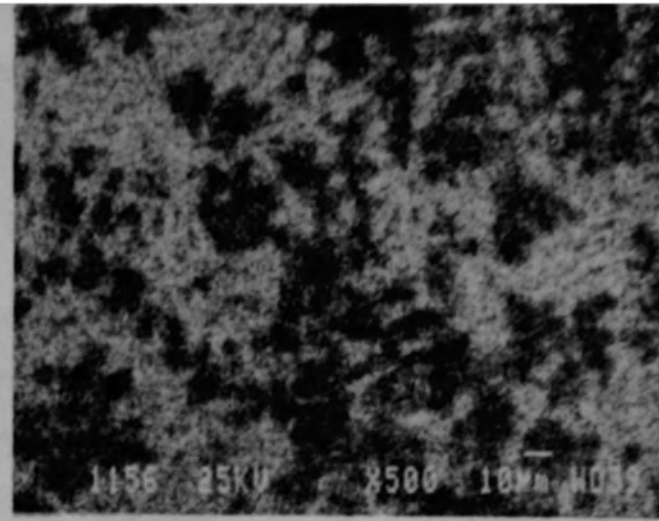
HCA 87-1154

Figure E-220. (Continued)



In dot map

HCA 87-1155



Ag dot map

HCA 87-1156



Cd dot map

HCA 87-1157

Figure E-220. (Continued)

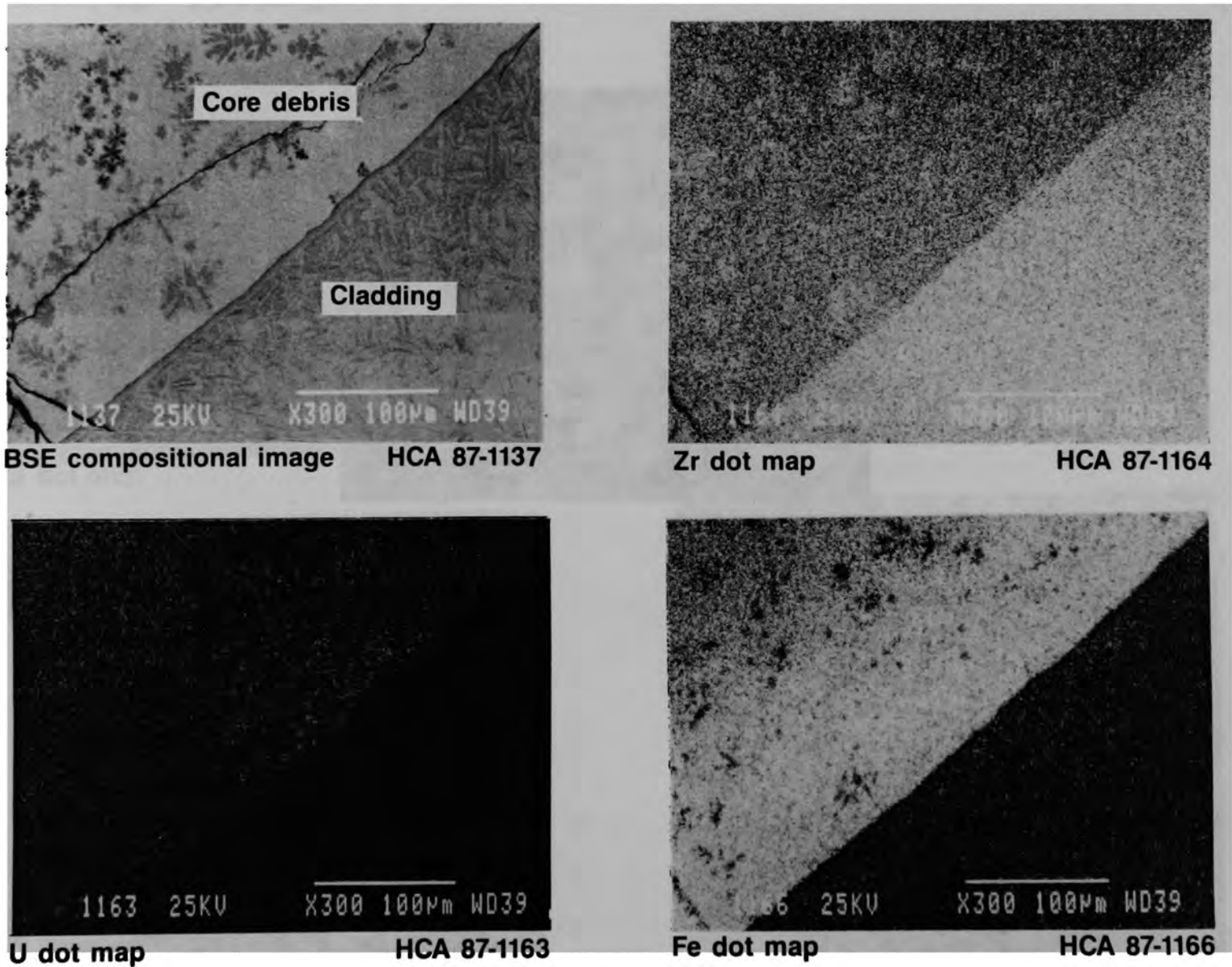


Figure E-221. Interaction at cladding/core debris interface (G08-R3-6M Area C).

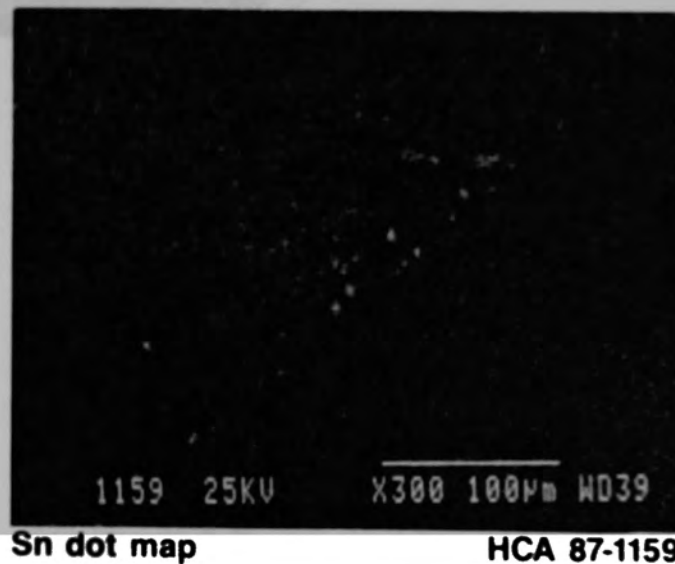
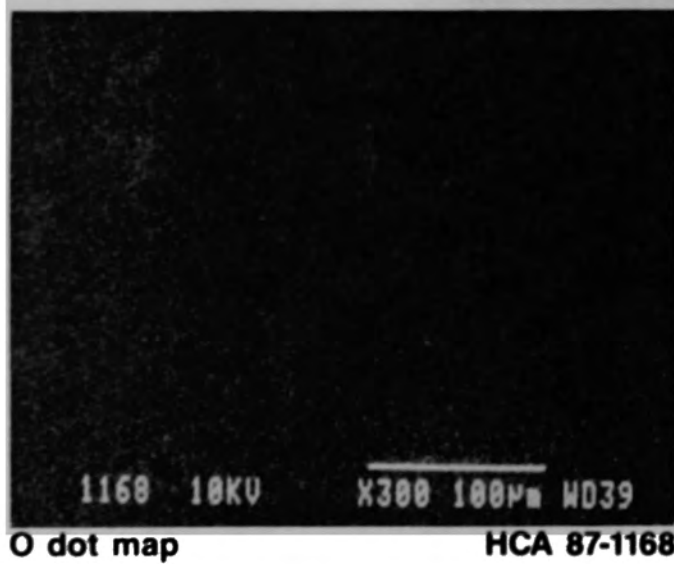
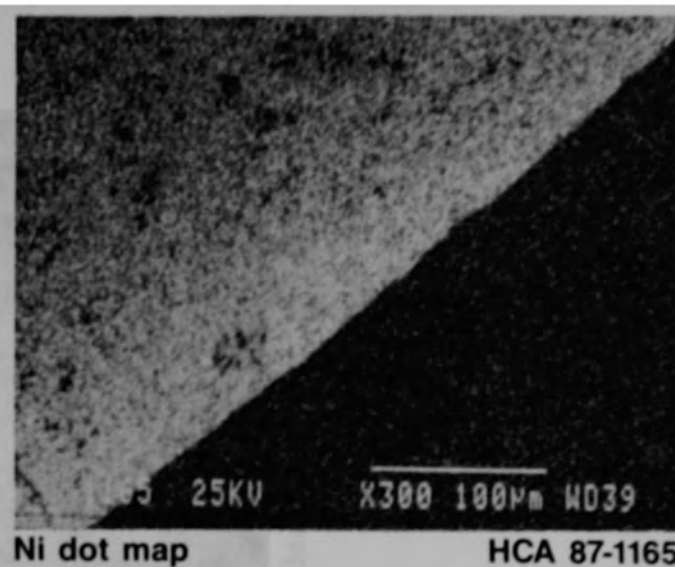
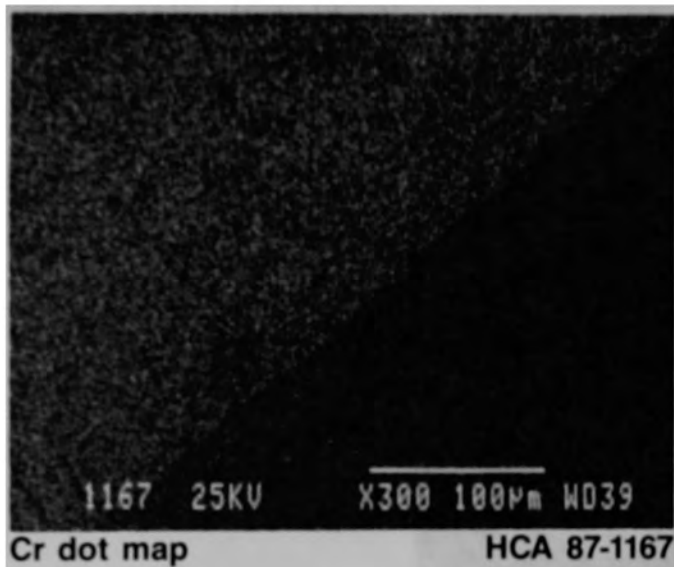


Figure E-221. (Continued)

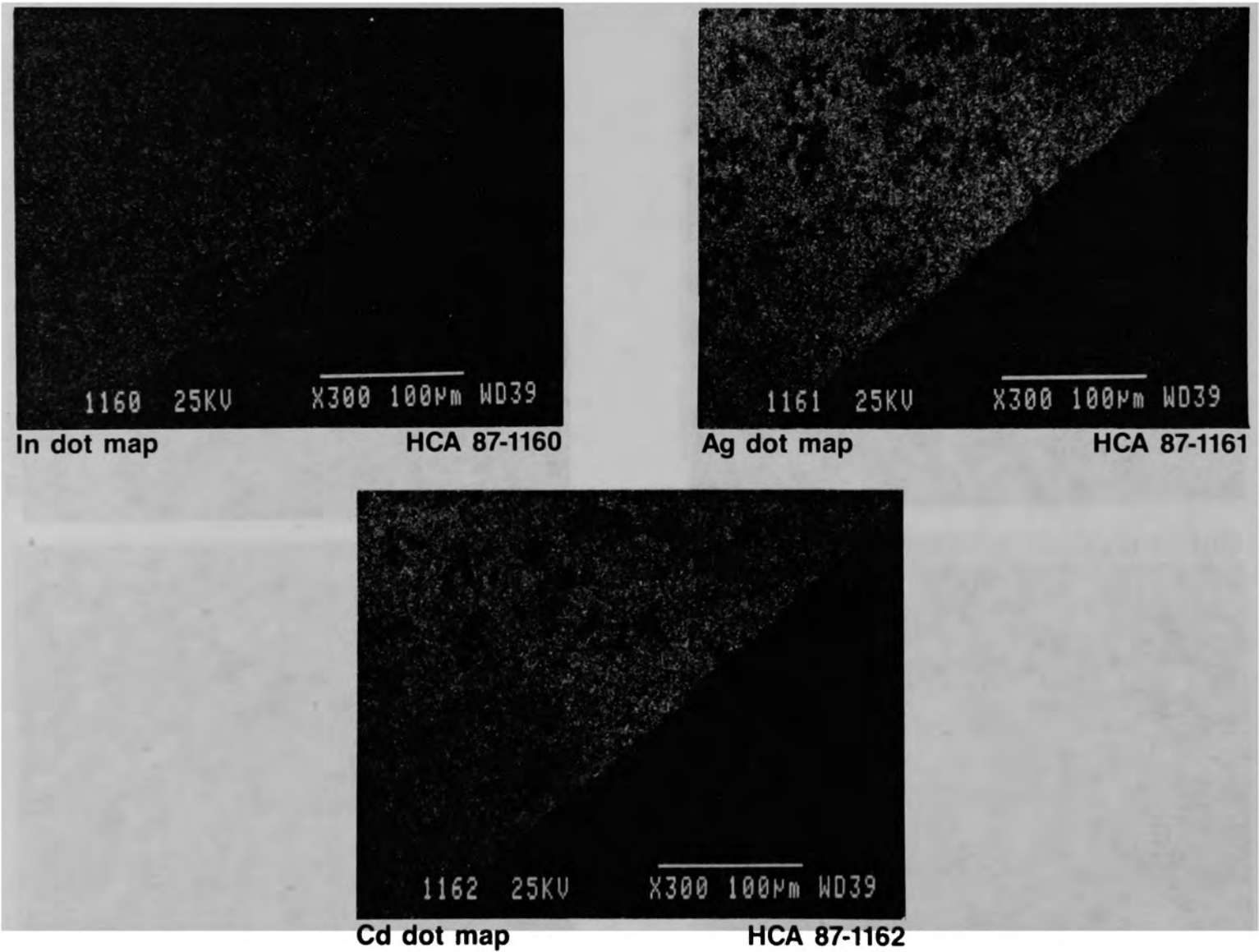


Figure E-221. (Continued)

APPENDIX F

BETA-GAMMA AUTORADIOGRAPHY





## APPENDIX F

### BETA-GAMMA AUTORADIOGRAPHY

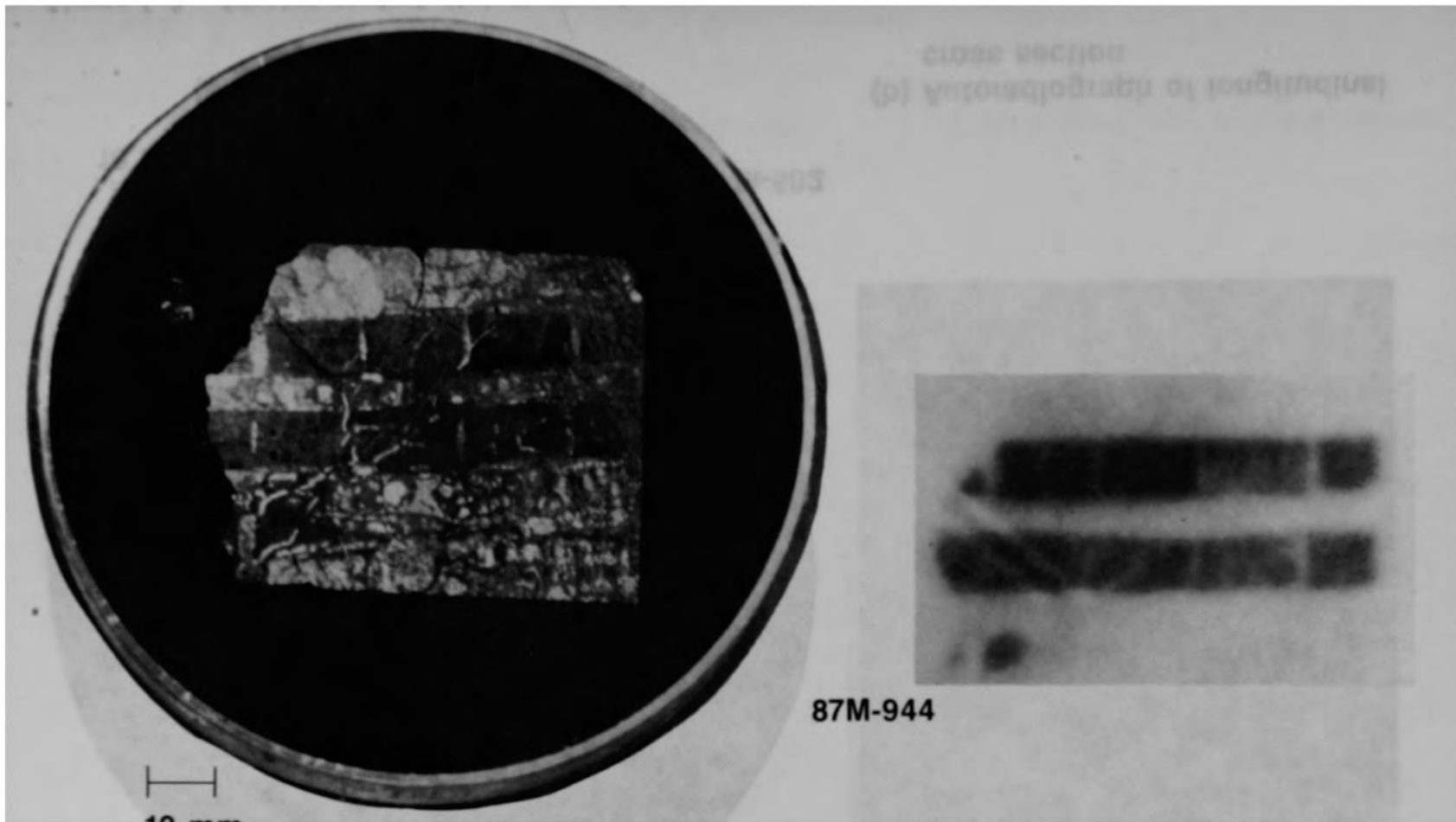
Beta-gamma autoradiographs were obtained for each of the samples to be examined by the scanning electron microscope (SEM) in order to determine the distribution of the fission products between the ceramic and metallic phases, and to ascertain any special features or locations that would warrant more detailed SEM examinations. Although autoradiographs were obtained for all 22 SEM samples, not all will be discussed because those from the rod stubs and small rocks did not show anything significantly different from those autoradiographs discussed below.

The autoradiographs from the lower crust and the upper crust of the central core bore K09 are shown respectively in Figures F-1 and F-2. In Figure F-1, the autoradiograph shows that the radioactivity is concentrated in the fuel, rather than in the metallics around the fuel. In contrast, the autoradiograph of the upper crust in Figure F-2 shows that the radioactivity is concentrated in the metallic inclusions rather than in the ceramic matrix. The primary difference between the two crusts is that the ceramic phase in the upper crust had been molten, which allowed the fission products that have the propensity to be in the metallic phase to be scavenged by the metallic phase. The lower crust fuel had not been previously molten, so that the scavenging process did not occur.

Figure F-3 shows an autoradiograph of upper crust sample G08-P11. This autoradiograph shows various radioactivity levels in both the fuel pellets and the metallic melt.

The autoradiographs of four cross sections from upper, peripheral, and lower crusts are compared with photomicrographs of the cross sections in Figure F-4. The sections K09-P1-G and D08-P2-A2 are from the lower crust that contained fuel pellets surrounded with prior-molten metallic debris. The radioactivity in these two cross sections is associated with the fuel. The radioactivity in upper crust sample D08-P3 is associated with the ceramic melt, and the radioactivity in peripheral crust sample G12-P1-D3 is also associated with the ceramic melt.

Figure F-5 shows the autoradiographs of some samples from the consolidated core region, compared with photomicrographs of their cross sections. The section from N05-P1-D contains a fuel rod remnant surrounded by metallic melt. The autoradiograph indicates that, in this case, the fuel pellet as well as the metallic materials are radioactive. Particle 007-P6 is metallic, and particle G08-P6-B is ceramic. The autoradiographs for sections from these two particles show that the metallic particle is more radioactive than the ceramic particle. The particle G08-P10-A contains metallic phases distributed in a ceramic matrix, and the autoradiograph shows that the metallic phase is more radioactive than the ceramic phase. Because all four of these sections were exposed for the same length of time, the degree of blackness indicates the relative activity of each specimen. For the metallics in each particle, the blackness is about the same for all cross sections.

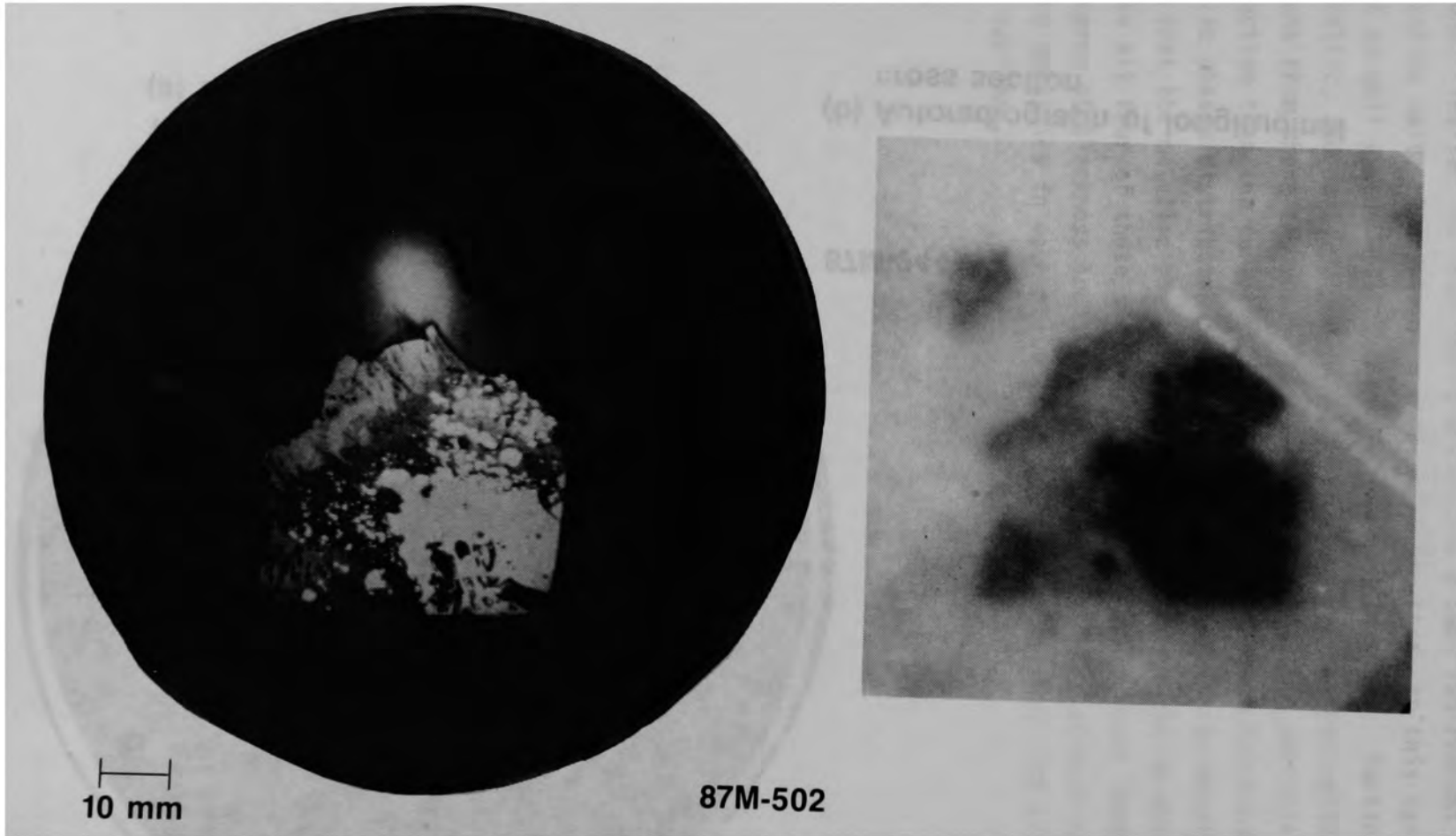


10 mm  
(a) Longitudinal cross section

87M-944  
(b) Autoradiograph of longitudinal cross section

Figure F-1. Fission product distribution in lower crust sample from core bore K09 (K09-P1-D).

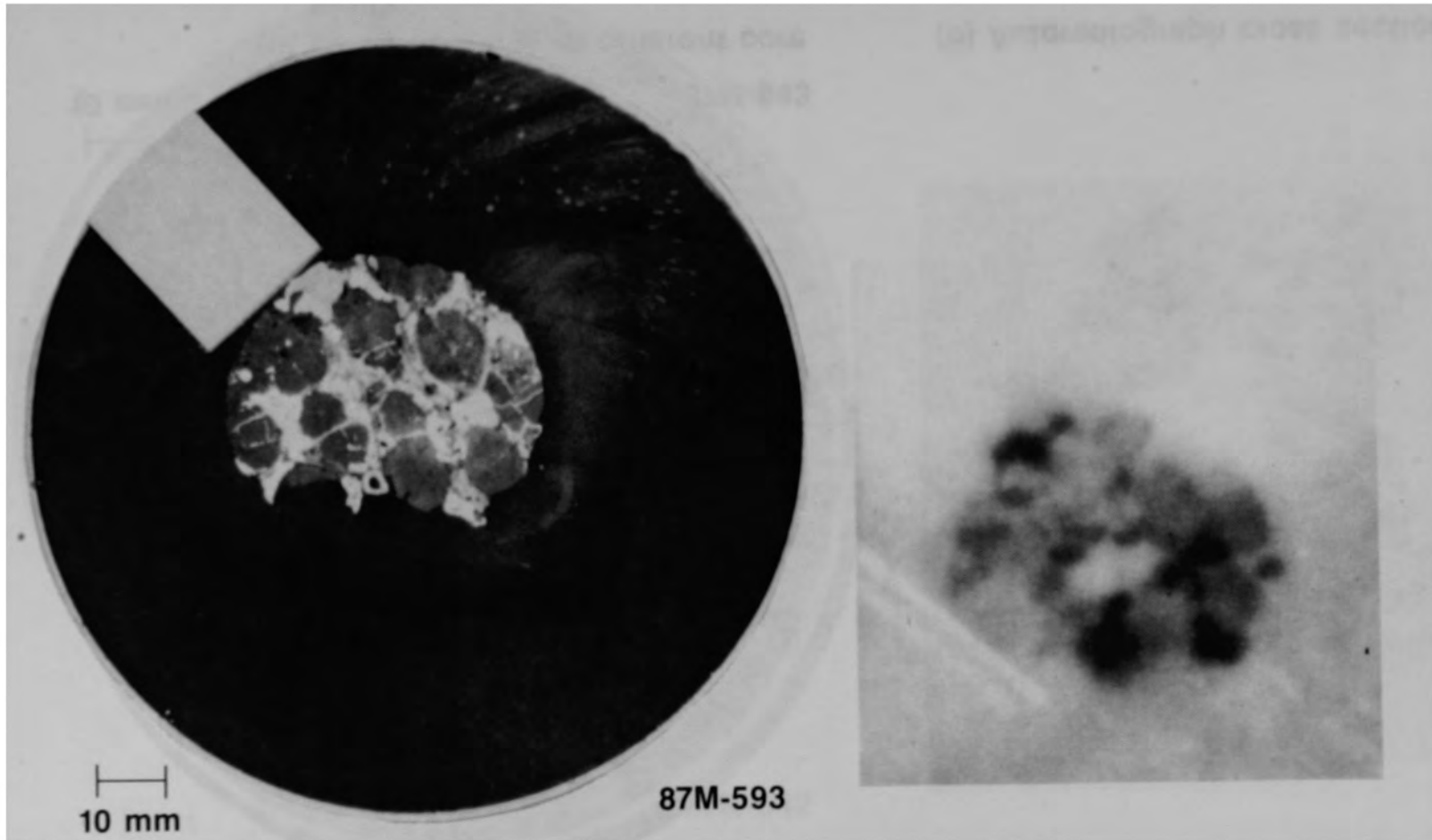
F-6



(a) Longitudinal cross section

(b) Autoradiograph of longitudinal cross section

Figure F-2. Fission product distribution in upper crust sample from K09 core bore (K09-P2-D).



(a) Transverse cross section

(b) Autoradiograph of transverse cross section

Figure F-3. Fission product distribution in upper crust sample from G08 core bore (G08-P11-C).

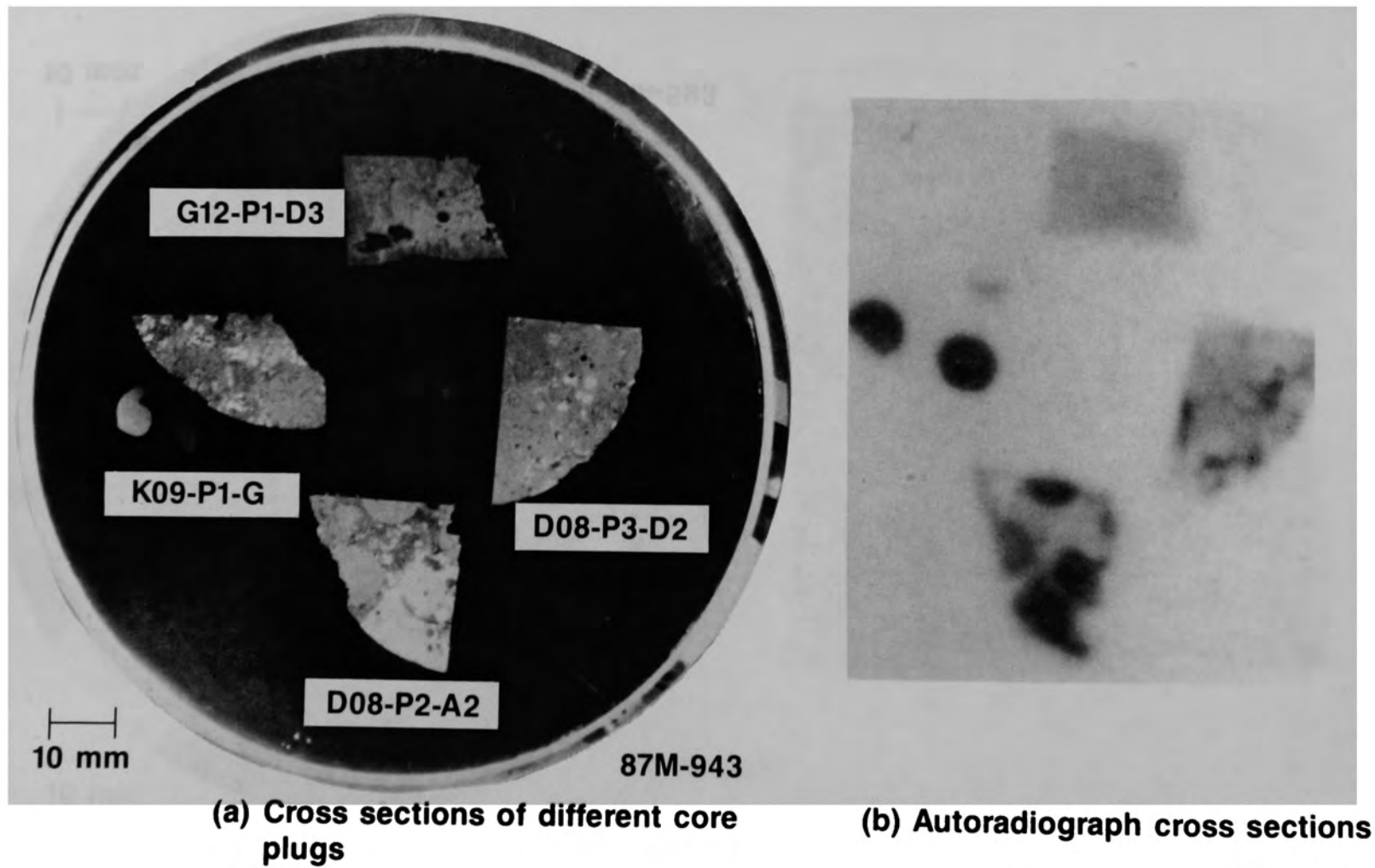
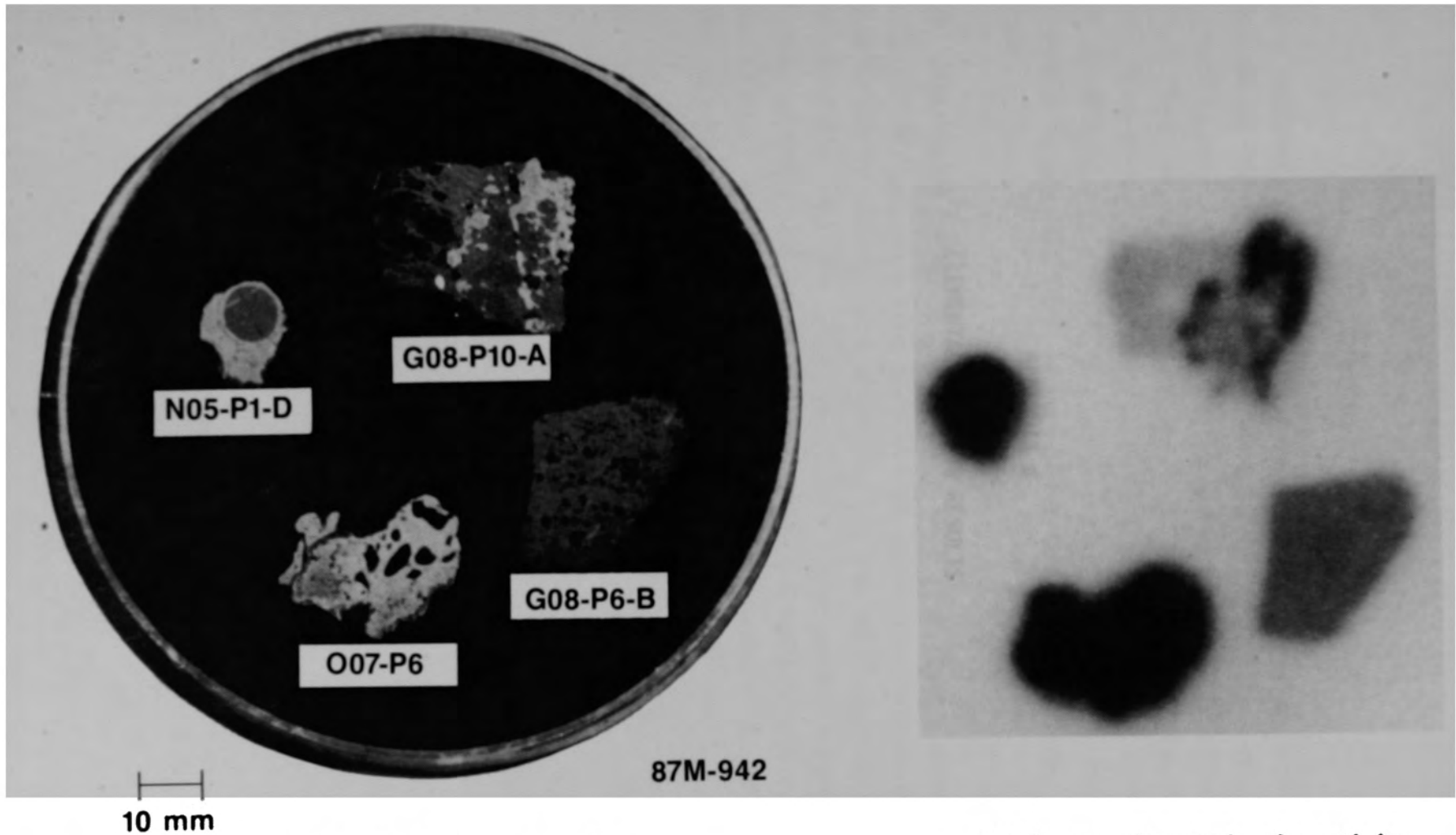


Figure F-4. Fission product distribution in TMI-2 core bore crust samples.



(a) Particle cross sections

(b) Autoradiograph of particle cross sections

Figure F-5. Fission product distribution in TMI-2 core bore particles.





**APPENDIX G**  
**ELEMENTAL ANALYSIS RESULTS**



## APPENDIX G

### ELEMENTAL ANALYSIS RESULTS

This Appendix presents results of the elemental analyses performed on samples removed from the lower core region using inductively coupled plasma (ICP) spectroscopy. This analysis was performed on the nonvolatile, dissolved liquid portions of the samples. The results are listed in weight percent. Many of the samples indicate a total measured elemental content from 60 to 85 wt%, depending on the composition of the sample. The balance of the sample is expected to be oxygen, which is not measurable by this technique.

The uncertainty quoted by the Battelle Pacific Northwest Laboratories where the ICP analyses were done is from 2 to 5% for the analysis and with sample dilution and weighing uncertainties, the total uncertainty is approximately 15%. However, some samples have higher uncertainties because of dilution or other problems identified during the analysis process. The results for these samples are included by a higher degree of uncertainty (typically 20 to 30%) associated with each sample.

TABLE G1. K9-P2-C ELEMENTAL CONCENTRATIONS  
(in Wt %)

Element	#1 (36)	#2 (17) <sup>a</sup>	#3 (54b)	#4 (57)
Ag	2.14E+00	9.32E+00	4.50E+00	4.94E-02
Al	1.32E-01	4.41E-01	1.23E-01	1.88E-01
B	<6.60E-03	1.28E-01	5.57E-02	9.88E-03
Cd	1.19E-01	9.49E-02	5.57E-02	9.88E-03
Cr	3.69E+00	3.28E+00	1.91E+00	3.36E-01
Cu	1.59E-01	9.37E+00	8.17E-02	4.94E-02
Fe	5.34E+01	1.66E+01	1.75E+01	7.80E-01
Gd	6.60E-03	6.14E-02	4.83E-02	4.94E-02
In	1.84E+00	1.57E+00	7.80E-01	<9.88E-03
Mn	3.30E-02	1.62E-01	6.32E-02	2.96E-02
Mo	2.15E+00	3.91E-01	7.02E-01	<2.96E-02
Nb	1.19E-01	1.51E-01	7.43E-02	1.28E-01
Ni	2.36E+01	1.45E+01	7.47E+00	9.88E-02
Si	1.65E-01	1.20E+00	2.79E-01	1.38E-01
Sn	3.71E+00	1.72E+00	1.20E+00	<9.88E-02
Te	3.30E-02	8.93E-02	4.09E-02	<9.88E-03
U	<3.30E-01	3.28E+01	3.22E+01	7.05E+01
Zr	<6.60E-03	8.76E+00	1.10E+01	1.95E+01
	9.17E+01	1.01E+02	7.80E+01	9.20E+01

a. Uncertainty up to 20% associated with result.

TABLE G2. G8-P11-B ELEMENTAL CONCENTRATIONS  
(in Wt %)

Element	G8-P11-B		
	#1 (40)	#2 (31)	#3 (52)
Ag	9.48E-02	5.21E+00	2.48E-01
Al	1.90E-01	2.76E-01	3.16E-01
B	3.38E-02	2.59E-01	<3.23E-03
Cd	<6.77E-03	1.99E-01	<3.23E-03
Cr	2.37E-01	1.79E+00	4.84E-01
Cu	1.42E-01	1.07E-01	7.42E-02
Fe	4.20E-01	5.61E+00	1.15E+00
Gd	8.80E-02	7.77E-02	7.10E-02
In	2.17E-01	1.30E+00	8.71E-02
Mn	2.71E-02	6.91E-02	5.16E-02
Mo	<2.03E-02	9.50E-02	9.68E-03
Nb	1.02E-01	1.35E-01	7.10E-02
Ni	6.77E-02	1.33E+00	2.07E-01
Si	5.08E-01	5.38E-01	3.13E-01
Sn	1.15E-01	9.79E-01	1.06E-01
Te	2.71E-02	4.61E-02	2.58E-02
U	6.67E+01	5.07E+01	6.20E+01
Zr	1.76E+01	1.72E+01	2.26E+01
	8.66E+01	8.59E+01	8.78E+01

TABLE G3. G8-P11-E ELEMENTAL CONCENTRATIONS  
(in Wt. %)

Element	G8-P11-E		
	#1 (20)	#2 (50)	#3 (18)
Ag	7.85E+00	2.12E-01	1.92E+00
Al	8.73E-02	2.30E-01	1.42E-01
B	2.55E-01	<4.51E-03	1.90E-01
Cd	3.20E-01	<4.51E-03	2.03E-02
Cr	3.85E+00	4.11E-01	1.00E+00
Cu	1.09E-01	6.32E-02	1.29E-01
Fe	2.44E+01	8.80E-01	2.87E+00
Gd	2.91E-02	7.22E-02	1.02E-01
In	1.77E+00	4.52E-02	7.04E-01
Mn	8.00E-02	4.52E-02	6.09E-02
Mo	1.02E+00	<1.35E-02	7.45E-02
Nb	1.75E-01	8.13E-02	3.25E-01
Ni	1.08E+01	1.35E-01	7.24E-01
Si	2.25E-01	3.03E-01	5.69E-01
Sn	3.36E+00	7.68E-02	3.72E-01
Te	2.91E-02	<4.51E-03	4.06E-02
U	1.51E+01	6.46E+01	7.04E+01
Zr	5.20E+00	2.21E+01	4.01E+00
	7.47E+01	8.92E+01	8.37E+01

TABLE G4. D8-P3-A ELEMENTAL CONCENTRATIONS  
(in Wt %)

Element	#1 (11) <sup>a</sup>	#2 (25)
Ag	6.78E+00	3.73E-01
Al	2.05E-01	1.77E-01
B	1.44E-01	1.44E-01
Cd	2.19E-01	1.31E-02
Cr	6.02E-01	1.56E+00
Cu	1.78E-01	9.16E-02
Fe	5.85E+00	2.74E+00
Gd	5.47E-02	1.05E-01
In	2.58E+00	6.21E-01
Mn	4.79E-02	4.58E-02
Mo	3.08E-01	1.05E-01
Nb	<6.84E-03	1.31E-01
Ni	2.95E+00	6.61E-01
Si	1.48E+00	9.42E-01
Sn	1.68E+00	1.44E-01
Te	<6.84E-03	2.62E-02
U	6.08E+01	6.09E+01
Zr	1.40E+01	1.12E+01
	9.79E+01	8.00E+01

a. Uncertainty up to 20% associated with results

TABLE G5. K9-P1-C ELEMENTAL CONCENTRATIONS  
(Wt %)

Element	#1 (51)	#2 (30)	#3 (28)	#4 (4)
Ag	3.68E+00	2.28E+00	3.91E+00	2.93E+00
Al	7.88E-01	1.58E-01	6.41E-01	8.34E-01
B	5.25E-02	1.09E-01	1.22E-01	1.29E-01
Cd	6.36E-02	1.98E-02	1.03E-01	1.10E-01
Cr	1.87E+00	3.06E-01	1.17E+00	2.06E+00
Cu	6.08E-02	8.89E-02	4.68E-02	5.48E-02
Fe	9.37E+00	1.76E+00	5.85E+00	1.02E+01
Gd	1.93E-02	9.88E-02	1.64E-02	2.62E-02
In	1.85E+00	7.51E-01	1.09E+00	1.11E+00
Mn	6.36E-02	1.98E-02	5.15E-02	7.39E-02
Mo	3.43E-01	8.89E-02	1.85E-01	3.77E-01
Nb	1.93E-01	8.89E-02	1.17E-01	2.10E-01
Ni	4.42E+00	1.04E+00	3.86E+00	5.05E+00
Si	2.13E-01	6.52E-01	2.11E-01	4.31E-01
Sn	1.41E+00	2.47E-01	1.52E+00	1.86E+00
Te	1.11E-02	<9.88E-03	2.57E-02	3.57E-02
U	1.74E+01	6.03E+01	7.20E+00	1.42E+01
Zr	4.45E+01	1.01E+01	3.67E+01	4.03E+01
	8.63E+01	7.81E+01	6.28E+01	8.00E+01



TABLE G6. D8-P1-C ELEMENTAL CONCENTRATIONS  
(Wt %)

Element	a		
	#1B (48b)	#2 (15)	#3 (68)
Ag	1.04E+01	4.66E+00	6.42E+00
Al	6.39E+00	1.42E-01	3.08E-01
B	1.18E-01	8.88E-02	1.12E-01
Cd	1.18E-01	8.88E-02	8.39E-02
Cr	4.06E+00	6.53E-01	3.23E+00
Cu	1.18E-01	1.29E-01	1.12E-01
Fe	3.40E+01	5.28E+00	2.82E+01
Gd	1.86E-02	2.92E+00	3.73E-02
In	1.74E+00	1.13E+00	1.93E+00
Mn	8.69E-02	2.66E-02	4.66E-02
Mo	1.33E+00	2.09E-01	1.14E+00
Nb	1.49E-01	<4.44E-03	1.40E-01
Ni	1.37E+01	2.09E+00	1.30E+01
Si	5.59E-01	1.11E+00	9.32E-02
Sn	3.12E+00	7.15E-01	2.92E+00
Te	<6.21E-03	<4.44E-03	6.53E-02
U	2.65E+00	8.79E+01	6.57E+00
Zr	1.17E+01	1.36E+01	1.38E+01
	9.03E+01	1.21E+02	7.82E+01

a. Uncertainty up to 30% associated with result.

TABLE G7. D8-P2-A ELEMENTAL CONCENTRATIONS  
(in Wt %)

Element	#1 (53b)	#2 (24)
Ag	5.09E+00	1.13E-00
Al	1.71E-01	1.86E-01
B	<1.32E-02	1.16E-02
Cd	1.32E-02	1.16E-02
Cr	4.62E-01	4.30E-01
Cu	2.58E-01	1.63E-01
Fe	2.91E+00	2.18E+00
Gd	<1.32E-02	9.29E-02
In	2.77E-01	2.90E-01
Mn	1.32E-02	2.32E-02
Mo	<3.96E-02	5.81E-02
Nb	<5.27E-02	1.51E-01
Ni	5.79E+00	5.23E-01
Si	<1.32E-01	4.99E-01
Sn	1.56E+00	3.02E-01
Te	<1.32E-02	6.97E-02
U	5.25E+01	5.96E+01
Zr	1.82E+01	8.57E+00
	8.75E+01	7.43E+01

TABLE G8. 07-P4-C ELEMENTAL CONCENTRATIONS  
(in Wt %)

Element	#1 (45)	#2 (61)	#3 (6)	#4 (56)
Ag	6.89E+00	5.39E+00	4.44E+00	1.88E+00
Al	4.66E-01	7.14E-02	1.08E-01	2.38E-01
B	1.10E-01	5.00E-02	1.88E-01	1.11E-01
Cd	4.20E-01	2.21E-01	8.74E-02	1.52E-02
Cr	3.76E+00	3.23E+00	1.61E+00	4.56E-01
Cu	1.10E-01	1.46E-01	1.31E-01	7.09E-02
Fe	2.89E+01	3.93E+00	1.98E+00	9.52E-01
Gd	1.51E-02	5.35E-02	8.07E-02	7.09E-02
In	2.73E+00	2.94E+00	1.25E+00	1.82E-01
Mn	6.44E-02	1.54E-01	7.06E-02	3.04E-02
Mo	1.18E+00	1.54E-01	3.36E-02	1.52E-02
Nb	9.85E-02	8.57E-02	1.08E-01	1.67E-01
Ni	1.26E+01	1.76E+00	3.09E-01	2.78E-01
Si	3.79E-01	3.75E-01	8.50E-01	5.82E-01
Sn	2.92E+00	2.75E+00	8.94E-01	2.23E-01
Te	3.03E-02	<3.57E-03	1.04E-01	2.03E-02
U	3.20E+00	5.32E+01	5.68E+01	6.63E+01
Zr	1.66E+01	4.39E+00	6.02E+00	1.70E+01
	8.05E+01	7.89E+01	7.51E+01	8.86E+01

TABLE G9. G12-P1-E ELEMENTAL CONCENTRATIONS  
(Wt %)

Element	#2 (59)	#3 (69)	#4 (70)
Ag	7.39E+00	3.77E-02	4.99E-02
Al	1.42E-01	2.45E-01	5.32E-01
B	8.21E-02	3.77E-02	4.16E-02
Cd	7.12E-02	<9.42E-03	8.31E-03
Cr	3.88E+00	3.86E-01	5.15E-01
Cu	9.31E-02	8.48E-02	6.65E-02
Fe	1.76E+01	8.39E-01	1.02E+00
Gd	2.74E-02	9.42E-02	8.31E-02
In	2.04E+00	3.77E-01	3.57E-01
Mn	4.00E-01	4.71E-02	4.16E-02
Mo	3.18E-01	3.77E-02	<2.49E-02
Nb	1.53E-01	1.51E-01	1.33E-01
Ni	8.76E+00	1.88E-01	2.49E-01
Si	2.08E-01	4.05E-01	1.51E+00
Sn	2.10E+00	1.60E-01	<1.25E-01
Te	7.67E-02	7.54E-02	1.16E-01
U	1.41E+01	5.38E+01	4.95E+01
Zr	2.32E+01	1.94E+01	1.77E+01
	8.05E+01	7.64E+01	7.21E+01

TABLE G10. G12-P1-D2 ELEMENTAL CONCENTRATIONS

Element	#1 (49)	#2 (43)
Ag	1.84E-01	2.13E-01
Al	2.04E-01	6.34E-01
B	<1.02E-02	<5.20E-03
Cd	<1.02E-02	<5.20E-03
Cr	4.49E-01	1.08E+00
Cu	4.08E-02	1.04E-01
Fe	1.08E+00	1.60E+00
Gd	5.10E-02	7.80E-02
In	<1.02E-02	1.82E-01
Mn	5.10E-02	5.20E-02
Mo	<3.06E-02	1.56E-02
Nb	1.33E-01	1.25E-01
Ni	1.74E-01	3.74E-01
Si	<1.02E-01	3.28E-01
Sn	<1.02E-01	1.25E-01
Te	2.04E-02	7.28E-02
U	6.32E+01	5.51E+01
Zr	2.21E+01	1.97E+01
	8.79E+01	7.98E+01

TABLE G11. K9 PARTICLES ELEMENTAL CONCENTRATIONS  
(in Wt %)

Element	k9-P3-A	K9-P3-D		K9-P3-F
	#1 (46)	#1 (62)	#2 (67)	#1 (19)
Ag	1.01E-01	2.24E-01	1.28E-01	2.60E-01
Al	1.34E+00	2.17E-01	3.23E-01	8.12E-01
B	8.68E-02	3.87E-02	2.78E-02	7.53E-02
Cd	<7.24E-03	<7.74E-03	5.56E-03	<8.37E-03
Cr	2.34E+00	4.41E-01	4.73E-01	5.94E-01
Cu	7.96E-02	8.51E-02	7.23E-02	1.26E-01
Fe	3.44E+00	9.44E-01	9.96E-01	1.46E+00
Gd	7.24E-02	8.51E-02	7.23E-02	9.21E-02
In	1.66E-01	3.10E-01	2.56E-01	2.51E-01
Mn	8.68E-02	4.64E-02	4.45E-02	5.86E-02
Mo	4.34E-02	3.10E-02	2.78E-02	3.35E-02
Nb	1.30E-01	1.24E-01	8.35E-02	2.43E-01
Ni	9.70E-01	2.71E-01	2.17E-01	7.37E-01
Si	3.76E-01	4.18E-01	3.95E-01	1.53E+00
Sn	1.88E-01	1.78E-01	1.45E-01	1.51E-01
Te	2.17E-02	5.42E-02	4.45E-02	1.00E-01
U	5.21E+01	5.59E+01	5.31E+01	5.47E+01
Zr	1.96E+01	2.04E+01	1.91E+01	1.98E+01
	8.12E+01	7.98E+01	7.55E+01	8.10E+01

TABLE G11. K9 PARTICLES ELEMENTAL CONCENTRATIONS (cont'd)  
(in Wt %)

Element	K9-P4-D	
	#1 (7)	#2 (47)
Ag	6.41E+00	6.49E-02
Al	1.03E+00	2.41E-01
B	1.85E-01	3.71E-02
Cd	3.21E-02	<9.27E-03
Cr	1.23E+00	5.19E-01
Cu	1.12E-01	6.49E-02
Fe	8.35E+00	1.06E+00
Gd	2.41E-02	8.35E-02
In	1.38E+00	2.41E-01
Mn	4.82E-02	4.64E-02
Mo	3.29E-01	<2.78E-02
Nb	1.69E-01	1.02E-01
Ni	4.44E+00	2.60E-01
Si	2.23E+00	5.47E-01
Sn	1.32E+00	2.32E-01
Te	1.61E-01	2.78E-02
U	1.91E+01	5.90E+01
Zr	3.45E+01	2.11E+01
	8.11E+01	8.37E+01

TABLE G12. G8 PARTICLE ELEMENTAL CONCENTRATIONS  
(in Wt %)

Element	G8-P5-B		G8-P6-B	
	#1 (14)	#2 (1)	1563 (34)	1689 (9)
Ag	3.02E-01	1.91E-01	2.19E-01	2.19E-01
Al	2.73E-01	2.41E-01	4.00E-01	2.77E-01
B	2.95E-02	6.02E-02	<9.52E-03	4.01E-02
Cd	<7.37E-03	1.00E-02	<9.52E-03	7.30E-03
Cr	4.72E-01	4.21E-01	5.52E-01	4.93E-01
Cu	1.84E-01	5.02E-02	1.14E-01	8.76E-02
Fe	9.58E-01	8.63E-01	1.29E+00	1.06E+00
Gd	8.84E-02	9.03E-02	7.62E-02	8.39E-02
In	5.16E-02	6.52E-01	1.62E-01	3.94E-01
Mn	5.16E-02	4.01E-02	5.71E-02	5.11E-02
Mo	1.47E-02	<3.01E-02	<1.90E-02	3.28E-02
Nb	2.21E-02	1.20E-01	2.38E-01	6.20E-02
Ni	3.61E-01	1.20E-01	2.67E-01	2.34E-01
Si	1.56E+00	5.62E-01	3.24E-01	4.31E-01
Sn	<1.11E-01	<1.50E-01	2.09E-01	<5.47E-02
Te	1.47E-02	3.01E-02	<9.52E-03	3.28E-02
U	8.70E+01	6.05E+01	5.67E+01	5.87E+01
Zr	2.78E+01	1.91E+01	2.15E+01	2.15E+01
	1.19E+02	8.32E+01	8.22E+01	8.38E+01

a. Uncertainty up to 30% associated with result.



TABLE G12. G8 PARTICLE ELEMENTAL CONCENTRATIONS (cont'd)  
(in Wt %)

Element	G8-P7-A	G8-P7-C		G8-P8-A
	#1 (39)	#1 (8)	#2 (32)	#1 (21)
Ag	2.20E-01	9.29E+00	2.12E-01	2.38E-01
Al	3.50E-01	4.56E-01	2.61E-01	2.17E-01
B	<5.94E-03	1.31E-01	<9.65E-03	4.89E-02
Cd	<5.94E-03	4.65E-01	<9.65E-03	6.99E-03
Cr	4.63E-01	4.20E+00	3.67E-01	4.47E-01
Cu	1.07E-01	9.64E-02	5.79E-02	7.69E-02
Fe	1.06E+00	3.15E+01	8.69E-01	9.50E-01
Gd	7.72E-02	1.75E-02	8.69E-02	9.08E-02
In	1.54E-01	1.42E+00	2.12E-01	5.59E-01
Mn	5.35E-02	7.89E-02	4.83E-02	4.89E-02
Mo	<1.19E-02	1.29E+00	<1.93E-02	2.10E-02
Nb	1.25E-01	1.49E-01	1.45E-01	1.12E-01
Ni	2.08E-01	1.41E+01	1.74E-01	1.89E-01
Si	3.86E-01	2.10E-01	4.05E-01	3.77E-01
Sn	1.31E-01	3.15E+00	<1.45E-01	<1.05E-01
Te	5.94E-02	5.26E-02	5.79E-02	4.19E-02
U	5.70E+01	3.93E+00	5.79E+01	5.83E+01
Zr	2.11E+01	1.82E+01	2.03E+01	2.12E+01
	8.15E+01	8.87E+01	8.13E+01	8.31E+01

TABLE G12. G8 PARTICLE ELEMENTAL CONCENTRATIONS (cont'd)  
(in Wt %)

Element	G8-P9-A #1 (2)	G8-P10-A	
		#1 (5)	#2 (10)
Ag	7.42E+00	7.95E-02	3.52E+00
Al	<9.79E-02	1.70E-01	1.73E-01
B	9.79E-02	6.53E-02	8.96E-02
Cd	8.32E-01	4.26E-03	2.88E-02
Cr	5.10E+00	2.78E-01	2.08E-01
Cu	1.71E-01	6.53E-02	1.34E-01
Fe	3.75E+01	1.01E+00	2.09E+00
Gd	2.45E-02	9.22E-02	9.92E-02
In	2.35E+00	3.58E-01	9.41E-01
Mn	7.34E-02	3.12E-02	2.24E-02
Mo	1.54E+00	1.56E-02	5.44E-02
Nb	2.20E-01	6.24E-02	4.16E-02
Ni	1.70E+01	5.96E-02	5.60E-01
Si	3.18E-01	5.01E-01	9.18E-01
Sn	4.63E+00	3.41E-02	6.02E-01
Te	2.45E-02	5.39E-02	9.28E-02
U	1.21E+00	6.57E+01	7.39E+01
Zr	1.20E+00	1.52E+01	6.98E+00
	7.98E+01	8.38E+01	9.05E+01

TABLE G13. DB PARTICLE ELEMENTAL CONCENTRATIONS  
(in Wt %)

Element	DB-P4-A		DB-P4-C		
	#1 (33)	#2 (60)	#1A (37a)	#1B (37b)	#2 (23)
Ag	1.22E+00	2.70E+00	1.74E-01	1.13E-01	7.11E-02
Al	1.26E-01	<1.04E-01	2.29E-01	1.86E-01	3.16E-01
B	<1.40E-02	<1.30E-02	<7.91E-03	3.99E-02	<7.89E-03
Cd	<1.40E-02	<1.30E-02	<7.91E-03	<6.64E-03	<7.89E-03
Cr	6.63E+00	3.90E-02	2.29E-01	2.26E-01	2.45E-01
Cu	1.96E-01	2.73E-01	5.54E-02	8.64E-02	1.34E-01
Fe	5.79E+01	5.03E+01	4.27E-01	4.52E-01	4.18E-01
Gd	<1.40E-02	<1.30E-02	8.70E-02	8.64E-02	9.47E-02
In	8.11E-01	3.25E-01	1.11E-01	3.12E-01	1.03E-01
Mn	9.79E-02	<1.30E-02	3.16E-02	3.32E-02	3.16E-02
Mo	2.25E+00	3.67E+00	<1.58E-02	<1.99E-02	<1.58E-02
Nb	2.24E-01	<1.30E-02	1.58E-01	7.31E-02	1.42E-01
Ni	2.45E+01	3.67E+01	5.54E-02	9.30E-02	1.74E-01
Si	3.35E-01	<1.30E-01	4.03E-01	4.85E-01	8.76E-01
Sn	3.98E+00	5.33E+00	<1.19E-01	1.13E-01	<1.18E-01
Te	5.59E-02	<1.30E-02	4.75E-02	1.99E-02	5.53E-02
U	<6.99E-01	<6.50E-01	6.08E+01	6.71E+01	6.58E+01
Zr	1.40E-02	<1.30E-02	1.68E+01	1.77E+01	1.73E+01
	9.90E+01	1.00E+02	7.98E+01	8.72E+01	8.59E+01

TABLE G14. 09 PARTICLE ELEMENTAL CONCENTRATIONS  
(in Wt %)

Element	09-P1-A		09-P1-B #1 (64)
	#1 C (35)	#2 P (44) <sup>a</sup>	
Ag	1.96E+00	2.61E-01	3.78E-01
Al	8.49E-02	1.75E-01	1.45E-01
B	1.06E-01	4.47E-02	2.91E-02
Cd	2.12E-02	<3.72E-03	<5.82E-03
Cr	6.55E+00	1.49E-01	1.40E-01
Cu	1.91E-01	1.08E-01	8.15E-02
Fe	5.56E+01	3.09E-01	2.62E-01
Gd	8.49E-02	1.23E-01	8.73E-02
In	1.09E+00	3.01E-01	3.14E-01
Mn	9.19E-02	2.98E-02	2.33E-02
Mo	2.28E+00	1.12E-02	2.91E-02
Nb	2.05E-01	5.58E-02	9.31E-02
Ni	2.43E+01	6.70E-02	5.82E-02
Si	1.84E-01	5.81E-01	3.90E-01
Sn	4.02E+00	8.56E-02	9.89E-02
Te	<4.95E-02	4.47E-02	4.66E-02
U	<3.54E-01	9.34E+01	6.17E+01
Zr	<7.07E-03	2.21E+01	1.56E+01
	9.71E+01	1.18E+02	7.95E+01

a. Uncertainty up to 30% associated with result.

TABLE G15. G12 PARTICLE ELEMENTAL CONCENTRATIONS  
(in Wt %)

Element	G12-P2-B		G12-P4-A	G12-P9-A1
	#1 (29)	#2 (42)	#1 (58)	#1 (22)
Ag	2.08E-01	9.90E-02	2.00E-01	4.68E+00
Al	1.50E-01	1.93E-01	2.47E-01	6.95E-01
B	4.04E-02	3.13E-02	8.67E-02	1.08E-01
Cd	1.15E-02	<5.21E-03	6.67E-03	1.54E-02
Cr	1.96E-01	1.51E-01	4.47E-01	8.26E-01
Cu	7.50E-02	8.34E-02	8.67E-02	9.27E-02
Fe	3.92E-01	3.70E-01	1.07E+00	4.49E+00
Gd	9.23E-02	8.86E-02	8.00E-02	8.49E-02
In	4.62E-01	1.72E-01	2.93E-01	7.34E-01
Mn	2.89E-02	4.17E-02	4.67E-02	6.18E-02
Mo	2.89E-02	1.56E-02	2.00E-02	7.72E-02
Nb	9.81E-02	6.78E-02	1.00E-01	1.24E-01
Ni	1.33E-01	5.21E-02	2.07E-01	2.38E+00
Si	4.27E-01	5.11E-01	4.27E-01	3.94E-01
Sn	<8.66E-02	< 7.82E-02	1.27E-01	5.02E-01
Te	2.89E-02	3.65E-02	4.00E-02	2.32E-02
U	5.83E+01	6.20E+01	5.51E+01	5.08E+01
Zr	1.68E+01	1.65E+01	2.00E+01	1.41E+01
	7.76E+01	8.05E+01	7.86E+01	8.02E+01

TABLE G16. N5 PARTICLE ELEMENTAL CONCENTRATIONS  
(in Wt %)

Element	N5-P1-D			N5-P1-H	
	#1A (12a)	#1B (12b)	#2 (63)	#1 (13)	#2 (65)
Ag	1.50E+00	2.01E-01	1.29E+00	7.70E+00	<2.70E-02
Al	4.43E-01	8.24E-02	1.91E-01	4.19E-01	9.17E-01
B	2.32E-01	5.15E-02	5.45E-02	5.63E-02	5.39E-02
Cd	2.06E-02	5.15E-03	<1.36E-02	3.13E-01	<2.70E-02
Cr	2.72E+00	4.17E-01	1.08E+00	1.88E-01	6.74E-01
Cu	7.21E-02	6.18E-02	1.23E-01	1.50E-01	1.08E-01
Fe	3.02E+01	5.11E+00	1.36E+01	3.07E-01	1.11E+00
Gd	1.55E-02	6.18E-02	8.18E-02	1.25E-02	1.08E-01
In	4.69E-01	4.12E-01	6.95E-01	3.54E+00	7.01E-01
Mn	2.06E-02	1.03E-02	1.36E-02	1.25E-02	5.39E-02
Mo	1.34E+00	2.42E-01	6.68E-01	<1.25E-02	<8.09E-02
Nb	3.09E-02	7.72E-02	2.04E-01	<6.26E-03	3.78E-01
Ni	1.30E+01	2.32E+00	6.13E+00	3.82E-01	1.35E-01
Si	4.02E-01	2.94E-01	3.82E-01	1.16E+00	9.71E-01
Sn	1.83E+00	4.74E-01	1.55E+00	2.08E+00	6.74E-01
Te	4.64E-02	2.58E-02	4.09E-02	<6.26E-03	2.43E-01
U	1.47E+00	4.11E+01	5.04E+01	3.24E+01	5.74E+01
Zr	2.59E+01	1.30E+00	3.95E+00	3.74E+01	1.38E+01
	7.97E+01	5.23E+01	8.05E+01	8.61E+01	7.75E+01

TABLE G17. D4 and 07 PARTICLE ELEMENTAL CONCENTRATIONS  
(in Wt %)

Element	07-P1-A	07-P6		D4-P2-A
	#1 (26)	#1 (16)	#2 (27)	#1 (38)
Ag	1.36E+00	5.92E+00	5.64E+00	3.45E+01
Al	3.50E-01	1.60E-01	1.60E-01	<2.58E-01
B	<2.19E-02	3.21E-02	2.91E-02	<3.23E-02
Cd	<2.19E-02	<1.60E-02	1.45E-02	5.81E-01
Cr	1.97E-01	3.67E+00	4.87E+00	1.61E+00
Cu	5.91E-01	2.56E-01	2.47E-01	1.94E-01
Fe	5.06E+01	5.47E+01	4.45E+01	2.61E+01
Gd	<2.19E-02	<1.60E-02	1.45E-02	<3.23E-02
In	7.66E-01	1.17E+00	1.10E+00	7.65E+00
Mn	<2.19E-02	6.41E-02	1.02E-01	<3.23E-02
Mo	2.30E+00	2.87E+00	2.27E+00	1.39E+00
Nb	2.85E-01	2.40E-01	2.62E-01	5.81E-01
Ni	2.82E+01	2.18E+01	1.74E+01	1.39E+01
Si	1.44E+00	7.05E-01	1.60E-01	<3.23E-01
Sn	4.90E+00	5.16E+00	4.24E+00	7.52E+00
Te	1.31E-01	1.12E-01	1.45E-02	1.29E-01
U	<1.09E+00	<8.01E-01	1.55E+00	<1.61E+00
Zr	8.76E-02	<1.60E-02	3.20E-01	1.61E-01
	9.24E+01	9.77E+01	8.29E+01	9.66E+01





**APPENDIX H**  
**RADIOCHEMICAL ANALYSIS RESULTS**



## APPENDIX H

### RADIOCHEMICAL ANALYSIS RESULTS

This Appendix presents the results of the radiochemical analyses of the lower core region samples. Analytical techniques are discussed in Appendix B. The uncertainty listed for the results is that associated with counting statistics. To this uncertainty must be added uncertainties due to dilution, weighing, and handling of the samples. The total uncertainty associated with the analytical results is approximately 15%. All radionuclide activities have been decay corrected to April 1, 1987, 8 y after the accident.

TABLE H-1. CORE BORE K9 RADIONUCLIDE CONCENTRATIONS  
( $\mu\text{Ci/g}$  on April 1, 1987)

Identification	Co-60	Sr-90		Ru-106	Sb-125
	$\mu\text{Ci/g} \pm \text{Error}$	$\mu\text{Ci/g} \pm \text{Error}$		$\mu\text{Ci/g} \pm \text{Error}$	$\mu\text{Ci/g} \pm \text{Error}$
K9-P1-C- #1 (51)	3.90E+02 +/-1.64E+00	1.41E+02	+/-1.13E+01	4.21E+02 +/-3.24E+00	2.49E+02 +/-1.04E+00
#2 (28)	3.37E+02 +/-1.28E+00	7.76E+02	+/-6.21E+01	7.24E+01 +/-1.98E+00	2.52E+02 +/-1.29E+00
#3 (30)	7.29E+01 +/-1.42E+00	7.04E+03	+/-5.63E+02	1.19E+02 +/-5.73E+00	9.06E+01 +/-3.14E+00
#4 (4)	1.87E+03 +/-6.74E+00	3.28E+03	+/-2.62E+02	8.23E+02 +/-8.89E+00	1.33E+03 +/-5.44E+00
K9-P2-C #1 (36)	1.43E+03 +/-5.42E+00	3.64E+00	+/-2.90E-01	7.44E+02 +/-8.48E+00	1.28E+03 +/-4.22E+00
#1A (36a)	1.39E+03 +/-3.88E+00	3.33E+00	+/-2.66E-01	8.11E+02 +/-9.24E+00	1.24E+03 +/-4.82E+00
#1B (36b)	1.43E+03 +/-5.16E+00	1.20E+00	+/-9.60E-02	2.01E+02 +/-5.09E+00	1.26E+03 +/-5.03E+00
#2 (17)	2.52E+02 +/-1.01E+00	1.46E+02	+/-1.17E+01	2.86E+02 +/-2.51E+00	5.66E+02 +/-1.13E+00
#3A (54a)	3.52E+02 +/-1.72E+00	6.59E+02	+/-5.27E+01	6.63E+02 +/-2.38E+00	1.44E-01 +/-2.88E-02
#3B (54b)	4.92E+02 +/-1.67E+00	2.42E+02	+/-1.94E+01	7.00E+02 +/-4.55E+00	4.58E+02 +/-2.29E+00
#4 (57)	9.21E+00 +/-1.94E-01	2.56E+03	+/-2.05E+02	<2.20E+0	1.06E+00 +/-2.62E-01
K9-P3-A #1 (46)	6.97E+01 +/-2.99E-01	8.97E+02	7.18E+01	<3.67E+0	1.91E+00 +/-2.02E-01
K9-P3-D #1 (62)	1.73E+01 +/-1.69E-01	5.02E+03	4.02E+02	5.39E+00 +/-5.52E-01	4.63E+00 +/-2.00E-01
#2 (67)	1.85E+01 +/-1.66E-01	1.86E+03	1.49E+02	2.72E+00 +/-3.75E-01	1.78E+00 +/-1.81E-01
K9-P3-F #1 (19)	2.24E+01 +/-1.81E-01	8.28E+03	6.62E+02	3.72E+00 +/-6.96E-01	1.45E+00 +/-1.82E-01
K9-P4-D #1 (7)	3.67E+02 +/-1.06E+00	2.51E+03	2.01E+02	4.22E+02 +/-2.70E+00	3.28E+02 +/-1.48E+00
#2 (47)	1.99E+01 +/-1.90E-01	1.08E+03	8.64E+01	9.95E+00 +/-7.13E-01	1.33E+00 +/-2.30E-01

TABLE H-1. (continued)

Identification	1-129	Cs-134	Cs-137	Cs-144
	UCI/g +/- Error	UCI/g +/- Error	UCI/g +/- Error	UCI/g +/- Error
K9-P1-C #1 (51)	1.10E-04 +/- 2.00E-05	<1.12E+0	2.45E+01 +/- 2.97E-01	1.08E+01 +/- 1.60E+00
#2 (28)	3.40E-05 +/- 8.50E-06	8.40E+00 +/- 2.16E-01	3.92E+02 +/- 1.69E+00	<3.77E+0
#3 (30)	4.60E-03 +/- 9.50E-04	1.24E+02 +/- 1.72E+00	5.30E+03 +/- 1.01E+01	2.38E+02 +/- 7.72E+00
#4 (4)	2.66E-05 +/- 2.00E-07	5.62E+00 +/- 7.84E-01	1.93E+02 +/- 1.96E+00	7.15E+01 +/- 6.17E+00
K9-P2-C #1 (36)	7.10E-04 +/- 1.60E-04	<2.66E+0	<3.27E+0	<1.37E+0
#1A (36a)	7.10E-04 +/- 1.40E-04	<1.17E+0	<1.75E+0	<2.45E+0
#1B (36b)	2.30E-02 +/- 4.80E-03	<1.24E+0	<2.20E+0	<2.87E+0
#2 (17)	6.00E-04 +/- 1.10E-04	3.10E+00 +/- 1.61E-01	1.33E+02 +/- 4.64E-01	5.44E+01 +/- 2.23E+00
#3A (54a)	2.50E-04 +/- 4.58E-05	1.68E+01 +/- 3.17E-01	8.03E+02 +/- 1.77E+00	1.11E+02 +/- 1.94E+01
#3B (54b)	3.00E-04 +/- 6.24E-05	9.27E+00 +/- 3.03E-01	4.50E+02 +/- 2.70E+00	8.15E+01 +/- 2.94E+00
#4 (57)	2.80E-06 +/- 4.37E-06	3.81E-01 +/- 6.70E-02	1.83E+01 +/- 3.86E-01	1.70E+02 +/- 9.69E+00
K9-P3-A #1 (46)	7.10E-06 +/- 1.69E-06	6.49E-01 +/- 6.86E-02	3.29E+01 +/- 2.31E-01	2.51E+02 +/- 9.26E+00
K9-P3-D #1 (62)	4.40E-05 +/- 1.03E-05	8.69E-01 +/- 7.97E-02	3.44E+01 +/- 2.65E-01	2.13E+02 +/- 6.27E+00
#2 (67)	1.10E-05 +/- 2.29E-06	1.12E+00 +/- 5.80E-02	5.27E+01 +/- 3.63E-01	1.92E+02 +/- 7.77E+00
K9-P3-F #1 (19)	1.70E-05 +/- 1.68E-05	6.59E-01 +/- 5.41E-02	2.96E+01 +/- 2.19E-01	2.10E+02 +/- 9.72E+00
K9-P4-D #1 (7)	1.60E-04 +/- 3.78E-05	<8.79E+0	2.52E+00 +/- 2.52E-01	7.47E+01 +/- 2.01E+00
#2 (47)	1.50E-06 +/- 3.99E-06	7.81E-01 +/- 7.05E-02	3.44E+01 +/- 3.06E-01	2.04E+02 +/- 9.00E+00

TABLE H-1. (continued)

Identification	Eu-154	Eu-155	U-235 (mg)		U-238 (mg)	
	uCi/g +/- Error	uCi/g +/- Error	mg/Sam +/- Error		mg/Sam +/- Error	
K9-P1-C- #1 (51)	2.67E+00 +/-0.189694	4.32E+00 +/-2.40E-01	--a--		--a--	
#2 (28)	<5.86E-0	<1.22E+0	1.02E-01 +/-8.00E-03		4.20E+00 +/-4.90E-01	
#3 (30)	5.05E+01 +/-1.004353	6.43E+01 +/-1.75E+00	1.10E+00 +/-1.60E-02		5.96E+01 +/-9.10E-01	
#4 (4)	1.48E+01 +/-0.892712	2.58E+01 +/-1.22E+00	3.00E-02 +/-7.00E-03		8.82E-01 +/-5.06E-01	
K9-P2-C #1 (36)	<2.07E+0	<4.87E+0	--A--		--A--	
#1A (36a)	<1.37E+0	<3.76E+0	--A--		--A--	
#1B (36b)	<1.30E+0	5.24E+00 +/-1.14E+00	--A--		--A--	
#2 (17)	1.33E+01 +/-3.30E-01	1.65E+01 +/-6.27E-01	1.90E-01 +/-8.00E-03		8.68E+00 +/-5.20E-01	
#3A (54a)	3.71E+01 +/-4.11E-01	4.73E+01 +/-4.26E-01	2.02E+00 +/-2.20E-02		9.40E+01 +/-1.40E+00	
#3B (54b)	1.81E+01 +/-3.68E-01	2.60E+01 +/-5.44E-01	--B--		--B--	
#4 (57)	4.61E+01 +/-2.53E-01	5.99E+01 +/-4.91E-01	--A--		--A--	
K9-P3-A #1 (46)	3.65E+01 +/-2.08E-01	4.67E+01 +/-4.62E-01	4.06E+00	3.50E-02	1.84E+02	1.92E+00
K9-P3-D #1 (62)	4.56E+01 +/-2.19E-01	5.88E+01 +/-3.76E-01	4.51E+00	3.70E-02	1.92E+02	2.01E+00
#2 (67)	4.37E+01 +/-1.79E-01	5.68E+01 +/-4.71E-01	8.73E+00	6.00E-02	3.77E+02	6.22E+00
K9-P3-F #1 (19)	4.12E+01 +/-2.02E-01	5.30E+01 +/-3.82E-01	--A--		--A--	
K9-P4-D #1 (7)	2.29E+01 +/-2.47E-01	2.99E+01 +/-5.35E-01	1.45E-01	8.00E-03	6.07E+00	2.39E-01
#2 (47)	4.60E+01 +/-2.57E-01	5.93E+01 +/-4.75E-01	2.87E+00	2.70E-02	6.54E+01	9.90E-01

TABLE H-2. CORE BORE G8 RADIONUCLIDE CONCENTRATIONS  
( $\mu\text{Ci/g}$  on April 1, 1987)

Identification	Co-60	Sr-90	Ru-106	Sb-125
	$\mu\text{Ci/g}$ +/- Error	$\mu\text{Ci/g}$ +/- Error	$\mu\text{Ci/g}$ +/- Error	$\mu\text{Ci/g}$ +/- Error
GB-P11-B #1 (40)	5.18E+00 +/- 9.17E-02	1.69E+03 +/- 1.35E+02	<2.04E+0	<6.36E-0
#2 (31)	5.98E+01 +/- 1.37E-01	7.42E+02 +/- 5.94E+01	2.78E+01 +/- 9.05E-01	2.60E+02 +/- 1.25E+00
#3 (52)	2.06E+01 +/- 1.38E-01	4.71E+03 +/- 3.77E+02	6.14E+00 +/- 5.37E-01	1.45E+00 +/- 1.07E-01
GB-P11-E #1 (20)	6.60E+02 +/- 2.97E+00	5.44E+02 +/- 4.35E+01	1.51E+03 +/- 1.04E+01	5.90E+02 +/- 2.30E+00
#2 (50)	1.42E+01 +/- 1.93E-01	6.30E+03 +/- 5.04E+02	2.19E+00 +/- 3.95E-01	3.92E-02 +/- 1.33E-02
#3 (18)	3.35E+01 +/- 9.45E-01	9.04E+02 +/- 7.23E+01	7.97E+01 +/- 1.22E+01	1.07E+02 +/- 5.43E+00
GB-P5-B #1 (14)	1.13E+01 +/- 2.05E-01	4.32E+03 +/- 3.46E+02	1.39E+01 +/- 4.85E-01	1.89E+00 +/- 1.34E-01
#2 (1)	2.56E+02 +/- 3.51E+00	3.01E+03 +/- 2.41E+02	<2.43E+0	1.78E+01 +/- 6.21E+00
GB-P6-B #1 (34)	2.29E+01 +/- 3.05E-01	4.35E+03 +/- 3.48E+02	3.14E+00 +/- 6.19E-01	2.20E+00 +/- 1.63E-01
#2 (9)	1.78E+01 +/- 1.47E-01	5.69E+03 +/- 4.55E+02	4.92E+00 +/- 3.50E-01	1.28E+00 +/- 1.43E-01
GB-P7-A #1 (39)	<2.05E-03	4.44E+03 3.55E+02	1.61E-01 +/- 1.39E+01	<1.64E-0
GB-P7-C #1 (8)	9.16E+02 +/- 4.58E+00	1.47E+02 +/- 1.18E+01	1.57E+03 +/- 7.21E+00	8.48E+02 +/- 1.95E+00
#2 (32)	1.35E+01 +/- 1.36E-01	5.07E+03 +/- 4.06E+02	2.50E+01 +/- 8.04E-01	1.87E+00 +/- 2.00E-01
GB-P8-A #1 (21)	1.73E+01 +/- 1.66E-01	6.06E+03 +/- 4.85E+02	<3.73E+0	1.41E+00 +/- 1.74E-01
GB-P9-A #1 (2)	9.80E+02 +/- 3.14E+00	2.52E+02 +/- 2.02E+01	2.68E+03 +/- 4.29E+00	1.35E+03 +/- 3.92E+00
GB-P10-A #1 (5)	5.62E+01 +/- 7.64E-01	7.19E+03 +/- 5.75E+02	<1.47E+0	<3.06E+0
#2 (10)	2.21E+01 +/- 2.04E-01	1.66E+03 +/- 1.33E+02	6.42E+01 +/- 1.06E+00	1.51E+02 +/- 6.05E-01

a. Radionuclide not detected

H-7

TABLE H-2. (continued)

Identification	I-129	Cs-134	Cs-137	Ce-144
	uCi/g +/- Error	uCi/g +/- Error	uCi/g +/- Error	uCi/g +/- Error
G8-P11-B #1 (40)	2.10E-06 +/-6.59E-07	5.44E-01 +/-5.26E-02	2.65E+01 +/-2.09E-01	1.45E+02 +/-7.92E+00
#2 (31)	3.50E-04 +/-8.05E-05	1.37E+01 +/-1.98E-01	6.43E+02 +/-1.54E+00	3.38E+01 +/-1.18E+00
#3 (52)	1.30E-05 +/-4.29E-06	9.18E-01 +/-6.60E-02	4.01E+01 +/-1.72E-01	2.04E+02 +/-4.55E+00
G8-P11-E #1 (20)	1.80E-04 +/-3.73E-05	3.02E+01 +/-5.48E-01	1.36E+03 +/-3.94E+00	1.21E+01 +/-5.28E+00
#2 (50)	2.10E-05 +/-8.40E-06	2.44E-01 +/-5.23E-02	1.08E+01 +/-7.98E-02	1.81E+02 +/-6.32E+00
#3 (18)	4.50E-05 +/-1.03E-05	2.17E+02 +/-2.21E+00	9.60E+03 +/-2.40E+01	7.45E+01 +/-1.17E+01
G8-P5-B #1 (14)	8.60E-06 +/-2.57E-06	5.45E-01 +/-5.69E-02	3.17E+01 +/-2.70E-01	1.83E+02 +/-7.01E+00
#2 (1)	2.41E-06 +/-3.30E-07	1.61E+01 +/-9.53E-01	7.05E+02 +/-8.32E+00	3.53E+03 +/-1.14E+02
G8-P6-B #1 (34)	1.30E-05 +/-3.51E-06	6.10E-01 +/-6.39E-02	3.06E+01 +/-2.69E-01	2.14E+02 +/-6.76E+00
#2 (9)	--a--	4.28E-01 +/-3.89E-02	1.96E+01 +/-1.25E-01	1.92E+02 +/-4.70E+00
G8-P7-A #1 (39)	8.00E-06 +/-6.16E-06	<2.62E-0	1.25E-02 +/-1.27E+01	<1.89E-0
G8-P7-C #1 (8)	6.00E-05 +/-1.25E-05	<1.25E+0	2.31E+01 +/-5.03E-01	<1.54E+0
#2 (32)	9.80E-06 +/-3.63E-06	4.75E-01 +/-6.95E-02	2.49E+01 +/-2.31E-01	2.03E+02 +/-8.06E+00
G8-P8-A #1 (21)	1.00E-05 +/-3.10E-06	8.14E-01 +/-5.22E-02	3.46E+01 +/-1.90E-01	2.07E+02 +/-8.80E+00
G8-P9-A #1 (2)	8.49E-05 +/-7.00E-07	1.67E+00 +/-8.19E-01	9.72E+01 +/-8.16E-01	<1.01E+0
G8-P10-A #1 (5)	2.75E-06 +/-1.60E-07	1.44E+01 +/-4.18E-01	6.57E+02 +/-2.76E+00	1.39E+03 +/-3.97E+01
#2 (10)	1.50E-04 +/-2.80E-05	4.27E+00 +/-5.85E-02	1.88E+02 +/-5.82E-01	6.71E+01 +/-5.05E+00



TABLE H-2. (continued)

Identification	Eu-154	Eu-155	U-235 (mg)		U-238 (mg)	
	$\mu\text{Ci/g} \pm \text{Error}$	$\mu\text{Ci/g} \pm \text{Error}$	$\text{mg/Sam} \pm \text{Error}$		$\text{mg/Sam} \pm \text{Error}$	
GB-P11-B #1 (40)	4.12E+01 $\pm$ 2.27E-01	5.31E+01 $\pm$ 4.35E-01	4.00E+00 $\pm$ 3.40E-02		1.82E+02 $\pm$ 1.91E+00	
#2 (31)	1.61E+00 $\pm$ 1.40E-01	1.34E+01 $\pm$ 4.15E-01	1.12E+00 $\pm$ 1.60E-02		5.79E+01 $\pm$ 8.90E-01	
#3 (52)	4.28E+01 $\pm$ 1.71E-01	5.65E+01 $\pm$ 4.64E-01	3.09E+00 $\pm$ 2.90E-02		1.36E+02 $\pm$ 1.53E+00	
GB-P11-E #1 (20)	<1.54E+0	<6.33E+0	8.60E-01	1.50E-02	5.05E+01	8.40E-01
#2 (50)	4.23E+01 $\pm$ 2.07E-01	5.50E+01 $\pm$ 4.95E-01	3.74E+00 $\pm$ 3.30E-02		1.62E+02 $\pm$ 1.75E+00	
#3 (18)	9.22E+00 $\pm$ 9.22E-01	4.12E+01 $\pm$ 2.02E+00	7.74E+00 $\pm$ 5.30E-02		3.80E+02 $\pm$ 3.51E+00	
GB-P5-B #1 (14)	4.34E+01 $\pm$ 2.78E-01	5.58E+01 $\pm$ 2.84E-01	2.24E+00 $\pm$ 2.40E-02		1.06E+02 $\pm$ 1.29E+00	
#2 (1)	7.80E+02 $\pm$ 4.53E+00	1.06E+03 $\pm$ 1.11E+01	9.14E-02 $\pm$ 7.40E-03		4.19E+00 $\pm$ 5.40E-01	
GB-P6-B #1 (34)	4.30E+01 $\pm$ 2.54E-01	5.55E+01 $\pm$ 5.55E-01	5.15E+00 $\pm$ 4.10E-02		2.27E+02 $\pm$ 2.28E+00	
#2 (9)	4.18E+01 $\pm$ 1.46E-01	5.46E+01 $\pm$ 3.66E-01	4.36E+00 $\pm$ 3.60E-02		2.02E+02 $\pm$ 2.18E+00	
GB-P7-A #1 (39)	<4.23E-0	<3.26E-02	1.72E+00	2.00E-02	7.61E+01	1.05E+00
GB-P7-C #1 (8)	1.92E+00 $\pm$ 5.06E-01	<2.95E+0	1.12E-01	8.00E-03	4.40E+00 $\pm$ 5.44E-01	
#2 (32)	4.28E+01 $\pm$ 1.76E-01	5.55E+01 $\pm$ 4.10E-01	1.82E+00 $\pm$ 2.10E-02		7.95E+01 $\pm$ 1.08E+00	
GB-P8-A #1 (21)	4.86E+01 $\pm$ 2.33E-01	6.28E+01 $\pm$ 4.71E-01	3.49E+00 $\pm$ 3.10E-02		1.60E+02 $\pm$ 1.73E+00	
GB-P9-A #1 (2)	<2.10E+0	ND	--B--		--B--	
GB-P10-A #1 (5)	3.65E+02 $\pm$ 1.97E+00	4.88E+02 $\pm$ 4.44E+00	--B--		--B-- $\pm$ --	
#2 (10)	7.96E+00 $\pm$ 1.30E-01	2.05E+01 $\pm$ 2.31E-01	2.47E+00	2.50E-02	1.34E+02 $\pm$ 1.51E+00	

TABLE H-3. CORE BORE D8 RADIONUCLIDE CONCENTRATIONS  
( $\mu\text{Ci/g}$  on April 1, 1987)

Identification	Co-60	Sr-90	Ru-106	Sb-125
	$\mu\text{Ci/g}$ +/- Error	$\mu\text{Ci/g}$ +/- Error	$\mu\text{Ci/g}$ +/- Error	$\mu\text{Ci/g}$ +/- Error
D8-P1-C #1 (48)	1.10E+01 +/-2.03E-01	2.71E+01 +/-2.17E+00	1.33E+01 +/-7.60E-01	8.27E+02 +/-1.90E+00
#1B (48b)	1.01E+03 +/-2.93E+00	8.21E+01 +/-6.57E+00	1.53E+03 +/-6.13E+00	1.06E+03 +/-3.29E+00
#2 (15)	1.04E+02 +/-9.54E-01	5.48E+03 +/-4.38E+02	2.61E+02 +/-5.38E+00	2.92E-01 +/-4.82E-02
#3 (68)	8.87E+02 +/-2.84E+00	1.36E+01 +/-1.09E+00	1.74E+03 +/-8.55E+00	9.25E+02 +/-2.03E+00
D8-P2-A1 #1 (53a)	7.43E+01 +/-4.83E-01	1.91E+03 +/-1.53E+02	6.90E+01 +/-1.61E+00	1.50E+02 +/-8.71E-01
#1B (53b)	2.70E+02 +/-1.57E+00	4.63E+03 +/-3.70E+02	3.80E+02 +/-3.16E+00	4.71E+02 +/-2.12E+00
#2 (24)	3.40E+01 +/-2.72E-01	6.43E+03 +/-5.14E+02	1.28E+02 +/-2.05E+00	7.91E+01 +/-4.03E-01
D8-P3-D1 #1 (11)	1.40E+02 +/-7.54E-01	3.01E+03 +/-2.41E+02	2.01E+02 +/-2.61E+00	3.98E+02 +/-1.51E+00
#2 (25)	3.70E+01 +/-3.11E-01	1.01E+03 +/-8.08E+01	4.39E+01 +/-2.01E+00	3.89E+01 +/-6.54E-01
D8-P4-A #1 (33)	1.54E+03 +/-4.15E+00	5.76E+00 +/-4.60E-01	3.17E+03 +/-1.59E+01	1.31E+03 +/-2.76E+00
#2 (60)	1.64E+03 +/-7.69E+00	2.52E+01 +/-2.02E+00	7.71E+03 +/-3.39E+01	2.91E+03 +/-9.60E+00
D8-P4-C #1 (37a)	5.69E+00 +/-5.92E-02	4.49E+03 +/-3.59E+02	<2.14E+0	<4.54E-0
#1B (37b)	1.06E+01 +/-2.15E-01	--a--	7.21E+00 +/-1.03E+00	1.24E+00 +/-3.77E-01
#2 (23)	5.36E+00 +/-8.84E-02	2.54E+03 +/-2.03E+02	<1.29E+0	<4.47E-0

a. Not detected

b. Uranium below detection limit

TABLE H-3. (continued)

Identification	I-129	Cs-134	Cs-137	Co-144
	uCi/g +/- Error	uCi/g +/- Error	uCi/g +/- Error	uCi/g +/- Error
D8-P1-C #1 (48)	4.70E-04 +/- 8.93E-05	<1.21E-0	1.84E+00 +/- 8.45E-02	<1.1E+0
#1B (48b)	2.30E-04 +/- 1.02E-04	<1.02E+0	3.79E+01 +/- 9.58E-01	<1.14E+0
#2 (15)	1.00E-03 +/- 2.29E-04	7.30E+01 +/- 8.47E-01	4.04E+03 +/- 3.64E+00	1.25E+02 +/- 2.52E+01
#3 (68)	1.70E-04 +/- 3.50E-05	6.89E+00 +/- 3.95E-01	3.07E+02 +/- 1.84E+00	2.82E+01 +/- 2.95E+00
D8-P2-A1 #1 (53a)	9.40E-05 +/- 1.96E-05	1.63E+00 +/- 1.41E-01	7.85E+01 +/- 8.87E-01	4.28E+02 +/- 3.51E+01
#1B (53b)	1.50E-04 +/- 3.75E-05	1.59E+00 +/- 3.01E-01	1.52E+01 +/- 6.35E-01	2.21E+02 +/- 2.36E+01
#2 (24)	9.00E-04 +/- 1.98E-04	1.33E+00 +/- 7.98E-02	6.64E+01 +/- 6.11E-01	1.98E+02 +/- 1.24E+01
D8-P3-O1 #1 (11)	2.70E-04 +/- 6.21E-05	1.11E+01 +/- 1.75E-01	5.05E+02 +/- 1.96E+00	7.25E+01 +/- 1.46E+01
#2 (25)	1.00E-04 +/- 2.40E-05	1.45E+01 +/- 1.70E-01	6.61E+02 +/- 2.18E+00	1.40E+02 +/- 1.29E+01
D8-P4-A #1 (33)	4.90E-05 +/- 1.52E-05	<2.25E+0	9.74E+00 +/- 6.40E-01	<1.05E+0
#2 (60)	5.80E-04 +/- 1.04E-04	<2.10E+0	<7.91E00	<2.72E+0
D8-P4-C #1 (37a)	1.40E-05 +/- 9.46E-06	3.94E-01 +/- 4.29E-02	1.69E+01 +/- 2.18E-01	1.54E+02 +/- 4.68E+00
#1B (37b)	1.40E-05 +/- 4.34E-06	9.42E-01 +/- 9.03E-02	4.12E+01 +/- 1.24E-01	2.84E+02 +/- 1.18E+01
#2 (23)	2.00E-06 +/- 2.80E-06	<5.51E-0	2.56E+01 +/- 1.46E-01	1.50E+02 +/- 6.08E+00

H-11

TABLE H-3. (continued)

Identification	Eu-154	Eu-155	U-235 (mg)	U-238 (mg)
	uCi/g +/- Error	uCi/g +/- Error	mg/Sam +/- Error	mg/Sam +/- Error
D8-P1-C #1 (48)	<3.32E-0	<3.00E+0	--b--	--b--
#1B (48b)	<3.39E+0	3.57E+00 +/-1.30E+00	--c--	--c--
#2 (15)	4.87E+01 +/-1.07E+00	5.08E+01 +/-1.25E+00	3.05E+00 +/-2.90E-02	1.67E+02 +/-1.76E+00
#3 (68)	6.10E+00 +/-4.10E-01	1.09E+01 +/-5.65E-01	1.18E+00 +/-1.70E-02	6.70E+01 +/-3.73E+00
D8-P2-A1 #1 (53a)	8.68E+01 +/-8.60E-01	1.42E+02 +/-1.81E+00	3.38E+00 +/-3.10E-02	1.54E+02 +/-1.68E+00
#1B (53b)	3.50E+01 +/-4.72E-01	4.44E+01 +/-4.17E-01	--c-- +/-	--c-- +/-
#2 (24)	3.98E+01 +/-3.27E-01	5.31E+01 +/-5.09E-01	1.90E+00 +/-2.20E-02	9.38E+01 +/-1.18E+00
D8-P3-D1 #1 (11)	2.14E+01 +/-2.97E-01	3.91E+01 +/-6.80E-01	1.15E+00 +/-1.70E-02	5.08E+01 +/-8.50E-01
#2 (25)	2.22E+01 +/-2.17E-01	4.20E+01 +/-3.95E-01	5.70E-01 +/-1.10E-02	2.56E+01 +/-6.50E-01
D8-P4-A #1 (33)	<1.05E+0	<3.50E+0	--b--	--b--
#2 (60)	<2.61E+0	<6.20E+0	--b--	--b--
D8-P4-C #1 (37a)	4.02E+01 +/-2.37E-01	5.19E+01 +/-1.87E-01		
#1B (37b)	7.43E+01 +/-5.28E-01	1.28E+02 +/-1.05E+00		
#2 (23)	4.13E+01 +/-2.19E-01	5.34E+01 +/-5.44E-01		

TABLE H-4. CORE BORE G12 RADIONUCLIDE CONCENTRATIONS  
( $\mu\text{Ci/g}$  on April 1, 1987)

Identification	Co-60	Sr-90	Ru-106	Sb-125
	$\mu\text{Ci/g} \pm \text{Error}$	$\mu\text{Ci/g} \pm \text{Error}$	$\mu\text{Ci/g} \pm \text{Error}$	$\mu\text{Ci/g} \pm \text{Error}$
G12-P1-D2 #1 (49)	1.79E+01 $\pm$ 2.20E-01	8.26E+02 $\pm$ 6.61E+01	<2.93E+0	<8.12E-0
#2 (43)	1.65E+00 $\pm$ 1.01E-02	2.46E+03 $\pm$ 1.97E+02	2.37E-01 $\pm$ 2.50E-02	1.45E-01 $\pm$ 7.00E-03
#2B (43b)	5.01E+00 $\pm$ 4.41E-02	a	6.50E-01 $\pm$ 2.01E-01	3.94E-01 $\pm$ 5.67E-02
G12-P1-E #1 (3)	8.25E-01 $\pm$ 1.85E-02	1.56E+02 $\pm$ 1.25E+01	2.43E-01 $\pm$ 6.73E-02	3.30E-01 $\pm$ 2.11E-02
#2 (59)	4.69E+02 $\pm$ 2.16E+00	6.37E+02 $\pm$ 5.10E+01	2.55E+02 $\pm$ 5.09E+00	5.70E+02 $\pm$ 2.16E+00
#3 (69)	1.49E+01 $\pm$ 1.83E-01	1.98E+03 $\pm$ 1.58E+02	<3.44E+0	1.03E+00 $\pm$ 2.48E-01
#4 (70)	1.99E+01 $\pm$ 1.52E-01	1.50E+03 $\pm$ 1.20E+02	<5.35E+0	2.17E+00 $\pm$ 1.91E-01
G12-P2-B #1 (29)	5.49E+00 $\pm$ 9.22E-02	1.89E+03 $\pm$ 1.51E+02	<1.42E+0	2.68E-01 $\pm$ 1.33E-01
#2 (42)	4.52E+00 $\pm$ 9.23E-02	7.74E+00 $\pm$ 6.19E-01	<1.15E+0	4.23E-01 $\pm$ 1.11E-01
G12-P4-A #1 (58)	1.91E+01 $\pm$ 2.01E-01	5.86E+03 $\pm$ 4.69E+02	<2.03E+0	1.62E+00 $\pm$ 2.20E-01
G12-P9-A1 #1 (22)	1.38E+02 $\pm$ 4.98E-01	3.14E+03 $\pm$ 2.51E+02	1.60E+02 $\pm$ 1.73E+00	1.91E+02 $\pm$ 1.15E+00
#2 (55)	9.30E+01 $\pm$ 5.95E-01	6.15E+00 $\pm$ 4.92E-01	3.44E+01 $\pm$ 9.08E-01	2.98E+00 $\pm$ 3.10E-01

a. Not measured

TABLE H-4. (continued)

Identification	I-129	Cs-134	Cs-137	Ce-144
	uCi/g +/- Error	uCi/g +/- Error	uCi/g +/- Error	uCi/g +/- Error
G12-P1-D2 #1 (49)	6.70E-06 +/-5.15E-06	4.09E-01 +/-5.95E-02	2.04E+01 +/-2.86E-01	1.86E+02 +/-7.81E+00
#2 (43)	9.90E-06 +/-2.77E-06	7.08E-02 +/-2.71E-03	3.22E+00 +/-1.51E-02	1.07E+01 +/-4.01E-01
#2B (43b)	--a--      --a--	1.08E-01 +/-1.36E-02	5.92E+00 +/-5.45E-02	5.04E+01 +/-1.85E+00
G12-P1-E #1 (3)	2.12E-06 +/-4.00E-07	5.43E-02 +/-5.51E-03	2.56E+00 +/-3.36E-02	4.89E+00 +/-7.88E-02
#2 (59)	3.00E-04 +/-6.87E-05	2.32E+01 +/-3.46E-01	1.05E+03 +/-4.41E+00	2.06E+01 +/-2.34E+00
#3 (69)	3.90E-06 +/-8.89E-07	6.27E-01 +/-7.35E-02	2.56E+01 +/-2.25E-01	1.71E+02 +/-1.47E+01
#4 (70)	8.40E-06 +/-6.38E-06	5.56E-01 +/-5.92E-02	2.95E+01 +/-2.39E-01	1.88E+02 +/-8.75E+00
G12-P2-B #1 (29)	5.20E-07 +/-2.90E-09	2.11E-01 +/-4.70E-02	1.08E+01 +/-1.18E-01	1.70E+02 +/-5.83E+00
#2 (42)	<2.7E-7	2.51E-01 +/-3.79E-02	7.23E+00 +/-7.16E-02	1.63E+02 +/-6.33E+00
G12-P4-A #1 (58)	7.70E-06 +/-4.40E-08	4.14E-01 +/-5.73E-02	1.71E+01 +/-1.82E-01	2.02E+02 +/-5.99E+00
G12-P9-A1 #1 (22)	2.40E-04 +/-4.97E-05	3.27E+00 +/-1.42E-01	1.64E+02 +/-8.18E-01	1.80E+02 +/-2.03E+00
#2 (55)	7.70E-06 +/-6.55E-06	3.84E+00 +/-1.05E-01	1.75E+02 +/-8.75E-01	1.45E+02 +/-1.03E+01

TABLE H-4. (continued)

Identification	Eu-154	Eu-155	U-235 (mg)	U-238 (mg)
	$\mu\text{Ci/g} \pm \text{Error}$	$\mu\text{Ci/g} \pm \text{Error}$	$\text{mg/Sam} \pm \text{Error}$	$\text{mg/Sam} \pm \text{Error}$
G12-P1-D2 #1 (49)	4.19E+01 $\pm$ 2.56E-01	5.47E+01 $\pm$ 5.74E-01	4.90E+00 $\pm$ 4.00E-02	2.24E+02 $\pm$ 2.26E+00
#2 (43)	2.12E+00 $\pm$ 9.73E-03	2.71E+00 $\pm$ 1.44E-02	3.19E+00 $\pm$ 3.00E-02	1.39E+02 $\pm$ 1.56E+00
#2B (43b)	1.16E+01 $\pm$ 4.52E-02	1.48E+01 $\pm$ 1.61E-01	--a--	--a--
G12-P1-E #1 (3)	9.97E-01 $\pm$ 1.68E-02	1.21E+00 $\pm$ 3.37E-02	--b--	--b--
#2 (59)	5.30E+00 $\pm$ 4.00E-01	1.37E+01 $\pm$ 6.37E-01	7.43E-01 $\pm$ 1.30E-02	3.31E+01 $\pm$ 7.10E-01
#3 (69)	4.15E+01 $\pm$ 1.91E-01	5.44E+01 $\pm$ 4.08E-01	1.03E+01 $\pm$ 6.90E-02	4.51E+02 $\pm$ 6.85E+00
#4 (70)	4.32E+01 $\pm$ 2.47E-01	5.58E+01 $\pm$ 4.41E-01	5.34E-01 $\pm$ 1.20E-02	2.05E+01 $\pm$ 3.42E+00
G12-P2-B #1 (29)	4.68E+01 $\pm$ 2.20E-01	5.96E+01 $\pm$ 3.99E-01	9.04E+00 $\pm$ 6.30E-02	4.13E+02 $\pm$ 3.82E+00
#2 (42)	4.58E+01 $\pm$ 2.06E-01	5.91E+01 $\pm$ 3.31E-01	1.81E+00 $\pm$ 2.10E-02	8.06E+01 $\pm$ 1.08E+00
G12-P4-A #1 (58)	4.44E+01 $\pm$ 2.26E-01	5.72E+01 $\pm$ 4.58E-01	3.98E+00 $\pm$ 3.40E-02	1.62E+02 $\pm$ 1.76E+00
G12-P9-A1 #1 (22)	2.06E+01 $\pm$ 2.06E-01	2.76E+01 $\pm$ 5.25E-01	2.65E+00 $\pm$ 2.60E-02	1.28E+02 $\pm$ 1.46E+00
#2 (55)	2.55E+01 $\pm$ 2.22E-01	3.49E+01 $\pm$ 5.10E-01	3.48E+00 $\pm$ 3.10E-02	1.48E+02 $\pm$ 1.64E+00

H-15

TABLE H-5. CORE BORES 07, D5, N5 AND 09 RADIONUCLIDE CONCENTRATIONS  
( $\mu\text{Ci/g}$  on April 1, 1987)

Identification	Co-60	Sr-90	Ru-106	Sb-125
	$\mu\text{Ci/g}$ +/- Error	$\mu\text{Ci/g}$ +/- Error	$\mu\text{Ci/g}$ +/- Error	$\mu\text{Ci/g}$ +/- Error
07-P4-C #1 (45)	8.87E+02 +/-3.10E+00	1.55E+02 +/-1.24E+01	5.00E+02 +/-6.30E+00	8.44E+02 +/-1.69E+00
#2 (61)	9.53E+01 +/-6.95E-01	1.40E+03 +/-1.12E+02	2.67E+02 +/-3.36E+00	1.27E-01 +/-1.09E-02
#3 (6)	1.24E+01 +/-1.36E-01	7.58E+02 +/-6.06E+01	5.36E+01 +/-8.04E-01	2.62E+02 +/-1.10E+00
#4 (56)	1.50E+01 +/-2.28E-01	3.49E+02 +/-2.79E+01	8.88E+00 +/-8.00E-01	6.32E+01 +/-4.80E-01
07-P1-A #1 (26)	1.70E+03 +/-5.25E+00	5.50E+00 +/-9.35E-01	4.12E+03 +/-1.53E+01	1.77E+03 +/-4.79E+00
07-P6 #1 (16)	1.23E+03 +/-8.24E+00	1.18E+01 +/-9.44E-01	5.10E+03 +/-2.24E+01	2.31E+03 +/-7.40E+00
#2 (27)	9.95E+02 +/-4.68E+00	1.22E+02 +/-9.76E+00	5.72E+03 +/-1.83E+01	1.86E+03 +/-5.56E+00
D4-P2-A #1 (38)	8.11E+02 +/-3.81E+00	3.61E+01 +/-2.89E+00	1.53E+03 +/-8.69E+00	1.59E-01 +/-3.20E-02
N5-P1-H #1 (13)	3.54E+00 +/-1.92E-01	3.54E+03 +/-2.83E+02	1.15E+01 +/-1.27E+00	5.03E+02 +/-2.11E+00
#2 (65)	5.97E+00 +/-2.05E-01	9.32E+03 +/-7.46E+02	1.03E+01 +/-2.99E+00	8.23E+00 +/-1.48E+00
N5-P1-A #1 (41)	1.19E+02 +/-9.31E-01	1.25E+01 +/-1.00E+00	2.98E+02 +/-3.97E+00	3.56E+02 +/-1.64E+00
N5-P1-D #1 (12a)	7.68E+02 +/-3.61E+00	1.01E+02 +/-8.08E+00	7.27E+02 +/-5.67E+00	6.26E+02 +/-2.00E+00
#1B (12b)	2.13E+02 +/-2.30E+00	1.31E+04 +/-1.05E+03	8.13E+02 +/-9.10E+00	3.15E+02 +/-4.91E+00
#2 (63)	3.35E+02 +/-2.35E+00	7.82E+03 +/-6.26E+02	1.29E+03 +/-7.76E+00	3.76E+02 +/-5.41E+00
09-P1-A #1 (35)	1.52E+03 +/-7.61E+00	8.82E+00 +/-7.06E-01	3.64E+03 +/-1.35E+01	1.27E+03 +/-2.41E+00
#2 (44)	2.85E+00 +/-4.51E-02	8.93E+02 +/-7.14E+01	<1.13E+0	3.53E+00 +/-1.20E-01
09-P1-B #1 (64)	4.04E+00 +/-6.79E-02	3.99E+03 +/-3.19E+02	<1.19E+0	1.10E+01 +/-1.21E-01



TABLE H-5. (continued)

Identification	1-129	Cs-134	Cs-137	Cs-144
	uCi/g +/- Error	uCi/g +/- Error	uCi/g +/- Error	uCi/g +/- Error
07-P4-C #1 (45)	2.20E-05 +/- 1.27E-05	<1.34E+0	1.34E+01 +/- 4.15E-01	<9.79E+0
#2 (61)	1.20E-04 +/- 2.75E-05	3.86E+00 +/- 1.50E-01	1.77E+02 +/- 1.04E+00	9.88E+01 +/- 1.18E+01
#3 (6)	1.50E-04 +/- 2.70E-05	1.43E+01 +/- 1.63E-01	6.66E+02 +/- 1.87E+00	1.43E+02 +/- 6.39E+00
#4 (56)	7.30E-05 +/- 1.75E-05	7.43E+00 +/- 1.22E-01	3.32E+02 +/- 3.98E-01	8.26E+01 +/- 5.42E+00
07-P1-A #1 (26)	1.20E-04 +/- 3.28E-05	<1.43E+0	7.03E+00 +/- 7.90E-01	<3.32E+0
07-P6 #1 (16)	5.40E-04 +/- 9.99E-05	<2.75E+0	<3.58E+0	<2.82E+0
#2 (27)	5.60E-04 +/- 1.28E-04	<2.22E+0	1.03E+01 +/- 8.97E-01	<1.34E+0
04-P2-A #1 (38)	8.30E-04 +/- 1.90E-04	<2.08E+0	3.20E+00 +/- 6.25E-01	<1.81E+0
N5-P1-N #1 (13)	2.70E-04 +/- 4.97E-05	1.45E+01 +/- 1.92E-01	7.16E+02 +/- 2.15E+00	6.05E+01 +/- 6.82E+00
#2 (65)	1.60E-04 +/- 3.17E-05	4.27E+01 +/- 3.46E-01	2.01E+03 +/- 5.22E+00	2.02E+02 +/- 2.09E+01
N5-P1-A #1 (41)	3.00E-04 +/- 6.21E-05	3.15E+01 +/- 6.45E-01	1.42E+03 +/- 3.83E+00	1.47E+02 +/- 2.19E+01
N5-P1-D #1 (12a)	1.10E-04 +/- 2.62E-05	<1.76E+0	7.59E+01 +/- 5.61E-01	<9.80E+0
#1B (12b)	1.90E-03 +/- 4.33E-04	1.23E+02 +/- 1.86E+00	6.67E+03 +/- 8.00E+00	1.99E+02 +/- 9.74E+00
#2 (63)	1.80E-03 +/- 3.73E-04	9.55E+01 +/- 2.10E+00	4.92E+03 +/- 7.38E+00	1.57E+02 +/- 9.44E+00
09-P1-A #1 (35)	2.40E-04 +/- 4.97E-05	<2.47E+0	<3.39E+0	<2.93E+0
#2 (44)	2.50E-05 +/- 5.20E-06	3.26E-01 +/- 5.00E-02	1.31E+01 +/- 2.35E-01	1.54E+02 +/- 5.00E+00
09-P1-B #1 (64)	1.50E-04 +/- 3.09E-05	2.28E-01 +/- 4.23E-02	9.94E+00 +/- 1.66E-01	1.52E+02 +/- 4.57E+00

H-17

TABLE H-5. (continued)

Identification	Eu-154	Eu-155	U-235 (mg)	U-238 (mg)
	uCi/g +/- Error	uCi/g +/- Error	mg/Sam +/- Error	mg/Sam +/- Error
07-P4-C #1 (45)	<1.38E+0	2.00E+00 +/-9.33E-01	4.70E-02 +/-7.00E-03	1.34E+00 +/-4.50E-01
#2 (61)	1.90E+01 +/-2.67E-01	3.44E+01 +/-5.19E-01	1.71E+00 +/-2.00E-02	8.28E+01 +/-1.10E+00
#3 (6)	2.62E+01 +/-1.70E-01	4.07E+01 +/-3.33E-01	2.53E+00 +/-2.60E-02	1.41E+02 +/-1.60E+00
#4 (56)	1.20E+01 +/-1.22E-01	1.83E+01 +/-2.12E-01	6.49E-01 +/-1.30E-02	2.92E+01 +/-6.80E-01
07-P1-A #1 (26)	<2.31E+0	<3.66E+0	--a--	--a--
07-P6 #1 (16)	<2.44E+0	9.66E+00 +/-2.06E+00	--a--	--a--
#2 (27)	<1.93E+0	<4.62E+0	6.60E-02 7.00E-03	1.95E+00 4.60E-01
D4-P2-A #1 (38)	<2.42E+0	7.82E+00 +/-1.85E+00	--a--	--a--
N5-P1-H #1 (13)	1.18E+01 +/-1.96E-01	2.31E+01 +/-4.51E-01	1.16E+00 +/-1.70E-02	5.25E+01 +/-8.60E-01
#2 (65)	4.54E+01 +/-4.04E-01	5.98E+01 +/-1.33E+00	4.48E-01 +/-1.10E-02	1.76E+01 +/-5.90E-01
N5-P1-A #1 (41)	2.50E+01 +/-4.70E-01	4.13E+01 +/-1.27E+00	2.70E+00 +/-2.60E-02	1.19E+02 +/-1.39E+00
N5-P1-D #1 (12a)	<1.46E+0	<2.00E+0	7.36E+00 +/-5.20E-02	3.24E+02 +/-3.09E+00
#1B (12b)	3.16E+01 +/-1.36E+00	6.30E+01 +/-2.25E+00	--b-- +/-	--b-- +/-
#2 (63)	2.31E+01 +/-1.42E+00	4.59E+01 +/-1.97E+00	7.96E+00 +/-5.70E-02	3.21E+02 +/-3.08E+00
09-P1-A #1 (35)	<2.90E+0	<4.12E+0	--a-- --a--	
#2 (44)	4.23E+01 +/-1.78E-01	5.55E+01 +/-4.60E-01	7.50E+00 +/-5.50E-02	3.40E+02 3.21E+00
09-P1-B #1 (64)	4.64E+01 +/-2.32E-01	5.90E+01 +/-5.01E-01		

**APPENDIX I**  
**DATA QUALIFICATION**



## APPENDIX I

### DATA QUALIFICATION

A data qualification program was performed as part of this examination program. Duplicate samples were obtained from some core bores, and in some cases, split samples were analyzed after an individual sample had been dissolved. The results of these examinations are listed in Appendices G and H. An analysis of these results indicates that the split (dissolved) sample results produce reproducible results within 5 to 10%; however, the duplicate samples removed from individual microcores had variations up to 100%. This effect results from the heterogeneity of the microcores and does not compromise the results, which are indicative of chemical and fission product phenomena. Normalization of the results to uranium content tends to remove biases associated with variation in the material content of the sample. Consequently, each sample is generally indicative of the chemical and fission product behavior in that part of the core when normalized to the elemental or chemical form of interest. Multiple samples are required to evaluate radionuclide retention or relocation in a particular portion of the reactor core.



APPENDIX J  
QUANTITATIVE WDS ANALYSIS





## APPENDIX J

### QUANTITATIVE WDS ANALYSIS

Wavelength dispersive X-ray spectrometry (WDS) provides the capability of performing quantitative microanalysis of materials in a scanning electron microscope. This technique was utilized to analyze phases in a number of the TMI lower core samples. The compositions were quantified for thirteen points on five samples: two samples from the upper crust (G8-P11-C2, K9-P2-D1), two from the lower crust (K9-P1-D1, K9-P1-D2), and one from a ceramic particle (K9-P4-D). However, only selected representative point analyses are presented in this appendix.

The basic technique of WDS was described in Appendix B. The procedure for obtaining quantitative information from WDS spectra consists of comparing, for a given element in a phase of unknown composition, the intensity of the characteristic X-ray signal (generated by the SEM electron beam hitting the sample) between the unknown and a well-characterized standard. To a very rough first approximation, a phase composed 50% of a given element will give a characteristic X-ray signal 50% as intense as would a pure standard of that element. However, the atomic processes of electron beam/material and X-ray/material interaction are extremely complex, and accurate quantitative analyses can only be achieved by correcting for these effects. This is especially important for material of highly dissimilar elemental constituents such as heavy metal oxides.

Quantification is performed by means of a set of correction equations that take into account such convoluting factors as electron backscattering and retardation, matrix X-ray absorption, and secondary X-ray fluorescence, all of which act to change the signal intensity from that anticipated on a simple compositional percentage basis. This experiment used a computer program for electron probe correction developed by Dr. J. Armstrong at the California Institute of Technology. The program (CITZAF) allows choices of various computational schemes for correction factors that catenate to generate the overall correction for

the peak height, from which element concentrations are calculated. The choice of specific schemes for correction factors depends on the nature of the sample material and the experimental conditions.

Despite the sophisticated correction schemes that have been developed for WDS microanalysis, there are still computational errors associated with any such procedure, due again to the very complex nature of the problem. That is why the CITZAF program allows the user to choose between different sets of correction equations; different equations perform better than others depending on the experimental conditions (beam voltage, sample composition, sample configuration). The only possible situation without computational error is the case of both unknown and standard being the exact same material, where the correction factors reduce to unity. In such a situation only measurement errors are of concern. Computational errors grow as the number of elements in a phase increases, and this was a problem for the TMI material, as many of the samples contained phases with a dozen or more elements.

In the examination of TMI samples experimental difficulties caused by the high radiation fields of the material had to be overcome before accurate quantitative analyses could be performed. Samples ranged from 1 to 60 R/h (contact beta-gamma). This radiation generated a very high background in the WDS detectors that interfered with the acquisition of spectral peaks from low concentration elements, and from oxygen. The high fields also necessitated fully remote sample handling, which prevented the use of a standard carbon coater for specimen preparation. The methods used to handle these difficulties are described below.

### High Spectral Background

The background observed in a WDS spectrum of TMI material is composed of two parts: electron beam induced background (primarily Bremsstrahlung radiation) and beam independent background caused by radioactive decay. The decay background is the dominant effect, in some cases an order of magnitude greater in intensity than the beam-induced signal. Although W shielding was placed where possible between the sample holder and X-ray

detectors, it was not possible to shield them through their full range of travel because the detectors moved along a large arc. The resulting background is shown in Figure J-1, a spectrum acquired with the electron beam off. The spectrum thus contains no compositional information, and the variation of intensity is purely a function of the radiation field. The decrease with increasing spectrometer position is caused by the motion of the detector, which travels in an arc away from the specimen for most of its range. The small increase at the high end (high wavelength/low energy) of the range results because the detector reaches a maximum distance, and then begins to approach the sample. The change in slope of the decrease is from the W shielding.

Decay background degraded the ability of the system to detect and quantify trace elements, but did not greatly affect the acquisition of major constituents, with the significant exception of oxygen. Because oxygen X-rays are of very low energy and, as a result, highly absorbed in the sample material, measurable peak intensity is low. A diffracting crystal with a large d-spacing is required because of the long X-ray wavelength, resulting in a very broad peak. These factors, coupled with a rising decay background in the peak region, make it difficult to find the true peak height required for quantification (Figure J-2).

The following procedure was used for the broad, low intensity oxygen peaks on a rising background. A WDS spectrum of the peak area was acquired with the TAP crystal. The resulting spectrum included most of the peak, although a portion of the low energy tail could not be acquired because of mechanical limits in spectrometer travel (Figure J-3). The spectrum is composed of three superimposed spectra: the two background components mentioned above and the characteristic (peak-forming) X-ray signal. In order to find the true height of the peak, four measurements were made: A, at the peak position with the beam on; B, at a higher energy peak position beyond the tail of the peak with the beam on; C, at the same position as B with the beam off; and D, at the peak position with the beam off (Figure J-4). With the beam off only the radiation background is

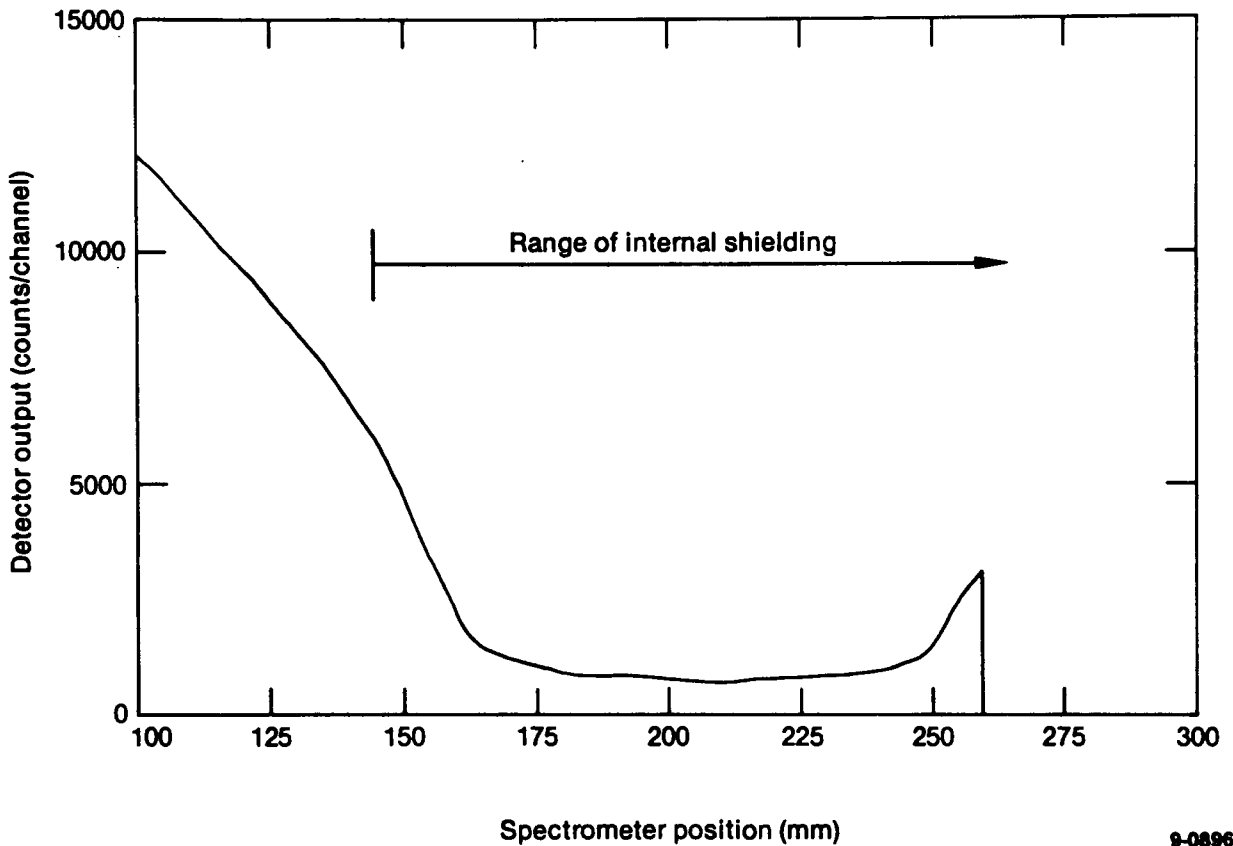
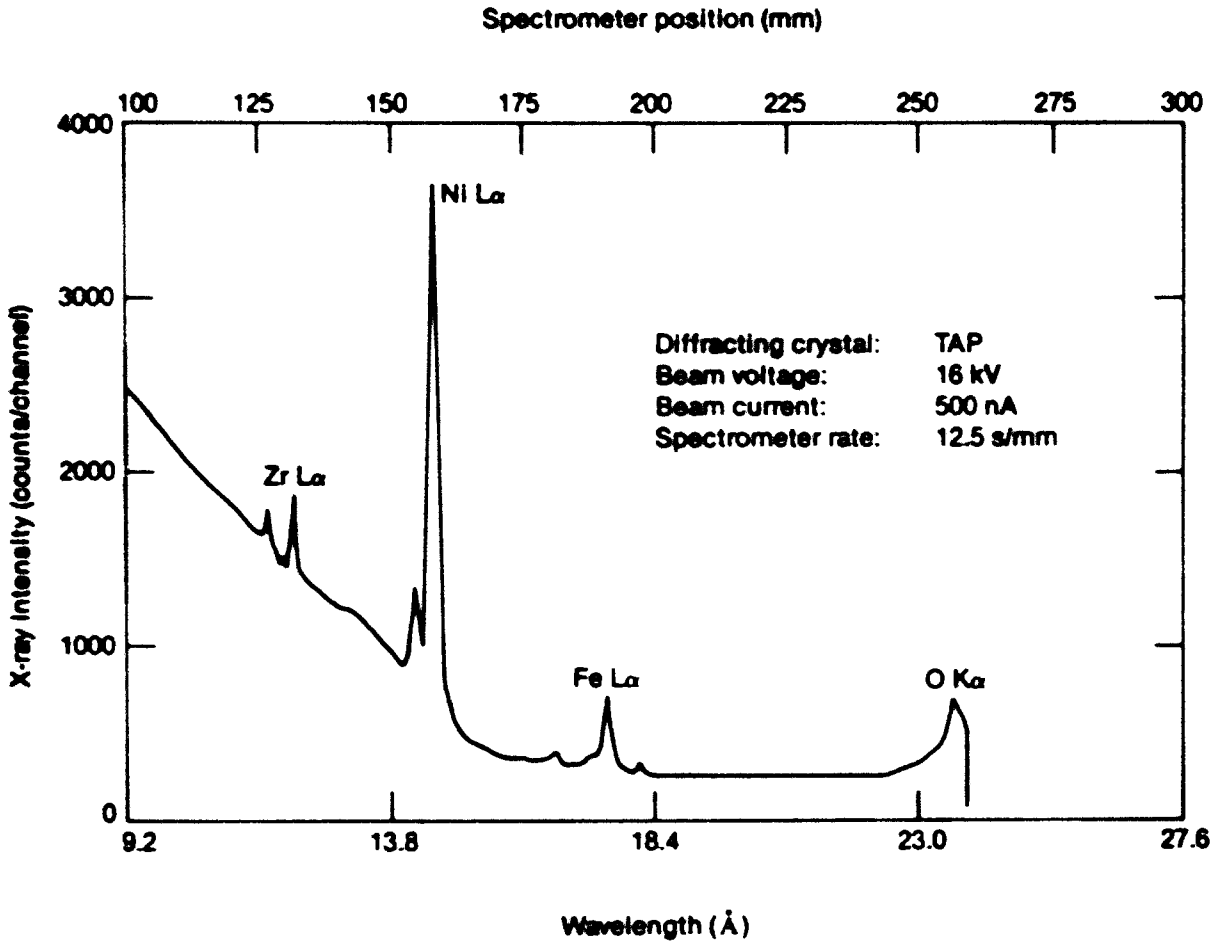


Figure J-1. WDS spectrometer background due to radiation from sample (30 R/h contact beta-gamma) with no beam. Variation due to changing sample detector distance. Change in slope at 145 mm is caused by internal tungsten shielding.



9-0894

Figure J-2. WDS spectrum of oxidized steel from TMI core. Comparison with Figure J-1 shows that the broad, weak oxygen peak is located on a rising background, making background subtraction difficult.

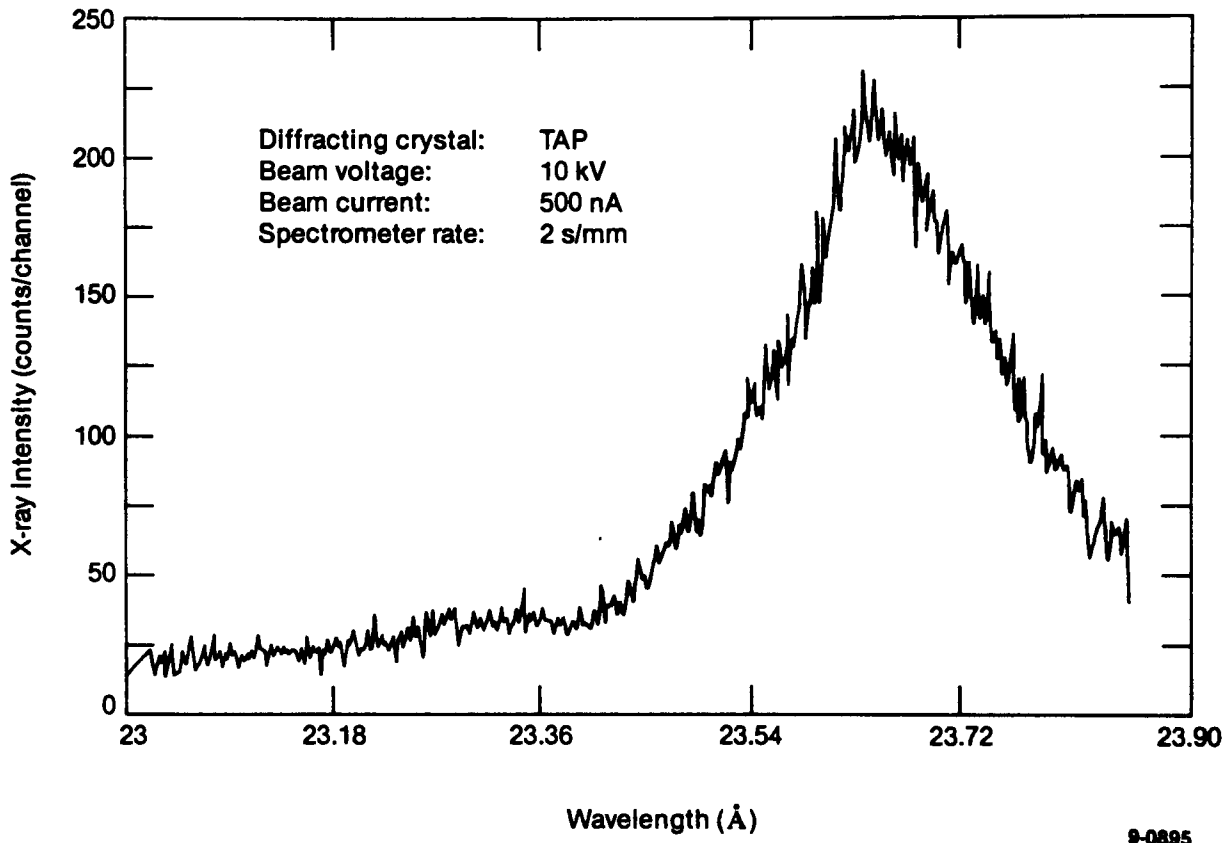
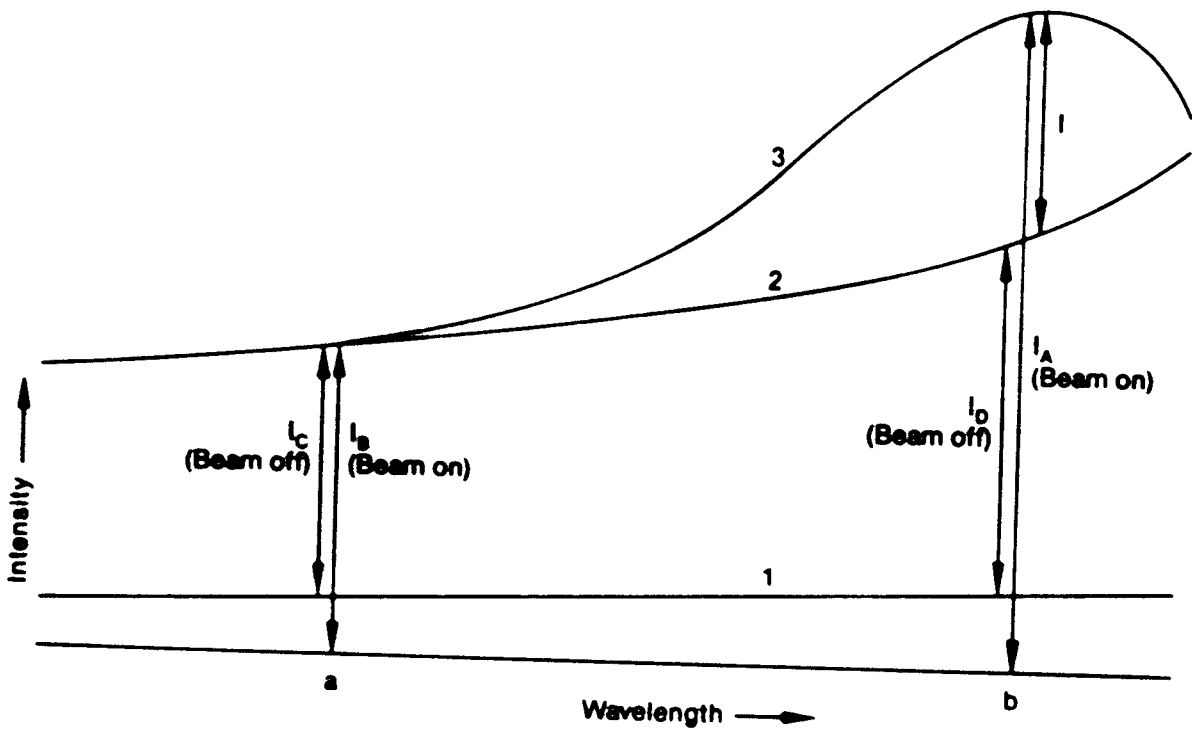


Figure J-3. WDX oxygen peak from oxidized TMI steel. The low wavelength tail (right) is cut off because of spectrometer geometry.



9-0893

Figure J-4. Oxygen peak background subtraction method for radioactive samples. Curves 1, 2, and 3 correspond to beam-induced background, radiation background, and the true peak, respectively. True peak height ( $I$ ) can be closely approximated by appropriate addition of four measurements ( $I_A$ ,  $I_B$ ,  $I_C$ , and  $I_D$ ).

measured, and if the beam-induced background is assumed to be constant for a given beam current and voltage over the range of measurement, then

$$I_P = (I_A + I_C) - (I_B + I_D)$$

where  $I_P$  is the true oxygen peak intensity and  $I_A$ ,  $I_B$ ,  $I_C$ , and  $I_D$  are measured intensities at the points listed above.

### Specimen Coating

The high radiation fields of the samples necessitated fully remote operations, including sample coating. All nonconductive samples placed in an SEM must have a conductive surface coating applied to them to prevent static charging under the electron beam. For quantitative analysis the coating is usually carbon, which is highly electron and X-ray transparent and, therefore, does not interfere with the analysis. Carbon coatings are applied with various forms of evaporative systems, usually involving thin carbon rods heated by a large current. Such a system could not be utilized for the TMI quantitative analysis, because remote operation of such a system did not afford enough control over the rapid evaporative process to reproduce consistent coating thicknesses. Accuracy in analysis requires that surface coatings of samples and standards be of equal thickness.

A gold sputter coater (Ernest Fullam Mini-Coater) achieved more uniform specimen coating. Sputtering has the advantages of simplicity of operation, making it ideal for remote usage, and a slow deposition rate, allowing great control over layer thickness. The disadvantages of having a gold surface layer on a SEM specimen are 1) a large number of characteristic peaks generated by gold can interfere by overlapping the peaks of other elements, and 2) sputtering cannot be used on a sample where gold might be intrinsically present, for the obvious reason that it would bias the data. Overlapping higher order peaks presented no difficulties; the layer required to prevent charging was thin enough so that only the principal gold peak was detectable and did not interfere with any other element. The latter problem was not of concern in the present examination.



## Data Acquisition

In acquiring quantitative WDS data, beam voltage, beam current, and acquisition time were adjusted to provide optimum measurements. The nature of the sample material determined the best values for each variable. The elemental composition of every analysis point was considered individually in determining the experimental conditions.

Electron primary beam voltage was adjusted to maximize the X-ray signal. For heavy elements, higher voltage results in higher count rates, but for oxygen, low voltage produces X-rays most efficiently. A beam potential of 10-15 kV was found to be the most effective compromise.

The most intense signal is generated at high primary beam currents, although a current greater than 100 nA was found to produce instability in peak heights of some oxide phases. Due to this instability, and because a low current and long counting time lead to system drift errors, measurements were made with a beam current of 100 nA or less, and acquisition times were limited to 200 seconds.

Selection of sample points was based on both an examination of SEM images and WDS dot maps and a semi-quantitative analysis of a large number of possible points. This analysis consisted of using a 'canned' computer program to acquire WDS peak height data (Tracor/Northern TASK V on T/N 5500-5600 coupled systems). The program controlled both spectrometer and sample motion in the SEM, finding peak heights and backgrounds for numerous pre-selected points. The program involved a sequence of operations that did not include actual spectral retention, did not take into account background anomalies such as nearby peaks or (for oxygen) the background slope caused by sample radiation, and did not vary the electron beam current or voltage for different material compositions to maximize the signal, as described above. Although the results generated included large errors, especially for oxygen, they provided an idea of the general composition.

Points selected for final analysis had to meet certain physical requirements: each point was located in a uniform, single-phase region; the region was large enough to prevent generation of fluorescent X-rays from surrounding phases (a minimum diameter of 10  $\mu\text{m}$  was desired); and the surface was both flat and smooth. Accuracy in quantitative microanalysis can be achieved only when these requirements are fulfilled.

The analyses used a set of element and compound standards prepared by the C.M. Taylor Corporation. These standards included pure elements for every component found in the TMI core material with the exceptions of O and In (InP was used for In). The oxides  $\text{ZrO}_2$ ,  $\text{UO}_2$ , and  $\text{Fe}_2\text{O}_3$  were variously employed as O standards, depending on the analysis point composition. Best results are obtained with standards as close as possible in composition to the unknown. Also, for this reason  $\text{UO}_2$  was used as the U standard, since most of the U in the bundle had oxidized; and because, due to the high potential for oxidation, the elemental U standard always developed a surface layer of  $\text{UO}_2$  which rendered it of little value as a quantitative standard. Standards used in the several point analyses are listed along with the data in Tables J-1 through J-9, which are introduced in the following sections.

The present system has not acquired enough data to provide a precise uncertainty for the calculated element concentrations. The uncertainties are a function of experimental and computational uncertainties, and the latter is, in turn, a function of the complexity of the sample composition. More elements generate greater probable error. For sample points of eight or ten elements, the uncertainty is greater than 10%. For points of two or three elements with standards close in composition to the unknown [e.g., regions of Zr-rich  $(\text{U,Zr})\text{O}_2$  in the ceramic melt region], the uncertainty is less than 10%.

TABLE J-1. WDS QUANTITATIVE ANALYSIS, Sample G8-P11-C2

<u>Sample Point</u>	<u>Element</u>	<u>Wt%</u>	<u>Normalized wt%</u>	<u>Atom%</u>
1	O	12.92	13.86	64.0
	Fe	1.30	1.40	1.9
	Zr	14.83	15.91	12.9
	U	64.14	68.83	21.4
2	O	25.46	25.97	67.0
	Zr	70.84	72.25	32.7
	U	1.74	1.78	0.3

Primary beam voltage: 10kV

Element/standard: O/ZrO<sub>2</sub>  
 Fe/Fe<sub>2</sub>O<sub>3</sub>  
 Zr/ZrO<sub>2</sub>  
 U/UO<sub>2</sub>

Correction program: Caltech ZAF with the following correction procedures

Backscatter correction of Love/Scott  
 Mean ionization potentials of Berger/Seltzer  
 Phi (0) Equation of Love/Scott  
 Phi-rho-Z absorption correction of Armstrong  
 Atomic number correction of Love/Scott

TABLE J-2. WDS QUANTITATIVE ANALYSIS, Sample K9-P2-D1

Sample Point	Element	<u>Wt%</u>	<u>Normalized Wt%</u>	<u>Atom%</u>
3	Fe	3.20	3.39	5.1
	Ni	34.66	36.72	52.5
	Sn	56.54	59.89	42.4

Primary beam voltage: 15kV

Element/standard: Fe/Fe  
 Ni/Ni  
 Sn/Sn

Correction program: Caltech ZAF with the following correction procedures

Backscatter correction of Love/Scott  
 Mean ionization potentials of Berger/Seltzer  
 Phi (0) Equation of Reuter  
 Phi-rho-Z absorption correction of Philibert  
 Atomic number correction of Duncumb/Reed

TABLE J-3. WDS QUANTITATIVE ANALYSIS, SAMPLE K9-P1-D1

<u>Sample Point</u>	<u>Element</u>	<u>Wt%</u>	<u>Normalized wt%</u>	<u>Atom%</u>
4	Ag	87.58	90.98	91.5
	In	8.69	9.02	8.5
5	Ag	85.99	84.66	85.4
	In	15.59	15.34	14.6

Primary beam voltage: 15kV

Element/standard: Ag/Ag  
In/InP

Correction program: Caltech ZAF with the following correction procedures

Backscatter correction of Love/Scott  
Mean ionization potentials of Berger/Seltzer  
Phi (0) Equation of Reuter  
Phi-rho-Z absorption correction of Philibert  
Atomic number correction of Duncumb/Reed

TABLE J-4. WDS QUANTITATIVE ANALYSIS, SAMPLE K9-P1-D1

---

<u>Sample Point</u>	<u>Element</u>	<u>Wt%</u>	<u>Normalized Wt%</u>	<u>Atom%</u>
6	Cr	6.86	7.35	9.8
	Fe	35.39	37.88	47.2
	Ni	5.90	6.32	7.5
	Zr	42.88	45.90	34.9
	U	2.38	2.54	0.7

---

Primary beam voltage: 15kV

Element/standard: Cr/Cr  
 Fe/Fe  
 Ni/Ni  
 Zr/Zr  
 U/UO<sub>2</sub>

Correction program: Caltech ZAF with the following correction procedures

Backscatter correction of Love/Scott  
 Mean ionization potentials of Berger/Seltzer  
 Phi (0) Equation of Reuter  
 Phi-rho-Z absorption correction of Philibert  
 Atomic number correction of Duncumb/Reed

TABLE J-5. WDS QUANTITATIVE ANALYSIS, SAMPLE K9-P1-D1

<u>Sample Point</u>	<u>Element</u>	<u>Wt%</u>	<u>Normalized Wt%</u>	<u>Atom%</u>
7	O	15.93	15.88	44.7
	Cr	6.65	6.63	5.8
	Fe	31.39	31.29	25.3
	Ni	7.81	7.79	6.0
	Zr	36.60	36.48	18.0
	U	1.94	1.94	0.4

Primary beam voltage: 10kV

Element/standard: O/Fe<sub>2</sub>O<sub>3</sub>  
 Cr/Cr  
 Fe/Fe<sub>2</sub>O<sub>3</sub>  
 Ni/Ni  
 Zr/Zr  
 U/UO<sub>2</sub>

Correction program: Caltech ZAF with the following correction procedures

Backscatter correction of Love/Scott  
 Mean ionization potentials of Berger/Seltzer  
 Phi (0) Equation of Love/Scott  
 Phi-rho-Z absorption correction of Armstrong  
 Atomic number correction of Love/Scott

TABLE J-6. WDS QUANTITATIVE ANALYSIS, SAMPLE K9-P1-D1

<u>Sample Point</u>	<u>Element</u>	<u>Wt%</u>	<u>Normalized Wt%</u>	<u>Atom%</u>
8	Fe	1.52	1.59	2.5
	Ni	24.99	26.02	37.4
	Zr	43.28	45.05	41.7
	Ag	5.55	5.78	4.5
	In	16.98	17.67	13.0
	U	3.75	3.90	1.4

Primary beam voltage: 15kV

Element/standard: Fe/Fe  
 Ni/Ni  
 Zr/Zr  
 Ag/Ag  
 In/InP  
 U/UO<sub>2</sub>

Correction program: Caltech ZAF with the following correction procedures

Backscatter correction of Love/Scott  
 Mean ionization potentials of Berger/Seltzer  
 Phi (0) Equation of Reuter  
 Phi-rho-Z absorption correction of Philibert  
 Atomic number correction of Duncumb/Reed



TABLE J-7. WDS QUANTITATIVE ANALYSIS, SAMPLE K9-P1-D1

---

<u>Sample Point</u>	<u>Element</u>	<u>Wt%</u>	<u>Normalized wt%</u>	<u>Atom%</u>
9	O	11.30	11.70	66.3
	U	85.35	88.30	33.7

---

Primary beam voltage: 10kV

Element/standard: O/UO<sub>2</sub>  
U/UO<sub>2</sub>

Correction program: Caltech ZAF with the following correction procedures

Backscatter correction of Love/Scott  
Mean ionization potentials of Berger/Seltzer  
Phi (0) Equation of Reuter  
Phi-rho-Z absorption correction of Philibert  
Atomic number correction of Duncumb/Reed

TABLE J-8. WDS QUANTITATIVE ANALYSIS, SAMPLE K9-P1-D2

<u>Sample Point</u>	<u>Element</u>	<u>Wt%</u>	<u>Normalized Wt%</u>	<u>Atom%</u>
10	O	16.81	16.94	47.0
	Cr	0.58	0.59	0.5
	Fe	33.29	33.54	26.7
	Ni	9.31	9.38	7.1
	Zr	37.16	37.45	18.2
	U	2.09	2.10	0.4

Primary beam voltage: 10kV

Element/standard: O/Fe<sub>2</sub>O<sub>3</sub>  
 Cr/Cr  
 Fe/Fe<sub>2</sub>O<sub>3</sub>  
 Ni/Ni  
 Zr/ZrO<sub>2</sub>  
 U/UO<sub>2</sub>

Correction program: Caltech ZAF with the following correction procedures

Backscatter correction of Love/Scott  
 Mean ionization potentials of Berger/Seltzer  
 Phi (0) Equation of Love/Scott  
 Phi-rho-Z absorption correction of Armstrong  
 Atomic number correction of Love/Scott

TABLE J-9. WDS QUANTITATIVE ANALYSIS, SAMPLE K9-P1-D2

<u>Sample Point</u>	<u>Element</u>	<u>Wt%</u>	<u>Normalized wt%</u>	<u>Atom%</u>
13	O	23.53	23.02	65.7
	Zr	64.66	63.26	31.7
	U	14.02	13.72	2.6

Primary beam voltage: 10kV

Element/standard: O/ZrO<sub>2</sub>  
 Zr/ZrO<sub>2</sub>  
 U/UO<sub>2</sub>

Correction program: Caltech ZAF with the following correction procedures

Backscatter correction of Love/Scott  
 Mean ionization potentials of Berger/Seltzer  
 Phi (0) Equation of Love/Scott  
 Phi-rho-Z absorption correction of Armstrong  
 Atomic number correction of Love/Scott

## Results

### Upper Crust

Two points from the upper crust ceramic material were analyzed from sample G8-P11-C2 (points 1 and 2, Table J-1, Figure J-5). This ceramic proved to be  $(U,Zr)O_2$ . The composition of point 1 was in the U-rich side of the single-phase solid solution, and contained a small quantity of Fe. Eutectic solidification of  $UO_2$  and Fe-Cr oxide took place extensively around point 1; the presence of 1.9 molecular wt% of Fe at point 1 is consistent with a mechanism in which prior-oxidized Fe from stainless steel and Inconel is dissolved in molten  $(U,Zr)O_2$  before solidifying eutectically. The minimum melting temperature for a composition equivalent to point 1 minus the Fe is 2810 K; the Fe in solution would have depressed the melting point less than 100 degrees. Point 2 was in a region of oxidized zircaloy cladding. The composition was  $ZrO_2$  with 0.9 molecular wt%  $UO_2$ .

A detail of the upper crust interface between two metallic regions is seen in Figure J-6 (sample K9-P2-D1). The region that appears darker in the backscattered electron image is Fe-Ni-Cr; the lighter region is control rod Ag-In with a small amount of Sn. The structural material elements are immiscible with the control rod elements, but a mediating Sn-rich phase is present at the interface. Quantitative analysis (point 3) gives the composition of this phase as shown in Table J-2. The phase corresponds to the intermetallic  $Ni_3Sn_2$  with a melting temperature of 1537 K. It is present at the interface as the only phase containing components of both metallic regions.

### Lower Crust

Two samples from the lower crust were investigated with quantitative WDS, K9-P1-D1 and K9-P1-D2. These samples contained prior-molten material from between fuel pellet stacks (K9-P1-D1) and from a pellet-pellet interface region (K9-P1-D2). Backscattered electron images showing the

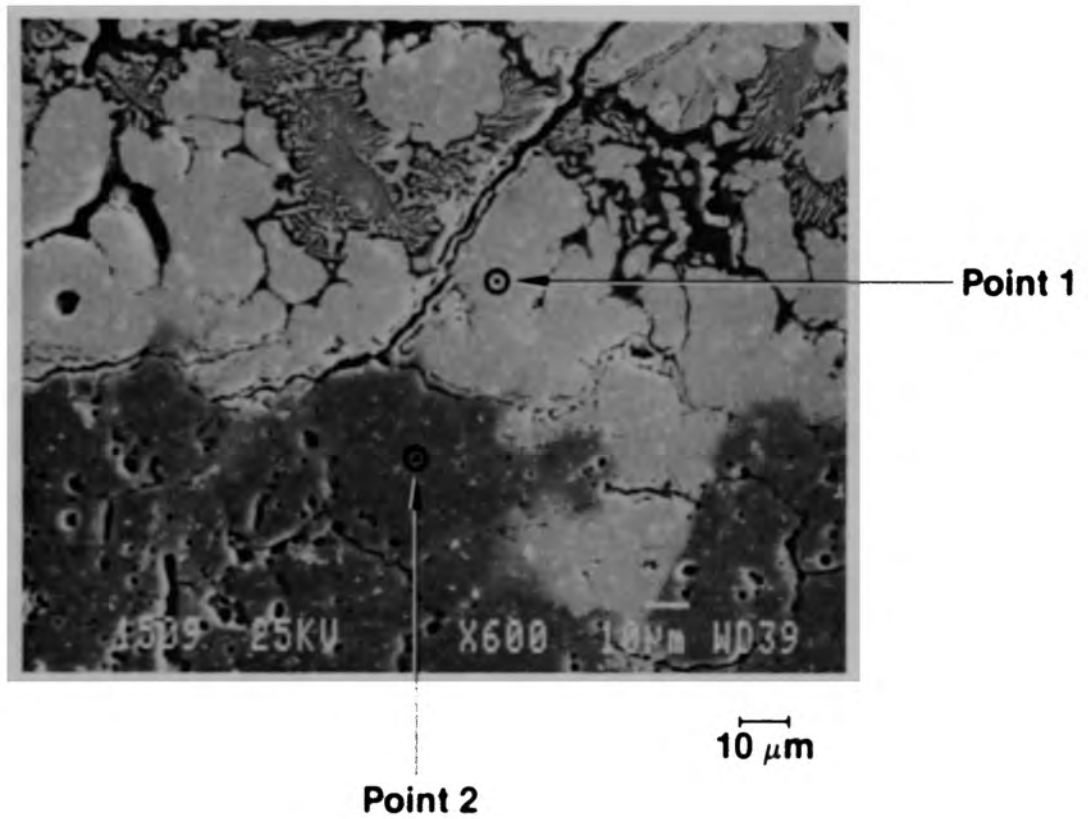


Figure J-5. Secondary electron image of G8-P11-C2 Area 1, showing locations of quantitative WDS points 1 and 2.

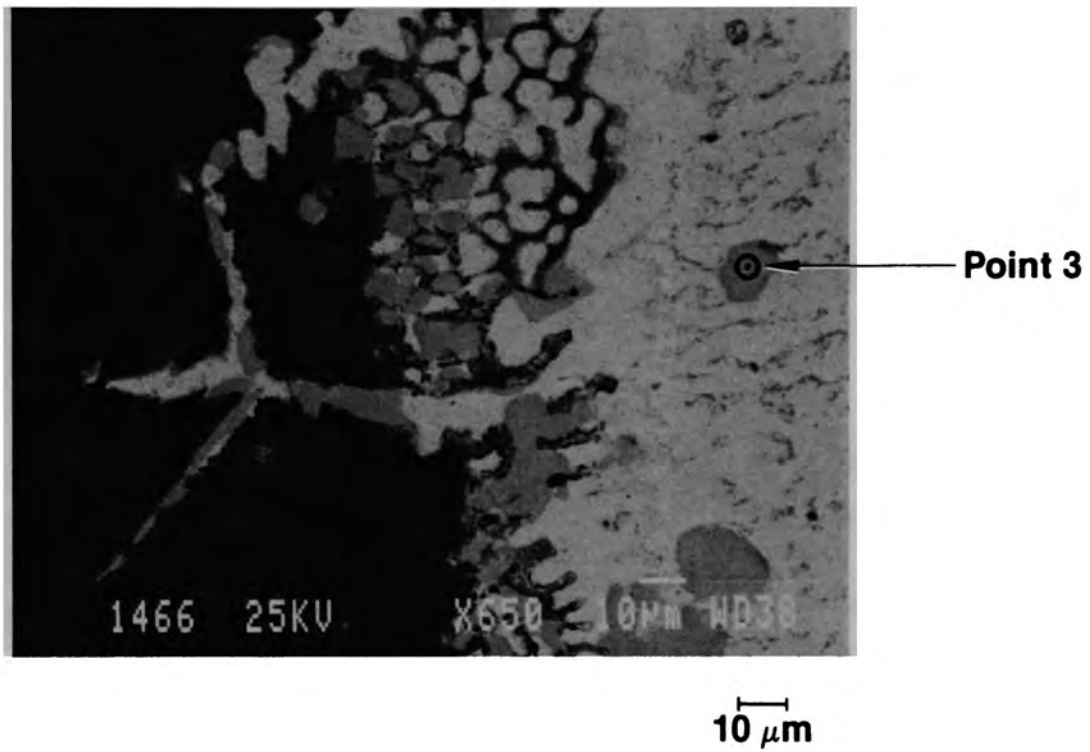


Figure J-6. Backscattered electron image of K9-P2-D1 Area 1, showing location of quantitative WDS point 3.

locations of point analyses for sample K9-P1-D1 are shown in Figures J-7 and J-8. Backscattered electron images showing the locations of point analyses for sample K9-P1-D2 are shown in Figures J-9 and J-10.

Control rod material in both the inter-rod and inter-pellet regions was analyzed (points 4 and 5, Table J-3). No Cd remained in the alloy, and Ag was enriched with respect to In from the original .80Ag-.15In-.05Cd alloy. This enrichment is consistent with the fact that In underwent extensive solution in a number of phases present in the TMI material, principally in combination with Sn and Ni, while Ag was less interactive and tended to remain in the original alloy, and Cd is very volatile.

A large percentage of the prior-molten material of the lower crust is composed of a mixed structural material, a zircaloy phase which exists in both metallic and oxidized states. Point 6 (Table J-4) is the metallic state, while point 7 (Table J-5) is the oxide. Iron and Zr predominate, with smaller amounts of Ni and Cr and a trace of dissolved U. The compositions are proportionally close to  $ZrM_2$ , where M represents Fe+Ni+Cr, which has been identified by Kleykamp of KfK as one of two principal metallic alloys of Zr in TMI lower crust material (the other being  $Zr_2M$ ). Iron forms an intermetallic  $Fe_2Zr$ , with a melting point of 1918 K which is probably close to that of the material examined.

The oxidation of lower crust  $ZrM_2$  results in a material with a metal-oxygen ratio of somewhat greater than one. This is true for point 7 as well as point 10 on sample K9-P1-D2 (Table J-8). This ratio does not correspond easily to any simple and reasonable oxide formula. The oxidation state of this material is unclear.

Point 8 on sample K9-P1-D1 is an example of one of the phases mentioned above that is enriched with In from control rod alloy. As shown in Table J-6, the Ni/In ratio corresponds to the intermetallic  $Ni_3In$ , with a melting point of 1179 K.

Within the fuel pellet sectioned in sample K9-P1-D1, point 9 was selected for analysis (Table J-7). The composition was, as expected,

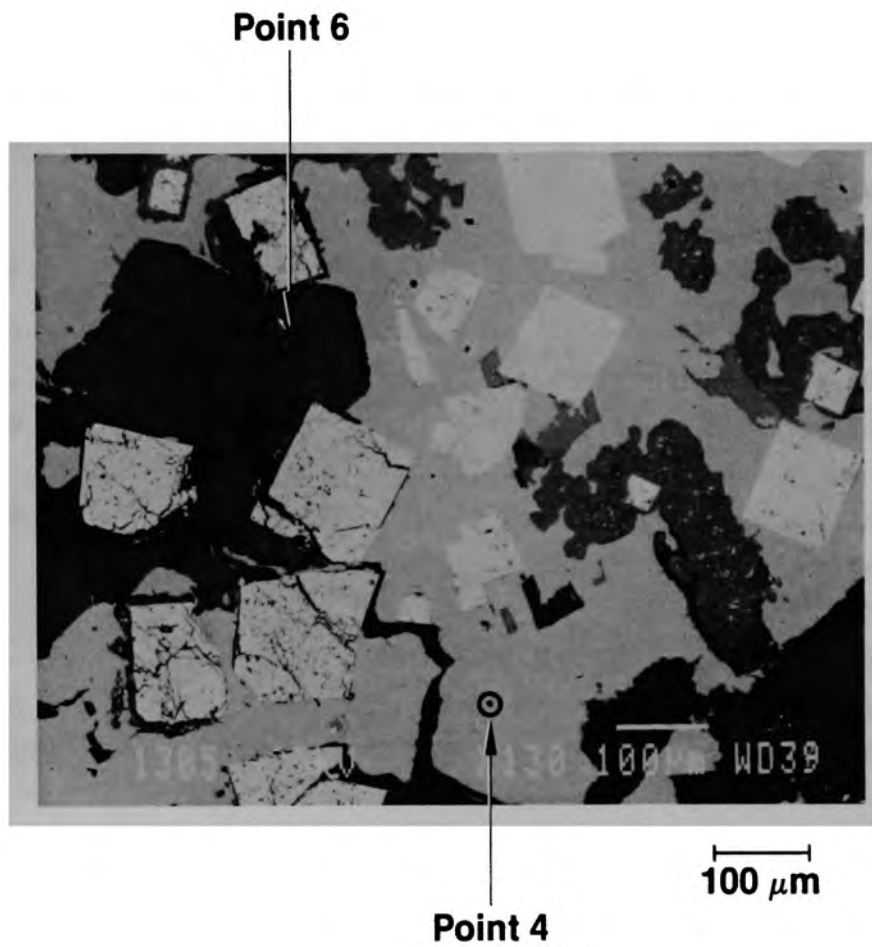


Figure J-7. Backscattered electron image of K9-P2-D1 Area 2, showing locations of quantitative WDS points 4 and 6.



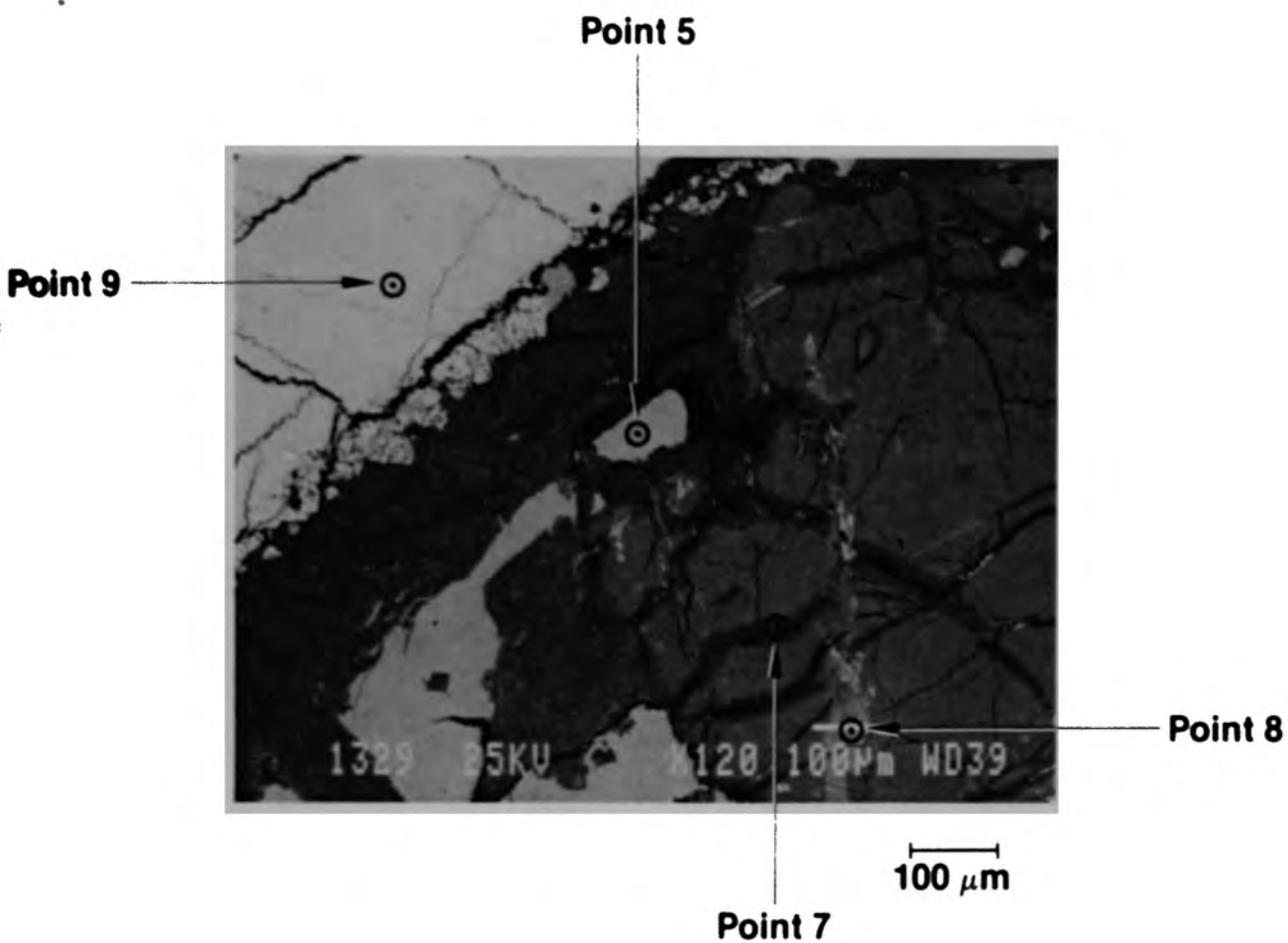
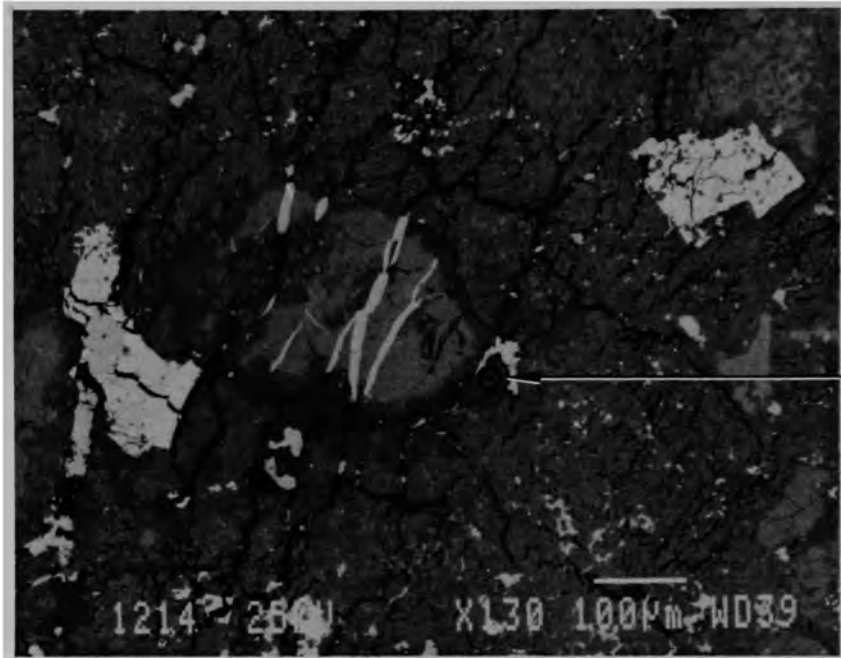


Figure J-8. Backscattered electron image of K9-P1-D1 Area 6, showing locations of quantitative WDS points 5 and 7 - 9.



**Point 10**

100 µm

Figure J-9. Backscattered electron image of K9-P1-D2 Area 1, showing location of quantitative WDS point 10.

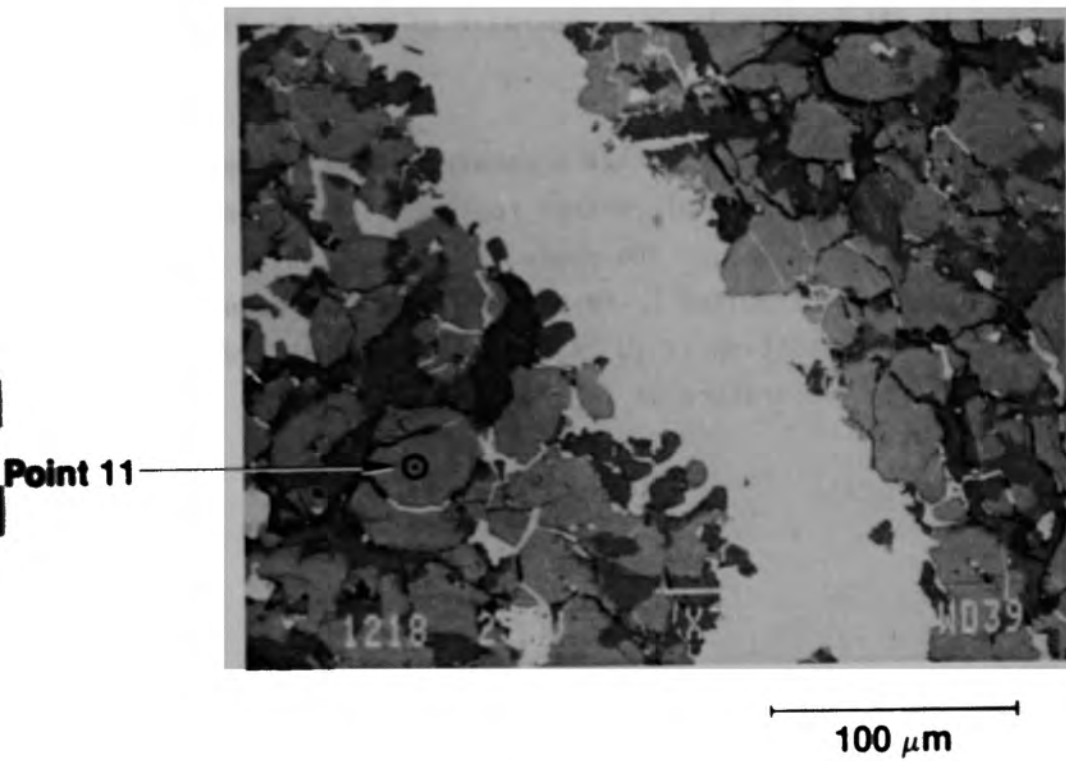


Figure J-10. Backscattered electron image of K9-P1-D2 Area 3, showing location of quantitative WDS point 11.

UO<sub>2</sub>; the analysis demonstrates the accuracy obtainable with the WDS system for a simple phase using good standards.

In sample K9-P1-D2 a point was selected on the periphery of a metallic Fe-Ni-Zr inclusion within a ZrO<sub>2</sub> matrix (point 10, Table J-8, Figure J-9). The periphery had been oxidized by contact with the ZrO<sub>2</sub>, and WDS analysis (point 10, Table J-8) revealed that the oxide was the same material as found in the pellet-pellet interface of K9-P1-D1, with the exception that it was lacking in Cr. The ratio of metal to oxygen was the same, slightly greater than one.

Point 11 was selected in a phase within a complex mixture of phases next to a fuel pellet, where a vein of control rod material had penetrated the matrix (Figure J-10, Table J-9). The phase of interest is an oxidized U-Zr oxide interspersed with oxidized Zr-Fe-Ni-Cr-Sn phases. Quantitative analysis shows that the composition is (U,Zr)O<sub>2</sub> with 8 molecular wt% UO<sub>2</sub>, indicating a melting temperature of 2825 K.

